I. R. IRAN

ISSN: 1728-144X
e-ISSN: 1735-9244

International Journal of Engineering

Journal Homepage: www.ije.ir

MERC

TRANSACTIONS B: APPLICATIONS

Volume 33, Number 07, August 2020

Materials and Energy Research Center

In the Name of God

INTERNATIONAL JOURNAL OF ENGINEERING
Transactions B: Applications

International **J**ournal of **E**ngineering *Transactions A: Basics* (ISSN 1728-1431) (EISSN 1735-9244)
International **J**ournal of **E**ngineering *Transactions B: Applications* (ISSN 1728-144X) (EISSN 1735-9244)
International **J**ournal of **E**ngineering *Transactions C: Aspects* (ISSN 2423-7167) (EISSN 1735-9244)
Web Sites: www.ije.ir & www.ijeir.info E-mails: ije.editor8@gmail.com, Tel: (+9821) 88771578, Fax: (+9821) 88773352
Materials and Energy Research Center (MERC)

ISSN: 1728-144X, e-ISSN: 1735-9244

International Journal of Engineering, Volume 33, Number 8, August 2020

CONTENTS:

ISSN: 1728-144X, e-ISSN: 1735-9244

International Journal of Engineering, Volume 33, Number 8, August 2020

ISSN: 1728-144X, e-ISSN: 1735-9244

International Journal of Engineering, Volume 33, Number 8, August 2020

IJE TRANSACTIONS B: Applications Vol. 33, No. 8, (August 2020) 1440-1449

International Journal of Engineering

Journal Homepage: www.ije.ir

Numerical Modeling of Non-equilibrium Plasma Discharge of Hydrogenated Silicon Nitride ($SiH_4/NH_3/H_2$)

M. Grari*, C. Zoheir

Mohamed first University, Department of Physics, LETSER Laboratory, Oujda, Morocco

P A P E R I N F O

Paper history:
Received 25 April 2020
Received in revised form 11 June 2020
Accepted 12 June 2020

Keywords:
Numerical Modeling
Non-equilibrium Electron Energy Distribution Function
Radio Frequency Plasma Discharge
Silicon Nitride
Capacitive Coupled Plasma Reactor

A B S T R A C T

In this work, we model a radiofrequency discharge of hydrogenated silicon nitride in a capacitive coupled plasma reactor using Maxwellian and non-Maxwellian electron energy distribution function. The purpose is to investigate whether there is a real advantage and a significant contribution using non-Maxwellian electron energy distribution function rather than Maxwellian one for determining the fundamental characteristics of a radiofrequency plasma discharge. The results show the evolution of the non-Maxwellian electron energy distribution function, the mobility and the diffusion coefficient required to determine the fundamental characteristics of the radiofrequency plasma discharge of a hydrogenated silicon nitride deposit at low pressure and low temperature, between the two electrodes of the capacitive coupled plasma reactor. By comparing these results using non-Maxwellian electron energy distribution function with those calculated using the Maxwellian one, we conclude that the use of non-Maxwellian electronic energy distribution function is more efficient for describing the evolution of a radiofrequency plasma discharge in a capacitive reactor, which will improve the quality of the deposition of thin films.

***doi**: 10.5829/ije.2020.33.08b.01*

NOMENCLATURE

B	Magnetic induction	m_e	Electron mass ($9.11\ 10^{-31}$ kg)
D_e	Electron diffusion coefficient	V_{rf}	Amplitude of the alternative voltages
D_ε	energy transport diffusion	x_k	Molar fraction
E	Electric field	z	Axial cylindrical coordinate
F	Lorentz force	**Greek Symbols**	
f	Equilibrium distribution function	$\mathcal{E}$	Energy
F_0	Non- Equilibrium electronic energy distribution function	ε_0	Vacuum permittivity
K	Number of collision	ϕ	Particle relaxation time
K_B	Boltzmann's constant ($1.381\ 10^{-23}$ J/K)	γ	Acceleration of a particle
K_r	Kinetic coefficient	γ_p	Secondary electron emission coefficient
M	Mass of the species.	λ	Renormalization factor
N	Gas density	μ_e	Electron mobility
N_n	Total density of neutral	μ_{eN}	Energy mobility
n_e	Electron density	π	3.1416
n_i	Ion density	σ_k	effective momentum-transfercross-cross
p	Pressure	σ_m	The total momentum-transfer cross-section
q	Electric charge	Γ	Particle flux

*Corresponding Author Email: *grarimery@gmail.com* (M. Grari)

Please cite this article as: M. Grari, C. Zoheir, Numerical Modeling of Non-equilibrium Plasma Discharge of Hydrogenated Silicon Nitride ($SiH_4/NH_3/H_2$), International Journal of Engineering (IJE), IJE TRANSACTIONS B: Applications Vol. 33, No. 8, (August 2020) 1440-1449

$\boldsymbol{r}$	Spatial vector	$\boldsymbol{\Gamma}_e$	Electron flux
S	Term source	$\boldsymbol{\Gamma}_i$	Ion flux
T	Particles temperature	$\boldsymbol{\Gamma}_\varepsilon$	Energy flux
u	Average velocity	v_{th}	Thermal velocity of electron
v	Velocity vector	$\Delta\varepsilon_k$	Energy loss

1. INTRODUCTION

Hydrogenated silicon nitride has attracted the interest of researchers over the last decades because of its wide application in thin films [1,2]. Hydrogenated amorphous silicon nitride films can be deposited in a capacitive coupled plasma (CCP) reactor because of high electron density and low electron temperature, leading to high-rate depositions of silicon films [3,4]. The plasma discharge in CCP reactor combines several phenomena during deposition: creation of electrical charges by radiofrequency (RF) excitation, fluid flow and chemical reactions on the surface.

The RF plasma discharge is a method that allows obtaining a plasma medium with specific parameters, both geometrically and in terms of the fluid itself. Moreover, it is a method well suited to the description of non-linear phenomena. RF discharges attracted the attention of physicists before their practical applications in the field of physics were known [5-8]. The capacitive RF discharge allows to define a frequency range between 1 and 100 MHz, gas pressure between 1 mTorr and few Torrs with a dimension of about a few cm and a power between 1 and 10 watts. Under these conditions, the RF discharge plasma is weakly ionized and out of thermodynamic equilibrium. The temperature value of the electrons depends in particular on the gas pressure and the discharge conditions.

In order to obtain a high quality of deposition, it is necessary to seek the better characteristics of the plasma discharge in CCP reactor. The fluid model can be used to determine the characteristics of the plasma discharge. The resolution of the fluid model equations is usually done by assuming a Maxwellian electron energy distribution function (EEDF). However, in the sheath regions of the fluid model of a RF discharge, the electron temperature is much higher than the temperature of heavy particles. That is why it is more likely that the real EEDF is non-Maxwellian because of its capability to describe an out-of-equilibrium system with high density and temperature gradients compared to the EEDF Maxwellian one.

Much attention is devoted to the non-equilibrium EEDF, because of their applications in many technological fields [1,9]. Godyac (1990,1995) has shown the existence of two electron groups, characterized by a weak inter-interaction, a significative different temperatures and their energy distribution can be a bi-Maxwellian EEDF [10,11]. Hageleer and Pitchford (2005) [12] developed a new resolution model of the Boltzmann equation (BE) to obtain transport coefficients and diffusion coefficients applicable for fluid models describing much more general conditions.

In this work, we are interested in studying the fundamental characteristics of the capacitive RF plasma discharge of silicon nitride using a non-Maxwellian EEDF which we calculated based on the Boltzmann model developed by Hageleer and Pitchford [12]. Thus, we intend to validate the choice of using the non-Maxwellian EEDF. Then, we focus on comparing the plasma discharge characteristics obtained using the non-Maxwellian EEDF with those calculated by a Maxwellian distribution function.

This article is organized as follows. In Section 2, we briefly describe the hypothesis and mathematical formulations used for determining non-equilibrium EEDF and transport coefficients. In Section 3, we describe hybrid physical model of plasma discharge using a non equilibrium EEDF. In Section 4, we present and compare the simulation results obtained by using a non-Maxwellian and Maxwellian EEDF. Finally, the conclusion is set out in Section 5.

2. CALCULATION OF EEDF, MOBILITY AND DIFFUSION COEFFICIENTS

2. 1. EEDF Calculation In general, the transport of charged species in the plasma can be described by the Boltzmann equation:

$$\frac{\partial f}{\partial t} + \mathbf{v}\nabla_r f + \frac{\mathbf{F}}{m_e}\nabla_v f = C[f] \quad (1)$$

which is a continuity equation in phase space (***r***, **v**). The right side of equation (1) is the collision operator, which describes the interaction between the particles in the system.

In our adopted model, we have three approximations:

- The initiating electric field and the probability of collision are uniform.
- The distribution of the electrons is then symmetrical around the direction of the electric field.
- In position, the electron distribution space can only change in the direction of the applied electric field.

Using the spherical coordinates in velocity space and choosing the direction *z* we obtain:

$$\frac{\partial f}{\partial t}+v\cos\theta\frac{\partial f}{\partial z}+\frac{e}{m_e}E\left(\cos\theta\frac{\partial f}{\partial v}+\frac{sin^2\theta}{v}\frac{\partial f}{\partial\cos\theta}\right)=C[f] \quad (2)$$

Such as $v=\left(v_x{}^2+v_y{}^2+v_z{}^2\right)^{1/2}$

The function f in Equation (2) depends on four variables: z, v, θ and t. Using the two-term approximation [12-14] we can simplify the dependence of the function f on θ to obtain Equation (3):

$$f(z,v,\theta,t)=f_0(z,v,t)+\cos\theta f_1(z,v,t) \quad (3)$$

The function f is the sum of a part isotrope f_0 and a small anisotropic perturbation f_1 [12,15].

According to the work [13,15] we can separate the energy dependence of f from its dependence on time and space by assuming that :

$$f(\varepsilon,z,t)=\frac{1}{2\pi\gamma^3}F_0(\varepsilon)n(z,t) \quad (4)$$

with F_0 is the energy distribution function which is constant in time and space, and $\gamma=\left(\frac{2e}{m_e}\right)^{1/2}$.

A further simplification on f in Equation (4) can be made with respect to time. Indeed, the electric field and the distribution of electrons can be considered to be stationary or oscillating at high frequency.

Based on the previous simplifications and the collision term calculation, Hageleer and Pitchford [12] have shown Equation (5).

The term to the left of Equation (5) represents a convection part with negative flow velocity $\tilde{W}$ and a diffusion part with coefficient $\tilde{D}$.

$$\frac{\partial}{\partial\varepsilon}\left(\tilde{W}F_0-\tilde{D}\frac{\partial F_0}{\partial\varepsilon}\right)=\tilde{S}$$

$$\tilde{W}=-\gamma\varepsilon^2\sigma_\varepsilon-3a\frac{n}{N}A_1$$

$$\tilde{D}=\frac{\gamma}{3}\left(\frac{E}{N}\right)^2\frac{\varepsilon}{\tilde{\sigma}_m}+\frac{\gamma k_BT}{e}\varepsilon^2\sigma_\varepsilon+2a\frac{n}{N}\left(A_2+\varepsilon^{3/2}A_3\right)$$

where:

$$a=\frac{q^2\gamma}{24\pi\varepsilon_0{}^2}ln\Lambda \quad ; \quad \Lambda=\frac{12\pi\left(\varepsilon_0k_BT_e\right)^{3/2}}{e^3n^{1/2}} \quad (5)$$

$$\sigma_m=\sum_{k=all}x_k\sigma_k \quad ;\sigma_\varepsilon=\sum_{k=elastic}2\left(\frac{m_e}{M}\right)x_k\sigma_k$$

$$\tilde{\sigma}_m=\sigma_m+\frac{\lambda}{\varepsilon^{1/2}} \quad ; \tilde{\sigma}_m=\sigma_m+\frac{\lambda}{\varepsilon^{1/2}};$$

$$A_1=\int_0^\varepsilon u^{\frac{1}{2}}f(u)du; \quad A_2=\int_0^\varepsilon u^{\frac{3}{2}}f(u)du$$

$$A_3=\int_0^\infty f(u)du$$

The source term $\tilde{S}$ represents the energy loss due to inelastic collisions. It can be broken down into three parts: attachment, excitation and ionization.

$$\tilde{S}=\sum_{k=inelastic}C_{0,k}+G$$

$$C_{0,k_{exitation}}=-\gamma x_k\left[\varepsilon\sigma_k(\varepsilon)f(\varepsilon)-(\varepsilon+\Delta\varepsilon_k)\sigma_k(\varepsilon+\Delta\varepsilon_k)f(\varepsilon+\Delta\varepsilon_k)\right]$$

$$C_{0,k_{attachment}}=-\gamma x_k\varepsilon\sigma_k(\varepsilon)f(\varepsilon) \quad (6)$$

$$C_{0,k_{ionization}}=-\gamma x_k\left[\varepsilon\sigma_k(\varepsilon)f(\varepsilon)-(\varepsilon+\Delta\varepsilon_k)\sigma_k(\varepsilon+\Delta\varepsilon_k)f(\varepsilon+\Delta\varepsilon_k)\right]+\delta\gamma x_k\varepsilon\sigma_k(\varepsilon)f(\varepsilon)$$

$$G=-\gamma\lambda f\varepsilon^{1/2}$$

The term λ is a scalar renormalization factor, which ensures that the EEDF has the following property:

$$\int_0^\infty f\varepsilon^{1/2}d\varepsilon=1$$

The left side of Equation (3) is discretized by the exponential scheme [15].

2. 2. Mobility and Electrons Diffusion The knowledge of the distribution function has allowed us to determine a number of important parameters, such as the ionization rate by collision of electrons, the mobility of electrons, the diffusion rate, the average energy of electrons, etc.

For the electrons transport, the mobility and diffusion of electrons are given by Equations (7) and (8):

$$\mu_e=-\frac{\gamma}{3}\int_0^\infty\frac{\varepsilon}{\hat{\sigma}}\frac{\partial F_0}{\partial\varepsilon}d\varepsilon \quad (7)$$

$$D_e=\frac{\gamma}{3}\int_0^\infty\frac{\varepsilon}{\hat{\sigma}}F_0d\varepsilon \quad (8)$$

For the energy transport, the mobility and diffusion of electrons are given by Equations (9) and (10):

$$\mu_\varepsilon=-\frac{\gamma}{3\bar{\varepsilon}}\int_0^\infty\frac{\varepsilon^2}{\hat{\sigma}}\frac{\partial F_0}{\partial\varepsilon}d\varepsilon \quad (9)$$

$$D_\varepsilon=\frac{\gamma}{3}\int_0^\infty\frac{\varepsilon^2}{\hat{\sigma}}F_0d\varepsilon \quad (10)$$

3. Hybrid Physical Model Like other reactors used in industry [16-21], the CCP reactor involves a set of fairly complex physico-chemical processes. The physical model must describe the dynamics of the plasma medium. In addition, it must take into account chemical reactions that best describe the source terms. We used a macroscopic-microscopic hybrid model where the fluid equations describe the kinetics of the system and the source terms are computed from the non-equilibrium EEDF.

The plasma dynamics is described by taking into account excitation phenomena, radical, ion dissociation, and their collisions with electrons. Efficient cross-sections were considered over a wide range of energy. This allows us to better describe the chemical reactions in volume of the species generated by the dissociation and recombination of neutral and radical particles, as well as the surface reactions on the substrate. The fluid flow rate describes the transfer of heat and mass into the reactor. All these phenomena are modeled by a system of equations, non-linear and dispersive, described in the following sections. The differential equations are solved using the finite element method.

To summerize the research methodology adapted in this article, we present this flowchart in Figure 1.

3. 1. CCP Reactor Figure 2 shows a synoptic scheme of a symmetrical CCP reactor which is composed of two parallel conductive electrodes, a gas pump and a substrate. The working gases are introduced at the inlet, and then brought into the reaction chamber,

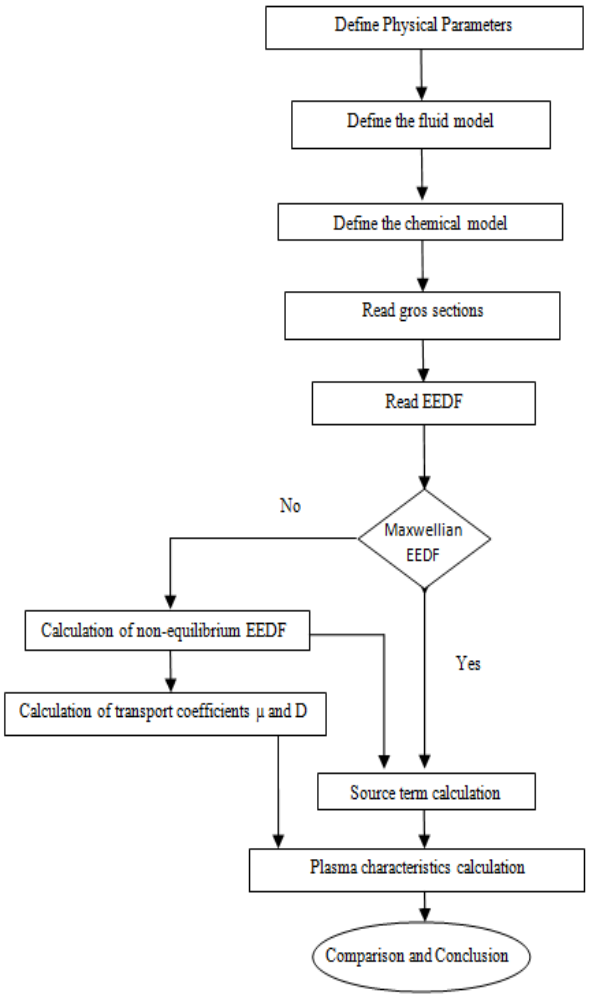

Figure 1. Flowchart of the proposed research methodology

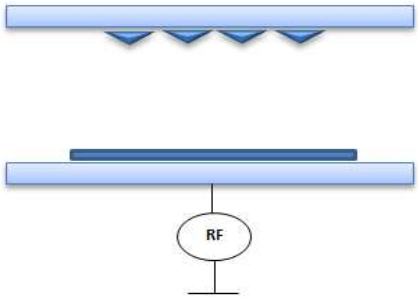

Figure 2. Synoptic scheme of CCP reactor used for plasma deposition of thin films

where a series of volume and surface reactions take place resulting in a deposition of thin films on the substrate.

The plasma in the CCP reactor are at low pressure, low electronic temperature and low ionization rate. In a mixture of ammonia and hydrogen silicon, the gas pressure between 0.2 and 0.5 Torr, the frequency is about 13.56 MHz, the voltage is 130 V, and the space between electrodes varies between 2.7 and 6 cm.

3. 2. Equations The general equations for a plasma discharge [15, 22] are calculated taking into account the following hypotheses:

-The gas is weakly ionized.
-The pressure is low.
-No magnetic field is applied.
-The electrons are supposed to have a non-Maxwellian energy distribution function.
-The mobility and the diffusion coefficients are calculated by the non-Maxwellian EEDF.

In our model we solve the system of equations (11)-(16) corresponding to a set of low temperature plasma evolution equations related to the self-coherent field $\boldsymbol{E}$ by Poisson's equation (17).

-Electron and ion transport

$$\frac{\partial n_e}{\partial t} + \nabla \boldsymbol{\Gamma}_e = S_e \tag{11}$$

$$\frac{\partial n_i}{\partial t} + \nabla \boldsymbol{\Gamma}_i = S_i \tag{12}$$

-Electron and ion flux

$$\boldsymbol{\Gamma}_e = -n_e \mu_e \boldsymbol{E} - \nabla(n_e D_e) \tag{13}$$

$$\boldsymbol{\Gamma}_i = -n_i \mu_i \boldsymbol{E} - \nabla(n_i D_i) \tag{14}$$

-Electron energy

$$\frac{\partial n_\varepsilon}{\partial t} + \nabla \boldsymbol{\Gamma}_\varepsilon + \boldsymbol{E}\boldsymbol{\Gamma}_e = S_\varepsilon \tag{15}$$

-Energy flux

$$\Gamma_\varepsilon = -n_\varepsilon \mu_\varepsilon E - \nabla(n_\varepsilon D_\varepsilon) \quad (16)$$

-Electric field

$$\varepsilon_0 \nabla E = e(n_e - n_i) \quad (17)$$

-Source terms

$$S_e = \sum x_r k_r N_n n_e \quad (18)$$

$$S_i = \sum x_r k_r N_n n_i \quad (19)$$

$$S_\varepsilon = \sum x_r k_r N_n n_e \varepsilon_r \quad (20)$$

$$k_r = \sqrt{2e/m_e} \int \varepsilon \sigma_r(v) F_0(\varepsilon) d\varepsilon \quad (21)$$

F_0 is the non-Maxwellian EEDF.

3. 3. Chemical Reactions The calculation of the source term equations (18)-(21), in the fluid model is based on the distribution function calculated by the model of Boltzmann F0 plus gross sections $\sigma_r(v)$ which takes into account the most reactive elastic and inelastic excitation and ionization collisions, presented in Table 1.

The cross sections data used in simulation, SiH_4 and NH_3 collisions are given by Hayashi [23].

The chemical species considered in this work are presented in Table 2. These species are very important for plasma chemistry and have an influence on the deposition process.

3. 4. Boundary Conditions The boundary conditions used in this section are similar to those presented by Bavafa et al. [2] and Xia et al. [24].

-The boundary condition for Poisson's equation is the potential value on the electrodes:

$V = 0$ electrical potential at the cathode.

TABLE 1. Energy of reactions NH3 SiH4

Reactions	Energy (eV)
1 : e+NH_3 => e+NH_3^*	0.202
2 : e+NH_3 => e+NH_3^*	0.42
3 : e+NH_3 => e+NH_3^*	5.72
4 : e+NH_3 => e+NH_3^*	8.65
5 : e+NH_3 => 2e+NH_3^+	10.2
6 : e+SiH_4 => e+SiH_4^*	0.115
7 : e+SiH_4 => e+SiH_4^*	0.27
8 : e+SiH_4 => e+SiH_4^*	8.01
9 : e+SiH_4 => e+SiH_4^*	8.92
10 : e+SiH_4 => 2e+SiH_4^+	12.9

TABLE 2. Kinetic coefficient of reactions NH_3 SiH_4

Reactions	Kinetic Coefficient $m^3/(s.mol)$
7 : SiH_4 + SiH_2 => Si_2H_6	2.8 10^7
8 : SiH_4 + H => SiH_3 + H_2	1.9 10^6
9 : SiH_4 + NH => $HSiNH_2$ + H_2	3.6 10^6
10 : SiH_4 + NH_2 => SiH_3 + NH_3	2.4 10^6
11 : SiH_4 + NH => SiH_3 + NH_2	2.4 10^7

$V_{rf} = V_0 \sin(\omega t)$ electrical potential at the anode.

- The boundary condition for electrons has a flow proportional to their thermal velocity, while for ions it has a zero gradient near the walls:

$$\Gamma_e = 5\frac{v_{th} n_e}{4} - \gamma \Gamma_i$$

$$\Gamma_i = -\mu_i n_i \nabla V$$

-Quantities v_{th} and q_e are calculated by:

$$q_e = \frac{v_{th} k_B}{4} \qquad v_{th} = \sqrt{\frac{8 k_B T_e}{\pi m_e}}$$

4. RESULTS AND DISCUSSION

To investigate the plasma discharge characteristics in the CCP reactor, the fluid approach are considered. Using the Boltzmann equation [12] we calculate the non-Maxwellian EEDF, the mobility and diffusion coefficients. Based on these factors we proceed to the resolution of the fluid model equations. Thus, we obtain the plasma discharge characteristics that will be used in the start to validate the choice of the non-Maxwellian EEDF, then to compare them with the plasma discharge characteristics obtained using Maxwellian EEDF.

In our simulations, the CCP reactor is driven by a sinusoidal voltage with a frequency of 13.56 MHz at a temperature of 573 K. Silicon diluted with hydrogen and ammoniac mixture is used as a deposition precursor gas. The RF voltage taken has an amplitude of 130 V, applied to the anode for an inter-electrode distance d and a variable pressure p. The results are presented at a final relaxation calculation time of around 7.37 μs.

Figure 3 shows the evolution of non-Maxwellian EEDF for $SiH_4/NH_3/H_2$ gases in energy range between 3 and 10 eV. The non-Maxwellian EEDF is calculated from the reactions presented in Table 1, the initial energy is $\varepsilon = 3\text{eV}$. This non-Maxwellian EEDF will be used in the source terms of the fluid model to calculate the density and the energy electrons.

The mobilities equations (7) and (9) and diffusion coefficients equations (8) and (10), calculated by the non-Maxwellian EEDF, are shown in Figure 4. They

will be used to calculate electron ion and energy flux in Equations (13), (14) and (16).

For the validation of the non-Maxwellian EEDF, we will discuss Figures 4-9. Therefore, Figures 5-7 show the variation of electron density, temperature and electric field as a function of pressure, taking a pressure margin between 0.2 and 0.5 Torr for an inter-electrode distance of 2.7 cm. Keeping the pressure at 0.3 Torr and varying the distance between 3 and 6 cm, Figures 8-10 show respectively the variation of the electron density, the temperature and the electric field as a function of the distance. Finally, Figures 11-13 show the comparison of density, temperature and electric field calculated by a Maxwellian and non-Maxwellian EEDF.

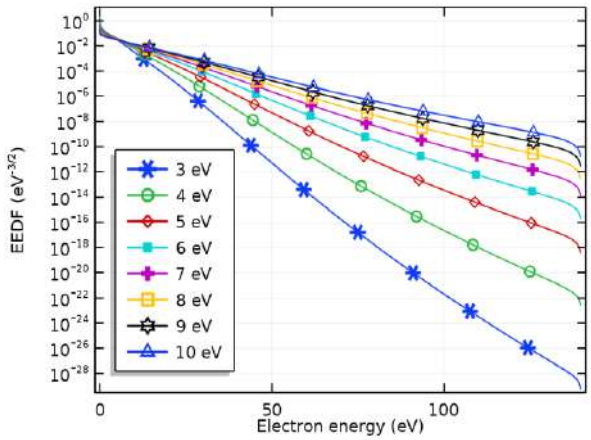

Figure 3. The evolution of Boltzmann's EEDF of SiH_4 NH_3 plasma in an energy range between 3 and 10 eV

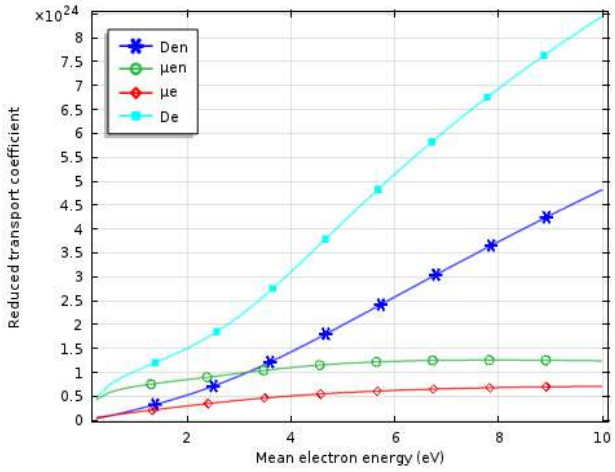

Figure 4. Reduced transport coefficients calculated by the non-Maxwellian EEDF

where, De: Reduced electron energy diffusivity (1/(m*s)), Den: Reduced electron diffusivity (1/(m*s)), μen: Reduced electron energy mobility (s^2 *A/(m^3*kg)), μe: Reduced electron mobility (s^2 *A/(m^3*kg))

By increasing the pressure in the deposition system, the density of radicals grows as the density of precursors increases (Figure 5). Another effect of the increase in the pressure of the deposition chamber is the fact that it leads to the accumulation of radicals in the area between ducts, which reduces the temperature in this area (Figure 6).

An electric field is introduced and added to the field created by the charges in the plasma. Figure 7 shows that it becomes important when the pressure increases, causing a significant displacement of electrons and ions. The field perceived by the electrons is very strong and allows the electrons to accelerate towards the anode. The migration of electrons from the cathode to the anode produces a higher temperature at the anode and therefore the temperature attenuation at the cathode, which is verified in Figure 6. These results are consistent with Daoxin et al. [25].

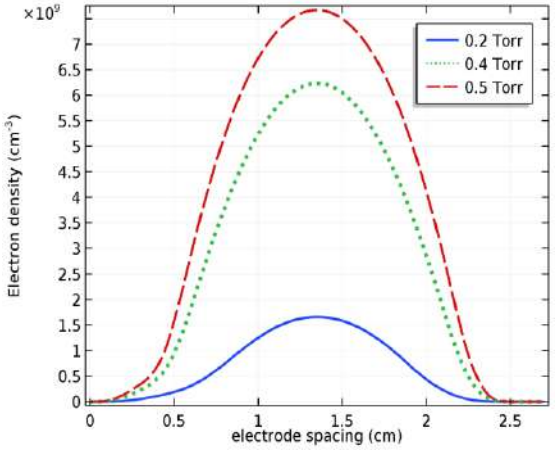

Figure 5. Variation of the electronic density as a function of pressure using non-Maxwellian EEDF

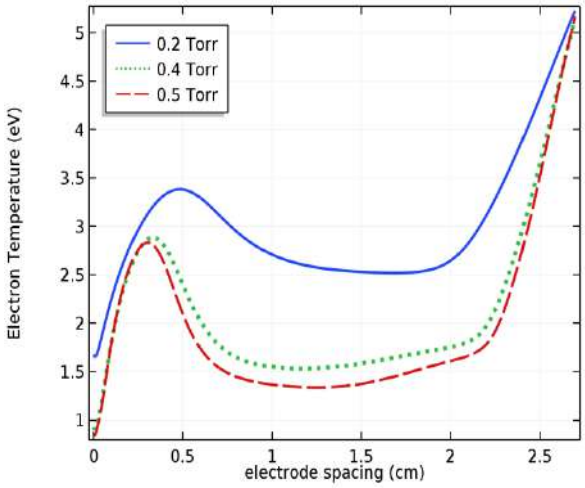

Figure 6. Variation of the electronic temperature as a function of pressure using non-Maxwellian EEDF

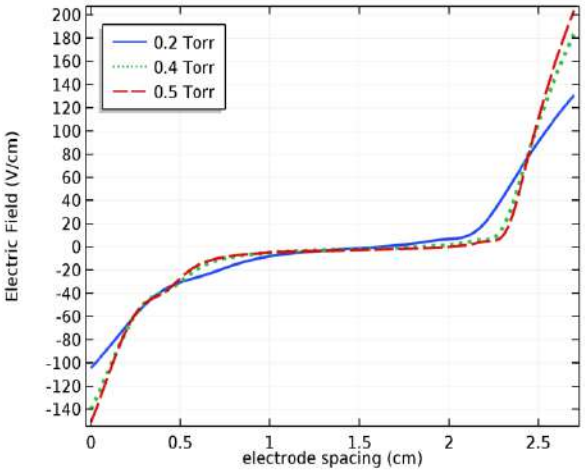

Figure 7. Variation of the electric field as a function of pressure using non-Maxwellian EEDF

The influence of the inter-electrode distance on the discharge is shown in Figures 8-10. When the distance becomes larger, collisions between electrons decrease and therefore the creation of secondary electrons will be low. In addition, as the distance increases, there is an expansion of the density towards the electrodes. These results are the same to that of Bavefa et al. [2] and Samir et al. [26] with respect to electron density, electron temperature and electric field distributions.

Summing up, according to these results and based on the comparison with theoretical [15, 22] and practical literature works [2, 9, 27-29], we validate the choice of the non-Maxwellian distribution function. Indeed, the plasma caracteristics resulting from the use of the non-Maxwellian EEDF satisfy the normal evolution of RF plasma discharge.

For an inter-electrode distance of 5 cm, and a pressure of 0.3 Torr, Figures 11-13 show respectively the variation in electron density, temperature and electric field, determined using the Maxwellian and non-Maxwellian EEDF.

Figure 11 shows that the density calculated based on a non-Maxwellian EEDF is much higher than that calculated using a Maxwellian EEDF. Indeed, the non-Maxwellian EEDF provides an electron density of about 3.9 $x10^9$ cm^{-3} while the Maxwellian EEDF barley reaches 2.5 $x10^9$ cm^{-3}. This significant difference in electron density means that there is another type of faster electrons added which couldn't be shown by using Maxwellian EEDF, while the use of the non-Maxwellian EEDF has succeed to reveal it. Figure 12 shows that the electron temperature calculated using a non-Maxwellian EEDF (about 13 eV) is higher than the calculated one using a Maxwellian EEDF (about 9 eV). This result is due to the high speed of electrons (about 3.4 $x10^8$cm/s) obtained using non-Maxwellian EEDF compared to that using Maxwellian EEDF (about 2.5x 10^8 cm/s) shown in Figure 13. These electrons have a self-coherent field source, hence the increase in the amplitude of the electric field at the cathode (Figure 14).

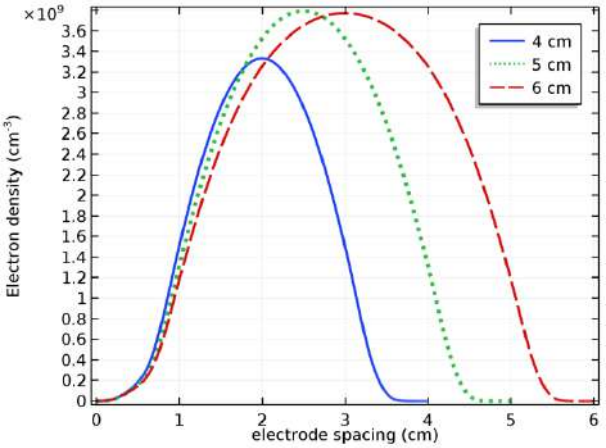

Figure 8. Variation of the electronic density as a function of distance using non-Maxwellian EEDF

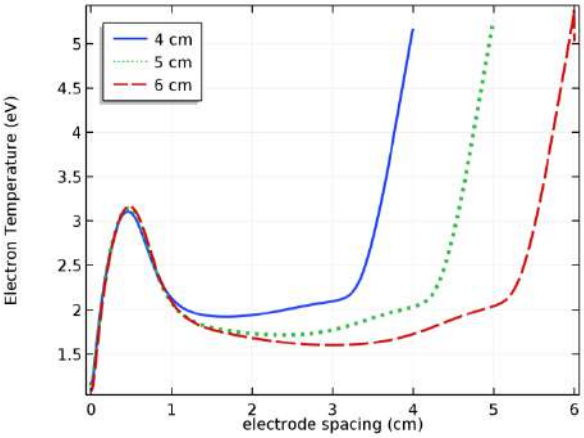

Figure 9. Variation of the electronic temperature as a function of distance using non-Maxwellian EEDF

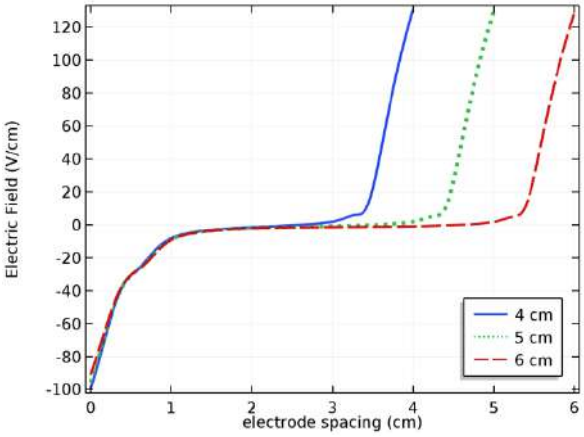

Figure 10. variation of the electric field as a function of distance using non-Maxwellian EEDF

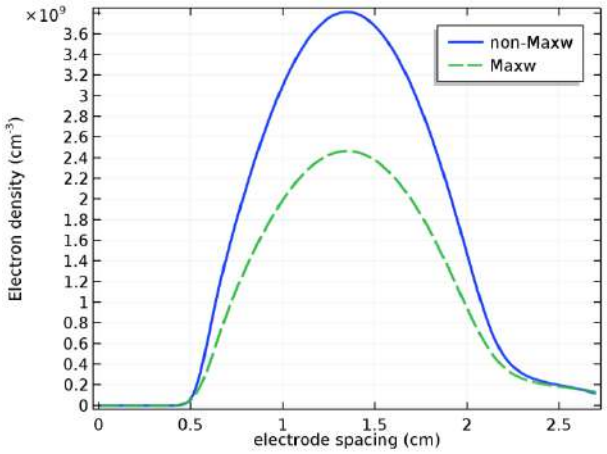

Figure 11. Electron density comparison using Maxwellian and non-Maxwellian EEDF

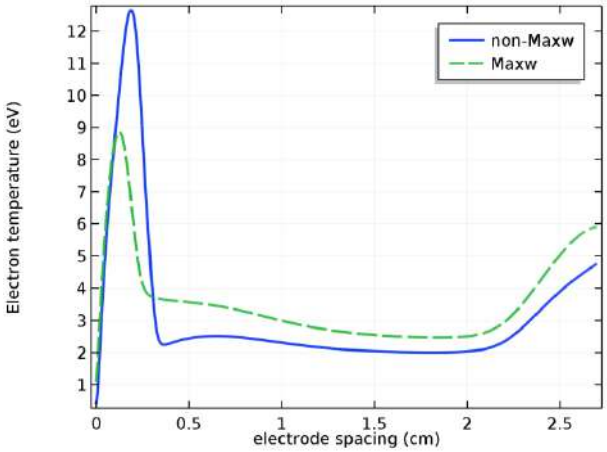

Figure 12. Electron temperature comparison using Maxwellian and non-Maxwellian EEDF

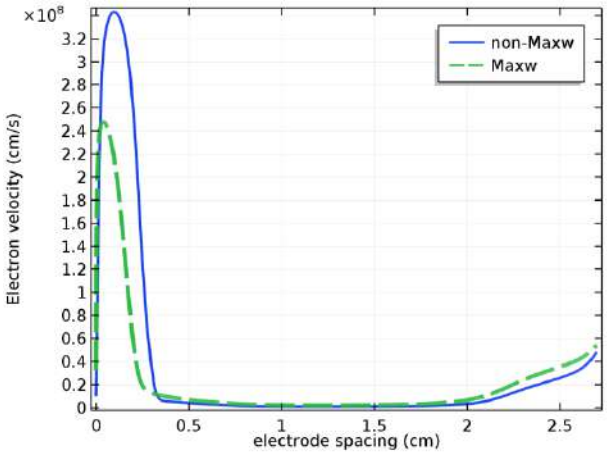

Figure 13. Electron velocity comparison using Maxwellian and non-Maxwellian EEDF

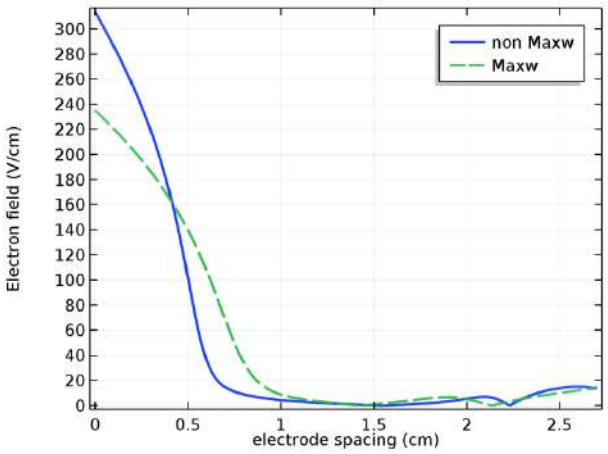

Figure 14. Electric field comparison using Maxwellian and non-Maxwellian EEDF

The field allows electrons to accelerate towards the anode. This migration produces a higher temperature at the anode, and hence temperature attenuation at the cathode (Figure 12).

5. CONCLUSION

In this work, we used a one-dimensional fluid model based on a non-Maxwellian electron energy distribution function to describe the characteristics of capacitive coupled plasma excited by an RF source using silane diluted with ammoniac and hydrogen ($SiH_4/NH_3/H_2$). The discharge operates at 13.56 MHz with RF voltage amplitude of 130 V and simulated at variable pressures and inter-electrode distances. The aim was to validate the choice of the non-Maxwellian EEDF and to compare the evolution of the plasma discharge characteristics obtained using the non-Maxwellian EEDF with those calculated by using a Maxwellian one.

By varying the pressure and distance between electrodes, we validated the choice of the non-Maxwellian EEDF and the type of the used gas. Indeed, the results show a significant increase in density when the gas pressure grows in the range of 0.2 to 0.5 Torr, similarly, when the inter-electrode distance increases in the range of 4 to 6 cm.

The use of a non-Maxwellian EEDF allowed us to reveal the existence of another faster type of electrons, which was not detected when a Maxwellian EEDF was used. Indeed, in the non-Maxwellian case an average electron velocity of about 3.4 $x10^8$ cm/s and an electron temperature of 13 eV were obtained at the cathode, whereas in the Maxwellian case an average electron velocity of about 2.4 $x10^8$ cm/s and an electron temperature of 9 eV were barely reached at the cathode. In addition, compared with the Maxwellian EEDF the

plasma discharge obtained using the non-Maxwellian EEDF has a higher electron density of about 3.8 $x10^9cm^{-3}$ which increases the deposition rate, and a reduced temperature at the anode of about 4.8 eV which results in a better distribution of species at the surface.

We deduce that the non-Maxwellian approximation of the electron energy distribution function is more effective to describe the evolution of an RF plasma discharge in a capacitive reactor than the Maxwellian one. Thus, in order to ensure better deposition of thin films, it is recommended to define the electron transport properties by an electron energy distribution function using a non-Maxwillian EEDF, which is a closer assumption to the real conditions of the physical model. Consequently, the application of this function in our fluid model for the discussion of gas type selection, pressure and inter-electrode distance, will provide better characteristics to enhance the quality of CCP reactor.

Finally, it will be interesting in a future work to seek optimal deposition of thin films by studying a two-dimensional simulation using a non-Maxwellian EEDF.

6. REFERENCES

1. Su, L. W., Chen, W., Uchino, K., and Kawai, Y., "Two-dimensional simulations of multi-hollow VHF SiH4/H2 plasma", ***AIP Advances***, Vol. 8, No. 2, (2018), 025316. DOI: 10.1063/1.5003911.
2. Bavafa, M., Ilati, H., Rashidian, B., "Comprehensive simulation of the effects of process conditions on plasma enhanced chemical vapor deposition of silicon nitride", ***Semiconductor Science and Technology***, Vol. 23, No. 9, (2008), 095023. DOI: 10.1088/0268-1242/23/9/095023.
3. Kim, H. J., Wonkyun Y., and Junghoon J., "Effect of electrode spacing on the density distributions of electrons, ions, and metastable and radical molecules in SiH4/NH3/N2/He capacitively coupled plasmas", ***Journal of Applied Physics***, Vol. 118, No. 4, (2015), 043304. DOI: 10.1063/1.4927531.
4. Kim, H. J., and Hae June L., "2D fluid model analysis for the effect of 3D gas flow on a capacitively coupled plasma deposition reactor", ***Plasma Sources Science and Technology***, Vol. 25, No. 3, (2016), 035006. DOI: 10.1088/0963-0252/25/3/035006
5. Graves, D. B., and Jensen, K. F, "A continuum model of DC and RF discharges", ***IEEE Transactions on Plasma Science***, Vol. 14, No. 2, (1986), 78-91. DOI: 10.1109/TPS.1986.4316510.
6. Passchier, J. D. P., and Goedheer, W. J., "A twodimensional fluid model for an argon rf discharge", ***Journal of Applied Physics***, Vol. 74, No. 6, (1993), 3744-3751. DOI: 10.1063/1.354487.
7. Li, X. S., Bi, Z. H., Chang, D. L., Li, Z. Wang,C., S., Xu, X., Xu, Y., Lu, W. Q., Zhu, A. M., and Wang, Y. N., "Modulating effects of the low-frequency source on ion energy distributions in a dual frequency capacitively coupled plasma", ***Applied Physics Letters***, Vol. 93, (2008), No. 3, 031504. DOI: 10.1063/1.2945890.
8. Grari, M., and Zoheir, C., "Numerical Modeling of Plasma Silicon Discharge for Photovoltaic Application", ***Materials Today: Proceedings***, Vol. 13, (2019), 882-888. DOI: 10.1016/j.matpr.2019.04.052.
9. Wang, X. F., Jia, W. Z., Song, Y. H., Zhang, Y. Y., Dai, Z. L., and Wang, Y. N., "Hybrid simulation of electron energy distributions and plasma characteristics in pulsed RF CCP sustained in Ar and SiH4/Ardischarges", ***Physics of Plasmas***, Vol. 24, No. 11, (2017), 113503. DOI: 10.1063/1.5009416.
10. Godyak, V. A., and Piejak, R. B., "Abnormally low electron energy and heating-mode transition in a low-pressure argon rf discharge at 13.56 MHz", ***Physical Review Letters***, Vol. 65, No. 8, (1990), 996. DOI: 10.1063/1.5009416.
11. Godyak, V. A., Meytlis, V. P., and Strauss, H. R., "Tonks-Langmuir problem for a bi-Maxwellian plasma", ***IEEE Transactions on Plasma Science***, Vol. 23, No. 4, (1995), 728-734. DOI: 10.1109/27.467995.
12. Hagelaar,G. J. M., and Pitchford, L. C., "Solving the Boltzmann equation to obtain electron transport coefficients and rate coefficients for fluid models", ***Plasma Sources Science and Technology***, Vol. 14, No. 4, (2005), 722. DOI: 10.1088/0963-0252/14/4/011.
13. Pitchford, L. C., and Phelps, A. V., "Comparative calculations of electron-swarm properties in N2 at moderate E/N values", ***Physical Review A***, Vol. 25, No. 1, (1982), 540. DOI: 10.1103/PhysRevA.25.540.
14. Godyak, V. A., "Nonequilibrium EEDF in gas discharge plasmas", ***IEEE Transactions on Plasma Science***, Vol. 34, No. 3, (2006), 755–766. DOI: 10.1109/TPS.2006.875847.
15. Lieberman, M. A., and Lichtenberg, A. J., "Principles of plasma discharges and materials processing", John Wiley & Sons, 2005.
16. Abdelaal, A. M., Attalla, E. M., and Elshemey, W. M., "Estimation of Out-of-Field Dose Variation using Markus Ionization Chamber Detector", ***SciMedicine Journal***, Vol. 2, No. 1, (2020), 8-15. DOI: 10.28991/SciMedJ-2020-0201-2
17. Sanito, R. C., You, S. J., Chang, G. M., and Wang, Y. F., "Effect of shell powder on removal of metals and volatile organic compounds (VOCs) from resin in an atmospheric-pressure microwave plasma reactor", ***Journal of Hazardous Materials***, (2020), 122558. DOI: 10.1016/j.jhazmat.2020.122558.
18. Ali, A., Ejaz, N., Nasreen, S., Nasir, A., Qureshi, L. A., and Al-Sakkaf, B. M. "Enhanced Degradation of Dyes present in Textile Effluent by Ultrasound Assisted Electrochemical Reactor", ***Civil Engineering Journal***, Vol. 5, No. 10, (2019), 2131-2142. DOI: 10.28991/cej-2019-03091399.
19. Shoukat, R., and Khan, M. I., "Synthesis of nanostructured based carbon nanowalls at low temperature using inductively coupled plasma chemical vapor deposition (ICP-CVD)". ***Microsystem Technologies***, Vol. 25, No. 12, (2019), 4439-4444. DOI: 10.1007/s00542-019-04463-7.
20. Archin, S., "Optimization of Process Parameters by Response Surface Methodology for Methylene Blue Removal Using Cellulose Dusts", ***Civil Engineering Journal***, Vol. 4, No. 3, (2018). DOI: 10.22090/JWENT.2018.02.007.
21. Ghorbani, H., Poladi, A., and Hajian, M., "Pulsed DC-Plasma Assisted Chemical Vapor Deposition of α-rich Nanostructured Tantalum Film: Synthesis and Characterization", ***International Journal of Engineering***, ***Transactions A: Basics,*** Vol. 30, No. 4 , (2017), 551-557. DOI: 10.5829/idosi.ije.2017.30.04a.13.
22. Capitelli, M. R., Celiberto, Colonna, G., Esposito, F., Gorse, C., Hassouni, K., Laricchiuta, A., and Longo, S., "Fundamental aspects of plasma chemical physics: kinetics", Springer Science and Business Media, 2015.
23. Hayashi database, www.lxcat.net, retrieved on October 27, 2016.
24. Xia, H., Xiang, D., Yang, W., Mou, P., "Multi-model simulation of 300mm silicon-nitride thin-film deposition by PECVD and experimental verification", ***Surface and Coatings Technology***, Vol. 297, (2016), 1-10. DOI: 10.1016/j.surfcoat.2016.04.034.

25. Daoxin, H., Jia, C., Linhong, J. and Yuchun, S., "Simulation of cold plasma in a chamber under high-and low-frequency voltage conditions for a capacitively coupled plasma", ***Journal of Semiconductors***, Vol. 33, No. 10, (2012), 104004. DOI: 10.1088/1674-4926/33/10/104004.

26. Samir, T., Liu, Y., Zhao, L.L. and Zhou, Y.W., "Effect of driving frequency on electron heating in capacitively coupled RF argon glow discharges at low pressure", ***Chinese Physics B***, Vol. 26, No. 11, (2017), 115201. DOI: 10.1088/1674-1056/26/11/115201.

27. Ghorbani, H., and Poladi, A., "MD-Simulation of Duty Cycle and TaN Interlayer Effects on the Surface Properties of Ta Coatings Deposited by Pulsed-DC Plasma Assisted Chemical Vapor Deposition", ***International Journal of Engineering, Transactions B: Applications*** Vol. 33, No. 5, (2020), 861-869. DOI: 10.5829/ije.2020.33.05b.18.

28. Kim, H. J., and Lee, H. J. "Analysis of intermediate pressure SiH4/He capacitively coupled plasma for deposition of an amorphous hydrogenated silicon film in consideration of thermal diffusion effects", ***Plasma Sources Science and Technology***, Vol. 26, No. 8, (2017), 085003. DOI: 10.1088/1361-6595/aa78b4.

29. Rastani, S., "Process Optimization of Deposition Conditions for Low Temperature Thin Film Insulators used in Thin Film Transistors Displays", ***International Journal of Engineering, Transactions B: Applications,*** Vol. 31, No. 5, (2018), 712-718. DOI: 10.5829/ije.2018.31.05b.05.

Persian Abstract

چکیده

در این پژوهش، یک تخلیه‌ی بسامد رادیویی از نیترید سیلیکون هیدروژنه در یک راکتور پلاسمای خازنی با استفاده از توابع توزیع انرژی الکترونی ماکسولی و غیرماکسولی مدل‌سازی شده است. هدف بررسی این مطلب است که آیا با استفاده از عملکرد توزیع انرژی غیرماکسولی به جای ماکسولی برای تعیین خصوصیات اساسی تخلیه پلاسمای بسامد رادیویی یک مزیت واقعی و کمک چشم‌گیری حاصل می‌شود یا نه. نتایج تکامل تابع توزیع انرژی الکترونیکی غیرماکسولی تحرک و ضریب انتشار مورد نیاز برای تعیین ویژگی‌های اساسی تخلیه پلاسمای بسامد رادیویی یک رسوب نیترید سیلیکونی هیدروژنه در فشار کم و دمای پایین بین دو الکترود راکتور پلاسمای خازنی را نشان می‌دهد. از مقایسه نتایج به دست آمده با استفاده از تابع توزیع انرژی الکترونیکی غیرماکسولی با نتایج محاسبه شده از طریق ماکسولی نتیجه می‌گیریم که استفاده از عملکرد توزیع انرژی الکترونیکی غیرماکسولی برای توصیف تکامل تخلیه پلاسمای بسامد رادیویی در یک راکتور خازنی کارآمدتر است، که باعث افزایش کیفیت رسوب فیلم های نازک می‌شود.

International Journal of Engineering

Journal Homepage: www.ije.ir

Early Age Shrinkage Behavior of Triple Blend Concrete

V. N. Kanthe*, S. V. Deo, M. Murmu

Department of Civil Engineering, National Institute of Technology Raipur, Chhattisgarh, India

P A P E R I N F O

Paper history:
Received 27 April 2020
Received in revised form 28 May 2020
Accepted 12 June 2020

Keywords:
Rice Husk Ash
Fly Ash
Concrete
Early Age Shrinkage

A B S T R A C T

The early age shrinkage is responsible for the early age cracking of concrete. It is very critical for durability of concrete. The change in volume of concrete due to evaporation of water or dehydration process is known as shrinkage. To reduce the early age shrinkage utilized the supplementary cementitious material (SCM) in concrete. In present research industrial and agricultural waste byproduct like fly ash (FA) and rice husk ash (RHA) along with cement were used as SCM. The triple blend concrete was prepared by the combination of 20%, 30% and 40% partial cement replacement with FA and RHA for 0.30, 0.35 and 0.40 water-cement ratio. The concrete samples were tested by advanced instrument as shrinkage cone meter were used for measure the shrinkage. The result shows that the early age shrinkage reduced with increasing the SCM content. The microstructure characteristics enhanced with raising the content of FA and RHA up to 30% replacement; that was due to the dense particle packing.

***doi**: 10.5829/ije.2020.33.08b.03*

1. INTRODUCTION

Shrinkage in concrete is a change in the volume of concrete with respect to time. Shrinkage occurs due to movement of water within concrete due to segregation, bleeding, chemical reaction, during hydration process and evaporation. The volume of product generated by the chemical reaction is less than the initial volume of ingredients. Hence a tensile stress develops and pulls the cement paste closer [1]. The shrinkage can be split in two phase. The early age shrinkage occurred in first five hours and other is long-term shrinkage which happened after 5 hours. The early age shrinkage mainly occurs due to evaporation of water, whereas long-term shrinkage occurs due to hydration of cement paste [2]. For low water-cement ratios, the early age shrinkage plays an important role. In this case, the early age strain occurs at a time when concrete is developing stiffness at a faster rate than its strength. Hence shrinkage cracks develop at a faster rate in lower water-cement ratios [3]. Due to the hydrostatic tension absorbed water held by small capillaries was reduced in drying process of concrete. The reduction in free moisture trying to developed tensile forces and due to this concrete shrink resulting development of cracks in concrete. This will affect the strength and durability of concrete. In respect to durability of structure understanding the shrinkage of concrete is important. Large shrinkage could be produced initial cracking of concrete [4]. These cracks will responsible to increased rate of corrosion for reinforcement in concrete structure, reduced structural strength and finally causes the early structural failure. The plastic shrinkage occurs while concrete is placed in form in fresh state. Generally drying shrinkage will continue throw out the life of the concrete. Hence early age shrinkage study is an important specially for such type of triple blend concrete made by industrial and agricultural byproducts. The concrete made with fly ash and pond ash with glass fiber can be reduce early age shrinkage as reported by several researchers [5, 6]. The durability test (shrinkage) of concrete is most vital aspect for checking the long term life of concrete. The durable concrete required durable material and no maintenance. Most of researchers have reported shrinkage can be reduced by using various type of admixtures such as fly as and slag ternary blend concrete [8]. The shrinkage can be reduce using activators by heating at 60^0 temperature [9, 10]. From the literature it shows that very less data

*Corresponding Author Email: *kanthevn@gmail.com* (V.N. Kanthe)

Please cite this article as: V. N. Kanthe, S. V. Deo, M. Murmu, Early Age Shrinkage Behavior of Triple Blend Concrete, International Journal of Engineering (IJE), IJE TRANSACTIONS B: Applications Vol. 33, No. 8, (August 2020) 1459-1464

available on early age shrinkage of triple blend concrete. The marginal materials are the byproduct of industrial and agricultural such as FA and rice husk ash [11]. FA is a generated from the combustion of coal mostly in thermal power plant. The huge quantity of FA available in India and disposal of such waste is an important issue; otherwise it polute the land, water and air. The utilization of such byproduct in concrete is one of the alternatives to address the issue of disposal waste. The FA is in pozzolanic in nature with smooth and spherical in shape. In the studied on early age shrinkage behavior of cement paste by replacing cement with FA and pond ash individually and in combined up to 80% by volume resulted in reduction of the shrinkage strain [5]. RHA is a byproduct of agriculture. RHA generated by combustion of rice husk at control temperature and grinding in fine powder form. Generally RHA have more than 90% silica content. The utilization of RHA in concrete as partial cement replacement is improved the strength and durability of concrete [12]. The use of RHA in concrete reduced the bleeding due to its rough surface texture. The shrinkage occurred in concrete at higher replacement of RHA [13]. To study the effect of FA and RHA along with ordinary Portland cement (OPC) on early age shrinkage of triple blend concrete using cementetious material particle packing approach is an interest in this research work. The ternary blend concrete was preferred for making sustainable high strength concrete and durable concrete using cementitious material [11,14]. Many of the waste byproduct producec from industries such as GGBS, slag, slurry, fly ash etc.[15,16,17,18]. And some of admixture are affect the properties of concrete such as antifreeze admixtures [19]. Less research was found in the study of particle packing of cementitious material. The dense particle packing can be achieved by selecting the several sizes of SCM particle so that it reduced voids between the particles. This fundamental of particle packing used in this research work, by using two types of the binder as FA and RHA finer along with OPC. The average particle size at D10 and D50 were found that 8μm and 32μm for ordinary Portland cement, 1μm and 20μm for type-1 rice husk ash, 2μm and 20μm for type-2 rice husk ash, 4μm and 21μm for type-3 rice husk ash, 5μm, and 22μm for FA particles and for OPC 32. The previous study on cement paste [20] and mortar [21] was reported that the particle packing increased the strength and durability of triple blend concrete than control concrete.

2. MATERIAL AND METHODS:

2. 1. Material The materials were used in this research work such as tap water, cement, local river sand, and 10 and 20mm size coarse aggregate, FA and RHA. The physical and chemical properties of OPC are summarized in Table 1 conformed from IS 8112-2013 [22]. The properties of fine aggregate were conformed from IS: 2386-1963 (part-III) and IS 383-1970. The grading of sand was conforming to Zone-II and 2.56 specific gravity. The properties of coarse aggregate were conformed from IS: 2386-1963 (part-III) and IS 383-1970 with specific gravity 2.62 and 2.64, respectively. The FA used as SCM in the present research work was collected from Bhilai, Chhattisgarh, India. Three types of amorphous RHA (Chhattisgarh, Odisha and Maharashtra state) were used as another SCM in this research work having greater than 90% of silica content was collected from a local vendor. The efficiency of RHA and FA was reported in previously work, as 10%RHA and 10%FA attained maximum strength [12]. The polycarboxylate-based superplasticizer with a 1.2 specific gravity was used to provide the water drop up to 20% without affecting the workability.

2. 2. Experimental Work Triple blend of concrete mix is prepared with 0.30, 0.35 and 0.40 water-cement ratio. The mix design of concrete prepared concerning standards IS 10262-2009 [23]. The detailed description and designation of blended concrete mix design are tabulated in Table 2. The fine aggregate for 0.30, 0.35 and 0.40 watercement ratio 637, 626 and 642.3 kg/m^3 were used, coarse aggrregate 1226, 1205 and 1236 kg/m^3 were used, water 148, 166 and 166 kg/m^3 were used, and chemical admixture 4.05, 2.63 and 1.20 kg/m^3 were used in concrete mixes. The control concrete mix represent by C100-R0-F0 that is 100% OPC content, 0% RHA and 0% FA. The triple blend concrete mixes are C80-1R10-F10 represent that means 80% OPC content, 10% Type-1RHA, Type-2RHA and Type-3RHA with 10% FA. Another combination of replacement of cement by FA and RHA as 70% and 60% for all water cement ratios. For concrete preparation weight batching was used for all the ingredients of concrete for various mixes. The concrete mixing was done by laboratory pan mixture. For

TABLE 1. Physical and Chemical Properties of OPC, FA, and RHA

Chemical Composition	Mass Content (%)				
	OPC	FA	1R	2R	3R
(SiO_2)	15.7	63.78	92.45	90.49	89.39
(CaO)	68.51	1.12	1.94	1.71	1.65
(Al_2O_2)	4.65	24.44	0.79	0.68	0.51
(Fe_2O_3)	3.76	5.01	0.74	0.52	0.66
(MgO)	1.66	0.48	0.37	0.32	0.35
(K_2O)	2.35	2.46	0.22	1.03	1.11
(Na_2O)	0.37	0.11	0.41	0.12	0.13
Specific Gravity	3.14	2.2	2.5	2.4	2.36

mixing all ingredients were placed in pan mixture. It was mixed for 2 to 4 minutes up to getting a uniform colored and homogeneous concrete. And by observing it insured that all surface of aggregate were coated with binder paste uniformly. At last concrete mix were removed and placed in a tray for slump test and casting of various mold.

2. 3. Srinkage Cone Test The shrinkage at early age consider as critical parameter for concrete. The loss of water due to hydration process referred to as drying shrinkage. The shrinkage in concrete developed tensile stresses and it lead to form cracks. In this research, the mainly focused on the effect of early age shrinkage. The Shrinkage Cone apparatus were used in this research work as shown in Figure 1. The apparatus consist of conical mould of diameter 14.5 cm and height 12.5 cm. The stand assembly was consisting with laser and platform for placing the cone mould. Before the fresh concrete poured in conical mould the thin foil placed in mould for easy of separation of concrete after testing from mould. The reflector was placed on centre of concrete in mould, the laser beam striking in it. The readings were taken out through the shrinkage meter and computer software. The laser beams offset were fixed at 2000μm. The total system was control through computer and software.

TABLE 2. Concrete Mix Proportion (kg/m^3)

Concrete Mix	C/W	OPC	RHA	FA
C100-R0-F0	0.3	450	0	0
C80-1R10-F10		396	49.5	49.5
C70-1R10-F20		346.5	49.5	99
C60-1R10-F30		297	49.5	148.5
C100-R0-F0	0.35	438	0	0
C80-1R10-F10		385.42	48.2	48.2
C70-1R10-F20		337.24	48.2	96.36
C60-1R10-F30		289.06	48.2	144.54
C100-R0-F0	0.40	383.2	0	0
C80-1R10-F10		337.2	42.2	42.2
C70-1R10-F20		295.0	42.2	84.30
C60-1R10-F30		252.9	42.2	126.46

Figure 1. Shrinkage Cone Test setup

2. 4. Prediction Model In the ACI 209R-92 code have a guideline for predicting the shrinkage of concrete [24]. In the literature it was reported that the modified Gardner model is more easy and accurate for prediction of shrinkage of concrete. In ACI model or Ross model both required ultimate drying shrinkage which can calculate using various complicated terms. In the present research work modified Gardner model was used for predicting the early age shrinkage of triple blend concrete. Equation (1) referred to modified Gardner model [24,25]:

$$\varepsilon_{sh}(t) = -\beta(h)\,\beta(t)\,\varepsilon_{sh\infty} \quad (1)$$

$$\beta(h) = 1 - 1.18\,h^4 \quad (2)$$

$$\beta(t) = \left(\frac{t}{t+0.15\left(\frac{v}{s}\right)z}\right)^{0.5} \quad (3)$$

$$\varepsilon_{sh\infty} = 1000 \times 1.15\left(\frac{30}{fcm_{28}}\right)^{0.5} \times 10^{-6} \quad (4)$$

where,($\varepsilon_{sh\infty}$)denotes national ultimate shrinkage strain calculated from regression analysis, $\beta(h)$denotes correction term according to relative humidity, $\beta(t)$denotes correction term for effect of time on shrinkage, (t) denotes time curing period, (v) volume of concrete for given conical apparatus, (s) surface area in contact with atmosphere, (fcm_{28})denotes 28days compressive strength of concrete, (h) denotes relative humidity as 70%.

3. RESULT AND DISCUSSION

3. 1. Early Age Shrinkage of Triple Blend Concrete During the shrinkage test on the sample for 24 hours, it was observed that the shrinkage increased up to first 7 hours after the addition of water in the mix and then it marginal. The shrinkage test was conducted for all blended concrete mixes with 0.30, 0.35 and 0.40 water-cement ratio. The results of early age shrinkage for 0.30 water-cement ratio blended concrete were shown in Figure 2. For 0.35 water-cement ratio blended concrete mix result were shown in Figure 3. And for 0.40 water-cement ratio, the shrinkage result was shown in Figure 4. In triple blend concrete made by FA and RHA, early age shrinkage was reduced over control concrete. The shrinkage was observed for the 0.30 water-cement ratio. The triple-blend concrete of 20, 30 and 40% partial cement replacement by FA type-1 RHA the shrinkage reduction was observed as 18.33, 29.81 and 34.57% over control concrete. The triple-blend concrete of 20%, 30% and 40% partial cement replacement concrete mix with FA and type-2 RHA the shrinkage reduction was observed as 15.60, 22.79 and 32.81% over control concrete. The triple-blend concrete of 20, 30 and 40% partial cement replacement concrete mix with FA and

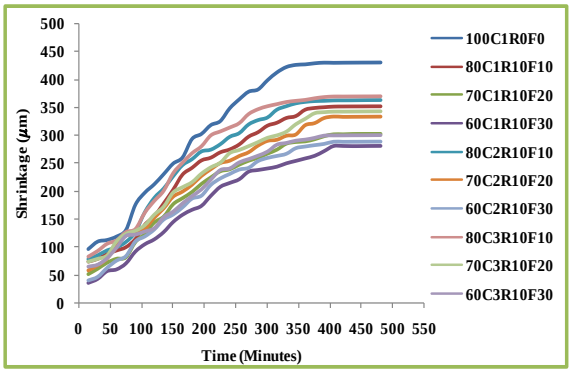

Figure 2. Early Age Shrinkage for 0.30 w/c concrete

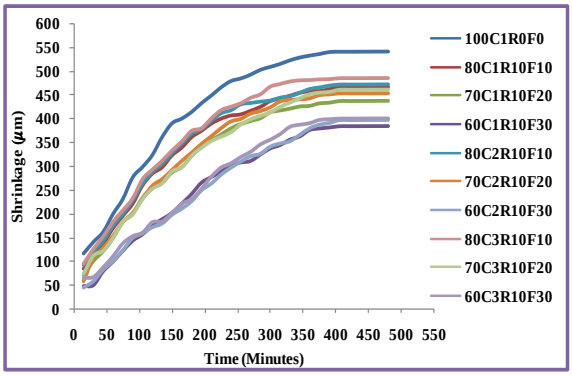

Figure 3. Early Age Shrinkage for 0.35 w/c concrete

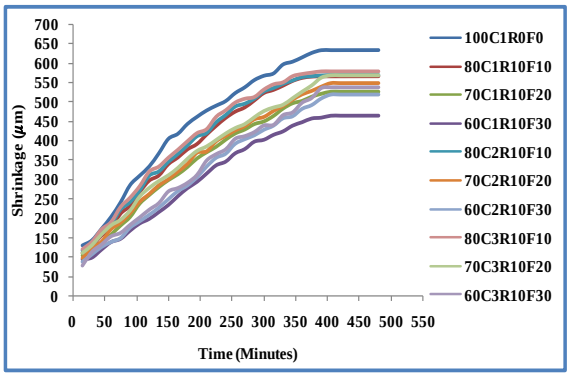

Figure 4. Early Age Shrinkage for 0.40 w/c concrete

type-3 RHA the shrinkage reduction was observed as 13.98, 20.24 and 30.02% over control concrete. Where as the maximum variation of shrinkage reduction for 0.35 water cement ratio observed as 29.06% over control concrete. And for the maximum variation of shrinkage reduction for 0.40 water cement ratio observed as 26.65% over control concrete. According to Neville and Adam [1] autogenous shrinkage and chemical shrinkage are very small as compared to early shrinkage. Hence only early shrinkage is included in present research. It was also noticed that the type-1 RHA blend results getting 2.74 and 4.35% more shrinkage reduction than type-2 and type-3 RHA blend of concrete. The shrinkage is more affected by water-cement ratios. It was observed that the rate of shrinkage is more for higher water-cement ratio concrete due to the higher bleeding possibility in concrete and lower matrix strength. In case of higher water-cement ratio, porosity increased and pore diameter accelerated the reduction in water content and rides capillary pressure in specimen; hence, increased in the early age shrinkage of concrete [7]. The shrinkage was reduced due to reduction in bleeding of concrete. The water stored in the rough surface of RHA. The stored water worked as the internal curing agent. It leads to the vulnerability of early age shrinkage cracking. The slow diffusion of water in fresh concrete also reduced the shrinkage and microcracks. In triple blend concrete, it was also noticed that the shrinkage reduced with the increase in cement replacement. It has happened due to the reduction in heat due to lesser cement content at an early age. In respect to triple blend concrete mix with type-1 and type-2 RHA was reduced more percentage of shrinkage than type-3 RHA blend and control concrete. It was because of reduction in bleeding by the addition of fine particles of RHA and FA. It makes dense particle packing internal concrete matrix and on the surface of concrete, hence the less chance of evaporation and micro cracks [26].

3. 2. Prediction of Early Age Shrinkage for Triple Blend Concrete In the modified Gardner model equation for predicting the shrinkage of triple blend concrete. The independent variable was the time of exposure (days) and dependant variable was early age shrinkage observed in particular time which was noted as $\epsilon_{sh}(t)$ in (μm). In ACI 209 code required ultimate drying shrinkage. In the present research experimental determined early age shrinkage of triple blend concrete at the period of exposure of 7 hours was used as ultimate drying shrinkage. The regression equation can be used for the determining the ultimate drying shrinkage of concrete. The regression equation used for predicting the ultimate drying shrinkage in present work. The concrete containing various ingredients but for developing the regression equation only cementetious material was selected as FA, RHA and OPC. In the equation variables are denoted as (X1), (X2) and (X3) for FA, RHA and OPC. The least square analysis used to determine the regression coefficient. The final equation for predicting the ultimate drying shrinkage of triple blend concrete shown in Equation (5). The R square for the given regression model is 0.864, hence it may considered as the given regression model is adequate for optimized the experimental work. However, it may be noted that the prediction model are specific to the variables and its properties hence cannot be generalized, but are very useful in predicting the result from the given response.

$$\varepsilon_{sh}(t) = \left[(1 - 1.18\,h^4) \cdot \left(\frac{t}{t+0.15\left(\frac{v}{s}\right)^2}\right)^{0.5} \cdot (2910)\right] - [(2.59 \cdot X1) - (0.82 \cdot X2) - (3.36 \cdot X3) + (1530)] \quad (5)$$

Table 3 illustrate the results drawn from analysis of modified mathematical model for early age shrinkage of triple blend concrete with variation of composations. It was observed that there is less difference between experimental and predicted values with 0.98 R-square. It was also noticed that the response is not much affected even changing the constituents. It is because of the equation structuraly strong. Hence it may considered as the given model is adequate. However, it may be noted that the prediction model are specific to the variables and its properties.

TABLE 3. Sensitivity analysis for mathematical model

OPC	RHA	FA	Exp. Shrinkage	Pred. Shrinkage	Differ.	R^2
450	0	0	430.45	431.43	-0.98	0.98
396	49.5	49.5	363.32	364.38	-1.06	
346.5	49.5	99	332.34	326.27	6.07	
297	49.5	148.5	289.23	288.15	1.08	
360	0	90	378.41	362.13	15.87	
270	0	180	290.86	292.83	-2.83	

4. CONCLUSIONS

The following are the conclusions drawn from the test results:

1. The triple blend concrete with type-1 RHA can reduce up to 34.57% the early age shrinkage resulting increased durability of concrete.
2. The fine, smooth and spherical structure of FA reduced the shrinkage of concrete and rough surface of RHA reduced the bleeding of concrete resulting reduced shrinkage.
3. The modified Gardner model for prediction of early age shrinkage for triple blend concrete can be used to predict early age shrinkage of triple blend concrete and minimise the experimental work.
4. The combined use of FA and RHA as partial cement replacement up to 30% can reduce the use of cement and environmental issues.
5. The proposed triple blend concrete is strongly recommended for reduce the early age shrinkage of concrete for long durability and sustainable concrete.

5. ACKNOWLEDGEMENT

The writer would like to acknowledge to TEQIP- phase-III, NIT Raipur, for purchase the required material. The author acknowledge to Department of Metallurgy, NIT Raipur for help in testing work through Scanning Electron Microscope (SEM). The author also acknowledge head of department of civil engineering, NIT Raipur for continuous support.

6. CONFLICT OF INTEREST

There is no conflict of interest for this research.

7. REFERENCES

1. A. M. Neville, Adam, M. *Properties of Concrete*, Fifth edition, Pearson Education Limited, 2011.
2. R. K. Mishra, R. K. Tripathi, and V. Dubey, "Early age shrinkage pattern of concrete on replacement of fine aggregate with industrial by-product" ***Journal of Radiation Research and Applied Sciences,*** Vol. 9, No. 4, (2016), 386-391, https://doi.org/10.1016/j.jrras.2016.05.003
3. P. Nath and P. K. Sarker, "Effect of Mixture Proportions on the Drying Shrinkage and Permeation Properties of High Strength Concrete Containing Class F Fly Ash," ***KSCE Journal of Civil Engineering,*** Vol. 17, No. 6, (2013), 1437-1445, doi: 10.1007/s12205-013-0487-6.
4. A. Castel, S. J. Foster, T. Ng, J. G. Sanjayan, and G. R. I., "Creep and drying shrinkage of a blended slag and low calcium fly ash geopolymer Concrete," ***Materials and Structures,*** Vol. 49, (2016), 1619-1628.doi: 10.1617/s11527-015-0599-1.
5. Rath Badrinarayan, D. Shrish, and R. Gangadhar, "A Study on Early Age Shrinkage Behaviour of Cement Paste with Binary and Ternary Combination of Fly Ash and Pond Ash," ***Indian Journal of Science and Technology***., Vol. 9, No. 9, (2016), 1-6. doi: 10.17485/ijst/2016/v9i44/95189.
6. Raut, M. V., and S. V. Deo. "Use of high volume fly ash on early age shrinkage in concrete for local hot and dry condition." ***Journal of Engineering Science and Technology***, Vol. 13, No. 7 (2018), 2036-2046.
7. Hu, X., Shi, Z., Shi, C., Wu, Z., Tong, B., Ou, Z. and De Schutter, G., "Drying shrinkage and cracking resistance of concrete made with ternary cementitious components," ***Construction and Building Materials,*** Vol. 149, (2017), 406-415, doi: 10.1016/j.conbuildmat.2017.05.113.
8. X. Hu, C. Shi, Z. Shi, B. Tong, and D. Wang, "Early age shrinkage and heat of hydration of cement-fly ash-slag ternary blends," ***Construction and Building Materials,*** Vol. 153, (2017), 857-865. doi: 10.1016/j.conbuildmat.2017.07.138.
9. S. Dueramae, W. Tangchirapat, P. Chindaprasirt, and C. Jaturapitakkul, "Autogenous and drying shrinkages of mortars and pore structure of pastes made with activated binder of calcium carbide residue and fly ash," ***Construction and Building Materials,*** Vol. 230, (2020), 116962. doi: 10.1016/j.conbuildmat.2019.116962.
10. B. Singh, M. R. Rahman, R. Paswan, and S. K. Bhattacharyya, "Effect of activator concentration on the strength , ITZ and drying shrinkage of fly ash/ slag geopolymer ***Construction and Building Materials,*** Vol. 118, (2016), 171-179, doi:

10.1016/j.conbuildmat.2016.05.008.

11. Kanthe, V., Deo, S. and Murmu, M., "Use of Mineral Admixture in Concrete for Sustainable Development," ***International Journal of Innovative Research in Science and Engineering***, Vol. 3, No. 3, (2017), 279-284.
12. Kanthe, V., Deo, S. and Murmu, M., "Combine use of fly ash and rice husk ash in concrete to improve its properties", ***International Journal of Engineering-Transactions A: Basics***, Vol. 31, No. 7, (2018), 1012-1019. doi: 10.5829/ije.2018.31.07a.02
13. A. L. G. Gastaldini, M. P. Da Silva, and F. B. Zamberlan, "Total shrinkage, chloride penetration, and compressive strength of concretes that contain clear-colored rice husk ash," ***Construction and Building Materials,*** Vol. 54, (2014), 369-377. doi: 10.1016/j.conbuildmat.2013.12.044.

[14. G. Shafabakhsh and S. Ahmadi, "Evaluation of Coal Waste Ash and Rice Husk Ash on Properties of Pervious Concrete Pavement," ***International Journal of Engineering, Transaction B: Applications***, Vol. 29, No. 2, (2016), 192-201, doi: 10.5829/idosi.ije.2016.29.02b.08.

15. V. Sai Giridhar Reddy and V. Ranga Rao, "Eco-friendly Blocks by Blended Materials," ***International Journal of Engineering Transaction B: Applications***,, Vol. 30, No. 5, (2017), 636–642. doi: 10.5829/idosi.ije.2017.30.05b.02
16. S. Sharma, T. Gupta, and R. K. Sharma, "Assessment of Mechanical Properties of Concrete Containing Granite Slurry Waste," ***International Journal of Engineering***, ***Transaction B: Applications,*** Vol. 29, No. 5, (2016), 599-605. doi: 10.5829/idosi.ije.2016.29.05b.021.
17. Sharma, S. Kant Ransinchung, G D R NKumar and A. P.Roy,Kumar, "Comparison of Permeability and Drying Shrinkage of Self Compacting Concrete Admixed with Wollastonite Micro Fiber and Fly Ash," ***International Journal of Engineering, Transaction B: Applications,*** Vol. 30, No. 11, (2017), 1681-1690. doi: 10.5829/ije.2017.30.11b.08
18. D. B. Zhang, Y. Zhang, T. Cheng, "New Analytic Method for Subgrade Settlement Calculation of the New Cement Fly ash Grave Pile slab Structure," ***International Journal of Engineering, Transactions A: Basics,*** Vol. 29, No. 10, (2016), 1364-1371. doi: 10.5829/ije.2016.29.10a.06
19. P. N. Reddy and J. A. Naqash, "Effect of Antifreeze Admixtures on Cold Weather Concrete," ***International Journal of Engineering, Transactions C: Aspects***, Vol. 32, No. 3, (2019), 366-372. doi: 10.5829/ije.2019.32.03c.03.
20. V. N. Kanthe, S. V. Deo, and M. Murmu, "Effect of Fly Ash and Rice Husk Ash as Partial Replacement of Cement on Packing Density and Properties of Cement," ***International Journal of Innovative Technology Exploring Engineering***, Vol. 8, No. 7, (2019), 1940-1945. *Retrieval Number: G6316058719/19©BEIESP.*
21. V. N. Kanthe, S. V Deo, and M. Murmu, "Effect of fly ash and rice husk ash on strength and durability of binary and ternary blend cement mortar," ***Asian Journal of Civil Engineering,*** Vol. 19, No. 8, (2018), 963-970. doi: 10.1007/s42107-018-0076-6.
22. IS: 8112-2013, "Ordinary Portland cement 43 Grade-Specification," ***Buro of Indian Standard,*** No. 2, (2013), 1-14.
23. IS: 12062-2009, "Concrete Mix Proportioning- Guidelines," ***Buro of Indian Standard,*** No. 1, (2009), 1–21.
24. American Concrete Institute, "Guide for Modeling and Calculating Shrinkage and Creep in Hardened Concrete," *ACI 209.2R-08*, (2008), 2-48.
25. N. J. Gardner and J. W. Zhao, "Creep and Shrinkage Revisited," ***Material Journal,*** Vol. 91, No. 2, (1994), 204-211.
26. V. Kanthe, S. Deo, and M. Murmu, "Effect on Autogenous Healing in Concrete by Fly Ash and Rice Husk Ash," ***Iranica (Iranian) Journal of Energy and Environment,*** Vol. 10, No. 2, (2019), 154-158. doi: 10.5829/ijee.2019.10.02.13.

Persian Abstract

چکیده

انقباض زودرس موجب ترک زودرس بتن است. برای دوام بتن بسیار حیاتی است. تغییر حجم بتن به دلیل تبخیر آب یا فرآیند کم آبی ، به عنوان کوچک شدن شناخته می شود. برای کاهش انقباض بتن ، از مواد سیمانی تکمیلی (SCM) در بتن استفاده شده است. در پژوهش حاضر از فرآورده های زائد صنعتی و کشاورزی مانند خاکستر احتراق (FA) و خاکستر پوسته برنج (RHA) به همراه سیمان به عنوان SCM استفاده شده است. بتن مخلوط سه گانه با ترکیب ۲۰٪ ، ۳۰٪ و ٤۰٪ جایگزینی سیمان جزئی با FA و RHA برای ۰.۳۰، ۰.۳۵ و ۰.٤۰ نسبت سیمان آب تهیه گردید. نمونه های بتنی با استفاده از دستگاه پیشرفته مورد آزمایش قرار گرفتند. نتیجه نشان می دهد که با افزایش محتوای SCM ، انقباض بیش از حدکاهش می یابد. خصوصیات ریزساختار با افزایش محتوای FA و RHA تا ۳۰٪ جایگزینی افزایش یافته است. این به دلیل بسته بندی ذرات متراکم بود.

International Journal of Engineering

Journal Homepage: www.ije.ir

Generation Process and Performance Evaluation of Engineered Microsphere Agarose Adsorbent for Application in Fluidized-bed Systems

R. Mofidian[a,b], A. Barati*[a], M. Jahanshahi[b], M. H. Shahavi[c]

[a] *Department of Chemical Engineering, Faculty of Engineering, Arak University, Arak, Iran*
[b] *Nanotechnology Research Institute, Babol Noshirvani University of Technology, Babol, Iran*
[c] *Faculty of Engineering Modern Technologies, Amol University of Special Modern Technologies (AUSMT), Amol, Iran*

PAPER INFO

Paper history:
Received 27 April 2020
Received in revised form 30 May 2020
Accepted 12 June 2020

Keywords:
Adsorbent
Agarose
Engineered Microsphere
Fluidized-bed
Streamline™

ABSTRACT

In this research, the generation process of engineered microsphere agarose adsorbent has been explained that has surfaces with different active sites to adsorb protein nanoparticles into the fluidized-bed system. Also, excellent selectivity of protein nanoparticles, high adsorption capacity, and fast equilibrium rate through the eco-friendly polymeric adsorbents were vital aims in here. Hence, agarose as a cheap, and abundant natural polymer, with a ferromagnetic condenser, and dye-ligand adsorbents, were employed to generate the engineered microsphere agarose adsorbent. Then, the performance of produced adsorbents was evaluated in the batch and fluidized-bed system. Scanning electron microscopy, atomic force microscopy, and optical microscope were used. Results showed the shape of adsorbents is spherical, with the size distribution range of 50-250 µm, the porosity of around 90%, and the wet density of 2.6 g/mL. Then, to compare the performance of the engineered adsorbents in a fluidized-bed system, the dye ligand was immobilized on the Streamline™. The obtained results were compared at the same conditions. In batch adsorption tests, the results of lactoferrin nanoparticle adsorption were shown higher dynamic binding capacity with engineered microsphere agarose adsorbents. Also, the results demonstrated that more than 75% of the adsorption process occurred in the first half-hour, which is a very suitable time for a fluidized-bed system. Also, adsorption equilibrium data were evaluated with isothermal adsorption models, and Langmuir's model suits the data, and the maximum of adsorption was close to 45.3 mg/mL adsorbent. The fluidized-bed adsorption tests showed that engineered adsorbents gained a sound breakthrough performance at high flow velocity and upper dynamic binding capacity compared to commercial adsorbents. The dynamic binding capacity at 10% breakthrough achieved 71% of the flooded adsorption process at the major fluid velocity of 348 cm/h, so the engineered adsorbent has been proved the good potential for use in high flow rate fluidized-bed systems.

***doi**: 10.5829/ije.2020.33.08b.02*

1. INTRODUCTION

Based on chemical engineering knowledge, one can develop a new multi-functional adsorbents for efficient protein nanoparticle adsorption in fluidized-bed systems. In the generation process of engineered microsphere polymeric adsorbents, excellent selectivity of nanoparticles, high adsorption capacity, and the fast equilibrium rate through economic polymeric substances are vital factors produced in every industrial system [1-3]. Accordingly, the use of natural origin polymeric substances is significant. Agarose is a natural-originated marine polysaccharide polymer having unique characteristics that give reason to consider it for engineering applications. There are several types of agarose available in the chemical market. One of the most important of them is low-melting agarose, which is used in the adsorption process. The agglomeration of agarose increases by adding metal elements such as nickel, zinc, or fill materials such as cellulose bead, silica gel, zirconium oxide, titanium oxide, and stainless steel. Solid filler materials and other porous solids can be used to increase the density of these products [4-6]. A metallic core adsorbent with a porous surface is an ideal choice

*Corresponding Author Email: *a-barati@araku.ac.ir* (A. Barati)

Please cite this article as: R. Mofidian, A. Barati, M. Jahanshahi, M. H. Shahavi, Generation Process and Performance Evaluation of Engineered Microsphere Agarose Adsorbent for Application in Fluidized-Bed Systems, International Journal of Engineering (IJE), IJE TRANSACTIONS B: Applications Vol. 33, No. 8, (August 2020) 1450-1458

for this purpose. Choosing the right metal core results in adsorption with a specific density and excellent performance [7-9]. Nickel is corrosion resistant, highly malleable, and fully recyclable so that it is an excellent choice for strengthening composites. Nickel has high polarizability (α=6.8), and low ion radius (Ni^{2+}=0.69 Å, Ni^{3+}=0.62 Å) compared to other metals; therefore, it is used as an absorbent core [10, 11].

By balancing the surface of an oil-impregnated object with water droplets deposited by adhesion force, oil droplets can be changed from hydrophobic to hydrophilic conditions. This physical phenomenon is defined as a three-phase emulsion. There are four main phases embedded in three-phase emulsion systems: water, oil, nanoparticles, and the substrate [12, 13]. Thus, three possible contact interfaces can form (1) oil/water, (2) water/substrate, and (3) oil/substrate. The ease of emulation depends on a variety of factors: interfacial surface tension, viscosity, chemical composition, the content of low molecular weight, and adsorption of different biological substances from intraocular fluids and tissues (emulsifiers). Studies have shown that all of these can have a role in the emulsification process. The affinity of a substance to emulsify and disperse into droplets over time is also reliant on its viscosity. Silicone oils have a high viscosity (1–5.00 cp), and because of their viscosity and their ability to repel water, they are referred to as oils [14-17].

Fluidized-bed adsorption (FBA) is an efficient technique for direct capture of target proteins from unrefined raw materials, as well as improved productivity and process economy. FBA is an ingenious chromatography technique to integrate illumination, concentration, and initial purification into an independent path [18, 19]. Adsorption has long been a research topic in the area of environmental science and engineering, and there is a large number of scientific and technical papers in this area [20, 21]. Adsorption is the process through which a substance, initially present in one phase, is removed from that phase by accumulation at the interface between that phase and a separate (solid) phase [22, 23]. Two essential properties of each adsorbent are size distribution of the particles and high density to provide a stable fluidized-bed, which also encompasses the hydrodynamic properties of the fluidized-bed and the packed bed. High density is needed for a steady operation at higher flow velocity, and the suitable size distribution contributes significantly to a complete mixture in the column [24-26]. A high compressive adsorbent does not need to be recovered because it can hold more adsorbate per unit weight. An essential way to increase the density of the absorbent structure is to increase the flow intensity and consequently increase the particle size. Many types of supporting matrices for FBA have been developed, and their preparation methods have gradually been commercialized [27].

The agarose-nickel adsorbent was initially developed by Asghari et al. [28]. They formulated the novel adsorbent by using the water-in-oil emulsification method. Desirable adsorbents had a spherical appearance, and suitable size distribution, the appropriate wet density of 1.95 g/mL, and porosity of 91.93% [28]. Also, Rezvani et al. [29] showed a higher adsorption rate and binding capacity compared to that of the Streamline™. They prepared two different agarose-nickel bead size with the sizes (75-150 & 150-300 µm) in the subject of hydrodynamic stability and adsorption properties [29]. Mohsenkhani et al. [30] invented a cost-effective series of support matrix named as k-carrageenan-zink. The new matrix had a wide size distribution of 50–350 µm and a mean diameter of 160–230 µm. They were found that increasing the fluid velocity and viscosity could compromise the FBA stability. However, the high flow velocity is most likely required to achieve high productivity and high viscosity in biological feedstocks [30]. In other work, super porous κ-Carrageenan-nickel adsorbent beads have been fabricated and evaluated using water in oil emulsification and granule leaching methods by Abatari et al. [31]. The results indicated that the particles had normal size distribution with the range of 60–320 µm. As a result of physical properties measurements, a proper wet density at the range of 1.43–2.42 g/mL has resulted in the adsorbent beads [31].

In this research, the engineered microsphere agarose (EMA) adsorbent was generated and presented as an adsorbent that has surfaces with different active sites to adsorb protein nanoparticles on the FBA systems. Scanning electron microscopy (SEM), atomic force microscopy (AFM), and optical microscope (OM) techniques have been employed to measure the formation of protein model, shape, and morphology of EMA adsorbents. Also, commercial Streamline™ adsorbent, which is an agarose-based anion exchanger, was prepared with the same dye ligand in a similar technique. Then, EMA was compared with Streamline™ based on contact time with various initial concentrations value of Lactoferrin (LF) nanoparticles as a protein model, and breakthrough curves with different flow velocity in the fluidized-bed system and obtaining adsorption isotherms parameters are the ultimate aims of this research.

2. MATERIALS & METHOD

2. 1. Materials Ultrapure low gelling temperature agarose, acetone, and glycerol were purchased from Merck (Germany). Sorbitan monooleate (Span® 80), Silicone oil and nickel powder with a bulk density of 1500-2600 Kg/m^3 and an average particle size of 10 µm were supplied by Sigma (MO, USA). Commercial Streamline™ adsorbent was purchased from Amersham

Biosciences (Uppsala, Sweden), and Cibacron Blue 3GA dye ligand was bought from AG Scientific Inc. (CA, USA).

2. 2. Generation Process of EMA Adsorbent The main generation process setup of EMA adsorbents shown in Figure 1. In this research, a cylindrical double wall jacketed glass reactor (T_1) with a diameter (D) of 0.04 m, height (H) of 0.06 m, and a stainless steel Ruston turbine (d = 0.01 m) was placed in it. A second glass vessel (D = 0.04 m (T_2), H = 0.06 m)) was used for slurry EMA adsorbents preparation.

In this process, 300 mL of silicon oil with a certain amount of Span® 80 was poured into a double-layer glass reactor. The reactor was connected by a pump to a water bath at 85 °C heated for 30 min. On the other side, a certain amount of agarose powder was stimulated for 5 min at 80°C in a vessel. Then, the nickel powder was added, and the mixing process lasted for 10 min. The contents of the second reactor were transferred to the vessel and mixed for 20 min at a uniform rate. The oil phase was cooled to 15 ◦C by replacing the hot water with cold water in the water bath. Subsequently, the oil production and the semi-ready adsorbent beads were centrifuged for about 20 min at around 11000 rpm to dissolve the oil and solid phases. Then, the solid phase was transferred from the centrifuge vials with acetone into a flask and placed on a shaker at 150 rpm for 2 hours at ambient temperature to achieve uniform particles. After that, the beads were washed by distilled water to remove oil droplets well from the adsorbents. Finally, the pellets were screened by metal sieves according to their size fraction.

Finally, chemical cross-linking was used by epichlorohydrin, to maintain the composite structure and mechanical strength of EMA beads. The EMA beads with a volume equal to 1M sodium hydroxide containing 5 g/L sodium borohydride were placed on a shaker for 30 min at 150 rpm. Then, epichlorohydrin (up to 2% v/v) was added to the mixture. After that, at 25°C, the solution was stirred at 150 rpm for 6 hours on a shaker. Subsequently, the beads were washed with distilled water to separate the ex-reactions. Here, Cibacron Blue 3GA (CB3) was immobilized on the structure of the adsorbent base to prepare EMA adsorbents finally for the processes of adsorption in the fluidized-bed system. The Streamline™'s adsorbent was modified with CB3 by the same method.

2. 3. Adsorption Application To study the hydrodynamic properties of the EMA adsorbents on the fluidized-bed system, a simple column with an internal diameter of 1 cm and a height of 25 cm was used [32]. A certain amount of adsorbents (around 6 cm bed height) was transferred to the column and allowed to sediment homogeneously. Scheme view of the setup in the fluidized-bed system shown in Figure 2. The adsorbents were washed several times with a 10 mM Tris/HCl buffer at pH 7 to balance its acidity. Then, a certain amount of the adsorbents transferred into the column, and the flow was expanded via the pump. In this study, the acetone solution (10% by volume), and Lf nanoparticles were filled at the floor of the column, and the output effluent of the column was captured in 280 nm wavelength via a spectrophotometer apparatus (Jenway 6305, Germany) [33].

2. 4. Adsorption Characterization The wet density (ρ_w) was measured by the water replacement method in a test pit and was measured by Equation (1) as below:

$$\rho_p = \frac{M_1 \rho_\omega}{M_1 + M_2 - M_3} \quad (1)$$

where ρ_p and ρ_ω represent the wet density and water density, respectively. M_1, M_2, and M_3 represent the mass of wet adsorbents, the mass of bottle filled with water, and the mass of bottle filled with water and adsorbents. The porosity of the adsorbents was estimated by Equation (2):

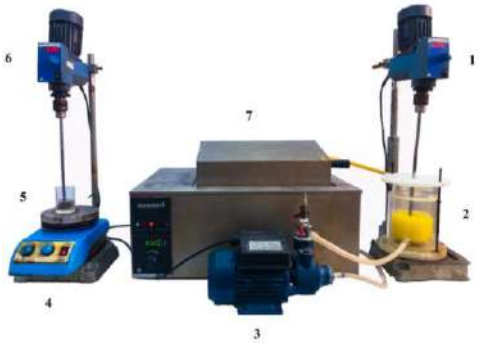

Figure 1. The main setup and its various components; (1, 6) Mixtures (2) Reactor T1 (3) Pump (4) Heater (5) Reactor T2 (7) Waterbath

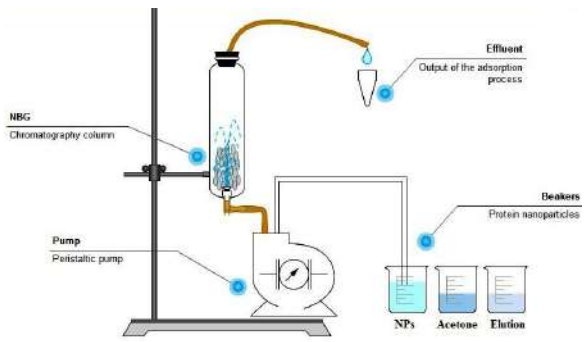

Figure 2. Scheme view of adsorbents application in the FBA systems

$$P = \frac{\omega \rho_p}{\rho_\omega} \times 100\% \quad (2)$$

where ω, is the water content (%) and obtained by Equation (3):

$$\omega = \frac{m_2 - m_3}{m_2 - m_1} \times 100\% \quad (3)$$

where m_1, m_2, and m_3 represent the mass of the weighing bottle, the adsorbent, and weighing bottle before and after drying, respectively [28].

2. 5. Adsorption Isotherms In the kinetic study of adsorption, a batch experiment was carried out using Lf nanoparticles. In summary, 0.9 mL of synthetic adsorbents were poured into a set of 25 mL beakers filled with 10 mL protein of different concentrations as binding for Lf adsorption, and a 1M Tris-HCl buffer stock solution was used. Adsorption trials were perfumed at 20 °C at an incubator speed of 150 rpm to realize the equilibrium. At the end of the process, the protein solution was used to identify protein concentration using a UV detector at a wavelength of 280 nm.

The Langmuir isotherm represents the equilibrium distribution of metal ions between the solid and liquid phases. Based on these assumptions, Langmuir described the following linear Equation (4) [34, 35]:

$$\frac{C_e}{q_e} = \frac{1}{q_m K_L} + \frac{C_e}{q_m} \quad (4)$$

where C_e is equilibrium concentration of adsorbent (mg/mL), q_e is the capacity of adsorption at equilibrium (mg/mL), q_m is the maximum capacity of adsorption (mg/mL) and K_L is the Langmuir isotherm constant. The values of q_m and K_L were calculated based on the slope and intercept of the Langmuir plot of $1/C_e$ versus $1/q_e$.

The Freundlich adsorption isotherm is relative to the adsorption process that occurs on a heterogonous surface. This isotherm provides an expression, which explains the surface heterogeneity. Also, it shows the exponential distribution of active sites and their energies. The linear Equation (5) of the Freundlich isotherm is as follows [36, 37]:

$$\log q_e = \log K_F + \frac{1}{n} \log C_e \quad (5)$$

where K_F and n are the Freundlich isotherm constants that are related to the capacity and intensity of adsorption, respectively. In kinetic reactions, the protein solution is used as a sample to measure the concentration of protein. Equation (6) estimated the sum of adsorbed proteins at each moment [38]:

$$q_t = \frac{C_0 V_0 - C_t V_t}{V_d} \quad (6)$$

where q_t is the volume of dye adsorbed per unit of adsorbent mass (mg/mL), C_0 is initial concentration, and C_t is the concentration of dye (mg/mL) at time t. Moreover, V_0, V_t and V_d are initial volume, the volume of dye solution at time t, and the volume of drained adsorption, respectively.

2. 6. Fluidized Bed Adsorption Dynamic binding capacity (DBC) of a column describes the maximum amount of target protein that can be loaded onto the column without causing unnecessary loss. It is measured under experimental conditions (default flow-rate, real protein sample). As stated above, samples were taken at a specific time interval from the output of the column. The breakthrough curve is obtained by plotting the adsorbed concentration or normalized concentration as a function of the time or flow rate for the given bed height (C/C_0). The shape of this chart may change dramatically in different situations. Here, it is considered as fatigue time when the output concentration reaches 10% of the input concentration ($C/C_0 = 0.1$), and as the time of infiltration ($C/C_0 = 0.9$) when the concentration of output reaches 90%. Since the surface below the infiltration curve represents the amount of protein not absorbed from the column, the dynamic adsorption capacity at the time of infiltration is 10% of the following relationship. This number corresponds to a point in equilibrium temperatures. The following formula measured the DBC of 10% breakthrough curve as Equation (7) [39]:

$$(DBC) q_{10\%} = \frac{C_0 \int_0^{V_{10\%}} (1 - C/C_0) dV}{V_d} \quad (7)$$

where $q_{10\%}$ is the DBC at 10% breakthrough curve and C and C_0 are the outlet and initial concentration of protein, respectively.

2. 7. Preparation of Lf Nanoparticles The Lf nanoparticles were used in the fluidized-bed system to evaluate the new adsorbents. The nanoparticles were prepared in our previous work [40]. Summarily, 3 g Lf powder was poured into 25 mL of distilled water and stirred for 1 hour. Then, the pH of the solution was adjusted to 7. Meanwhile, the Lf solution was heated slowly at a constant rate of 5 °C/min to the final temperature of 90 °C.

3. RESULTS AND DISCUSSION

3. 1. Images Analysis To achieve a microspherical adsorbent is one of the highlights of this work. That as demonstrated in Figure 2a via an optical microscope (Nikon, model YS 100, Japan), the generated EMA particles were to be spherical and micro-sized. As depicted, the particles are defragmented to each other, and all these adsorbent particles have a regular shape. The size range of the EMA adsorbents was 50-250 μm. All adsorbents have physical independence, and there is no adhesion. Schematic of EMA adsorbent drawn in

Figure 2b. As can be seen, nickel particles have shown with black circles that are scattered in the natural agarose polymer. In addition, dye ligands, which are indicated by the blue triangle in Figure 2b, plays an important role due to the mechanism of adsorbent, which acts as a cross-linker between nanoparticles and adsorbents.

Also, the morphology and surface properties of EMA adsorbent were investigated by an SEM (Tescan, Vega XMU-II, Czech Republic) [41]. The acceleration voltage mode of this microscope was changeable between 200 V up to 30 kV, and the resulting magnification could being from 500× up to 3500×. Figures 3a and 3b showed the SEM images of EMA adsorbent. These images can see the porous surface, and the highly reticular structure of adsorbent is evident. Suitable spherical shape and sufficient porosity are of the prominent points in the production of adsorbents. The cavities on the adsorbent are clearly shown in Figure 3b. Also, based on Equation (2), the porosity of particles was measured close to 90%, which is a perfect result for adsorbents.

Lf nanoparticles synthesized and employed in the adsorption process of the fluidized-bed system as a protein model. Morphology and direct physical particle sizes of the Lf nanoparticles determine the AFM images. These images were taken under ambient conditions in the air using an EasySacn II® (NanoSurf Co. Ltd, Liestal, Switzerland). AFM image of Figure 4a shows that the protein model prepared are in nano-scale and spherical. That indicates that the smaller the particle size, the more surface area is available to the adsorbent, and as a consequence, the higher the number of the binding site available to adsorb it. As can be seen in Figure 4b, the average particle size of Lf nanoparticles in this study was close to 100 nm.

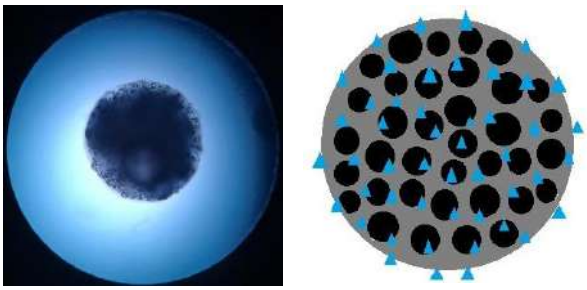

(a) (b)

Figure 2. EMA adsorbent (a) optical microscopy image; and (b) schematic image: ▲ dye ligand, ● nickel, ■ agarose

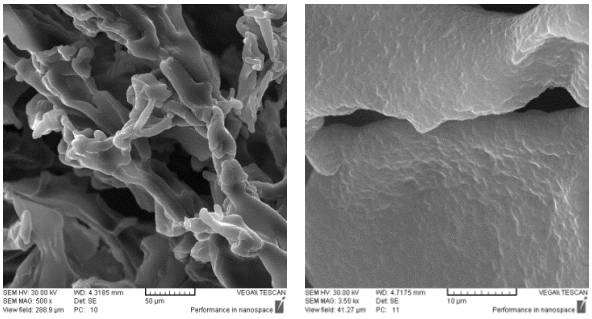

(a) (b)

Figure 3. SEM images of a EMA adsorbent (a) 30 kV, magnification 500, (b) 30 kV, magnification 3500

3. 2. Effect of Contact Time It is shown in Figure 5 that for both adsorbents, rapid adsorption of Lf nanoparticle occurred in the very early stages of FBA, which ensured the system equilibrium. As expected, more than 75% of the protein uptake (EMA, 1 mg/mL) occurred during the first half-hour, which is due to soluble droplet inside the column. As can be seen, EMA adsorbents in various concentrations had more adsorption capacity against modified Streamline™ adsorbents. It may be, cause of higher density and porosity of engineered adsorbents. After an hour, the adsorbent function was close to equilibrium for absorbing protein, and the adsorption continued constantly. In a similar study, the same result found that the sorption reached at equilibrium state after 1 hour and revealed an adsorption

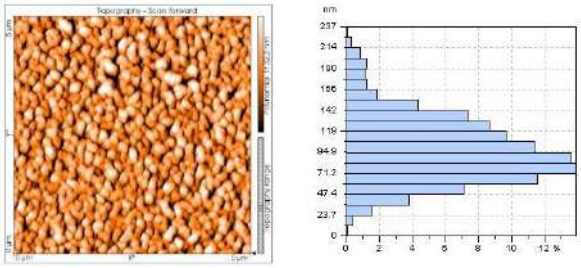

(a) (b)

Figure 4. AFM of Lf nanoparticles (a) morphology image, (b) Particle size distribution graph

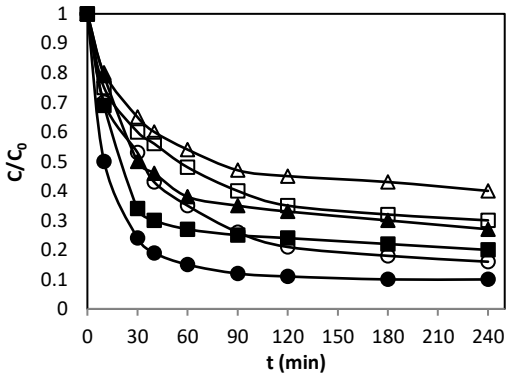

Figure 5. The Effect of contact time on Lf adsorption against on generated adsorbents with different initial concentrations: (●) EMA, 1 mg/mL; (■) EMA, 2 mg/mL; (▲) EMA, 3 mg/mL; (○) Streamline™, 1 mg/mL; (□) Streamline™, 2 mg/mL; (Δ) Streamline™, 3 mg/mL

efficiency of 98 % [42] whereas, for EMA adsorbents, this occurred after 4 hours, which is due to the presence of porosity that is evident in the synthesized adsorbent. This porosity causes a delay in the equilibrium of the adsorption process, which is a significant factor and increases the adsorptive properties - i.e., DBC [38].

3. 3. Adsorption Isotherms Analyses The Lf nanoparticles adsorption experimental data obtained from the batch system were used to find the appropriate isotherm model. Freundlich and Langmuir adsorption isotherms were plotted in Figure 6 (q_e versus C_e). According to Equation (4), q_m is related to C_e, q_e, and K_L. Also, from Table 1 could be found the isotherm parameters for the adsorbents by linear regression appear to give acceptable fits to the experimental data with respective regression coefficients (R^2) close to unity. Overall, the Langmuir isotherm has the highest R^2 values, whereas the Freundlich values are considerably lower. The Langmuir monolayer adsorption capacity (q_m) and equilibrium constant (k_L) for Lf nanoparticles adsorbed by EMA are 47 mg/mL and 0.0168 mg/mL, respectively. Also, at the same variables process condition (such as dye-ligand type, contact time, and etc.) the value of the modified Streamline™ adsorption capacity was obtained 43.4 mg/mL. The Langmuir isotherm provide a reasonable description due to the easiness and good agreement with experimental data. Simultaneously, this tentative model supposes monolayer adsorption; in which adsorption can only turn up at a limited number of particular localized sites, which are identical and equivalent, with no costal interaction between the adsorbed molecules, even on adjacent sites [43, 44].

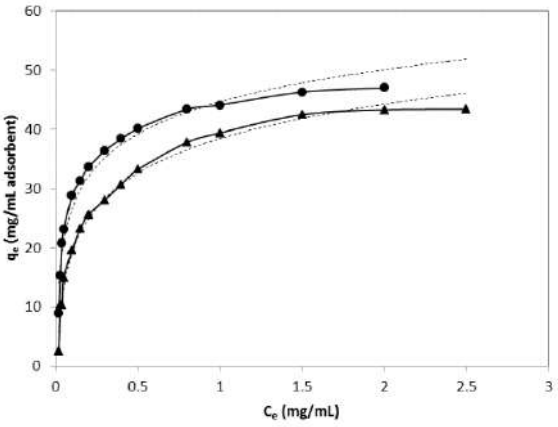

Figure 6. Equilibrium of adsorption isotherms of Lf for (●), EMA; (▲), modified Streamline™; and simulation curves: Langmuir equation (solid lines), Freundlich equation (dashed lines)

TABLE 1. Parameters of equilibrium isotherms (Langmuir and Freundlich)

Adsorbents	q_{max}	Langmuir model			Freundlich model		
		q_m	K_L	R^2	K_F	n	R^2
EMA	45.3	47	0.0168	0.967	26.4	1.16	0.9443
modified Streamline	40.2	43.4	0.0247	0.977	22.9	1.11	0.9503

3. 4. Breakthrough Curve The breakthrough curve happens when the concentration of the feed target protein is equal to the concentration of output target protein. It indicates when to stop the loading, depending on how much bed remains unused and lost. Figure 7 shown the breakthrough curve of Lf during binding to EMA and modified Streamline™ adsorbents in the FBA system at the stream rate of 174 cm/h, and a bed height of 6 cm. The results of the breakthrough diagram clearly shown that the adsorption capacity is perfect for the EMA adsorbent ($q_{10\%}$), which can reach more than 90% of the saturated adsorption. This result indicates the size of the small adsorbent beads, which can affect the order of film mass transfer and the mass resistance inside the beads. The sharp breakthrough curve for Streamline™ was obtained even when adsorption was carried out either in highly viscous solutions or at a high velocity of 174 cm/h. However, using frontal analysis, the breakpoint was found to vary in an approximately linear manner with the degree of bed expansion. The breakpoint was also found to occur much earlier when adsorption was carried out at this superficial velocity. This may be the result of either increased mass transfer resistance between Lf in the bulk liquid and adsorption sites in the EMA beads in a high viscosity solution or substantial axial mixing in both the

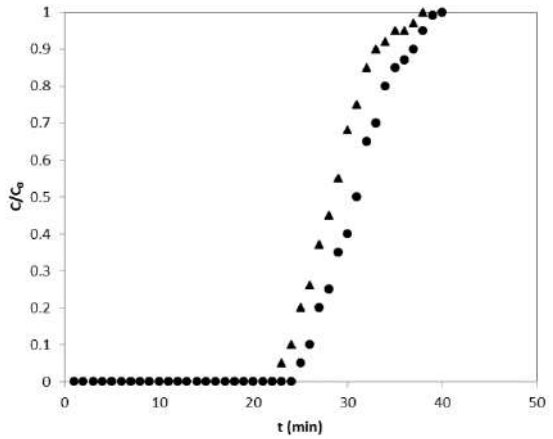

Figure 7. Lf nanoparticles breakthrough at the FBA system: (●) EMA, and (▲) modified Streamline™

liquid and solid phases of the adsorbent beds. Similar works have been shown that the shape and position of the breakthrough curves can be affected by the effective diffusivity, external film mass transfer, and solid/liquid phase axial dispersion coefficient.

Moreover, by increasing the flow intensity of 348 cm/h (about 2×) to achieve double bed expansion, the amount of adsorption capacity increased to 10 mg/mL adsorbent, which is very close to the adsorption capacity (9.43 mg/mL adsorbent) for the initial amount of commercial adsorbent (see Figure 8). At this flow rate, the maximum adsorption capacity value is 71%, which is suitable for FBA systems. The results also show that the synthesized EMA adsorbent performs well for high flow rates. As expected, 6 cm bed height is very suitable for commercial adsorption or EMA adsorption to achieve a high DBC.

The EMA adsorbents had an appropriate wet density of 2.6 g/mL. Obviously, the EMA particles with a higher density are suitable for major flow velocity. In comparison with the Streamline™ commercial adsorbents wet density of 1.15 g/mL, novel adsorbents had higher density and an equal range of adsorbents size, which results in less mass transfer resistance and high efficiency for application in fluidized-bed systems.

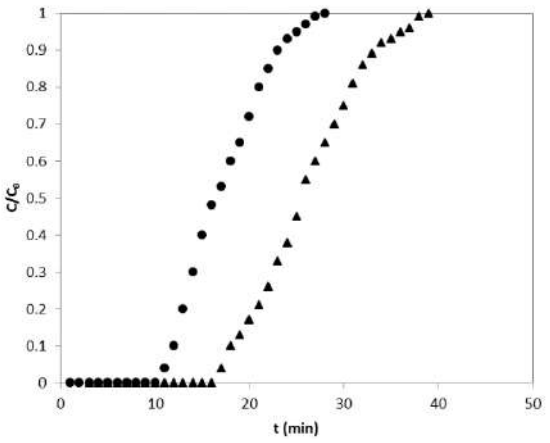

Figure 8. Lf breakthrough curves at 2-fold bed expansion in the FBA system: (●) EMA, and (▲) modified Streamline™

4. CONCLUSION

The preparation of EMA adsorbent was performed using a three-phase emulsion method, and the effects of contact time, adsorption isotherm, DBC, and breakthrough curve on the physical and fluidized bed properties of the beads were investigated. EMA adsorbent immobilized by dye-ligand and showed higher stability in adsorption processes. Suitable porosity, higher density, biodegradability, and ease of operation are the advantages of EMA adsorbent. As mentioned above, the obtained EMA pellets had an average size of 50-250 µm, a wet density of 2.6 g/mL, and a porosity of 90%. The synthesized adsorbent showed better adsorption efficiency under optimal conditions compared to modified Streamline™ with the same dye-ligand into the FBA system. AFM and OM techniques have been shown the formation of protein model, shape, and morphology of generated EMA adsorbents were to be spherical and micro-sized, respectively. Also, SEM images deliberated that the EMA adsorbents have the porous surface and the highly reticular structure of the adsorbent. Effect of contact time in batch adsorption shows that more than 75% of protein uptake of Lf nanoparticles occurred in the first half of the process that is a good accomplishment since the contact time in FBA systems is not too much. Adsorption isotherms were discussed in this work, and in contrast, the results coincided with the Langmuir model, which indicates that the adsorption was maintained in a single layer. Obviously, in the FBA system, DBC at 10% breakthrough curve and a fluid velocity of 348 cm/h were close to 71%, which helped column efficiency, so the engineered adsorbent has been proved the excellent potential for use in high flow rate fluidized-bed systems.

6. ACKNOWLEDGEMENT

The data for this article was extracted from a Ph.D. dissertation in chemical engineering. The authors gratefully acknowledge the facilities provided and support given by Nanotechnology Research Institute of Babol Noshirvani University of Technology.

7. REFERENCES

1. Wang, P., Dai, J., Ma, Y., Chen, L. and Pan, J., "Fabrication and evaluation of aminoethyl benzo-12-crown-4 functionalized polymer brushes adsorbents formed by surface-initiated atrp based on macroporous polyhipes and postsynthetic modification", ***Chemical Engineering Journal***, Vol. 380, (2020), 122495. https://doi.org/10.1016/j.cej.2019.122495

2. Shahavi, M.H., Hosseini, M., Jahanshahi, M. and Najafpour Darzi, G., "Optimization of encapsulated clove oil particle size with biodegradable shell using design expert methodology", ***Pakistan Journal of Biotechnology***, Vol. 12, (2015), 149-160.

3. Arahman, N., Fitri, R.A., Wirakusuma, A., Fahrina, A. and Bilad, M.R., "Adsorption performance of low-cost java plum leaves and guava fruits as natural adsorbents for removal of free fatty acids from coconut oil", ***International Journal of Engineering, Transactions A: Basics***, Vol. 32, No. 10, (2019), 1372-1378. doi: 10.5829/ije.2019.32.10a.06.

4. Vesali-Naseh, M., Barati, A. and Vesali Naseh, M.R., "Efficient copper removal from wastewater through montmorillonite-supported hydrogel adsorbent", ***Water Environment Research***, Vol. 91, No. 4, (2019), 332-339. doi: 10.1002/wer.1047.

5. Pérez Quiñones, J., Brüggemann, O., Kjems, J., Shahavi, M.H. and Peniche Covas, C., "Novel brassinosteroid-modified polyethylene glycol micelles for controlled release of

agrochemicals", ***Journal of Agricultural and Food Chemistry***, Vol. 66, No. 7, (2018), 1612-1619. doi: 10.1021/acs.jafc.7b05019.

6. Mofidian, R., Barati, A., Jahanshahi, M. and Shahavi, M.H., "Fabrication of novel agarose–nickel bilayer composite for purification of protein nanoparticles in expanded bed adsorption column", ***Chemical Engineering Research and Design***, Vol. 159, (2020), 291-299. doi: 10.1016/j.cherd.2020.03.024.
7. Mofidian, R., Barati, A., Jahanshahi, M. and Shahavi, M.H., "Agar-zinc adsorbent synthesis with nano cavities to absorb protein nanoparticles", in The 6th International Conference on Composites Characterization, Fabrication and Application (CCFA-6), Iran University of Science and Technology, Tehran, Iran. (2018 of Conference).
8. Hanish, H.H.H., Edrees, S.J. and Shukur, M.M., "The effect of transition metals incorporation on the structural and magnetic properties of magnesium oxide nanoparticles", ***International Journal of Engineering, Transactions A: Basics***, Vol. 33, No. 4, (2020), 647-656. doi: 10.5829/ije.2020.33.04a.16.
9. Alizadeh, M., Hosseinzadeh, K., Shahavi, M. and Ganji, D., "Solidification acceleration in a triplex-tube latent heat thermal energy storage system using v-shaped fin and nano-enhanced phase change material", ***Applied Thermal Engineering***, Vol. 163, (2019), 114436. doi: 10.1016/j.applthermaleng.2019.114436.
10. Rad, A.S., Samipour, V., Movaghgharnezhad, S., Mirabi, A., Shahavi, M.H. and Moghadas, B.K., "X12n12 (x= al, b) clusters for protection of vitamin c; molecular modeling investigation", ***Surfaces and Interfaces***, Vol. 15, (2019), 30-37. doi: /10.1016/j.surfin.2019.02.001.
11. Mashhadzadeh, A.H., Fathalian, M., Ahangari, M.G. and Shahavi, M.H., "Dft study of ni, cu, cd and ag heavy metal atom adsorption onto the surface of the zinc-oxide nanotube and zinc-oxide graphene-like structure", ***Materials Chemistry and Physics***, Vol. 220, (2018), 366-373. doi: 10.1016/j.matchemphys.2018.09.016.
12. Shahavi, M.H., Hosseini, M., Jahanshahi, M., Meyer, R.L. and Darzi, G.N., "Evaluation of critical parameters for preparation of stable clove oil nanoemulsion", ***Arabian Journal of Chemistry***, Vol. 12, No. 8, (2019), 3225-3230. doi: 10.1016/j.arabjc.2015.08.024.
13. Hosseini, M. and Shahavi, M.H., "Electrostatic enhancement of coalescence of oil droplets (in nanometer scale) in water emulsion", ***Chinese Journal of Chemical Engineering***, Vol. 20, No. 4, (2012), 654-658. doi: 10.1016/S1004-9541(11)60231-0.
14. Lashkenari, A.S., Najafi, M., Peyravi, M., Jahanshahi, M., Mosavian, M.T.H., Amiri, A. and Shahavi, M.H., "Direct filtration procedure to attain antibacterial tfc membrane: A facile developing route of membrane surface properties and fouling resistance", ***Chemical Engineering Research and Design***, Vol. 149, (2019), 158-168. doi: 10.1016/j.cherd.2019.07.003.
15. Shahavi, M.H., Hosseini, M., Jahanshahi, M., Meyer, R.L. and Darzi, G.N., "Clove oil nanoemulsion as an effective antibacterial agent: Taguchi optimization method", ***Desalination and Water Treatment***, Vol. 57, No. 39, (2016), 18379-18390. doi: 10.1080/19443994.2015.1092893.
16. Hosseini, M., Shahavi, M.H. and Yakhkeshi, A., "Ac & dc-currents for separation of nano-particles by external electric field", ***Asian Journal of Chemistry***, Vol. 24, No. 1, (2012), 181-184.
17. Kazemeini, H., Azizian, A. and Shahavi, M.H., "Effect of chitosan nano-gel/emulsion containing bunium persicum essential oil and nisin as an edible biodegradable coating on escherichia coli o157:H7 in rainbow trout fillet", ***Journal of Water and Environmental Nanotechnology***, Vol. 4, No. 4, (2019), 343-349. doi: 10.22090/jwent.2019.04.008.
18. Driessen, R.T., van der Linden, J.J.Q., Kersten, S.R.A., Bos, M.J. and Brilman, D.W.F., "Characterization of mass transfer in a shallow fluidized bed for adsorption processes: Modeling and supporting experiments", ***Chemical Engineering Journal***, Vol. 388, (2020), 123931. doi: 10.1016/j.cej.2019.123931.
19. Shahavi, M., Jahanshahi, M., Najafpour, G., Ebrahimpour, M. and Hosenian, A., "Expanded bed adsorption of biomolecules by nbg contactor: Experimental and mathematical investigation", ***World Applied Sciences Journal***, Vol. 13, No. 2, (2011), 181-187.
20. Taheri, E.S., Jahanshahi, M., Hamed Mosavian, M.T. and Shahavi, M.H., "Investigation of hydrodynamic parameters in a novel expanded bed configuration: Local axial dispersion characterization and an empirical correlation study", ***Brazilian Journal of Chemical Engineering***, Vol. 29, No. 4, (2012), 725-739. doi: 10.1590/S0104-66322012000400005.
21. Mofidian, R., Shahavi, M.H., Barati, A. and Jahanshahi, M., "Engineering mechanisms for protein nanoparticles adsorption", in The 2th International Conference on Modern Technologies in Sciences, Mazandaran, Iran. (2019 of Conference), 866-871.
22. Asadpour, R., Sapari, N.B., Hasnain Isac, M. and Kakooei, S., "Further study of adsorption of crude oils onto acetylated corn silk and its kinetics and equilibrium isotherm", ***International Journal of Engineering, Transactions B: Applications***, Vol. 32, No. 2, (2019), 229-235. doi: 10.5829/ije.2019.32.02b.07.
23. Najafpour, G.D., Shahavi, M.H. and Neshat, S.A., "Assessment of biological hydrogen production processes: A review", ***IOP Conference Series: Earth and Environmental Science***, Vol. 36, (2016), 012068. doi: 10.1088/1755-1315/36/1/012068.
24. Askari, M., Salehi, E., Ebrahimi, M. and Barati, A., "Application of breakthrough curve analysis and response surface methodology for optimization of a hybrid separation system consisting of fixed-bed column adsorption and dead-end depth filtration", ***Chemical Engineering and Processing-Process Intensification***, Vol. 143, (2019), 107594. doi: 10.1016/j.cep.2019.107594.
25. Shahavi, M.H., Najafpour, G.D. and Jahanshahi, M., "Hydrodynamic behaviour and biochemical characterization of a simple custom expanded bed column for protein purification", ***African Journal of Biotechnology***, Vol. 7, No. 23, (2008), 4334-4344.
26. Aminayi, P., Allaedini, G. and Tasirin, S.M., "Hydrodynamic studies of fluidized bed chemical vapor deposition reactors to produce carbon nano tubes via catalytic decomposition over co/pd mgo", ***International Journal of Engineering, Transactions C: Aspects***, Vol. 28, No. 12, (2015), 1693-1701. doi: 10.5829/idosi.ije.2015.28.12c.01.
27. Jahanshahi, M. and Shahavi, M.H., Advanced downstream processing in biotechnology, in Biochemical engineering and biotechnology, G. Najafpour Darzi, Editor. 2015, Elsevier. 495-526.
28. Asghari, F., Jahanshahi, M. and Ghoreyshi, A.A., "Preparation and characterization of agarose–nickel nanoporous composite particles customized for liquid expanded bed adsorption", ***Journal of Chromatography A***, Vol. 1242, (2012), 35-42. doi: 10.1016/j.chroma.2012.04.019.
29. Rezvani, A., Jahanshahi, M. and Asghari, F., "Characterization of a novel agarose–nickel composite matrix for protein nanoparticles affinity chromatography in expanded bed", ***Chromatographia***, Vol. 77, No. 19-20, (2014), 1267-1274. doi: 10.1007/s10337-014-2727-4.
30. Mohsenkhani, S., Jahanshahi, M. and Rahimpour, A., "Cross-linked κ-carrageenan polymer/zinc nanoporous composite matrix for expanded bed application: Fabrication and hydrodynamic characterization", ***Journal of Chromatography A***, Vol. 1408, (2015), 178-186. doi: 10.1016/j.chroma.2015.07.018.
31. Abatari, M.N., Emami, M.R.S., Jahanshahi, M. and Shahavi, M.H., "Superporous pellicular κ-carrageenan–nickel composite

beads; morphological, physical and hydrodynamics evaluation for expanded bed adsorption application", ***Chemical Engineering Research and Design***, Vol. 125, (2017), 291-305. doi: 10.1016/j.cherd.2017.07.012.

32. Shahavi, M.H., Najafpour, G. and Jahanshahi, M., "Design and fabrication of expanded bed adsorption column (named nbg-nano bio group) for nanobioproducts separation", **Patent no. IR49023**, 2008, Iran.
33. Shahavi, M.H., Jahanshahi, M., Najafpour, G.D., Ebrahimpour, M. and Hosenian, A.H., "Expanded bed adsorption of biomolecules by nbg contactor: Experimental and mathematical investigation", ***World Applied Sciences Journal***, Vol. 13, No. 2, (2011), 181-187.
34. Khavarpour, M., "Adsorption of malachite green from aqueous solution by nanozeolite clinoptilolite: Equilibrium, kinetic and thermodynamic studies", ***International Journal of Engineering, Transactions A: Basics***, Vol. 31, No. 1, (2018), 1-11. doi: 10.5829/ije.2018.31.01a.01.
35. Jafari, B., Khatamnejad, H., Shahavi, M.H. and Domeyri Ganji, D., "Simulation of dual fuel combustion of direct injection engine with variable natural gas premixed ratio", ***International Journal of Engineering, Transactions C: Aspects***, Vol. 32, No. 9, (2019), 1327-1336. doi: 10.5829/ije.2019.32.09c.14.
36. Alzeyadi, A., Al-Ansari, N., Laue, J. and Alattabi, A., "Study of biomass bottom ash efficiency as phosphate sorbent material", ***Civil Engineering Journal***, Vol. 11, No. 5, (2019), 2392-2401. doi: 10.28991/cej-2019-03091419.
37. Jaafar, J., Goh, P.S., Lau, W.J., Shahrin, S. and Fauzi Ismail, A.F., "Adsorptive removal of cr(vi) and cu(ii) ions from water solution using graphene oxide-manganese ferrite (gmf) nanomaterials", ***International Journal of Engineering, Transactions B: Applications***, Vol. 31, No. 8, (2018), 1341-1346. doi: 10.5829/ije.2018.31.08b.24.
38. Jahanshahi, M., Najafpour, G., Ebrahimpour, M., Hajizadeh, S. and Shahavi, M.H., "Evaluation of hydrodynamic parameters of fluidized bed adsorption on purification of nano-bioproducts", ***physica status solidi c***, Vol. 6, No. 10, (2009), 2199-2206. doi: 10.1002/pssc.200881737.
39. Chu, K.H., "Breakthrough curve analysis by simplistic models of fixed bed adsorption: In defense of the century-old bohart-adams model", ***Chemical Engineering Journal***, Vol. 380, (2020), 122513. doi: 10.1016/j.cej.2019.122513.
40. Mofidian, R., Barati, A., Jahanshahi, M. and Shahavi, M.H., "Optimization on thermal treatment synthesis of lactoferrin nanoparticles via taguchi design method", ***SN Applied Sciences***, Vol. 1, No. 11, (2019), 1339. doi: 10.1007/s42452-019-1353-z.
41. Theingi, M., Tun, K.T. and Aung, N.N., "Preparation, characterization and optical property of lafeo3 nanoparticles via sol-gel combustion method", ***SciMedicine Journal***, Vol. 1, No. 3, (2019), 151-157. doi: 10.28991/SciMedJ-2019-0103-5.
42. Bhatti, Z.A., Qureshi, K., Maitlo, G. and Ahmed, S., "Study of pan fiber and iron ore adsorbents for arsenic removal", ***Civil Engineering Journal***, Vol. 6, No. 3, (2020), 548-562. doi: 10.28991/cej-2020-03091491.
43. Palash, M.L., Jahan, I., Rupam, T.H., Harish, S. and Saha, B.B., "Novel technique for improving the water adsorption isotherms of metal-organic frameworks for performance enhancement of adsorption driven chillers", ***Inorganica Chimica Acta***, Vol. 501, (2020), 119313. doi: 10.1016/j.ica.2019.119313.
44. Seliem, M.K., Barczak, M., Anastopoulos, I. and Giannakoudakis, D.A., "A novel nanocomposite of activated serpentine mineral decorated with magnetic nanoparticles for rapid and effective adsorption of hazardous cationic dyes: Kinetics and equilibrium studies", ***Nanomaterials***, Vol. 10, No. 4, (2020), 684. doi: 10.3390/nano10040684.

Persian Abstract

چکیده

در این تحقیق، فرآیند تولید جاذب میکروکره آگارزی مهندسی شده که دارای سطوح با سایت‌های فعال مختلف جهت جذب نانوذرات پروتئین در سیستم بستر سیال است شرح داده شده است. همچنین ، انتخاب عالی نانوذرات پروتئینی ، ظرفیت جذب بالا و سرعت تعادل سریع از طریق جاذب‌های پلیمری سازگار با محیط زیست از اهداف مهم در اینجا بود. از این رو ، آگارز به عنوان یک پلیمر طبیعی ارزان و فراوان ، با یک ماده چگال فرومغناطیسی به همراه مولکول های رنگی به عنوان عامل جذب کننده، برای تولید جاذب میکروکره آگارزی مهندسی شده به کار گرفته شد. سپس عملکرد جاذب‌های تولید شده در سیستم ناپیوسته و بستر سیال مورد بررسی قرار گرفت. میکروسکوپ الکترونی روبشی، میکروسکوپ نیروی اتمی و میکروسکوپ نوری مورد استفاده قرارگرفتند. نتایج نشان داد شکل جاذب‌ها کروی هستند و دامنه توزیع آن ۵۰ تا ۲۵۰ میکرومتر ، تخلخل حدود ۹۰٪ و چگالی مرطوب ۲/٦ گرم در میلی لیتر است. سپس، برای مقایسه بهتر عملکرد جاذب‌های مهندسی شده در یک سیستم بستر سیال، لیگاند رنگی بر روی جاذب تجاری استریم لاین تثبیت شد و در شرایط یکسان مورد بررسی و مقایسه قرار گرفت. در جذب ناپیوسته، نتایج جذب نانوذره پروتئینی لاکتوفرین نشان از ظرفیت اتصال دینامیکی بالاتر جاذب میکروکره آگارز مهندسی شده داشت. همچنین، نتایج نشان داد که ۷۵٪ فرآیند جذب در نیم ساعت اول اتفاق می افتد که برای جذب نانوذرات پروتئینی در سیستم بستر سیال بسیار مناسب است. همچنین ، داده های تعادل جذب با مدل های جذب ایزوترمال ارزیابی شدند و مدل لانگمیر داده هـــا را بهتر توصیف می نماید و حداکثر جذب نزدیک به ٤٥/۳ میلی گرم در میلی لیتر جاذب بود. تست‌های جذب بستر سیال نشان داد که جاذب‌های مهندسی شده در سرعت جریان بالای خوراک ورودی نیز ظرفیت اتصال دینامیکی بالایی در مقایسه با جاذب های تجاری با سرعت جریان مشابه دارند. همچنین، نتایج بررسی منحنی های رخنه در سرعت جریان بالا ۳٤۸ سانتی متر بر ساعت خوراک ورودی حدود ۷۱ درصد محاسبه شد، بنابراین جاذب مهندسی شده پتانسیل خوبی برای استفاده در سیستم های بستر سیال با سرعت بالا را نشان داده است.

International Journal of Engineering

Journal Homepage: www.ije.ir

Mechanical Behavior of Hybrid Fiber Reinforced High Strength Concrete with Graded Fibers

S. R. R. Teja Prathipati*[a], C. B. K. Rao[a], N. R. Dakshina Murthy[b]

[a] *Department of Civil Engineering, National Institute of Technology Warangal, Telangana, India*
[b] *Civil Engineering Department, Chaitanya Bharathi Institute of Technology, Gandipet, Hyderabad, Telangana State, India*

P A P E R I N F O

Paper history:
Received 19 April 2020
Received in revised form 06 June 2020
Accepted 12 June 2020

Keywords:
Crimped Steel Fiber
Alkali-resistant Glass Fiber
High Strength Concrete
Hybrid Fiber Reinforced High Strength Concrete
Hybrid Graded Fiber Reinforced High Strength Concrete

A B S T R A C T

Brittleness, which was the inherent weakness in High Strength Concrete (HSC), can be avoided by reinforcing the concrete with discontinuous fibers. Reinforcing HSC with more than one fiber is advantageous in an overall improvement of the mechanical performance of the composite. In this experimental study, Hybrid Fiber Reinforced High Strength Concrete (HyFR-HSC) mixes were formed by blending single length glass fiber and single length steel fiber with a total volume fraction of 1.65% into the concrete and Hybrid Graded Fiber Reinforced High Strength Concrete (HyGrFR-HSC) mixes were obtained by mixing different lengths of glass fiber with different length of steel fibers at a total volume fraction of 1.65% into the concrete. A comparative study was made between HyFR-HSC and HyGrFR-HSC specimens to investigate the effect of fiber grading on strength properties and the uniaxial compressive behaviour of HSC with hybrid fibers. In both HyFRC and HyGrFRC mixes, glass fibers improved the pre-peak behaviour, and steel fibers improved the post-peak behaviour of concrete, thereby exhibiting a positive synergy in combining glass and steel fiber into the concrete. Among the two-hybrid FRC's, HyGrFRC outperformed HyFRC with substantial improvement in both strength and ductility. Among all the HyGrFRC mixes, HyGr9 mix, which contain a higher amount of long-length fibers exhibited better improvement in peak strain, ductility factor, total energy and toughness index. The replacement of single length of fibers with graded length fibers at higher volume fraction in HyFRC is useful in improving workability, thereby providing better fiber dispersion and thus enhances both the pre-peak and post-peak performance of the concrete. From this investigation, it can be inferred that grading of fibers improved the mechanical behaviour of HyFRC by exhibiting positive synergy from both fiber geometry and fiber type.

***doi**: 10.5829/ije.2020.33.08b.04*

NOMENCLATURE

PM	Plain Mix	GrFRC	Graded Fiber Reinforced Concrete
HSC	High Strength Concrete	HyFR-HSC	Hybrid Fiber Reinforced High Strength Concrete
FRC	Fiber Reinforced Concrete	HyGrFR-HSC	Hybrid Graded Fiber Reinforced High Strength Concrete (HSC)

1. INTRODUCTION

Due to the higher strength and dense microstructure of High Strength Concrete (HSC), its application in diversified structures reduces the overall dimensions of the structural element with reduced dead weight, making it technically and economically viable solution in large scale infrastructure projects. At larger stress levels, HSC materials have performed effectively [1]. Despite abundant advantages of High Strength Concrete (HSC) over normal strength concrete, HSC was considered to be brittle material due to its minor fracture process zone [2]. So there is a need to enhance the strength and ductility of HSC by adding fibers, which

*Corresponding Author Email: *praviteja@student.nitw.ac.in* (S. R. R. Teja Prathipati)

Please cite this article as: S. R. R. Teja Prathipati, C. B. K. Rao, N. R. Dakshina Murthy, Mechanical Behavior of Hybrid Fiber Reinforced High Strength Concrete with Graded Fibers, International Journal of Engineering (IJE), IJE TRANSACTIONS B: Applications Vol. 33, No. 8, (August 2020) 1465-1471

can control crack coalescence and propagation in concrete.

The mechanism of fiber action in the formation and propagation of crack growth in conventional FRCs is that after the formation of the first crack, the presence of fiber will prevent sudden failure and allows the load transfer across the crack [3,4]. The utilisation of discontinuous steel fibers into composite has improved the load-carrying capacity [5-7]. Addition of glass fibers in HSC was proved to be efficient in changing the failure mode of the composite from brittle to ductile [8]. Fiber-reinforced concretes produced today consist of a single fiber type that is only effective up to a limited level [9]. Reinforcing concrete with more than one fiber has been proved to be efficient in improving the strength and ductility of the composite [10].

Hybrid Fibre Reinforced concrete (HyFRC) is one of the versatile kinds of composite that uses more than one fiber, which improves the mechanical properties and arrests the multi-scale cracking in the concrete [11,12]. The use of steel fibers and glass fibers in the concrete under uniaxial stress will eliminate sudden failure as well as improves strength and toughness [13,14]. Fiber synergy can be achieved by combining different lengths, different diameters, and different Young's modulus of the fibers [15]. The inclusion of fibers of different lengths into the concrete will be useful in arresting cack at different levels, thereby improving the pre-peak and post-peak performance of the composite. The mechanical properties and the workability of the concrete will be enhanced by blending two different lengths of fibers instead of adding single length fiber at higher volume fraction [16]. The blending of different length fibers into concrete is termed as Graded Fiber Reinforced Concrete (GrFRC) [17]. GrFRC is a sub-classification of HyFRC. The strength and deformation behaviour under uniaxial stress was significantly improved by adding graded glass fibers into the concrete [17]. Addition of graded fibers into the concrete was proved to be advantageous and therefore, in this study hybridisation of graded steel fibers and graded glass fibers for use in concrete was attempted.

The majority of the research work was carried out on Hybrid Fiber Reinforced High Strength Concrete (HyFR-HSC) using different Young's modulus of the fibers and different geometries of fibers individually. According to some researchers, addition of fibers at lower volume is not much effective in enhancing the properties of concrete. But at higher volume fraction, due to the workability issues caused by higher relative surface area, there was not much improvement in the mechanical properties of the HyFRC. Therefore a new type of Hybrid FR-HSC called Hybrid Graded Fibre Reinforced High Strength Concrete (HyGrFR-HSC) in which different types of fibers are added in different lengths into the concrete was developed to overcome the problem of lower workability and improve the mechanical behaviour. A limited amount of research work was carried out on the behaviour of HyFR-HSC obtained by combining different types of fibers in graded form. In this study, the strength and uniaxial compressive behaviour of HyGrFR-HSC was investigated and reported. In this research work, crimped steel fibers 25mm and 50mm with aspect ratio 50 and 100 respectively and AR glass fibers 6 mm and 12 mm with aspect ratio 428 and 856 were used, and they are graded independently at first, and then they are hybridised to form HyGrFR-HSC. The objective of this research work is to study the behaviour of HyFR-HSC and HyGrFR-HSC under uniaxial stress.

Following the introduction section, the structure of the manuscript is designed as follows: Materials, mixing and curing, and testing methodology are described in section 2. Results and discussions are given in section 3 and finally concluding remarks are reported in section 4.

2. EXPERIMENTAL PROGRAM

Figure 1 represents the research methodology used in this study.

2. 1. Materials Ordinary Portland Cement (OPC) having a compressive strength of 53 Mpa with a specific gravity of 3.11, standard consistency of 33%, initial setting time is 48 mins, and final setting time is 125 mins was used in the mix. Fine aggregate from a nearby river source with a specific gravity of 2.68 and fineness modulus of 3.44 was used. Crushed granite of 10 mm nominal size as coarse aggregate with a specific gravity of 2.78 and fineness modulus of 7.1 was used. The water used for mixing and curing is Potable water. Superplasticizer used in the mix is Conplast SP430. Class F fly ash conforming to ASTM C618 [19] was used in the study. The fibers used in the study were

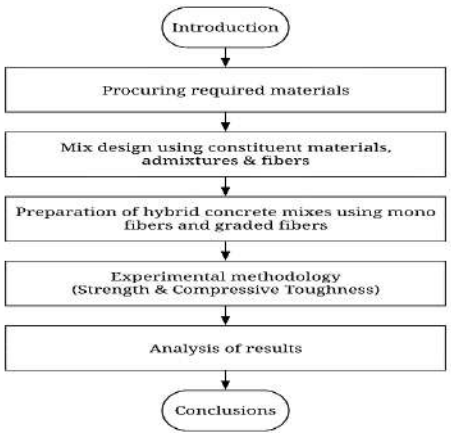

Figure 1. Research Methodology Flow chart

crimped steel fiber of length 25mm and 50mm with a constant diameter 0.5mm and Alkali Resistant glass fiber of length 6mm and 12mm with filament diameter 13.5 μ was used in the study. Table 1 provides information about the properties of fibers used in the study.

2. 2. Mix Proportions High strength concrete mix was designed as per ASTMC192 [20], and the mix proportions are tabulated in Table 2.

2. 3. Volume Proportions of Fibers Used In this investigation, alkali-resistant glass fibers of two different lengths and crimped steel fibers of two different lengths with a total fiber volume fraction of 1.65% were mixed in varying percentages and combinations to the concrete to obtain 13 HyFR-HSC and HyGrFR-HSC mixes. The first four HyFR-HSC mixes, Hy1 to Hy4 was obtained by blending glass and steel fiber in the mono form to the concrete. Mixes HyGr1 to HyGr9 mixes were obtained by hybridising graded glass and graded steel fibers into the concrete. Table 3 provides a schematic view of the experimental program used in this study.

2. 4. Mixing and Curing Fine and coarse aggregates were combined together into a homogeneous blend. Cement and fly ash were independently blended, and then glass fibres were scattered into the cement and fly ash blend. The contents were then placed into the pan mixer limit of 100 kg. Steel fiber was added to the mixer and mixed for another one minute. Finally, water was added along with superplasticiser and the contents thoroughly mixed. Proper homogeneous mixing was ensured by continuous mixing for 4-8 min. A slump test was conducted to ensure the workability of the plain concrete mix, HyFRC mixes and HyGrFRC mixes before casting. After the completion of the casting, all the specimens were kept to maintain the ambient conditions for 24 hours. The specimens were removed from the mould and were cured for 28 days.

TABLE 1. Fiber Properties

Property	Steel Fiber		Glass Fiber	
Length (mm)	25	50	6	12
Diameter (mm)	0.5	0.5	0.0135	0.0135
Aspect ratio	50	100	444	888
Elastic modulus (GPa)	200	200	73	73
Tensile strength (MPa)	1168	1168	1400	1400

TABLE 2. Mix Proportions

Cement (kg/m^3)	Flyash (kg/m^3)	Silica Fume (kg/m^3)	Water (kg/m^3)	Coarse Agg. (kg/m^3)	Fine Agg. (kg/m^3)
500	100	38	198	970	664

TABLE 3. Mix Designation

Specimen	Glass fiber length		Steel fiber length	
	6mm (G1)	12mm (G2)	25mm (S1)	50mm (S2)
	V_f (Glass) = 0.4%		V_f (Steel) = 1.25%	
PM	–	–	–	–
Hy1	100%	–	100%	–
Hy2	–	100%	100%	–
Hy3	100%	–	–	100%
Hy4	–	100%	–	100%
HyGr1	75%	25%	75%	25%
HyGr2	50%	50%	75%	25%
HyGr3	25%	75%	75%	25%
HyGr4	75%	25%	50%	50%
HyGr5	50%	50%	50%	50%
HyGr6	25%	75%	50%	50%
HyGr7	75%	25%	25%	75%
HyGr8	50%	50%	25%	75%
HyGr9	25%	75%	25%	75%

2. 5. Testing of Specimens A total number of forty-two cubical specimens (100 x 100 x 100 mm^3) and forty-two beam specimens (100 x 100 x 500 mm^3) for fourteen mixes were cast and tested for compressive strength and flexural strength. Forty-two cylindrical specimens (300mm height and 150mm diameter) were cast and tested to obtain stress-strain curves in compression. In this study, a 1000 kN servo-controlled test machine was used for testing specimens, which was shown in Figure 2.

3. RESULTS AND DISCUSSION

The uniaxial compressive and uniaxial tensile behaviour for the HyFR-HSC and HyGrFR-HSC specimens were discussed in the below sections.

3. 1. Compressive Strength For a total of 14 mixes, which include plain, hybrid, and hybrid graded mixes, the compressive strength values are given in Table 4. The compressive strength of the plain concrete mix was 78.65 Mpa. The compressive strength values for HyFR-HSC and HyGrFR-HSC are presented in Figure 3. The compressive strength improved marginally by using hybrid fibers at higher volume fraction. The percentage improvement of strength was

Figure 2. 1000kN servo-controlled test setup

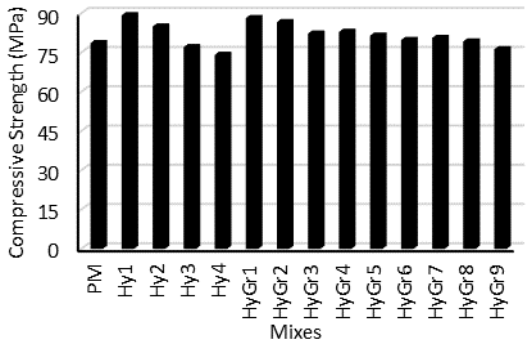

Figure 3. Compressive strength variation for different hybrid mixes

around 14%. The obtained values of compressive strength improvement were in good agreement with Vandewalle, L [11]. Among the hybrid mixes, the mixes which contain a higher amount of short fibers exhibited better performance in the enhancement of compressive strength, and this may be due to the better dispersion of short length fibers that arrest micro crack and improves the peak strength. In the hybrid combination, glass fiber with short length has contributed towards the increment of compressive strength, and this may be due to more number of fiber availability in the mix. Hy4 has the lowest compressive strength value among all the hybrid FR-HSC's, and this may be due to the balling effect of fibers, which was caused by using higher aspect ratio fibers at higher volume fraction.

3. 2. Flexural Strength The flexural strength of the plain concrete mix was 7.38 Mpa. The flexural strength values for HyFR-HSC and HyGrFR-HSC mixes are presented in Figure 4. The maximum improvement of flexural strength was 44% for the HyGr9 combination. Dawood et al. [10] also reported that similar improvement in flexural strength was observed with the addition of hybrid fibers. Hybrid fiber mixes exhibited a significant increase of flexural strength, and this may be due to the crack arresting mechanism by hybrid fiber, which delays the crack formation and propagation. It was evident that there was an apparent bridging effect provided by hybrid fibers, which reduced the crack widths and improved the flexural strength. The mixes which contain the longer fibers were much useful in the improvement of flexural strength, and this may be due to the enhanced bridging effect of larger cracks by longer fibers.

3. 3. Stress-Strain Behavior in Compression The uni-axial compressive stress-strain curves for plain concrete, HyFR-HSC, and HyGrFR-HSC specimens were drawn in Figure 5 for each mix by taking an average of three specimens. Addition of glass/steel fibers to the concrete exhibited a large number of cracks

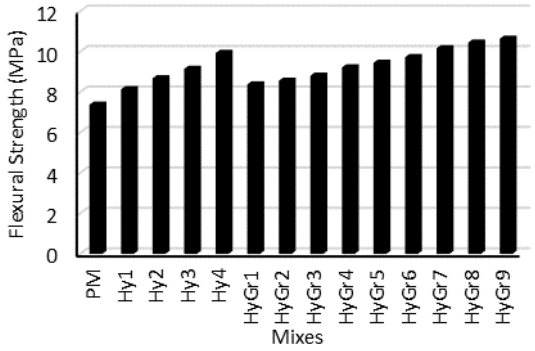

Figure 4. Flexural strength variation for different hybrid mixes

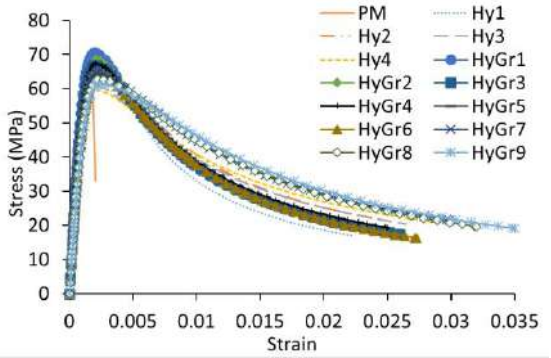

Figure 5. Uniaxial compressive stress-strain curve for hybrid mixes

before failure, thereby modifying the brittle failure pattern of the plain concrete. The softening part of the stress-strain curve of FR-HSC was improved with the addition of steel fiber/glass fiber.

The initial portion of the ascending part of the stress-strain curve of FRC was linear, and after reaching the peak stress, the stress values gradually decreased in the descending part at higher strain values. The salient properties that represent the uniaxial compressive stress-strain behaviour are peak stress, peak strain, ductility factor, and energy absorption capacity. From the stress-strain curves, for both the HyFR-HSC and HyGrFR-HSC specimens, the before said properties were extracted and presented in Table 4.

Plain concrete specimens without fibers exhibited brittle failure without any improvement in post-peak toughness. Both HyFR-HSC and HyGrFR-HSC specimens have shown ductile failure due to the bridging effect which was provided by hybrid fiber. Similar findings were given by Lihua Xu et al. [15], in which they stated that reinforcing concrete with hybrid fiber has a favorable effect in the improvement of the ductility. Glass fibers that were present in the hybrid FR-HSC were useful in the pre-peak zone by contributing towards the improvement of the peak stress of concrete by arresting the micro-cracks and the steel fibers will be effective in the post-peak behavior of concrete by capturing macro crack and by increasing toughness of the composite. Both the HyFR-HSC and HyGrFR-HSC specimens obtained by blending steel and glass fibers into the concrete arrested the cracks at different levels and improved both the strength and toughness of the composite.

With the addition of hybrid fiber into the concrete, the maximum improvement of peak stress was about 17% whereas the improvement of peak strain was 25%. By reinforcing hybrid fibers and hybrid graded fibers into the concrete, there was a significant improvement in the ductility factor, energy absorption and toughness index. Similar behaviour was observed by Ahmed et al. [18], in which they reported that hybrid fiber has a favorable reinforcement effect on uniaxial compression.

From Figure 6, it was clearly understood that the post-peak part of the stress-strain curve of HyGrFR-HSC specimens was significantly improved by hybridizing the graded fibers, which were not exhibited by HyFR-HSC specimens and the similar behaviour was reported by Kasagani, Hanuma et al. [16] . This was attributed to the multiple cracking failure pattern (formation of microcracks in the vicinity of the macro crack) of HyGrFR-HSC specimens. Among all the hybrid combinations, HyGr9 performed much better in terms of ductility factor, energy absorbed, and toughness index values.

TABLE 4. Salient Properties of Stress-Strain curve of Hybrid FRC under uniaxial compression

Mix	Peak Stress	Peak Strain	Ductility Factor	Total Energy (kJ/m^3)	Tough-ness Index
PM	60.73	0.00208	-	84.01	-
Hy1	70.85	0.02228	3.44	77 7.84	9.26
Hy2	67.79	0.02454	4.63	949.48	10.31
Hy3	60.74	0.02645	5.01	968.58	11.25
Hy4	59.41	0.02857	5.35	1018.18	12.12
HyGr1	69.61	0.02385	3.81	867.29	10.32
HyGr2	68.33	0.02385	3.89	906.67	10.79
HyGr3	66.93	0.02599	4.21	950.21	11.31
HyGr4	68.44	0.02498	4.25	942.27	11.22
HyGr5	67.27	0.02567	4.47	974.78	11.63
HyGr6	65.87	0.02730	4.54	1048.27	12.48
HyGr7	67.48	0.02985	4.94	1171.18	13.94
HyGr8	66.41	0.03212	5.52	1285.82	15.31
HyGr9	66.24	0.03558	5.82	1468.81	17.48

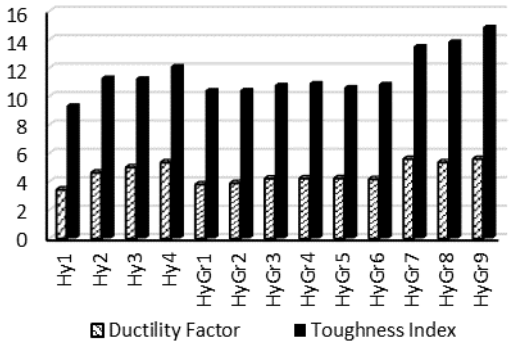

Figure 6. Ductility Factor and Toughness Index for different hybrid mixes

4. CONCLUSIONS

With an increasing in frequency of the applications of HyFRC in the present days, an understanding of the effect of different types of graded fibers on the properties of HyFRC is needed. In this paper, the mechanical behaviour of high strength concrete incorporating graded steel fiber and graded glass fiber in hybrid form was evaluated in terms of strength and toughness properties. Compressive strength, flexural strength, and uniaxial compressive stress-strain curves for HyFR-HSC and HyGrFR-HSC mixes have been investigated, and the following conclusions were drawn:

1. In both the HyFR-HSC and HyGrF-HSRC mixes, addition of short length glass fibers and short length

steel fibers have proved to be advantageous in the enhancement of peak stress, and this may be due to the more number of fiber availability with better dispersion in the composite.

2. HyGrFR-HSC mixes with a higher percentage of large fiber have exhibited significant improvement in flexural strength, and this may be due to the enhanced fiber bridging capacity of long-length fibers.

3. In HyFR-HSC and HyGrFR-HSC mixes, glass fibers improved the pre-peak behaviour of concrete by controlling the microcrack propagation and steel fiber is to enhance the post-peak response by seizing the broadening of macro crack.

4. Among the hybrid fiber mixes, HyGr9 performed much better in terms of failure strain, ductility factor, energy absorbed, and toughness index values performed better in all aspects.

5. The improvement in ductility, energy absorption, and toughness index of HyGrFR-HSC specimens was significant when compared to that of HyFR-HSC specimens at 1.65% fiber volume fraction, and this may be due to the advantage of hybridising the graded fibers.

Addition of graded steel and graded glass fibers into the high strength concrete have improved the ductility and toughness of the composite and thereby it can be used in the beam-column joints. Hybrid graded fiber-reinforced beam-column joints could be an excellent choice in the high seismic zones where high energy absorption capacity is required. From the above study, it can be deduced that utilisation of graded steel fibers and graded glass fibers in the HyFRC has proven to be a promising beneficial alternative to the use of mono fibers in the HyFRC.

5. REFERENCES

1. Ramtekkar, Gangadhar, Shirish Deo, and Badrinarayan Rath. "Durable glass fiber reinforced concrete with supplimentary cementitious materials." ***International Journal of Engineering, Transactions A: Basics,*** Vol. 30, No. 7, (2017), 964-971, doi: 10.5829/ije.2017.30.07a.05.
2. Gettu, Ravindra, Zdenek P. Bazant, and Martha E. Karr. "Fracture properties and brittleness of high-strength concrete." ***ACI Materials Journal,*** Vol. 87, No. 6, (1990), 608-618.
3. Wong, John Kok Hee, Sien Ti Kok, and Soon Yee Wong. "Fibers, Geopolymers, Nano and Alkali-Activated Materials for Deep Soil Mix Binders." ***Civil Engineering Journal,*** Vol. 6, No. 4, (2020), 830-847, doi: 10.28991/cej-2020-03091511.
4. Chowdary, Bhavita, V. Ramanamurty, and Rakesh J. Pillai. "Fiber reinforced geopolymer treated soft clay–An innovative and sustainable alternative for soil stabilization" ***Materials Today: Proceedings***, (2020), doi: 10.1016/j.matpr.2020.03.574
5. Majeet, Anas Hameed, and Ahmad Jabbar Hussain Alshimmeri. "The Performance of Self-Compacted High Strength Concrete Columns with Laced Steel Section" ***Civil Engineering Journal,*** Vol. 4, No. 11, (2018), 2606-2617, doi: 10.28991/cej-03091185.
6. Paluri, Yeswanth, Sudhakar Mogili, Heeralal Mudavath, and Rathish Kumar Pancharathi. "A study on the influence of steel fibers on the performance of Fine Reclaimed Asphalt Pavement (FRAP) in pavement quality concrete." ***Materials Today: Proceedings,*** (2020), doi: 10.1016/j.matpr.2020.03.147.
7. Khamees, Shahad S., Mohammed M. Kadhum, and Nameer A. Alwash. "Effects of Steel Fibers Geometry on the Mechanical Properties of SIFCON Concrete" ***Civil Engineering Journal***, Vol. 6, No. 1, (2020), 21-33, doi: 10.28991/cej-2020-03091450.
8. Hilles, Mahmoud M., and Mohammed M. Ziara. "Mechanical Behavior of High Strength Concrete Reinforced with Glass Fiber Reinforced Polymer" ***Journal of Engineering Research and Technology,*** Vol. 5, No. 3, (2018).
9. Betterman, L. R., C. Ouyang, and Surendra P. Shah. "Fiber-matrix interaction in microfiber-reinforced mortar." Advanced Cement Based Materials 2, No. 2, (1995), 53-61, doi: 10.1016/1065-7355(95)90025-X.
10. Dawood, Eethar Thanon, and Mahyuddin Ramli. "Contribution of hybrid fibers on the properties of high strength concrete having high workability", ***Procedia Engineering,*** Vol. 14 (2011): 814-820, doi: 10.1016/j.proeng.2011.07.0103.
11. Vandewalle, Lucie. "Hybrid fiber reinforced concrete." Measuring, monitoring and modeling concrete properties. Springer, Dordrecht, 2006. 77-82, doi: 10.1007/978-1-4020-5104-3_
12. Shubbar, Hasanain A., and Nameer A. Alwash. "The Fire Exposure Effect on Hybrid Reinforced Reactive Powder Concrete Columns", ***Civil Engineering Journal,*** Vol. 6.2 (2020), 363-374, doi: 10.28991/cej-2020-03091476.
13. Prathipati, SRR Teja, and C. B. K. Rao. "A study on the uniaxial behavior of hybrid graded fiber reinforced concrete with glass and steel fibers", ***Materials Today: Proceedings*** (2020), doi: 10.1016/j.matpr.2020.03.558.
14. Salim, Lamyaa Gh, Haider M. Al-Baghdadi, and Haitham H. Muteb. "Reactive Powder Concrete with Steel, Glass and Polypropylene Fibers as a Repair Material." ***Civil Engineering Journal***, Vol. 5, No. 11 (2019), 2441-2449, doi: 10.28991/cej-2019-03091422.
15. Xu, Lihua, Le Huang, Yin Chi, and Guodong Mei. "Tensile behavior of steel-polypropylene hybrid fiber-reinforced concrete." ***ACI Materials Journal***, Vol. 113, No. 2, (2016), 219, doi: 10.14359/51688641.
16. Kasagani, Hanuma, Sri Ram Ravi Teja Prathipati, and Chittem Butchi Kamiswara Rao. "Influence of Graded Glass Fibers on Strain Hardening and Strain Softening behaviour of GFRC under uniaxial stress." ***Magazine of Concrete Research***, (2019), 1-52, doi: 10.1680/jmacr.19.00303.
17. Kasagani, Hanuma, and C. B. K. Rao. "Effect of graded fibers on stress strain behaviour of Glass Fiber Reinforced Concrete in tension." ***Construction and Building Materials,*** Vol. 183 (2018), 592-604, doi: 10.1016/j.conbuildmat.2018.06.193.
18. Ahmed, Shaikh Faiz Uddin, and Hirozo Mihashi. "Strain hardening behavior of lightweight hybrid polyvinyl alcohol (PVA) fiber reinforced cement composites" ***Materials and Structures,*** Vol. 44, No. 6 (2011), 1179-1191, doi: 10.1617/s11527-010-9691-8.
19. ASTM C61-12a, Standard Specification for Coal Fly Ash and Raw or Calcined Natural Pozzolan for Use in Concrete, ASTM International, West Conshohocken, PA, (2012), www.astm.org.
20. ASTM C192 / C192M-16a, Standard Practice for Making and Curing Concrete Test Specimens in the Laboratory, ASTM International, West Conshohocken, PA, (2016), www.astm.org.

Persian Abstract

چکیده

شکنندگی، که ضعف ذاتی در بتن با مقاومت بالا (HSC) بوده ، با تقویت بتن با الیاف ناپیوسته می توان از آن جلوگیری کرد. تقویت HSC با بیش از یک فیبر در بهبود کلی عملکرد مکانیکی کامپوزیت سودمند است. در این مطالعه تجربی ، مخلوط بتن با مقاومت بالا از جنس فیبر ترکیبی (HyFR-HSC) با مخلوط کردن الیاف شیشه ای تک طول و الیاف فولادی تک طول با کسری از حجم ۱.٦٥ به داخل بتن و بتن با مقاومت بالا تقویت شده با فیبر ترکیبی تشکیل شد مخلوط (HyGrFR-HSC) با مخلوط کردن طول های مختلف الیاف شیشه ای با طول های مختلف الیاف فولادی در کسری از حجم کلی ۱.٦٥٪ در بتن بدست آمد. یک مطالعه مقایسه ای بین نمونه های HyFR-HSC و HyGrFR-HSC برای بررسی تأثیر درجه بندی فیبر بر خواص مقاومت و رفتار فشاری یک محوره HSC با الیاف ترکیبی انجام شد. در هر دو مخلوط HyFRC و HyGrFRC ، الیاف شیشه ای رفتار پیش از اوج را بهبود بخشیده و الیاف فولادی رفتار پس از اوج بتن را بهبود بخشیده و از این طریق یک هم افزایی مثبت در ترکیب شیشه و فیبر فولادی در بتن به نمایش می گذارند. در میان FRC دو هیبریدی ، HyGrFRC از پیشرفت HyFRC با پیشرفت چشمگیر در قدرت و انعطاف پذیری بالاتر عمل کرده است. در بین تمام مخلوط های HyGrFRC ، مخلوط HyGr9 ، که حاوی مقدار بیشتری از الیاف با طول طولانی است ، پیشرفت بهتری در کرنش اوج ، ضریب انعطاف پذیری ، کل انرژی و شاخص چقرمگی نشان می دهد. جایگزینی الیاف طول یکنواخت با الیاف طول درجه بندی شده در کسر حجمی بالاتر در HyFRC در بهبود کارآیی مفید است ، از این طریق پراکندگی بهتر فیبر را فراهم می کند و بدین ترتیب عملکرد قبل از اوج و پس از اوج بتن را افزایش می دهد. از این تحقیق ، می توان نتیجه گرفت که درجه بندی الیاف با نشان دادن هم افزایی مثبت از هر دو هندسه فیبر و نوع فیبر ، رفتار مکانیکی HyFRC را بهبود بخشیده است.

International Journal of Engineering

Journal Homepage: www.ije.ir

Numerical Analysis of Stress Distribution During Tunneling in Clay Stone Rock

D. H. Ali, H. O. Abbas*, T. H. Abdullah

Department of Civil Engineering, University of Diyala, Diyala, Iraq

P A P E R I N F O

Paper history:
Received 09 April 2020
Received in revised form 01 May 2020
Accepted 12 June 2020

Keywords:
Tunnel
Clay Stone
Stress
Numerical

A B S T R A C T

In recent years, modern technology has been applied to build tunnels by means of drilling machines (TBM) that were used for civil engineering work in large cities to reduce the harmful effects of spending on the surface of the earth significantly. To build the tunnel, numerical modeling was used on the basis of the finite element method to predict stress behavior during the tunnel construction process. Tunnel simulation model by using the numerical method (FEM) with the Hoek-Brown model, which includes calculating the behavior of predicting stress-that surrounds the tunnel and analysis during the process of building the tunnel and compared with the natural state of the rocks during the different tunnel construction stages. Vertical stresses at the top and bottom of the tunnel are reduced during the advance of tunneling while horizontal stresses are increased. TBM progression is reflected in phases through one to five by performing an axial symmetric FE analysis, math calculation results revealed significant stress changes occurring in rock regions near the boundary of the tunnel. In other words, proximity to rocks is mostly affected by the tunnel. These pressure variations decrease as you move away from the tunnel horizontally and the seams reach extremely small values for distances greater than (2D) meters from the edge of the tunnel, where D is the diameter of tunnel.

***doi**: 10.5829/ije.2020.33.08b.05*

1. INTRODUCTION

An increase in economic and social development made the need to build tunnels significant due to its multiple functions such as transportation and water supply. The construction and design of the tunnel is different from other engineering fields. The tunnel design procedures in a rock mass affect the strength of the rocks, pressure behavior, and other measures [1]. Shot concrete is a crucial component of tunnels and underground structures as protection. To determine the time-dependent nature of a tunnel boring machine (TBM) tunnel liner under high site stress a new fundamental model of sprayed concrete is being implemented. The Shotcrete model is based on a versatile plasticity system designed to more accurately view the non-linear and time-dependent behavior of concrete materials [2]. Horizontal rock strata is a geological state of rock that is often encountered in tunnel construction and has a major impact on tunnel construction, it is important to examine and study the stability of horizontal rock strata in tunnel construction to ensure the safety and efficiency of tunnel construction. By using the "Xishan Highway Tunnel" as the focus of study and using the numerical simulation method [3].

Thus, for the purpose of overcoming problems of insufficient information about ground conditions and in order to predict the condition of the land under loading after drilling, some have used numerical analysis [4, 5].

Modeling rock mass is a very difficult task due to interruptions, heterogeneous, and inflexible nature of the rock mass, using experimental and modern methods [6, 7]. The complex nature and various formations make rock blocks a difficult material for experimental and numerical modeling. The RS2 numerical modeling technique was used by analytical methods to validate the support proposed. The data obtained from field and laboratory test results were used for the classification of rock mass and the determination of rock mass unit qualities along the tunnel alignment. RMR described the rocks as good to bad, and Q-system moderate to very bad. The RMR suggested bolt support and Shotcrete mounted in RS2 software models decreases the total displacement

*Corresponding Author Email: *temimi71@yahoo.com* (H. O. Abbas)

Please cite this article as: D. H. Ali, H. O. Abbas, T. H. Abdullah, Numerical Analysis of Stress Distribution During Tunneling in Clay Stone Rock, International Journal of Engineering (IJE), IJE TRANSACTIONS B: Applications Vol. 33, No. 8, (August 2020) 1472-1478

and thickness of the plastic zone around the tunnel [8]. Site Response Analyses (SRA) will assess the seismic excitation at the surface to compensate for the site's unique soil properties. However, the results obtained are largely determined by the choice and setting of the model and by the depth of the soil layer considered. Proposes a streamlined 3D analytical approach, by OPENSEES platform use. Special attention has been paid to the role of the soil depth considered in determining the seismic input from the surface [9]. During the initial stages of drilling projects, detailed data are not available on strength characteristics, model deformation, on-site pressure, and hydrological rock masses [10].

Digital modeling is receiving more attention in civil and rock engineering to predict the response of the rock mass to various drilling activities [11]. Numerical methods are convenient, less expensive, and less time consuming to analyze redistributive stresses and their effects on rock mass behavior and design the structures are in the center of the environmental stone block. numerical methods mathematical equation rest in problems in governance and engineering Input parameters physical and strong determinants of rock parameters [12, 13]. A more detailed examination of stress concentrations around the tunnel and in areas close to it is permitted in three-dimensional analysis using numerical modeling. The effects of three-dimensional stress have proven to be an important factor when the tunnel side is present, especially advanced with regard to induced stress concentrations and rock strength degradation [14, 15].

In general, estimating site stresses requires detailed descriptions of site geology and considerable judgment. Models (physical or numerical) can be developed to explore the influence of parameters such as the rock's foundational model, loading date, critical geological structures, terrain, and boundary conditions on-site pressures. It is common practice to make two basic assumptions when estimating the stress state at any depth, z, in a rock mass. The first assumption is that the stress condition can be described with two components: vertical component, (σv), due to the rock's excess weight at this depth equal to γz, A uniform horizontal component, σh = (σH equals K times σv. The second assumption is that both σv and σh are two main stresses. Another expression often used in the literature for the coefficient of K is Ko = v / (1 -v) where v is the Poisson ratio of the rock.

This expression was derived by assuming (1) that the rock mass is half of an ideal linear homogeneous linear parallel area with the surface of the horizon, (2) that the rock mass is under gravity alone with the disappearance of horizontal positions, and (3) that the loading record has no effect on how it accumulated pressure on the site [16]. The main objective of this study is to predict the horizontal and vertical stresses around the tunnel during the advance of tunneling with TBM progress in the rocks.

2. CASE STUDY

The purpose of the numerical analysis of a mechanical tunnel model is that it takes into account the large number of operations performed during tunnel excavation and construction. The 3D object model consists of several different components such as rock parameters, rock layers, tunnel boring machine, hydraulic jacks, tunnel liner application, all of these parameters are analyzed and simulated in the 3D FEM model.

2. 1. Model Dimensions and Rock Properties

The simulation of the tunnel construction is carried out using FEM, and because the model is symmetric, half of the tunnel model is taken for calculations by a numerical solution. The tunnel diameter (D) assumes 6m and its length is 9m. The geometrical shape of the tunnel and the estimated network are shown in Figure 1.

The tunnel model depends on the actual data of the rock properties. The criteria obtained from the basic tests on the rock hole of the project and some other standards were adopted from literature [17]. The obtain data from field and laboratory tests of the project are shown in Table 1. In this study, the model has used the behavior of rock is the Hoek-Brown model (HB).

2. 2. Type of Element Used in Numerical Study In engineering problems (geotechnical problems) and in order to obtain accuracy, for the three-dimensional finite element, the grid with the nested four-dimensional nested elements is used which is also used to model the tunnel lining. The functions of the shape Ni has the size of the

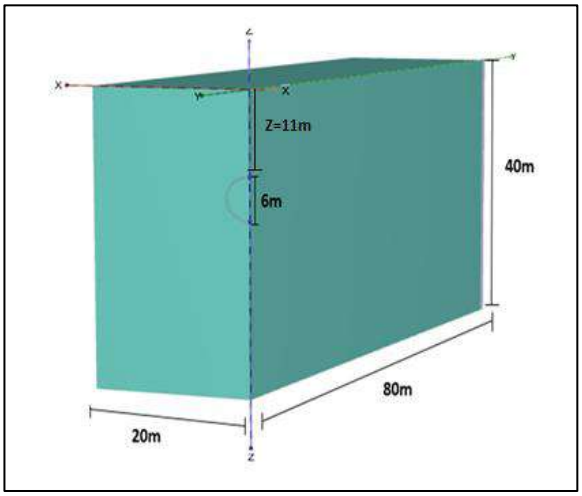

Figure 1. The geometry of the tunnel for the 3D model

TABLE 1. The rock parameters of the Hoek-Brown model (HB)

Depth(m)	40
Saturated unit weight of rock (kN\m³)	23
Unsaturated unit weight of rock (kN\m³)	23
Young's modulus×10^6 * (kN\m²)	14
Uni-axial compressive Strength×10^3 * (kN\m²)	25
Intack Rock parameter*	4
Geological Strength Index*	38
Disturbance factor	0
Poisson's Ratio *	0.3

*[17]

function equal to the unit in node i and zero in the other nodes. Interface elements are observed with a limited thickness, in some program output diagrams, but the coordinates of each node pair are identical in the formulation of the finite element (FE), meaning that the interface element has zero thickness. The stiffness matrix of trigonometric elements depends on the characteristics specified in the material data sets that were acquired by Gaussian integration using 6 integration points.

2. 3. Structural Elements Properties Tunnel boring machine (TBM) is designed as plate elements and is supposed to be 9m in length, and segmental tunnel liner is designed as plate elements. Table 2 shows the parameters of the tunnel machine [17]. In the concrete lining used, each part is assumed to be 1.5m wide, and so, TBM advances 1.5m in each severity of the tunneling stages. The segments of the concrete lining are formed by using structural elements with flexible linear behavior of the formed properties. The material properties of lining elements are shown in Table 3.

TABLE 2. Material of properties of the TBM [17].

Parameter	Unite	TBM
Thickness	Meter	0.35
Elastic Modulus	(kN\m^2)	23.0*10^6
Unit Weight	(kN\m^3)	70
Poisson's Ratio	-	0.1

TABLE 3. The material properties of the concrete lining element.

Parameter	Unite	Lining	TBM
Thickness	Meter	0.25	0.35
Elastic Modulus	(kN\m^2)	23.5 *10^6	23.0*10^6
Unit Weight	(kN\m^3)	25	70
Poisson's Ratio	-	0.1500	0.1

In this paper, the volume of the face pressure is determined in relation to the vertical pressure caused by the weight of the rock deposits and is related to the unit weight of the bentonite suspension while the volume of the pressure has been defined by increasing the face pressure at the crown of the tunnel. The pressure of the filling increases linearly from the crown of the tunnel to its reversal as a face pressure depending on the weight of the unit of the plaster material.

The first six drilling steps represent a 9-meter advance at long TBM, and the veneer elements are activated with the dedicated TBM material, then the liner is fixed by setting the liner material to the corresponding veneer elements [17].

2. 4. Mesh Generation In PLAXIS 3D, an unstructured, automatically generated network that can be chosen to improve the local and global network is used. PLAXIS 3D shows five network density options spread from a very rough mesh to a very fine mesh. In this paper, a medium network is applied. The network is refined in areas where stresses and strains are expected to be high and critical, i.e. the tunnel, the liner of the tunnel, and the surrounding rocks, as shown in Figure 2.

3. RESULTS AND DISCUSSION OF NUMERICAL MODEL

The modeling process for building a tunnel using TBM is a summary of the construction stages that include rock drilling and the installation of a lined concrete part. The results obtained from rock tunnel pressure by using a finite element method with rock failure criteria are the HB model, displaying the location of sections taken tunnel model at x-direction shown in Figure 3.

3. 1. Stresses of Section A-A This section represents the data through tunnel (x=0 with variations at x-direction=26.5m, and different depths z). It should be noted that the stress depth curves in this case show the vertical and horizontal stress at different depths, while y-

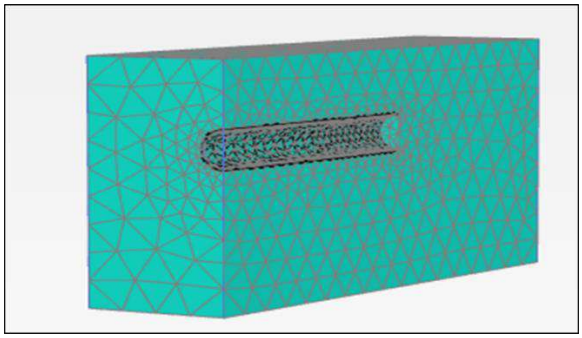

Figure 2. Medium type mesh of 3D geometrical of the tunnel for (HB) model

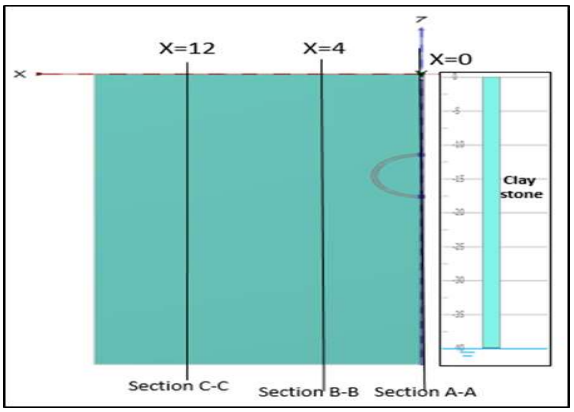

Figure 3. Displaying location of sections taken tunnel model at x-direction

direction = 26.5 with deviations and x-direction = 0 with deviations. The first stage marks the beginning of TBM construction work and the drilling of the first part of the tunnel liner, in addition to the following other phases that will serve as a model for 1.5m rendering.

Figure 4 represents the distribution of the vertical stresses during the construction stages of the tunnel model. In general, the vertical stress decreases with increasing the depth from all phases. During the advancing of TBM in rock, the vertical stress from the upper region of the tunnel begins less than native rock at a percentage of 75%. This is due to machine vibration of TBM and the effect of lateral stress. For the region under the tunnel, the vertical stress from all phases also less than native rock at percentage 42% and became close to the native rock with increasing the depth because the effect of tunneling is not significant. Figure 5 represents the total horizontal pressure distribution during the construction stages of the tunnel model. In general, the horizontal stress increase with increasing the depth from

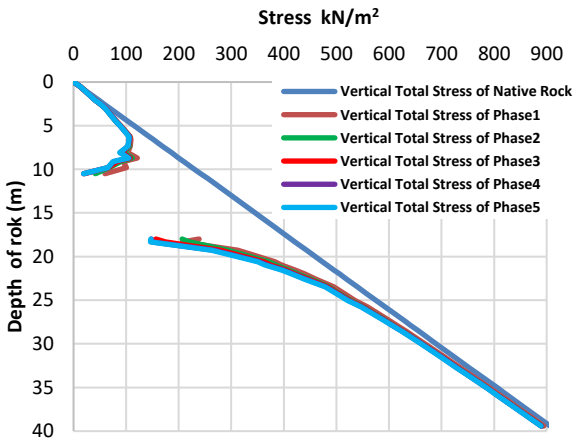

Figure 4. Distribution of the total vertical stress during construction phases of tunnel at x=0 with find deviations

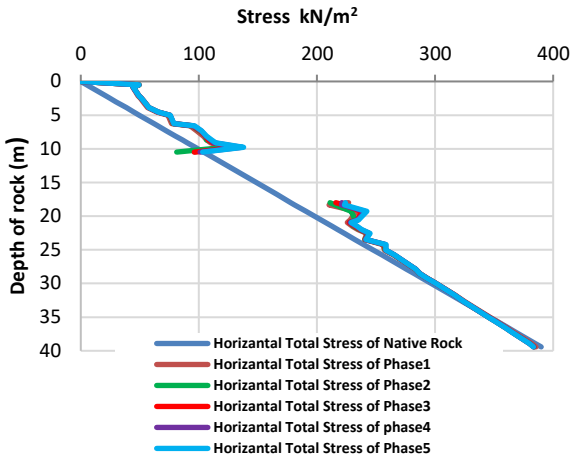

Figure 5. Distribution of the total horizontal stress during construction phases of tunnel at x=0 with find deviations

the native and all phases. During the advancing of TBM in rock, the horizontal stress from the upper region of the tunnel begins more than native rock at a percentage of 30%. This is due to machine vibration of TBM and the effect of horizontal ratio k. For the region under the tunnel the horizontal stress from all phases also more than native rock at percentage 22% and became close to the native rock after depth 30m because the effect tunneling is not significant beyond this depth.

3. 2. Stresses of Section B-B It is obvious from Figure 6 that the vertical stresses increase with increasing depth for native rock and all phases. During the advancing of TBM in rock the differences in vertical stress is begin approximately at a depth of 9m from ground surface. For the region between depth (9-19)m, the vertical stress of all phases is more than the native

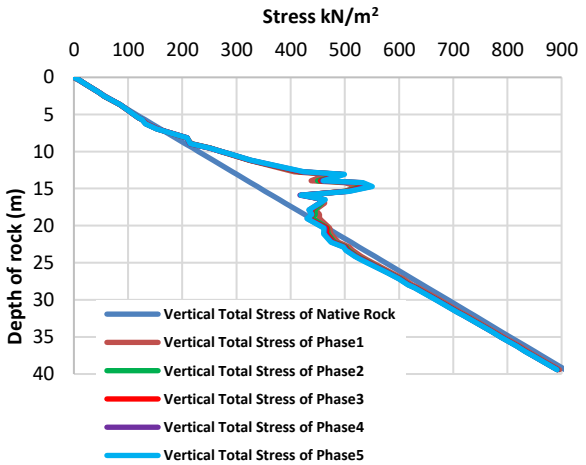

Figure 6. Distribution of the total vertical stress during construction phases of tunnel at x=4 with find deviations

rock at a percentage of 29%. This is due to tunneling in this region and the effect of lateral stresses. In addition, for the region between(19m and 30m) the vertical stress of all phases begins to decrease and become less than native rock at a percentage of 5%. This is because of lateral forces induced from TBM machine. Beyond the depth of 30m the vertical stress of native and all phases are similar, the effect of tunneling is not significant beyond this depth.

From Figure 7, it is obvious that the horizontal stress in the upper region of the tunnel can be seen the same behavior of deviation at all stages, at depth o.5m appear largely deviation due to several reason such as machine vibration (TBM) during drilling and the effect of horizontal ratio k. For the region between depth (7m-22m) the horizontal stress of phases less than the native rock at percentage 24% except phase one and phase two at depth(13m-15m) became more the native rock at percentage 26% for phase one and 3% for phase two and return less after this depth. This is due to tunneling in this region and the effect of horizontal ratio k. For the depth (22-40)m the horizontal stress of native rock and all phases are similar because the effect of tunneling is not significant beyond this depth.

3. 3. Stresses of Section C-C In this section, we focused on the distance from X-direction =12m Y-direction=26.5m and different depth of Z. It is obvious from Figure 8 that the vertical stresses of all phases close to the vertical stress of native rock because this region is located far away from the drilling zone of the tunnel.

Figure 9 shows the distribution of the horizontal stresses through the stages of building the tunnel model. In general, the overall horizontal stress behavior can be clearly observed and is the same as the direction of

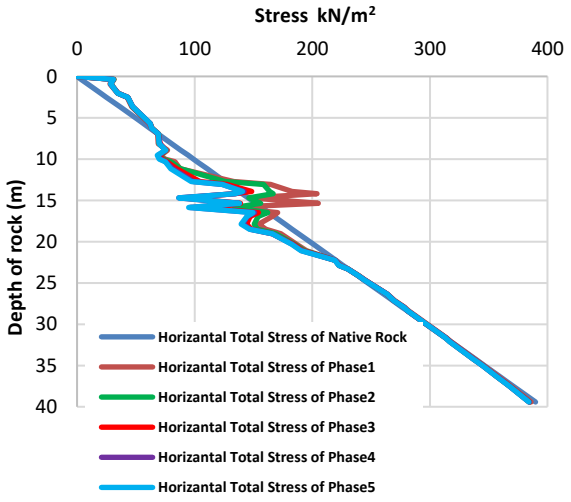

Figure 7. Distribution of the total horizontal stress during construction phases of tunnel at x=4 with find deviations

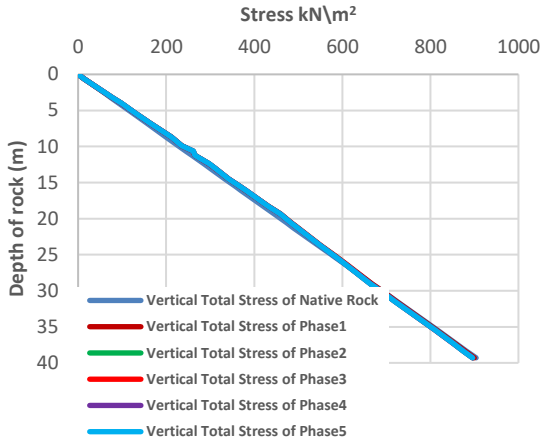

Figure 8. Distribution of the total vertical stress during construction phases of tunnel at x=12 with find deviations

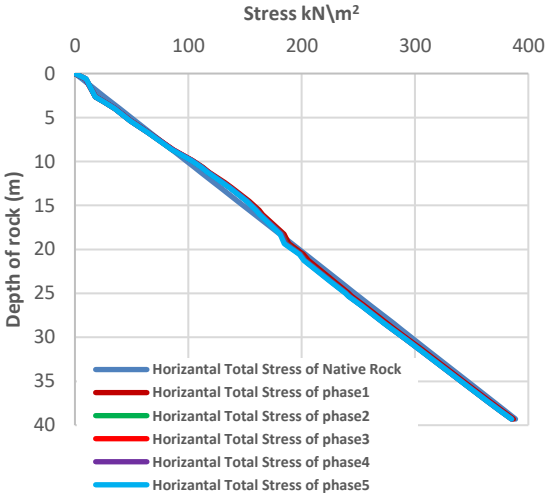

Figure 9. Distribution of the total horizontal stress during construction phases of tunnel at x=12 with find deviations

behavior for all stages with a slight difference between all stages. This is due to several reasons such as the distance is far away from the machine vibrations (TBM) during drilling of the tunnel, (the effect of the horizontal ratio (K).

4. CONCLUSIONS

In this study, the analysis focuses completely on the difference of state (pressure) before and after TBM construction. Thus, all the curves presented in this research are displayed rock stress conditions for pre-drilling state (original rock state) with rock stress during construction of the tunnel. The following points are drawn:

i. The vertical stress in the centreline of the tunnel(X/ D = 0), at the top of the tunnel for all phases, is 75% less than the original rocks, while at the bottom of the tunnel is 42% less than the original rocks. This is due to several reasons, including the vibrations of the TBM tunnelling machine during the progress of the tunnel and the effect of lateral pressure. As for the horizontal stress, the top of the tunnel is 30% larger than the original rocks, while the bottom of the tunnel is 22% more than the original rocks. This is due to the advancing of the TBM machine and the effect of horizontal ratio k.

ii. At each side of the tunnel (X/ D = 0.67), the vertical stress values for the phases of the original rocks within the depth are increased from 9 m to 19 m, with an increase of 29%, due to the tunnel in this area and the side effect pressure after depth (19-30)m. The vertical pressure of all stages has become 5% less than the original rock due to the effect of induced stress, after depth 30m the stress values of the original rock have converged with the rest of the stages. As for the horizontal stress, it will be at all stages less than the original rocks at depth from 7m to 22m, with a decrease of 24% except for the depths from 13m to 15m. Then it returns to diminishing after this depth 22m and the reason for that is the presence of the tunnel in this area and the effect of the ratio of horizontal stress k until the values of horizontal stress for all stages converge with the stress of the original rocks.

At each side of the tunnel (X/ D =2), the vertical stress values for all the phases close to the original rocks, due to this region away from the drilling zone. As for the horizontal stress, it will be at all stages close to the original rocks with slightly difference due to the effect of the ratio of horizontal stress k. Tunneling progress is not affected by stresses in rock mass beyond (X/ D=2).

5. REFERENCES

1. Maynar, M.J. and Rodríguez, L.E., "Discrete numerical model for analysis of earth pressure balance tunnel excavation", ***Journal of Geotechnical and Geoenvironmental Engineering***, Vol. 131, No. 10, (2005), 1234-1242. https://doi.org/10.1061/(ASCE)1090-0241(2005)131:10(1234)
2. Shaalan, H.H., Azit, R. and Ismail, M.A.M., "Numerical analysis of tbm tunnel lining behavior using shotcrete constitutive model", ***Civil Engineering Journal***, Vol. 4, No. 5, (2018), 1046-1065. Doi.org/10.28991/cej-0309155
3. Zhang, N., Wang, W., Yang, Z. and Zhang, J., "Numerical simulation on the stability of surrounding rock of horizontal rock strata in the tunnel", ***Civil Engineering Journal***, Vol. 3, No. 12, (2017). Doi.org/10.28991/cej-030948
4. Beer, G., "Numerical simulation in tunnelling, Springer Science & Business Media, (2003). https://doi.org/10.1007/978-3-7091-6099-2
5. Jing, L. and Hudson, J., "Numerical methods in rock mechanics", ***International Journal of Rock Mechanics and Mining Sciences***, Vol. 39, No. 4, (2002), 409-427. https://doi.org/10.1016/S1365-1609(02)00065-5
6. Harrison, J.P., Hudson, J.A. and Popescu, M., "Engineering rock mechanics: Part 2. Illustrative worked examples", ***Appl. Mech. Rev.***, Vol. 55, No. 2, (2002), B30-B31. https://doi.org/10.1115/1.1451165
7. Jing, L., "A review of techniques, advances and outstanding issues in numerical modelling for rock mechanics and rock engineering", ***International Journal of Rock Mechanics and Mining Sciences***, Vol. 40, No. 3, (2003), 283-353. https://doi.org/10.1016/S1365-1609(03)00013-3
8. Akram, M.S., Ahmed, L., Ullah, M.F., Rehman, F. and Ali, M., "Numerical verification of empirically designed support for a headrace tunnel", ***Civil Engineering Journal***, Vol. 4, No. 11, (2018), 2575-2587. Doi.org/10.28991/cej-0391182
9. Forcellini, D., Tanganelli, M. and Viti, S., "Response site analyses of 3d homogeneous soil models", ***Emerging Science Journal***, Vol. 2, No. 5, (2018), 238-250. Doi.org/10.28991/esj-2018-01148
10. Andriani, G.F. and Parise, M., "Applying rock mass classifications to carbonate rocks for engineering purposes with a new approach using the rock engineering system", ***Journal of Rock Mechanics and Geotechnical Engineering***, Vol. 9, No. 2, (2017), 364-369. https://doi.org/10.1016/j.jrmge.2016.12.001
11. Vakili, A., "An improved unified constitutive model for rock material and guidelines for its application in numerical modelling", ***Computers and Geotechnics***, Vol. 80, No., (2016), 261-282. https://doi.org/10.1016/j.compgeo.2016.08.020
12. Bobet, A., "Numerical methods in geomechanics", ***The Arabian Journal for Science and Engineering***, Vol. 35, No. 1B, (2010), 27-48.
13. Rasouli, M., "Engineering geological studies of the diversion tunnel, focusing on stabilization analysis and support design, iran", ***Engineering Geology***, Vol. 108, No. 3-4, (2009), 208-224. https://doi.org/10.1016/j.enggeo.2009.07.007
14. Abel, J.F. and Lee, F.T., "Stress changes ahead of an advancing tunnel", in International Journal of Rock Mechanics and Mining Sciences & Geomechanics Abstracts, Elsevier. Vol. 10, No. 6, (1973), 673-697. https://doi.org/10.1016/0148-9062(73)90013-2
15. Martin, C.D., "Seventeenth canadian geotechnical colloquium: The effect of cohesion loss and stress path on brittle rock strength", ***Canadian Geotechnical Journal***, Vol. 34, No. 5, (1997), 698-725. https://doi.org/10.1139/t97-030
16. Hoek, E. and Brown, E., "Underground excavations in rock. Inst. Of mining and metallurgy", Stephan Austin And Sons London, 527s, (1980). http://worldcat.org/isbn/0900488557
17. Brinkgreve, R. and Vermeer, P., "Plaxis 3d-finite element code for soil and rocks analysis", Balkema, Rotterdam, The Netherlands, (2012).

Persian Abstract

چکیده

در سالهای اخیر از فن آوری مدرن برای ساخت تونل ها با استفاده از ماشین های حفاری (TBM) استفاده شده است که برای کارهای مهندسی عمران در شهرهای بزرگ مورد استفاده قرار می گرفت تا اثرات مضر هزینه ها را روی سطح زمین بطور قابل توجهی کاهش دهد. برای ساخت تونل ، از مدل سازی عددی بر اساس روش المان محدود برای پیش بینی رفتار تنش در طی مراحل ساخت تونل استفاده شده است. مدل شبیه سازی تونل با استفاده از روش عددی (FEM) با مدل هوک–براون ، که شامل محاسبه رفتار پیش بینی استرس–است که در طی فرایند ساخت تونل ، تونل و آنالیز را احاطه کرده و با وضعیت طبیعی سنگها در طول مراحل مختلف ساخت تونل. تنش های عمودی در بالا و پایین تونل در طول پیشروی تونل زنی کاهش می یابد در حالی که تنش های افقی افزایش می یابد. پیشرفت TBM در مراحل از طریق یک تا پنج با انجام یک تجزیه و تحلیل متقارن محوری محور FE منعکس می شود ، نتایج محاسبه ریاضی تغییرات تنش قابل توجهی را در مناطق سنگی نزدیک مرز تونل نشان می دهد. به عبارت دیگر ، نزدیکی به سنگها بیشتر تحت تأثیر تونل قرار دارد. این تغییرات فشار با کاهش فاصله از تونل به صورت افقی کاهش می یابد و درزها برای مسافت های بیشتر از (D۲) متر از لبه تونل ، جایی که D قطر تونل است ، به مقادیر بسیار کمی می رسند.

IJE TRANSACTIONS B: Applications Vol. 33, No. 8, (August 2020) 1479-1490

International Journal of Engineering

Journal Homepage: www.ije.ir

Ranking Passive Seismic Control Systems by Their Effectiveness in Reducing Responses of High-Rise Buildings with Concrete Shear Walls Using Multiple-Criteria Decision Making

M. S. Barkhordari, M. Tehranizadeh*

Department of Civil and Environmental Engineering, Amirkabir University of Technology, Tehran, Iran

P A P E R I N F O

Paper history:
Received 09 April 2020
Received in revised form 21 April 2020
Accepted 12 June 2020

Keywords:
Concrete Shear Walls
Multiple-Criteria Decision-Making Method
Opensees
Passive Control Systems
Tall Buildings

A B S T R A C T

In recent decades, the dual systems of steel moment-resisting frames and RC shear walls have found extensive application as lateral load-resisting systems for high-rise structures in seismically active areas. This paper investigated the effectiveness of tuned mass damper (TMD), viscous damper, friction damper, and the lead-core rubber bearing in controlling the damage and seismic response of high-rise structures with concrete shear walls. Five buildings (10, 15, 20, 25, and 30-story) with passive seismic control systems were analyzed in OpenSees using 50 seismic records. The structural responses (acceleration, drift, displacement, velocity, and base shear) were adopted as the criteria. The criteria were nondimensionalized by defining a measure to establish a relationship between the inputs (ground motions) and outputs (structural responses). At the end, Multi Criterion Decision Making (MCDM) method was employed to rank the passive seismic control systems and select the best one. The results showed application of the multiple-criteria decision-making methods in selecting a seismic upgrading strategy and earthquake engineering.

***doi**: 10.5829/ije.2020.33.08b.06*

NOMENCLATURE

D	seismic design category	S_S	maximum considered earthquake (MCE) spectral acceleration at short periods (g)
I	risk category	S_1	maximum considered earthquake (MCE) spectral acceleration at 1-s period (g)
EDP	Engineering Demand Parameter	Sa	seismic scale factor
x_{ij}	element of the decision matrix	r_{ij}	element of the normalized matrix
E_j	entropy of each criterion	m	number of alternatives
n	number of criteria	w_j	weight of each criterion
$[R]$	normalized decision matrix	d_j	uncertainty of jth criterion
$[V]$	weighted normalized decision matrix	C_j	relative distance to positive ideal alternative
S_i^+, S_i^-	distance from positive and negative ideal alternatives	$A^{(+)}, A^{(-)}$	Positive and negative ideal criterion

1. INTRODUCTION

In recent decades, the dual systems of steel moment-resisting frames and RC shear walls have found extensive application as lateral load-resisting systems for high-rise structures in seismically active areas and regions where buildings are exposed to high winds. This system is commonly used in residential, office, and hospital buildings. The underlying reason behind using a steel moment-resisting frame instead of a concrete moment-resisting frame is higher steel strength, smaller cross-section, and easy implementation. Moreover, the

*Corresponding Author Institutional Email: *tehranizadeh@aut.ac.ir* (M. Tehranizadeh)

Please cite this article as: M. S. Barkhordari, M. Tehranizadeh, Ranking Passive Seismic Control Systems by Their Effectiveness in Reducing Responses of High-Rise Buildings with Concrete Shear Walls Using Multiple-Criteria Decision Making, International Journal of Engineering (IJE), IJE TRANSACTIONS B: Applications Vol. 33, No. 8, (August 2020) 1479-1490

concrete curing process in reinforced concrete moment-resisting frames can affect its quality. On the other hand, the concrete shear wall is coupled with the steel moment-resisting frame to enhance structural resistance to lateral loads exerted by wind, earthquake, or the reduction of cross-section area. Structures equipped with this system typically perform well against collapse [1]. Nevertheless, they might suffer from severe damages from significant lateral loads exerted by an earthquake or the wind, which can cause substantial economic losses in turn. An example would be the impacts of the Christchurch Earthquake on structures with this system [2]. This earthquake caused considerable damage to several buildings with the shear wall-frame dual lateral resisting system. Since the repair of the concrete shear wall is complicated and may impair the structural performance, it was decided to demolish several shear wall-reinforced structures, inflicting economic and social burdens to many urban areas.

Seismic energy-dissipation mechanisms are commonly considered in design techniques. For example, considering specific places for plastic hinges (at the base of the shear wall and two ends of the beam) allows these points to enter the nonlinear area and energy dissipation in them. An alternative method for energy dissipation is the use of energy dissipation devices. Each device has a specific dissipation mechanism. Madsen et al. [3] investigated the effect of using dampers in different areas of coupling shear walls and found that the placement of dampers between two walls and near the connective beam results in the improvement of responses. Faridani and Capsoni [4] investigated the effects of using viscous damping on coupled shear walls with flexural and shear mechanisms. Analysis results showed that the bending and shear damping mechanisms performed better than the linear classical damping. Ahmed [5] used fluid viscous dampers in reinforced-concrete core wall buildings and showed the reduction of deformation, rotation, and energy demands. Hejazi et al. [6] analyzed structures with concrete shear walls under seismic loading using a 3D model. They sought an optimal place for viscous dampers and found that its placement over the shear wall frame resulted in maximum reduction of placement and element loading. Muscat [7] carried out similar studies. Aydin et al. published a paper in which they investigated the optimum design of viscous dampers in multistorey buildings [8]. Cetin et al. [9] carried out similar studies. The TMD is another type of damper used and investigated by researchers to control the responses of concrete moment-resisting frames [10–13]. For example, Hessabi et al. [14] have examined the application of the tuned mass dampers for improving the performance of base-isolated structures. Chung et al. [15] proposed a new friction damper to control the responses of the RC shear wall system. They showed that the performance of the new friction damper was higher than the coupled wall with a rigid beam. Ahn et al. [16], Bagheri and Oh [17] also conducted similar studies. Base isolators are another structure control strategy. Osgooei et al. [18] used rectangular fiber-reinforced elastomeric isolators to control the responses of a structure with a concrete shear wall and showed that the maximum response is considerably reduced in a structure with an isolator. There are similar studies into the effect of isolators on the response of structures with concrete shear walls [19, 20]. Another critical topic is concrete shear wall modeling. Previous studies relied on certain models for macro modeling of concrete shear walls that were incapable of taking into account the interaction between axial/flexural and shear behavior. Experimental studies have shown the effect of shear deformation even in the responses of slender walls [21–24]. Ignoring the interactions between axial, flexural, and shear loads results in an underestimation of flexural compressive strains and overestimation of lateral load-resisting capacity and shear load demand in the plastic hinge area [25–27]. In addition to the importance of controlling failure and collapse in concrete shear walls, it is essential to reduce the damages of shear wall components. Therefore, there is no clear solution to the problem of selecting the (more efficient) energy dissipation systems between dampers and isolators. As a result, this paper intends to investigate and rank dampers and isolators' effectiveness in controlling and reducing damages in concrete shear walls. On the other hand, such factors as diverse selection criteria and effective parameters (e.g., effect of frequency content of ground motions) make the decision-making problematic to the extent that the existing criteria no longer facilitate the selection or ranking of optimal alternatives and the use of more straightforward methods. As a result, the most common weighting method (entropy weigh method) and multiple attribute decision making method (MCDM) (TOPSIS-Technique for Order Preference by Similarity to Ideal Solution) are employed [28–30].

2. BUILDING SPECIFICATIONS

Five buildings (10, 15, 20, 25, and 30-story) were examined in this paper. The employed systems for these buildings are concrete shear wall-steel frame dual lateral resisting system. Figure 1 shows the typical plan and elevation of the buildings. The building plan consisted of five bays having a width of 4m. The typical height of each story is 4m. The design dead and live loads are, respectively, 5.5 and $2KN/m^2$. The compressive strength of concrete used in wall is assumed to be $40MPa$. The longitudinal rebars with a yield stress of $470MPa$ and the transverse rebars as well as stirrups with a yield stress of $430MPa$ are used as reinforcement. The nominal yield strength of the steel (the steel beams

and columns of the frame) is assumed to be $350MPa$. The dimensional details of the beams, columns, and rebar sections of the concrete shear wall are presented in Appendix A. Damping induced by the structural components (concrete shear wall, beams, and columns) are considered to be 2% and applied using the Rayleigh damping. The gravity framing is considered using the leaning column which is linked to the main structure (Figure 2). Rigid truss elements are used to link the shear wall-steel frame and leaning columns and transfer the P-Delta effect. Table 1 characterizes the building site and design parameters. The design was conducted based on ACI 318 and ASCE 7 [31, 32]. The building was designed based on the modal response spectrum analysis [32]. The first 15 modes were used in the design.

Four different systems were designed and used (viscous damper, friction damper, tuned mass damper, and lead-rubber isolation bearing) for controlling structural response [33]. A similar target damping was considered for all systems-dampers and LRB isolators. In other words, isolators and dampers were designed to provide a 15% damping. Tables 2-5 present the passive seismic control systems specifications. The modal periods of the buildings are shown in Table 6. The viscous damper is modeled with a Two Node Link Element using OpenSees [34, 35]. This element follows a viscous damper hysteretic response [36]. To simulate the friction damper in OpenSees an equivalent uniaxial material composed of different materials that are already available in the OpenSees library with a Two Node Link Element are used [37]. The LRB isolator is modeled with a ZeroLength Element and a uniaxial KikuchiAikenLRB material object. This material model produces nonlinear hysteretic curves of lead-rubber bearings [38]. To simulate the nonlinear response of the reinforced concrete shear walls, a nonlinear Timoshenko element and a nDMaterial MCFT material are utilized [24]. Tuned mass damper is modeled with a ZeroLength Element and Viscous and Elastic materials [39]. Columns and beams are modeled using DispBeamColumn elements, Steel02 material, and Concrete02 material [34, 35].

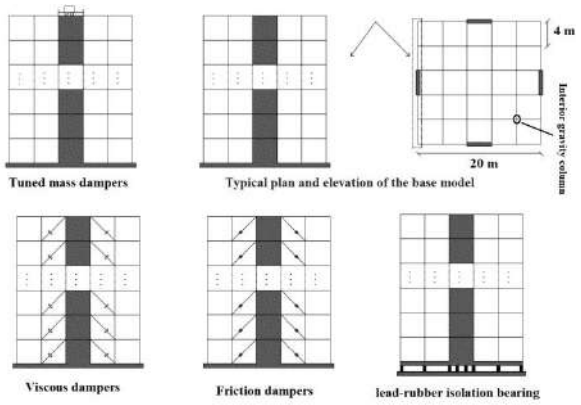

Figure 1. Typical plan and elevation of buildings

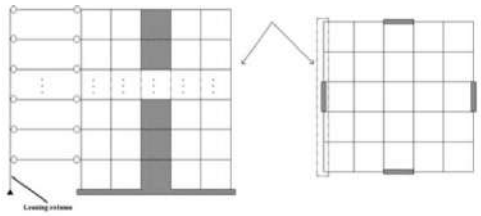

Figure 2. Modeling gravity framing using the leaning column

TABLE 1. Strouhal number for different geometric cases

Latitude	Longitude	Seismic design Cat.	Risk Cat.	Soil classification	S_S (g)	S_1 (g)
35.653 $\circ N$	-120.440 $\circ W$	D	I	D	1.5	0.6

TABLE 2. Viscosity coefficient of nonlinear viscous dampers

Story	10	15	20	25	30
$C\frac{KN\cdot sec^{0.5}}{m^{0.5}}$	400	597	611	810	992

TABLE 3. Slip-load of friction dampers

Story	10	15	20	25	30
Yield strength (slip load) KN	240	170	130	141	150

TABLE 4. Tuned mass dampers

Story	10	15	20	25	30
Mass (ton)	30	45	60	75	90
Stiffness (KN/m)	384	342.5	217.5	248.1	206
C_d $(N.sec/m)$	22550	26050	26784	28728	28512

TABLE 5. Lead-rubber isolation bearing

Story	10	15	20	25	30
Area of rubber (m^2)	0.385	0.442	0.570	0.7	1.227
Thickness of rubber (m)	0.5	0.65	0.8	0.95	1.15
Area of lead plug (m^2)	0.0201	0.024	0.038	0.038	0.057
Yield stress of lead plug $(N/m^2)\times 10^6$	8.82				
Shear modulus of rubber $(N/m^2)\times 10^4$	64				

TABLE 6. Modal periods of the prototype buildings

	Modal periods (sec)				
Story	**10**	**15**	**20**	**25**	**30**
Fixed based	1.61	2.66	3.17	3.8	4.3
Friction	0.98	1.59	1.86	2.08	2.63
LRB	1.81	2.98	3.39	3.89	4.38
TMD	1.79	2.98	3.41	4.06	4.6
Viscous	1.63	2.81	3.22	3.82	4.34

Given that the frequency content of earthquakes differed, which in turn affected the structural responses. This study investigated structures using 50 seismic records. Details of seismic records are presented in Appendix A. Earthquake records with a velocity pulse in the near field are selected from the database of the Pacific Earthquake Engineering Research (PEER) [40]. The minimum magnitude of near-field records is taken as 6.0 and near-field records are within a distance less than 15km to the fault. Given these criteria, total 18 earthquake records (the near field records) are obtained from the PEER database. The first 18 records are the near-field ground motions, and the remaining records are the far-field ground motions. These ground motions were scaled for the maximum considered earthquake (MCE) hazard level. Record scaling in the PEER Ground Motion Database (PGMD, [40]) is accomplished by applying a linear scale factor that does not alter the relative frequency content of the acceleration time series. There are two options for scaling in the PGMD. In this study, the records are scaled to match the target spectrum over a period range (from 0.2T to 1.5T where T is the first mode of vibration). In other words, the average value of the 5% damped response spectra for the suit of motions is not less than ASCE design response spectrum [32]. As an example, responses of the buildings (10, 15, 20, 25, and 30 stories) subjected to the ground motion (No. 1) recorded at the Brawley Airport station during the 1979 Imperial Valley earthquake are illustrated. Figures 3-7 show the responses.

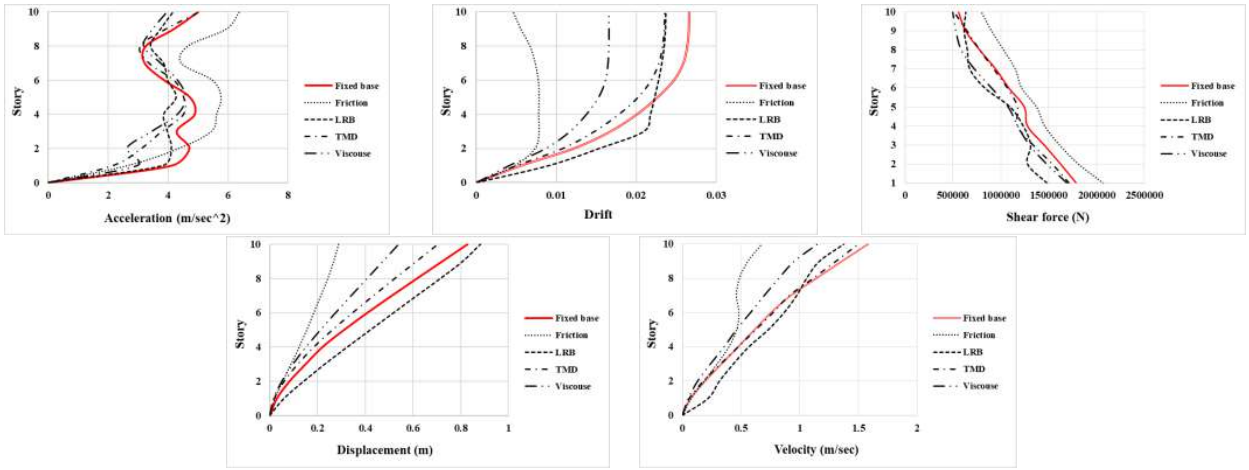

Figure 3. Responses of the 10-story buildings subjected to ground motion No. 1

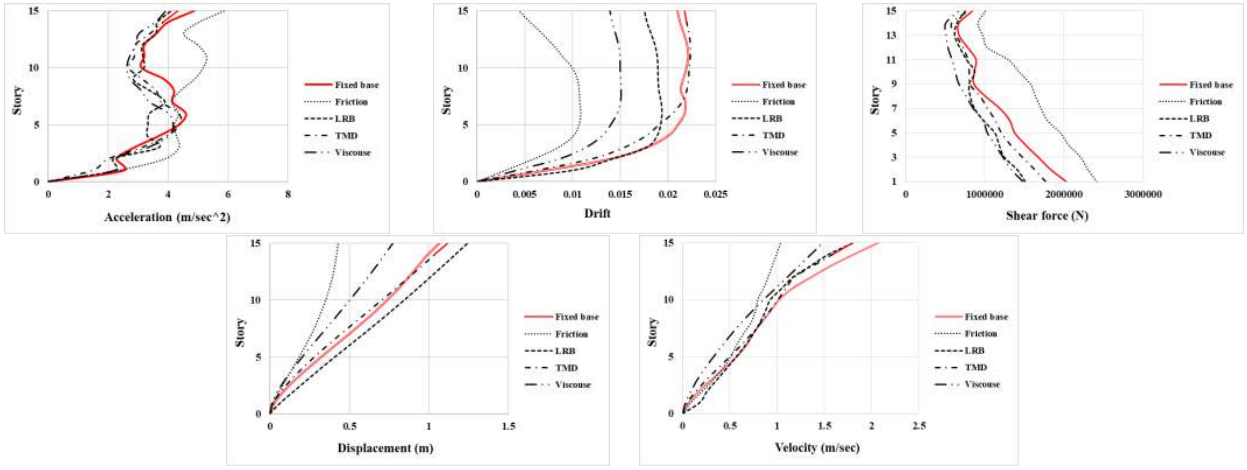

Figure 4. Responses of the 15-story buildings subjected to ground motion No. 1

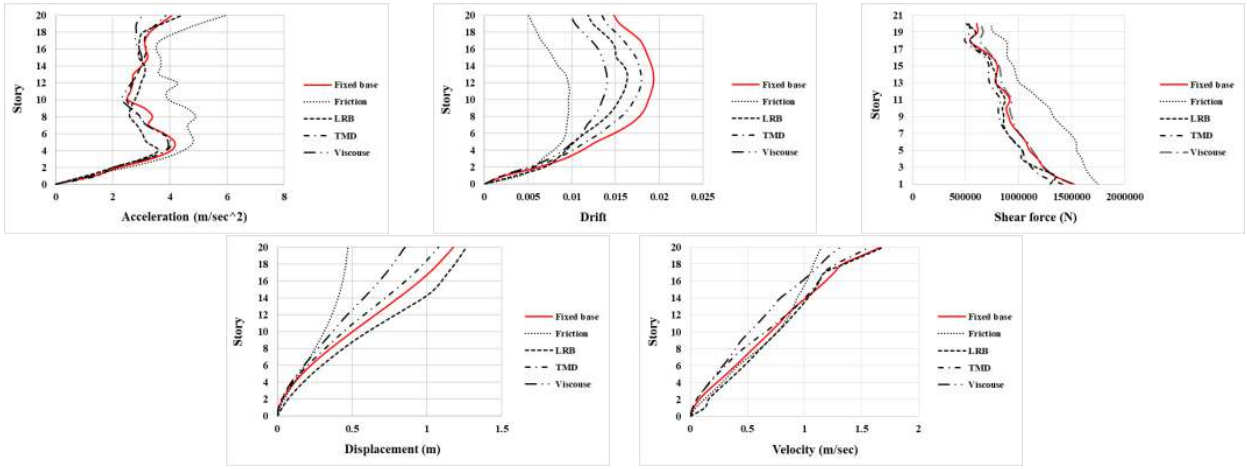

Figure 5. Responses of the 20-story buildings subjected to ground motion No. 1

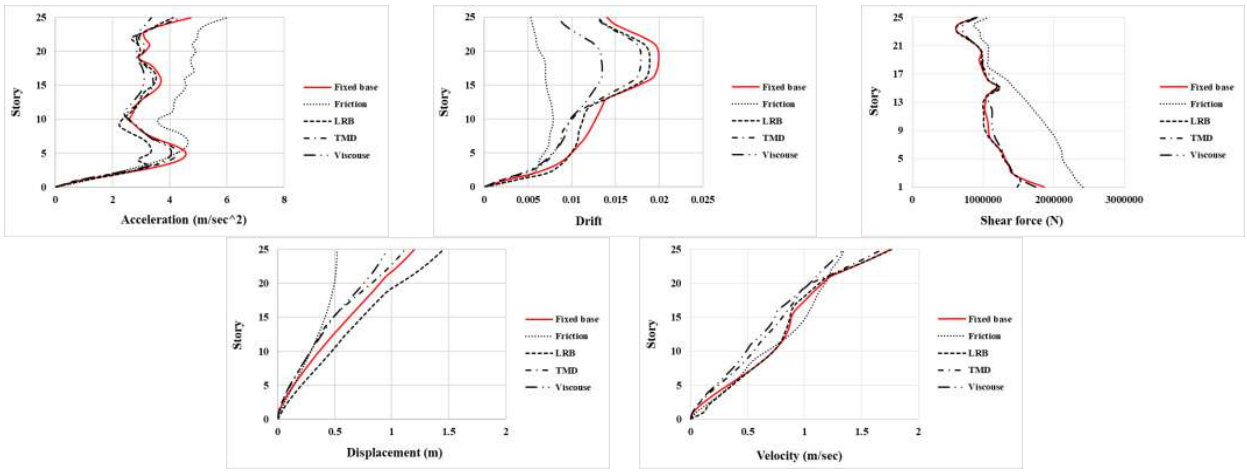

Figure 6. Responses of the 25-story buildings subjected to ground motion No. 1

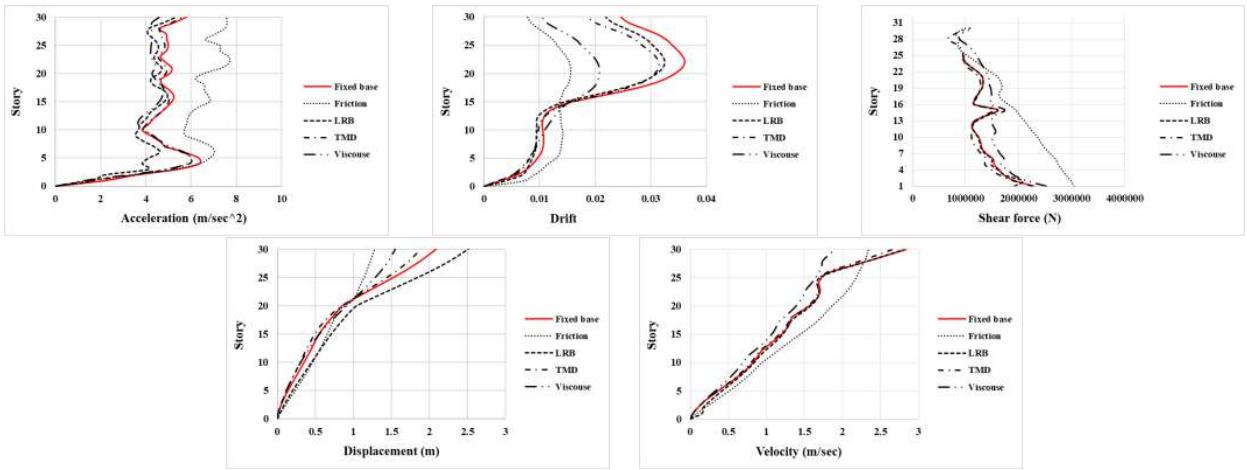

Figure 7. Responses of the 30-story buildings subjected to ground motion No. 1

3. MCDM

In the majority of cases, decision making is convenient when it is based on some measure or criterion. We can use the multiple-criteria decision-making method (MCDM) to deal with definite and explicit criterion. In fact, the MCDM was used to solve a decision making problem by identifying the best alternative that fulfilled a

set number of criteria. The story drift, base shear, the story displacement, story velocity, and story acceleration of different systems can be regarded as criteria to form the decision matrix. One way to calculate these criteria is by using the maximum obtained for each system under the 50 seismic records. However, this approach does not outline the relationship between the ground motion and the given criterion explicitly. For example, a structure subjected to a seismic excitation with the scale factor of 1.2 may have the maximum drift of 1.5%; whereas, its maximum drift under another seismic excitation with the scale factor of 0.5 is 2.1%, which is because the ground motion naturally undergoes random changes and has different frequency contents. For high-rise structures, the effects of the higher modes are also significant. As a result, it was tried to define a measure to consider it via establishing a relationship between the scale factor and criteria (story drift, base shear, story velocity, and acceleration) and used the values of this measure instead of direct use of criteria in the decision matrix.

3. 1. Measure Describing the System Reaction

As was mentioned earlier, the decision matrix should express the relationship between input and output. Regarding section 2 and that earthquakes are scaled using the scale factor, the establishment of a relationship between the scale factor and story drift, story displacement, base shear, story velocity, and story acceleration can contribute to a better understanding of the effect of ground motion frequency content on structural response and its effect on the decision matrix. As a result, the rate of the scale factor against each structural response was adopted as a criterion. The numerical value of each criterion was calculated using Equation (1):

$$Indicator\,Value\,(IV) = \Delta EDP - \Delta Sa$$
$$where:$$
$$\Delta EDP = \left(\frac{EDP_n - EDP_{\min}}{EDP_{\max} - EDP_{\min}}\right) - \left(\frac{EDP_{n-1} - EDP_{\min}}{EDP_{\max} - EDP_{\min}}\right) \quad (1)$$
$$\Delta Sa = \left(\frac{Sa_n - Sa_{\min}}{Sa_{\max} - Sa_{\min}}\right) - \left(\frac{Sa_{n-1} - Sa_{\min}}{Sa_{\max} - Sa_{\min}}\right)$$

In Equation (1), the Engineering Demand Parameter (EDP) is a structural response (e.g., Drift), and Sa represents the seismic scale factor. In Equation (1), the maximum value of structural responses is considered for EDP with different value. For example, there are 15 drift values for a 15-story building, out of which the maximum value is considered for a specific seismic excitement. As a result, the decision matrix has five criteria (story drift, base shear, story velocity, story displacement, and story acceleration), each of which is related to a measure, and their values are calculated using Equation (1). The concept of negative criterion in decision-making suggests the criterion utility (e.g., cost) reduces as it increases in value. Here too, we are dealing with negative criteria since an increase in these criteria is indicative of weak system performance. The first step in the MCDM is forming the decision matrix (Table 7). Table 7 is obtained using the results of simulations and Equation (1). Each row of this matrix indicates the existing alternatives, and each column represents the score of the alternative for each criterion. The second step is the matrix normalization. Normalization is a column-specific operation and distinctively applied to the column specific to each criterion. If each element of the decision matrix is represented by x_{ij}, the element of the normalized matrix will be calculated by Equation (2):

$$r_{ij} = \frac{x_{ij}}{\sum_{i=1}^{m} x_{ij}} \quad (2)$$

In Equation (2), m is the number of alternatives. Table 8 shows the normalized matrix.

TABLE 7. Decision matrix

10 story	**Index value**				
	Accel.	**Disp.**	**Drift**	**Base Shear**	**Vel.**
Friction	7.89	7.68	6.55	7.54	7.02
LRB	7.27	11.8	11.49	7.23	8.97
TMD	8.126	10.765	7.79	7.21	8.27
Viscous	5.79	10.32	9.02	5.21	9.02
15 story	**Index value**				
	Accel.	**Disp.**	**Drift**	**Base Shear**	**Vel.**
Friction	9.712	8.554	7.02	7.066	7.62
LRB	9.435	12.224	8.594	6.648	9.493
TMD	9.921	11.486	8.488	6.709	7.785
Viscous	9.284	8.971	7.893	7.132	7.968
20 story	**Index value**				
	Accel.	**Disp.**	**Drift**	**Base Shear**	**Vel.**
Friction	7.812	5.465	4.839	4.593	5.611
LRB	7.874	10	7.24	5.829	6.823
TMD	7.777	8.675	7.831	6.468	7.308
Viscous	7.834	10.851	9.227	6.385	7.373
25 story	**Index value**				
	Accel.	**Disp.**	**Drift**	**Base Shear**	**Vel.**
Friction	5.983	4.734	4.731	4.734	5.581
LRB	6.786	9.052	6.612	5.422	6.194
TMD	7.08	9.2	7.325	5.07	5.542
Viscous	7.166	9.927	9.147	5.334	6.04
30 story	**Index value**				
	Accel.	**Disp.**	**Drift**	**Base Shear**	**Vel.**
Friction	4.214	5.744	5.114	5.027	5.109
LRB	6.958	11.539	8.123	4.784	4.501
TMD	7.232	13.198	9.095	5.128	5.499
Viscous	7.299	8.929	6.198	4.664	5.152

TABLE 8. The normalized decision matrix

10 story	Index value				
	Accel.	**Disp.**	**Drift**	**Base Shear**	**Vel.**
Friction	0.2713	0.1893	0.1879	0.2773	0.2109
LRB	0.2500	0.2908	0.3297	0.2659	0.2695
TMD	0.2794	0.2653	0.2235	0.2651	0.2485
Viscous	0.1991	0.2544	0.2588	0.1916	0.2710
15 story	**Index value**				
	Accel.	**Disp.**	**Drift**	**Base Shear**	**Vel.**
Friction	0.2532	0.2074	0.2194	0.2564	0.2318
LRB	0.2460	0.2964	0.2686	0.2412	0.2888
TMD	0.2586	0.2785	0.2652	0.2434	0.2368
Viscous	0.2420	0.2175	0.2466	0.2588	0.2424
20 story	**Index value**				
	Accel.	**Disp.**	**Drift**	**Base Shear**	**Vel.**
Friction	0.2496	0.1561	0.1660	0.1973	0.2069
LRB	0.2515	0.2857	0.2484	0.2504	0.2516
TMD	0.2484	0.2479	0.2687	0.2778	0.2695
Viscous	0.2503	0.3101	0.3166	0.2743	0.2719
25 story	**Index value**				
	Accel.	**Disp.**	**Drift**	**Base Shear**	**Vel.**
Friction	0.2214	0.1438	0.1700	0.2302	0.2389
LRB	0.2511	0.2750	0.2377	0.2637	0.2651
TMD	0.2620	0.2795	0.2633	0.2465	0.2372
Viscous	0.2652	0.3016	0.3288	0.2594	0.2585
30 story	**Index value**				
	Accel.	**Disp.**	**Drift**	**Base Shear**	**Vel.**
Friction	0.1639	0.1457	0.1792	0.2564	0.2521
LRB	0.2707	0.2927	0.2847	0.2440	0.2221
TMD	0.2813	0.3348	0.3187	0.2615	0.2714
Viscous	0.2839	0.2265	0.2172	0.2379	0.2542

After the normalization, all criteria are converted into positive criteria using Equation (3):

$$r_{ij}^{+} = 1 - r_{ij} \tag{3}$$

Hereafter, these matrices are used to calculate the weights of criteria.

3. 2. Indicators Weight In this step, the importance of each criterion relative to others is determined by the entropy method. This method uses the elements of the decision matrix to determine the weight of the criteria. Based on this method, the importance of a criterion grows with increasing the dispersion of its value. The weights of criteria are calculated in the following steps:

1. Normalizing the decision matrix with m alternatives and n criteria

2. Calculating the entropy of each criterion using Equation (4):

$$E_j = -\frac{1}{ln(m)} \cdot \left(\sum_{i=1}^{m} r_{ij}^{+} \cdot ln(r_{ij}^{+})\right) \tag{4}$$

3. Determining uncertainty of j[th] criterion using Equation (5):

$$d_j = 1 - E_j \tag{5}$$

4. Determining the weight of each criterion using Equation (6):

$$w_j = \frac{d_j}{\sum_{j=1}^{m} d_j} \tag{6}$$

The weight of each criterion was calculated using the entropy method and presented in Table 9.

3. 3. Decision-Making Model The last decision-making step is selecting a decision-making model to prioritize the criteria. For this purpose, the TOPSIS [41] technique was employed. Based on this technique, the selected criterion should have the minimum distance from the positive ideal solution (the best solution) and the maximum distance from the negative ideal solution (the worst solution). The solution steps are as follows:1) Formation of decision matrix, 2) Normalization of decision matrix and conversion of negative criteria into positive ones$[R]$3) Outlining the measure weight vector, 4) Forming of weighted normalized decision matrix $[V] = \{W\}[R]$, 5) Determining positive and negative ideal alternatives (Equation (7)). The positive ideal criterion is actually a vector of the best alternatives on each column; whereas, the worst alternatives in each column are used as the negative ideal criterion.

$$\begin{aligned} A^{(+)} &= \{Max(V_{i1}) \quad \dots \quad Max(V_{in})\} \\ A^{(-)} &= \{Min(V_{i1}) \quad \dots \quad Min(V_{in})\} \end{aligned} \tag{7}$$

6) Calculation of distance from positive and negative ideal alternatives using using Equation (8):

$$S_i^{+} = \sqrt{\sum_{j=1}^{n}(V_{ij} - A_j^{+})^2}, S_i^{-} = \sqrt{\sum_{j=1}^{n}(V_{ij} - A_j^{-})^2} \tag{8}$$

TABLE 9. Weight of each criterion using Entropy method

Building	Acc.	Disp.	Drift	Base Shear	Velocity
10-story	0.1454	0.2089	0.3833	0.1751	0.0871
15- story	0.0209	0.5868	0.2594	0.0282	0.1044
20-story	0.0014	0.4282	0.3613	0.1262	0.0827
25-story	0.0381	0.5219	0.3987	0.0220	0.0191
30-story	0.2352	0.4651	0.2626	0.0086	0.0283

7) The last step was the calculation of the relative distance to positive ideal alternative using Equation (9):

$$C_j = \frac{S_j^{(-)}}{S_j^{(+)}+S_j^{(-)}} \quad (9)$$

The parameter C_j remains in the 0-1 range. A criterion gets closer to the positive ideal alternative with increasing C_j. The criteria are ranked based on the greater C_j which is taken as the score for each criterion. The score or value of C_j for each criterion is presented in Tables 10.

4. DISCUSSION

According to Tables 10, based on the criteria of choice and conditions, the friction damper ranked first for all buildings (10, 15, 20, 25, and 30 stories). In other words, the use of the friction dampers results in better control over structural behavior under seismic excitement, which can be attributed to the characteristics of this damper. In the nonlinear viscous damper, the damping ratio of the nonlinear viscous damper depends on the vibration frequency (ω) and maximum displacement of the two ends of the damper (u_{max} or modal displacement shape

TABLE 10. Score and rank of each criterion in buildings

	System	Score	Rank
10-story	Friction	0.38838	1
	LRB	0.03746	4
	TMD	0.3057	2
	Viscous	0.26846	3
15-story	Friction	0.4667	1
	LRB	0.0049	4
	TMD	0.1233	3
	Viscous	0.4051	2
20-story	Friction	0.599	1
	LRB	0.1794	3
	TMD	0.2185	2
	Viscous	0.0031	4
25-story	Friction	0.62039	1
	LRB	0.21506	2
	TMD	0.16359	3
	Viscous	0.00096	4
30-story	Friction	0.564	1
	LRB	0.1242	3
	TMD	0.0035	4
	Viscous	0.3081	2

(Equation (10)). As a result, the superiority of the friction damper over the nonlinear viscous damper is due to the former's independence of velocity and vibration frequency [42].

$$F_D = C_{NL} \cdot |u|^{\alpha} \cdot \mathrm{sgn}(u) \quad , \quad \alpha = 0.5 \, , \qquad C_{NL} = C_L \cdot \frac{\pi}{\lambda} \cdot (u_{\max} \cdot \omega)^{1-\alpha} \quad (10)$$

Although the friction damper causes extra structural stiffness, this stiffness is eliminated after damper slip and used to resist small seismic and wind excitements.

Another point is the effect of higher modes on the behavior of structures with concrete shear walls [43]. The second and even the third vibration modes in high-rise structures can increase the shear and flexural force demand. For instance, Yang et al. [44] showed that structural responses increase with increasing the magnitude of an earthquake due to the involvement of higher modes; besides, the deformation of different modes and related internal forces increases after the formation of a plastic hinge at the wall base. This behavior can result in formation of other plastic hinges in the height of the wall. The tuned mass damper is designed based on the first mode frequency. Studies have shown that the TMD sensitivity to frequency changes results in yield reduction. Results showed that the TMD ranked last among other alternatives for 30-story building. As an advantage of such systems (TMDs), they can respond to small levels of excitation. But, the performance of TMD is very sensitive to the natural frequency of structures and damping percentage of the damper. In addition, the effectiveness of a tuned mass damper is constrained by the maximum weight that can be practically placed on top of the structure. One solution is to investigate the use of the multiple mass dampers vertically distributed in the height of the structure in tall buildings based on modal analysis, which is recommended for future studies. A large number of base-isolated high-rise buildings were built (Thousand Tower with a height of 135 m, Sendai MT building with a height of 84.9 m, and super high-rise building in Japan with a height of 177.4 m [45, 46]) in recent decades. In the low-rise and mid-rise buildings, the use of base isolators extends the first period, which in turn reduces the load exerted on the structure. However, the extension of the period is negligible in high-rise buildings. The main reason for using base isolators in high-rise buildings (e.g., Tokyo Skytree East Tower, Taiwan Tan Tzu Medical center, and Japan Thousand Tower and Sendai MT building) is to dissipate large portions of seismic energy. Nevertheless, numerical results indicated that this system failed in obtaining a good score and rank. In addition, recent study suggests that, even for design-level earthquake, base isolation is not effective for near-field earthquakes [47]. Therefore, it did not meet the main goal, i.e., the seismic energy attraction and dissipation, and thus did not adequately

control structural responses relative to other existing alternatives. One solution, that should be examined, is using multiple base isolators vertically distributed in the height of the structure -or another type of isolator, such as friction pendulum isolators in high-rise buildings. Considering the above paragraphs, it can be concluded that it is difficult to determine and select a seismic passive control system without using a multi-criteria decision-making method.

5. CONCLUSION

This study investigated the control and reduction of seismic responses of high-rise buildings with concrete shear walls using viscous dampers, friction dampers, TMD, and lead-rubber isolation bearings. Five buildings with 10, 15, 20, 25, and 30 stories were reinforced with four passive control systems mentioned earlier. Next, the structures were subjected to 50 seismic records. The structural responses (acceleration, drift, velocity, displacement, and base shear) were adopted as criteria, and quantitative indicators were defined to establish a relationship between the inputs (ground motions) and the outputs (responses). At the end, the TOPSIS was found to be the best method of reinforcement and controlling the damage and responses of the concrete shear wall. Based on the criteria of choice and systems conditions, results showed that the friction damper had the highest score, ranking first among the discussed dampers in all buildings, followed by other dampers, with differences based on the number of stories. For example, the TMD ranked second and fourth in 20-story and 30-story buildings, respectively. Therefore, structural characteristics (e.g., periods of the first to third modes) and their relationship with the mode level, selected control system characteristics (e.g., the dependence of viscous damper performance on velocity), and frequency content is among parameters that affect the structural responses. Due to the complexity of the problem, it is recommended to use the multi criterion decision making (MCDM) under these scenarios.

6. REFERENCES

1. Lu, X., Lu, X., Guan, H., and Ye, L. "Collapse simulation of reinforced concrete high-rise building induced by extreme earthquakes." ***Earthquake Engineering and Structural Dynamics***, Vol. 42, No. 5, (2013), 705–723. https://doi.org/10.1002/eqe.2240
2. Xu, Z., Lu, X., Cheng, Q., Guan, H., Deng, L., and Zhang, Z. "A smart phone-based system for post-earthquake investigations of building damage." ***International Journal of Disaster Risk Reduction***, Vol. 27, (2018), 214–222. https://doi.org/10.1016/j.ijdrr.2017.10.008
3. Madsen, L. P. B., Thambiratnam, D. P., and Perera, N. J. "Seismic response of building structures with dampers in shear walls." ***Computers and Structures***, Vol. 81, No. 4, (2003), 239–253. https://doi.org/10.1016/S0045-7949(02)00441-8
4. Moghadasi Faridani, H., and Capsoni, A. "Investigation of the effects of viscous damping mechanisms on structural characteristics in coupled shear walls." ***Engineering Structures***, Vol. 116, (2016), 121–139. https://doi.org/10.1016/j.engstruct.2016.02.031
5. Ahmed, M. "Fluid viscous dampers locations in reinforced-concrete core wall buildings." ***Proceedings of the Institution of Civil Engineers - Structures and Buildings***, Vol. 170, No. 1, (2017), 33–50. https://doi.org/10.1680/jstbu.16.00007
6. Hejazi, F., Ostovar, N., and Bashir, A. "Seismic response of shear wall with viscous damping system." In Lecture Notes in Civil Engineering (Vol. 9, pp. 595–607). Springer. https://doi.org/10.1007/978-981-10-8016-6_46
7. Muscat, O. "Examination of Shear Walls Retrofitted with Fluid Viscous Dampers." ***International Journal of Pure and Applied Mathematics***, Vol. 118, No. 24, (2018), 1–10. Retrieved from https://acadpubl.eu/hub/2018-118-24/4/631.pdf
8. Aydin, E., Öztürk, B., and Dutkiewicz, M. "Analysis of efficiency of passive dampers in multistorey buildings." ***Journal of Sound and Vibration***, Vol. 439, (2019), 17–28. https://doi.org/10.1016/j.jsv.2018.09.031
9. Cetin, H., Aydin, E., and Ozturk, B. "Optimal Design and Distribution of Viscous Dampers for Shear Building Structures Under Seismic Excitations." ***Frontiers in Built Environment***, Vol. 5, No. 90, (2019), 1–13. https://doi.org/10.3389/fbuil.2019.00090
10. Jiang, Q., Lu, X., Guan, H., and Ye, X. "Shaking table model test and FE analysis of a reinforced concrete mega-frame structure with tuned mass dampers." ***The Structural Design of Tall and Special Buildings***, Vol. 23, No. 18, (2014), 1426–1442. https://doi.org/10.1002/tal.1150
11. Mate, N. U., Bakre, S. V., and Jaiswal, O. R. "Seismic Pounding Response of Singled-Degree-of-Freedom Elastic and Inelastic Structures Using Passive Tuned Mass Damper." ***International Journal of Civil Engineering***, Vol. 15, No. 7, (2017), 991–1005. https://doi.org/10.1007/s40999-017-0178-7
12. Kamgar, R., Samea, P., and Khatibinia, M. "Optimizing parameters of tuned mass damper subjected to critical earthquake." ***The Structural Design of Tall and Special Buildings***, Vol. 27, No. 7, (2018), e1460. https://doi.org/10.1002/tal.1460
13. Reza, M. S., Jaafar, K., Shams, S., and Azad, A. K. "Tube shear wall interaction of high rise building and influence of damper on its dynamic behavior." In 7th Brunei International Conference on Engineering and Technology (BICET 2018) (Vol. 2018, pp. 1–4). Institution of Engineering and Technology. https://doi.org/10.1049/cp.2018.1609
14. Hessabi, R. M., Mercan, O., and Ozturk, B. "Exploring the effects of tuned mass dampers on the seismic performance of structures with nonlinear base isolation systems." ***Earthquake and Structures***, Vol. 12, No. 3, (2017), 285–296. https://doi.org/10.12989/eas.2017.12.3.285
15. Chung, H.-S., Moon, B.-W., Lee, S.-K., Park, J.-H., and Min, K.-W. "Seismic performance of friction dampers using flexure of rc shear wall system." ***The Structural Design of Tall and Special Buildings***, Vol. 18, No. 7, (2009), 807–822. https://doi.org/10.1002/tal.524
16. Ahn, T.-S., Kim, Y.-J., and Kim, S.-D. "Large-Scale Testing of Coupled Shear Wall Structures with Damping Devices." ***Advances in Structural Engineering***, Vol. 16, No. 11, (2013), 1943–1955. https://doi.org/10.1260/1369-4332.16.11.1943
17. Bagheri, B., and Oh, S. H. "Seismic Design of Coupled Shear Wall Building Linked by Hysteretic Dampers using Energy Based Seismic Design." ***International Journal of Steel Structures***, Vol.

18, No. 1, (2018), 225–253. https://doi.org/10.1007/s13296-018-0318-1

18. Osgooei, P. M., Tait, M. J., and Konstantinidis, D. "Seismic Isolation of a Shear Wall Structure Using Rectangular Fiber-Reinforced Elastomeric Isolators." ***Journal of Structural Engineering***, Vol. 142, No. 2, (2016), 04015116. https://doi.org/10.1061/(ASCE)ST.1943-541X.0001376
19. Li, A., Yang, C., Xie, L., Liu, L., and Zeng, D. "Research on the Rational Yield Ratio of Isolation System and Its Application to the Design of Seismically Isolated Reinforced Concrete Frame-Core Tube Tall Buildings." ***Applied Sciences***, Vol. 7, No. 11, (2017), 1191–1210. https://doi.org/10.3390/app7111191
20. Wang, W., Li, A., and Wang, X. "Seismic performance of precast concrete shear wall structure with improved assembly horizontal wall connections." ***Bulletin of Earthquake Engineering***, Vol. 16, No. 9, (2018), 4133–4158. https://doi.org/10.1007/s10518-018-0348-2
21. Massone, L., and Wallace, J. "Load-deformation responses of slender reinforced concrete walls." ***Structural Journal***, Vol. 101, No. 1, (2004), 103–113. Retrieved from https://www.concrete.org/publications/internationalconcreteabstractsportal/m/details/id/13003
22. Thomsen, J., and Wallace, J. Displacement based design of reinforced concrete structural walls: an experimental investigation of walls with rectangular and t-shaped cross-sections: a dissertation, Doctoral dissertation, Clarkson University, Potsdam, United States (1995).
23. Tran, T. A., and Wallace, J. W. "Cyclic Testing of Moderate-Aspect-Ratio Reinforced Concrete Structural Walls." ***ACI Structural Journal***, Vol. 112, No. 6, (2015), 653–665. Retrieved from 110.14359/51687907
24. Barkhordari, M. S., Tehranizadeh, M., and Scott, M. H. "Numerical modeling strategy for predicting the response of RC walls using Timoshenko theory." ***Magazine of Concrete Research***, (2020), 1–70. https://doi.org/10.1680/jmacr.19.00542
25. Kolozvari, K., Orakcal, K., and Wallace, J. W. "Modeling of Cyclic Shear-Flexure Interaction in Reinforced Concrete Structural Walls. I: Theory." ***Journal of Structural Engineering***, Vol. 141, No. 5, (2015), 04014135. https://doi.org/10.1061/(ASCE)ST.1943-541X.0001059
26. Orakcal, K., and Wallace, J.W., "Flexural Modeling of Reinforced Concrete Walls— Experimental Verification." ***ACI Structural Journal***, Vol. 103, No. 2, (2006), 196–206. https://doi.org/10.1061/(ASCE)0733-9445(2004)130:4(618)
27. Kolozvari, K., and Wallace, J. W. "Practical Nonlinear Modeling of Reinforced Concrete Structural Walls." ***Journal of Structural Engineering***, Vol. 142, No. 12, (2016), G4016001. https://doi.org/10.1061/(ASCE)ST.1943-541X.0001492
28. Formisano, A., Castaldo, C., and Chiumiento, G. "Optimal seismic upgrading of a reinforced concrete school building with metal-based devices using an efficient multi-criteria decision-making method." ***Structure and Infrastructure Engineering***, Vol. 13, No. 11, (2017), 1373–1389. https://doi.org/10.1080/15732479.2016.1268174
29. Invidiata, A., Lavagna, M., and Ghisi, E. "Selecting design strategies using multi-criteria decision making to improve the sustainability of buildings." ***Building and Environment***, Vol. 139, (2018), 58–68. https://doi.org/10.1016/j.buildenv.2018.04.041
30. Mosalam, K. M., Alibrandi, U., Lee, H., and Armengou, J. "Performance-based engineering and multi-criteria decision analysis for sustainable and resilient building design." ***Structural Safety***, Vol. 74, (2018), 1–13. https://doi.org/10.1016/j.strusafe.2018.03.005
31. ACI 318-08, "Building code requirements for structural concrete (ACI 318-08) and commentary", American Concrete Institute, (2014).
32. ASCE Standard, "Minimum design loads for buildings and other structures", American society of civil engineers/structural engineering institute, Reston, Virginia, (2010).
33. Takewaki, I. Building control with passive dampers: optimal performance-based design for earthquakes. John Wiley & Sons, (2011).
34. McKenna, F., Scott, M. H., and Fenves, G. L. "Nonlinear Finite-Element Analysis Software Architecture Using Object Composition." ***Journal of Computing in Civil Engineering***, Vol. 24, No. 1, (2010), 95–107. https://doi.org/10.1061/(ASCE)CP.1943-5487.0000002
35. Mazzoni, S., McKenna, F., Scott, M. H., and Fenves, G. L., "OpenSees command language manual", Pacific Earthquake Engineering Research (PEER) Center, (2007).
36. Akçelyan, S., and Lignos, D. "Dynamic Analyses of 1-Story Moment Frame with Viscous Dampers", (2015).
37. Aiken, I. D., Nims, D. K., Whittaker, A. S., and Kelly, J. M. "Testing of Passive Energy Dissipation Systems." ***Earthquake Spectra***, Vol. 9, No. 3, (1993), 335–370. https://doi.org/10.1193/1.1585720
38. Kikuchi, M., Nakamura, T., and Aiken, I. D. "Three-dimensional analysis for square seismic isolation bearings under large shear deformations and high axial loads." ***Earthquake Engineering & Structural Dynamics***, Vol. 39, No. 13, (2010), 1513–1531. https://doi.org/10.1002/eqe.1042
39. Ramezani, M., Bathaei, A., and Ghorbani-Tanha, A. K. "Application of artificial neural networks in optimal tuning of tuned mass dampers implemented in high-rise buildings subjected to wind load." ***Earthquake Engineering and Engineering Vibration***, Vol. 17, No. 4, (2018), 903–915. https://doi.org/10.1007/s11803-018-0483-4
40. Ancheta, T., Darragh, R., Stewart, J., and Seyhan, E. "PEER 2013/03: PEER NGA-West2 Database." Pacific Earthquake Engineering Research, (3013).
41. Papathanasiou, J., and Ploskas, N. Multiple Criteria Decision Aid (Vol. 136, pp.57-89), Springer International Publishing, (2018). https://doi.org/10.1007/978-3-319-91648-4
42. Hanson, R., and Soong, T. Seismic design with supplemental energy dissipation devices. Earthquake Engineering Research Institute, (2001).
43. Rodriguez, M. E., Restrepo, J. I., and Carr, A. J. "Earthquake-induced floor horizontal accelerations in buildings." ***Earthquake Engineering and Structural Dynamics***, Vol. 31, No. 3, (2002), 693–718. https://doi.org/10.1002/eqe.149
44. Yang, T.Y., and Moehle, J.P., "The Tall Buildings Initiative." In 14th World Conference on Earthquake Engineering (Vol. 12). Airiti Press, Inc., (2008). https://doi.org/10.5297/ser.1201.002
45. Komuro, T., Nishikawa, Y., Kimura, Y., and Isshiki, Y. "Development and Realization of Base Isolation System for High-Rise Buildings." ***Journal of Advanced Concrete Technology***, Vol. 3, No. 2, (2005), 233–239. https://doi.org/10.3151/jact.3.233
46. Wang, S., Du, D., and Liu, W. "Research on key issues about seismic isolation design of high-rise buildings structure." In Proceedings of the 11th World Conference on Seismic Isolation, Energy Dissipation and Active Vibration Control of Structures, (2009), 17–21.
47. Bhandari, M., Bharti, S. D., Shrimali, M. K., and Datta, T. K. "The Numerical Study of Base-Isolated Buildings Under Near-Field and Far-Field Earthquakes." ***Journal of Earthquake Engineering***, Vol. 22, No. 6, (2018), 989–1007. https://doi.org/10.1080/13632469.2016.1269698

7. APPENDIX A

TABLE A.1. Shear wall section of the prototype buildings

Building	No. of story	Thickness (cm)	Longitudinal Rein.	Transverse Rein.
10-story	1-4	35	#6@20cm	$8.8cm^2/m$
	5-8	30	#5@20cm	$7.5cm^2/m$
	9-10	25	#4@20cm	$6.3cm^2/m$
15-story	1-5	30	#5@20cm	$7.5cm^2/m$
	6-10	30	#4@25cm	$6.3cm^2/m$
	11-15	25	#4@25cm	$6.3cm^2/m$
20-story	1-5	35	#6@20cm	$8.8cm^2/m$
	6-10	30	#5@20cm	$7.5cm^2/m$
	11-15	25	#4@20cm	$6.3cm^2/m$
	16-20	25	#4@25cm	$6.3cm^2/m$
25-story	1-5	35	#6@15cm	$8.8cm^2/m$
	6-10	30	#6@20cm	$7.5cm^2/m$
	11-15	30	#5@20cm	$7.5cm^2/m$
	16-20	30	#4@20cm	$7.5cm^2/m$
	21-25	25	#4@25cm	$6.3cm^2/m$
30-story	1-5	35	#7@20cm	$8.8cm^2/m$
	6-10	35	#6@20cm	$8.8cm^2/m$
	11-15	30	#5@20cm	$7.5cm^2/m$
	16-20	30	#5@25cm	$7.5cm^2/m$
	21-25	25	#4@20cm	$6.3cm^2/m$
	26-30	25	#4@25cm	$6.3cm^2/m$

TABLE A.2. Characteristics of the selected records

No.	Earthquake Name	Station	year	Mag.
1	"Imperial Valley-06"	"Brawley Airport"	1979	6.53
2	"Imperial Valley-06"	"El Centro Array #10"	1979	6.53
3	"Loma Prieta"	"Gilroy - Historic Bldg."	1989	6.93
4	"Loma Prieta"	"Gilroy Array #2"	1989	6.93
5	"Loma Prieta"	"Gilroy Array #3"	1989	6.93
6	"Loma Prieta"	"Saratoga - W Valley."	1989	6.93
7	"Chi-Chi_ Taiwan"	"CHY101"	1999	7.62
8	"Duzce_ Turkey"	"Bolu"	1999	7.14
9	"Chuetsu-oki_ Japan"	"Joetsu Kakizakiku "	2007	6.8
10	"Dar. _ New Zealand"	"Riccarton High School "	2010	7
11	"El Mayor _ Mexico"	"El Centro Array #12"	2010	7.2
12	"El Mayor _ Mexico"	"Westside Elementary "	2010	7.2
13	"Imperial Valley-06"	"El Centro Array #11"	1979	6.53
14	"Superstition Hills-02"	"Poe Road (temp)"	1987	6.54
15	"Superstition Hills-02"	"Westmorland Fire Sta"	1987	6.54
16	"Northridge-01"	"Beverly Hills - 14145"	1994	6.69
17	"Kobe_ Japan"	"Amagasaki"	1995	6.9
18	"Kocaeli_ Turkey"	"Duzce"	1999	7.51
19	"Iwate_ Japan"	"MYG005"	2008	6.9
20	"El Mayor _ Mexico"	"CERRO PRIETO "	2010	7.2
21	"El Mayor _ Mexico"	"MICHOACAN DE "	2010	7.2
22	"El Mayor _ Mexico"	"RIITO"	2010	7.2
23	"El Mayor _ Mexico"	"EJIDO SALTILLO"	2010	7.2
24	"Dar. _ New Zealand"	"DFHS"	2010	7
25	"Chri. _ New Zealand"	"Papanui High School "	2011	6.2
26	"Northern Calif-03"	"Ferndale City Hall"	1954	6.5
27	"Coalinga-01"	"Parkfield - Fault Zone 14"	1983	6.36
28	"Loma Prieta"	"Hollister - South & Pine"	1989	6.93
29	"Loma Prieta"	"Hollister City Hall"	1989	6.93
30	"Kobe_ Japan"	"Sakai"	1995	6.9
31	"Kobe_ Japan"	"Yae"	1995	6.9
32	"Chi-Chi_ Taiwan"	"TCU038"	1999	7.62
33	"Chi-Chi_ Taiwan"	"TCU112"	1999	7.62
34	"Chi-Chi_ Taiwan"	"TCU117"	1999	7.62
35	"Chi-Chi_ Taiwan"	"TCU118"	1999	7.62
36	"St Elias_ Alaska"	"Icy Bay"	1979	7.54
37	"Chi-Chi_ Taiwan-03"	"CHY025"	1999	6.2
38	"Chi-Chi_ Taiwan-03"	"TCU065"	1999	6.2
39	"Chuetsu-oki_ Japan"	"Joetsu City"	2007	6.8
40	"Iwate_ Japan"	"Nakashinden Town"	2008	6.9
41	"Iwate_ Japan"	"Semine Kurihara City"	2008	6.9
42	"Iwate_ Japan"	"Yokote Masuda Tamati Masu"	2008	6.9
43	"El Mayor _ Mexico"	"TAMAULIPAS"	2010	7.2
44	"El Mayor _ Mexico"	"El Centro - Meloland "	2010	7.2
45	"El Mayor _ Mexico"	"El Centro - Geotechnic"	2010	7.2

Persian Abstract

چکیده

در این مقاله توانایی میراگر جرمی تنظیم‌شونده، میراگر ویسکوز، میراگر اصطکاکی و جداگر هسته سربی در کاهش خرابی و پاسخ‌های سازه‌های بلند دارای دیوار برشی بتنی مورد بررسی قرار گرفته است. پنج ساختمان با تعداد طبقات۱۵،۱۰، ۲۰،۲۵ و ۳۰ طبقه به همراه سیستم‌های کنترل لرزه‌ای غیرفعال تحت اثر ۵۰ رکورد زلزله با استفاده از نرم‌افزار OpenSees تحلیل شده‌اند. پاسخ‌های سازه (شتاب، دریفت، جابه‌جایی، سرعت و برش پایه) به عنوان معیار در نظر گرفته شده است. برای ایجاد ارتباط بین ورودی (زلزله) و خروجی (پاسخ‌های سازه) با تعریف کردن یک شاخص، مقدار کمی بی‌بعد برای هر معیار محاسبه شده است. در نهایت با استفاده از روش تصمیم‌گیری چند معیاره، گزینه‌های موجود برای مقاوم‌سازی و کنترل پاسخ سازه‌ها رتبه‌بندی شده اند.

International Journal of Engineering

Journal Homepage: www.ije.ir

Assessment of Changes in Shear Strength Parameters for Soils below Circular Machine Foundation

K. W. Abdul Kareem[a], M. Y. Fattah*[a], Z. S. M. Khaled[b]

[a] *Department of Civil Engineering, University of Technology, Baghdad, Iraq*
[b] *Department of Civil Engineering, Al-Nahrain University, Baghdad, Iraq*

PAPER INFO

Paper history:
Received 08 April 2020
Received in revised form 19 April 2020
Accepted 12 June 2020

Keywords:
Circular Machine Foundation
Clay
Sand
Shear Strength
Strain

ABSTRACT

This paper focuses on the response of circular machine foundation resting on different soils (sand and clay) through studying the variation of soil shear strength parameters and strain with the number of cycles. The objective of the current study is to explore the results related to the parameters of the dynamic load (number of loading cycles and frequency of load) related to the circular footing of a machine on the dynamic shear strength parameters (for sand soil (ϕ°dyn) and for clay soil (Cudyn)) in addition to the amplitude strain foundation. A special setup was designed and manufactured to simulate the vertical vibration of a circular machine foundation. A steel circular machine foundation with a diameter of 150 mm was used to represent the footing. A total of 6 cases were examined to take into account the effects of different parameters including different frequencies (0.5, 1, and 2 Hz); state of sand (medium and dense) which corresponded to relative densities of (50 and 80%), while the state of clay (medium and stiff) corresponded to undrained shear strengths (50 and 70 kPa). All tests were carried out under load amplitude of 2.5 kN. It was found that the rate of increase in shear strength parameters for the soil under a circular machine foundation decreases remarkably when increasing the frequency for both types of soil under the footing. While little change in the shear strength parameters, or even no change was observed under the effect of other locations. Moreover, the amplitude strain decreased when increasing the frequency for both types of soil.

***doi**: 10.5829/ije.2020.33.08b.07*

1. INTRODUCTION

The machine foundations should be designed to transmit the dynamic forces of machines to the soil through the foundation thus reducing the harmful effects due to vibration [1]. The response of the soil to dynamic loads differs from that in static loads, and it is a fact of great importance to the stability of structures. Soil strain behavior can be recognized as highly hysteresis and non-linear, and the actual behavior of the soil is usually flexible plastic, which reveals closer estimates of displacement when exposed to a working load. Soil type also influences the responses under dynamic loading conditions. The most influential factors that separate the different soil types are the particle size distribution. Well-graded materials are unlikely to lose energy under dynamic loading, while uniform soils are likely to lose their dynamic load carrying capacity [2].

In the design of the shallow foundation, the bearing capacity of the soil has an essential role in the spectrum. Foundation transmits projected loads to the soil below without failure. The minimum value of the ultimate dynamic bearing capacity of shallow foundations on sands obtained between static to dynamic loading range can be estimated by using a friction angle ϕ^{o}_{dyn} (internal friction angle under dynamic load), such that in Equation (1) [3]. While ultimate bearing-capacity of foundations resting on clay soils can be considering the strain-rate influence caused by dynamic loading is taken into account in the undrained cohesion determination. In contrast with sand, the, undrained cohesion of soaked clays rises with the strain rate increasing, Carroll [4] suggested that:

$$\phi^{\circ}_{dyn} = \phi^{\circ}_{stat} - 2 \quad \text{(in sand)} \quad (1)$$

$$Cu_{dyn} = 1.5\, Cu_{stat} \quad \text{(in clay)} \quad (2)$$

*Corresponding Author Email: *myf_1968@yahoo.com (M. Y. Fattah)*

Please cite this article as: K. W. Abdul Kareem, M. Y. Fattah, Z. S. M. Khaled, Assessment of Changes in Shear Strength Parameters for Soils below Circular Machine Foundation, International Journal of Engineering (IJE), IJE TRANSACTIONS B: Applications Vol. 33, No. 8, (August 2020) 1491-1498

Baidya et al. [5] declared an experimental exploration for the dynamic reaction of foundation on limited stratum underlain by a solid layer. The stratum thickness effect and the dynamic reaction of the foundation system were experimentally investigated, by conducting "the vertical vibration test" using mechanical oscillator on different stratum depths with different static weights and different eccentric angles "ϕ". With an increase in the constant weight, the natural regularity and the amplitude reduce, and with an increase in ϕ, the natural regularity reduces and the sounding amplitude also increases.

Fattah et al. [6] investigated the experimental behavior of dry sandy soil under foundations subjected to vertical cyclic stress load. It was believed that there is a rise in the angle of internal friction after testing under periodic load with different foot models. The rate of increase of sand shear strength (friction angle) depends on the rate of development of permanent stress.

Investing dynamics properties is therefore very sensitive and challenging task. This demads complex mathematical analysis for the incorporation of various aspects of design. Kirar et al. [7] presented a discussion about various dynamic soil properties those are essential in the machine foundation design and the methods to evaluate them. Some of the established correlations between the important dynamic soil properties and general soil properties are also presented. It was observed that the resonant frequency of the soil-foundation system decreased with an increase in the excitation force while resonant amplitude increases with an increase in the excitation force level.

Bender-element (BE) tests were conducted by Cabalar et al. [8] on clay-sand mixtures to investigate the variation of small strain-shear modulus (Gmax) with the sand content and the physical characteristics (size, shape) of the sand grains in the mixtures. Three different gradations (0.6–0.3 mm, 1.0–0.6 mm and 2.0–1.0 mm) of sands having distinct shapes (rounded, angular) were added to a low-plasticity clay with mixture ratios of 10, 20, 30, 40 and 50% clean clay. The tests indicated that both the G_{max} and unconfined compressive strength (q_u) values of the specimens with angular sand grains were measured to be lower than those with rounded sand grains, for all sizes and percentages. As the percentage of sand in the mixture increases, the G_{max} values increase, while the q_u values decrease.

Venkateswarlu and Hegde [9] carried out numerical analyses to understand the performance of the machine foundations resting on the geocell reinforced beds. The analyses were carried out by using finite element software PLAXIS 2D. The hypothetical case of the circular machine foundation of 1 m diameter resting on the saturated silty sand was analyzed. Mohr-Coulomb failure criteria was used to simulate the behavior of the soil. Initially, the numerical model was validated with the existing results reported in the literature. Three different cases, namely, unreinforced, geogrid reinforced and geocell reinforced were considered. The depth of the placement of the geocell and geogrid was also varied. At the optimum location of geocell, 61% reduction in the displacement amplitude was observed as compared to unreinforced foundation bed. Similarly, as compared to geogrid, more than 50% reduction in the displacement was observed in the presence of geocell. In addition,163% increase in the damping ratio of the soil was observed in the presence of geocell. In this way, the study highlights the possible new applications of geocell in supporting the machine foundations.

A rigid circular foundation with diameter of 150 mm was subjected to two modes of vibration each mode applies with two frequencies by Fattah et al. [10]. The foundation was placed at three depths within dry sand with two relative densities in a test model with dimensions of (800×800×1000) mm. It was concluded that the edge points stresses for circular foundation showed an increase from one side to another (the increase in the direction of the rocking mode) by150-100%, while most test models subjected to vertical vibration mode had a depression under the center of the foundation making peak stress levels just around the center of footing.

The objective of the current study is to explore the results related to the parameters of the dynamic load (number of loading cycles and frequency of load) related to the circular footing of a machine on the dynamic shear strength parameters (for sand soil (ϕ°_{dyn}) and for clay soil (Cu_{dyn})) in addition to the amplitude strain of the foundation.

2. TESTING MATERIAL AND TEST PROGRAM

Two types of soil are used in this research; the first type is sand which was brought out of Karbala city in Iraq. The physical properties of the sand are illustrated in Table 1. Figure 1 shows the sample soil grain size distribution. The second type of soil used in this research is clay which had been brought from a river embankment

TABLE 1. Physical properties of sand soil

Index properties	Value	Specification Ref.
Specific gravity, Gs	2.66	[11]
Uniformity coefficient, C_u	3.91	[11]
Curvature coefficient, C_c	0.77	[11]
Classification of soil-USCS	SP	[11]
Maximum dry-unit weight (kN/m³)	18.63	[11]
Minimum dry-unit weight (kN/m³)	15.71	[11]
Maximum void-ratio	0.66	-
Minimum void-ratio	0.4	-
Angle of internal-friction ϕ° at R.D =50%	39.5°	[11]

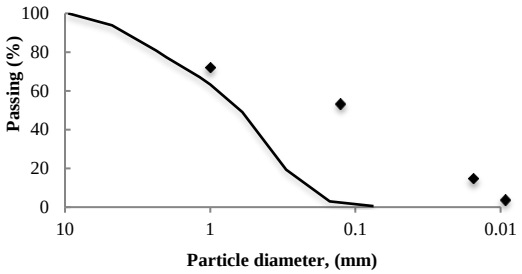

Figure 1. Grain size distribution curve of sandy soil

in the south of Baghdad (Iraq). Its physical properties are listed in Table 2. Consolidation test was carried out on clayey soils prepared at two undrained shear strengths; 50 and 70 kN/m^2 according to ASTM D2435 specifications [11]. The results are presented in Table 3.

The experimental work was carried out using a steel tank of dimensions (800 x 800 x 1000 mm) made of steel plate with a thickness of 6 mm, double-sided, to hold the soil. These dimensions were chosen to persuade the boundary effects of physical models subject to dynamic loading. To get uniform density along the depth of the model, layers of soil of thickness 100 mm each were laid consequently and manually pressed to the specified levels.

TABLE 2. Physical properties of clay used

Test	Value	Specification
Liquid limit (LL) %	46	
Plastic limit (PL) %	21	[11]
Plasticity index %	25	
Specific gravity (Gs)	2.65	[11]
Gravel%	0	
Sand%	4	[11]
Silt%	35	
Clay%	61	
Activity	0.41	-
Expansion index, Cr	0.05	0.039

TABLE 3. Consolidation test results for medium and stiff clay

Parameter	Medium State	Stiff State
Undrained shear strength, Cu	50 kN/m^2	70 kN/m^2
Initial void ratio, e_o	0.38	0.23
Dry unit weight, γ_{dry}	19.3	21.2
Saturated unit weight, γ_{sat}	21.6	23.3
Compression index, Cc	0.1	0.059

3. MODEL SETUP

In order to simulate conditions as close as possible to those occurring in the field, a special testing machine has been designed and manufactured with attachments. The loading system is operated hydraulically and fixed to the rigid structure of the machine to adequately withstand the loading capacity as shown in Figure 2. The load application device was constructed from the following parts: 1. the steel loading-frame, 2. the system of electrical hydraulic, 3. loading-spreader plate, 4. settlement-measuring device, 5. the system of data monitoring and acquisition. Steel container (800*800*1000 mm).

3. 1. Angle of Internal Friction Measurement Device The concept of such tool was borrowed from the laboratory tool known as "Making ring Penetrometer" made by ELE company for laboratory tools manufacturing. A similar tool comprising of 60 mm distance across cone having a length of 40 mm plus a shank of a breadth of 25 mm plus a length of (120 mm) had been fabricated. This device is used to find the internal friction angle of the sand used in the tests at any loading cycle. This device is connected to the hydraulic cylinder system through the work of the grooves that allow to be installed in the structure of the machine as shown in Figure 3. When the cone completely penetrates the soil, the soil reaction (F) required to maintain this penetration is recorded.

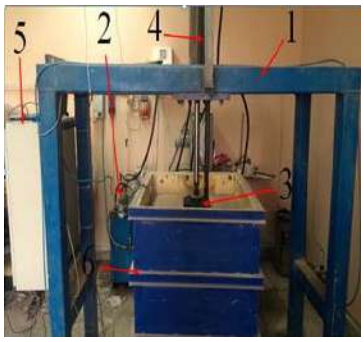

Figure 2. Details of the loading system

(a) (b)

Figure 3. Measuring device for soil shear resistance; a. Components, b. Measuring device

It is important to note that when the cyclic load is used, the frequency as well as the form of the desired function must be determined as a relationship between time (in seconds) and the applied force. This is done by using a unit called C-type. The mathematical form is slightly different from that of the function in practice, as shown in Figure 4.

The load amplitude was 2.5 kN applied at differenet frequencies; 0.5, 1 and 2 Hz.

3. 2. Estimating the Angle of Internal Friction After Dynamic Loading To estimate the angle of internal friction after number of cycles of loading, a procedure had been implemented. The relationship between the reaction of soil (F) and the angle of internal friction ϕ° was found by preparing thirteen soil model samples at different relative densities ranging from loose (R.D. = 30%) to very dense (R.D. = 90%). The direct shear test device was used to measure the angle of internal friction of the thirteen samples. For calculating the response of the used sand, a steel loading cone was put on a small example having the dimensions of (300×300×300 mm) as shown in Figure 5. The soil reaction was measured via a loading cell in addition to a digital display device. To this end, the tool velocity had been set at (2 mm/min.) for all measurements with applied pressure of (2.5 kN). The results of the soil reaction, unit weight and the angle of internal friction for the thirteen samples at relative densities are presented in Table 4. The relation of soil resistance to penetration (F) with the soil unit weight and relation between the soil resistance (F) along with the relative density of sand can be seen in Figures 6 and 7.

$$\text{Unit weight} = 0.0033\ F + 15.98 \quad (3)$$

$$\text{Relative density} = 0.104\ F + 6.531 \quad (4)$$

A pressure/tension loading cell from "SEWHA", model S-beam type (SS300), was used to calculate the persistent loading applied. The cell was linked to a numerical weight indicating tool in order to display loading amounts.

3. 3. Measuring of the Undrained Cohesion of Clay The second point was determining the variation of shear strength after carrying out dynamic tests on model footings on clayey soil. The undrained shear strength was measured using a portable vane shear device.

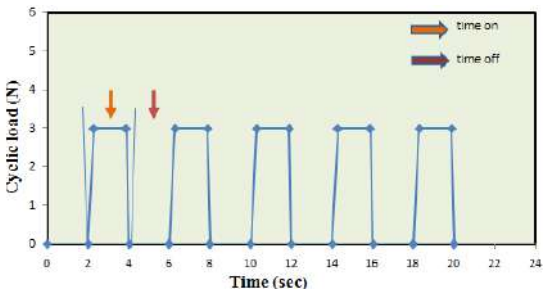

Figure 4. Realistic load-time relationship

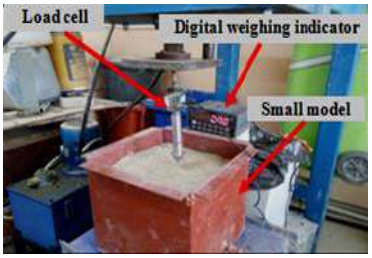

Figure 5. Manufactured apparatus for measuring the angle of friction

TABLE 4. Mobilized soil-reaction, unit weight, and angle of internal friction of sand

Test No.	Relative density R.D.%	Unit weight γ_d in kN/m^3	Angle of internal friction ϕ°	Reaction of soil F in N
1	30	16.48	35.2	245.77
2	30.2	16.49	37.8	247.41
3	37.3	16.68	38.3	305.58
4	44.2	16.87	39.4	320.78
5	50	17.04	39.5	360.97
6	55	17.19	40.2	404
7	60	17.34	40.4	541.14
8	64	17.46	40.4	590.21
9	70.4	17.66	40.8	620.60
10	76.6	17.85	41.2	654.81
11	80	17.96	42	708.15

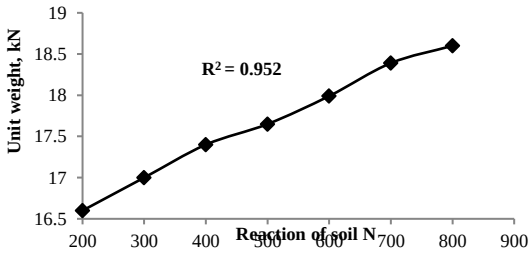

Figure 6. Soil reaction vs. unit weight

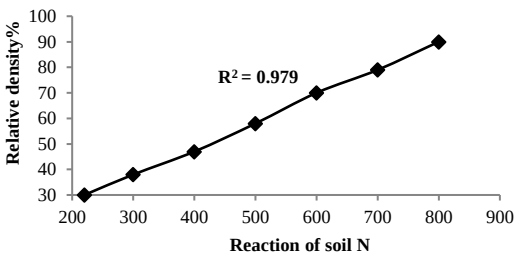

Figure 7. Soil reaction vs. relative density

4. RESULETS AND DISCUSSION

The bearing capacity of shallow foundations under static loads has been extensively studied and data are reported in literature. However, foundations can be subjected to dynamic loads which could be in different modes and directions. Such loading may induce large permanent deformation in soil by affecting its shear strength [12]. Thus the bearing capacity of foundations under dynamic loads has also been extensively studied and reported in literature. Nevertheless, most of the previous studies have been based on theoretical procedures with no supportive experimental data especially when examining the behavior of the bearing capacity of machine foundation under dynamic loading. Therefore, this research comes to study the bearing capacity under machine foundation by experimental work.

4. 1. Effect of Dynamic Load on the Angle of Internal Friction of Sand The shear strength of soil is of special relevance among geotechnical soil properties for it is one of the essential parameters for analyzing and solving stability problems, besides bulk density. In all tests, the angle of internal friction was measured under the footing at the middle and the end of the test (i.e., after 500 and 1000 loading cycles, respectively). It was also measured at different locations in the model before and after the dynamic load test.

Figure 8 shows the variation in the angle of friction before, during and after the tests of circular model of footing on medium and dense sand. The results are summarized in Table 5. It is noticed in Table 5 that the angle of internal friction of the soil located under the footing is considerably affected, while little change in the angle of internal friction on points located at the footing

TABLE 5. After test values of internal friction angle of sand

Load = 0.25 ton	After 1000 cycles at edge	After 500 cycles at center	After 1000 cycles at center
a. Medium sand			
f_o= 0.5 Hz	39.72	39.92	40.153
f_o=1 Hz	39.66	40.00	40.08
f_o= 2 Hz	39.61	39.74	39.97
b. Dense sand			
f_o= 0.5 Hz	42.34	42.64	43.12
f_o= 1 Hz	42.27	42.57	42.84
f_o= 2 Hz	42.25	42.32	42.65

edge or other location in model. The reason for this is that the soil particles in the failure zone do not always follow the path of least resistance, resulting in higher shear strength of soil, which leads to higher bearing capacity.

During cyclic loading, the sand undergoes recoverable and irrecoverable strains. Under a given cyclic load, the recoverable strain is reasonable constant and the irrecoverable strain accumulates with number of cycles [13].

4. 2. Undrained Shear Strength under Dynamic Load Because it is necessary to know the strength and some deformation characteristics of soil under dynamic loading, the undrained shear strength has been measured at different locations below the center and edge of footing, using portable vane shear device, before and after the dynamic loading test was performed. Figure 9. shows the variation of the undrained shear strength under dynamic loading. It can be noticed that the undrained shear strength of clay increased about 9 -25%. This is

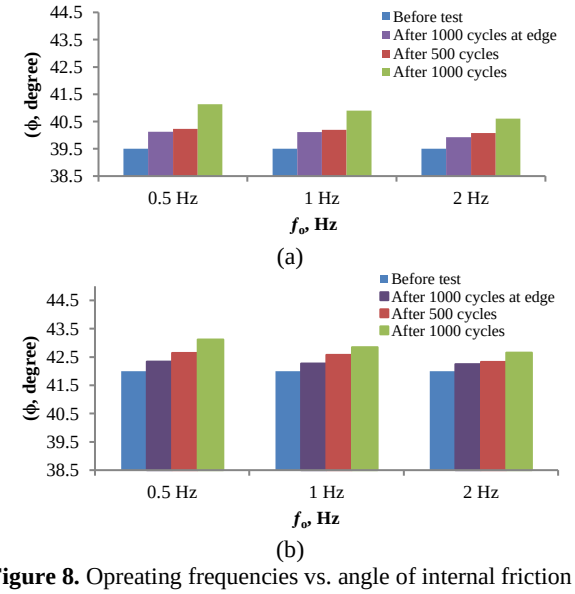

Figure 8. Opreating frequencies vs. angle of internal friction of sand; a. Medium sand, b. Dense sand

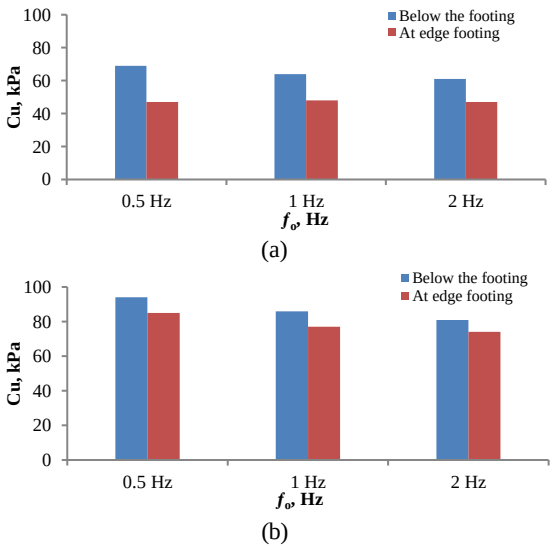

Figure 9. Opreating frequency vs. undrained shear strength; a. Medium clay, b. Stiff clay

because of compression of clay caused by dynamic loads. In addition, there is a rapid reorientation of soil particles which overides the repulsive forces between clay particles and brings them close together resulted in strong structure of the clay. Table 6 illustrates the value of undrained shear strength at different frequencies for medium and stiff clayey soil.

4. 3. Cumulative of Strain for Soil The response of soils subjected to dynamic loading is affected by different factors. The most important factors are soil type, stress or settlement and specific test conditions. In addition, the loading conditions, of a given dynamic test, imposed on soil affect its response. In particular, the dynamic response of such soils depends on the frequency and type of dynamic loading.

Figures 10 and 11 show the relationship between number of load cycles and strain of soil (S_N/H) where (S_N) is the settlement of the surface footing at any number of cycles and (H) is the thickness of the soil layer in the steel box. Table 7 presents the strain values at the end of 1000 cycles at different frequencies for both types soil. It can be seen that the strain decreases with the frequency. This is caused by low load frequency that provides enough time for the soil compression and so this results in increased rate of strain.

The strain has increased with decreased frequency. There was a sharp increase in strain up to the cycle (500) and then there was a gradual increase until it levels out at (800) to (1000) cycles depending on the frequency used. This increase can be attributed to the increase in the period of loading time during each cycle. In addition, the total period taken by the slow frequency test was greater than the period taken by the rapid frequency test within the same number of cycles.

The trend of the strain confirms with the findings reported by [14, 15] who found that the behavior of foundation settlement under the load frequency has three main modes; the first mode during the dynamic excitation, the second mode during the free vibration of the system, and the third mode during the time that the soil-foundation system reached to its physical equivalence (i.e reach the strain to the stability stage).

TABLE 6. Undrained shear strength after 1000 cycles in clay

Location	After 1000 cycles at edge	After 1000 cycles below footing
Cu, kPa		**50**
f_o = 0.5 Hz	48	69
f_o =1 Hz	46	65
Cu, kPa		**70**
f_o = 0.5 Hz	85	94
f_o =1 Hz	74	86

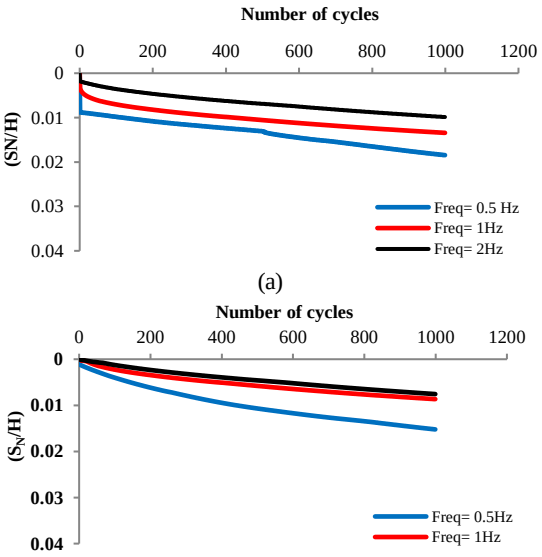

Figure 10. Number of cycles vs. rate of strain in sand for load amplitude (0.25 ton); a. Medium sand, b. Dense sand

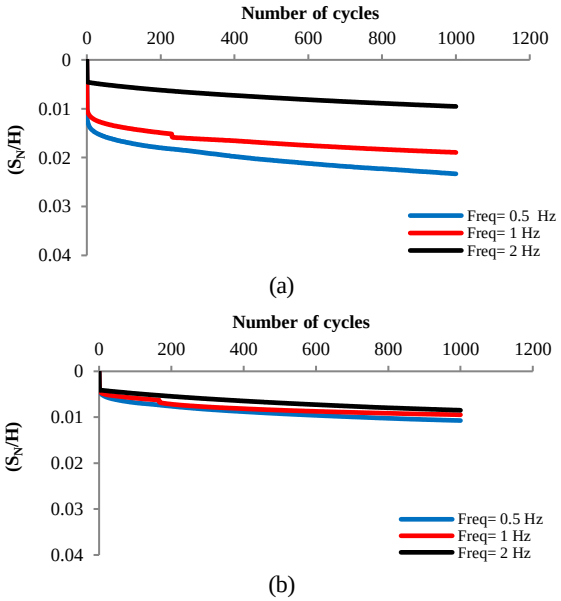

(b)

Figure 11. Number of cycles vs. rate of strain in clay for load amplitude (0.25 ton); a. Medium clay, b. Stiff clay

TABLE 7. The values of cyclic strain at different frequencies for both soils.

Soil type	Sand		Clay	
f_o, Hz	Medium	Dense	Medium	Stiff
0.5	0.018	0.014	0.022	0.015
1	0.013	0.008	0.018	0.008
2	0.009	0.006	0.010	0.006

4. LIMITATIONS OF THE PRESENT WORK

The present work, which deals with the dynamic response of machine foundations to steady state dynamic loading, clarifies the response of soil and foundation to such loading condition. The present work cannot be considered as a complete study of the response of machine foundations to dynamic loading (in addition to the data available inliterature), which are restricted to the number of variables studied especially for the measurements of stresses inside soil media. Other parameters that influence the behavior of such machine foundations have not been taken intoconsideration in this work because of the limited time available and cost. Hence, the limitations within the testing program are the footing size, the soil is sand and clay with specific properties in addition to the type of the manufactured machine with harmonic loading fuction.

5. CONCLUSIONS

1. The shear strength parameters for footings under dynamic load had increased according to the dynamic strain amplitude. The higher the dynamic strain amplitude, the higher was the rate of shear strength parameters increase.
2. The induced shear strength parameters after the application of the dynamic load decrease when the load frequency increases from (0.5) to (2) Hz. This is because more energy is carried away by the waves, which originate not only from the base of the foundation, but also from the vertical faces of the foundation in contact with the soil.
3. The strain has increased with decreased frequency. There was a sharp increase in strain up to the cycle (500) and then there was a gradual increase until it levels out at (800) to (1000) cycles depending on the loading frequency.
4. Higher strains were obtained for model footing on looser sand or softer clay.

6. REFERENCES

1. Tripathy, S., and Desai, A. K. "Seismic analysis of turbo machinery foundation: Shaking table test and computational modeling." ***Earthquake and Structures***, Vol. 12, No. 6, (2017), 629–641. https://doi.org/10.12989/eas.2017.12.6.629
2. Richart, F. E., and Whitman, R. V. "Comparison of Footing Vibration Tests with Theory." ***Journal of the Soil Mechanics and Foundations Division***, Vol. 93, No. 6, (1967), 143–168. Retrieved from https://trid.trb.org/view/126866
3. Vesic, A. S. "Analysis of Ultimate Loads of Shallow Foundations." ***Journal of the Soil Mechanics and Foundations Division***, Vol. 99, No. 1, (1973), 45–73. Retrieved from https://trid.trb.org/view/125905
4. Carroll, W. "Dynamic Bearing Capacity of Soils: Vertical Displacements of Spread Footings on Clay: Static and Impulsive Loadings." Technical Report No. 3-599, Report 5, U.S. Army Corps of Engineers, Waterways Experiment Station, Vicksburg, Mississippi, (1963).
5. Baidya, D. K., Muralikrishna, G., and Pradhan, P. K. "Investigation of Foundation Vibrations Resting on a Layered Soil System." ***Journal of Geotechnical and Geoenvironmental Engineering***, Vol. 132, No. 1, (2006), 116–123. https://doi.org/10.1061/(ASCE)1090-0241(2006)132:1(116)
6. Fattah, M. Y., Karim, H. H., and Al-Qazzaz, H. H. "Cyclic Behavior of Footings on Dry Sand under Different Rates of Loading." ***International Journal of Construction Engineering and Management***, Vol. 6, No. 6, (2017), 240–253. https://doi.org/10.5923/j.ijcem.20170606.03
7. Kirar, B., Krishana, A. M., and Rangwala, H. M. "Dynamic properties of soils for the design of machine foundations." In Proceedings of Indian Geotechnical Conference, (2016), 1–4. Retrieved from http://www.igs.org.in:8080/portal/igc-proceedings/igc-2016-chennai-proceedings/theme5/IGC_2016_paper_265.pdf
8. Cabalar, A. F., Khalaf, M. M., and Karabash, Z. "Shear modulus of clay-sand mixtures using bender element test." ***Acta Geotechnica Slovenica***, Vol. 15, No. 1, (2018), 3–15. https://doi.org/10.18690/actageotechslov.15.1.3-15.2018
9. Venkateswarlu, A., and Hegde, A. "Numerical Analysis of Machine Foundation Resting on the Geocell Reinforced Soil Beds." ***Geotechnical Engineering Journal of the SEAGS & AGSSEA***, Vol. 49, No. 4, (2018), 55–62. Retrieved from https://www.researchgate.net/publication/329451307
10. Fattah, M. Y., Salim, N. M., and Alwan, K. K. "Contact pressure distribution under circular shallow foundation subjected to vertical and rocking vibration modes." ***Journal of Building Engineering***, Vol. 26, (2019), 100908. https://doi.org/10.1016/j.jobe.2019.100908
11. American Society for Testing and Materials. Annual Book of ASTM Standards, (2007).
12. Ranjan, G. and Rao, A.S.R., Basic and applied soil mechanics. New Age International, (2007).
13. O'reilly, M. P., and Brown, S. F. "Observations on the resilient shear stiffness of granular materials." ***Geotechnique***, Vol. 42, No. 4, (1992), 631–633. https://doi.org/10.1680/geot.1992.42.4.631
14. Tutunchian, M. A., Shahnazari, H., Salehzadeh, H., and Asadi, M. "Study on Dynamic Behavior of Shallow Foundations on Liquefiable Sand, Using Video Processing Technique." ***Electronic Journal of Geotechnical Engineering***, Vol. 16, (2011), 945–960. Retrieved from https://www.researchgate.net/publication/265119640
15. Fattah, M. Y., Al-Mosawi, M. J., and Al-Americ, A. F. I. "Stresses and pore water pressure induced by machine foundation on saturated sand." ***Ocean Engineering***, Vol. 146, (2017), 268–281. https://doi.org/10.1016/j.oceaneng.2017.09.055

Persian Abstract

چکیده

در این مقاله با بررسی تغییر پارامترهای مقاومت برشی خاک و کرنش با تعداد چرخه‌ها، بر پاسخ فونداسیون دستگاه دایره‌ای که روی خاک‌های مختلف (شن و ماسه) استراحت می‌کند، تمرکز می‌شود. هدف از مطالعه حاضر، کشف نتایج مربوط به پارامترهای بار دینامیکی (تعداد چرخه بارگیری و فرکانس بار) مربوط به پایه دایره‌ای یک دستگاه بر روی پارامترهای مقاومت برشی پویا (برای خاک شنی (ϕ°_{dyn}) و برای خاک رس (Cu_{dyn}) علاوه بر فونداسیون کرنش دامنه، است. برای شبیه‌سازی لرزش عمودی یک پایه ماشین دایره‌ای، یک مجموعه ویژه طراحی و ساخته شده است. یک پایه ماشین دایره‌ای فولادی با قطر ۱۵۰ میلی‌متر برای نشان دادن پایه استفاده شد. در مجموع ٦ مورد برای در نظر گرفتن اثر پارامترهای مختلف از جمله فرکانس‌های مختلف (۰/۵، ۱ و ۲ هرتز) مورد بررسی قرار گرفت. حالت شن (متوسط و متراکم) که با تراکم نسبی (۵۰ و ۸۰٪) مطابقت داشت، در حالی که حالت رس (متوسط و سفت) مطابق با مقاومت برشی زهکشی‌نشده (۵۰ و ۷۰ کیلو پاسکال) بود. تمام آزمایشات تحت دامنه بار ۲/۵ KN انجام شد. مشخص شد که سرعت افزایش پارامترهای مقاومت برشی برای خاک تحت یک دستگاه دایره‌ای قابل ملاحظه‌ای هنگام افزایش فرکانس برای هر دو نوع خاک زیر پایه کاهش می‌یابد. در حالی که تغییر کمی در پارامترهای مقاومت برشی یا حتی هیچ تغییری تحت تأثیر مکان‌های دیگر مشاهده نشده است. علاوه بر این، کرنش دامنه هنگام افزایش فرکانس برای هر دو نوع خاک کاهش یافته است.

IJE TRANSACTIONS B: Applications Vol. 33, No. 8, (August 2020) 1499-1511

International Journal of Engineering

Journal Homepage: www.ije.ir

Experimental Study of the Combined Use of Fiber and Nano Silica Particles on the Properties of Lightweight Self Compacting Concrete

M. Ghanbari, O. Kohnehpooshi*, M.Tohidi

Civil Engineering Department, Sanandaj Branch, Islamic Azad University, Sanandaj, Iran

PAPER INFO

Paper history:
Received 11 March 2020
Received in revised form 20 May 2020
Accepted 12 June 2020

Keywords:
Lightweight Concrete
Scoria Aggregate
Nano Silica Particles
Glass Fiber
Pozzolanic Materials
Self Compacting Concrete

ABSTRACT

In fiber concretes, microcracks in the boundary area between the cement paste and the surface of aggregates or fibers are higher. Natural and artificial pozzolans can be used for reinforcing this area. In this research, the combination of glass fiber, zeolite, and nano silica particles were used in lightweight self-compacting concrete containing scoria. Fiber volume fractions between 0% to 1.5% in combination with 0% to 6% nano silica particles were examined. The scoria aggregates and zeolite were considered constant in all mixes. The fresh and hardened properties of specimens were evaluated using T50, slump flow, V-funnel, L-box, compressive strength, splitting tensile strength, flexural strength, ultrasonic, electrical resistivity, and water absorption tests. Also, the microstructure of concrete was investigated using scanning electron micrograph images. The combined use of nano silica particles and glass fiber increased the splitting tensile strength by about 3 to 56%. Also, the use of nano silica particles increased electrical resistivity by 136 to 194%. Nano silica particles, due to their high specific surface and high reactivity, result in consuming calcium hydroxide that is quickly organized within the hydration, filling pores of the calcium silicate gel structure and eventually producing more and more compacting hydrated products.

***doi**: 10.5829/ije.2020.33.08b.08*

1. INTRODUCTION

Despite the major benefits of concrete, there are two major disadvantages inherent in it, one is low tensile strength and the other is relatively high density [1]. There are generally two different methods to resolve the relatively high weight of concrete buildings. The first method is based on increasing concrete strength to reduce dimensions of elements and thereby to decrease volume of concrete and weight of rebar. The second method is based on the density reduction of concrete and the use of lightweight concrete. However, tensile weakness of concrete, which results in low ductility and high brittle, is considered as a weak point. To solve this problem, fibers that are uniformly dispersed in the concrete volume are used. Destruction and deterioration of concrete are highly dependent on the formation of cracks and micro cracks due to loading or environmental impacts. Heat and moisture transfers in the cement paste result in the formation of microcracks, and such microcracks are concentrated on the surface of coarse grains [2–6].

Ehsani Yeganeh et al. [4] evaluated the attributes of self compacting concrete containing fiber. Three types of high density polyethylene fibers, crumb rubber and polyvinyl alcohol were used. The results showed that adding fibers improves compressive, tensile and flexural strengths and increases the cracks [4]. Badogiannis et al. [7] evaluated the behavior of steel and polypropylene lightweight concrete. For this purpose, pumice was used as a lightweight aggregate. Based on this study, fiber can improve the cracking strength of concrete [7]. Wu et al. [8] evaluated the microstructural characteristics of steel and carbon fibers lightweight concretes. Five different lightweight aggregates were used and volume percentage of fibers was considered 0.3, 0.6 and 0.9. The results showed that the use of fibers in lightweight concrete has

*Corresponding Author Email: *Omidkohnehpooshi@gmail.com*
(O. Kohnehpooshi)

Please cite this article as: M. Ghanbari, O. Kohnehpooshi, M.Tohidi, Experimental Study of the Combined Use of Fiber and Nano Silica Particles on the Properties of Lightweight Self Compacting Concrete, International Journal of Engineering (IJE), IJE TRANSACTIONS B: Applications Vol. 33, No. 8, (August 2020) 1499-1511

little effect on compressive strength but increases tensile strength. The water-cement ratio and the properties of aggregates can also influence the results [8].

In the studies mentioned above, it was observed that making fiber concrete is an effective step in preventing the propagation of microcracks and cracks and compensating for the tensile strength weakness of concrete. The energy-absorption property of concrete can greatly reduce the risk of failure of concrete structures, especially in areas which are under repeated seismic loads. However, addition of some types of fibers such as steel fibers to structural lightweight concrete, especially with a volume greater than 1%, increases the density of lightweight concrete they have low strength against corrosion. To solve this problem, other fibers such as carbon, aramid, polypropylene (PP), polyethylene (PE) and polyvinyl alcohol, polyester, and glass fiber (GF) can be used, either in single or in combination with lightweight concrete to improve the strengths and ductility.

To reinforce the boundary area between the cement paste and the surface of aggregates or fibers, nano silica particles (nSPs) can be used as a highly active artificial pozzolan which is from nanotechnology products. The presence of nSPs can increase the bonding strength of aggregate with paste as well as fibers with cement paste. Senff et al. [9] indicated that setting time of cement was decreased by adding nSPs to the cement. Naniz and Mazloom [10] investigated the characteristics of self compacting lightweight concrete containing nSPs and silica fume. The evaluations indicated that the combined use of silica fume and nSPs significantly improve the concrete characteristics [10]. Mohammad et al. [11] evaluated the effects of nSPs on the characteristics of concrete containing fly ash as a replacement for a part of cement. NSPs decreased the porosity of cement to 13.4% [11]. Abd Elrahman et al. [12] evaluated lightweight concrete containing of nSPs. The results indicated that nSPs modify the structure of the fine pores and thereby improve the concrete transport attributes [12].

On the other hand, a lot of research has been done on the use of different fillers such as fly ash, zeolite, metakaolin, etc [13–19]. It is more important to use filler that has both filler and pozzolanic properties and to participate in the hydration reaction. Zeolite is one of the fillers that has been considered as a pozzolanic filler in concrete in various studies and has had many positive effects. Nanoparticles with different fillers can exhibit different behaviors and optimum percentages. Therefore, the investigation of nanoparticles together with various fillers is important.

This study investigated the impact of GF, nSPs and zeolite on the characteristics of self compacting lightweight concrete which were made with scoria aggregates. The fresh concrete attributes were evaluated using slump flow, T50, V-funnel, L-Box and the properties of hardened concrete were investigated using compressive, tensile, flexural and ultrasonic tests. The durability of concrete specimens was also determined by electrical resistivity and concrete water absorption tests.

2. SCHEME OF EXPERIMENTAL INVESTIGATIONS

2. 1. Materials The materials include Portland cement (Type II), sand, scoria mineral shell, drinking water, superplasticizer, GF, zeolite, and nSPs. The coarse aggregates were the scoria lightweight aggregates which were obtained from Qorveh (Iran). In general, scoria is created by entering volcanic melting materials into aquatic environments such as seas and lakes and rapid cooling. Its color is black, light gray and dark brown. It also has irregular open and closed pores and has an uneven, angular surface. The largest scoria aggregate size used in this study is 12.5 mm. Its density is 0.68 g/cm^3.

The characteristics of the scoria are introduced in Table 1. The bulk density of sand is 1800 kg/m^3 and the water absorption rate is 3.2%. ASTM C136 [20] was used for gradation of aggregates. The sand gradation and scoria characteristics are introduced in Table 2. This table shows the allowable range of ASTM C330. The range of gradation is between the upper and lower boundaries of the ASTM C330 [21].

Potable water was used with a pH of about 7.5. The cement is Portland cement type II, a product of Hegmatan plant with a density of 3.15 g/cm^3. The physical and chemical properties of this cement are presented in Table 1. The nSPs are in powder form with a size of 15 to 20 nm. The physical properties and chemical analysis of

TABLE 1. Properties of Portland cement, Scoria, Zeolite and nSPs

Item	Scoria	Portland cement	Zeolite	nSPs
SiO_2 (%)	58.8	21.54	67.79	99.98 ≥
Al_2O_3 (%)	32.16	4.95	13.66	-
Fe_2O_3 (%)	3.98	3.82	1.44	-
CaO (%)	3.28	63.24	1.68	-
MgO (%)	1.5	1.55	1.20	-
SO_3 (%)		2.43	0.5	-
K_2O (%)	-	0.54	1.42	-
Na_2O (%)	-	0.26	2.04	-
Loss on ignition (%)	3.02	-	10.23	1.00 ≤
Specific gravity (g/cm^3)	0.68	0.75	1.1	0.5
Specific surface area (m^2/g)	-	326	1.1	200

TABLE 2. Gradation properties of aggregates and their comparison with ASTM-C33

Sieve size (mm)	ASTM-C33 limits for coarse aggregates	Percentage passing (Scoria)	ASTM-C33 limits for fine aggregates	Percentage passing (Sand)
12.5	90-100	91	-	-
9.5	40-80	63	-	-
4.75	0-20	10	-	-
2.36	0-10	6	95-100	95
1.18	-	-	40-80	60
0.3	-	-	10-35	25
0.15	-	-	5-25	17

these nSPs are introduced in Table 1. The chemical analysis of zeolite-based on ASTM C311 [22] is presented in Table 1. The fibers used in this study are A/type. The characteristics of GF are presented in Table 3. The superplasticizer function is the separation and dispersion of cement by repulsive forces caused by static electric load. This product works well when silica additives are used in the mixed design for preventing slump drop. It is chlorine free and is in adjustment with ASTM-C494 [23]. Its color is light brown and it has a pH of 6 to 7 and a density of 1.2 g/cm^3.

2. 2. Mixed Design The properties of mixed design and the amounts of each consuming materials are presented in Table 4. The mixed design was obtained by the use of previous experimental studies and trial and

TABLE 3. Properties of GF

Length (mm)	Diameter	Tensile strength (MPa)	Module of elasticity (GPa)
12	0.02	1400	77

TABLE 4. Mixed design

Mix ID	Water-binder ratio	Cement	Nanosilica		Zeolite		Glass fiber (%)	Water (kg)	Sand (kg)	Scoria (kg)	Superplasticizers	
			Percent	Content (kg)	Percent	Content (kg)					Percent	Content (kg)
NS0F0	0.4	405	0	0	10	45	0	180	950	393	1.62	7.45
NS0F0.25	0.4	405	0	0	10	45	0.25	180	950	393	1.62	7.45
NS0F0.50	0.4	405	0	0	10	45	0.5	180	950	393	1.62	7.45
NS0F0.75	0.4	405	0	0	10	45	0.75	180	950	393	1.62	7.45
NS0F1	0.4	405	0	0	10	45	1	180	950	393	1.62	7.45
NS0F1.5	0.4	405	0	0	10	45	1.5	180	950	393	1.62	7.45
NS2F0	0.4	396.9	2	9	10	44.1	0	180	950	393	1.62	7.45
NS2F0.25	0.4	396.9	2	9	10	44.1	0.25	180	950	393	1.62	7.45
NS2F0.50	0.4	396.9	2	9	10	44.1	0.5	180	950	393	1.62	7.45
NS2F0.75	0.4	396.9	2	9	10	44.1	0.75	180	950	393	1.62	7.45
NS2F1	0.4	396.9	2	9	10	44.1	1	180	950	393	1.62	7.45
NS2F1.5	0.4	396.9	2	9	10	44.1	1.5	180	950	393	1.62	7.45
NS4F0	0.4	388.8	4	18	10	43.2	0	180	950	393	1.62	7.45
NS4F0.25	0.4	388.8	4	18	10	43.2	0.25	180	950	393	1.62	7.45
NS4F0.50	0.4	388.8	4	18	10	43.2	0.5	180	950	393	1.62	7.45
NS4F0.75	0.4	388.8	4	18	10	43.2	0.75	180	950	393	1.62	7.45
NS4F1	0.4	388.8	4	18	10	43.2	1	180	950	393	1.62	7.45
NS4F1.5	0.4	388.8	4	18	10	43.2	1.5	180	950	393	1.62	7.45
NS6F0	0.4	380.7	6	27	10	42.3	0	180	950	393	1.62	7.45
NS6F0.25	0.4	380.7	6	27	10	42.3	0.25	180	950	393	1.62	7.45
NS6F0.50	0.4	380.7	6	27	10	42.3	0.5	180	950	393	1.62	7.45
NS6F0.75	0.4	380.7	6	27	10	42.3	0.75	180	950	393	1.62	7.45
NS6F1	0.4	380.7	6	27	10	42.3	1	180	950	393	1.62	7.45
NS6F1.5	0.4	380.7	6	27	10	42.3	1.5	180	950	393	1.62	7.45

error in accordance with ACI-211 [24]. The studied variables were nSPs (0, 2, 4 and 6 % by weight of cement) and GF (0, 0.25, 0.50, 0.75 and 1 and 1.5 % by weight of cement), respectively. After making and molding, the specimens were kept in the mold for 24 hours. Then they were removed from the mold and moisture curing was performed until the age of the tests.

2. 3. Procedure The fresh concrete tests include slump flow, T50, V-funnel, L-box, respectively and the hardened concrete tests are compressive, splitting tensile, flexural, ultrasonic, electrical resistivity, water absorption and scanning electron micrograph (SEM), respectively. Tests related to evaluation of self-compacting concrete were performed according to the European guildlines for self-compacting concrete (EFNARC) [25]. Compressive, tensile and flexural behavior of concrete specimens were performed in accordance with ASTM C39 [26], ASTM C496 [27] and ASTM-C293 [28], respectively (Figure 1). For compressive strength, cubic molds with dimensions of 150×150×150 mm were used. In the splitting tensile strength test, a standard cylindrical mold with dimensions of 300×150 mm was used. The load was increased uniformly at a rate of 0.8 to 1.2 MPa/min until the specimen was failed. The maximum load was recorded and the splitting tensile strength was obtained from Equation (1)

$$T = \frac{2p}{\pi Ld} \quad (1)$$

T and P represent tensile stress and failure load, respectively. Also, L and d represent the length and diameter of specimen.

Prismatic specimens with dimensions of 100×100×400 mm were prepared for flexural strength test. The flexural strength was calculated by Equation (2).

$$S_f = \frac{3pl}{2bh^2} \quad (2)$$

where S_f is the flexural strength, p is the applying force in the middle of the span, b is the section width, h is the section height in mm, and l is the distance between the two supports.

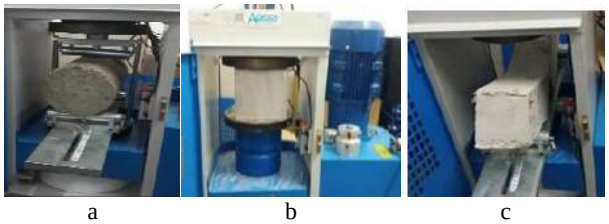

a b c

Figure 1. Experimental set up; a: Compressive strength, b: Splitting tensile strength, c: Flexural strength

Ultrasonic pulse velocity (UPV) test was performed by ultrasonic device on concrete specimens in accordance with ASTM C597 [29] (Figure 2). Ultrasonic test is a common method used to analyze the structure of concrete and to reveal its internal weaknesses (such as hole, cracking, lamination, etc) [30, 31].

The water absorption test conducted in accordance with ASTM C642 at 28 days of age. For this purpose, cubic specimens (100×100×100 mm) were heated at 50 degrees Celsius for 14 days. The specimens were immersed in a tank filled with water after the temperature of the specimens had been remained constant with the laboratory temperature and their initial weight had been read. After 1 and 24 hours of immersion, the specimens were weighed. The water absorption percentage of the specimens was obtained using Equation (3).

$$\omega = \frac{m - m_0}{m_0} \times 100 \quad (3)$$

where m and m_0 are the weight of wet and dry specimens, respectively.

Electrical resistivity is an indicator of the relationship between holes. This indicator determines concrete strength against penetration of liquid or gas through concrete surface that is in contact with the outside environment. Electrical resistivity is one of the intrinsic properties of materials, that is dependent on the nature and topography of the structure of the holes, moisture conditions, temperature and density of soluble ions in the environment. A device for measuring the electrical resistivity with a variable frequency of 10 to 10,000 Hz was used. Copper plates were used to attach the two heads of specimen to the device. In order to prevent the copper plates from attaching to the floor and the worktable, 150×150 mm plastic molds were used, and the copper plates were positioned 100 mm apart. Because a conductive material is essential to entirely bond the copper plates to the specimen surface, a cement paste was used. The cement paste, on the one hand, has a large number of free ions which is an electrical conductor with a low strength and on the other hand, it makes a perfect connection between the concrete surface and the copper plates. The method of measuring the electrical resistivity

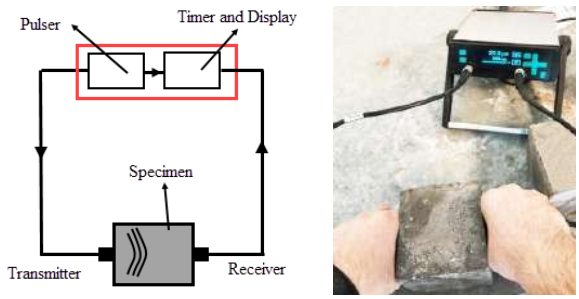

a b

Figure 2. Ultrasonic test; a: Schematic image, b: Real image

is that some cement paste was first placed on one of the copper plates and spread by a spatula. The specimen, which was in saturated surface dry conditions, was placed on the cement paste. Then, the top level of the specimen was covered with cement paste and the top copper plate was placed on the specimen with weight. Each of the wires of the device was connected to one of the copper plates, the frequency of the device was set at 10 Hz, and the electrical resistivity number was recorded [32–35]. Figure 3 shows the specimen and copper plates and the process of measuring electrical resistivity of hardened concrete. The electrical resistivity was calculated using Equation (4).

$$\rho = \frac{R.L}{A} \quad (4)$$

where, ρ is the specific electrical resistivity of concrete in ohms-meters; R is the electrical resistivity that has been read from the device in ohms-meters, A represents the surface area of concrete (m^2) and L represents the distance between positive and negative poles in meters. Estimation of corrosion probability of buried rebars in concrete based on electrical resistivity is presented in Table 5.

The compressive strength test was performed at 7, 28 and 90 days. Also, splitting tensile, flexural, electrical strength, ultrasonic, and water absorption tests were performed 28 days after curing of specimens. Three specimens were constructed for each experiment and the average was presented as the ultimate number. According to the variables and the tests, a total of 576 specimens were made and various tests were performed on them.

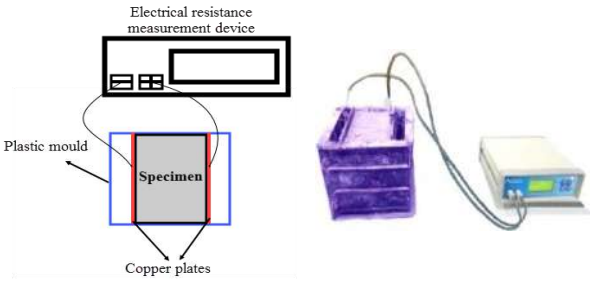

a b

Figure 3. Electrical resistivity device; a: Schematic image, b: Real image

TABLE 5. Estimation of corrosion probability of buried rebars in concrete based on electrical resistivity [34, 35]

Electrical resistivity (kΩ-cm)	Estimation of corrosion probability
Less than 50	Very high
Between 50 and 100	High
Between 100 and 200	Low
More than 200	Very low

3. RESULTS

3. 1. Fresh Concrete Test It was first tried to evaluate the concrete performance to ensure the minimum quality required for having self-compacting capabilities. Because the major physical and mechanical difference between self compacting concrete and usual concrete is the difference in efficiency and ease of transport and molding, it is necessary to control its performance. Control of fresh self compacting concrete properties is presented according to EFNARC [25] in Table 6. As it can be seen, the results of the tests on fresh concrete show that all the lightweight concrete specimens have self-compacting concrete conditions and are within

TABLE 6. Fresh concrete results

Mix ID	Slump flow		V-funnel time (sec)	L-box (H_2/H_1)
	D (mm)	T_{50} (s)		
NS0F0	747	3	8.1	0.93
NS0F0.25	733	3.2	8.7	0.92
NS0F0.50	721	3.3	8.9	0.89
NS0F0.75	716	3.3	9.3	0.88
NS0F1	691	3.5	9.5	0.86
NS0F1.5	683	3.5	9.9	0.84
NS2F0	717	3.1	9.1	0.9
NS2F0.25	713	3.3	9.6	0.89
NS2F0.50	677	3.4	9.6	0.88
NS2F0.75	656	3.4	9.9	0.87
NS2F1	645	3.6	10.1	0.85
NS2F1.5	635	3.7	10.6	0.84
NS4F0	692	3.3	9.9	0.88
NS4F0.25	684	3.5	10.2	0.87
NS4F0.50	665	3.8	10.6	0.86
NS4F0.75	642	3.9	10.6	0.85
NS4F1	614	4	10.9	0.83
NS4F1.5	609	4.2	11.3	0.82
NS6F0	677	3.7	10.6	0.81
NS6F0.25	667	3.9	10.9	0.79
NS6F0.50	642	4	11.2	0.77
NS6F0.75	619	4.3	11.5	0.76
NS6F1	608	4.6	11.7	0.74
NS6F1.5	601	4.8	11.9	0.72
EFNARC recommendatis [29]				
Min.	550	2	6	0.8
Max.	850	5	12	1

the EFNARC standard range. According to the EFNARC [25], the slump flow range should be between 550 and 850 mm and all the investigated specimens are in this range. According to EFNARC [25], the allowable range of the H_2/H_1 relation is between 0.80 and 1 and the allowable range of V-funnel is between 6 to 12 seconds and the investigated specimens are in this range. Therefore, according to the mentioned values, the investigated concrete specimens are considered self-compacting.

As shown in Table 6, it is observed that as the percentage of GF and nSPs decreases, the slump flow decreases, so that the lowest slump value occurred in the NS6F1.5 mixed design and the slump value corresponding to the control specimen became approximately 1.24 times more than the slump value corresponding to NS6F1. As it is expected, the addition of fibers reduces the slump flow, that is, it increases the locking probability. This is due to the higher value of fibers and their internal strength against flow, as well as increasing friction and internal collisions between aggregates and fibers [36]. On the other hand, the results of T50 test show that T50 increases with increasing the percentage of GF and nSPs. In the NS2F0, NS4F0 and NS6F0 modes, the T50 increased by 3.3, 10 and 23.3%, respectively; while, in the NS0F0.25, NS0F0.50, NS0F0.75, NS0F1 and NS0F1.5 modes, T50 increased by 7.5, 10, 30, 60 and 77.5%, respectively.

The effect of GF and nSPs on flow time of V-funnel and blockage ratio are presented in Table 6. The results show that the presence of fibers in self-compacting lightweight concrete containing scoria increases the viscosity of concrete and the funnel discharge time increases with increasing fiber percentage. Also, all the times obtained from the V funnel test conform to the allowable range set by EFNARC [25] (6 to 12 seconds). The use of nSPs significantly increases the V-funnel time, so that the discharge time of concrete from V funnel for each specimen containing 0.25, 0.5, 0.75, 1 and 1.5% GF in which 6% of the nSPs were used became 31, 25.3, 25.8, 23.7, 23.2 and 20.2% higher than those corresponding to the specimens without nSPs. High specific surface area and high water absorption of nanoparticles are the most important reasons that have reduced the concrete flowability. The results of the L-box test show that all designs have a good filling ability. However, observations indicate that increasing the fiber percentage led to a decrease in the H_2/H_1 ratio. In other words, the presence of fibers reduces concrete passing ability through rebars and decreases with increasing percentage of concrete passing ability of fibers. According to the results obtained by Mohsenzadeh et al. [6], adding fibers reduces the flowability and this reduction is exacerbated by increasing fiber value. This issue is also considered in this study. In a study by Sivakumar et al. [37], it was shown that adding GF to self-compacting concrete reduces the concrete fluidity and for compensating this fluidity decline, it was attempted to have a high fluidity in the initial mixture. Taheri Fard et al. [38] also stated that the use of fibers has negative effects on the rheological attributes of self-compacting concrete.

3. 2. The Results of Hardened Concretes

3. 2. 1. Density The compositions in self compacting concrete are such that they have a higher density than the conventional concrete and they have a less empty space. In a study about comparing the characteristics of self compacting concrete and conventional concrete, Persson [39] stated that, the density of self compacting concrete is higher than the conventional concrete. Weight loss of a building or structure that is related to the density of self compacting concrete has the greatest effect on reducing the risk of earthquake acceleration. The density of lightweight self compacting concrete specimens after molding is presented in Table 7. Each recorded number has a density mean of 3 cubic specimens of 150×150×150 mm. According to ACI 213R-03 [40], the density of lightweight concrete should be between 1120 and 1920 kg/m^3. According to the obtained values, all investigated concrete specimens are in the range of lightweight concrete because the obtained density is in the range of 1885 to 1897 kg/m^3. The addition of nSPs and GF increased the density of the specimens by a very small percentage (about 0.6%). Although the addition of fibers has created cavities in concrete, the use of silica nanoparticles has had a positive effect on the microstructure of concrete and increased its density, which has led to a slight increase in the density of concrete.

3. 2. 2. Compressive Strength Compressive strength of specimens at agaes of 7, 28 and 90 days is presented in Figure 4. Also, the changes of compressive strength compared to the control specimens are shown in Figure 5. The use of GF in self compacting lightweight concrete specimens was not effective and in some cases,

TABLE 7. The density of specimens (kg/m^3)

Glass fiber	Nano Silica Particles			
	NS0	NS2	NS4	NS6
F0	1886	1888	1890	1893
F0.25	1885	1890	1890	1893
F0.5	1887	1890	1892	1894
F0.75	1888	1891	1891	1895
F1	1888	1892	1893	1896
F1.5	1890	1891	1894	1897

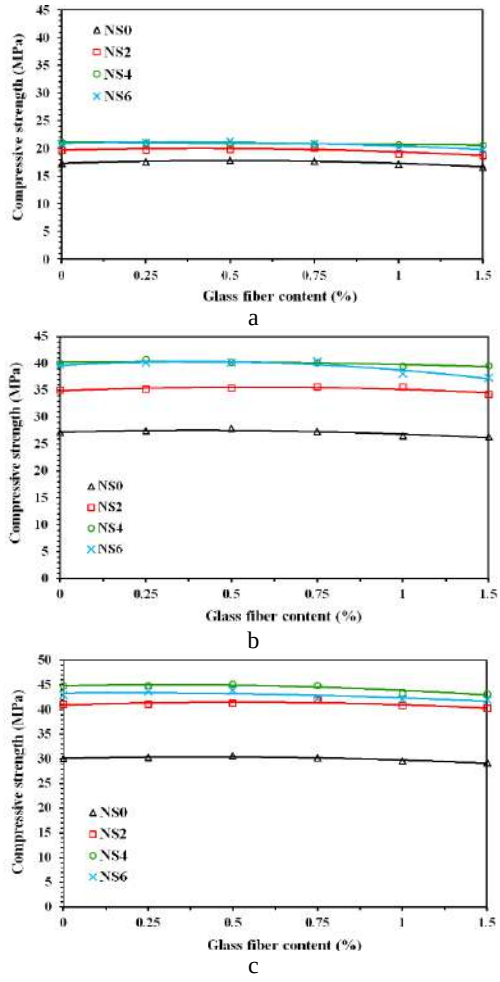

Figure 4. The results of compressive strength test; a: After 7 days, b: After 28 days, c: After 90 days

it even reduced the compressive strength at ages of 7, 28 and 90 days. The highest compressive strength obtained from adding GF is related to the specimens in which 0.5% GF were used, so that the 7, 28 and-day compressive strength of concrete specimens containing 0.5% GF (without nSPs) increased by 3.6, 2.6 and 1.75%, respectively, compared to the control specimen.

By increasing GF in self compacting lightweight concrete, their compressive strength decreased, so that the 7, 28, and 90-day strengths of specimens containing 1.5% of GF (without nSPs) decreased by 3.3, 2.9 and 3%, respectively. The decreasing process of compressive strength in lightweight concrete due to increasing fiber percentage can be ascribed to the balling phenomenon. If the percentage of fiber growth exceeds the optimum value, there is an uneven distribution of fibers followed by inappropriate fiber collision with the cement matrix and this reduces the effectiveness possibility of fibers to improve concrete structure [41]. This can be seen using the SEM images shown in Figure 6. By Examination of compressive strength of self compacting lightweight concrete specimens, it was revealed that the highest strength after 7, 28 and 90 days was related to concrete specimens containing 4% nSPs and 0.5% GF. The results showed that the use of nSPs can compensate for (or slightly increase) the compressive strength caused by adding GF. So that the 7, 28 and 90-day compressive strength of NS4F0.5 specimens grew by 21, 47.8 and 49.8%, respectively. NSPs, due to their high specific surface and high reactivity, result in consuming calcium hydroxide that is quickly organized within the hydration, filling pores of the calcium silicate gel structure and eventually producing more and more compacting hydrated products. The mentioned subject presented in the SEM images (Figure 6).

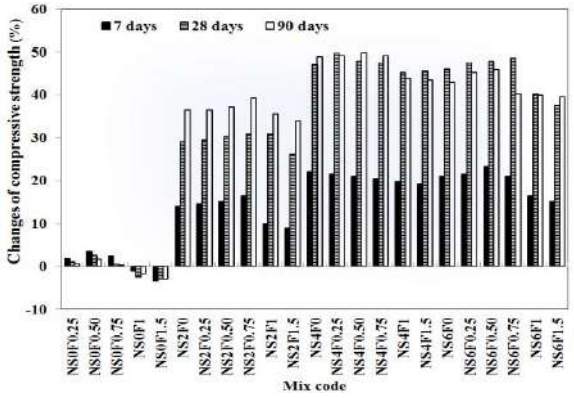

Figure 5. Changes of compressive strength

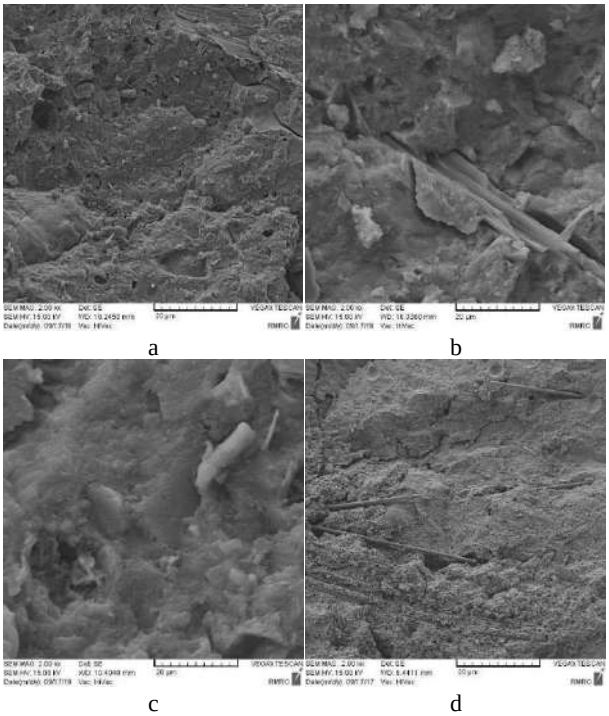

Figure 6. SEM pictures of some of the examined concrete specimens a: NS0F0 b: NS0F1.5 c: NS4F0 d: NS4F1.5

When the nano silica particles are distributed in the concrete, each particle is placed in a cubic pattern and acts as a nucleus. When hydration is started, nanoparticles, due to their high activity, accelerate to hydration and surround the hydrated products of nanoparticles as a nucleus. If the amount and distance of the nanoparticles are appropriate, the calcium hydroxide crystal growth will be restricted and the cement matrix will be more homogeneous. The smaller calcium silicate gel which usually has higher hardness is formed. By too much increasing of nanoparticles, the distance between them decreases, and the calcium hydroxide crystal cannot grow sufficiently. The use of 6% nSPs seems to be high in combination with the "free lime produced in the hydration process" and this caused the strength to decrease. A part of cement is replaced with a material that does not help the strength increase and leads to defects in strength. Another reason is that nanoparticles tend to become bulky because of their high surface energy, the content of nanoparticles which are more than the required amount results in uneven distribution, and nanoparticles appear as weak mass regions [42–44]. 4% nSPs showed the highest compressive strength among three different percentages of used nanosilica. Therefore, the optimum amount of using nSPs in concrete was obtained to increase the compressive strength of 4% by weight of cement. One possible cause of decrease in strength of the specimen containing 6% nSPs compared to the specimen containing 4% is the agglomeration of nSPs at high percentages of consumption.

3. 2. 3. Tensile Strength The tensile strengths of 24 lightweight concrete specimens were compared in Figure 7. The tensile strength in the specimens varied from 2.19 to 3.41 MPa. The combined use of nSPs and GF also had a significant effect on self compacting lightweight concrete containing zeolite and scoria aggregates. Splitting tensile strength at 28 days increased from 3 to 56% depending on the content of GF and nSPs (Figure 8). Using 0.25, 0.5, 0.75, 1 and 1.5% GF in lightweight concrete specimens containing zeolite and scoria aggregates increased the tensile strength by 2.7, 4.1, 8.7, 11.9 and 13.7%, respectively. The reason for increasing strength of GF can be due to increase in tensile strain tolerance through transfer of stresses from matrix to the fibers. Also, the use of 2, 4 and 6% nSPs in lightweight concrete specimens containing zeolite and scoria aggregates increased the tensile strength by 13.2, 47.5 and 34.7%, respectively.

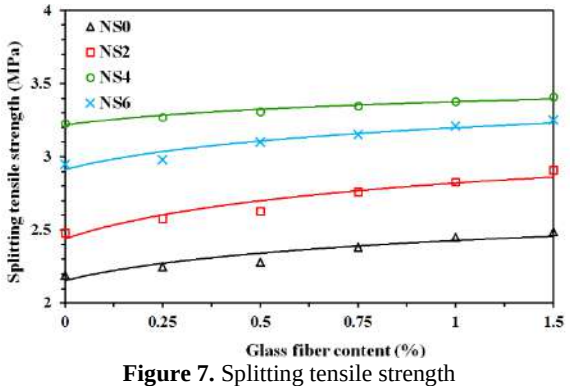

Figure 7. Splitting tensile strength

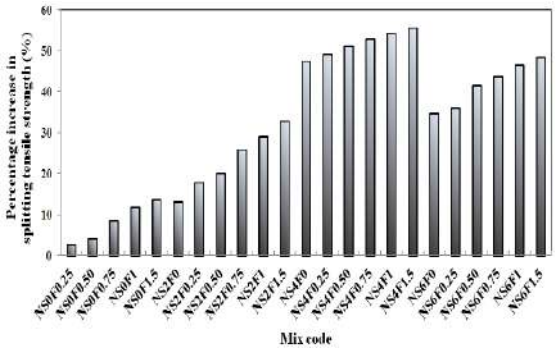

Figure 8. Percentage increase in splitting tensile strength

The highest improvement of tensile strength was due to the combined use of GF and nSPs in a specimen containing 4% nSPs and 1.5% GF and its tensile strength increased by approximately 56%. The positive effect of nSPs on increasing tensile strength also mentioned in previous studies [45]. The pozzolanic activity of nSPs with products formed in Portland cement hydration and their penetration into the pores of scoria aggregates and the creation of better aggregate interlockes with cement paste leads to the compatibility of strength between light weight aggregates and cement paste and this reason is the main reason for the increase in tensile strength of lightweight concrete. This is because as the hardness of the Scoria aggregates increases in the rupture path, the tensile strength of the lightweight concrete also increases. In lightweight concrete, cracking is usually started and passed through the lightweight aggregates. Therefore, with the presence of nanosilica and the penetration of cement paste into the aggregates, their hardness increases and eventually the cracking strength of concrete increases. The results also show that the effect of nSPs on increasing tensile strength is much greater than the effect of GF on increasing tensile strength. The reason for this is that nanosilica, by reducing cavities and increasing the density of the mixture, creates more contact surface between the cement and the aggregates compared to the fibers, and causes the tensile strength to grow more.

ACI318-95 [46] and EN1992-1 [47] codes introduce a range for tensile strength based on cylindrical compressive strength. The mention relationships were for cylindrical specimen and the investigated specimens are cubic. Therefore, the cubic compressive strengths were converted to cylindrical compressive strength by applying coefficients. Figure 9 illustrates the correlation between tensile and compressive strengths of this study

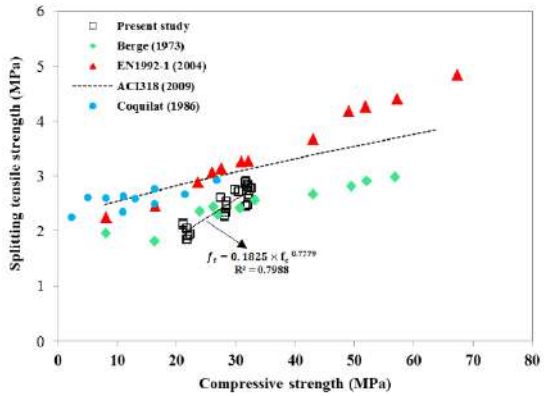

Figure 9. Correlation between tensile strength and compressive strength of lightweight concrete containing nSPs, zeolite and GF

and the mentioned codes as well as the studies of Berge [48, 49]. The strengths values of this study are very close to the experimental curves introduced by ACI 363-92 [50] and ACI318-99 [51]. Equation (5) is presented based on Figure 9.

$$f_t = 0.1825 f_c^{0.7779} \quad (5)$$

f_t and f_c are splitting tensile strength and compressive strength, respecetively.

3. 2. 3. Flexural Strength The flexural strength and its percentage increase are shown in Figures 10 and 11, respectively. The combined use of nSPs and GF in all mixed designs increased the 28-day flexural strength. As the load increases, the fibers collide with the cracks, and the fibers with their tensile strength modify the crack propagation and concrete release to achieve the tensile strength. This creates a mechanism for extra energy absorption and results in reducing stresses in the area of microcracks near the apex of the cracks, and as the crack depth decreases, the modulus of rupture increases. The highest increase in flexural strength was 35% and was obtained in a specimen in which 4% nSPs and 1.5% GF were used. Nano silica particles, with their filler and

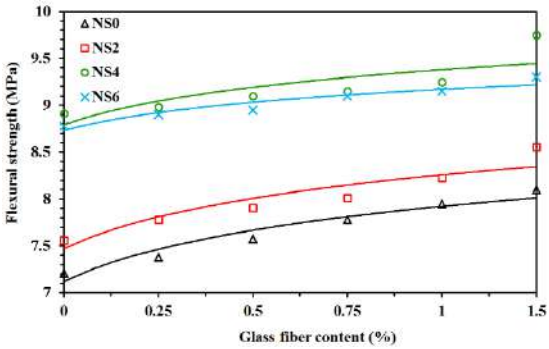

Figure 10. Flexural strength

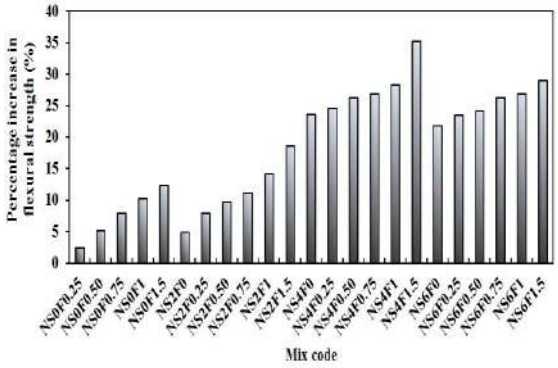

Figure 11. Percentage increase in flexural strength

pozzolanic effect, improve the properties of the cement paste contact area with fibers and aggregates and increase the adhesion of the contact areas.

3. 2. 4. Ultrasonic Pulse Velocity (UPV) The UPV test is an important non-destructive procedure. This method does not afford any damage even on the concrete surface and it can be done with low cost and fast velocity. These factors confirm the suitability of the above method for evaluation. In this study, the process of ultrasonic wave velocity changes in different designs at age of 28 days was investigated for 100×100×100 mm specimens. Table 8 and Figure 12 show the results of velocity of ultrasonic waves against compressive strength. Whitehurst [52] divided the velocity of ultrasonic waves of concrete in terms of quality into five categories: excellent (greater than 4500 m/s), good (3500 to 4500 m/s), suspicious (3000 to 3500 m/s), weak (2000 to 300 m/s) and very weak (smaller than 2000 m/s). Therefore, all mixes fall within the good range. Higher porosity results in lower velocity of waves. According to Figure 12, it can be stated that the combined use of nSPs and zeolites have an effect on filling the voids and reducing the porosity of the concrete. This can be attributed to the growing process of cement paste hydration and the filling of holes and capillary pores with cementitious reaction products and thereby compaction of cement. However, the growth of wave velocity was less than the compressive strength.

3. 3. Results of Concrete Durability Tests

3. 3. 1. Electrical Resistivity Determination of electrical resistivity is one of the tests related to durability and reliability of concrete for achieving corrosion probability of buried rebars. Electrical resistivity is defined by the movement of ions such as Na^+, k^+, OH^-, SO_4^{2-} and Ca^{2+} in the pores in the concrete mass under the influence of the electric field or the difference in ion concentration [33]. Therefore, the amount of electrical resistivity is affected by the concentration of ions in the concrete pores. For example,

TABLE 8. Ultrasonic wave velocity and cubic compressive strength (28 days)

Mix ID	UPV (m/s)	Compressive strength (MPa)
NS0F0	3891	27.2
NS0F0.25	3887	27.1
NS0F0.50	3881	26.9
NS0F0.75	3878	26.5
NS0F1	3868	26.4
NS0F1.5	3858	26.3
NS2F0	3923	35.1
NS2F0.25	3921	35.1
NS2F0.50	3920	34.9
NS2F0.75	3911	34.6
NS2F1	3895	34.5
NS2F1.5	3893	34.3
NS4F0	4001	40
NS4F0.25	3995	39.9
NS4F0.50	3991	39.8
NS4F0.75	3990	39.7
NS4F1	3990	39.5
NS4F1.5	3989	39.6
NS6F0	3999	39.7
NS6F0.25	3992	39.1
NS6F0.50	3991	38.9
NS6F0.75	3990	38.8
NS6F1	3990	38.7
NS6F1.5	3988	38.4

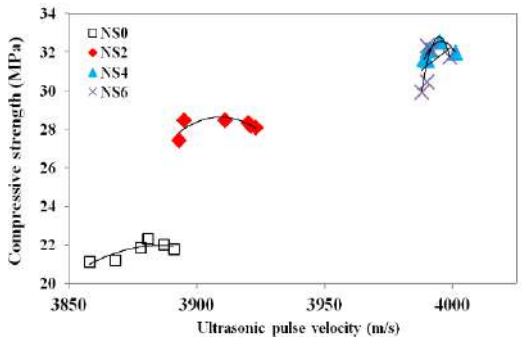

Figure 12. Correlation between cylindrical compressive strength and UPV at age of 28 days

the electrical resistivity can depend on the concentration of the Cl ion, which is one of the factors affecting the corrosion of the rebar. It is on this basis that electrical resistivity can be used as an auxiliary tool to investigate the corrosion probability of buried rebars in concrete. The electrical resistivity of concrete specimens was measured (Figure 13). The process of interpreting the results of the electrical resistivity is described in Section 2.3.

According to Figure 13, electrical resistivity of lightweight concrete specimens containing nSPs, zeolites and GF are in the range of 55 to 162 kHz/m. Hence, according to the classification provided by Song and Saraswathy [34] and Elkey and Sellevold [35], all specimens have very low corrosion probability. The results also show that the presence of GF has little effect on the electrical resistivity of the test specimens and electrical resistivity is reduced by increasing fibers. On the other hand, the use of 2, 4, 6% nSPs in specimens without GF increased the electrical resistivity of concrete by 136, 174 and 194%, respectively. The pozzolanic behavior of silica and zeolite nanoparticles increases the hydration process of concrete and fills cavities and spaces as fillers. As a result, they improve electrical resistivity.

3. 3. 2. Water Absorption Percentage Water absorption is defined as the movement of liquids in pores of solid masses due to surface tension in capillary pores. The water absorption of self compacting lightweight concrete containing zeolite, nSPs, GF and scoria aggregates were calculated and the results are presented in Figure 14. The CEB [53] divides the concrete into three categories of poor quality (above 5%), average (between 3% and 5%) and good (less than 3%). According to the CEB classification, all specimens in which nSPs were not used are in average and near-poor category. According to the durability aspect, water absorption above the scoria lightweight aggregates is an important disadvantage because most corrosive substances penetrate the concrete through water. The use of nSPs largely reduces this problem. The initial water absorption percentage of self-compacting lightweight concrete containing nSPs is in the range of 1.73 to 1.91%;

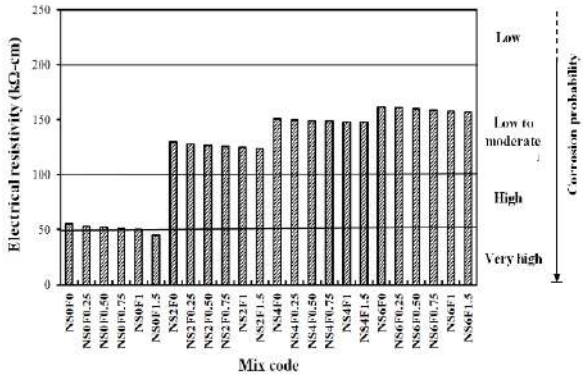

Figure 13. Electrical resistivity of self-compacting lightweight concrete containing zeolite, nSPs, GF and scoria aggregates

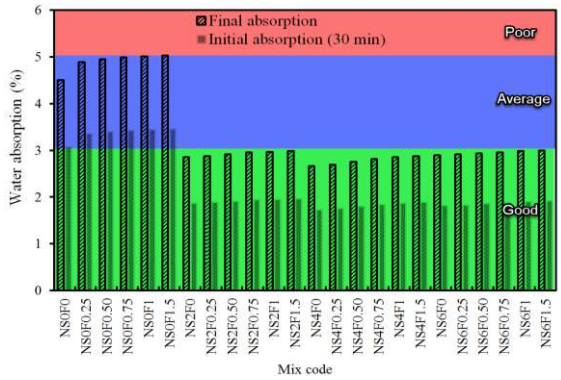

Figure 14. Water absorption percentage of the specimens containing zeolite, nanosilica, GF and scoria aggregates

According to the aforementioned classification, it can be stated that all of the lightweight concrete specimens in which zeolite and nSPs are used are in good quality range. In fact, the use of nSPs in all mixed designs reduced the water absorption percentage of concrete. For example, the use of 4% nSPs reduced the initial and final water absorption of lightweight concrete by 43 and 41%, respectively. The high pozzolanic activity of nSPs and the C-S-H gel production, the filling property of concrete porosity and the removal of fine holes in the silicate gel structure are the main reasons of this improvement.

There was no significant difference between the water absorption percentage of the specimens containing 2, 4 and 6 percent nanoparticles. The combined use of nanoparticles and zeolite has reduced the water absorption percentage to a certain extent, and then due to the presence of more than the required amount of nanoparticles to combine with the free lime produced during the hydration process, it washes more than the silica limit is reduced [44, 54]. For example, the water absorption percentage of specimens containing 6% of silica nanoparticles is much higher than the corresponding values of specimens containing 4%. In fact, part of the cement has been replaced with a material that does not help reduce water absorption further.

4. CONCLUSIONS

In this research, the effect of nSPs and zeolite on the mechanical, rheological properties and durability of self compacting lightweight concrete containg GF and scoria aggregates were investigated. The variables were nSPs (0, 2, 4 and 6 wt % by weight of cement) and GF (0, 0.25, 0.5, 0.75, 1 and 1.5% by volume of concrete). The scoria aggregates and zeolite were considered constant in all mixes. The fresh and hardened properties of specimens were evaluated using T50, slump flow, V-funnel and L-box, compressive strength, splitting tensile strength, flexural strength, ultrasonic, electrical resistivity, and water absorption tests. In this section, the most important results are presented.

- The decreasing process of compressive strength in lightweight concrete due to increasing fiber percentage can be attributed to the balling phenomenon. If the percentage of fiber growth exceeds the optimum value, there is an uneven distribution of fibers followed by inappropriate fiber collision with the cement matrix and this reduces the effectiveness possibility of fibers to improve concrete structure. The use of nSPs can compensate for (or slightly increase) the compressive strength caused by the addition of GF. So that the 7, 28, and 90-day compressive strength of NS4F0.5 specimens increased by 21, 47.8 and 49.8%, respectively.
- The combined use of nSPs and GF has a significant effect on self-compacting lightweight concrete containing zeolite and Scoria aggregates; Depending on the amount of GF and nSPs, the splitting tensile strength increased by about 3 to 56% at age of 28 days.
- The use of GF in lightweight concrete specimens containing zeolite and scoria aggregates increased the tensile strength by about 3 to 14% depending on the fiber content. The reason for increasing strength of GF can be due to increasing tensile strain tolerance through the transfer of stresses from the matrix to the fibers. The use of nSPs in lightweight concrete specimens containing zeolite and Scoria aggregates also increased the tensile strength by about 13 to 35% depending on the amount of nano.
- NSPs, due to their high specific surface and high reactivity, result in consuming calcium hydroxide that is quickly organized within the hydration, filling pores of the calcium silicate gel structure and eventually producing more and more compacting hydrated products.
- The highest increase in tensile strength was due to the combined use of GF and nSPs in a specimen in which 4% nSPs and 1.5% GF were used and its tensile strength increased by approximately 56%.
- The presence of GF has little effect on the electrical resistivity of the testing specimens and decreases with increasing fiber strength. On the other hand, the use of nSPs in specimens that do not have GF increased the electrical resistivity of the concrete from 136 to 194% depending on the number of nSPs.
- From the sustainability aspect, water absorption above the scoria lightweight aggregates is an important disadvantage because most harmless and corrosive substances penetrate the concrete through water. The use of nSPs largely reduces this problem. In fact, the use of nSPs in all mixed designs decreased the water absorption rate of concrete. This improvement can be attributed to the high pozzolanic activity of the nSPs, the gel production, the C-S-H porosity and the filling of the concrete pores, and the removal of fine holes in the silicate gel structure.

5. REFERENCES

1. Kashani, H., Ito, Y., Han, J., Liu, P., and Chen, M. "Extraordinary tensile strength and ductility of scalable nanoporous graphene." ***Science Advances***, Vol. 5, No. 2, (2019). https://doi.org/10.1126/sciadv.aat6951
2. Hassanpour, M., Shafigh, P., and Mahmud, H. Bin. "Lightweight aggregate concrete fiber reinforcement - A review." ***Construction and Building Materials***. Vol. 38, (2012), 452-461. https://doi.org/10.1016/j.conbuildmat.2012.07.071
3. Ting, T. Z. H., Rahman, M. E., Lau, H. H., and Ting, M. Z. Y. "Recent development and perspective of lightweight aggregates based self-compacting concrete." ***Construction and Building Materials***. Vol. 201, (2019), 763-777. https://doi.org/10.1016/j.conbuildmat.2018.12.128
4. Ehsani Yeganeh, A., Kouroshnezhad, F., Dadsetan, S., Hossain, K. M. A., and Lachemi, M. "Experimental Investigation on Mechanical Properties of Fiber Reinforced Lightweight Self-consolidating Concrete." In RILEM Bookseries (Vol. 23, pp. 536–543). Springer Netherlands. https://doi.org/10.1007/978-3-030-22566-7_62
5. Hilal, N. N., Sahab, M. F., and Mohammed Ali, T. K. "Fresh and hardened properties of lightweight self-compacting concrete containing walnut shells as coarse aggregate." ***Journal of King Saud University - Engineering Sciences***, (2020). https://doi.org/10.1016/j.jksues.2020.01.002
6. Mohsenzadeh, S., Maleki, A., and Lotfollahi-Yaghin, M. A. "Experimental and Numerical Study of Energy Absorption Capacity of Glass Reinforced SCC Beams." ***International Journal of Engineering, Transactions C: Aspects***, Vol. 32, No. 12, (2019), 1733–1744. https://doi.org/10.5829/ije.2019.32.12c.06
7. Badogiannis, E. G., Christidis, I., and Tzanetatos, G. E. "Evaluation of the mechanical behavior of pumice lightweight concrete reinforced with steel and polypropylene fibers." ***Construction and Building Materials***, Vol. 196, (2019), 443–456. https://doi.org/10.1016/j.conbuildmat.2018.11.109
8. Wu, T., Yang, X., Wei, H., and Liu, X. "Mechanical properties and microstructure of lightweight aggregate concrete with and without fibers." ***Construction and Building Materials***, Vol. 199, (2019), 526–539. https://doi.org/10.1016/j.conbuildmat.2018.12.037
9. Senff, L., Labrincha, J. A., Ferreira, V. M., Hotza, D., and Repette, W. L. "Effect of nano-silica on rheology and fresh properties of cement pastes and mortars." ***Construction and Building Materials***, Vol. 23, No. 7, (2009), 2487–2491. https://doi.org/10.1016/j.conbuildmat.2009.02.005
10. Afzali Naniz, O., and Mazloom, M. "Effects of colloidal nano-silica on fresh and hardened properties of self-compacting lightweight concrete." ***Journal of Building Engineering***, Vol. 20, , (2018), 400–410. https://doi.org/10.1016/j.jobe.2018.08.014
11. Mohammed, B. S., Liew, M. S., Alaloul, W. S., Khed, V. C., Hoong, C. Y., and Adamu, M. "Properties of nano-silica modified pervious concrete." ***Case Studies in Construction Materials***, Vol. 8, , (2018), 409–422. https://doi.org/10.1016/j.cscm.2018.03.009
12. Abd Elrahman, M., Chung, S. Y., Sikora, P., Rucinska, T., and Stephan, D. "Influence of nanosilica on mechanical properties, sorptivity, and microstructure of lightweight concrete." ***Materials***, Vol. 12, No. 19, (2019). https://doi.org/10.3390/ma12193078
13. Kanthe, V., Deo, S., and Murmu, M. "Combine Use of Fly Ash and Rice Husk Ash in Concrete to Improve its Properties." ***International Journal of Engineering, Transactions A: Basics***, Vol. 31, No. 7, (2018), 1012–1019. https://doi.org/10.5829/ije.2018.31.07a.02
14. Hashemi, S. H., and Mirzaeimoghadam, I. "Influence of Nano-silica and Polypropylene Fibers on Bond Strength of Reinforcement and Structural Lightweight Concrete." ***International Journal of Engineering, Transactions B: Applications***, Vol. 27, No. 2, (2014), 261–268. https://doi.org/10.5829/idosi.ije.2014.27.02b.10
15. Shen, D., Jiao, Y., Kang, J., Feng, Z., and Shen, Y. "Influence of ground granulated blast furnace slag on early-age cracking potential of internally cured high performance concrete." ***Construction and Building Materials***, Vol. 233, (2020), 117083. https://doi.org/10.1016/j.conbuildmat.2019.117083
16. Zaroudi, M., Madandoust, R., and Aghaee, K. "Fresh and hardened properties of an eco-friendly fiber reinforced self-consolidated concrete composed of polyolefin fiber and natural zeolite." ***Construction and Building Materials***, Vol. 241, (2020), 118064. https://doi.org/10.1016/j.conbuildmat.2020.118064
17. Sadeghi-Nik, A., Berenjian, J., Alimohammadi, S., Lotfi-Omran, O., Sadeghi-Nik, A., and Karimaei, M. "The Effect of Recycled Concrete Aggregates and Metakaolin on the Mechanical Properties of Self-Compacting Concrete Containing Nanoparticles." ***Iranian Journal of Science and Technology - Transactions of Civil Engineering***, Vol. 43, No. 1, (2019), 503–515. https://doi.org/10.1007/s40996-018-0182-4
18. Mehrinejad Khotbehsara, M., Mohseni, E., Ozbakkaloglu, T., and Ranjbar, M. M. "Durability Characteristics of Self-Compacting Concrete Incorporating Pumice and Metakaolin." ***Journal of Materials in Civil Engineering***, Vol. 29, No. 11, (2017), 04017218. https://doi.org/10.1061/(ASCE)MT.1943-5533.0002068
19. Najimi, M., Sobhani, J., Ahmadi, B., and Shekarchi, M. "An experimental study on durability properties of concrete containing zeolite as a highly reactive natural pozzolan." ***Construction and Building Materials***, Vol. 35, (2012), 1023–1033. https://doi.org/10.1016/j.conbuildmat.2012.04.038
20. ASTM C136 / C136M-19, Standard Test Method for Sieve Analysis of Fine and Coarse Aggregates, ASTM International, West Conshohocken, PA, (2019).
21. ASTM C330 / C330M-17a, Standard Specification for Lightweight Aggregates for Structural Concrete, ASTM International, West Conshohocken, PA, (2017).
22. ASTM C311 / C311M-18, Standard Test Methods for Sampling and Testing Fly Ash or Natural Pozzolans for Use in Portland-Cement Concrete, ASTM International, West Conshohocken, PA, (2018).
23. ASTM C494 / C494M-17, Standard Specification for Chemical Admixtures for Concrete, ASTM International, West Conshohocken, PA, (2017).
24. ACI Committee 211, American Concrete Institute, Farmington Hills, Michigan, (1991).
25. Self-Compacting Concrete European Project Group, The European guidelines for self-compacting concrete: Specification, production and use. International Bureau for Precast Concrete (BIBM), (2005).
26. ASTM C39 / C39M-18, Standard Test Method for Compressive Strength of Cylindrical Concrete Specimens, ASTM International, West Conshohocken, PA, (2018).
27. ASTM C496 / C496M-17, Standard Test Method for Splitting Tensile Strength of Cylindrical Concrete Specimens, ASTM International, West Conshohocken, PA, (2017).
28. ASTM C293 / C293M-16, Standard Test Method for Flexural Strength of Concrete (Using Simple Beam With Center-Point Loading), ASTM International, West Conshohocken, PA, (2016).
29. ASTM C597-09, Standard Test Method for Pulse Velocity Through Concrete, ASTM International, West Conshohocken, PA, (2009).
30. Vasconcelos, G., Lourenço, P. B., Alves, C. A. S., and Pamplona, J. "Ultrasonic evaluation of the physical and mechanical properties of granites." ***Ultrasonics***, Vol. 48, No. 5, (2008), 453–466. https://doi.org/10.1016/j.ultras.2008.03.008

31. Lafhaj, Z., Goueygou, M., Djerbi, A., and Kaczmarek, M. "Correlation between porosity, permeability and ultrasonic parameters of mortar with variable water / cement ratio and water content." ***Cement and Concrete Research***, Vol. 36, No. 4, (2006), 625–633. https://doi.org/10.1016/j.cemconres.2005.11.009
32. ASTM C642-13, Standard Test Method for Density, Absorption, and Voids in Hardened Concrete, ASTM International, West Conshohocken, PA, (2013).
33. Sengul, O., and Gjorv, O. E. "Electrical Resistivity Measurements for Quality Control During Concrete Construction." ***ACI Materials Journal***, Vol. 106, No. 6, (2008), 541–547. Retrieved from https://trid.trb.org/view/876465
34. Song, H. W., and Saraswathy, V. "Corrosion Monitoring of Reinforced Concrete Structures - A Review ." ***International Journal of Electrochemical Science***, Vol. 2, (2007), 1–28. Retrieved from http://cecri.csircentral.net/683/
35. Elkey, W., and Sellevold, E. "Electrical Resistivity of Concrete", Publication No. 80, Norwegian Road Research Laboratory, Oslo, Norway, (1995).
36. AL-Ameeri, A. "The Effect of Steel Fiber on Some Mechanical Properties of Self Compacting Concrete." ***American Journal of Civil Engineering***, Vol. 1, No. 3, (2013), 110. https://doi.org/10.11648/j.ajce.20130103.14
37. Sivakumar, V. R., Kavitha, O. R., Prince Arulraj, G., and Srisanthi, V. G. "An experimental study on combined effects of glass fiber and Metakaolin on the rheological, mechanical, and durability properties of self-compacting concrete." ***Applied Clay Science***, Vol. 147, (2017), 123–127. https://doi.org/10.1016/j.clay.2017.07.015
38. Taheri Fard, A. R., Soheili, H., Ramzani Movafagh, S., and Farnood Ahmadi, P. "Combined effect of glass fiber and polypropylene fiber on mechanical properties of self-compacting concrete." ***Magazine of Civil Engineering***, Vol. 62, No. 2, (2016), 26–31. https://doi.org/10.5862/MCE.62.3
39. Persson, B. "A comparison between mechanical properties of self-compacting concrete and the corresponding properties of normal concrete." ***Cement and Concrete Research***, Vol. 31, No. 2, (2001), 193–198. https://doi.org/10.1016/S0008-8846(00)00497-X
40. ACI 213R-03, Guide for Structural Lightweight-aggregate Concrete. ACI 213R-03, American Concrete Institute, Farmington Hills, MI. (2003).
41. De Schutter, G., Bartos, P. J., Domone, P., and Gibbs, J. Self-Compacting Concrete. Whittles Publishing, Dunbeath, Caithness Scotland. Retrieved from https://trid.trb.org/view/863702
42. Arefi, M., Javeri, M., and Mollaahmadi, E. "To study the effect of adding Al2O3 nanoparticles on the mechanical properties and microstructure of cement mortar." ***Life Science Journal***, Vol. 8, No. 4, (2011), 613–617. Retrieved from https://www.academia.edu/download/30702744/082_7488life0804_613_617.pdf
43. Nazari, A., Riahi, S., Riahi, S., Fatemeh Shamekhi, S., and Khademno, A. "Influence of Al2O3 nanoparticles on the compressive strength and workability of blended concrete ." ***Journal of American Science***, Vol. 6, No. 5, (2010), 6–9. Retrieved from http://www.americanscience.orgeditor@americanscience.org
44. Faez, A., Sayari, A., and Manie, S. "Mechanical and Rheological Properties of Self-Compacting Concrete Containing Al2O3 Nanoparticles and Silica Fume." ***Iranian Journal of Science and Technology - Transactions of Civil Engineering***, (2020), 1–11. https://doi.org/10.1007/s40996-019-00339-y
45. Mukharjee, B. B., and Barai, S. V. "Influence of Nano-Silica on the properties of recycled aggregate concrete." ***Construction and Building Materials***, Vol. 55, (2014), 29–37. https://doi.org/10.1016/j.conbuildmat.2014.01.003
46. ACI Committee 318. Building Code Requirements for Structural Concrete (ACI318-95) and Commentary (ACI 318-R95). American Concrete Institute, Farmington Hills, Mich., (1995).
47. European Committee for Standardisation (CEN). European (draft) Standard EN 1992-1- 1: Eurocode 2; Design of concrete structures, Part 1-1: General rules and rules for buildings. Brussels, (2004).
48. Berge, O. "Reinforced structures in lightweight concrete." PhD Thesis, Stockholm, (1973).
49. Bogas, J. A., and Nogueira, R. "Tensile strength of structural expanded clay lightweight concrete subjected to different curing conditions." ***KSCE Journal of Civil Engineering***, Vol. 18, No. 6, (2014), 1780–1791. https://doi.org/10.1007/s12205-014-0061-x
50. ACI Committee 363, State-of-the-art report on high-strength concrete (ACI 363R-92), American Concrete Institute, Farmington Hills, Michigan, 55. (1992).
51. ACI 318-99, Building Requirements for Structural Concrete and Commentary, American Concrete Institute, Farmington Hills, Michigan, 393, (1999).
52. Whitehurst, E. A. "Evaluation of Concrete Properties from Sonic Tests." ***American Concrete Institute Monograph***, Vol. 326, , (2006), 16–21. Retrieved from https://ci.nii.ac.jp/naid/10018411018
53. CEB-FIP. Diagnosis and assessment of concrete, structures-state of art report, CEB Bulletin 83. (1989).
54. Agarkar, S., and Joshi, M. "Study of effect of Al2O3 nanoparticles on the compressive strength and workability of blended concrete." ***International Journal of Current Research***, Vol. 4, No. 12, (2012), 382–384.

Persian Abstract

چکیده

میزان ریز ترک‌ها در بتن‌های الیافی در ناحیه مرزی بین خمیر سیمان و سطح سنگدانه یا الیاف بیشتر می‌باشد که برای تقویت این ناحیه می‌توان از پوزولان‌های طبیعی و مصنوعی استفاده کرد. در مطالعه حاضر، اثر استفاده ترکیبی از نانو ذرات سیلیس و زئولیت بر خصوصیات مکانیکی، رئولوژیکی و دوام بتن‌های سبک خود متراکم ساخته شده با سنگدانه‌های اسکوریا که با الیاف شیشه مسلح شده است، مورد بررسی قرار گرفت. الیاف شیشه به مقدار ۰ تا ۱.۵ درصد در ترکیب با ۰ تا ٦ درصد نانوذرات سیلیس ارزیابی شد. خصوصیات بتن تازه و بتن سخت شده با انجام آزمایش‌های جریان اسلامپ، T50، قیف V، جعبه L، مقاومت فشاری، مقاومت کششی دو نیم شدن، مقاومت خمشی، تراسونیک، مقاومت الکتریکی و جذب آب انجام شد. همچنین ریز ساختار نمونه‌های بتنی با استفاده از عکسبرداری میکروسکوپ الکترونی SEM مورد بررسی قرار گرفت. استفاده ترکیبی از نانوذرات سیلیس و الیاف شیشه در بتن‌های سبک خودتراکم حاوی زئولیت و سنگدانه‌های اسکوریا اثر قابل توجهی دارد؛ بطوریکه بسته به مقدار الیاف شیشه و نانوذرات سیلیس، مقاومت کششی دو نیم شدن حدوداً از ۳ تا ٥٦ درصد افزایش یافته است. استفاده از نانوذرات سیلیس مقاومت الکتریکی بتن را بسته به مقدار نانوذرات از ۱۳٦ تا ۱۹٤ درصد افزایش داده است. نانو ذرات سیلیس به دلیل سطح مخصوص بالا و واکنش پذیری بالا منجر می گردد کلسیم هیدروکسید که در طول هیدراسیون به خصوص در سنین اولیه، به سرعت تشکیل می‌شود، مصرف گردد و منافذ ساختار ژل کلسیم سیلیکات پر شود و سرانجام محصولات هیدراته بیشتر و متراکم‌تر تولید می‌گردد.

IJE TRANSACTIONS B: Applications Vol. 33, No. 8, (August 2020) 1512-1521

International Journal of Engineering

Journal Homepage: www.ije.ir

Predicting Shear Capacity of Panel Zone Using Neural Network and Genetic Algorithm

M. Vajdian[a], S. M. Zahrai*[b], S. M. Mirhosseini[a], E. Zeighami[a]

[a] *Department of Civil Engineering, Arak Branch, Islamic Azad University, Arak, Iran*
[b] *Center of Excellence for Engineering and Management of Civil Infrastructures, School of Civil Engineering, College of Engineering, University of Tehran, Tehran, Iran*

PAPER INFO

Received 07 March 2020
Received in revised form 03 May 2020
Accepted 12 June 2020

Keywords:
Box-Shaped Cross-Sections
Genetic Algorithm
Neural Network
Shear Capacity of Panel Zone
Steel moment-Resisting Frame

ABSTRACT

Investigating the behavior of the box-shaped column panel zone has been one of the major concerns of scientists in the field. In the American Institute of Steel Construction the shear capacity of I-shaped cross- sections with low column thickness is calculated. This paper determines the shear capacity of panel zone in steel columns with box-shaped cross-sections by using artificial neural network (ANN) and genetic algorithm (GA). It also compares ABAQUS finite element software outputs and AISC relations. Therefore, neural networks were trained using parametric information obtained from 510 connection models in ABAQUS software. The results show that the predicted shear capacity of the NN and the GA in comparison with the AISC relations use a wide range of all effective parameters in the calculation of the shear capacity of panel zone. Therefore, the use of artificial intelligence can be a good choice. Finally, the GA, along with optimization of a mathematical relation, has been able to minimize the error in determining the shear capacity of panel zones of steel-based columns, even at high column thicknesses.

***doi**: 10.5829/ije.2020.33.08b.09*

1. INTRODUCTION

In recent decades, connections have been one of the most important concerns of scientists in the field. The major differences of recent approaches are paying more attention to the beam-to-column load transfer path and ensuring that this load transfer path is safe to the extent of the lateral load system behavior. Therefore, this study focuses on research and predicts the shear capacity of panel zones in steel boxes using NN method. Seismic behavior of panel zones has been the focus of numerous researchers for a long time. Research has begun in the late 1960s and early 1970s. In the last four decades, significant changes have been observed in the seismic design criteria of panel zones. Over the years, there have been many changes to panel zone by laws and guidelines. The 2002 AISC seismic criterion stated that the shear resistance required by panel zone must be determined by testing. In other words, it does not provide a quantitative relationship. However, as a minimum, the shear resistance required of panel zone must be determined from the sum of bending moments in the column resulting from the formation of expected bending moments at the points of formation of plastic hinge [1]. The 2010 AISC Seismic Code is the latest and the most up-to-date version of the seismic design criteria for steel structures. In the section on panel zones sections of the special bending reinforced frames, no changes were considered compared to the 2002 AISC criteria [2]. Mansouri et al. [3] proved that the AISC relations overestimate in I-shaped columns with relatively thick flanges. What seems to be necessary is that the shear capacity of panel zone depends primarily on the various geometrical parameters of the coupling components and, secondly, the AISC relations have acceptable errors for I-shaped cross-sections with low thicknesses. However, these errors became more pronounced at higher thicknesses and box-shaped cross-sections [3]. Today,

*Corresponding Author Institutional Email: *mzahrai@ut.ac.ir* (S. M. Zahrai)

Please cite this article as: M. Vajdian, S. M. Zahrai, S. M. Mirhosseini, E. Zeighami, Predicting Shear Capacity of Panel Zone Using Neural Network and Genetic Algorithm, International Journal of Engineering (IJE), IJE TRANSACTIONS B: Applications Vol. 33, No. 8, (August 2020) 1512-1521

NNs are used in almost all engineering sciences. NNs, also known as ANNs, are one of the learning algorithms in "machine learning" that are based on the biological concept of NNs. ANNs are the building blocks or neurons, very simple computing devices. Communication between neurons determines network function. The purpose of ANN training is to determine the appropriate relationship for solving different problems [4]. Many researchers have used ANN to study structures, for instance Hartman et al. [5] have investigated the use of ANN in assessing different levels of structures safety. Elhewy et al. [6] have investigated the ability of NNs to predict the failure of structures.

Optimization techniques include the recently developed random search methods. Among the new optimization techniques used today to solve many different problems are GA (GA), Simulated Annealing (SA), Ant Colony and more. Regardless of the type of calculation, these methods can be applied at different levels of engineering. In these methods, simple algorithms are used for complex calculations [7]. Jenkins' research [8] is one of the first studies in optimizing structures. Adeli [9] also explored the use of NNs to improve the responses of GAs to optimization problems. Sahoo and Maity [10] used a combination of NN and GA to predict structural damage .

Khalkhali et al [11] proved that neural networks are useful tools to predict the buckling capacity of vertically stiffened cylindrical shells.

Mallela et al [12] dealt with the development of an analytical and computationally efficient analysis tool using artificial neural networks (ANN) for predicting the buckling load of laminated composite stiffened panels subjected to in-plane shear loading. The results show that the trained neural network can predict the shear buckling load of laminated composite stiffened panels accurately and will be very useful in optimization applications [12].

Abmbres et al. [13] proposed an artificial neural network (ANN)-based formula to come up with estimates of the shear capacity of one-way reinforced concrete slabs under a concentrated load. A step-by-step assessment scheme for reinforced concrete slab bridges by means of the ANN-based model is also proposed, which results in an improvement of the current assessment procedures [13].

Hoang [14] relied on a piecewise multiple linear regression (PMLR) and artificial neural network (ANN) approaches to construct a prediction model that can approximate the mapping function between the punching shear capacity of SFRC flat slabs and its influencing factors. The algorithms of gradient descent and Levenberg-Marquardt backpropagation were employed to train the ANN based prediction models. Experimental results showed that SPMLR can deliver prediction outcome which was better than those of ANN as well as empirical design equations [14].

Jang et al. [15] reported the magnitudes of fiber optic sensor signals were used for estimating the distances between each sensor and impact location. Then, through the neural network training, the accuracy of estimating the distances from the signal magnitudes could be enhanced. Triangulation method showed the acceptable localization results about the non-trained impact points [15].

Hedayat et al. [16] were aimed to propose an integrated formula developed based on artificial neural network to predict the minimum resistance requirement of steel moment frames at any performance level and desired level of probabilistic response. In addition to the simple form of the proposed model, results generally indicated that this model was more accurate than the other available models [16].

In recent decades, due to the widespread use of these cross-sections in moment-resisting frame systems, investigating the behavior of the box-shaped column panel zone has been one of the major concerns of scientists in the field. As a rectangular area of column web, panel zone is enclosed between continuity plates and column flanges and plays an important role in the bonding behavior. The shear capacity of this region depends on various parameters, such as the geometrical dimensions of the beam cross-section, the geometrical dimensions of the column cross-section and the thickness of continuity plates. In the American Institute of Steel Construction (AISC), based on these parameters, the shear capacity of I-shaped cross-sections with low column thickness is calculated. However, no separate relations have been provided to determine the shear capacity of panel zone in metal columns with box-shaped cross-sections. The error of the AISC relations is particularly evident at high thicknesses. This paper determines the shear capacity of panel zone in metal columns with box-shaped cross-sections with artificial neural network (ANN) and genetic algorithm (GA). It also compares ABAQUS finite element software outputs and AISC relations. The parameters used to determine this shear capacity are height, flange thickness, beam and column thickness, thickness of continuity plates and axial force of the column.

In this study, an ANN and GA are designed to calculate the shear capacity of panel zone-loaded steel columns for the purpose of a separate relationship and reducing the errors mentioned in the AISC. To achieve this goal, first, an extensive parametric study is performed on the parameters affecting the performance of the connection source by ABAQUS software. These parameters include column flange thickness, column web thickness, beam flange thickness, column width, height of beam and thickness of continuity plates. Then, an ANN is designed and trained based on ABAQUS software outputs. This network is examined to predict the shear capacity of square columns or boxes with low to

high thickness ranges. The results are compared with the ABAQUS output and the AISC. Then, using the GA, an optimal function is determined to predict and calculate the shear capacity of the bending steel columns. After that, the performance of artificial intelligence in relation to the AISC relations is investigated in terms of shear capacity of the box-shaped columns with different column thicknesses.

2. CALCULATING THE SHEAR CAPACITY OF PANEL ZONE

2. 1. Calculating the Shear Capacity of Panel Zones in American Institute of Steel Construction (AISC)

The AISC Relations, based on the Crawinker Relations, yielded an acceptable result for relatively thin columns. However, for high column flange thicknesses, these relations need to be modified. It is important to note that the difference in shear capacity of panel zone is due to the high thickness and shape of the cross-section, so that the column with the box-shaped cross-section is not specified in the AISC as separate relation [17]. In recent AISC seismic design standards based on the LRFD design, the design resistance of panel zones is classified as follows, with or without the deformation of panel zones depending on the axial force applied to the column [2]:

A) When the deformation effect of panel zones is not considered in the frame, Rn is the capacity of panel zones as follows:

$$R_n = 0.6F_y.d_c.t_w \qquad P_r \le 0.4P_c \qquad (1)$$

$$R_n = 0.6\mathrm{F}_y.\mathrm{d}_c.\mathrm{t}_w(1.4 - \frac{P_r}{P_c}) \qquad P_r > 0.4P_c \qquad (2)$$

B) When considering the deformation effect of panel zone in the frame, the capacity of panel zone is as follows:

In Equations (1) to (4), the first part deals with the yield point and the second part concerns the final capacity of panel zone. In the above equations, F_y is the yield stress of column cross-section, dc is column cross depth, t_w is column web thickness, b_{cf} is column flange width, t_{cf} is column flange thickness, d_b is column depth, P_r is column design resistance and Pc is column axial yield resistance.

It can be stated that the AISC uses five physical parameters of panel zone to calculate the shear capacity. These parameters are: 1) Depth of column, 2) Thickness of column, 3) Width of column, 4) Thickness of column, 5) Depth of beam.

Figure 1 shows the calculated values of Vpz, shear capacity based on the AISC relations for 510 specimens. Vpz is the shear capacity of panel zone named R_n in the AISC.

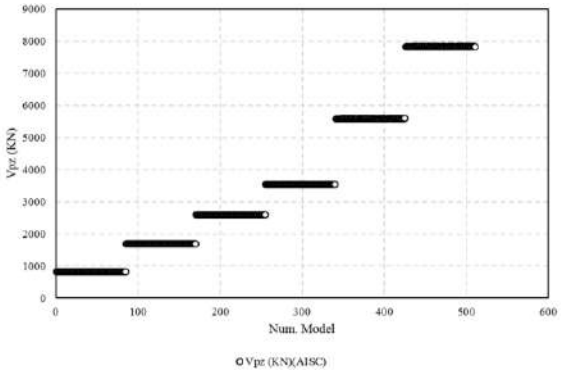

Figure 1. Shear capacity based on the AISC relations for 510 samples

2. 2. Finite Elements Modeling

2. 2. 1. Modeling Verification In this part, in order to ensure the accuracy of the numerical results of the performed analysis, a steel beam to column connection performed by Stojadinović et al. [18] is modeled in ABAQUS. In the following, the mentioned model is analyzed and the results of this analysis are compared to laboratory results [18].

2. 2. 2. Geometrical Properties and Materials of the Laboratory Specimens The laboratory specimen was built from a column with the W14 × 120 section; and for the beam, a W24 × 68 section was used. The model geometry and loading details are shown in Figure 2. The used materials in this experiment are steel plates for the stiffeners, beams, and columns with the yield resistance of 358 MPa and ultimate tensile resistance of 475 MPa as shown in Table 1.

$$R_n = 0.6\,F_y.d_c.t_w(1 + \frac{3b_{cf}.t_{cf}^{\,2}}{d_b.d_c.t_w}) \qquad P_r \le 0.75P_c \qquad (3)$$

$$R_n = 0.6F_y.d_c.t_w(1 + \frac{3b_{cf}.t_{cf}}{d_b.d_c.t_w})(1.9 - \frac{1.2P_r}{P_c}) \qquad P_r > 0.75P_c \qquad (4)$$

2. 2. 3. Meshing In order to model the beam, column and the stiffener plates, the shell and solid elements were used. Also, the modeled geometry was partitioned for regular meshing with the partitioning command.

2. 2. 4. Boundary Condition and Loading The boundary condition of the laboratory specimen requires that the displacement of all the nodes in the above and below the column were tightly restrained. Also, for the out-of-plane buckling, the beam was restrained. All the boundary and support conditions are applied in modeling. The loading was in the form of displacement application to the beam end with the amount of 195 mm.

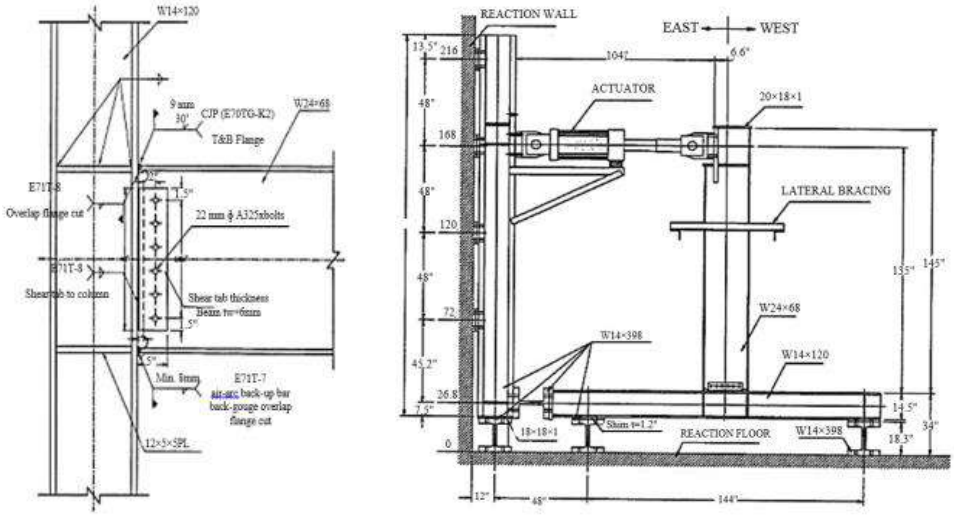

Figure 2. Specimen geometry specifications

TABLE 1. The specifications of the materials used in the experiment

Young's modulus (GPa)	Poisson's Ratio	Ultimate Tensile Resistance (MPa)	Yield Resistance (MPa)	Material
210	0.3	475	358	Steel

2. 2. 5. The Results of the Load-Displacement Analysis The answers of load-final displacement resulted from the analysis results for the numerical sample with the answers of the load-displacement of the laboratory specimen are illustrated in Figure 3. As it can be observed in this figure, the load-displacement curves are almost coincident. In fact, from the beginning, the aim of the sample calibration was to accommodate the load-displacement curve of the numerical model with the laboratory sample.

2. 2. 6. Parametric Studies with ABAQUS Software and Calculation of Shear Capacity of Panel Zones ABAQUS software version 2017 was used for parametric modeling and calculation of shear capacity of panel zone. In this part of the research, the details of modeling using finite element method are presented. In this section, the model made in the previous section is used for modeling, with the exception of the box-shaped column instead of the H-shaped column. In the models, it is assumed that the steel beam-column connections are rigid and welded. Variable parameters are used in modeling 510 models, namely change in beam flange thickness, beam web, continuity plate, column web thickness and column flange thickness. The boundary conditions are similar to the model boundary conditions made in the previous section. Four thicknesses of 8, 10, 15 and 20 mm were used for the beam flange, beam web and continuity plate thickness parameters. In addition, 6 thicknesses of 8, 10, 15, 20, 30 and 40 mm were used for column web and column flange thickness (Table 2).

The beam and column dimensions used in parametric studies are I500X250 and BOX400X400, respectively. For the used material in this study, the yield resistance of 345 MPa and ultimate tensile resistance of 510 MPa are assumed.

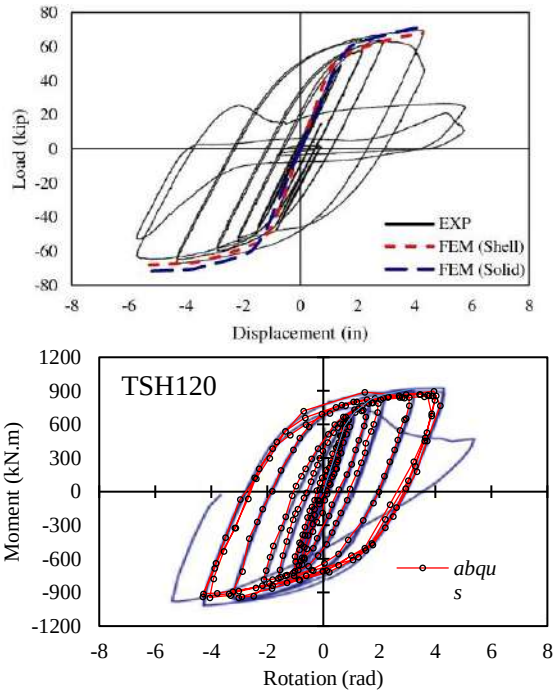

Figure 3. Comparison of load-displacement results for the numerical model and the experimental specimen

TABLE 2. Dimensions of parametric study models

Model	$t(mm)$
Beam flange Beam web Continuity Plate	8,10,15,20
Column flange Column web	8,10,15,20,30,40

The boundary conditions of the parametric models were such that the displacement of all the nodes located at the top and bottom of the column which was constrained to be clamped. In addition, it was bound for the buckling off the beam plate. The loading was applied to the end of the beam by a displacement of 150 mm. The steel beam connections are rigid and welded. Therefore, the 9 cross-sectional geometrical parameters for calculating the shear capacity of panel zones are effective: 1) column length, 2) column width, 3) column flange thickness, 4) column web thickness, 5) beam flange width, 6) beam height (x to X beam flange), 7) beam flange thickness, 8) beam web thickness, and 9) thickness of panel zone stiffeners. To accelerate the modeling process, the S4R quadruple shell element was used to construct the cross-sections. To improve the accuracy, in the areas close to the connection and panel zones, a fine mesh was selected. In all cases, 3500 mm beam length and 3000 mm column length were considered. Figure 4 shows an overview of the model built into ABAQUS software.

In the modeling performed, the proposed equations in literature [19] are used to calculate panel zone cut. In addition, the equations proposed in literature [20] are used to calculate the shear strain of panel zone.

$$V_{pz} = \frac{PL}{h_t}\left(1 - \frac{h_t}{H}\right) \quad (5)$$

$$\gamma = \frac{\Delta^+ + \Delta^-}{2}\left(\frac{\sqrt{d_{pz}^2 + b_{pz}^2}}{d_{pz} b_{pz}}\right) \quad (6)$$

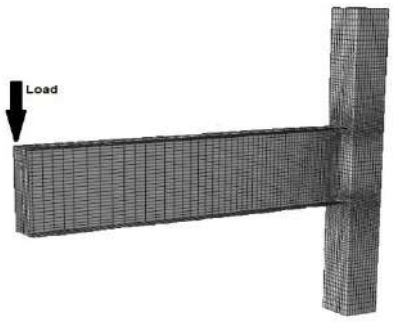

Figure 4. An overview of the model built into ABAQUS software

In Equations (5) and (6), p is the force applied to the end of the beam, L is the distance from the beam to the column, h_t is the distance to the center of the beam flange, H is the height of the column, Δ is the diameter of panel zones, d_{pz}, b_{pz} are the vertical and horizontal spacing of panel zones, respectively. Figure 5 shows the parameters in the connection source.

Figure 6 shows the calculated values of shear capacity in ABAQUS software and Equations (5) and (6) for 510 samples.

4. NN DESIGN AND GA TO PREDICT SHEAR CAPACITY OF THE CONNECTION SOURCE

4. 1. NN Design

In general, there are several types of NNs. The study will use a "Feedforward NN" or "Perception NNs". This ANN relays data directly from front to back. Feedforward neuron training often requires back-propagation, which is a network of corresponding sets of inputs and outputs. When the input data is transferred to the neuron, it is processed and an output is generated. Basically, a NN is a combination of the following components:

- An input layer that receives the data
- Several hidden layers

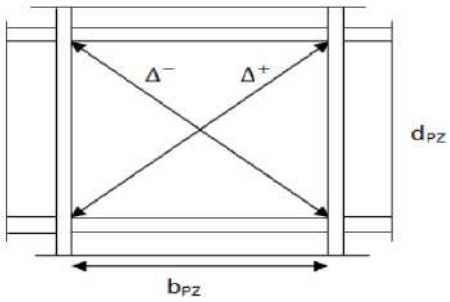

Figure 5. Details of the parameters in the connection source

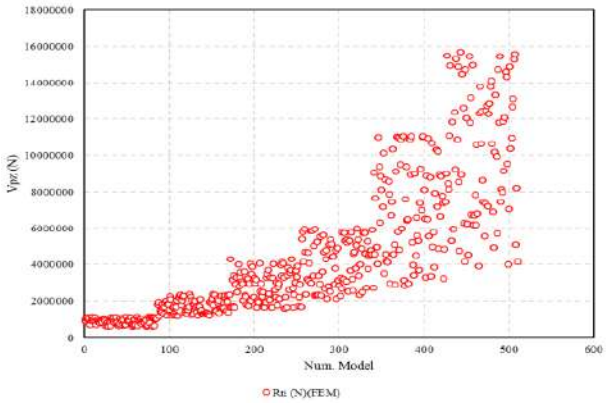

Figure 6. Shear capacity values in ABAQUS software for 510 samples

- An output layer
- Weights and bias between layers
- A deliberate activation function for each hidden layer. In this paper, the function of "tangent sigmoid" (tansig) will be used. This function maps each value to a value from 0 to 1 and helps to normalize the sum of the input weights [21].

In this step, the NN is trained to make accurate predictions. Each input will have a weight (positive or negative). This implies that an input with a large number of positive weights or a large number of negative weights will further influence the output result. It should also be remembered that initializing the weights by assigning a random number to any weight will happen. At each step, 9 geometric variables were assigned to 9 input layer neurons for training. Output data from ABAQUS software, we will have one number for every 9 inputs, introduced for training on NN. It should be noted that 510 samples are available as databases in this section. In other words, we will have 510 data outputs from ABAQUS as target and 510 * 9 data as input. 70% of this data was used for training, 10% for validating or averaging, and 20% for NN testing. For this problem, after trial and error, 6 hidden layers were considered. The next step was to determine the number of neurons in each layer. Each sample has 9 inputs and 1 output. As a result, we will have 9 neurons in the input layer and 1 neuron in the output layer. The number of neurons for secretory layers 1-6 was considered equal to 20, 30, 45, 35, 25 and 10. After several trials and errors, these neurons were selected to specify the number of layers. In the next step, it was necessary to specify the activation functions of each layer. By selecting the appropriate activation function for a layer, this activation function applied to all neurons in the same layer. Table 3 shows the used functions.

For the data of this paper, the tansig function (Sigmoid tangent) was used for individual layers and the purelin activation function (pair) for even layers, which showed relatively good convergence in outputs. Figure 7 shows the NN training process for training, test and intermediate data.

The four categories of data examined in this form are training data, test data, midterm data, and finally total data. Figure 8 shows the normal distribution of the error as a histogram during the training process.

4. 2. GA Design and Optimization As a computational optimization algorithm, by considering a set of answer space points in each computational iteration, the GA searches the different regions of the answer space efficiently. In the search mechanism, although the target function value of the whole answer space is not calculated, the calculated value of the target function for each point is involved in the statistical averaging of the objective function for each point, in the statistical averaging of the target function in all subfields to which the point depends Is. These subfields are statistically averaged in terms of the objective function. This process leads the space search to areas where the statistical mean of the objective function is high and the possibility of an absolute optimal point is greater. Because, unlike single-path methods, this method searches for an all-encompassing answer space, there is less chance of convergence to a local optimal point. This article uses the AISC Equation to derive shear capacity for system identification. In addition to the AISC equation, the combination of polynomial functions was also used to better identify different states. Equation (7) is the equation that the GA seeks to optimize by applying changes in the values of the $a_i$coefficients. In this

TABLE 3. Activation functions for each NN layer

No.	First layer	Second layer	Third layer	Fourth layer	Fifth layer	Sixth layer
Activation function	tansig	purelin	tansig	purelin	tansig	purelin

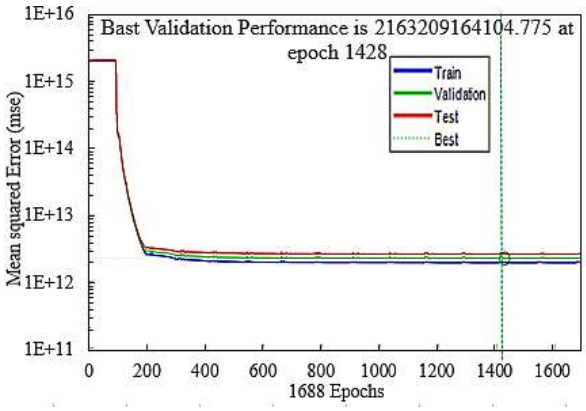

Figure 7. NN training diagram for training, test and intermediate data

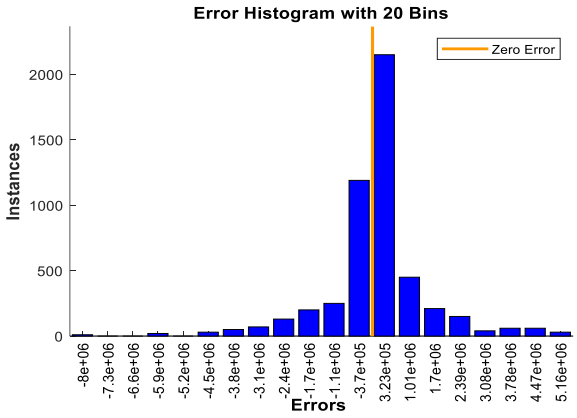

Figure 8. Histogram of error rate during training process for NN in the first case

equation, the $x_i$represents the inputs. It should be noted that by deriving a common denominator of Equation (7) and simplification, we arrive at a linear equation. However, this practice is not defined for the GA. In other words, the response of the algorithm to the linear function obtained from the simplification of Equation (7) will be different from the answer to Equation (7) itself. Table 4 shows coefficients 1-9 of the three optimized algorithms. In general, the outputs of the GA are expressed in three different states, namely the output of the project for one, two and three GAs that will work concurrently.

$$y \approx \sum_{i=1}^{9} \alpha_i (x_i + \frac{x_i^3}{x_i^2}) \quad (7)$$

5. VALIDATION AND COMPARISON OF RESULTS

A series of graphs are plotted as colored contours, each of which determines the percentage error of the data part. In Figures 9-12, the percentage of NN output error and the GA are shown with the actual value. Taking a look at these color contours and the calculated error rate in each house from this checkerboard, we find that the GA worked well. Only one error point represents about 80% and most points below 10%.

To evaluate the performance of the networks, the mean squared error (MSE) method with an ideal value of zero was used. Mean Square Error (MSE) is one of the

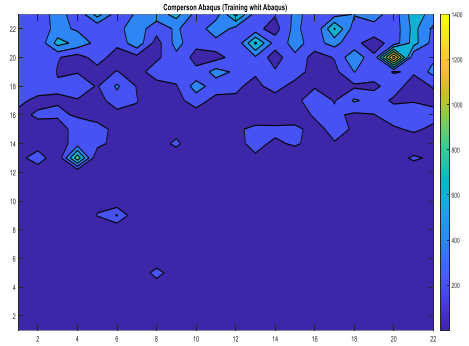

Figure 10. Comparison of the NN output with the actual output value of ABAQUS software as thermal graph

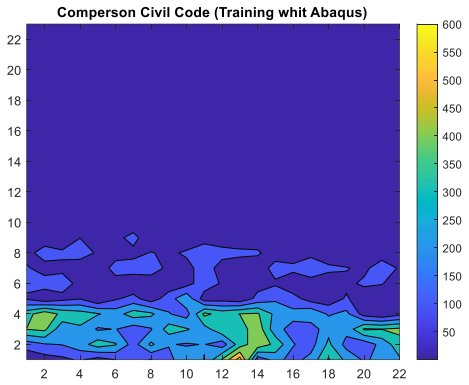

Figure 11. Comparison of the output of the NN with the output value of the AISC as a thermal graph

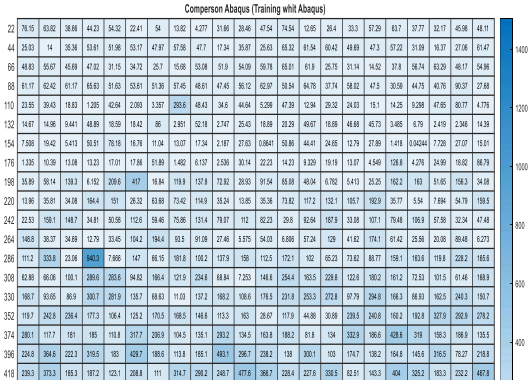

Figure.9. NN Output Error Percentage with Real Value (ABAQUS Software)

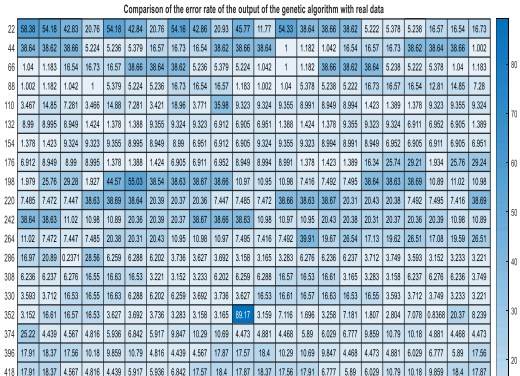

Figure 12. GA Output Error Percentage with Real Value (ABAQUS Software)

TABLE 4. Coefficients 1-9 of the three optimized algorithms

	a_9	a_8	a_7	a_6	a_5	a_4	a_3	a_2	a_1
Algorithm 1	49.21	49.22	49.08	2.52×10^{-5}	0.0019	678.38	532.64	2.68×10^{-5}	3.85×10^{-5}
Algorithm 2	90.35	90.71	88.26	0.0013	0.0012	42.61	238.70	0.0014	0.0005
Algorithm 3	98.55	97.67	90.012	0.0042	0.0316	38.54	40.65	0.0074	0.0033

statistical tools for finding prediction accuracy in modeling [21].

$$MSE = \sum_1^n \frac{(obs-calc)^2}{N} \quad (8)$$

N is Total number of training and test data pairs, obs is Training data, and Calc is Test data corresponding to training data. In this comparison, the data are divided into two categories. The first category relates to training data. This input data together with their response is provided to the smart method. Then, try to test the prediction performance using the second set of data, namely X data. Therefore, it is generally expected that the error of the training data is less than the test data. This is well seen in both Figures 13 and 14. In Figure 15, the error rate between the output of the NN and the output of the GA for ABAQUS data is calculated and shown.

The first point to note is the low error of prediction of the results by the GA compared to the NN in all different modes. This suggests that the choice of GA would be more appropriate in this particular case.

6. SENSITIVITY ANALYSIS

For sensitivity analysis, all input data were normalized to the range of 0 to 1. These parameters include column flange thickness, column web thickness, beam flange thickness, column width, height of beam and thickness of

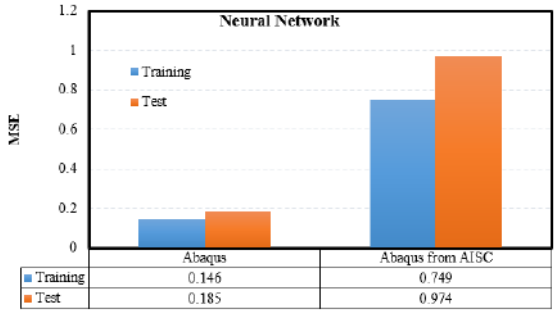

Figure 13. Values of the MSE NN

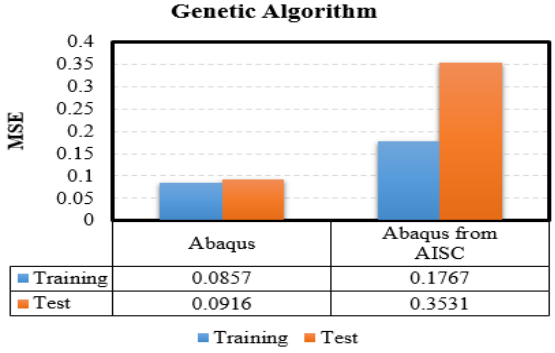

Figure 14. Values of the MSE GA

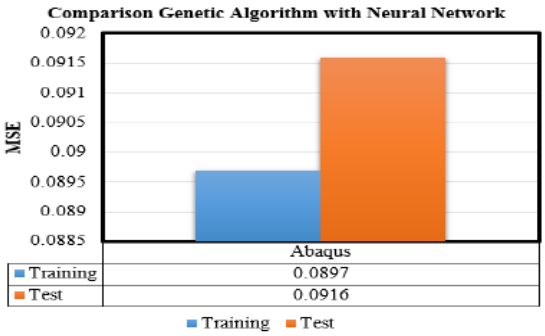

Figure 15. The error rate between the output of the NN and the output of the GA

continuity plates. The NN and GA are designed based on these parameters. If the output function is $f = R_n$, for the variations in the variable input, the input x_i is considered as follows:

$$\frac{\partial R_n}{\partial x_i} = \frac{f(x_i + \Delta x_i) - f(x_i - \Delta x_i)}{2\Delta x_i} \quad (9)$$

Considering $\Delta x_i = 0.05$, $\frac{\partial R_n}{\partial x_i}$ values were calculated as reported in Figure 16.

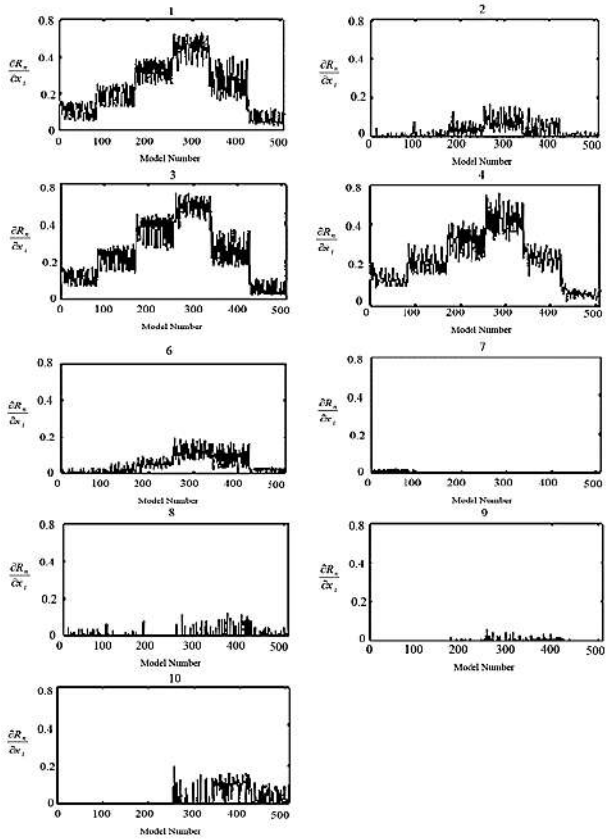

Figure 16. Sensitivity analysis for 9 parameters influencing the shear capacity of panel zone

In this figure, the x-axis represents 510 data and the y-axis represents $\frac{\partial R_n}{\partial x_i}$. The number shown at the top of each figure represents the input variable input. According to Figure 16, compared to other parameters, the three counters, namely 1, 3 and 4, are more effective in calculating the shear capacity. These parameters are column width, column thickness, flange and column web, respectively. This proves that the AISC relations are not efficient for calculating the shear capacity of panel zones at high thicknesses.

7. DISCUSSION AND CONCLUSION

In this comparison, the data are divided into two categories. The first category relates to training data. This input data is provided along with their response to the smart method. Then, we try to test the prediction performance using the second set of data, the X data. When ABAQUS data is selected as training and test data, smart methods perform best. However, in another case, if the test data are selected from the AISC data, the error rate will increase sharply. The present study presents a model using multilayer perceptron ANN and regression analysis method. This model is capable of measuring the shear capacity of a steel-shaped box-shaped column panel zone using 9 effective parameters (i.e., column length, column width, column flange thickness, column web thickness, beam width, beam height (X to X beam flange), beam flange thickness, beam web thickness, stiffener thickness). The results of the designed NN and GA refer to the following.

1) What is evident is the error of the AISC relations to determine the shear capacity of the box-shaped column panel zone. The AISC relations calculates shear capacity based on four parameters. However, the artificial intelligence networks in this study are trained on 9 parameters and predict the shear capacity of the coupling source, which reduces the error rate.

2) Sensitivity analysis based on a large parametric study of low to high thicknesses. In the AISC, the unstructured relations have shown that at high thicknesses, both the column thickness and the thickness of the bond plates affect the shear capacity. Therefore, by using the optimized equation of GA, a wide range of shear capacity of box-shaped columns with different column thicknesses can be obtained.

3) Artificial Intelligence Networks This study is based on 9 training parameters and predicts the shear capacity of the coupling source. Each of these AIs has errors with respect to ABAQUS output, which calculates the actual amount of shear capacity. Based on their performance evaluation, it can be concluded that the GA reduces the error to below 10% by using optimization.

8. REFERENCES

1. Arabzadeh, A., and Hizaji, R. "A Simple Approach to Predict the Shear Capacity and Failure Mode of Fix-ended Reinforced Concrete Deep Beams based on Experimental Study." ***International Journal of Engineering, Transactions A: Basics***, Vol. 32, No. 4, (2019), 474–483. https://doi.org/10.5829/ije.2019.32.04a.03
2. AISC 360-05,Specification for structural steel buildings. Chicago(IL): American Institute of Steel Construction; (2010).
3. Mansouri, I., and Saffari, H. "A fast hybrid algorithm for nonlinear analysis of structures." ***ASIAN Journal of Civil Engineering (BHRC)***, Vol. 15, No. 2, (2014), 213–229. https://www.sid.ir/en/journal/ViewPaper.aspx?ID=353421
4. Chithra, S., Kumar, S. R. R. S., Chinnaraju, K., and Alfin Ashmita, F. "A comparative study on the compressive strength prediction models for High Performance Concrete containing nano silica and copper slag using regression analysis and Artificial Neural Networks." ***Construction and Building Materials***, Vol. 114, (2016), 528–535. https://doi.org/10.1016/j.conbuildmat.2016.03.214
5. Hartmann, S. "Project Scheduling with Multiple Modes: A Genetic Algorithm." ***Annals of Operations Research***, Vol. 102, No. 1–4, (2001), 111–135. https://doi.org/10.1023/A:1010902015091
6. Elhewy, A. H., Mesbahi, E., and Pu, Y. "Reliability analysis of structures using neural network method." ***Probabilistic Engineering Mechanics***, Vol. 21, No. 1, (2006), 44–53. https://doi.org/10.1016/j.probengmech.2005.07.002
7. VANLUCHENE, R. D., and SUN, R. "Neural Networks in Structural Engineering." ***Computer-Aided Civil and Infrastructure Engineering***, Vol. 5, No. 3, (1990), 207–215. https://doi.org/10.1111/j.1467-8667.1990.tb00377.x
8. Jenkins, W. M. "Plane Frame Optimum Design Environment Based on Genetic Algorithm." ***Journal of Structural Engineering***, Vol. 118, No. 11, (1992), 3103–3112. https://doi.org/10.1061/(ASCE)0733-9445(1992)118:11(3103)
9. Adeli, H. "Neural networks in civil engineering: 1989-2000." ***Computer-Aided Civil and Infrastructure Engineering***, Vol. 16, No. 2, (2001), 126–142. https://doi.org/10.1111/0885-9507.00219
10. Sahoo, B., and Maity, D. "Damage assessment of structures using hybrid neuro-genetic algorithm." ***Applied Soft Computing Journal***, Vol. 7, No. 1, (2007), 89–104. https://doi.org/10.1016/j.asoc.2005.04.001
11. Khalkhali, A., Nariman-Zadeh, N., Khakshournia, S., and Amiri, S. "Optimal Design of Sandwich Panels using Multi-objective Genetic Algorithm and Finite Element Method." ***International Journal of Engineering, Transactions C: Aspects***, Vol. 27, No. 3, (2014), 395–402. https://doi.org/10.5829/idosi.ije.2014.27.03c.06
12. Mallela, U. K., and Upadhyay, A. "Buckling load prediction of laminated composite stiffened panels subjected to in-plane shear using artificial neural networks." ***Thin-Walled Structures***, Vol. 102, (2016), 158–164. https://doi.org/10.1016/j.tws.2016.01.025
13. Abambres, M., and Lantsoght, E. O. L. "Neural network-based formula for shear capacity prediction of one-way slabs under concentrated loads." ***Engineering Structures***, Vol. 211, (2020), 110501. https://doi.org/10.1016/j.engstruct.2020.110501
14. Hoang, N. D. "Estimating punching shear capacity of steel fibre reinforced concrete slabs using sequential piecewise multiple linear regression and artificial neural network." ***Measurement: Journal of the International Measurement Confederation***, Vol.

137, (2019), 58–70. https://doi.org/10.1016/j.measurement.2019.01.035

15. Jang, B. W., and Kim, C. G. "Impact localization of composite stiffened panel with triangulation method using normalized magnitudes of fiber optic sensor signals." ***Composite Structures***, Vol. 211, (2019), 522–529. https://doi.org/10.1016/j.compstruct.2019.01.028
16. Hedayat, A. A., Ahmadi Afzadi, E., Kalantaripour, H., Morshedi, E., and Iranpour, A. "A new predictive model for the minimum strength requirement of steel moment frames using artificial neural network." ***Soil Dynamics and Earthquake Engineering***, Vol. 116, , (2019), 69–81. https://doi.org/10.1016/j.soildyn.2018.09.046
17. Krawinkler, H., Popov, E., and Bertero, V. "Shear behavior of steel frame joints." ***Journal of the Structural Division***, Vol. 101, No. 11, (1975), 2317–2336. Retrieved from https://cedb.asce.org/CEDBsearch/record.jsp?dockey=0006323
18. Stojadinović, B., Goel, S. C., Lee, K. H., Margarian, A. G., and Choi, J. H. "Parametric tests on unreinforced steel moment connections." ***Journal of Structural Engineering***, Vol. 126, No. 1, (2000), 40–49. https://doi.org/10.1061/(ASCE)0733-9445(2000)126:1(40)
19. Mansouri, I., and Saffari, H. "A new steel panel zone model including axial force for thin to thick column flanges." ***Steel and Composite Structures***, Vol. 16, No. 4, (2014), 417–436. https://doi.org/10.12989/scs.2014.16.4.417
20. Bayo, E., Loureiro, A., and Lopez, M. "Shear behaviour of trapezoidal column panels. I: Experiments and finite element modelling." ***Journal of Constructional Steel Research***, Vol. 108, (2015), 60–69. https://doi.org/10.1016/j.jcsr.2014.10.026
21. Ho, S. L., Xie, M., and Goh, T. N. "A comparative study of neural network and Box-Jenkins ARIMA modeling in time series prediction." ***Computers and Industrial Engineering***, Vol. 42, No. 3-4, 371–375. https://doi.org/10.1016/S0360-8352(02)00036-0

Persian Abstract

چکیده

بررسی رفتار چشمه اتصال ستون باکسی شکل یکی از مهمترین دغدغه‌های دانشمندان علم سازه بوده است. در آیین‌نامه فولاد آمریکا ظرفیت برشی مقاطع I شکل با ضخامت کم ستون محاسبه می‌شود. در این مقاله ظرفیت برشی چشمه اتصال در ستون‌های فلزی با مقاطع باکسی شکل با شبکه عصبی و الگوریتم ژنتیک تعیین می‌گردد و با خروجی‌های نرم‌افزار اجزا محدود آباکوس و روابط آیین‌نامه فولاد آمریکا مقایسه شده است. بنابراین با اطلاعات پارامتریک بدست آمده از ۵۱۰ مدل اتصال در نرم‌افزار آباکوس، شبکه عصبی آموزش داده شدند.نتایج نشان می‌دهد ظرفیت برشی که شبکه عصبی و الگوریتم ژنتیک پیش‌بینی می‌کند، طیف وسیعی از کلیه پارامترهای تاثیرگذار در محاسبه میزان ظرفیت برشی چشمه اتصال نسبت به روابط آیین‌نامه آمریکا استفاده می‌کند. بنابراین هوش‌های مصنوعی به کار رفته می‌تواند گزینه مناسبی باشد. در نهایت الگوریتم ژنتیک به همراه بهینه کردن یک رابطه ریاضی توانسته است میزان خطا را در تعیین ظرفیت برشی چشمه اتصال ستون‌های باکسی شکل فلزی حتی در ضخامت‌های بالای ستون به حداقل برساند.

International Journal of Engineering

Journal Homepage: www.ije.ir

Durability Performance of Self Compacting Concrete Incorporating Alccofine and Fly Ash

B. V. Kavyateja*[a], J. G. Jawahar[b], C. Sashidhar[a]

[a] *Department of Civil Engineering, Jawaharlal Nehru Technological University, Anantapur, India*
[b] *Department of Civil Engineering, Annamacharya Institute of Technology and Sciences, Tirupati, India*

PAPER INFO

Paper history:
Received 15 February 2020
Received in revised form 16 April 2020
Accepted 11 June 2020

Keywords:
Carbonation Test
Chloride Permeability Test
Electrical Resistivity
Self Compacting Concrete
Water Absorption Test
Water Permeability Test

ABSTRACT

The cost associated with the application of large volume of cement and synthetic admixtures was one of the major drawbacks of Self Compacting Concrete (SCC), which can be reduced by the use of supplementary cementitious materials (SCM). When the demand of cement reduces, the release of carbon dioxide (CO_2) from cement industries will come down, which has a positive impact on global warming. The present paper reports an attempt in this direction by experimental examination on the fresh properties and durability performance of SCC by replacing cement with SCM such as fly ash (FA) and ultra-fine Ground Granulated Blast Furnace Slag (GGBS) in varying ratios. SCC mix was obtained by fixing the water-binder ratio and superplasticizer (SP) dosage with respect to total cementitious content. Along with the Fresh properties, SCC mixes incorporating both alccofine and fly ash at 10 and 25%, respectively; which gave the best fresh properties were selected to assess the durability issues. Incorporating 10% alccofine and 25% fly ash gave the best result in both fresh and durability studies in comparison with other combinations.

***doi**: 10.5829/ije.2020.33.08b.10*

1. INTRODUCTION

Self compacting concrete (SCC) was developed in Japan due to the reduction of skilled labour force and the subsequent reduction of quality in construction industry. The first paper presentation in 1989 on SCC by Ozawa augmented its international attention. Positive aspects of SCC include reduction in labour, safety due to decrease in human risk, less construction time, refined filling capacity, better interfacial transitional zone (ITZ), decreased permeability, improved durability, more freedom in designing, superior quality production and good structural implementation [1]. One of the major drawbacks of SCC was its cost due to the utilization of high amounts of cement and chemical admixtures. The use of pozzolanic materials improves the durability of concrete which in turn reduces the usage of cement. This will result in strong structures which require fewer repairs during its life span. Addition of Supplementary Cementitious Materials (SCM) in SCC can upgrade the strength, durability, economic aspect and the effects due to inadequate compaction [2]. The durability of concrete with SCM was improved due to the pozzolanic reaction which occurs during the process of hydration in cement. The most commonly used SCMs were silica fume (SF), fly ash, ground granulated blast furnace slag (GGBS), metakaolin, rice husk ash etc. During cement hydration, calcium hydroxide (CH) and calcium silicate hydrate (C–S–H) gels were formed. CH which is the most soluble hydration product was a fragile linkage in cement [3]. When concrete was open to water, the CH will dissolve which increases the porosity and makes concrete more sensitive to further leaching and chemical intrusion. The pozzolanic materials added in SCC makes the pore refinement which blocks the passage of water and other chemicals [4].

Compared to ordinary concrete SCC has a lower viscosity and, therefore, a more significant flow rate when pumped. To achieve a high workability, SCC requires control on the nominal maximum size (NMS),

*Corresponding Author Email: *kavyateja2014@gmail.com* (B. V. Kavyateja)

Please cite this article as: B. V. Kavyateja, J. G. Jawahar, C. Sashidhar, Durability Performance of Self Compacting Concrete Incorporating Alccofine and Fly Ash, International Journal of Engineering (IJE), IJE TRANSACTIONS B: Applications Vol. 33, No. 8, (August 2020) 1522-1528

amount and grading of the aggregate. So to maintain consistency of fresh mixture of SCC, and to reduce settlement effects, the practice was to utilize high range water reducers, to restrict the maximum size of coarse aggregate and content, and to utilize low water powder proportions or viscosity modifying agent (VMA) to modify the flow properties and rheology of SCC. The properties of fresh SCC were influenced by water to cement content (w/c) and water to powder content (w/p) ratios [5]. Flow ability and stability of SCC can be maintained either by increasing the paste content by, raising the cement content or some mineral admixtures, or by using a viscosity-modifying agent (VMA).

SCC has not yet improved all its widespread responses as a development material and its application stays constrained [6]. The improvement of a SCC with remarkable properties in the fresh and hardened state was essential for the response of such a concrete. Blend of high strength along with its self compacting property offers prospective advantages to construction world. The distinctive mix design along with the absence of vibration makes distinct changes in durability properties in SCC. The degradation of the cementitious material are extremely affected by the perviousness of the material. As the pore structure may be distinctive for SCC compared with normal concrete, a few changes in durability behaviour may be taken care. SCC was utilized without knowledge of the natural durability of the material itself and this could be the reason for the durability issues identified with the usage of SCC [7].

In the present paper an investigation was carried out on the practicality of developing a self-compacting concrete by replacing cement with SCM such as fly ash and ultra-fine slag [8–13]. It highlights the outcomes of the fresh properties and different durability studies of SCC mixtures. The paper moreover looks into the effects of using fly ash and alccofine on durability performance of SCC. Hence the paper addresses the improvement of SCC blended with SCM and examines its various properties like fresh and durability which will lead to a sustainable construction.

2. MATERIALS AND METHODS

2. 1. Materials The constituent materials used for the preparation of the conductive SCC included Ordinary Portland cement 53 grade conforming to BIS: 12269-1987 [14], coarse aggregates of 10 mm maximum size and fine aggregate of zone III conforming to IS: 383 – 1970 [15]. High range water reducer (HRWR) based on modified sulfonated nathalene formaldehyde (SNF) – Conplast SP 430 [16] was used as a superplasticizer to mobilize the flow of the concrete to acquire self-compacting properties.

Alccofine (AL-1203) was obtained from Ambuja Cement Ltd, Goa having the specific gravity of 2.9 confirming to ASTM C989-1999 [17] was used in entire study. The properties (i.e. physical and chemical) of the cement used are tabulated in Tables 1 and 2, respectively. The physical properties and chemical properties of AL-1203 are given in Tables 3 and 4, respectively. Fly ash Class F was obtained from Rayalaseema Thermal power Plant (RTPP), Muddanur, Aandhra Pradesh, India and confirming to ASTM C 618. The physical properties and chemical composition are represented in Table 5. The Microstructural properties of the cement, fly ash and alccofine used are shown in Figures 1, 2 and 3, respectively.

TABLE 1. Physical properties of cement

Characteristics	Test Results	Requirements as per BIS code
Grade	53	53
Specific gravity	3.10	-
Standard consistency	30%	-
Initial setting time	94 min	>30 min
Final setting time	280 min	< 600 min
Specific surface area (m^2/kg)	340	-

TABLE 2. Chemical properties of cement

CaO	SiO_2	Al_2O_3	Fe_2O_3	SO_3	MgO
60.84%	16.34%	6.95%	5.38%	1.99%	2.32%

TABLE 3. Physical properties of AL-120

Characteristics	Test Results
Specific gravity	2.90
Specific surface area [m^2/kg]	1200
Bulk density [kg/m^3]	680
Particle Size in Micron	
D10	1.5
D50	5
D90	9

TABLE 4. Chemical Properties of AL form EDAX

Characteristics of Element	Results for EDAX	
	Weight %	Atomic %
C K	45.69	57.64
O K	35.26	33.39
Al K	4.01	2.25
Si K	6.38	3.44
Ca K	8.66	3.27

TABLE 5. Physical properties and chemical composition of class F Fly ash

Particulars	Class F Fly ash	ASTM C 618 Class F Fly ash
Physical properties		
Fineness (m^2/kg)	360	Min 225
Specific gravity	2.23	-
Chemical composition		
Silica	65.6	Silica + Alumina + Iron oxide >70
Iron oxide	3.0	
Alumina	28.0	
Magnesia	1.0	
Lime	1.0	
Sulphur trioxide	0.2	Max 5.0
Titanium oxide	0.5	
Loss on Ignition	0.29	Max 6.0

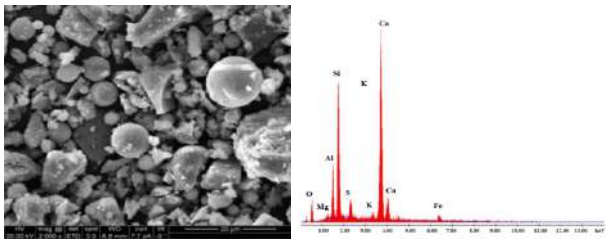

(a) (b)

Figure 1. Microstructural analysis of cement using (a) SEM (b) EDAX

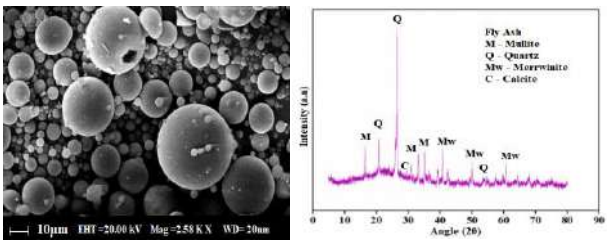

(a) (b)

Figure 2. Microstructural analysis of fly ash using (a) SEM (b) XRD

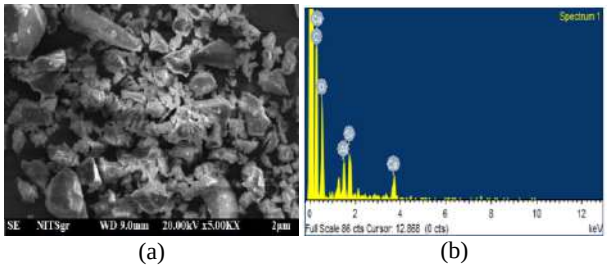

(a) (b)

Figure 3. Microstructural analysis of alccofine using (a) EDAX (b) SEM

2. 2. Fabrication of Concrete In the present investigation, M25 grade normal concrete mix design carried out according to BIS: 10262-2009 [18]. Mix proportions: 1:1.66:2.97:0.52. Self-compact ability largely affected by the characteristics of materials and mix proportions. In this experimental study, three types of self-compacting concrete mixture proportions adopted. The mortar or the paste in the self-compacting concrete requires high viscosity and deformability, thereby the water-powder ratio has been adopted as 0.36 (as per EFNARC guidelines) constantly. The concrete is drenched into steel moulds and left to harden. After 24 hours, these cubes are exiled from the moulds for curing. A total of four altered mixes with constant dosage of fly ash and 1.2% of SNF and with varying dosages of alccofine have been prepared. The concrete mix proportion details are given in Table 6.

2. 3. Methods

2. 3. 1. Frsh Properties To decide the fresh stage properties of SCC blends, individual workability test like Slump Flow, T50 Slump Flow, V-Funnel and L-box etc. were completed according to EFNARC specifications [19].

2. 3. 2. Water Absorption Test Measurement of water absorption test on cube sample of size 150 mm was carried out under ASTM C642-06 at 28 days. Initially, the cube specimens had been placed in an oven at a temperature of 105ºC for 24 hours. Later, the specimens were taken out from the oven, cooled and were weighted (B). The specimens were immersed in water for two days and weighted (A). The water absorption value of the cube specimen was determined as per Equation 1 below.

$$\text{Water absorption (\%)} = \frac{A-B}{B} \quad (1)$$

where, A is saturated surface dry weight of specimens (g) and B is oven dry weight of specimens (g).

2. 3. 3. Electrical Resistivity of Concrete Electrical resistivity (ρ) of a material is characterized as its ability to withstand the exchange of ions exposed to an electrical field. It is reliant on the concrete microstructure properties such as pore size and state of the interconnections; by this the durability of concrete can be judged. Leader RCON™ Concrete Electrical Resistivity Meter has been used to measure the electrical resistance of concrete as per standards guidelines in ASTM C1202-19. The test was done for 150 mm size cubical specimens at one predetermined position on each specimen for normal concrete with and without addition of fly ash and alccofine at a curing period of 28 days. The electrical resistivity of concrete cubes is expressed as follows:

$$\rho = \frac{RA}{l} \quad (2)$$

where, ρ is electrical resistivity (unit: Ω-m), R is electrical resistance (unit: Ω), l is electrical path length in the specimen (unit: m), and A is the cross-sectional area of the specimen (unit: m^2).

2. 3. 4. Rapid Chloride Penetration Test As per ASTM C1202 test, the water statured concrete specimens having a thickness of 50 mm and a diameter of 100 mm are placed in a vacuum desiccator to eliminate air particles and these specimens were exposed to 60 V DC voltage supply for 6 hours with the RCPT apparatus and having three cell arrangement as illustrated in Figure 4. The specimens were placed among the cells without a bit of air gap and the boundaries were coated with silicon glue to prevent the escape of chemical solution. There is a 0.3M NaOH solution in one reservoir and a 3% NaCl solution in another reservoir. The total charge carried out in coulombs at an interval of 30 minutes for 360 minutes was used to measure the concrete resistance against chloride ion penetration. The total charge passed is assessed and used to measure the concrete quality as per the criteria set out in Table 7.

3. ESULTS AND DISCUSSION

3. 1. Fresh Properties The fresh mixes of SCC with inclusion of 25% fly ash and varying dosage of alccofine (0%, 5%, 10% and 15%) were tested to check its rheological properties. As discussed earlier the SCC should have four main characteristics, namely flowability, viscosity, passing ability and smooth surface after de- moulding. Tests described in Table 8 were performed on freshly prepared concrete: as per the procedure as explained in EFNARC and ACI 237R code.

Fresh mix prepared was tested for slump flow to check its flow-ability. Test results are shown in Table 9. From obtained results, it can be seen that the measured diameter of flow is within the prescribed limits of EFNARC for all the mixes. It was observed that as alccofine volume increases flow of SCC slightly increases (Upto 10%). The required time for flowing concrete for a diameter of 500mm i.e. T500 was also found and is tabulated in Table 9. It was observed that all the results fall within the limits prescribed by EFNARC.

Table 10 gives the test results of L-box test. This test was conducted to check the flowing and passing ability of SCC through reinforcement. Results obtained for all the mixes fall within the prescribed limits of EFNARC. In L-box test results H1 represent horizontal distance on L-box filled with concrete and H2 represents vertical distance on L-box filled with concrete.

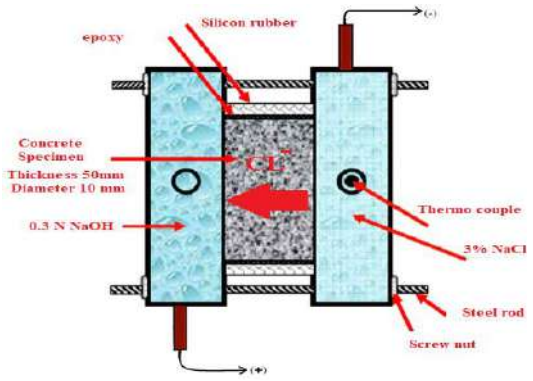

Figure 4. Schematic picture of the RCPT apparatus

TABLE 7. Chloride ion penetration of concrete according to ASTM C1202

Charge passed	Chloride ion penetration
<100	Negligible
100-1000	Very low
1000-2000	Low
2000-4000	Moderate
>4000	High

TABLE 8. Tests and purpose

Test Name	Purpose
Slump flow	To check the flowability of the freshly prepared mix
V – funnel	For knowing Viscosity property of fresh SCC
L-box	To check Passing ability and filling of SCC in between the bars

TABLE 9. Slump flow test results

Specimen Mix designation	Flow Dia (mm) Obtained in 30 seconds	Permissible range as per EFNARC	Time for 500mm Dia (T_{500}) (s)	Permissible range for T_{500} as per EFNARC
SCC0	655	650-800	4.1	2-5 s
SCC 1	671		3.7	
SCC 2	682		3.4	
SCC 3	631		4.5	

V-funnel test was also conducted to check the filling ability and viscosity of freshly prepared SCC. In this test, V-funnel was filled with freshly mixed concrete and concrete was left to fall freely under the force of gravity noting the time for emptying the funnel. All the results obtained were within prescribed limits of EFNARC and are shown in Table 11.

3. 2. Water Absorption Test Water absorption test is one of the most important parameters for finding the durability of concrete. The perforation of gases, water and ions depend on the microstructure and porosity of concrete. From Figure 5, it can be observed that normal concrete had high water absorption values than alccofine added concrete. The mixes with constant fly ash quantity and varying dosage of alccofine i.e. SCC0, SCC1, SCC2 and SCC3 showed the reduction in water absorption percentage values of 0.58%, 0.247%, 0.225% and 0.214%, respectively, with respect to NM (i.e. 1.02%) at 28th day. From the results, alccofine added concrete mixture showed low water absorption values because of high surface area of alccofine particles which settled in micro spaces in concrete [8–13]. The low water absorption percentage results in fly ash-alccofine based self compacting concrete mixes is due to occurrence of higher pozzolanic effect by alccofine and fly ash due to their micro and nano particle size which made the concrete more denser, more compacted and also improved the pore structure of the concrete which helped to reduces the water absorption percentage.

3. 3. Electrical Resistivity of Concrete The electrical resistivity of concrete is the resistance offered by concrete against the flow of electrical current and is its material property [20]. This material property is used

TABLE 10. L Box test results

Specimen Mix	H2/H1	Permissible limits of H2/H1
SCC0	0.75	0.8-1
SCC 1	0.83	
SCC 2	0.86	
SCC 3	1.0	

TABLE 11. V-funnel test results

Specimen Mix designation	V-funnel flow time (s)	Permissible range as per EFNARC (s)
SCC 0	9.62	6–12
SCC 1	8.91	
SCC 2	8.75	
SCC 3	11.5	

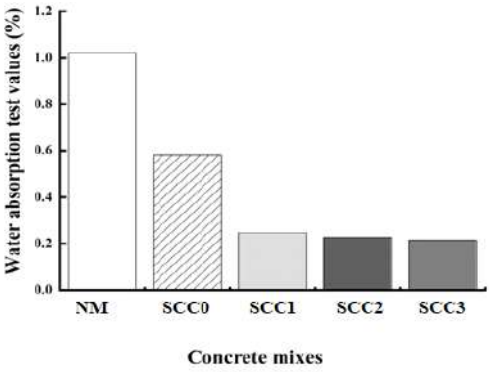

Figure 5. Graphical representation of water absorption test of fly ash-alccofine based self compacting concrete

in condition surveying of concrete structures. Figure 6 shows electrical resistivity results of concrete with constant dosage of fly ash and varying dosages of alccofine. The mixes with constant fly ash quantity and varying dosage of alccofine i.e. SCC0, SCC1, SCC2 and SCC3 showed enhancement in electrical resistivity values of 2.04%, 11.26%, 8.14% and 2.97%, respectively with respect to NM at 28th day [20]. It is noticed that concrete cubes with adding of fly ash (25% by mass) and 5% of AL had high electrical resistivity. It was also noticed that the resistivity of concrete increases with increasing dosage of alccofine up to 5%. This improvement is due to the filling of pores with alccofine and formation of ettringite was followed by the combination of alccofine and fly ash. The reduction in electrical resistivity of concrete at higher dosages of alccofine is because of over precipitation of calcite at the surface region.

3. 4. Rapid Chloride Penetration Test From Table 12, it can observe that replacement of cement with constant fly ash and varying alccofine dosages decreases the chloride ion penetration. NM showed the RCPT value of 2468 coulombs and shows medium chloride

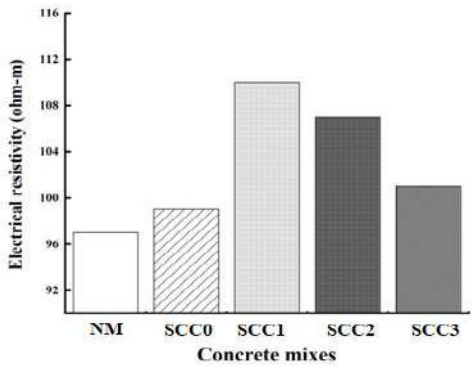

Figure 6. Graphical representation of electrical resistivity of fly ash-alccofine based self compacting concrete

TABLE 12. RCPT values of concrete with constant fly ash quantity and varying dosage of alccofine

Mix No	Mix Name	RCPT value in coulombs	Chloride penetration as per ASTM C1202
Mix 1	NM	2468	Medium
Mix 2	SCC0	1235	Low
Mix 3	SCC 1	232	Very Low
Mix 4	SCC 2	112	Very Low
Mix 5	SCC 3	104	Very Low

permeability as per ASTM C1202. With increasing the dosage of alccofine (i.e., 0%, 5%, 10% and 15%) into fly ash based concrete (i.e. Constant dosage of cement replaced with 25% fly ash by mass) showed from 1235 to 104 RCPT values and shows a low to very low permeability class in ASTM code. The reason behind that with adding of alccofine and fly ash showed better homogeneity in concrete, its help to improved pore microstructure and also reduce the RCPT values [21].

4. CONCLUSION

We investigated five different combinations of mixtures for Fresh properties, water absorption test, electrical resistivity and rapid chloride penetration test. With the constant dosage of fly ash and 10% alccofine showed better improvement in water absorption test, electrical resistivity, rapid chloride penetration test and fresh properties. SCC can be easily achieved with incorporation of SCM to the concrete. All the mixes showed good workability properties, which satisfied the EFNARC guidelines. From the water absorption test results, the concrete with adding of alccofine and fly ash showed a reduction of water absorption values compared to normal and fly ash based concrete due to filling of pores by alccofine particles. Resistivity of concrete has increased with adding of alccofine and fly ash because of homogeneity mixture up to 5% of alccofine and it decreased the further increment of alccofine dosage because of over precipitation of calcite at the surface region. Concrete with adding of constant fly ash quantity and 10% alccofine showed less RCPT value compared to other mixtures and showed chloride ion penetration changes from 1235 to 104 RCPT values with increasing alccofine dosages.

5. ACKNOWLEDGEMENTS

The authors acknowledge the facilities provided by Jawaharlal Nehru Technological University, Anantapur and Annamacharya Institute of Technology and Sciences, Tirupathi for research works in the field of concrete technology at the Department of Civil Engineering (CE).

6. REFERENCES

1. Shi, C., Wu, Z., Lv, K., and Wu, L. "A review on mixture design methods for self-compacting concrete." ***Construction and Building Materials***. Vol. 84, (2015), 387– 398. https://doi.org/10.1016/j.conbuildmat.2015.03.079
2. Ramanathan, P., Baskar, I., Muthupriya, P., and Venkatasubramani, R. "Performance of self-compacting concrete containing different mineral admixtures." ***KSCE Journal of Civil Engineering***, Vol. 17, No. 2, (2013), 465–472. https://doi.org/10.1007/s12205-013-1882-8
3. Owsiak, Z., and Grzmil, W. "The evaluation of the influence of mineral additives on the durability of self-compacting concretes." ***KSCE Journal of Civil Engineering***, Vol. 19, No. 4, (2015), 1002–1008. https://doi.org/10.1007/s12205-013-0336-7
4. Le, H. T., and Ludwig, H. M. "Effect of rice husk ash and other mineral admixtures on properties of self-compacting high performance concrete." ***Materials and Design***, Vol. 89, (2016), 156–166. https://doi.org/10.1016/j.matdes.2015.09.120
5. Guru Jawahar, J., Sashidhar, C., Ramana Reddy, I. V., and Annie Peter, J. "Micro and macrolevel properties of fly ash blended self compacting concrete." ***Materials and Design***, Vol. 46, (2013), 696–705. https://doi.org/10.1016/j.matdes.2012.11.027
6. Uysal, M., and Sumer, M. "Performance of self-compacting concrete containing different mineral admixtures." ***Construction and Building Materials***, Vol. 25, No. 11, (2011), 4112–4120. https://doi.org/10.1016/j.conbuildmat.2011.04.032
7. El-Chabib, H., and Syed, A. "Properties of Self-Consolidating Concrete Made with High Volumes of Supplementary Cementitious Materials." ***Journal of Materials in Civil Engineering***, Vol. 25, No. 11, (2013), 1579–1586. https://doi.org/10.1061/(ASCE)MT.1943-5533.0000733
8. Goh, C. S., Gupta, M., Jarfors, A. E. W., Tan, M. J., and Wei, J. "Magnesium and Aluminium carbon nanotube composites." ***Key Engineering Materials***, Vol. 425, , (2010), 245–261. https://doi.org/10.4028/www.scientific.net
9. Reddy, P. N., and Naqash, J. A. "Development of high early strength in concrete incorporating alccofine and non-chloride accelerator." ***SN Applied Sciences***, Vol. 1, No. 7, (2019), 1–11. https://doi.org/10.1007/s42452-019-0790-z
10. Reddy, P. N., and Naqash, J. A. "Effect of Alccofine on Strength and Durability Index Properties of Green Concrete." ***International Journal of Engineering, Transactions C: Aspects***, Vol. 32, No. 6, (2019), 813–819. https://doi.org/10.5829/ije.2019.32.06c.03
11. Reddy, P. N., and Naqash, J. A. "Experimental study on TGA, XRD and SEM Analysis of Concrete with Ultra-fine Slag." ***International Journal of Engineering, Transactions B: Applications***, Vol. 32, No. 5, (2019), 679–684. https://doi.org/10.5829/ije.2019.32.05b.09
12. Reddy, P. N., and Naqash, J. A. "Properties of concrete modified with ultra-fine slag." ***Karbala International Journal of Modern Science***, Vol. 5, No. 3, (2019), 151–157. https://doi.org/10.33640/2405-609X.1141
13. Reddy, P. N., and Naqash, J. A. "Effectiveness of polycarboxylate ether on early strength development of alccofine concrete." ***Pollack Periodica***, Vol. 15, No. 1, (2020), 79–90. https://doi.org/10.1556/606.2020.15.1.8
14. BIS 12269, Ordinary Portland cement 53 Grade-Specification, New Delhi, India, (2013).
15. BIS 383, Specification for Coarse and Fine Aggregates from

Natural Sources for Concrete, New Delhi, India, (2016).,

16. ASTM C494, Standard specification for chemical admixtures for concrete, Philadelphia: American Society for Testing and Materials, (2004).
17. ASTM C989, Standard Specification for Ground Granulated Blast-furnace Slag for Use in Concrete and Mortars, West Conshohocken, USA, (1999).
18. BIS 10262, Concrete Mix Proportioning—Guideline. Bureau of Indian Standards, New Delhi, India, (2009).
19. EFNARC, The European Guidelines for Self-Compacting Concrete (EFNARC), Specification, production and use, (2005).
20. Azarsa, P., and Gupta, R. "Electrical Resistivity of Concrete for Durability Evaluation: A Review." ***Advances in Materials Science and Engineering***, Vol. 2017, (2017), 1–30. https://doi.org/10.1155/2017/8453095
21. T. Subbulakshmi, and Dr. B. Vidivelli. "Rapid Chloride Permeability Test on HPC Incorporating Industrial Byproducts." ***Middle-East Journal of Scientific Research***, Vol. 24, No. 2, (2016), 247–431. https://doi.org/10.5829/idosi.mejsr.2016.24.02.22935

Persian Abstract

چکیده

هزینه مرتبط با استفاده از حجم زیادی از سیمان و مواد افزودنی مصنوعی یکی از مهمترین ایرادات بتن خود متراکم (SCC) است که با استفاده از مواد اضافی سیمانی (SCM) قابل کاهش است. وقتی تقاضای سیمان کاهش یابد، میزان دی اکسید کربن (CO_2) آزاد شده از صنایع سیمان کم می‌شود که این امر تأثیر مثبتی در مسئله گرمایش کره زمین دارد. مقاله حاضر با استفاده از یک بررسی آزمایشگاهی در خصوص خواص تازه و عملکرد دوام SCC با جایگزینی سیمان با SCM مانند خاکستر حاصل از احتراق (FA) و سرباره کوره گرانول فوق العاده ریز (GGBS) در نسبت‌های مختلف، سعی در این راستا دارد. مخلوط SCC با تثبیت نسبت چسب–آب و دوز سوپر پلاستیسته با توجه به محتوای سیمان کل به دست آمد. همراه با خواص تازه، مخلوط‌های SCC که شامل دو گروه آلکوفیین و خاکستر حاصل از احتراق به ترتیب ۱۰٪ و ۲۵٪ به ترتیب که بهترین خواص تازه را به دست می‌آورند، برای ارزیابی مسائل مربوط به دوام انتخاب شدند. ترکیب ۱۰٪ آلکوکسین و ۲۵٪ خاکستر حاصل از احتراق در مقایسه با سایر ترکیبات بهترین نتیجه را در مطالعات تازه و دوام داشته است.

IJE TRANSACTIONS B: Applications Vol. 33, No. 8, (August 2020) 1529-1543

International Journal of Engineering

Journal Homepage: www.ije.ir

Numerical and Experimental Investigations on the Behavior of Steel-reinforced Concrete Columns Subjected to Eccentric Loading

M. Ahmadi[a], M. Naghipour*[a], M. Nematzadeh[b]

[a] *Faculty of Civil Engineering, Babol Noshirvani University of Technology, Babol, Iran*
[b] *Department of Civil Engineering, University of Mazandaran, Babolsar, Iran*

PAPER INFO

Paper history:
Received 27 March 2020
Received in revised form 21 May 2020
Accepted 23 May 2020

Keywords:
Composite Column
Steel-Reinforced Concrete
Finite Element Model
Ductility Index
Load-Bearing Capacity
Eccentric Loading

ABSTRACT

Steel-reinforced concrete (SRC) columns, which are classified as composite columns, became the most widely used in recent years; because of their extensive advantages over the reinforced concrete and the steel columns. In this paper, the ductility index and its influential factors were explored to investigate the behavior of SRC columns. A straightforward approach was then proposed by establishing the necessary equations based on the plastic stress distribution method. Accordingly, an experimental program was performed on six SRC column specimens with two H- and cross-shaped steel sections and three eccentricity ratios of 0.4, 0.55, and 0.7. In addition, a finite element model was developed for numerical analysis using Abaqus software, which was verified by the experimental results. A total of 30 columns were thus analyzed for the parametric study where the effects of geometric and material variables, including steel percentage, concrete compressive strength, lateral tie spacing, and geometrical shape of the steel core on the ductility index of these columns were assessed. The results confirm that for the H-shaped column, reducing the lateral tie spacing ratio from 0.6 to 0.2 not only increases the ductility index to as much as 72%, it also induces a post-yield hardening in the load-displacement curve and increases the bearing capacity by 20%. Subsequently, load-bending moment interaction curves were developed according to plastic stress distribution method cited in EC4 Code and then compared with those obtained through the software. Thus, normalized curves were presented as a means to design these columns.

***doi**: 10.5829/ije.2020.33.08b.11*

1. INTRODUCTION

The application of SRC columns is particularly desirable due to many architectural, structural, and economic expediencies over the concrete or steel columns. Besides, the constant need to improve materials and reduce the dimensions and size required in the structural systems became critical, especially in high-rise buildings. In this context, SRC columns are utilized because of their high bearing capacity, high stiffness, and ductility. These columns, distinguished as a type of composite column, have significant advantages such as good shear strength, no local buckling of steel components, and proper fire resistance since the steel parts are encased within the concrete [1-5].

In recent years, numerous studies on composite columns have been carried out. For instance, the research done by An et al. [6], a numerical model was created in Abaqus to present a column containing an embedded steel tube section. The model was subsequently verified by experiment to evaluate the flexural performance of the column. Distinct regions of concrete confinement were also considered in modeling in order to improve accuracy. The steel tube sustained no local buckling, and developed its plastic strength. According to plastic stress distribution method, a relation was proposed to estimate flexural capacity of SRC sections. Ellobody et al. [7, 8] introduced different confinement regions into the numerical model using Abaqus by examining the SRC columns with H-shaped

*Corresponding Author Institutional Email: *m-naghi@nit.ac.ir* (M. Naghipour)

Please cite this article as: M. Ahmadi, M. Naghipour, M. Nematzadeh, Numerical and Experimental Investigations on the Behavior of SRC Columns Subjected to Eccentric Loading, International Journal of Engineering (IJE), IJE TRANSACTIONS B: Applications Vol. 33, No. 8, (August 2020) 1529-1543

steel section under the combination of axial load and bending moment. They demonstrated that incorporating such regions into numerical modeling leads to a good agreement between the experimental and numerical results. In their research, fixed rectangular zones were used to partition the confinement regions in numerical modeling. Lin and Chen [9] proposed a numerical model to estimate the bearing capacity of SRC columns with different I-, H-, cross-, and T-shaped sections and different lateral tie spacing. In this numerical model, two types of behavior were presented for the longitudinal reinforcement and the steel section. The method given by Mander et al. [10] was practiced to consider the effects of concrete confinement. The findings denoted that taking the impact of confinement into account would increase the load-bearing capacity of the column. Wang et al. [11] performed a numerical study via Abaqus on several SRC columns subjected to eccentric loading and verified the numerical model with the experimental results. A parametric study was then carried out to examine the factors counting the concrete strength, steel yield stress, and eccentricity of loading on the strength and behavior of these columns. The results were also compared with some regulations. The results indicated that the plastic stress distribution method, adopted by the codes, may not always be conservative. Han and An [12] studied the behavior of SRC columns with steel tube sections, emphasizing that the use of these sections in the construction of high-rise structures and bridges is perceived to be growing. They prepared a numerical model by Abaqus to study the behavior of the columns. The nonlinear behavior of the materials, as well as the interaction between the steel tube and the concrete, either the external part or the core concrete, were considered. Different regions of concrete confinement were defined in the software modeling so that three zones of highly-confined core concrete, moderately-confined steel tube exterior, and the unconfined concrete cover with distinct stress-strain behavior were included in the modeling. It was affirmed that the results obtained from the simulation were in good accord with the predicted values as a consequence of considering different regions of concrete confinement. A relationship was therefore recommended to estimate the bearing capacity of the column. Zhou et al. [13] conducted multiple numerical and experimental studies on the behavior of H-shaped steel sections of SRC columns subjected to eccentric compression. No less than eight specimens were tested to screen the effects of load eccentricity, width-to-thickness ratio of the steel section, and the shear studs. The results were put together with those of Abaqus modeling. In this regard, they exercised Li et al.'s [14] relationships to model the behavior of concrete in the software, considering the two confined and unconfined concrete regions. The outcomes exhibited a proper consistency between the measured values with those of the software predictions. Moreover, several analytical and experimental investigations have been previously conducted on the SRC columns with H- or cross-shaped sections, including Mirza and Skrabek [15], Mirza et al. [16], El-Tawil and Deierlein [17], Munoz and Hsu [18], Bogdan et al. [19], Lelkes and Gramblicka [20], among others.

According to literature so far, the behavior of SRC columns can be credited to several factors, one of which has been acknowledged to be the ductility. On this account, a number of SRC columns with different steel sections and load eccentricities were experimented in the present study. After the necessary tests and measurements, the specimens were modeled and validated through the Abaqus software, so that the proposed model could be used for further investigation. Afterward, a parametric study was accomplished on a total of 30 SRC columns, geometrical and material variables, including the section steel percentage, concrete compressive strength, lateral tie spacing, and the geometrical shape of steel section were discussed. Finally, some relationships were established to estimate the ductility index of columns with different steel sections. The required relationships for plotting the axial load-bending moment interaction curves of these columns were also derived based on the plastic stress distribution method. Furthermore, specific curves were presented, from which an inventory of SRC columns could be conveniently designed once these curves were generalized.

2. SUMMARY OF EXPERIMENTAL INVESTIGATION

Ahmadi et al. [21] performed an experimental and numerical study on six specimens of SRC columns. Figure 1 provides details of the experimental specimens. As it is inferred, the span length of all specimens is $460mm$, and the section dimensions are $150\times150mm$.The longitudinal reinforcement bars comprise $4\Phi10$, the ties are made of $\Phi8@60mm$, and the concrete cover thickness over the ties is $15mm$. As shown in this figure, grooved steel plates were used at both column ends so as to represent the hinged supports and apply different values of eccentricity ratios (e/B), including 0.4, 0.55 and 0.7. These experiments were performed in the structural laboratory of Noshirvani University of Babol, and thus, due to the limited load-bearing capacity of the testing device, such values were selected so that all specimens could be experimented.

It should be noted that the eccentricity, e, was measured relative to the plastic centroid of the section. Two types of steel sections were encased in the concrete, which makes up a total of 6 specimens given

the three eccentricity ratios. Table 1 summarizes the specimen specifications along with their notations.

A linear variable differential transformer (LVDT) was installed at midspan, perpendicular to column direction, to record the lateral displacement. Two other LVDTs were also instrumented on the sides of the specimen to measure the axial deformations. Mix design in preparing the concrete cylinders conformed to ACI211.1-91[22] with average 28-day compressive strength of 30MPa. Steel properties were determined according to the tension test recommended by ASTM E8/E8M[23], the results of which are reported in Table 2.

All laboratory specimens, with hinged boundary conditions at both ends, were subjected to eccentric compression. The overall schematic of the testing system, along with its boundary element, is given in Figure 2.

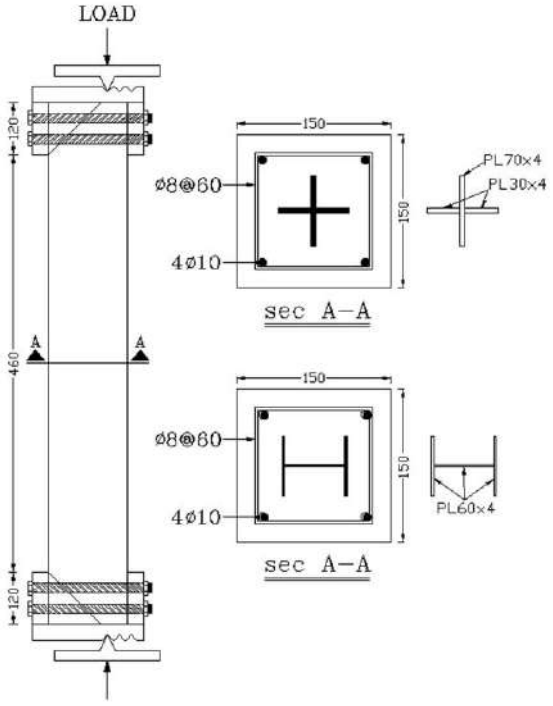

Figure 1. Overall dimensions of column with H- and cross-shaped sections

TABLE 1. Specifications of the tested SRC columns

Notation	Steel Core	Column Dimensions (mm)	Eccentricity (mm)
SRC-X60	Cross	150×150×700	60
SRC-X82	Cross	150×150×700	82.5
SRC-X105	Cross	150×150×700	105
SRC-H60	H	150×150×700	60
SRC-H82	H	150×150×700	82.5
SRC-H105	H	150×150×700	105

TABLE 2. Results of tensile test on plate and reinforcements

	Yield Stress (MPa)	Ultimate Stress (MPa)
Steel Plate	243	367
Longitudinal Rebar	302	430
Transvers Rebar	297	388

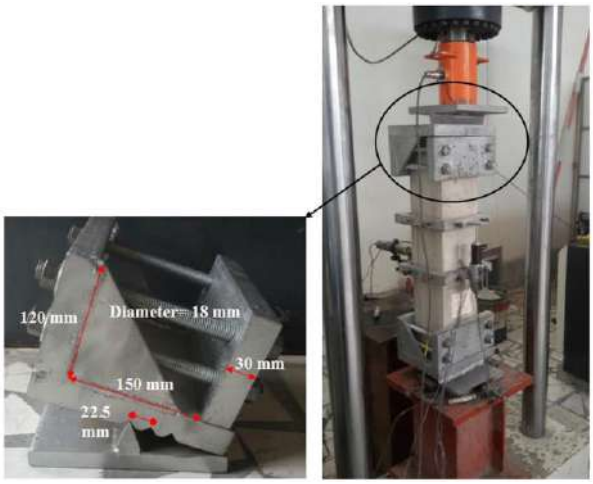

(a) Supporting plate to apply the eccentric load

(b) Overall testing system

Figure 2. Test setup with measuring arrangements

The results obtained for the SRC column with cross-shaped steel core in terms of three cases of eccentricity are sketched and compared in the form of axial load-axial displacement and axial load-midspan lateral displacement curves in Figure 3. In specimens SRC-X60 and SRC-X82, the ultimate yield and failure modes respectively happen to be cracking on the tensile face and concrete crushing on the compressive face at midspan. According to the figure, the load ramps up with a steep slope towards the peak load, while in specimen SRC-X105, there is an abrupt decline in the bearing capacity following the peak load, and thus the cracking and crushing occurs in the vicinity of the boundary element.

In like manner, the results of SRC columns with H-shaped steel core are illustrated in Figure 4. In specimens SRC-H60 and SRC-H82, the ultimate yield and failure modes, respectively, take place as cracking on the tensile face and crushing on the compressive face adjacent to the boundary element. In this sense, the post-peak capacity drops with a relatively sharp slope, whereas in specimen SRC-H105, yielding and failure occur at midspan. As lateral displacement gradually increases at midspan, the tensile reinforcement exceeds the yield limit strain.

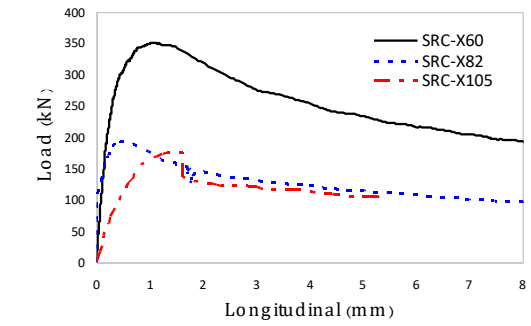

(a)

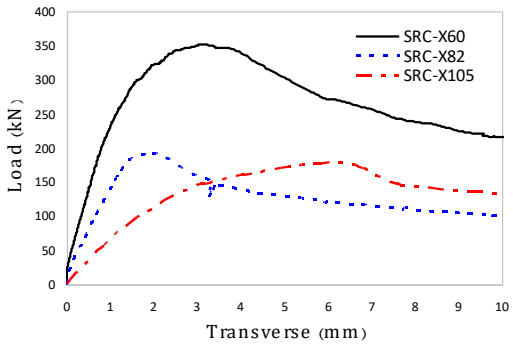

(b)

Figure 3. Laboratory specimens with cross-shaped steel core: (a)Axial load-longitudinal displacement curve; (b)Axial load-midspan lateral displacement curve

Figure 5 shows the failure mode in the ultimate state of all specimens.

3. FINITE ELEMENT ANALYSIS MODEL

The FE model developed in Abaqus, the steel section and the concrete were modeled using the S4R shell and C3D8R elements, respectively [24-25]. The three-

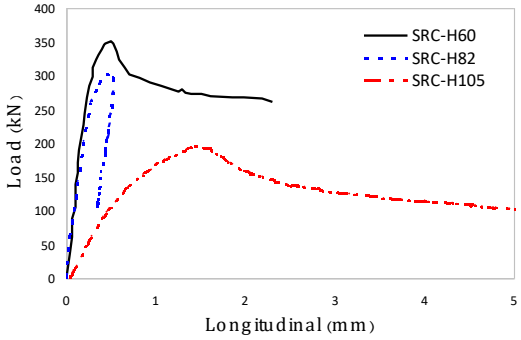

(a)

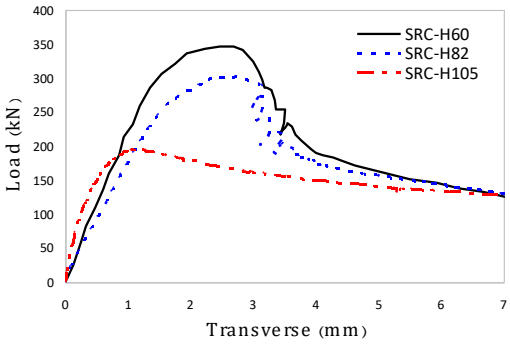

(b)

Figure 4. Laboratory specimens with H steel core: (a)Axial load-longitudinal displacement curve; (b)Axial load-midspan lateral displacement curve

dimensional two-noded T3D2 element was used for the simulation of longitudinal and lateral reinforcement bars. The steel components were embedded inside the concrete blocks to ensure an adequate bond between the steel sections, the concrete, and the reinforcements. Furthermore, the top and bottom of the specimen were supported by two rigid steel plates, to which R3D4 elements were selected and tied to the concrete surface in the defining step. The load was exerted to the top of the column with desired eccentricities in the displacement-control mode. The sketch of the numerical model is presented in Figure 6. In this model, the damaged plasticity model was implemented for the concrete material, which accounts for two fundamental principles of tensile cracking and compressive crushing during the failure mechanism. Besides $E = 4730\sqrt{f_c'}$ and $\nu = 0.2$ were postulated for concrete after the ACI318-11 [26], in which f_c' is the cylinder compressive strength in *MPa*. Also, the elastic-plastic model was adopted for steel material with $E = 200\ GPa$ and $\nu = 0.3$.

Figure 5. Ultimate yielding mode and failure of experimental specimens

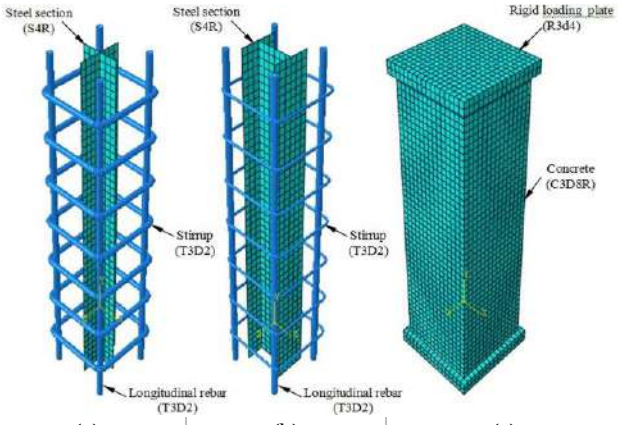

Figure 6. Finite element model of laboratory specimen: (a) cross-shaped section; (b) H-shaped section; (c) Overall configuration of the numerical model

The stress-strain behavior of the compression concrete was defined in the numerical model using the relations provided by Barr and Lee [27]. This model consists of a continuous function plus the sum of two exponential functions as given by Relation (1):

$$f_c(x) = C_1\left(e^{-C_2 x} - e^{-C_3 x}\right) \tag{1}$$

in which C_1, C_2, and C_3 are constants regulating the shape of the stress-strain curve and are calculated as follows:

$$x_{\max} = \frac{1}{C_3 - C_2}\ln\left(\frac{C_3}{C_2}\right) \tag{2}$$

$$C_1 = \frac{f_{\max}}{\left(\alpha^{\frac{1}{1-\alpha}} - \alpha^{\frac{\alpha}{1-\alpha}}\right)} \tag{3}$$

$$C_2 = \frac{\ln \alpha}{x_{\max}(\alpha - 1)} \tag{4}$$

where $f_{\max}$ is the uniaxial compressive strength, $x_{\max}$ the strain at ultimate load, and $\alpha = \frac{C_3}{C_2}$, which can be determined by Relation (5):

$$\begin{cases} \left(\frac{x_{\max}}{x_{0.2f_{\max}}}\right) \le 0.000572 \Rightarrow \alpha = 10^4 \\ 0.000572 < \left(\frac{x_{\max}}{x_{0.2f_{\max}}}\right) \le 0.026 \Rightarrow \alpha = 1.67\left(\frac{x_{\max}}{x_{0.2f_{\max}}}\right)^{-1.17} \\ 0.026 < \left(\frac{x_{\max}}{x_{0.2f_{\max}}}\right) \le 0.262 \Rightarrow \alpha = \sum_{i=0}^{6} \chi_i \left(\frac{x_{\max}}{x_{0.2f_{\max}}}\right)^i \\ \left(\frac{x_{\max}}{x_{0.2f_{\max}}}\right) \ge 0.262 \Rightarrow \alpha = 1.0001 \end{cases} \tag{5}$$

The above relationships, $x_{0.2f_{\max}}$ is the strain corresponding to 20% of the uniaxial compressive stress in the post-peak phase. The stress-strain relationships recommended by An et al. [6] is presented in Relation (6) to model the behavior of concrete in tension:

$$\frac{\sigma_t}{\sigma_{t0}} = \frac{\varepsilon_t/\varepsilon_{t0}}{0.31\sigma_{t0}^2\left[\left(\varepsilon_t/\varepsilon_{t0}\right) - 1\right]^{1.7} + \varepsilon_t/\varepsilon_{t0}} \tag{6}$$

where $\varepsilon_{t0} = \sigma_{t0}/E_C$, and the tensile cracking resistance σ_{t0} is estimated by $\sigma_{t0} = 1.4\left(f_c'/10\right)^{0.67}$ in which $E_C = 4730\sqrt{f_c'}$, and f_c' is the cylinder compressive strength is in *MPa*.

4. VERIFICATION OF FINITE ELEMENT MODEL

The numerical predictions were compared with those of the experiment to verify the proposed FE model. The comparison was made respecting the three columns of SRC-H105, SRC-X82, and SRC-X60 with specifications reported in Table 1; the results of which were then employed for verification of the numerical models.

4. 1. Axial Load-Axial Displacement Behavior The experimental results were compared with those obtained via FE modeling in terms of load-displacement behavior, as depicted in Figure 7. As for the three verified specimens, the load-axial displacement curves match the FE curves with a subtle difference at peak load, which is likely to be associated with a geometric and loading defect/imperfection generated through the experiment.

4. 2. Axial Capacity The ultimate axial loads were obtained from the numerical model and compared with those of the experiment. Table 3 compares the peak load of the laboratory specimens with the capacity derived from the FE analysis. The reported mean and standard deviation values highlight a favorable efficiency of the FE model in predicting the desired measures.

4. 3. Failure Modes The main yielding mode in the experimental specimens was the concrete crushing. Surface cracks in concrete are always an indication of reaching the yield state. The failure sequence of the tested columns started with cracking in the middle of the column as well as the top and bottom regions close to supports. Then, as the load increased, cracks became wider and the concrete cover spalling happened. Finally, concrete crushing began, followed by the yielding of the longitudinal rebars. The yielding modes of the SRC

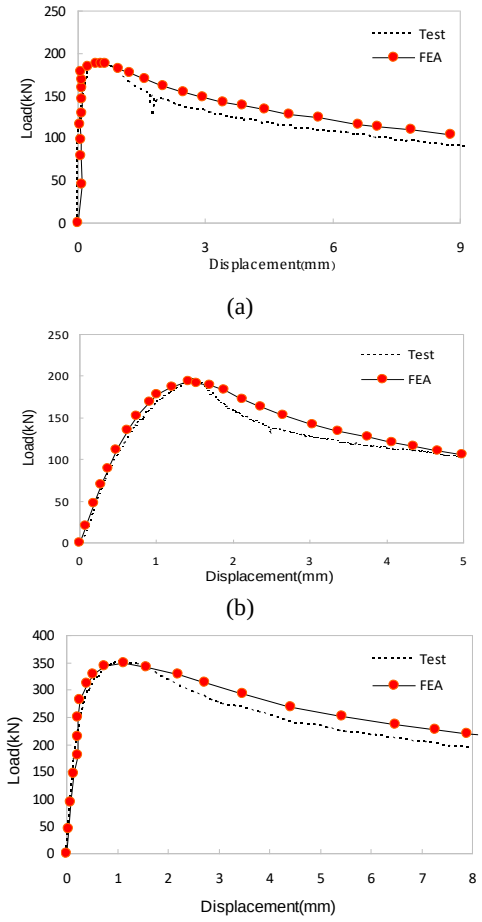

Figure 7. Comparison of load-longitudinal displacement: (a) SRC-X82; (b) SRC-H105; (c) SRC-X60.

TABLE 3. Comparison of the numerical and experimental results

Sample codes	Peak load(kN)		$\frac{P_{num}}{P_{exp}}$
	P_{exp}	P_{num}	
SRC-H105	196.1	193.2	0.985
SRC-X82	193.2	188.3	0.975
SRC-X60	351.1	348.6	0.993
Mean			0.984
Standard deviation			0.009

columns obtained from the finite element analysis were compared with those of the experimental specimens. A comparison between the yielding modes of experimental and numerical columns is demonstrated in Figure 8.

5. ANALYSIS AND DISCUSSIONS

Once validity of the numerical model was established, ensuring the behavioral model of materials, the correct interaction between different element parts, as well as the applied boundary conditions and loading procedure, a parametric study was embarked on by varying the geometric and material properties of the model so as to better understand the behavior of SRC columns. In this setting, the influence of several factors, embracing steel percentage, concrete compressive strength, lateral tie

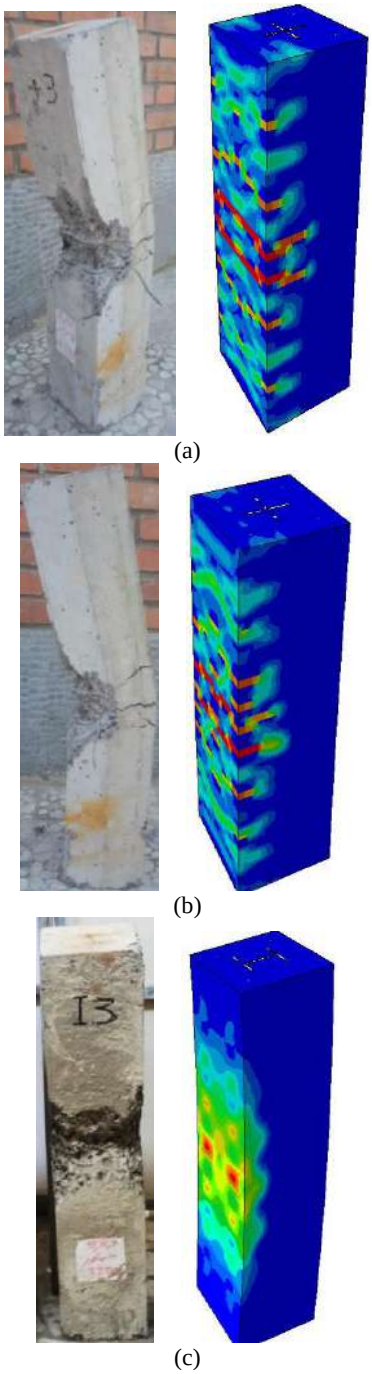

Figure 8. Comparison of yielding modes and failure of experimental and numerical specimens: (a) SRC-X60 column; (b) SRC-X82 column; (c) SRC-H105 column

spacing, and geometrical shape of steel sections were tackled. Thus, a total of 30 SRC columns were analyzed (as shown in Figure 9), the results of which are given in Tables 4, 5, and 6 accompanied by the specimens' specifications. In these tables, L denotes the specimen length, D the column side, S the lateral tie spacing, A_s the steel percentage, and f_c the standard cylinder compressive strength. In a general sense, both the high percentage of section steel and the low tie spacing enhance the ductility of the column. As a criterion to examine the ductility of SRC columns in this paper, the ductility index (μ) is defined as the ratio of displacement at a point corresponding to 85% of the peak load on the descending branch of the curve (Δu) to the yield point displacement (Δ_y) [28]:

$$\mu = \frac{\Delta_u}{\Delta_y} = f(A_s, f_c, \frac{S}{D}, steel\ core\ shape) \quad (7)$$

It is important to note that in the modeling settled by the Abaqus software, the possible slip between the steel section and the concrete surface, as well as the geometrical defects generated during the experiment, are not taken into account. Moreover, this research does not pursue the code recommendations at selecting the material properties and section dimensions, which can be regarded as a drawback to this study.

As reported in Table 4, the ductility index increases with an increase in the steel percentage of the section. In this table, three values of 1, 3, and 5% were assumed for the steel percentage. The ductility index marks the highest measure for the box-shaped section and the lowest value for the cross-shaped. It is discerned, based on the tabulated results, that the ductility index is escalated by 31.7% as the steel percentage of the H-shaped section increases from 1 to 5%. Such a gain is as much as 14.7 and 25% for the cross- and box-shaped sections, respectively.

The obtained results match the eccentricity ratio of 0.1, in which case the behavior of the column is closer to that of the steel, and thus, μ increases by increasing the steel percents (As).

Figure 10 illustrates the load-axial displacement curve of various sections for different percentages of steel. It is recognized that the box-shaped column features a higher bearing capacity in the post-yield phase than the other sections. This argument is connected with the higher confinement of concrete inside the box-shaped steel section, which in turn increases the ductility index. In some measure, the fact holds for the H-shaped section, owing to the confinement of concrete between the flanges and the web.

Three values of 15, 30, and 60 *MPa* were adopted for concrete compressive strength in Table 5 so as to evaluate its impact on the ductility index. It turns out that the ductility index downscales with increasing compressive strength of concrete such that in H-shaped section, the ductility index reduced by 38.4% as the compressive strength surged from 15 to 60 *MPa*. The commensurate values for the cross- and box-shaped sections were 32.4 and 26.2%, respectively. The obtained results match the eccentricity ratio of 0.1, in which case, similar to the column under axial load, an increase in fc makes the column to have a more brittle response.

Figure 11 depicts the load-axial displacement curve of various sections for different values of concrete compressive strength. As can be seen, the ultimate axial

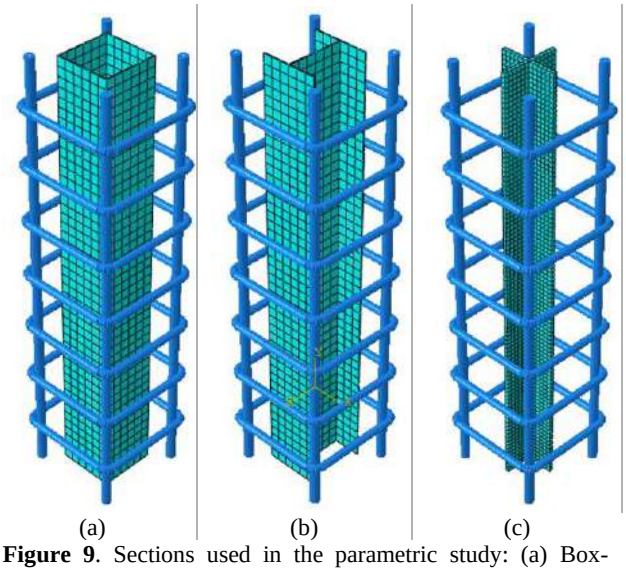

(a) (b) (c)

Figure 9. Sections used in the parametric study: (a) Box-shaped section; (b) H-shaped section; (c) Cross-shaped section removed

TABLE 4. Effect of steel percentage (As) on the column ductility index

Specimen	Steel Section (mm)	A_s (%)	Axial Capacity (kN)	Δ_y (mm)	Δ_u (mm)	μ
HN1	$3PL60\times1.25$	1	765.8	0.95	2.105	2.21
HN2	$3PL60\times3.75$	3	877.1	1	2.51	2.51
HN3	$3PL60\times6.25$	5	991.7	1.1	3.2	2.91
XN4	$2PL60\times1.91$	1	764.2	0.9	1.966	2.18
XN5	$2PL60\times5.92$	3	873.7	0.95	2.255	2.37
XN6	$2PL60\times10.25$	5	983.5	1	2.5	2.5
BN7	$60\times60\times0.95$	1	771.8	1	2.4	2.4
BN8	$60\times60\times2.95$	3	884.8	1	2.81	2.81
BN9	$60\times60\times5.12$	5	1004.3	1.25	3.75	3

* Column Dimensions (mm):150×150×460, L/D=3, S/D=0.4, f_c=30MPa, e/B=0.1

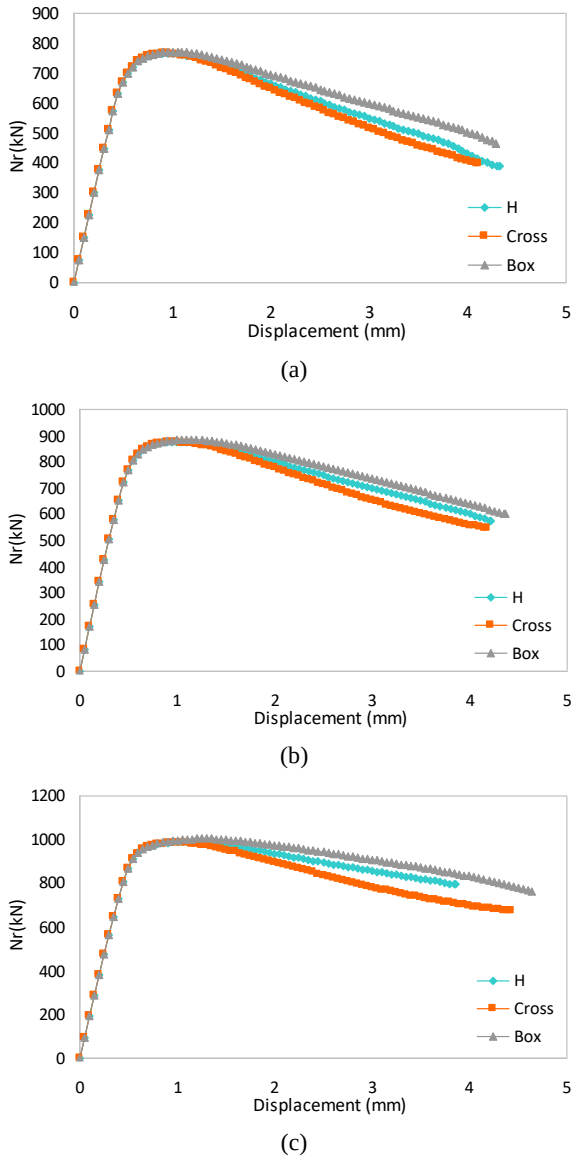

Figure 10. Comparison of load-axial displacement curves for column with various steel cores: (a) As=1%; (b) As=3%; (c) As=5%

TABLE 5. Effect of concrete compressive strength (fc) on the column ductility index

Specimen	A_s (%)	f_c (MPa)	Axial Capacity (kN)	Δ_y (mm)	Δ_u (mm)	μ
HL10	3	15	602.7	1.25	4.22	3.36
HN11	3	30	877.1	1	2.51	2.51
HH12	3	60	1448.8	0.85	1.763	2.07
XL13	3	15	597.7	1.2	3.45	2.87
XN14	3	30	873.7	0.95	2.255	2.37
XH15	3	60	1449.4	0.85	1.65	1.94
BL16	3	15	617.5	1.5	4.47	2.98
BN17	3	30	884.8	1	2.81	2.81
BH18	3	60	1449.3	0.85	1.863	2.2

* Column Dimensions (mm):150×150×460, L/D=3, S/D=0.4, e/B=0.1

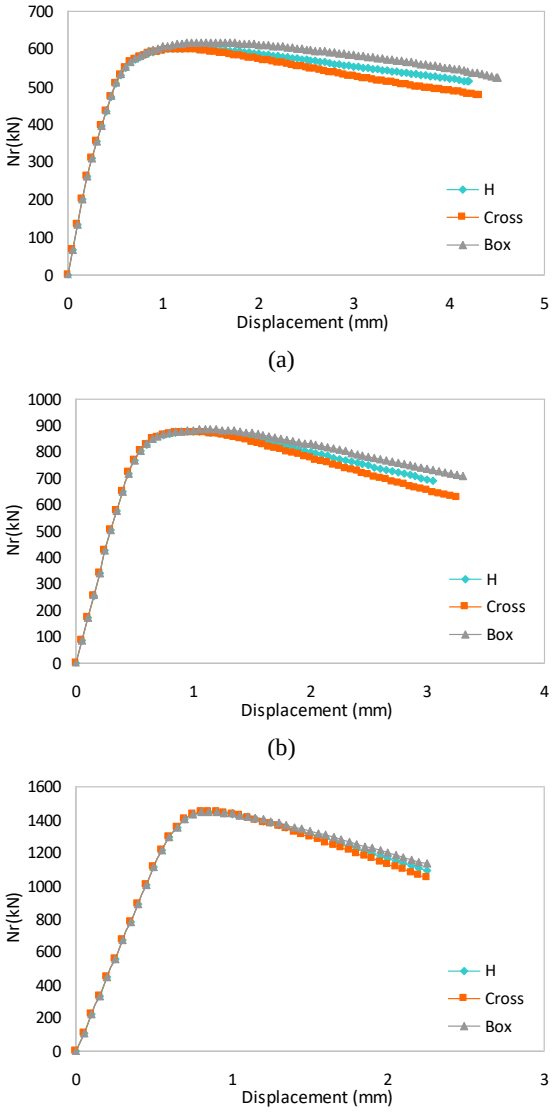

Figure 11. Comparison of load-axial displacement curves for column with various steel cores: (a) fc=15 MPa; (b) fc=30 MPa; (c) fc=60 MPa

load and the stiffness of the column were affected by concrete strength such that the curve captures a steep slope in the ascending portion as regards to the higher strength concrete and due to high elastic modulus. The descending portion of the curve takes even a steeper slope because of the brittleness of the section, which

reduces its ductility index compared to sections with lower compressive strengths.

Table 6 outlines the effect of tie spacing on the column ductility index, for which four values of spacing ratios 0.1, 0.2, 0.4, and 0.6 have been considered. It is well comprehended that the main objective of using ties in columns is to provide concrete confinement, to trigger suitable support for longitudinal bars so as to prevent their buckling, and to improve the shear strength of the section. Accordingly, the tie spacing is an influential factor on the ultimate capacity and the behavior of columns. Table 6 demonstrates that a reduction in the tie spacing increases the ductility index, characterizing the highest value for the box-shaped section and the lowest measure for the cross-shaped. The results also signify that with increasing tie spacing, the bearing capacity and the ductility index drastically fall. In this case, by varying spacing ratio (S/D) from 0.1 to 0.6 for the H-shaped section, the ductility index drops by 54.6%. The equivalent values are 56 and 51.4% for the cross- and box-shaped sections.

Figure 12 portrays the load-axial displacement curves concerning the different values of S/D. As can be seen, the ascending branch of the curves is identical for all columns and the discrepancy between different sections, influenced by the tie spacing, is observed in the post-yield phase so that there is a post-yield hardening area at spacing ratios of 0.1 and 0.2. This is mainly attributable to the evolution of high confinement and the reinforcement buckling prevention as per the lateral ties. Such impact subsides as the spacing increases, followed by a decline in the curve slope and subsequently a decrease in the bearing capacity and the ductility index.

Figure 12, for S/D= 0.1 and 0.2, due to the high confinement induced by the ties and the inhibition of the buckling of longitudinal bars, there is a post-yield hardening zone, and thus, the strength is significantly increased. Meanwhile, in the plotted curves, the criterion for calculating the ductility index, according to literature [28], the displacement is at 85% of the peak load in the descending branch, and hence, the end point of the curve does not indicate the failure point, and simply the curve continues based on the software output.

TABLE 6. Effect of tie spacing (S/D) on the column ductility index

Specimen	A_s (%)	$\frac{S}{D}$	Axial Capacity (kN)	Δ_y (mm)	Δ_u (mm)	μ
HN19	3	0.1	1163.45	0.7	3.69	5.27
HN20	3	0.2	1014.86	0.75	3.09	4.12
HN21	3	0.4	877.1	1	2.51	2.51
HN22	3	0.6	845.6	0.9	2.15	2.39
XN23	3	0.1	1160.4	0.7	3.55	5.07
XN24	3	0.2	1015.2	0.75	2.86	3.81
XN25	3	0.4	873.7	0.95	2.255	2.37
XN26	3	0.6	841.1	0.85	1.901	2.23
BN27	3	0.1	1176.1	0.7	3.862	5.52
BN28	3	0.2	1025.4	0.75	3.3	4.4
BN29	3	0.4	884.8	1	2.81	2.81
BN30	3	0.6	848.4	0.9	2.411	2.68

* Column Dimensions (mm):150×150×460, L/D=3, f_c=30MPa, e/B=0.1

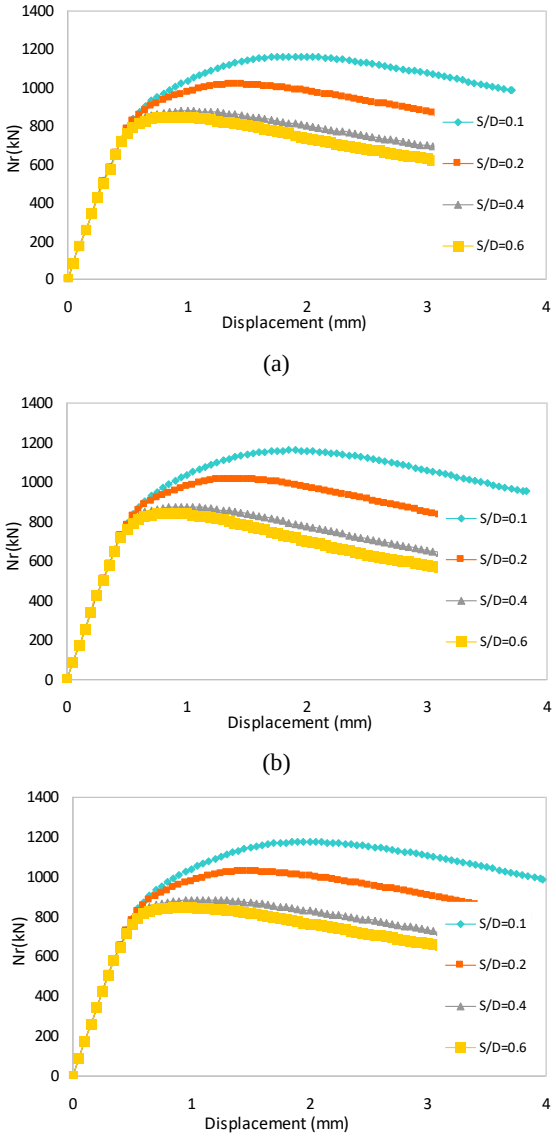

Figure 12. Load-axial displacement curves for column with various steel cores wrt different S/D ratios: (a) H-shaped section; (b) Cross-shaped section; (c) Box-shaped section

Based on the factors affecting the ductility index and the obtained results, appropriate relationships can be established for the ductility index of the H-, cross-, and box-shaped columns as follows:

$$\mu_H = \left[60.203 + 1308.34A_s - 2.931 f_c\right] \times \left(\frac{S}{D}\right)^2 + 125(A_s)^2 + 0.00726(f_c)^2 - 16.611A_s.f_c \times \left(\frac{S}{D}\right) \quad (8)$$

$$\mu_{Cross} = \left[55.047 + 1578.125A_s - 2.813 f_c\right] \times \left(\frac{S}{D}\right)^2 - 75(A_s)^2 + 0.00751(f_c)^2 - 20A_s.f_c \times \left(\frac{S}{D}\right) \quad (9)$$

$$\mu_{Box} = \left[69.693 + 1401.04A_s - 3.363 f_c\right] \times \left(\frac{S}{D}\right)^2 - 275(A_s)^2 + 0.00789(f_c)^2 - 16.056A_s.f_c \times \left(\frac{S}{D}\right) \quad (10)$$

In the above relations, A_s is the ratio of section steel area, f_c the cylinder compressive strength in *MPa*, S the tie spacing, and D is the sectional side in *mm*. It should be noted that the above relations are limited to when $\frac{e}{B}=0.1$, $f_c \geq 30MPa$ and $\frac{S}{D} \leq 0.4$. Three steel percentages of 1, 3, and 5% were assumed in plotting the axial load-bending moment interaction curves.

A total of six eccentricities, i.e., e/B= 0, 0.1, 0.2, 0.4, 0.8, and 2 were chosen to develop each interaction curve in Abaqus. The generated curves were then compared with the concrete section without the steel core. The dimensions selected for plotting the interaction curves are similar to those of laboratory specimens, yet differences in types and percentages of steel core. Figure 13 sketches the axial load-bending moment interaction curves for the cross-, H-, and box-shaped sections with three steel core percentage ratios of $A_S = 1$, 3, and 5%. The mentioned curves have been compared with that of the concrete section without the steel core for different values of steel core percentages.

It is proved that the interaction curves converge as for the cross-shaped column specifically at the balance point for 1 and 3% of steel. However, with increasing steel percentage to 5%, contours scatter especially at the balance point. Nevertheless, in the H-shaped column, the curves are close to each other in the compression-dominated region for the 3 and 5% of steel, though after the balance point, in the tension-dominated region, the curve related to 3% of steel approaches that of the 1% of steel. On the contrary, contours maintain relatively identical distances throughout the curve in the box-shaped section for different steel percentages.

As shown in the figure, the performance of H-, cross-, and box-shaped columns with A_s=1% is almost identical. As the steel percentage rises to A_s=3%,

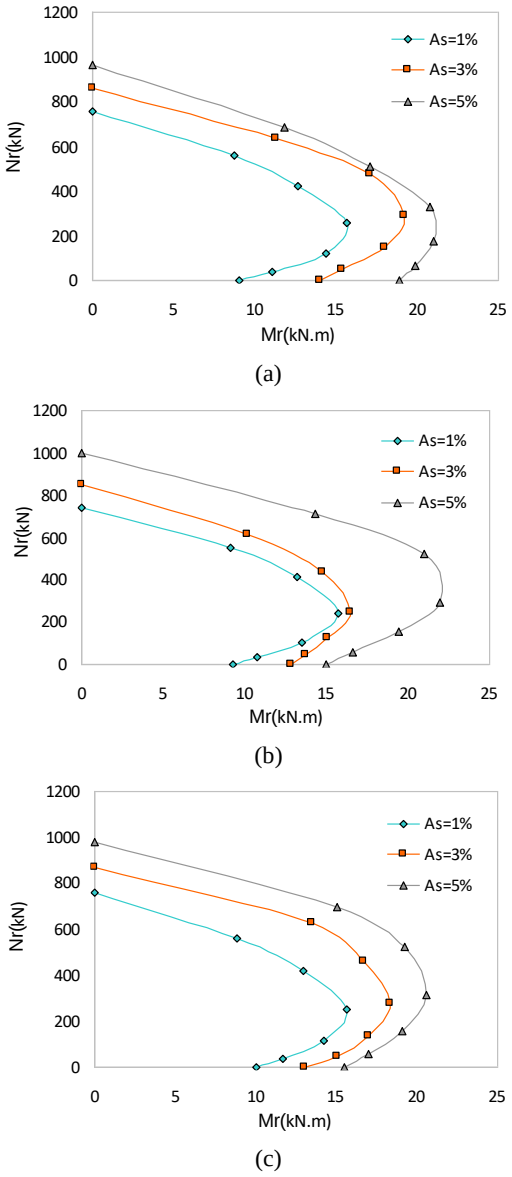

(a)

(b)

(c)

Figure 13. Interaction curves for column with different steel sections: (a) H-shaped section; (b) Cross-shaped section; (c) Box-shaped section

columns with H- and box-shaped sections demonstrate similar performances, whose curves possess more extensive areas as to the cross-shaped section. However, there is a shift in the trend as the steel percentage reaches A_s=5%. Interestingly, Figure 14 reveals that the box- and cross-shaped sections are comparable in performance in the compression- and tension-dominated regions. Yet, they perform unlike at the balance region, wherein the cross-shaped section marks a larger balance point. Furthermore, the H-shaped section sustains lower bearing capacity in the compression-dominated region and higher capacity in the tension-dominated zone when compared to the other two sections.

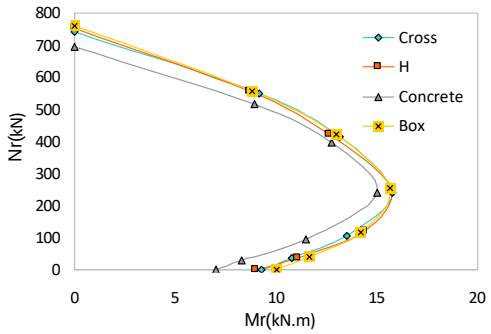

(a)

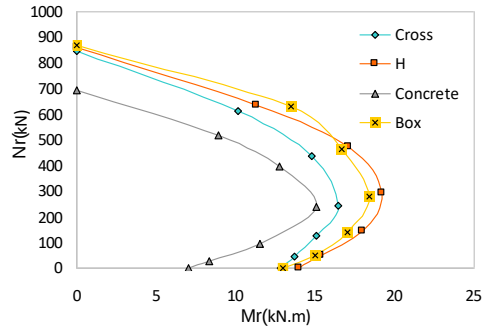

(b)

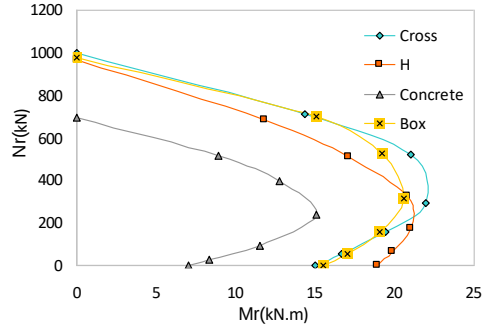

(c)

Figure 14. Comparison of interaction curves for column with different steel sections: (a) As=1%; (b) As=3%; (c) As=5%

In order to develop the interaction curves according to EC4 recommendations and compare them with numerical results, a specimen with an H-shaped section with dimensions and steel percentage similar to that of the laboratory sample was designated. The interaction curve in this code has been simplified to a polygon curve, so that in this study, the points required for plotting the interaction curves were computed based on the plastic stress distribution equations. The nominal compressive strength can be expressed by Relation (11):

$$P_{n0} = F_y.A_s + c_2.f_c(A_c + A_{sr}\frac{E_s}{E_c}) \quad (11)$$

Based on the plastic stress distribution concept, the flexural capacity, M_{max}, related to the balance point, which is larger than the pure flexure, can be calculated as the Relation (12) for the SRC with an H-shaped section around the strong axis and the reinforcements laid at both sides. In this case, the column is simultaneously subjected to bending and axial compression, and the plastic neutral axis lies at the center of the cross-section.

$$M_{max} = \frac{1}{8}c_2.f_c.A_c.h + F_y.A_s.d.\left[\frac{4A_f + A_w}{8A_f + 4A_w}\right] + \frac{1}{2}A_{sr}.F_{ysr}.(h-2d') \quad (12)$$

In the above relation, $A_c = b.h - A_s - A_{sr}$ is the net concrete area, $A_f = b_f \times t_f$ the H-shaped section flange area, $A_w = d \times t_w$ the web area, d the section height, and d′ is the distance from the centerline of the rebars to the nearest outer face of the column, A_{sr} and F_{ysr} are the area of reinforcements and their yield stress, respectively. The flexural capacity of the section can be calculated according to the plastic stress distribution method based on Figure 15. As it is observed, in this case, the plastic neutral axis is located above the center of the cross-section. Accordingly, the nominal flexural strength of the SRC column with an H-shaped section around the strong axis and with reinforcement placed at both sides is calculated as the following relations:

$$if \quad h_n = \frac{A_c}{2(b-t_w) + \frac{4F_y.t_w}{c_2.f_c}} \le \frac{h_w}{2} \quad \Rightarrow$$

$$M = \frac{1}{4}c_2.f_c\left[A_c - 2h_n(t_w - b)\right](\frac{h}{2} - h_n) + \frac{1}{2}A_{sr}.F_{ysr}(h-2d') + F_y.A_f(d-2t_f) + F_y.A_w(\frac{d}{4} - t_f) + F_y.t_w(h_n^2 + t_f^2) \quad (13)$$

$$if \quad \frac{h_w}{2} < h_n = \frac{c_2.f_c.b.h + 2F_y.b_f.d - 2F_y.A_s}{4F_y.b_f + 2c_2.f_c.b} \le \frac{d}{2} \quad \Rightarrow$$

$$M = \frac{1}{2}c_2.f_c.b.(\frac{h}{2} - h_n)^2 + \frac{1}{2}A_{sr}.F_{ysr}(h-2d') + F_y.A_f(2h_n + d) + F_y.b_f(h_n - \frac{d}{2})^2 + F_y.A_w(\frac{d}{2} - h_n) \quad (14)$$

$$if \quad h_n = \left[\frac{h}{2} - \frac{A_s.F_y}{c_2.f_c.b}\right] > \frac{d}{2} \quad \Rightarrow$$

$$M = \frac{1}{2}c_2.f_c.b.(\frac{h}{2} - h_n)^2 + A_s.F_y.h_n + \frac{1}{2}A_{sr}.F_{ysr}(h-2d') \quad (15)$$

where h_w is the net height of the H-shaped section.

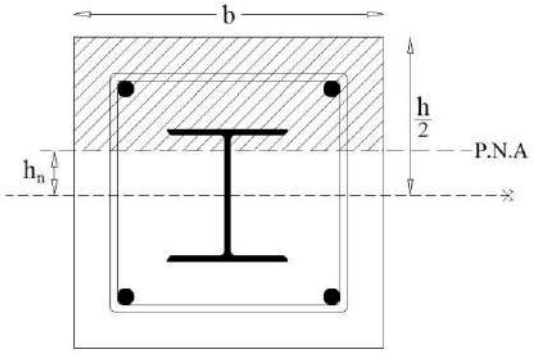

Figure 15. Column section for calculating the flexural capacity

Based on the calculations performed using the method stated in the code, and with the aid of the above relationships, as well as considering the numerical modeling of the experimental specimen, it is confirmed that the relations derived from the plastic stress distribution method are in favorably good agreement with the numerical model. The only conservative exception is witnessed at the axial compression and part of the compression-dominated region, which is shown in Figure 16.

Figures 17 and 18 illustrate the normalized interaction curves of the column with different section steel percentages and longitudinal reinforcement. In these curves, $\rho_{sr}=\frac{A_{sr}}{b.h}$ is the percentage of longitudinal reinforcement, $\rho_s=\frac{A_s}{b.h}$ the section steel percentage, N_{ro} the pure axial capacity, M_{ro} the pure flexural capacity, and $\gamma=\frac{h-2d'}{h}$. It is noted that these curves reflect the reciprocal influence of the rectangular and the H-shaped sections around the strong axis, with rebars distributed

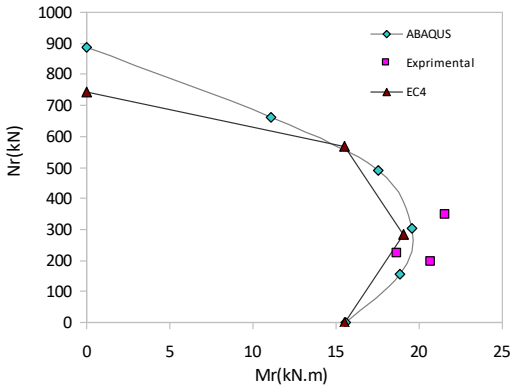

Figure 16. Comparison of the interaction curves for the column with H-shaped section and steel percentage of $A_s=3.2\%$

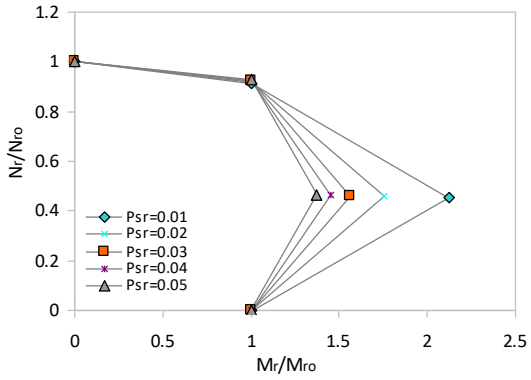

(a)

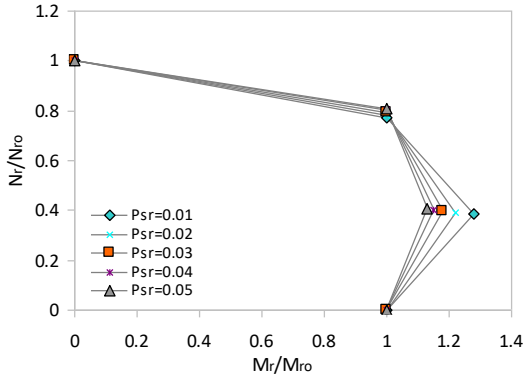

(b)

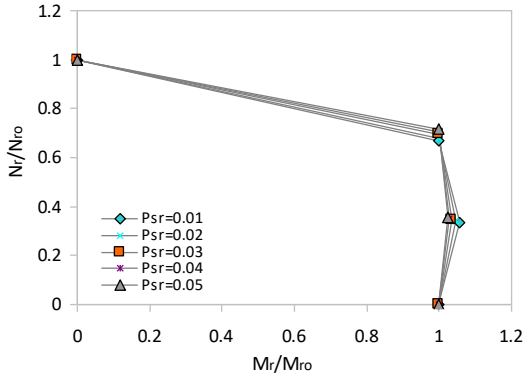

(c)

Figure 17. Normalized interaction curves for the H-shaped column in terms of ultimate strength for $\gamma=0.6$: (a) $\rho_s=0.01$; (b) $\rho_s=0.03$; (c) $\rho_s=0.05$

at both sides of the section. In Figure 17, the curves have been plotted in terms of the ultimate capacity $\frac{N_r}{N_{ro}}$ and $\frac{M_r}{M_{ro}}$. As shown in this figure, with increasing steel percentage, the maximum moment corresponding to the balance point approximately approaches the flexural capacity of the cross-section, and thus the curves overlie

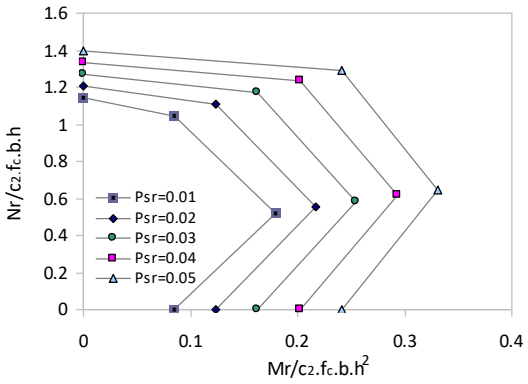

(a)

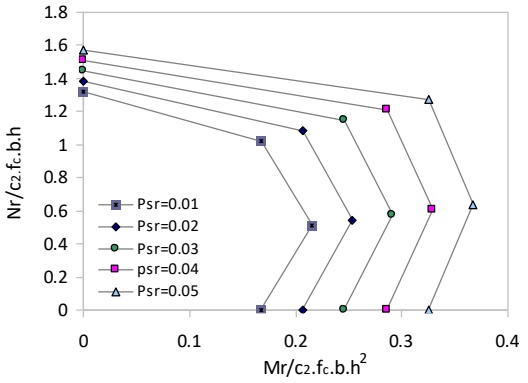

(b)

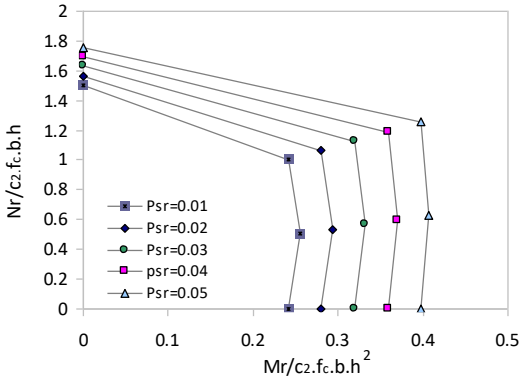

(c)

Figure 18. Normalized interaction curves for the H-shaped column in terms of concrete strength for $\gamma = 0.6$: (a) $\rho_s = 0.01$; (b) $\rho_s = 0.03$; (c) $\rho_s = 0.05$

for different percentages of longitudinal reinforcement. This specifies that as the steel core becomes stronger, the impact of the longitudinal reinforcement on the flexural capacity of the cross-section is mitigated, which is not the case for the lower percentages of section steel. In Figure 18, the normalized curves have been developed in terms of concrete strength $\frac{N_r}{c_2 . f_c . b.h}$ and $\frac{M_r}{c_2 . f_c . b.h^2}$. In this figure, as the steel percentage increases, the curves take a bi-linear form, and the balance point moment approximates the pure flexural capacity. By generalizing such curves for different values of γ and rebars positioned at four sides of the column section, more inclusive curves can be obtained for the design purpose of these columns.

6. CONCLUSION

The present study aimed to investigate the behavior of SRC columns subjected to the combination of axial load and bending moment. The conclusionss were drawn as follows:

1. As the steel percentage of the cross-section increases, the ductility index surges such that a rise in the steel percentage from 1 to 3% and from 3 to 5%, respectively, escalate the ductility index by 13.6 and 16%. The corresponding values are 8.7 and 5.5% for the cross-shaped section, and 17.1 and 6.8% for the box-shaped section.
2. With increasing concrete compressive strength, the ductility index decreases so that in columns with H-shaped sections, an escalation in the compressive strength from 15 to 60 *MPa* reduces the ductility index by 38.4%. Such a reduction is 32.4% for the cross-shaped and 26.2% for the box section.
3. As the lateral tie spacing increases, the bearing capacity and the ductility index sharply dropped, in such a way that by varying the spacing ratio from 0.1 to 0.6 for the H-shaped section, the ductility index slumped by 54.6%. The equivalent values are 56 and 51.4% for the cross-shaped and box-shaped sections.
4. The performance of columns with cross-, H-, and box-shaped steel cores is akin when $A_S = 1\%$, and the axial load-bending moment interaction curves roughly coincide.
5. As the steel percentage is raised to $A_S = 3\%$, the box- and H-shaped sections conform in performance. In this case, the axial load-bending moment interaction curves retain more extensive areas and higher distances, compared to that of the cross-shaped section, especially at the balance point.
6. Each of the studied sections features a distinct performance at $A_S = 5\%$ such that the box- and cross-shaped columns are analogous in the compression- and tension-dominated regions. Yet, they are different in the vicinity of the balance point in that the cross-shaped column captures a larger balance point. The column with an H-shaped steel core gains a lower bearing capacity in the compression-dominated region, though

its bearing capacity in the tension-dominated region excels, as compared to the other two sections.

7. It is perceptible in the normalized interaction curves, for column with the H-shaped section and $\rho_s = 0.01$, that the normalized moment $\frac{M_r}{M_{ro}}$, corresponding to the balance point of a section with $\rho_{sr} = 0.01$ is by 35.4% larger than that of a section with $\rho_{sr} = 0.05$.

8. It is noticeable in the normalized interaction curves, for column with the H-shaped section and $\rho_s = 0.03$, that the normalized moment $\frac{M_r}{M_{ro}}$, corresponding to the balance point of a section with $\rho_{sr} = 0.01$ is by 11.7% larger than that of a section with $\rho_{sr} = 0.05$.

9. It is visible in the normalized interaction curves, for column with the H-shaped section and $\rho_s = 0.05$, that the normalized moment $\frac{M_r}{M_{ro}}$, corresponding to the balance point of a section with $\rho_{sr} = 0.01$ is by 3.3% larger than that of a section with $\rho_{sr} = 0.05$.

10. The normalized interaction curves of short columns with the H-shaped section and $\gamma = 0.6$, provide a straightforward approach in designing the cited columns, where the generalization of such curves for various values of γ and the reinforcement placed at four sides of the column would contribute to even more developed curves.

7. ACKNOWLEDGEMENTS

The present study was conducted under the grant number BNUT925940001 at Babol Noshirvani University of Technology, which is hereby greatly appreciated.

8. REFERENCES

1. Shariati, M., Sulong, N.R., Shariati, A. and Kueh, A., "Comparative performance of channel and angle shear connectors in high strength concrete composites: An experimental study", ***Construction and Building Materials***, Vol. 120, (2016), 382-392 DOI: https://doi.org/10.1016/j.conbuildmat.2016.05.102.
2. Rahmani, Z., Naghipour, M. and Nematzadeh, M., "Flexural performance of high-strength prestressed concrete-encased concrete-filled steel tube sections", ***International Journal of Engineering***, Vol. 32, No. 9, (2019), 1238-1247 DOI: https://doi:10.5829/ije.2019.32.09c.03.
3. Nematzadeh, M., Naghipour, M., Jalali, J. and Salari, A., "Experimental study and calculation of confinement relationships for prestressed steel tube-confined compressed concrete stub columns", ***Journal of Civil Engineering and Management***, Vol. 23, No. 6, (2017), 699-711 DOI: https://doi.org/10.3846/13923730.2017.1281837.
4. ECS, "Eurocode 4: En 1994-1-2: 2004: Design of composite steel and concrete structures. Part1-1: General rules–structural rules for buildings, ECS Brussels, Belgium, (2004).
5. An, Y.-F., Han, L.-H. and Roeder, C., "Performance of concrete-encased cfst box stub columns under axial compression", ***Structures***, Vol. 3, (2015), 211-226 DOI: https://doi.org/10.1016/j.istruc.2015.05.001.
6. An, Y.-F., Han, L.-H. and Roeder, C., "Flexural performance of concrete-encased concrete-filled steel tubes", ***Magazine of Concrete Research***, Vol. 66, No. 5, (2014), 249-267 DOI: https://doi.org/10.1680/macr.13.00268.
7. Ellobody, E., Young, B. and Lam, D., "Eccentrically loaded concrete encased steel composite columns", ***Thin-walled Structures***, Vol. 49, No. 1, (2011), 53-65 DOI: https://doi.org/10.1016/j.tws.2010.08.006.
8. Ellobody, E. and Young, B., "Numerical simulation of concrete encased steel composite columns", ***Journal of Constructional Steel Research***, Vol. 67, No. 2, (2011), 211-222 DOI: https://doi.org/10.1016/j.jcsr.2010.08.003.
9. Chen, C.-C. and Lin, N.-J., "Analytical model for predicting axial capacity and behavior of concrete encased steel composite stub columns", ***Journal of Constructional Steel Research***, Vol. 62, No. 5, (2006), 424-433 DOI: https://doi.org/10.1016/j.jcsr.2005.04.021.
10. Mander, J.B., Priestley, M.J. and Park, R., "Theoretical stress-strain model for confined concrete", ***Journal of Structural Engineering***, Vol. 114, No. 8, (1988), 1804-1826 DOI: https://doi.org/10.1061/(ASCE)0733-9445(1988)114:8(1804).
11. Wang, H., Li, J. and Song, Y., "Numerical study and design recommendations of eccentrically loaded partially encased composite columns", ***International Journal of Steel Structures***, Vol. 19, No. 3, (2019), 991-1009 DOI: https://doi.org/10.1007/s13296-018-0179-7.
12. Han, L.-H. and An, Y.-F., "Performance of concrete-encased cfst stub columns under axial compression", ***Journal of Constructional Steel Research***, Vol. 93, (2014), 62-76 DOI: https://doi.org/10.1016/j.jcsr.2013.10.019.
13. Zhou, X., Yan, B. and Liu, J., "Behavior of square tubed steel reinforced-concrete (src) columns under eccentric compression", ***Thin-walled Structures***, Vol. 91, (2015), 129-138 DOI: https://doi.org/10.1016/j.tws.2015.01.022.
14. Li, B., Park, R. and Tanaka, H., "Stress-strain behavior of high-strength concrete confined by ultra-high-and normal-strength transverse reinforcements", ***ACI Structural Journal***, (2001), 395-406 DOI:http://hdl.handle.net/10220/8359.
15. Mirza, S.A. and Skrabek, B., "Statistical analysis of slender composite beam-column strength", ***Journal of Structural Engineering***, Vol. 118, No. 5, (1992), 1312-1332 DOI: https://doi.org/10.1061/(ASCE)0733-9445(1992)118:5(1312).
16. Mirza, S.A., Hyttinen, V. and Hyttinen, E., "Physical tests and analyses of composite steel-concrete beam-columns", ***Journal of Structural Engineering***, Vol. 122, No. 11, (1996), 1317-1326 DOI: https://doi.org/10.1061/(ASCE)0733-9445(1996)122:11(1317).
17. El-Tawil, S. and Deierlein, G.G., "Strength and ductility of concrete encased composite columns", ***Journal of Structural Engineering***, Vol. 125, No. 9, (1999), 1009-1019 DOI: https://doi.org/10.1061/(ASCE)0733-9445(1999)125:9(1009).
18. Munoz, P.R. and Hsu, C.-T.T., "Behavior of biaxially loaded concrete-encased composite columns", ***Journal of structural engineering***, Vol. 123, No. 9, (1997), 1163-1171 DOI: https://doi.org/10.1061/(ASCE)0733-9445(1997)123:9(1163).
19. Bogdan, T., Gerardy, J.C., Davies, D.W. and Popa, N., "Performance and capacity of composite "mega columns" with encased hot rolled steel sections", ***Euro Steel***, Vol. 1, No. 2-3, (2017), 1879-1888 DOI: https://doi.org/10.1002/cepa.232.
20. Lelkes, A. and Gramblička, Š., "Theoretical and experimental studies on composite steel–concrete columns", ***Procedia Engineering***, Vol. 65, (2013), 405-410 DOI: https://doi.org/10.1016/j.proeng.2013.09.063.

21. Nematzadeh, M., Fazli, S. and Hajirasouliha, I., "Experimental study and calculation of laterally-prestressed confined concrete columns", ***Steel and Composite Structures***, Vol. 23, No. 5, (2017), 517-527 DOI: https://doi.org/10.12989/scs.2017.23.5.517.
22. ACI, "Standard practice for selecting proportions for normal, heavyweight, and mass concrete(aci 211.1-91), ACI manual of concrete practice, (1996), 1-38.
23. ASTM, "E8/e8m-2013, standard test methods for tension testing of metallic materials, ASTM International, West Conshohocken, USA, (2013).
24. Nematzadeh, M. and Ghadami, J., "Evaluation of interfacial shear stress in active steel tube-confined concrete columns", ***Computers and Concrete***, Vol. 20, No. 4, (2017), 469-481 DOI: https://doi.org/10.12989/cac.2017.20.4.469.
25. Haghinejada, A. and Nematzadeh, M., "Three-dimensional finite element analysis of compressive behavior of circular steel tube-confined concrete stub columns by new confinement relationships", ***Latin American Journal of Solids and Structures***, Vol. 13, No. 5, (2016), 916-944 DOI: https://doi.org/10.1590/1679-78252631
26. ACI, "Building code requirements for structural concrete (aci 318-11), Detroit, MI, USA, (2011).
27. Barr, B. and Lee, M., "Modelling the strain-softening behaviour of plain concrete using a double-exponential model", ***Magazine of Concrete Research***, Vol. 55, No. 4, (2003), 343-353 DOI: https://doi.org/10.1680/macr.2003.55.4.343.
28. Zhao, X.-L., Han, L.-H. and Lu, H., "Concrete-filled tubular members and connections, CRC Press, (2010).

Persian Abstract

چکیده

ستون های بتنی مسلح شده با فولاد SRC نوعی از ستون های مرکب می باشند که به دلیل مزایای فراوانی که نسبت به ستون های بتن آرمه و فولادی تنها دارند، استفاده از آنها در سال های اخیر رواج زیادی پیدا کرده است. در این تحقیق، به جهت بررسی رفتار ستون های SRC، شاخص شکل پذیری این ستون ها و عوامل موثر بر آن مورد بررسی قرار گرفته و همچنین با محاسبه معادلات لازم بر اساس روش توزیع تنش پلاستیک، روشی ساده برای طراحی این ستون ها ارائه گردید. بر همین اساس، یک تست آزمایشگاهی بر روی 6 نمونه ستون SRC با دو نوع پروفیل فولادی H و صلیبی و با سه نسبت برون محوری 0.4، 0.55 و 0.7 انجام شد. همچنین یک مدل المان محدود به کمک نرم افزار آباکوس به جهت مطالعه عددی ایجاد شد که با نتایج مدل آزمایشگاهی اعتبارسنجی گردید. در مجموع 30 ستون برای مطالعه پارامتریک تحلیل گردیدند که متغیرهای هندسی و مصالح از قبیل درصد فولاد، مقاومت فشاری بتن، فاصله میلگردهای عرضی و شکل هندسی هسته فولادی بر شاخص شکل پذیری این ستون ها مورد بررسی قرار گرفتند که نتایج نشان داد که برای ستون با مقطع فولادی مانندH، کاهش نسبت فاصله آرماتورهای عرضی از 0.6 به 0.2 سبب افزایش شاخص شکل پذیری به میزان 72% می گردد که این کاهش فاصله، سبب ایجاد سخت شدگی پس از نقطه تسلیم در نمودار نیرو- تغییرمکان و افزایش ظرفیت باربری به میزان 20% نیز می گردد. همچنین بر اساس روش توزیع تنش پلاستیک ذکر شده در آیین نامه EC4، نمودارهای اندرکنش نیرو- لنگرخمشی ترسیم شده و با نمودارهای اندرکنش استخراج شده توسط نرم افزار مقایسه گردیدند و در نهایت نمودارهایی بدون بعد جهت طراحی این ستون ها ارائه شد.

IJE TRANSACTIONS B: Applications Vol. 33, No. 8, (August 2020) 1544-1552

International Journal of Engineering

Journal Homepage: www.ije.ir

The Efficiency of Hybrid BNN-DWT for Predicting the Construction and Demolition Waste Concrete Strength

M. Hashempour*[a], A. Heidari[b], M. Shahi jounaghani[b]

[a]*Department of Civil and Environmental Engineering, Amirkabir University of Technology, Tehran, Iran*
[b]*Department of Civil Engineering, Shahrekord University, Shahrekord, Iran*

P A P E R I N F O

Paper history:
Received 17 December 2019
Received in revised form 06 June 2020
Accepted 11 June 2020

Keywords:
Concrete
Waste Management
Backpropagation Network
Discrete Wavelet Transform
Sustainable Development

A B S T R A C T

The current study focuses on two main goals. First, with the use of construction and demolition (C&D) of building materials, a new aggregate was produced and it was utilized for green concrete production. The compressive strength test confirmed the good function of C&DW aggregate concrete. This concrete did not show significant differences with natural sand concrete. Second, Backpropagation neural network (BNN) was adjusted for C&DW concrete strength prediction at different curing times. Although BNN has good accuracy for strength prediction, due to the importance of 28th day of concrete strength the need to improve the accuracy was felt. So discrete wavelet transform (DWT) was used on BNN and a hybrid network was produced. DWT by filtering the noises can improve the homogeneity of the dataset. The results of DWT-BNN showed that the regression can increase to 98% and the MSE index reduces to 0.001. Continued research has shown that increasing the number of filters to four steps leads to reduced accuracy and increased computational cost. So using DWT-BNN as a hybrid network with one filter can improve prediction ability to the desired level but adding up the number of filters not recommended.

***doi**: 10.5829/ije.2020.33.08b.12*

NOMENCLATURE

X_i	Input units	E	Error function
X	Sample	m , n	Scaling parameters
$x_{\max}$	Maximum sample	A	Approximation
$x_{\min}$	Minimum sample	D	detail
w_{ij}	Weight on the connections	**Greek Symbols**	
b_j	Bias of each neuron	ξ	Trainng parameter
n	Number of input units	$\psi(t)$	Mother function
O_z	Actual output value	**Subscripts**	
t_z	Output of the network	j	Neuron counter

1. INTRODUCTION

Concrete is one of the common building material that has a large volume of production and consumption in the building industry [1, 2]. It produces in almost all countries [3, 4]. Therefore, various ways have proposed to reduce the cost of concrete production. One of the methods is the use of building waste in the manufacture process. Wastes such as glass, ceramic tiles, concrete, plastics, etc. are recommended materials for the construction of concrete. Researchers have evaluated the different dimensions of using these materials [5], whether

*Corresponding Author Institutional Email: *m.hashempour@aut.ac.ir* (M. Hashempour)

Please cite this article as: M. Hashempour, A. Heidari, M. Shahi jounaghani, The Efficiency of Hybrid BNN-DWT for Predicting the Construction and Demolition Waste Concrete Strength, International Journal of Engineering (IJE), IJE TRANSACTIONS B: Applications Vol. 33, No. 8, (August 2020) 1544-1552

cement or aggregate, as concrete ingredients or even soil stablizers [6]. For example, in the case of C&D waste as concrete aggregate, laboratory studies indicated an increase in water absorption and, in some cases, a decrease in compressive strength of concrete [7]. However, the use of recycled aggregate concrete with low old cement paste adhering to them could increase the quality of aggregates and improve the mechanical properties of concrete [8]. The use of tile and ceramic waste were also used to replace cement and aggregate in the manufacture of concrete [9, 10]. The use of tile and ceramic waste in cement manufacturing were also investigated. The use of them is appropriate in accordance with the relevant standard for the production of cement and using up to a maximum of 35% is allowed [11]. The use of brick waste could be used in the construction of a lightweight concrete compound [12]. Today, due to the development of technology, significant changes have been made in the experimental studies. Previously, due to material and sample making limitations it was not possible to decisively decide on the high precision deductions. So it took a lot of time to build prototype and study about experimental samples. But with the help of computer simulations, it was possible for discrete laboratory results to be converted to continuous results and avoid spending additional time and cost [13]. In the construction of concrete materials, various researchers have also used statistical methods and computer modeling to increase deduction precision. Artificial neural networks are one of the statistical tools that have been used successfully to estimate concrete features such as shear resistance [14], compressive strength [15, 16], elastic modulus [17], and corrosion of bars in reinforced concrete [18]. It is also possible to use neural networks in concrete mix designs modeling [19]. A series of studies have also shown that various types of networks, such as artificial neural network (ANN), automated neural network search (ANS), radial basis function (RBF), Support vector machine, and Support vector regression (SVR and SVM) are capable of solving laboratory problems [20, 21]. Another computational method is wavelet transform which is able to evaluate the performance of concrete structures [22, 23]. A wavelet transform with data separation capabilities has the potential to facilitate data analysis for the network. Using some transformations, such as discrete wavelet transforms, can separate data using upper and lower frequencies [24]. This can be used as a positive point in neural networks to reduce the time of data analysis. To date, numerical results have shown that the use of wavelet transforms as the neural network functions have beneficial effects in the increasing of the prediction accuracy [25]. What has been researched by the authors so far, using both wavelet and BNN with serial function have not been investigated, altough the DWT-fuzzy systems has been evaluated before [26]. In addition to, the influences DWT filters on network answers has not been studied. In this regard, for estimating the compressive strength of concrete containing recycled aggregate, first a BNN with using 165 laboratory samples, including the samples in different age, was made. In the next step, in order to increase the precision of the estimation, the compressive strength results were filtered by the help of discrete wavelet transformation (DWT). The new up and low frequencies which were obtained by DWT were used as BNN output. Afterward, the predicted values were reconstructed and the results were evaluated. This paper has 7 sections. First at section (2) experimental program is explained. At sections (3) and (4), BNN and DWT structures are investigated respectively. In section (5) the BNN-DWT is described. In section (6) the results of the networks were evaluated. In addition, section (7) shows a summary of the most important results.

2. EXPERIMENTAL PROGRAM

For the construction of recycled aggregate (RA) concrete, portland cement type 1-525, potable water, the aggregate mixture of natural aggregate (NA) and construction waste, and superplasticizer based on polycarboxylate copolymer were used. The RA was produced by the destruction of the building which was included concrete, stone, brick, and ceramic. It was replaced by 0 to 100% of the total consumed aggregate. Table 1 shows the mix design of the samples. As can be seen, a total of 55 concrete samples with different amounts of sand to cement ratio and recycled to natural sand were made. In this table, R, W, C, and S are used as recycled aggregate,

TABLE 1. Mix design

NA*	RA*	Label	Superplasticizer by S/C ratio**				
			1	1.5	2	2.5	3
100	0	R0	0	0	0.3	0.2	0.7
90	10	R10	0	0	0.3	0.3	0.7
80	20	R20	0	0	0.3	0.5	0.8
70	30	R30	0	0	0.3	0.7	0.1
60	40	R40	0	0	0.4	0.8	0.14
50	50	R50	0	0	0.6	0.11	0.16
40	60	R60	0	0.1	0.8	0.14	0.17
30	70	R70	0	0.1	0.11	0.17	0.2
20	80	R80	0	0.2	0.14	0.19	0.2
10	90	R90	0	0.3	0.17	0.2	0.2
0	100	R100	0.3	0.4	0.19	0.2	0.2

*(%wt. of total aggregate)
**(%wt. of cement)

water, cement, and sand respectively. It should be noted that for the results section (parts 4 and 6) the name of samples for better understanding has changed. For this reason, R used as recycled sand, the number after that shows the substitute percent with natural sand, S as sand to cement abbreviation and the number following is sand to cement ratio. For example, R0S1 means a sample with 0% recycled sand and sand to cement ratio of 1.

To make concrete, dry compounds, cement, and aggregate, were first combined in 5 liters mixer for 3 minutes, and then a solution of water and superplasticizer was added to the mixture. The mixing process continued for another 3 minutes (ASTM C 94). Then concrete was poured into 5 cm cubic molds. After one day, the molds were opened and the concrete samples were cured by water for 7 and 28 days. It is worth noting that after 1, 7, and 28th days, samples were broken by using a 2000 KN concrete compressive strength jack and their results were taken (ASTM C 109). Figure 1 shows the concrete sample under jack for compressive strength. It should be noted that based on ASTM C 109, for each day three samples were ready and broken by jack. The average of three samples' compressive strength was used as the final result.

2. 1. Compressive Strength Test Figure 2 shows the compressive strength results. As shown in Figure 2, the maximum compressive strength at 1th day was 18.1 MPa for a sample containing 40% of the RA and the ratio of sand to the cement of 2.5. After 7 days, compressive strength was observed and the highest compressive strength was related to samples containing 0 and 20% of waste with sand to cement ratio of 3. The compressive strength of 7th day in both samples was 54.13 and 54.6 MPa, respectively. At 28th day, compressive strength in both samples were for samples with 40 and 20% recycled sand replacement and the sand to cement ratio of 2.5 and 3, with the compressive strength of 56.56 and 58.68 MPa, respectively.

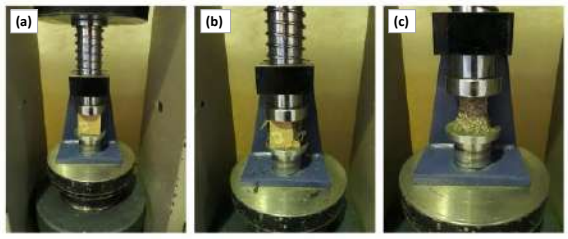

Figure 1. Process of the concrete sample breaking under hydraulic jack [27]

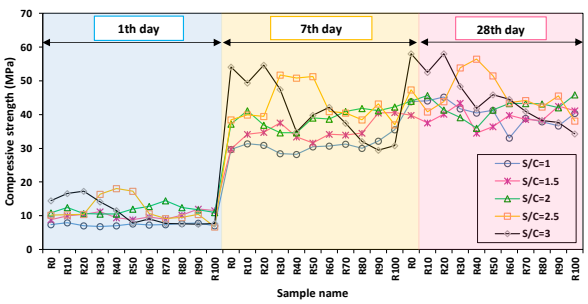

Figure 2. Compressive strength test results

3. BACKPROPAGATION NEURAL NETWORK

In this study, the Backpropagation neural network (BNN) is used to estimate the compressive strength of concrete at 1, 7, and 28 days. The neural network had three inputs: the recycled sand to sand ratio, the superplasticizer to cement ratio and the sand to cement ratio. This network had a hidden layer with 10 neurons. Also, the Levenberg Marquardt was used as a training function, and the Tangent Sigmoid and Linear functions were used as transfer functions. Therefore, the network had 3 inputs and 3 outputs (Figure 3). It should be noted that in this network 80% of the data was used for training and 10% was set aside for validation and 10% was used for the testing process. The BNN mechanism is as follows:

First, the inputs enter the network. Then, they processed based on the following equation:

$$Net_j = \sum_{i=1}^{n} x_i w_{ij} + b_j \quad (1)$$

In which x_i is used as input units, w_{ij} is the weight, i and j are the input and neuron counters, b_j is the bias of each neuron, and n is the number of input units. If the tangent sigmoid is used as a transfer function of the hidden layer, the following formula will be used:

$$O_j = f(Net_j) = \frac{-1+e^{-2Net_j}}{1+e^{-2Net_j}} \quad (2)$$

One more time, the data multiple by weight and sum with the bias. Then they entered into the second transfer function and enter into the output layer. This process is the same as before. In the end, the network error is calculated. The error general formula is as Equation (3):

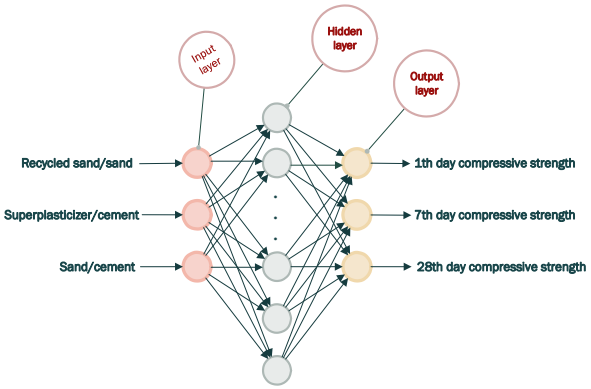

Figure 3. The BNN configuration in the current study

$$e_i = t_z - O_z \tag{3}$$

which t_z is the predicted value which is achieved by BNN and O_z is the real output value. For determining the error, the mean absolute error (MAE), mean square error (MSE), sum of squared error (SSE), and root-mean-squared error (RMSE) were used. The Equations (4)-(7) show the used error functions respectively.

$$E = \frac{\sum_{i=1}^{n} |e_i|}{n} \tag{4}$$

$$E = \frac{\sum_{i=1}^{n} e_i^2}{n} \tag{5}$$

$$E = \sum_{i=1}^{n} e_i^2 \tag{6}$$

$$E = \sqrt{\frac{\sum_{i=1}^{n} e_i^2}{n}} \tag{7}$$

The network training is the process of achieving the best-predicted value. To minimize the error, the weight parameter must be changed:

$$\nabla W_{jz} = -\xi\left(\delta E / \delta W_{jk}\right) \tag{8}$$

ξ and E are the training parameter and the error function respectively. The new weight for the next steps will be computed as:

$$W_{jz}(n+1) = W_{jz}(n) + \nabla W_{jz}(n) \tag{9}$$

This process continues until the network error reaches the desired level [17].

4. DISCRETE WAVELET TRANSFORM (DWT)

Wavelet transform is a powerful tool for separating high and low frequencies. This transformation for data separation and reconstruction can be a useful tool for analysis [28-30]. One of the wavelet transforms is the discrete wavelet transform, which is used for analyzing the signal at various scales. A discrete wavelet transform is defined as:

$$DWT(m,n) = 2^{-(\frac{m}{n})} \sum_{t=0}^{T-1} x(t)\psi[\frac{(t-n2^m)}{2^m}] \tag{10}$$

In the above equation, x (t) is the function that is related to t, where t is the horizontal axis points, m and n are the scaling factors and the translation factor, respectively. T is the number of points and is the mother wavelet function. In this study, Haar wavelet function is mother function and is used as follows.

$$\psi(t) = \begin{cases} 1 & 0 \le t < \frac{1}{2} \\ -1 & \frac{1}{2} \le t < 1 \\ 0 & otherwise. \end{cases} \tag{11}$$

In the discrete wavelet transformation, the primary wave is divided into two high-frequency and low-frequency. Then, the low frequency is divided into two new high and low-frequencies. This process continues for the n stage [22]. The following figure shows the wave separation. In Figure 4, D is an abbreviation of detail and A is used as an approximation. The number after D and A is illustrated as the step of filtration.

In this study, the results of compressive strength of concrete were filtered using discrete wavelet. The results of which were as follows:

As shown in Figure 5, with an increasing number of wave filtering levels, the low frequency is converted to a more smother wave. In the first phase filter, at the high-frequency wave, the first noise occurred in the compressive strength changes of 1st day to 7th day, which is associated with a jump. This jump is visible in

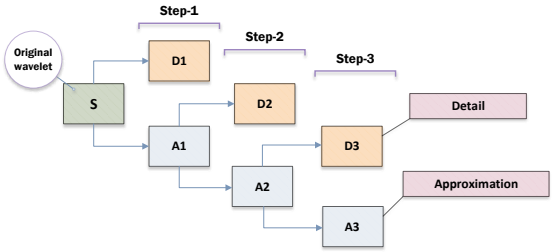

Figure 4. DWT mechanism

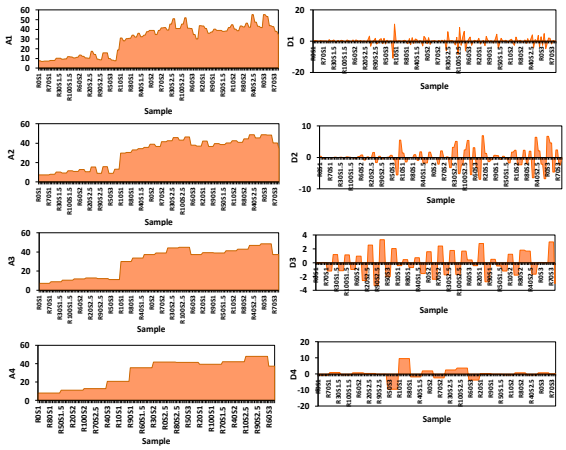

Figure 5. Using DWT in filtering the compressive strength function (4 step filtrations)

A1 (Figure 5). Afterward, the next noise occurred at a change in compressive strength of 7th day to 28th day, which was shown at a high frequency in the form of noise. But compared to the first noise, the second noise is less intense due to the more severe compressive strength on 7th day compared to the 28th day. The jumps due to compressive strength time are shown in Figure 6.

In the fourth stage filter, with lowering the compressive strength curve changes due to filtration, the high-frequency spectrum has fewer fluctuations, while the low frequency changes from oscillating shape to a relatively uniform state. It should be noted that the high-frequency curves have lower rates of variation. If the vertical axis of high-frequency changes as the same as the low-frequency axis, this curve has no significant variations.

5. DWT-BNN Analysis Since the compressive strength curve is highly noisy (Figure 2), for increasing the performance of the estimated data, a combination of a DWT and a BNN is used. The DWT-BNN methodology is as follows (see Figure 7).

In this method, first, the output data is entered into a discrete wavelet transform, and after filtering to up and down frequencies, the broken wave is given as a new output to the neural network. After training the neural network, the outputs are re-constructed. The reconstruction waves after 4 levels have done based on the following equation:

$$RC = A4 + D4 + D3 + D2 + D1 \quad (12)$$

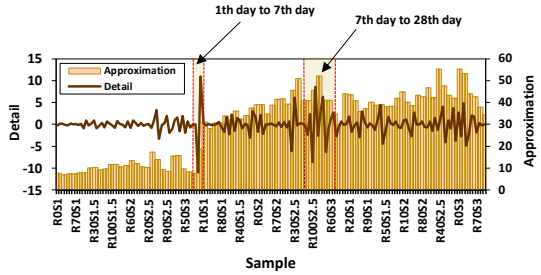

Figure 6. The presence of two main noises at 7th and 28th day of strength test

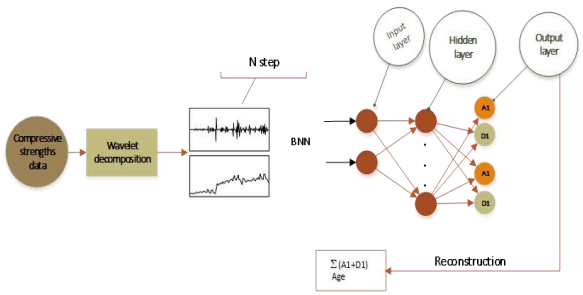

Figure 7. DWT-BNN mechanism

RC is the reconstructed wave, A and D are the approximation and detail, respectively. The number after them is used as a filtration step. Therefore, the compressive strength is again obtained from the above equation. Then the results of observations and predictions are compared with each other.

6. RESULTS AND DISCUSSION

6. 1. Backpropagation Neural Network In the first step, the linear regression method was examined by Excel software. The regression was 0.135. This amount indicates the failure of fitting. Therefore, a more powerful tool is needed. In the second step, the neural network was used. The recycled sand to the total sand, the superplasticizer to cement, and the sand to cement ratios were defined as the network input. Then compressive strength of 1st day, 7th day, and 28th day were considered as the network outputs. After analyzing the network around 38 to 40 times and ensuring complete training, the best result was chosen as its appropriate result. Figure 8 shows the result of fitting by BNN.

As can be seen, the neural network, having regression of 0.9722, has a good ability to estimate the compressive strength of concrete, which is approved by Alilou and Teshnehlab [31]. But it seems that with the increase of noisy manner of 28th day strength, the neural network loses its ability (Figure 9).

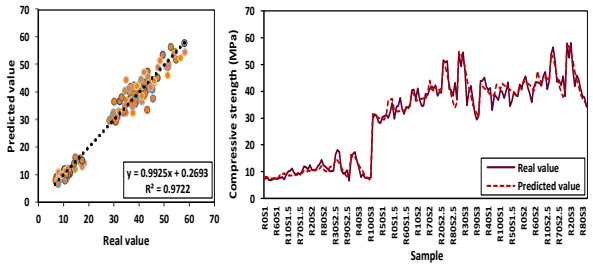

Figure 8. Regression and the real and predicted values by BNN

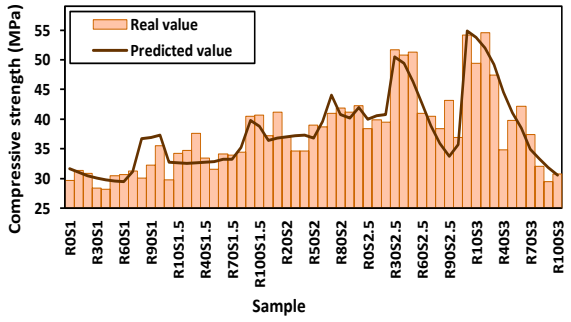

Figure 9. The lack of enough precision for predicting the 28th day compressive strength

The lowest error rate was observed for 1st-day concrete strength. At this time, the MSE error was 0.00056. Also, the error rate increases for the 28th day compressive strength. The MSE error rate is reached to 0.0021. The results are shown in Table 2.

6. 2. DWT 1-BNN In the next step, a DWT is used. For this, filtration of the compressive strength data (the desired output) was performed without reducing the number of data in just one level. Then the filtered data was entered into the neural network as a new output. From the combination of the neural network and the discrete wavelet (one filter level), the results of Figure 10 were obtained.

As shown in Figure 10, the new network regression was 0.9841 which had been 0.9722 before. At this stage, the MSE error index of the 28th day strength was decreased, and thus, the accuracy of the combination network improved. Providing a filtering tool by DWT can denoise the strength spectra and improve the homogeneity of the dataset. Increasing the R^2 factor is important proof for reducing the standard deviation and improving accuracy. The mean square error rate from 0.00157 reached the 0.000961 level (Table 3). Since the 28th day strength of concrete in many cases has a higher priority and importance than others ages for long term study, the combination of BNN and wavelet with a filtering stage is desirable from two perspectives: 1) having higher regression and less error index than BNN, 2) help to obtain more accurate estimation for 28th day compressive strength. It should be noted that the research conducted by Khademi et al. [32], ANN network with 91% R^2 factor is chosen as the best tool for predicting 28th day compressive strength. In the current work, the regression increases to 98% which is a more exact answer. So DWT can improve accuracy.

TABLE 2. Errors of BNN

Error	MAE	MSE	SSE	RMSE
1st day	0.0184	0.0005	0.0306	0.1751
7th day	0.0332	0.0021	0.1141	0.3378
28th day	0.0362	0.0021	0.1156	0.3400
average	0.0293	0.0015	0.2604	0.5103

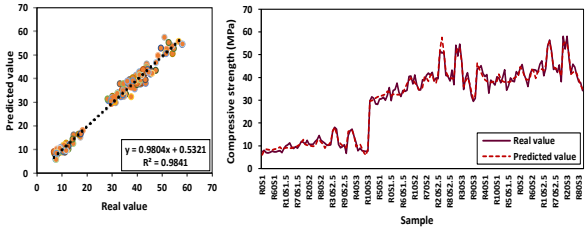

Figure 10. Regression and the real and predicted values differences by DWT 1-BNN

TABLE 3. Errors of DWT 1-BNN

Error	MAE	MSE	SSE	RMSE
1st day	0.0188	0.0005	0.0284	0.1685
7th day	0.0285	0.0012	0.0688	0.2624
28th day	0.0276	0.0011	0.0612	0.2475
average	0.0249	0.0009	0.1585	0.3981

6. 3. DWT 2-BNN In the next step, the DWT filtering was increased to two levels (Figure 11). In this step, the network error in the prediction of compressive strength of one day was decreased compared to the previous stage and the accuracy of the network was higher, but for the network at 7th and 28th days, the network error was increased. It seems that DWT removes important data instead of denoising them and it deviates BNN; which is approved by Altunkaynak and Wang [33] before. Filters are good for denoising. In this case that the error-index is not too high, using one filter is sufficient.

At one day, the MSE error index was reduced to 0.000255. The MSE error rate on 28th day was reached to 0.00183, while if the neural network had used with one filtering level, the MSE error-index could have been 0.001114. The results indicate an increase in the final errors of this method compared to the previous step (Table 4).

6. 4. DWT 3-BNN Next, the 3 levels filtering effects were evaluated (Figure 12). The results of the data evaluation showed that the 7th day strength error decreases compared to the use of two levels filter, but at the age of 1th and 28th days, the error of this method is higher than the two levels filtration (Table 5).

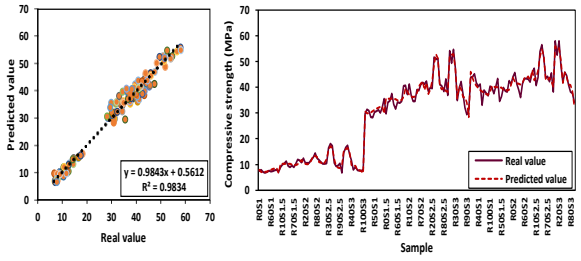

Figure 11. Regression and the real and predicted values differences by DWT 2-BNN

TABLE 4. Errors of DWT 2-BNN

Error	MAE	MSE	SSE	RMSE
1st day	0.0123	0.0002	0.0140	0.1184
7th day	0.0344	0.0018	0.1004	0.3169
28th day	0.0341	0.0018	0.1006	0.3172
average	0.0269	0.0013	0.2151	0.4637

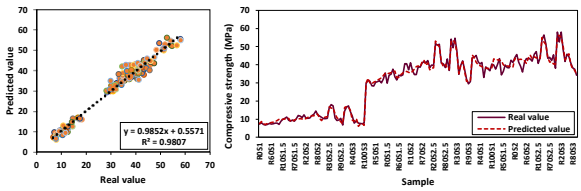

Figure 12. Regression and the real and predicted values differences by DWT 3-BNN

TABLE 5. Errors of DWT 3-BNN

Error	MAE	MSE	SSE	RMSE
1st day	0.0183	0.0005	0.0254	0.1593
7th day	0.0304	0.0015	0.0839	0.2896
28th day	0.0387	0.0025	0.1371	0.3703
average	0.0291	0.0015	0.2464	0.4964

It should also be noted that the MSE error-index on 28th day was increased to 0.002493. While the MSE error index for BNN had been 0.002102. Therefore, the recent state is not recommended for the estimation of 28th day compressive strength due to an increase in error index.

6. 5. DWT 4-BNN In the last step, using four levels filtration, a new network was created. The results are shown in Figure 13. As can be seen, the regression has a value of 0.9658 which was lower than BNN. The network errors were also greater in all ages than the primary backpropagation neural network (Table 6).

Therefore, it is not recommended to use four level filtrations. So the analysis was stopped at 4 step filtrations and the BNN-DWT with 2 level filtrations was introduced as the best network.

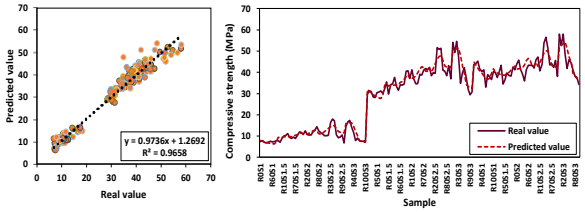

Figure 13. Regression and the real and predicted values differences by DWT 4-BNN

TABLE 6. Errors of DWT 4-BNN

Error	MAE	MSE	SSE	RMSE
1st day	0.023325	0.000975	0.053622	0.231564
7th day	0.056574	0.005304	0.291719	0.54011
28th day	0.059223	0.005264	0.289517	0.538067
average	0.046374	0.003848	0.634857	0.796779

7. CONCLUSION

The current study focuses on the evaluation of DWT-BNN efficiency on C&DW concrete strength prediction. The main results are summarized as follows.

- Previously, the compressive strength prediction has been done for 28th day compressive strength as standard strength. In the current study, it was shown that providing the separated networks for each day is essential.
-The presence of noises on 28th day spectra, deviate BNN from predicting the values with good precision. So the supplementary tool (DWT) added to the BNN.
- Adding DWT with one filter produced a network that as approximately 50% lower MSE error in comparison with BNN. In addition, the R^2 factor, as the main parameter of network function, increased to 98% which shows the high correlation of real and predicted value.
-This regression and low error indexes in comparison to similar researches, confirm the DWT efficiency.
-The good results of using DWT on BNN encouraged authors to investigate the higher number of filters.
- Evaluating the filters' numbers showed that increment of filters can accumulate errors by removing main data instead of noises. Further, augmentation of low and high passes can decrease the RUN speed and provide computational cost.
- According to the current results, based on the deviation of real and predicted values by BNN, the authors should decide whether to use DWT on BNN or not. If it is necessary to use DWT, adding one (two) filters on DWT is suggested. If the results are not satisfactory, the filters should be added one by one.
- For further investigation, the authors suggested evaluating the mother functions, symmetric or asymmetric, and the shape of wavelets on BNN results.

8. REFERENCES

1. Tavakoli, D., Hashempour, M. and Heidari, A., "Use of waste materials in concrete: A review", ***Pertanika Journal of Science and Technology***, Vol. 26, No. 2, (2018), 499-522.
2. Heidari, A., Hashempour, M. and Chermahini, M.D., "Influence of reactive mgo hydration and cement content on c&dw aggregate concrete characteristics", ***International Journal of Civil Engineering***, Vol. 17, No. 7, (2019), 1095-1106. doi: https://doi.org/10.1007/s40999-018-0361-5
3. Arunraj, E., Vincent Sam Jebadurai, S., Daniel, C., Joel Shelton, J. and Hemalatha, G., "Experimental study on compressive strength of brick using natural fibres", ***International Journal of Engineering, Transactions C: Aspects***, Vol. 32, No. 6, (2019), 799-804. doi: 10.5829/ije.2019.32.06c.01
4. Ehsani, M.R., Rajaie, H., ramezanianpour, A. and Momayez, A., "Experimental investigation of the methods of evaluating the bond strength between concrete substrate and repair materials", ***International Journal of Engineering***, ***Transactions B: Applications*** Vol. 15, No. 4, (2002), 319-332.
5. Adejuyigbe, I., Chiadighikaobi, P. and Okpara, D., "Sustainability comparison for steel and basalt fiber reinforcement, landfills, leachate reservoirs and multi-functional

structure", ***Civil Engineering Journal***, Vol. 5, No. 1, (2019), 172-180. doi: https://doi.org/10.28991/cej-2019-03091235.

6. Emeka, A., Chukwuemeka, A. and Benjamin.Okwudili, M., "Deformation behaviour of erodible soil stabilized with cement and quarry dust", ***Emerging Science Journal***, Vol. 2, (2018), 383. doi: https://doi.org/10.28991/esj-2018-01157.
7. Heidari, A., Hashempour, M., Javdanian, H. and Karimian, M., "Investigation of mechanical properties of mortar with mixed recycled aggregates", ***Asian Journal of Civil Engineering***, Vol. 19, No. 5, (2018), 583-593. doi: https://doi.org/10.1007/s42107-018-0044-1.
8. Verian, K.P., Ashraf, W. and Cao, Y., "Properties of recycled concrete aggregate and their influence in new concrete production", ***Resources, Conservation and Recycling***, Vol. 133, (2018), 30-49. doi: https://doi.org/10.1016/j.resconrec.2018.02.005.
9. Khaloo, A.R., "Crushed tile coarse aggregate concrete", ***Cement, Concrete and Aggregates***, Vol. 17, No. 2, (1995), 119-125.
10. Vejmelková, E., Keppert, M., Rovnaníková, P., Ondráček, M., Keršner, Z. and Černý, R., "Properties of high performance concrete containing fine-ground ceramics as supplementary cementitious material", ***Cement and Concrete Composites***, Vol. 34, No. 1, (2012), 55-61. doi: https://doi.org/10.1016/j.cemconcomp.2011.09.018.
11. Ay, N. and Ünal, M., "The use of waste ceramic tile in cement production", ***Cement and Concrete Research***, Vol. 30, No. 3, (2000), 497-499. doi: https://doi.org/10.1016/S0008-8846(00)00202-7.
12. Wongsa, A., Sata, V., Nuaklong, P. and Chindaprasirt, P., "Use of crushed clay brick and pumice aggregates in lightweight geopolymer concrete", ***Construction and Building Materials***, Vol. 188, (2018), 1025-1034. doi: https://doi.org/10.1016/j.conbuildmat.2018.08.176.
13. Heidari, A. and Hashempour, M., "Investigation of mechanical properties of self compacting polymeric concrete with backpropagation network", ***International Journal of Engineering, Transactions C: Aspects***, Vol. 31, No. 6, (2018), 903-909. doi: 10.5829/ije.2018.31.06c.06
14. Naderpour, H., Poursaeidi, O. and Ahmadi, M., "Shear resistance prediction of concrete beams reinforced by frp bars using artificial neural networks", ***Measurement***, Vol. 126, (2018), 299-308. doi: https://doi.org/10.1016/j.measurement.2018.05.051.
15. Heidari, A., Hashempour, M., Javdanian, H. and Nilforoushan, M.R., "The effects of reactive mgo on the mechanical properties of rock flour mortar", ***Iranian Journal of Science and Technology, Transactions of Civil Engineering***, Vol. 43, No. 3, (2019), 589-598. doi: https://doi.org/10.1007/s40996-018-0204-2.
16. Heidari, A., Hashempour, M. and Tavakoli, D., "Using of backpropagation neural network in estimating of compressive strength of waste concrete", ***Journal of Soft Computing in Civil Engineering***, Vol. 1, No. 1, (2017), 54-64. doi: https://doi.org/10.22115/scce.2017.48040.
17. Golafshani, E.M. and Behnood, A., "Application of soft computing methods for predicting the elastic modulus of recycled aggregate concrete", ***Journal of Cleaner Production***, Vol. 176, (2018), 1163-1176. doi: https://doi.org/10.1016/j.jclepro.2017.11.186.
18. Xu, Y. and Jin, R., "Measurement of reinforcement corrosion in concrete adopting ultrasonic tests and artificial neural network", ***Construction and Building Materials***, Vol. 177, (2018), 125-133. doi: https://doi.org/10.1016/j.conbuildmat.2018.05.124.
19. Kalman Šipoš, T., Miličević, I. and Siddique, R., "Model for mix design of brick aggregate concrete based on neural network modelling", ***Construction and Building Materials***, Vol. 148, No. Supplement C, (2017), 757-769. doi: https://doi.org/10.1016/j.conbuildmat.2017.05.111.
20. Reuter, U., Sultan, A. and Reischl, D.S., "A comparative study of machine learning approaches for modeling concrete failure surfaces", ***Advances in Engineering Software***, Vol. 116, (2018), 67-79. doi: https://doi.org/10.1016/j.advengsoft.2017.11.006.
21. Paul, S.C., Panda, B., Huang, Y., Garg, A. and Peng, X., "An empirical model design for evaluation and estimation of carbonation depth in concrete", ***Measurement***, Vol. 124, (2018), 205-210. doi: https://doi.org/10.1016/j.measurement.2018.04.033.
22. Patel, S.S., Chourasia, A.P., Panigrahi, S.K., Parashar, J., Parvez, N. and Kumar, M., "Damage identification of rc structures using wavelet transformation", ***Procedia Engineering***, Vol. 144, (2016), 336-342. doi: https://doi.org/10.1016/j.proeng.2016.05.141.
23. Montes-García, P., Castellanos, F. and Vásquez-Feijoo, J.A., "Assessing corrosion risk in reinforced concrete using wavelets", ***Corrosion Science***, Vol. 52, No. 2, (2010), 555-561. doi: https://doi.org/10.1016/j.corsci.2009.10.014.
24. Heidari, A. and Raeisi, J., "Optimum design of structures against earthquake by simulated annealing using wavelet transform", ***Journal of Soft Computing in Civil Engineering***, Vol. 2, No. 4, (2018), 23-33. doi: https://doi.org/10.22115/scce.2018.125682.1055.
25. Huang, L. and Wang, J., "Forecasting energy fluctuation model by wavelet decomposition and stochastic recurrent wavelet neural network", ***Neurocomputing***, Vol. 309, (2018), 70-82. doi: https://doi.org/10.1016/j.neucom.2018.04.071.
26. Hamidian, D., Salajegheh, J. and Salajegheh, E., "Damage detection of irregular plates and regular dams by wavelet transform combined adoptive neuro fuzzy inference system", ***Civil Engineering Journal***, Vol. 4, (2018), 305-319. doi: https://doi.org/10.28991/cej-030993.
27. Hashempour, M., Heidari, A. and Jounaghani, M.S., "The evaluation of the stress-strain characteristics of mcc concrete", ***Materials Today Communications***, Vol. 23, (2020), 101133. doi: https://doi.org/10.1016/j.mtcomm.2020.101133.
28. Belayneh, A., Adamowski, J., Khalil, B. and Quilty, J., "Coupling machine learning methods with wavelet transforms and the bootstrap and boosting ensemble approaches for drought prediction", ***Atmospheric Research***, Vol. 172-173, (2016), 37-47. doi: https://doi.org/10.1016/j.atmosres.2015.12.017.
29. Aghajani, A., Kazemzadeh, R. and Ebrahimi, A., "A novel hybrid approach for predicting wind farm power production based on wavelet transform, hybrid neural networks and imperialist competitive algorithm", ***Energy Conversion and Management***, Vol. 121, (2016), 232-240. doi: https://doi.org/10.1016/j.enconman.2016.05.024.
30. Golafshani, E.M., Behnood, A. and Arashpour, M., "Predicting the compressive strength of normal and high-performance concretes using ann and anfis hybridized with grey wolf optimizer", ***Construction and Building Materials***, Vol. 232, (2020), 117266. doi: https://doi.org/10.1016/j.conbuildmat.2019.117266.
31. Alilou, V. and Teshnehlab, M., "Prediction of 28-day compressive strength of concrete on the third day using artificial neural networks", ***International Journal of Engineering,*** Vol. 3, No. 6, (2010), 565-670.
32. Khademi, F., Jamal, S.M., Deshpande, N. and Londhe, S., "Predicting strength of recycled aggregate concrete using artificial neural network, adaptive neuro-fuzzy inference system and multiple linear regression", ***International Journal of Sustainable Built Environment***, Vol. 5, No. 2, (2016), 355-369. doi: https://doi.org/10.1016/j.ijsbe.2016.09.003.
33. Altunkaynak, A. and Wang, K.-H., "Estimation of significant wave height in shallow lakes using the expert system techniques", ***Expert Systems with Applications***, Vol. 39, No. 3, (2012), 2549-2559. doi: https://doi.org/10.1016/j.eswa.2011.08.106.

Persian Abstract

چکیده

مطالعه حاضر بر دو هدف متمرکز است. در بخش اول یک بتن دوستدار محیط زیست به کمک سنگدانه ساخته شده از ضایعات ساختمانی تولید شد. نتایج مقاومت فشاری نشان داد این نوع بتن تفاوت چندانی از لحاظ مقاومت فشاری با بتن ساخته شده از سنگدانه طبیعی ندارد. در بخش دوم با استفاده از شبکه عصبی مصنوعی انتشار برگشتی اقدام به پیش‌بینی مقاومت فشاری شد. نتایج نشان داد اگرچه مقاومت فشاری با کمک شبکه انتشار برگشتی قابل قبول است اما لازم است به دلیل اهمیت بالای مقاومت ۲۸ روزه بتن، دقت شبکه افزایش یابد. شبکه هیبریدی انتشار برگشتی–موجکی برای این امر پیشنهاد داده شد. استفاده از موجک توانست دقت شبکه را تا رگرسیون ۹۸ درصد بالا برده و خطا را تا ۰/۰۰۱ کاهش دهد. ادامه بررسی‌ها نشان داد افزایش تعداد فیلترها به جای کاهش نویزها منجر به افزایش خطا و زمان محاسبات می‌شود. بر این اساس شبکه هیبریدی انتشاربرگشتی–موجکی با یک فیلتر برای پیش‌بینی مقاومت فشاری این نوع بتن مناسب است و افزایش بیشتر فیلترها پیشنهاد نمی‌شود.

IJE TRANSACTIONS B: Applications Vol. 33, No. 8, (August 2020) 1553-1559

International Journal of Engineering

Journal Homepage: www.ije.ir

Evaluation of Dynamic Probing Testing Effect in Hand Excavated Pit on Test Results Using Numerical Modeling

S. M. S. Ghorashi*[a], M. Khodaparast[a], A. M. Rajabi[b]

[a] *Faculty of Engineering, University of Qom, Qom, Iran*
[b] *Department of Geology, University of Tehran, Tehran, Iran*

PAPER INFO

Paper history:
Received 08 February 2020
Received in revised form 09 June 2020
Accepted 11 June 2020

Keywords:
Abaqus
Dynamic Probing Test
Dynamic Resistance of Cone's Tip
Hand Excavated Pit
Numerical Modeling

ABSTRACT

In Iran, using the hand excavated pits (wells) have been more common compared to other countries. As a matter of fact, recent years, utilizing the dynamic probing test (DPT) in these types of pits has been significantly developed in Iran. This is while the standard state of doing this test is from the ground level. In this work, the dynamic probing test is carried out in two similar wells with diameter of 1 m and the depth of 10 m in two areas in city of Qom in Iran; one has silty sand soil and the other is clay. Then, both tests are simulated using numerical modeling in Abaqus software and the results are compared and calibrated with the values obtained at the mentioned sites. The results show a good agreement between the simulation data and tests done in the sites. After calibrating the simulated values with the values obtained from the site, we perform another simulation, this time, for the standard state (It means that the test is done from the ground level or with the assumption without well), as deep as 10 m and for both areas and with the mentioned soils specifications. The results show 35 and 22 percent difference in the dynamic resistance of cone's tip between the testing in standard state and hand excavated pit, for silty sand and clay soils, respectively. Finally, using the simulation, we present the relations between the depth of the test point and dynamic resistance of cone's tip for both states and both types of the soils studied in this paper.

***doi**: 10.5829/ije.2020.33.08b.13*

1. INTRODUCTION

The dynamic probing test (DPT) is one of the in-situ tests that has wide application in identifying soil properties. The primary type of this test was developed by Nicolaus Goldman in 1699, and one of the first standards was facilitated by the Germans in 1977, named DIN [1, 2]. In this test, depending on the type of the dynamic probing, the soil strength is estimated from number of blows needed for specified penetration between 10 to 20 cm. Thereafter, other standards were developed from this test [3–5]. In addition, in 2014 the first national standard was provided for this test in Iran [6]. Figure 1 shows different parts of a dynamic probing.

Boring and drilling are considered as the oldest method for the site investigation. In Iran, due to the existence of domestic expertise, and also considering the long-time experience of the Iranians in hand excavated pits (pits or wells), this method is less costly and hence, more practical. Also, advantages of pits compared to the boreholes such as exact determination of the log, possibility of in-situ density testing, in-situ shear testing and undisturbed sampling of soil, help a lot to identify the foundation of sites, specifically in big and sensitive civil projects. On the other hand, DPT has shown its advantages to use through its enormous applicability in different situations such as pits, which is why are motivated to use it here as well. Since in the standard state, DPT is continuously done from ground level, the direct use of the test result in pit bottom does not give an accurate estimation of soil resistance. Diameter of the pit can have a significant impact on the results of the DPT.

Numerical modeling with a valid computer software which is based on numerical methods is a simple, cheap and accurate way to evaluate the in-situ tests results and other geotechnical phenomena.

Most studies on numerical modeling of penetration tests so far are about the cone penetration tests (CPT) [7–13]. However, so far, only the empirical researches have been presented on DPT [14–18]. In this study, the aim is to evaluate the effect of the pit (well) on DPT (DPL type) results using numerical modeling. With the help of this method, without any cost, the difference of the cone's tip strength values in the standard state and the test in the pit

*Corresponding Author's Email: *mr.sms.ghorashi@gmail.com*
(S. M. S. Ghorashi)

Please cite this article as: S. M. S. Ghorashi, M. Khodaparast, A. M. Rajabi, Evaluation of Dynamic Probing Testing Effect in Hand Excavated Pit on Test Results Using Numerical Modeling, International Journal of Engineering (IJE), IJE TRANSACTIONS B: Applications Vol. 33, No. 8, (August 2020) 1553-1559

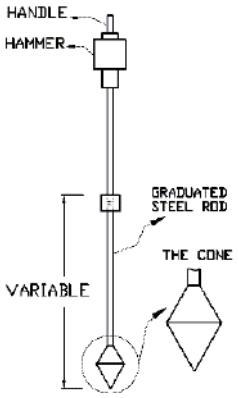

Figure 1. Schematic device structure of a dynamic probing

can be obtained. Therefore, after testing in the pit bottom, by modifying the values, the values of the foundation of the construction site are accurately measured. This study is novel and has been carried out for the first time.

2. TEST SPECIFICATIONS IN THE STUDY AREA

In this study, the DPT has been implemented using light dynamic probing (DPL) in two areas of Qom city in Iran. The site of performing the DPT is shown in Figure 2.

Tables 1 and 2 show the specification of DPL used for the calculation of dynamic resistance of the cone's tip (q_d) and properties of soil types in the study areas, respectively. Soil properties at the sites have been obtained in the laboratory in Qom city.

Figure 2. The site of study area

Table 3 shows the test results for the number of hammer blows in both types of soils in the site. Meanwhile, according to the standard of DPL, number of hammer blows is for specified penetration of 10 cm (N_{10}) [5].

The dynamic resistance of cone's tip (q_d) is achieved using the number of hammer blows, according to the following relationship [19]:

$$q_d = (\frac{m}{m+m'})r_d \quad (1)$$

$$r_d = \frac{mgh}{Ae} \quad (2)$$

where, m is hammer mass in kg, m' the total mass of penetrating cone, rod drive, anvil and guide rod (kg), g gravity acceleration in the unit of m/s^2, h the height of hammer fall in meter (m), A nominal base area (m^2) and e the average of penetration value in each blow (m) equal to $0.1/N_{10}$ based on DPL type.

As a result, according to the above relationship, the value of (q_d) in depth of 10 m for both types of clay and silty sand soil, equal to 2.56 and 4.26 MPa, respectively.

TABLE 1. The Specification of DPL used in study area

Soil types	Specific weight,γ (KN/m^3)	Elasticity modulus, E (MPa)	Poisson ratio, ν	Internal friction angle, ϕ' (°)	Cohesion, C' (kPa)
Silty sand	18.5	85	0.3	34	0
Clay	17	20	0.4	23	3.5

TABLE 2. The properties of soil types in the study areas

Specification	Value	Unit
Hammer mass	10	Kg
Height of hammer fall	0.5	m
Anvil, guide rod and penetrating-cone mass	6	Kg
Drive rods mass	3	Kg/m
Cone diameter	36	mm
Nominal base area	10	cm^2
Cone angle	90	(°) degree
Specific work per blow	49	(kJ/m^2)

TABLE 3. The results of DPT test in the study areas

Soil type	Number of hammer blows for penetration of 10 cm	Standard range of hammer blows in DPT [6]
Silty sand	40	3-50
Clay	24	3-50

3. NUMERICAL MODELING

3. 1. Geometry and Meshing of the Model In this study, the aim is to use Abaqus finite element software for numerical modeling of the DPL penetration

in soil. The cone of dynamic probing and soil environment are two main parts of the desired modeling. Thanks to the axial symmetry of the cone and soil environment, the simulation has been performed in two dimensions and for half of the cone and soil environment. The objects or environments that have axial symmetry can be simulated in two dimension and for half of them. Therefore, the elements are used in the model must be axisymmetric elements. With the help of this modeling, we can decrease the time of computing in Abaqus software without the minimum computational error.

Because of the higher stiffness of the cone compared to the soil, the cone and soil have been modeled as the rigid and deformable systems, respectively.

The soil environment used in the modeling has been assumed to have 1.5 *m* width and 3 *m* depth. The soil model has been meshed using 1811 elements, including CAX4R element (4-node, reduce integration, axisymmetric element) and the right and the bottom boundaries have been meshed using CINAX4 element (4-node, axisymmetric, infinite element).

Also, in order to increase the accuracy of simulation, the elements size is reduced, as it gets closer to the cone. The infinite elements have been used in the right and bottom boundaries of soil environment to reduce the effect of the boundary conditions. On the other side, there is an axis of symmetry in the left boundary and an overburden pressure is applied on the top of the soil model which is equivalent to the pressure value in the depth that DPT is performing. Also in the pit model, vertical displacement has been blocked in the area of non-overburden pressure.

Figure 3 depicts the model that has been created by Abaqus software for two testing cases: pit bottom and standard state with depth of 10 *m*. Since all tests have been done in depth 10 *m*, the same overburden pressure has been used for both soils.

To apply the effect of horizontal stresses in model, the coefficient of earth pressure at rest (k_0) has been estimated using Equations (3) and (4) [20]:

$$k_0 = 1 - sin\,\phi' \quad (3)$$

$$k_0 = 0.95 - sin\,\phi' \quad (4)$$

Equations (3) and (4) are for silty sand and clay soil, respectively.

3. 2. Loading Based on the standard instruction of DPT, penetrating of the cone in DPT must be continuously conducted into the ground. Also, the penetration rate must be kept between 15 to 30 blows per minute [5]. According to Table 3, the values of N_{10} in the site are 40 and 24 for silty sand and clay soil, respectively. Also, based on the standard considerations of DPT, the penetration rate of 30 and 20 blows per minute has been considered for silty sand and clay soil, respectively.

Therefore, considering the proportional relation between the values recorded in the site (N_{10}) and the value considered of the test standard range for 10 *cm* penetration, the penetration velocity of penetrometer in silty sand and clay soil has been achieved 0.00125 *m/s* and 0.00139 *m/s*, respectively.

3. 3. Interaction of Parts of Model The surface to surface contact [21] has been used in the definition of interaction between cone and soil. And the cone and soil are chosen to be master and slave surfaces respectively, based on the higher stiffness of the cone. In order to simplify the model, the friction coefficient between boundary surfaces of the cone and soil neglected to prevent interference of sleeve friction resistance in determining of the cone's tip resistance.

3. 4. Soil Behavior In this study, in order to determine the soil behavior, the Drucker-Prager model has been employed. Figure 4 shows the failure line of Drucker-Prager model in *p-q* plane [22].

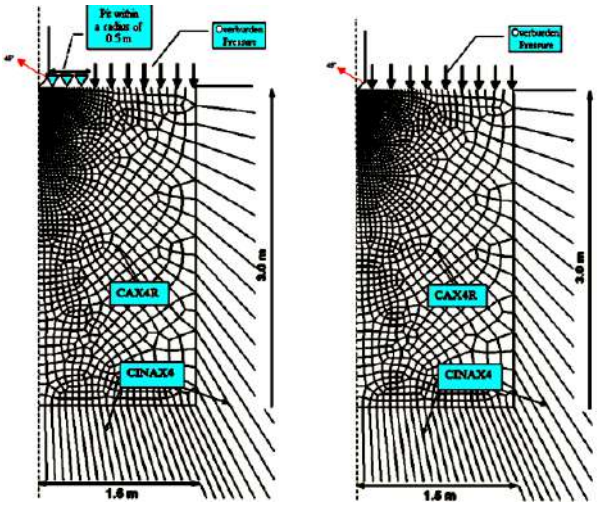

Figure 3. The model in state of testing at pit bottom (Left) and continuously from ground level (Right)

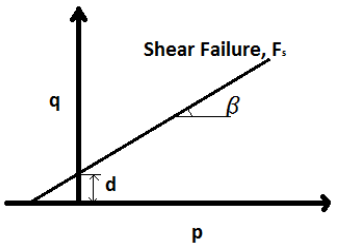

Figure 4. The failure line in yield criterion of Drucker-Prager model

To calculate the values of friction angle (β) and cohesion (d) in Drucker-Prager model using the soil parameters of ϕ' and C' in the site, following relationships can be used [23]:

$$tan\,\beta = \frac{6\sin\phi'}{3-\sin\phi'} \quad (5)$$

$$d = c'\frac{6\cos\phi'}{3-\sin\phi'} \quad (6)$$

Another parameter that is required to define the plastic area of soil in the Drucker-Prager model is the flow stress ratio, which ranges from 0.788 to 1 [23]. The parameters required in the definition of the Drucker-Prager model have been taken for the simulation in Abaqus from Table 4 for the silty sand and clay soil.

Another parameter needed in this model is the dilation angle. Because the experimental values of dilation angle are not available, it is calculated by using the values given in Table 5 employing following equation [24]:

$$\psi = \phi' - \phi_{cr} \quad (7)$$

where ψ and ϕ_{cr} are dilation and critical friction angles.

3. 5. The Method of Analyzing the Model In order to analyze the model, dynamic explicit method has been used. In addition, due to the creation of large displacement when the cone is penetrating, the Arbitrary Lagrangian Eulerian (ALE) technique has been employed in the vicinity of the cone. ALE technique combines the features of pure Lagrangian and pure Eulerian analysis. In other words, the mesh networking moves independent of material and hence a high quality of the meshing can be possible even in large deformations. Moreover, the Volume Smoothing (VS) method has been used to implement ALE analysis [21]. The VS approach relocates the position of nodes by computing a volume weighted average of the center of elements which surrounding the node. This approach is shown in Figure 5. Based on Figure 5, new position of node M is determined from the position of the element C1 to C4. The node M approaches to C3 from the C1 as result of VS scheme.

TABLE 4. The parameters needed of Drucker-Prager used in modeling

Soil type	$\beta°$	d	k
Silty sand	54	0	0.788
Clay	42	7.409	1

TABLE 5. The range of friction angles for soils [24]

Soil type	ϕ'	ϕ_{cr}
Silty sand	27-35	24-32
Clay	20-30	15-30

4. RESULT AND DISCUSSION

The q_d values are taken from the simulation by dividing the vertical reaction force of the cone tip over the cross section area of the cone's dynamic probing. It is noteworthy that the values obtained from the numerical modeling in both soils have been considered for the penetration of about 20 *cm*. Figure 6 shows the penetration of the cone into the soil environment that is modeled in Abaqus.

Table 6 shows the q_d values obtained from the numerical modeling in pit bottom in depth of 10 *m* for the different values of ψ. As is shown in Table 6, the closest values of modeling to the values obtained from DPT (DPL type) in pit bottom are achieved at angles of 0º and 9º for silty sand and clay soils, respectively.

Table 7 shows a good agreement between the values obtained from the site and modeling for corresponding dilation angles. Therefore, these data have been employed to estimate the effect of pit diameter on DPT (DPL type) results for both soils.

In addition of the values obtained from pit bottom, it the q_d values in the standard state are needed as well (it means that the test is continuously done from ground level); then, we can model DPT for both cases (pit bottom and standard state) in similar conditions.

Table 8 shows q_d values obtained from numerical modeling in both states mentioned above.

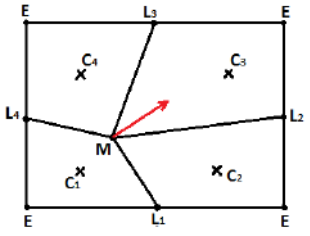

Figure 5. The VS approach used in modeling

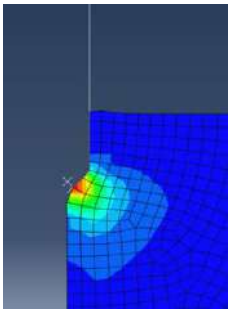

Figure 6. The penetration of cone in soil

TABLE 6. The q_d values versus ψ for soils

ψ(°)	$q_d(MPa)$	
	Silty sand	**Clay**
0	4.2	1.6
1	4.6	-
5	6.1	-
7	-	2.3
9	-	2.5

TABLE 7. The q_d values obtained in the modeling and the site

Soil type	ψ (°)	$q_d(Mpa)$	
		In the modeling	**In the site**
Silty sand	0	4.2	4.26
Clay	9	2.5	2.56

TABLE 8. The q_d values obtained at the case of testing in pit bottom and standard state

Soil type	$q_d(Mpa)$		**Difference (%)**
	In pit bottom	**In standard state**	
Silty sand	4.2	6.5	35
Clay	2.5	3.2	22

Figures 7 and 8 show the process of achieving q_d at the penetration depth (d_p) of about 20 *cm* in both the pit bottom and standard state for silty sand and clay soil.

To estimate the depth effect of DPL in both soils, in addition to the test modeling in depth of 10 *m* which was mentioned before, the modeling has been performed for depths of 2, 4, 6 and 8 *m* in both cases (pit bottom and standard state) and both soils.

As is shown in Figures 9 and 10, by increasing the depth of the test, which is followed by increasing the overburden pressure, the values of q_d increase. However,

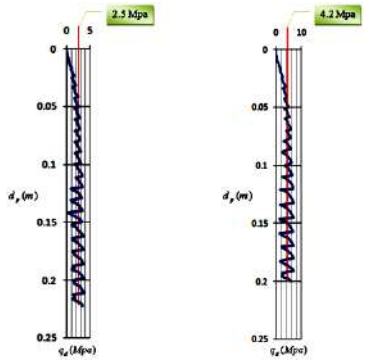

Figure 7. The q_d value for clay (Left) and silty sand (Right), in pit bottom

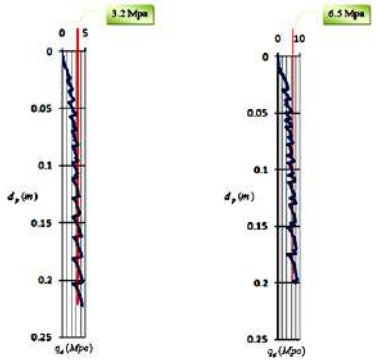

Figure 8. The q_d value for clay (Left) and silty sand (Right), in standard state

it should be noted that this increase is not linear, and in the higher depths, this increment is decreasing. It is also possible to obtain the relationship between the depth of the test (H_{dpl}) and the q_d values by fitting a second-degree curve for both soil types (Equations (7) to (10)).

In the following, Equations (8) and (9) render the values of q_d in terms of the depth of the test, at the pit bottom and the standard state for silty sand soil, respectively:

$$q_d = -0.03H_{DPL}^2 + 0.714H_{DPL} (R^2 = 0.999) \quad (8)$$

$$q_d = -0.062H_{DPL}^2 + 1.260H_{DPL} (R^2 = 0.996) \quad (9)$$

Similarly, the values of q_d are obtained using Equations (10) and (11) in terms of the depth of the test for clay soil:

$$q_d = -0.023H_{DPL}^2 + 0.48H_{DPL} (R^2 = 0.998) \quad (10)$$

$$q_d = -0.03H_{DPL}^2 + 0.621H_{DPL} (R^2 = 0.998) \quad (11)$$

As is clear, the fitted curves have a very good agreement with q_d values obtained from DPL test for both soils types in the pit bottom and standard state. In such way that the regression coefficient (R^2) is close to 1 for all equations. In addition, as shown in Figures 9 and 10, the difference in q_d values are significantly larger for silty sand in compare to clay soil. This is due to the lack of cohesion in silty sand.

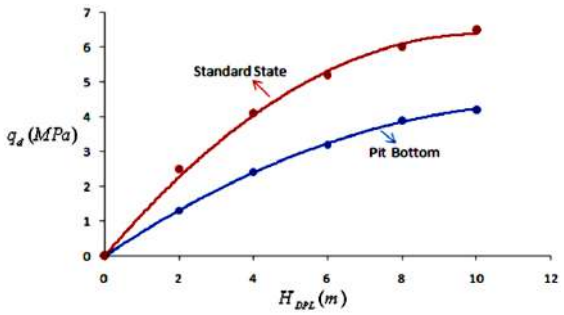

Figure 9. The relation of q_d values and H_{dpl} in pit bottom and standard state, for silty sand

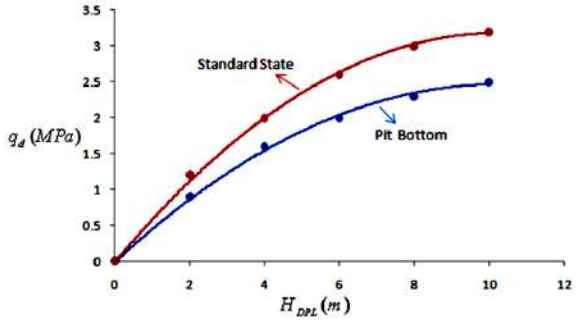

Figure 10. The relation of q_d values and H_{dpl} in pit bottom and standard state, for clay

Another point is that the q_d values on silty sand are higher than the q_d values of the clay soil in both standard state and pit bottom, due to. to the internal friction angle of the soil. In silty sand, although there is no cohesion, its internal friction angle is greater than the clay soil. Therefore, the q_d values of the silty sand are more.

5. CONCLUSION

It was found that by using values obtained from the numerical modeling via Abaqus, it presents an accurate calibration of q_d values for the results performed from DPT (DPL type) in pit bottom (diameter of 1 m and 10 m depth) for silty sand and clay soil in the sites mentioned. The values of q_d in pit bottom are smaller than the standard state case, which means the penetration of the cone is simpler in the former case. Furthermore, the differences of q_d values between pit bottom case (diameter of 1 m and 10 m depth) and the case where test is continuously done from the ground level (standard state) are calculated to be 35 and 22 percent for silty sand and clay soils, respectively. Therefore, cohesion in clay causes the soil particles to be held together. As a result, it causes the difference in q_d values of the pit being smaller than the standard state. However, this difference is higher in sandy soil due to lack of cohesion.

The internal friction angle has a more important role than cohesion to increase the q_d values. Nevertheless, cohesion plays a more important role than internal friction angle to decrease the q_d values in both the standard state and pi bottom.

Finally, a set of second-degree equations for the q_d values have been obtained. These equations had the best fit with the q_d values. It is found that q_d increases by increasing the depth of test, whereas the value of this increment decreases by increasing test depth. These results are true for both cases in both types of soils.

The main innovation of this work is that it is the first time a dynamic probing test is simulated with numerical modeling. In addition, since the DPT has been performed in the pit and the standard state of this test is from the ground level, so with the help of this method, it can be done at any depth of the ground. However, performing the DPT in the pit leads to easier penetration of the cone in the soil, and therefore the values obtained from this test in the pit in the desired depth are not real values. Therefore, using numerical modeling, the values in the site have been calibrated with the simulated values. Then, using the calibrated model, this time the simulation is carried out with the assumption of testing in the standard state and at the same depth. With the help of this method, in any depth, the test can be done and the obtained values can be modified using the numerical modeling and with the lowest possible errors.

6. REFERENCESS

1. Rejšek, K., Buchar, J., Vaníček, I., Hromádko, L., Vranová, V., and Marosz, K., "Results of dynamic penetration test-an indicator of the compaction of surface soil horizons by forestry machinery", ***Journal of Forest Science***, Vol. 57, No. 10, (2011), 439–450. https://doi.org/10.17221/4/2011-JFS
2. DIN 4094, "Dynamic and standard penetrometers, Part 1: Dimensions of apparatus and method of operation; Part 2: Application and evaluation", Deutsches Institut fur Normung, Berlin, (1980).
3. BS 1377, "British standard methods of test for soils; Part 9: In-situ tests", British Standards Institution, UK, (1990).
4. ASTM D6951 / D695 1M – 09, "Standard test method for use of the dynamic cone penetrometer in shallow pavement applications", American Society for Testing and Materials, Philadelphia, USA, (2015).
5. ISO 22476-2: 2005+A1, "Geotechnical investigation and testing -Field testing -Part 2: Dynamic probing", International Standardization Organization, (2011).
6. INSO 12305-2, "Geotechnical investigation and testing -Field testing -Part 2: Dynamic probing", Iranian National Standardization Organization, Iran (In Persian), (2014). View the download link
7. Ceccato, F., Beuth, L., Vermeer, P. A., and Simonini, P., "Two-phase Material Point Method applied to the study of cone penetration", ***Computers and Geotechnics***, Vol. 80, (2016), 440–452. https://doi.org/10.1016/j.compgeo.2016.03.003
8. Ciantia, M. O., Arroyo, M., Butlanska, J., and Gens, A., "DEM modelling of cone penetration tests in a double-porosity crushable granular material", ***Computers and Geotechnics***, Vol. 73, (2016), 109–127. https://doi.org/10.1016/j.compgeo.2015.12.001
9. Janda, A. and Ooi, J. Y., "DEM modeling of cone penetration and unconfined compression in cohesive solids", ***Powder Technology***, Vol. 293, (2016), 60–68. https://doi.org/10.1016/j.powtec.2015.05.034
10. Suzuki, Y. and Lehane, B. M., "Analysis of CPT end resistance at variable penetration rates using the spherical cavity expansion method in normally consolidated soils", ***Computers and Geotechnics***, Vol. 69, (2015), 141–152. https://doi.org/10.1016/j.compgeo.2015.04.019
11. Kouretzis, G. P., Sheng, D., and Wang, D., "Numerical simulation of cone penetration testing using a new critical state constitutive model for sand", ***Computers and Geotechnics***, Vol. 56, (2014), 50–60. https://doi.org/10.1016/j.compgeo.2013.11.002
12. Lin, C., Tu, F., Ling, D., and Hu C., "FEM-DEM coupled modeling of cone penetration tests in lunar soil", ***Journal of***

Central South University, Vol. 25, No. 2, (2018), 392–405. https://doi.org/10.1007/s11771-018-3745-4

13. Ahmadi, M. M. and Golestani Dariani, A. A., "Cone penetration test in sand: A numerical-analytical approach", ***Computers and Geotechnics***, Vol. 90, (2017), 176–189. https://doi.org/10.1016/j.compgeo.2017.06.010
14. Khodaparast, M., Rajabi, A. M., and Mohammadi, M., "The new empirical formula based on dynamic probing test results in fine cohesive soils", ***International Journal of Civil Engineering***, Vol. 13, No. 2B, (2015), 105–113. http://dx.doi.org/10.22068/IJCE.13.2.105
15. Lee, C., Kim, K. S., Woo, W., and Lee, W., "Soil Stiffness Gauge (SSG) and Dynamic Cone Penetrometer (DCP) tests for estimating engineering properties of weathered sandy soils in Korea", ***Journal of Engineering Geology***, Vol. 169, (2014), 91–99. https://doi.org/10.1016/j.enggeo.2013.11.010
16. Fakher, A., Khodaparast, M., and Jones, C. J. F. P., "The use of the Mackintosh Probe for site investigation in soft soils", ***Quarterly Journal of Engineering Geology and Hydrogeology***, Vol. 39, No. 2, (2006), 189–196. https://doi.org/10.1144/1470-9236-05-039
17. Gholami, A., Palassi, M., and Fakher, A., "Assessment of the Effect of Skin Friction on the Results of Dynamic Penetration Testing in Cohesionless Soil", ***Iranian Journal of Science and Technology - Transactions of Civil Engineering***, Vol. 44, No. 2, (2020), 715–721. https://doi.org/10.1007/s40996-019-00286-8
18. Rollins, K. M., Amoroso, S., Milana, G., Minarelli, L., Vassallo, M., and Di Giulio, G., "Gravel Liquefaction Assessment Using the Dynamic Cone Penetration Test Based on Field Performance from the 1976 Friuli Earthquake", ***Journal of Geotechnical and Geoenvironmental Engineering***, Vol. 146, No. 6, (2020), 1-14. https://doi.org/10.1061/(ASCE)GT.1943-5606.0002252
19. Butcher, A. P., Mcelmeel, K., Powel, J. J. M., "Dynamic probing and its use in clay soils", In: Advances in site investigation practice, Thomas Telford Publishing. (1995), 383-395.
20. Mesri, G. and Hayat, T. M., "The coefficient of earth pressure at rest", ***Canadian Geotechnical Journal***, Vol. 30, No. 4, (1993), 647–666. https://doi.org/10.1139/t93-056
21. Abaqus, Ver. 6.11, Providence, Dassault Systèmes Simulia Corp, RI, USA, (2011).
22. Drucker, D.C. and Prager, W., Soil mechanics and plastic analysis for limit design", ***Quarterly of Applied Mathematics***, Vol. 10, (1952), 157-165. https://doi.org/10.1090/qam/48291
23. Chen, W. and Saleeb, A., "Constitutive equations for engineering materials, Vol. 1: Elasticity and modeling". John Wiley & Sons, New York, (1982).
24. Budhu, M., Soil mechanics and foundations., John Wiley & Sons, New York, (2010).

Persian Abstract

چکیده

گمانه‌های دستی (چاه‌ها) در ایران نسبت به سایر کشورها رایج‌ترند. همچنین، اخیراً در ایران، استفاده از آزمون کاوشگردینامیکی در این گمانه ها به طور قابل توجهی توسعه یافته است. این در حالی است حالت استاندارد انجام این آزمایش از سطح زمین می باشد. در این مقاله، آزمون کاوشگر دینامیکی در دو چاه مشابه با قطر۱ متر و عمق ۱۰ متر در دو منطقه از شهر قم در ایران که یکی دارای خاک ماسه‌ای لای‌دار و دیگری رسی است، انجام شده است. سپس هر دو آزمون با استفاده از نرم‌افزار آباکوس شبیه‌سازی و نتایج به‌دست‌آمده از شبیه‌سازی با مقادیر به‌دست آمده از ساختگاه‌های ذکر شده مقایسه و کالیبره شده است. نتایج هم‌خوانی خوبی بین مقادیر به‌دست آمده از شبیه‌سازی و آزمون‌های انجام شده در ساختگاه‌ها را نشان می‌دهد. پس از کالیبره کردن مقادیر شبیه‌سازی شده با مقادیر به‌دست آمده از ساختگاه، این بار شبیه‌سازی را برای حالت استاندارد (به معنای انجام آزمایش به‌طور پیوسته از سطح زمین یا با فرض نبود چاه) در همان عمق ۱۰ متر و برای هر دو ناحیه و با مشخصات خاک‌های مذکور انجام می‌دهیم. نتایج به ترتیب، اختلاف ۳۵ و ۲۲ درصدی مقادیر مقاومت دینامیکی نوک مخروط به دست آمده از انجام آزمون کاوش‌گر دینامیکی در گمانه‌ی دستی با مقادیر به‌دست آمده در حالت استاندارد، برای خاک ماسه‌ای سیلتی و رسی را نشان می‌دهند. در نهایت با استفاده از شبیه‌سازی روابطی بین عمق انجام آزمون و مقاومت دینامیکی نوک مخروط برای هر دو حالت مذکور و هر دو نوع خاک مورد مطالعه، ارائه شده است.

International Journal of Engineering

Journal Homepage: www.ije.ir

Investigation of Wear Behavior of Biopolymers for Total Knee Replacements Through Invitro Experimentation

Y. Sandeep Kumar*, K. V. S. Rajeswara Rao, Y. Sunil R.

Department of Industrial Engineering and Management, Rashtreeya Vidyalaya College of Engineering, Bengaluru, India

P A P E R I N F O

Paper history:
Received 07 April 2020
Received in revised form 21 April 2020
Accepted 12 June 2020

Keywords:
Ti6Al4V
Polyether Ether Ketone
Ultra High Molecular Weight Poly Ethylene
Additive Manufacturing
Scanning Electron Microscopy
Analysis Of Variance

A B S T R A C T

The average life span of knee prosthesis used in Total Knee Replacement (TKR) is approximately 10 to 15 years. Literature indicates that the reasons for implant failures include wear, infection, instability, and stiffness. However, the majority of failures are due to wear and tear of the prosthesis. The most common biopolymer used in TKR is Ultra High Molecular Weight Polyethylene (UHMWPE). Prevailing research reports that implants are restrained by tiny UHMWPE debris generated by long term friction between the femoral component and polyethylene articulating surface. This necessitates an alternative material with high wear-resistance to reduce the wear rate. Polyether ether ketone (PEEK) is one of the biopolymers expected to possess better mechanical properties and biocompatibility with surrounding tissue and hence can be suitable for orthopedic applications. In this regard, a study on UHMWPE and PEEK biopolymers was carried out and tribological behavior was examined. The effect of process parameters such as normal load and speed on the tribological performance of biopolymers were evaluated. The experiment plan was designed as per Taguchi's Design of Experiments methodology. An empirical relation between wear and process parameters was established using linear regression analysis. Microanalysis and failure analysis of worn-out surfaces of both the biopolymers was carried out using Scanning Electron Microscopy(SEM). Results exhibit that UHMWPE had deep grooves as compared to finer grooves on PEEK indicating a low wear rate in the latter. This was also supported by the experimental results suggesting PEEK as a suitable alternative biopolymer for TKR.

***doi**: 10.5829/ije.2020.33.08b.14*

1. INTRODUCTION

The reduction of knee implant failures is the main concern for the orthopaedics. The reasons behind the failure of the prosthesis in Total Knee Replacement (TKR) include instability due to improper fixation and wear between the femoral component and tibia insert. These two factors are the major issues to focus on orthopaedic research. The proper fixation of knee prosthesis can be possible by modelling the patient-specific implants using medical image processing from Computerized axial Tomography/Magnetic Resonance Imaging [1, 2]. Another factor, which affects the failure of the prosthesis, is the generation of wear particles from biopolymers into the adjacent tissue. This is the major focus of ongoing research. The formation of wear particles depends on multiple factors including sliding distance, contact pressure, lubricating effect, the surface roughness of implant, and friction factor between the mating components. The friction factor for different biomaterials that are in contact can vary from 0.05 to 0.16. Literature reports that Ultra High Molecular Weight Poly Ethylene (UHMWPE) had maximum wear against Ti6Al4V [3].

The average life span of UHMWPE is 7.8 years with linear wear of 3.8 μm/year. To reduce the wear rate and improve the longevity of the implant, the alternative bearing materials have been introduced. In the 1990s, Polyetheretherketone (PEEK) and its carbon fiber composites were also introduced as a bearing material for TKR [4] but the results were unsatisfactory. A

*Corresponding Author Email: *ssandeep539@gmail.com* (Y. Sandeep Kumar)

Please cite this article as: Y. Sandeep Kumar, K. V. S. Rajeswara Rao, Y. Sunil R., Investigation of Wear Behavior of Biopolymers for Total Knee Replacements Through Invitro Experimentation, International Journal of Engineering (IJE), IJE TRANSACTIONS B: Applications Vol. 33, No. 8, (August 2020) 1560-1566

similar type of study was conducted with a combination of UHMWPE and carbon fiber, resulted in the enhancement of tribological wear performance. But, the biological tissue response was unsatisfactory [5 – 6]. This drawback made polymer composites non-biocompatible. The selected material for TKR surgery requires exposure to good wear resistance including biocompatibility.

Another way of reducing the wear rate is the application of lubricant. The tibia and femoral joints are enclosed with a synovial fluid which serves as a lubricant. The wear behaviour under the lubricating condition of synovial fluid was studied [7]. The different concentrations of Human Serum Albumin (HSA), Immunoglobulin G (IgG), and Dipalmitoylphosphatidylcholine (DPPC) of lubricating medium were investigated. The results showed minimization of wear rate by changing the additives in the lubricant. The amount of wear rate can be found by a suitable experimental setup as per the American Society for Testing and Materials (ASTM) standards. Several studies have been conducted to evaluate the wear rate of biopolymers for TKR. The results of a pin on disc study have been used for many years to evaluate wear characteristics [8]. It is observed that wear is increased by increasing the contact pressure in a lubricating medium. This contact pressure could be taken as the equivalent of the patient weight.

The statistical methods are applied in most of the fields that involve decision making. These methods play an important role in predicting the wear rate of polymers by modelling the suitable regression equation. Different process parameters are influencing the wear rate [9-12]. Analysis of variance (ANOVA) can investigate the relationship between several factors like process parameters which influence the dependant variable [13-15].

This research work involves investigating the wear rate of biopolymers in artificial knee implants. For this purpose, the pin on disc tribometer has been used with different operating conditions. The design of experiments is conducted as per Taguchi design and the process parameters are optimized.

2. MATERIALS AND METHODS

The different stages adopted for investigating wear characteristics of biomaterials are divided into preparation and characterization of biomaterials, evaluation of tribological behavior of biomaterials by a pin on disc, optimizing and developing regression equation by using ANOVA.

2. 1. Specimen Preparation The steps involved in the preparation of experimental specimens are detailed.

2. 1. 1. Additive Manufacturing Additive manufacturing is a process of building a part by adding a successive layer of the material rather than subtracting the material [16]. In this technique, there is no wastage of material compared with conventional manufacturing techniques. Figure 1 shows the flowsheet for optimization of wear rate.

The reason for adopting this technology is because the melting point temperature of Ti6Al4V is 1604^{O}C – 1660^{O}C and it is not possible to create a part by conventional manufacturing methods. Also, the present research is mainly focusing on the patient-specific knee implants, which are produced from the Magnetic Resonance Imaging (MRI) data. These MRI datasets could be converted into the specific 3-Dimensional model of the knee by using medical image processing software by generating Standard Tessellation Language (STL) files [17].

This layered manufacturing is divided into liquid, powder, and solid form, depending on the build material. In the present research, the print material Ti6Al4V is taken in the form of powder. So the suitable method should be taken for conversion of metal powder into desired 3D parts. In this regard, Direct Laser Metal Sintering (DMLS) was considered. In this technique, the

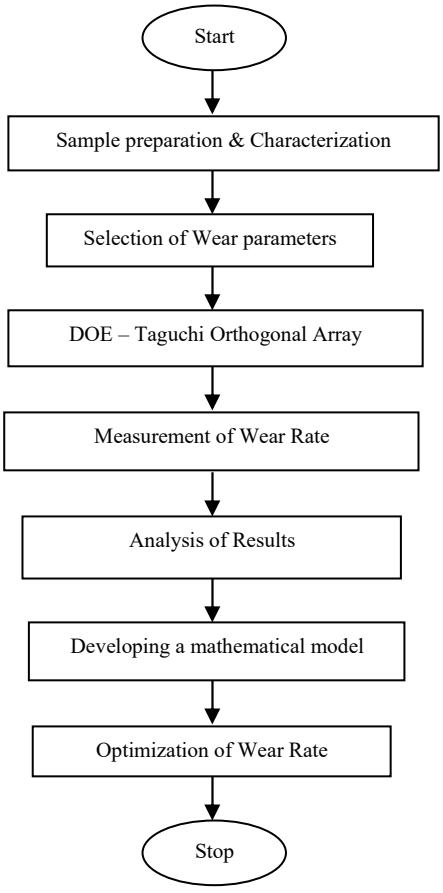

Figure 1. Flow chart for optimization of wear rate

power source was used in the form of laser to sinter the Ti6Al4V powder.

Figure 2 shows the formation of layers to build the model by rotating the roller. The closed chamber was used to control the entire process. However, the drawback of this method is oxidation; to minimize this nitrogen gas is filled in this chamber. The biodegradable metals like Ti6Al4v, CoCr, stainless steel and Ni based alloys etc. are used as build materials by this method.

The most common biomaterials which are used for the total knee replacement are Ti6Al4V and CoCrMo [18]. In the current research Ti6Al4V, powder particles are taken with the chemical composition of 90% of titanium, 6% of aluminium, and 4% of vanadium. The samples are prepared by using DMLS technology in the form of a 30 mm diameter and 10 mm thickness.

2. 1. 2. Blasting In general, the surface modification of a specimen can be done by the normal machining methods. By using this method, there may be a chance of changing the surface composition and the implant biocompatibility. Blasting is one of the techniques to reduce these surface contaminants. The abrasive particles like ceramics are used to minimize the surface roughness under high pressure. The size of abrasive particles can affect surface roughness. The surface roughness of samples can be set up as per the ASTM G75 test standards and the required R_a value of the implant. Biocompatibility is another factor to be considered when selecting the abrasive particles [20]. Figure 3 shows the PEEK specimens and chemical structure of PEEK.

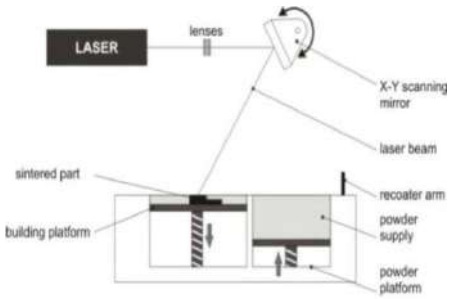

Figure 2. DMLS Technology

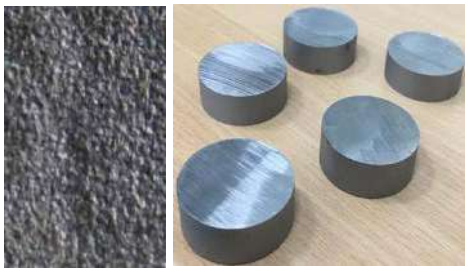

Figure 3. Ti6Al4V samples (a) before and (b) after blasting technique

2. 2. Experimental Details The prosthesis used in TKR consists of a femoral component, tibial tray, and tibial insert, which are made from CoCr alloy, titanium alloy, and UHMWPE respectively shown in Table 1. The mechanism that is observed in the knee joint, the femoral component and tibial tray are fixed rigidly whereas the tibial insert is mating with the femoral component. If these two components mesh with each other, it leads to the loosening of the implants due to wear and tear resulting in failure of the prosthesis. The minimization of this drawback can be possible by understanding the wear mechanism of UHMWPE or replacing it with another biopolymer. To fulfil this objective, the experiments were conducted through a pin on disc friction and wear testing machine [21]. In the present research, the UHMWPE is replaced with PEEK biopolymer to investigate the wear behavior.

In the pin on disc tribometer, the PEEK specimens shown in Figure 4 (rectangular shape of 8 x 8 x 32 mm^3) are held stationary while a cyclic rotation was applied to the Ti6Al4V disc with 30 mm diameter and 10 mm thickness.

The standard orthogonal arrays for three levels and two factors (3x2) design are L9, L18, and L27. In this present research, nine experiments are sufficient to optimize the parameters according to the Taguchi method. Each process parameter has three levels namely low (1 m/sec speed, 20 Kg weight), medium (2 m/sec, 40 Kg) and high (3 m/sec, 60 Kg) respectively. The wear rate was investigated through experimentation under dry and atmospheric condition in DUCOM pin on disc instrument as shown in Figure 5. This instrument is capable of measuring wear rate from 0µm to 2000µm with a least count of 1µm, and friction force from 0 N to 200 N with a least count of 0.1 N.

To explore the effect of normal load on the wear rate of biomaterials, the three values of normal forces 20 N, 40 N, and 60 N were considered. After completion of each test, the volume loss was calculated based on the difference between initial and final weight. The output values of wear and friction values are continuously stored with concerning test time.

TABLE 1. Properties of biomaterials [22-25]

Property of Material	Ti6Al4V	PEEK	UHMWPE
Modulus of Elasticity (GPa)	113	3.6	0.5
Poisons Ratio	0.34	0.37	0.42
Tensile Strength (MPa)	950	97	35
Density (kg/m^3)	4430	1320	970
Melting Point (^OC)	1600	340	137

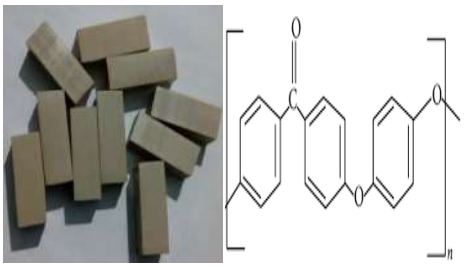

Figure 4. (a) PEEK specimens (b) chemical structure of PEEK

Figure 5. Pin on Disc experimental setup

3. RESULTS AND DISCUSSIONS

3. 1. Wear and Friction Behavior The major focus in orthopedic knee replacement research is to reduce the wear rate of polyethylene articulating surface. The generation of wear debris is the primary source of implant degradation and it leads to loosening of the patient implant. In the majority of cases, revision surgery is necessary due to this drawback.

In this study, the wear rate of different biopolymers has been investigated to minimize the revision surgery. Tables 2 gives clear information about the wear behavior of UHMWPE and PEEK. The amount of wear rate is calculated by measuring volume loss (∇v) from Equation (1).

$$\text{Wear Rate} = \frac{\nabla V}{W \times L} \quad (1)$$

where ∇V = Volume loss in mm^3
W = Normal load in N
L = Sliding distance in m

The linear wear rate was monitored using a LVDT (Linear Variable Differential Transducer) which is displayed on the controller. The generation of a graphical plot for wear and friction behaviour results are shown in Figures 6 and 7. These plots for both PEEK and UHMWPE were drawn for different loads concerning time variation of 0.064 sec.

3. 2. Sample Characterization The investigation of different phases presented in ti6al4v, uhmwpe and peek, the combination of x-ray diffraction and scanning electron microscopy characterization techniques were used [26]. To characterize the wear behaviour of these biopolymer surfaces, sem analysis of warn out surfaces was done. Figures 8 and 9 show typical micrographs for low and high wear out surfaces for these two polymer specimens respectively.

The worn out surfaces of the UHMWPE shown in Figure 8 reflects the high wear rate due to its deep grooves, whereas SEM images of PEEK shown in Figure 9 indicates the low wear rate due to its finer grooves.

3. 3. Taguchi Method To obtain optimum results with a minimum number of experiments, the Taguchi method is employed to design the experiments for the investigation of wear rate. Taguchi proposed the experimental designs which involve the usage of Orthogonal Array (OA) to organize the factors affecting the process to complete the experiments with a minimum number of trials which reduces time, money, and resources [27].

TABLE 2. L9 orthogonal array with wear rate

S.No	Load (Kg)	Speed (m/s)	PEEK			UHMWPE		
			Volume Loss	Wear Rate	S/N Ratio	Volume Loss	Wear Rate	S/N Ratio
1	20	1	0.151515152	7.57576E-06	102.411	0.322580645	1.6129E-05	98.848
2	40	1	0.151515152	3.78788E-06	**108.432**	0.430107527	1.07527E-05	99.373
3	60	1	0.454545455	7.57576E-06	102.411	0.322580645	5.37634E-06	**105.39**
4	20	2	0.227272727	1.13636E-05	98.890	0.430107527	2.15054E-05	93.349
5	40	2	0.227272727	5.68182E-06	104.910	0.430107527	1.07527E-05	99.370
6	60	2	0.454545455	7.57576E-06	102.411	1.075268817	1.79211E-05	94.933
7	20	3	0.303030303	1.51515E-05	96.391	0.322580645	1.6129E-05	95.848
8	40	3	0.378787879	9.4697E-06	100.473	0.537634409	1.34409E-05	97.431
9	60	3	0.378787879	6.31313E-06	103.995	0.322580645	1.79211E-05	94.933

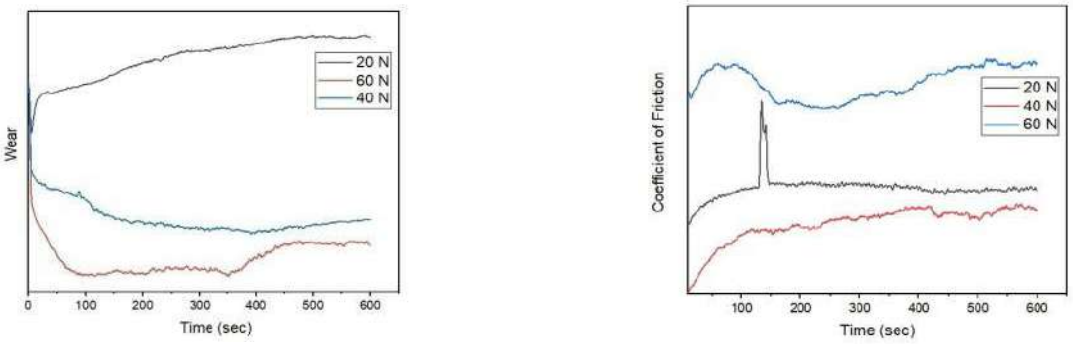

(a) (b)

Figure 6. (a) wear behaviour (b) friction coefficient for different loading conditions for PEEK material

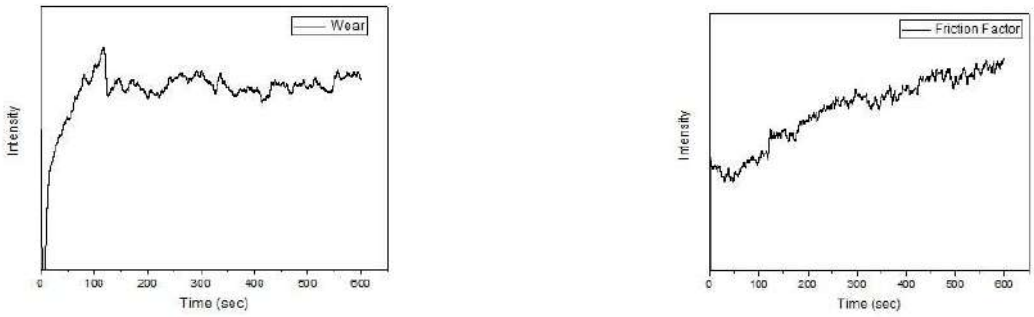

(a) (b)

Figure 7. Variation of (a) wear rate (b) friction coefficient on time for UHMWPE material

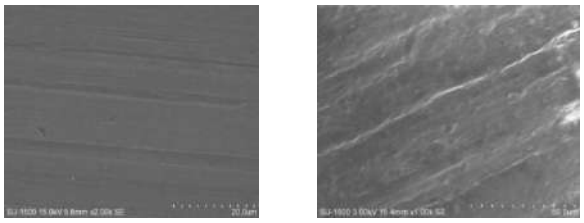

(a) (b)

Figure 8. (a) Scanning electron micrographs of UHMWPE specimen with low and (b) High wear rate

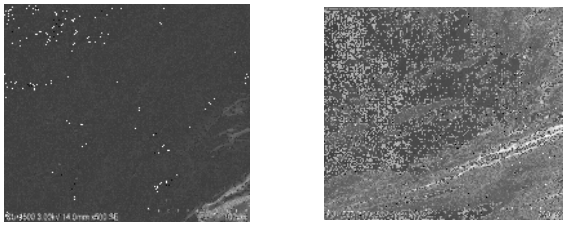

(a) (b)

Figure 9. (a) Scanning electron micrographs of PEEK specimen with low and (b) High wear rate

3. 4. S/N (Signal to Noise) Ratio The S/N ratio was used to find the sensitivity of process parameters affecting the wear rate. The main focus of this research is to minimize the wear rate of a biopolymer, hence it can enhance the life of the prosthesis. In this regard "Smaller–is–better" filter is applied. The S/N ratio's for different process conditions can be calculated by Equation (2).

$$= -10 \log_{10}\left(\frac{1}{n}\sum_{i=1}^{n} y_i^2\right)\frac{S}{N} \quad (2)$$

where n = no. of observations

The graphs are plotted under "smaller – the - better" condition to wear loss for both the cases and the same are shown in Figures 10 and 11 respectively.

3. 5. Regression Equation It is a widely used technique for prediction, forecasting the dependent

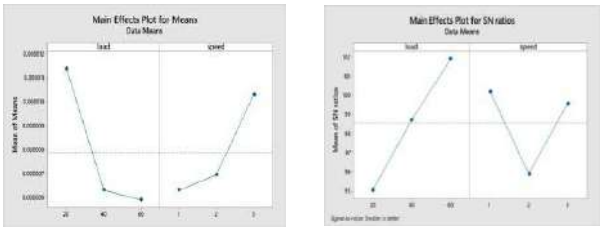

(a) (b)

Figure 10. Graphical representation of means and S/N Ratios of PEEK

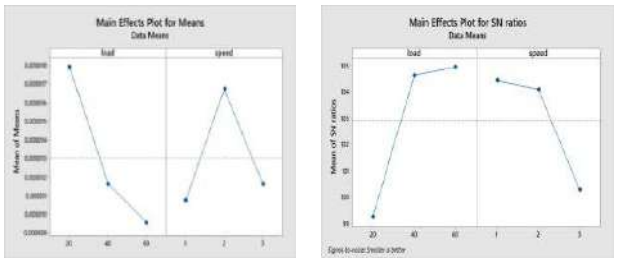

(a) (b)

Figure 11. Graphical representation of means and S/N Ratios of UHMWPE

variable [28]. The pin on disc instrument used for conducting wear tests is limited to 200N and 2000 rpm. The estimation beyond this range is difficult. In this regard, the regression equation (Equation (3)) is capable for prediction of wear rate.

$$\text{Wear Rate} = 0.000067 + 0.000004 \times \text{Normal Load} + 0.000067 \times \text{Speed} \quad (3)$$

4. CONCLUSIONS

The objective of this research is to propose an alternate material to UHMWPE that can have minimal wear rate and reduce the wear rate in a knee prosthesis. For this, a pin on disc tribometer was used. The effect of process parameters on wear performance was examined. The maximization of the S/N Ratio signifies the maximization of the desired effect i.e minimization of wear rate. Based on this study, an optimal combination of 40 kg load and 1 m/s speed for minimum wear rate of 3.78788E-06 with maximum S/N ratio 108.432db is suggested.

The linear regression equation helps in establishing the relation between process parameters and wear rate, which was beyond the scope of experimentation. Results indicate that PEEK is the best suitable material for TKR, as it exhibits a lesser wear rate compared to UHMWPE.

The present research is limited to the dry sliding condition only. The same methodology can also be carried out in a lubricating medium with synovial fluid as a lubricant. Surface modification of biopolymers can also be considered for further studies.

5. REFERENCES

1. Y Sandeep Kumar, Rajeswar Rao KVS, Sunil R Yalamalle, SM Venugopal, Sandeep Krishna. "Applications of 3D printing in TKR pre-surgical planning for design optimization–A case study". ***Proceedings of Elsevier Materials Today***, Vol. 5, (2018), 18833-18838. https://doi.org/10.1016/j.matpr.2018.06.230
2. Philipp Honigmann, Neha Sharma, Brando okola, Uwe Popp, Bilal Msallem, Florian M Thieringer. "Patient-specific surgical implants made of 3D printed PEEK: material", Technology, and Scope of Surgical Application, Hindawi BioMed Research International, (2018). https://doi.org/10.1155/2018/4520636
3. M Geetha, A.K Sigh, R Ashokamani, A.K Gogia. "Ti based biomaterials, the ultimate choice for orthopaedic implants – A review". ***Progress in Materials Science***, Vol. 54, (2009), 397-425. https://doi.org/10.1016/j.pmatsci.2008.06.004
4. L Brockett, S. Carbone, A.Abdelgained, J Fisher, L M Jennings. "Influence of contact pressure, cross shear and counterface material on the wear of PEEK and CFR-PEEK for orthopaedic applications". ***Journal of the Mechanical Behaviour of Biomedical Materials***, Vol. 63 (2016), 10-16. https://doi.org/10.1016/j.jmbbm.2016.06.005
5. Scholes. S, A. Unswarth. "Wear studies on the likely performance of CFR–PEEK/ CoCrMo for use as artificial joint bearing materials". ***Journal of Material Science, Materials in Medicine***, Vol. 20 (2009), 163-170. doi: 10.1007/s10856-008-3558-3
6. Ashley A Stratton powell, Kinga M pasko, Claire L Brockett, Joanne L Tipper. "The Biologic Response to PEEK wear particles in total joint replacements–A systematic review". ***Journal of clinical orthopaedics and related research***, Vol. 474 (2016), 2394-2404. doi: 10.1007/s11999-016-4976-z
7. Chen Ying Su, Shih shcean, Huanh, Hsu – weiFang. "Effect of major components of synovial fluid on the morphology and wear rate of polyether ether ketone particles under an accelerated wear process". ***MDPI Journal of polymers***, Vol. 10 (2018), 1-10. doi: 10.3390/polym10060635
8. H. Unal, A. Mimaroglu. "Friction and wear characteristics of PEEK and its composites under water lubrication**". *Journal of Reinforced plastic and composites***, Vol. 25, No. 16, (2014), 1659-1667. https://doi.org/10.1177/0731684406068406
9. Stephanie Hamilton, Patrica Munoz – Escalona. "Enhancement of wear properties of a polyetherether ketone polymer by incorporation of carbon and glass fibers". ***Journal of Applied Polymer Science***, Vol. 136, No. 22, (2019), 1-11. https://doi.org/10.1002/app.47587
10. S Y Gajjal, Aishwarya J Unkle, P S Gajjal. "Taguchi Technique for dry sliding wear behaviour of PEEK composite material". ***Proceedings of Elsevier Materials Today***, Vol. 5, (2018), 950-957. https://doi.org/10.1016/j.matpr.2017.11.170
11. Vesa Saikko. "In vitro wear simulation on Random POD wear testing system as a screening method for bearing materials intended for total knee arthroplasty". ***Journal of Biomechanics***, Vol. 5 (2014), 1-5. doi: 10.1016/j.jbiomech.2014.04.039.
12. SM Salehi, GH Ferrahi, S Sohrabpour "A Study on the Contact Ellipse and the Contact Pressure During the Wheel Wear through Passing the Tracks including Several Sharp Curves," ***International Journal of Engineering, Transactions B: Applications***, Vol. 31, No. 5, (2018), 826–833. doi: 10.5829/ije.2018.31.05b.19
13. Pruthvi serrao, Ravikanth prabhu, Chiranth B.P, Yazid Mohemmed. "Application of Taguchi method to predict the abrasive wear behaviour of CP titanium". ***Journal of Mechanical Engineering and Automation***, Vol. 6, (2016), 13-17. doi:10.5923/c.jmea.201601.03
14. H. Van Hoten, Gunawarman, I. Hari Mulyad, A. Kurniawan Mainil, P. Bismantolo, Nurbaiti "Parameters Optimization in Manufacturing Nanopowder Bioceramics of Eggshell with Pulverisette 6 Machine using Taguchi and ANOVA Method". ***International Journal of Engineering, Transactions A: Basics***, Vol. 31, No. 1, (2018), 45-49. doi: 10.5829/ije.2018.31.01a.07
15. E. C. Okafor, C. C. Ihueze, S. C. Nwigbo "Optimization of Hardness Strengths Response of Plantain Fibers Reinforced

Polyester Matrix Composites (PFRP) Applying Taguchi Robust Design". ***International Journal of Engineering, Transactions A: Basics***, Vol. 26, No. 1, (2013), 1-11. **doi:** 10.5829/idosi.ije.2013.26.01a.01

16. Kaufui V. Wong, Aldo Hernandez "A Review of Additive Manufacturing". ***International Scholarly Research Network***, Vol. 2012, 1-10. doi:10.5402/2012/208760
17. Y Sandeep Kumar**,** Rajeswar Rao KVS, Sunil R Yalamalle, S M Venugopal and Sandeep Krishna "Effect of slicing thickness and increment on the design of patient specific implant for total knee replacement(TKR) using Magnetic Resonance Imaging (MRI) – A case study". ***Springer "Smart Innovation, Systems and Technologies***, Vol. 169 (2020), 411-418. https://doi.org/10.1007/978-981-15-1616-0_40
18. Marjan Bahrami Nasb, Mohd Roshdi Hassan "Mettalic Biomaterials of knee and Hip–A Review". ***Trends in Biomaterials and Artificial Organs***, Vol. 24, No. 1, (2010), 69 - 82.
19. Caroline o Sullivan, Peter O Hare, Greg Byrne, Liam O Neil, Katie B Ryan and Abima M crean "A modified surface on Titanium deposited by a Blasting Process". ***Coatings***, Vol. 1, (2011), 53-71. doi:10.3390/coatings1010053
20. Pei-Bang Liao, Hsin-Chung Cheng, Chiung-Fang Huang, Yi Lin, Yung-Kang Shen, Yang-Ming Fan, Chang-Yu Lee, Chun-Wei Chang & Wei-Chiang Hung "The cell culture of titanium alloy surface modification by powder blasting and co blasting technique". ***Surface Engineering***, Vol. 35, (2019), 45-49. https://doi.org/10.1080/02670844.2019.1587570
21. E.M. Bortoleto, A.C. Rovani, V. Seriacopi, F.J. Profito, D.C. Zachariadis, I.F. Machado, A. Sinatora, R.M. Souza "Experimental and numerical analysis of dry contact in the pin on disc test". ***Wear***, Vol. 301, (2013), 19-26. https://doi.org/10.1016/j.wear.2012.12.005
22. Z˙ aneta Anna Mierzejewska, Radovan Hudák, and Jarosław Sidun "Mechanical Properties and Microstructure of DMLS Ti6Al4V Alloy Dedicated to Biomedical Applications". ***Materials***, Vol. 12, No. 176, (2019), 1-17. doi:10.3390/ma12010176
23. H.K. Rafi, N.V. Karthik, Haijun Gong, Thomas L. Starr, and Brent E. Stucker "Microstructures and Mechanical Properties of Ti6Al4V Parts Fabricated by Selective Laser Melting and Electron Beam Melting". ***Journal of Materials Engineering and Performance***, Vol. 23, No. 12, (2013), 3872-3885. DOI: 10.1007/s11665-013-0658-0
24. Muzamil Hussain y , Rizwan Ali Naqvi y, Naseem Abbas, Shahzad Masood Khan, Saad Nawaz , Arif Hussain , Nida Zahra and Muhammad Waqas Khalid, Sohrabpour "Ultra-High-Molecular-Weight-Polyethylene (UHMWPE) as a Promising Polymer Material for Biomedical Applications: A Concise Review," ***MDPI Polymers***, Vol. 12, No. 323, (2020), 826-833. doi:10.3390/polym12020323
25. P.J. Rae a, E.N. Brown a, E.B. Orler "The mechanical properties of poly(ether-ether-ketone) (PEEK) with emphasis on the large compressive strain response," ***Science Direct Polymers***, Vol. 48 (2007), 598-615. doi:10.1016/j.polymer.2006.11.032
26. Saravanan I, ElayaPerumalA, Balasubramanian V "A study of frictional wear behavior of Ti6Al4V and UHMWPE hybrid composite on TiN surface for bio-medical applications" ***Tribology International*** Vol. 98, (2016), 179-189. http://dx.doi.org/10.1016/j.triboint.2016.02.030
27. VC U.varaja, N. Natarajan, " Optimization on Friction and Wear Process Parameters Using Taguchi Technique" ***International Journal of Engineering and Technology,*** Vol. 2 No. 4, (2012), 694-699. doi: 10.5829/ije.2018.31.01a.07
28. Narasimha reddy, P., Ahmed Naqash. J "Effect of alccofine on mechanical and durability index properties of green concrete" ***International Journal of Engineering, Transactions C: Aspects***, Vol. 32, No. 6, (2019), 813-819. doi: 10.5829/ije.2019.32.06c.03

Persian Abstract

چکیده

طول عمر پروتز زانو مورد استفاده در جایگزینی توتال زانو ((TKRتقریباً ۱۰ تا ۱۵ سال است. ادبیات نشان می دهد که دلایل خرابی کاشت شامل سایش، عفونت ، بی ثباتی و سفتی است. با این حال، اکثر خرابی ها ناشی از ساییدگی و پارگی پروتز است. متداول ترین بیوپلیمر مورد استفاده در TKR ، پلی اتیلن با وزن مولکولی فوق العاده بالا (UHMWPE) است. گزارشهای تحقیقاتی حاکم بر اینکه ایمپلنت ها توسط آوارهای کوچک UHMWPE ایجاد شده توسط اصطکاک طولانی مدت بین اجزای استخوان ران و سطح مفصلی پلی اتیلن مهار می شوند. این امر به یک ماده جایگزین با مقاومت بالا در برابر سایش برای کاهش میزان سایش نیاز دارد. کتون پلی اتر اتر (PEEK) یکی از بیوپلیمرهایی است که انتظار می رود دارای خواص مکانیکی بهتری و سازگاری زیست سازگار با بافت اطراف باشد و از این رو می تواند برای کاربردهای ارتوپدی مناسب باشد. در همین راستا، مطالعه ای در مورد بیوپلیمرهای UHMWPE و PEEK انجام شد و رفتار تریبولوژیکی مورد بررسی قرار گرفت. تأثیر پارامترهای فرآیند مانند بار و سرعت عادی بر عملکرد ترسیمی بیوپلیمرها مورد بررسی قرار گرفت. این طرح طبق روش طراحی آزمایشات تاگوچی طراحی شده است. رابطه تجربی بین پارامترهای سایش و فرآیند با استفاده از تحلیل رگرسیون خطی برقرار شد. میکروآنالیز و تجزیه و تحلیل شکست سطوح فرسوده هر دو بیوپلیمر با استفاده از میکروسکوپ الکترونی روبشی (SEM) انجام شد. نتایج نشان می دهد که UHMWPE دارای شیارهای عمیق نسبت به شیارهای ظریف تر در PEEK است که نشان دهنده میزان سایش کم در دومی است. این همچنین توسط نتایج تجربی نشان می دهد PEEK به عنوان یک بیوپلیمر جایگزین مناسب برای TKR پشتیبانی می شود.

IJE TRANSACTIONS B: Applications Vol. 33, No. 8, (August 2020) 1567-1578

International Journal of Engineering

Journal Homepage: www.ije.ir

An Extension to the Economic Production Quantity Problem with Deteriorating Products Considering Random Machine Breakdown and Stochastic Repair Time

L. Poursoltan, S. M. Seyedhosseini*, A. Jabbarzadeh

Department of Industrial Engineering, Iran University of Science and Technology, Narmak, Tehran, Iran

PAPER INFO

Paper history:
Received 09 April 2020
Received in revised form 03 May 2020
Accepted 01 June 2020

Keywords:
Economic Production Quantity
Inventory Deterioration
Machine Breakdown
Stochastic Repair Time
Partial Backordering

ABSTRACT

The recent advances in manufacturing systems motivate several studies to focus on Economic Production Quantity (EPQ) problem. Althuogh there are several extentions to the EPQ, this paper provides a new extension by considering some of the real world parameters like: (a) shortages in the form of partial backordering, (b) inventory can deteriorate stochastically, (c) machine can break down stochastically, and (d) machine repair time may change stochastically based on the failure status of machine. As far as we know, there is no study treated all these suppositions in an EPQ framework. In addition to this development, two forms of uniformly- and exponentially-distributed repair times are formulated and necessary convexity conditions are discussed. Then, the corresponding optimality conditions are written that lead to finding the roots of two equations. Due to difficulty of achieving a closed-form solution, the solution is obtained numerically by means of Newton-Raphson method. Finally, some sensitivity analyses are provided to explain the models' applicability. The practicality and efficiency of the proposed method in this context lends weight to development of proposed EPQ with more complex elements and its application more broadly.

doi: *10.5829/ije.2020.33.08b.15*

1. INTRODUCTION

Production management is a difficult job when a manager should simultaneously consider many conflicting parameters through his/her decision making [1]. There are many models in the literature that each of them cast into specific working conditions of the plant. Economic Production Quantity (EPQ) problem is well-studied that can be extended into the many different cases in reality. For example, there is no inventory deterioration in the basic EPQ model. But, it can be observed in many products in the forms of decay, spoilage, vaporization, obsolescence, etc. In more details, many kinds of food and volatile liquids have a natural deteriorate-prone characteristic.

At first, as one of earliest studies, Misra [2] in 1975 developed an EPQ model with deterioration consideration. He studied the model with the fixed and variable deterioration rates and derived an estimation of expression for the size of production lot. Then, in 1999, Kim and Hong [3] studied EPQ with random process of the deteriorating production. They presented three deterioration models. Next, in 2004, Samanta [4] presented a production inventory model with allowable backlogging, where the items deterioration time follow the exponential distribution function.

In a similar manner, Baten and Kamil [5] developed the model of a production inventory considering Pareto distribution. They assumed that the time of deterioration follows from a generalized Pareto distribution with three parameters. They also assumed that a firm has no shortage and demand rate varies with time. In that model Pontryagin maximum principle is used to obtain an explicit solution under dealing with continuous review policy. In another integrated production-distribution system, Yang et. al., [6] did it for a deteriorating inventory item through a two-echelon supply chain with fixed deterioration rate. They derived the optimal

*Corresponding Author Email: *seyedhosseini@iust.ac.ir* (S. Seyedhosseini)

Please cite this article as: L. Poursoltan, S. M. Seyedhosseini, A. Jabbarzadeh, An Extension to the Economic Production Quantity Problem with Deteriorating Products Considering Random Machine Breakdown and Stochastic Repair Time, International Journal of Engineering (IJE), IJE TRANSACTIONS B: Applications Vol. 33, No. 8, (August 2020) 1567-1578

solution based on an algebraic method for the case that deteriorating rate is very small.

Another realistic working condition is that there is partial backlogging instead of two extremes of lost sales and backlogs. This means that β% of shortages are to be satisfied in the future and (1-β)% of the shortages can be considered as lost sales. In another word, in real-world concepts, a percentage of customers is selected to wait for backlogging until next replenishment. This backlogging rate depends on waiting time diminished the waiting time length. Up to our knowledge, Mak [7] proposed partial backorder and formulated a model for a production-inventory system. During each period, the demand is partially backlogged and the items are replenished by assuming a uniform rate. He supposed that the willingness for a customer waiting for backorder during the period of shortage is declining regarding the waiting time length. Later, Balkhi [8] proposed an inventory-production system considering deterioration and learning effect with allowable partial backorders. Next, Lo et. al., [9] introduced a new integration of production and inventory model considering the Weibull distribution deteriorating items under partial backlogging and imperfect production process. Then, as mentioned above, Yang et. al., [6] extended the inventory models considering deteriorating items along with partial backlogging in an inventory lot-size model.

On the other hand, machine unavailability is an inevitable phenomenon in many production industries that is the result of three main things; preventive maintenance, corrective maintenance and machine suddenly breakdown. There are some studies in literature in which the machine unavailability has been explored. For example, Cheung and Hausman [10] introduced an unreliable production system to illustrate a balance between the costs of safety stock and preventive maintenance. They considered the time to failure by Weibull and Gamma distributions and solved it with exponentially and constant repair time. Independently, Abboud [11] considered a production-inventory system considering exponential machine breakdown and general machine repairing time. They supposed that no backordering is allowed.

Later, Arreola-Risa et al. [12] studied an inventory problem. They assumed that the supply of the products was arbitrarily disrupted with regrads to the random duration periods. They entered partial backorder and lost sales in to their proposed model. In a different research, Giri et al. [13] proposed two mathematical models for EPQ problem with unreliable production and maintenance cost. The main difference of their research was the consideration of the production rate as a decision variable. Afterward, Chakraborty et al. [14] introduced an EPQ considering machine breakdown and deterioration. They considered preventive and corrective maintenance, simultaneously. The same authors [15] one year later, proposed an integration of production, inventory and maintenance activities in a manufacturing system to study the joint impacts of inspections, machine breakdown and process deterioration on the decisions of the optimal lot sizing.

From the last decade, several studies have focused on various modifications and improvements of EPQ with regards to uncertain parameters. In 2010, Widyadana and Wee [16] studied an EPQ to deteriorate the items with stochastic repair time and machine breakdown. They determined the production time and the lost sales, optimality. They added a deteriorating product item and price dependent demand in to their model. They proposed two models with uniform and exponential distributions for machine repair time. Because of the complexity of the given problem a Genetic algorithm (GA) is employed to address it optimally. The same authors [17] one year later, extended their paper by using an optimization technique to derive an optimal solution but for the case of constant and non-price dependent demand rate. In the same way, in 2011, Chung et al. [18] expanded the work of Widyadana and Wee [17]. They assumed that the lost sales takes place when an urgent need is requested by the buyer who cannot wait for the next replenishment. They considered the backorder taking the place when the buyer can wait for the next replenishment. In 2012, for a production system, Chiu et al. [19] obtained the optimal replenishment run time considering failure for reworking and machine breakdown. They studied the effect of Poisson breakdown on the replenishment run time.

Furthermore, Taleizadeh et al. [20] suggested a multi-product single-machine inventory-production model with production capacity and service level limitation while considering partial backlogging. After that in 2013, Sarkar [21] developed a production-inventory model for a deteriorating item. He considered three types of statistical functions including the Uniform, Triangular, and Beta for deterioration. However, the shortage was not allowed. An algebraically solution is applied to find the minimum total cost of these models. Subsequently, Chang [22] extended the work of Sarkar and Sarker [23] by developing an improved solution method. They [23] presented an Economic Manufacture Quantity (EMQ) with deterioration consideration. They considered exponential demand and time varying the production rate. The Euler-Lagrange formula of control theory is used to derive the maximization procedure. Lastly, the same authos [24] developed an inventory model with regads to the diversification of the deteriorating items. They assumed that demand is stock-dependent and shortage is partial backlogging.

In 2014, Taleizadeh [25] contributed an Economic Order Quantity (EOQ) to evaporate the items with partial consecutive prepayments and backordering. They applied it to a real case of gasoline stations in Iran. Similarly, De et al., [26] considered an EOQ under

uncertainty based on the backlogged. In their problem, the demand of customers is varied by sold price of the items. In addition, the demand in stock out is changed by duration of the shortage in each period. The total cost is included by set up cost, promotional effort costs, shortage cost and the inventory costs. Khan et al., [27], developed an integrated supply chain model under the learning curve effects in the production process. Also in their investigation defective products occur due to human errors. They assumed multi delivery EPQ policy for the vendor and traditional EOQ policy for the buyer.

In 2015, De et al., [28] in another work proposed EOQ with intuitionistic fuzzy inventory model with the possibility of backlogging. They used the score functions with the non-membership and membership functions. In addition, Palanivel and Uthayakumar [29] proposed an extension to the EOQ with non-instantaneous items. They contributed the price and advertisement dependent demand pattern. These suppositions are under the inflation factor and time value over a finite planning horizon.

In 2016, Pal et al., [30] developed an EPQ improvement by an integration of supplier, manufacturer and retailer. They considered the joint economic lot-sizing approach by considering imperfect quality and uncertain demand. Their main difference was to consider the production of supplier i.e., the raw material sending to the manufacturer as the decision variable. In addition, Mohanty et al., [31] offered another EPQ which is a two-warehouse inventory system with regards to non-instantaneous deteriorating products under uncertainty. They considered the shotages combining partial backlog and lost sales.

In 2017, Chanda and Kumar [32] developed an EOQ problem considering a firm selling the technology of the products in a finite planning horizon. The demand was dynamic and uncertain ceiling on the potential adoptions. This factor is sensitive with regards to the unit selling price and advertising expenditure. Manna et al., [33] extended an EPQ model with allowable shortages. In their model, imperfect items are reworked or disposed of then to reduce the defective items, the learning effect is considered in the production process.

In 2018, Qiu et al., [34] introduced closed loop production rooting problem with remanufacturing and reverse logistics activities under the vender managed inventory contract. They provided a comparison of system costs concerning the different remanufacturing parameters. In addition, Marchi et al., [35] offered a two-level (vendor-buyer) supply chain models considering two coordinated policies: classical and vendor-managed inventory with consignment stock, where the objective is to find the values of the decision variables that yield the minimum total supply chain cost. It includes the costs of holding inventory, green emissions and tax, energy usage, product and process quality, and transportation operations. The decision variables are the order quantity, the number of shipments, and the production rate.

More recently in 2019, Marchi et al., [36] investigated the learning effect in energy efficiency which is an essential factor in many manufacturing companies. Therefore, they proposed a lot-sizing problem to illustrate the interaction between learning in production and energy efficiency directly and indirectly and also an appropriate decision about the lot size quantity. Walid et al., [37] applied the learning effects in the mean and variance of non-conforming items which considered as a random variable. Therefore, they decrease under the effect of the learning process. Finally, Chen et al., [38] considered a firm (e.g., retailer) selling a single nonperishable product over a finite-period planning horizon. At the beginning of each period, the firm determines its selling price and inventory replenishment quantity with the objective of maximizing total profit, but it knows neither the average demand (as a function of price) nor the distribution of demand uncertainty a prior; hence, it has to make pricing and ordering decisions based on observed demand data.

Based on the reviewed studies the essential parameters should be considered in this problem are: shortage, machine breakdown and its repair time and deterioration. Also considering the stochastic nature of these parameters is an essential necessity to close the model to a reality which makes the model applicable to every industrial production company which is neglected in many previous studies. Our paper is a continuation of Chung et al. [18] and Widyadana and Wee [17]. The main difference of our paper with them is to consider the shortage and inventory levels stochastically for the first time. Taken together, as far as we know and based on the aforementioned papers, this study provides an extension to the EPQ problem by considering the following assumptions:

(a) Shortages are in the form of partial backordering,
(b) Inventory can deteriorate stochastically,
(c) Machine can break down stochastically due to its past workload, lubrication, etc.
(d) Machine repair time may change stochastically based on the failure status of machine. Also, two cases of uniformly- and exponentially-distributed repair times are formulated and necessary convexity conditions are discussed. Remaining parts of this paper is organized as follows: notation and proposed mathematical model is presented in section 2, computational results and sensitivity analysis are discussed in section 3, and finally some concluding remarks and guides for future research are given in section 4.

2. PROBLEM FORMULATION

The statement of our proposed problem is defined as follows: Figure 1 illustrates the variations of inventory/

shortage level during a working cycle for the proposed inventory-production model. During production time T_1, machine breakdown occurs stochastically. If machine doesn't break down over time segment T_1, the inventory reaches to its maximum level (I_m). When machine breaks down, the production process is stopped and a corrective repair process is started, where the repair time of T_p is a stochastic variable. In addition, products deteriorate continuously. Since production deterioration, machine breakdown and machine repair time are stochastic, shortage may occur in terms of partial backorders. In the partial backordering, backorders may change to the lost sales, stochastically. This section first provides a general formulation for the problem. Then, two models will be developed for the special cases of uniformly and exponentially distributed repair times.

Based on the above description, the following assumptions are existed in this paper:

- A plant produces a single product with constant rates of production and consumption (i.e. demand), where production rate is greater than the demand rate.
- There isn't any inventory at the start and the end of a working cycle.
- Machine breakdown can occur such that the time between two consecutive breakdowns follows from exponential distribution with parameter μ.
- After each breakdown, the machine needs repair and/or maintenance. Also, machine repair time is a stochastic variable with known distribution function. Also it is assumed that the machine repair time is independent of the time between two machine breakdowns.
- A fixed fraction of the inventory deteriorates per time unit. In addition, no repair or replacement of the deteriorated inventory is required during the planning period.
- Inventory deterioration can be considered in both production and consumption time of each cycle.
- The production manager aims to minimize the total costs of inventory holding, setups, lost sales, backorders and partial backorders.

The problem can be formulated by means of the following parameters and variables:

Input parameters:	
D	Demand rate
P	Production rate
Θ	Deterioration rate
K	Setup cost
H	Unit inventory holding cost
Π	Unit lost sales cost
$\hat{\pi}$	Unit backorder cost
C	Unit deterioration cost
M	Repair cost of machine
β	Parameter of partial backorder
μ	Breakdown rate of machine

Variables:	
I_m	Maximum inventory level of a cycle
I_1	Inventory level in a production period of a cycle
I_2	Inventory level in non-production period of a cycle
I	Total number of inventories per cycle
R	Total number of deteriorated items per cycle
I_L	Lost sales level of a cycle
I_b	Backorder level of a cycle
T_1	Production period of a cycle
T_2	Non-production period of a cycle
T_3	Shortage period of a cycle
T_p	Machine breakdown period of a cycle

The initial general calculations based on Widyadana and Wee [17] can be reviewed as follows:

At first, T_2 and T_3 are derived based on T_1. Equations (1) and (2) represent the inventory levels in production and non-production periods, respectively:

$$\frac{dI_1(t_1)}{dt_1} + \theta I_1(t_1) = p - d \qquad 0 \le t_1 \le T_1 \qquad (1)$$

$$\frac{dI_2(t_2)}{dt_2} + \theta I_2(t_2) = -d \qquad 0 \le t_2 \le T_2 \qquad (2)$$

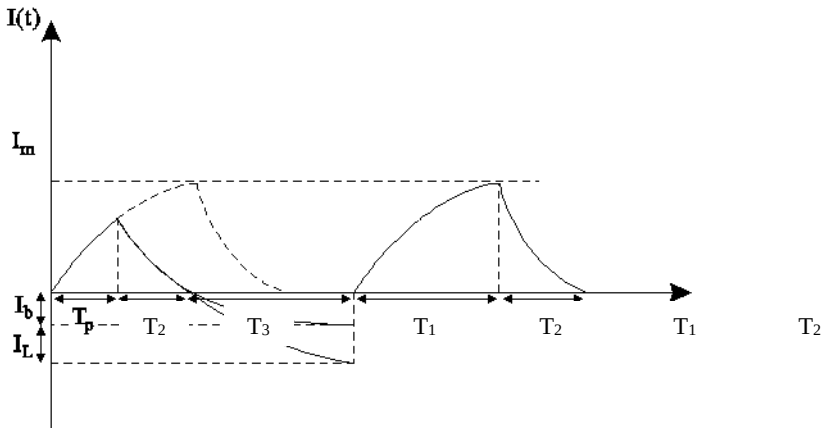

Figure 1. A working cycle of the studied inventory system

As shown in Figure 1, inventory level is zero at the end of T_2. So, inventory level in production and non-production periods can be formulated as follows:

$$I_1(T_1) = (\frac{p-d}{\theta})\left[1-e^{-\theta t_1}\right] \qquad 0 \le t_1 \le T_1 \qquad (3)$$

$$I_2(T_2) = \frac{d}{\theta}(e^{\theta(T_2-t_2)}-1) \qquad 0 \le t_2 \le T_2 \qquad (4)$$

At the top of inventory level, while t_1 equals to T_1 and t_2 is zero, I_1 (T_1) and I_2 (T_2) are equal. Then, we can write:

$$\frac{p-d}{\theta}(1-e^{-\theta T_1}) = \frac{d}{\theta}(e^{\theta T_2}-1) \qquad (5)$$

Further, ΘT can be approximated by means of Taylor expansion. Since the estimation error of the Taylor series is negligible after the third term, we can approximate ΘT as follows:

$$e^{\theta T} \approx 1+\theta T+\frac{\theta T^2}{2} \qquad (6)$$

According to Yang and Wee [39], the error of this estimation is lower than 0.2%. By replacing $e^{\theta T}$ approximation in Equation (5), the following equation is derived:

$$\frac{p-d}{\theta}(T_1-\frac{1}{2}\theta T_1^2) = \frac{d}{\theta}(T_2+\frac{1}{2}\theta T_2^2) \qquad (7)$$

Since θT_2 is a small value, $\theta {T_2}^2$ can be eliminated in Equation (7). Hence, T_2 can be approximated in terms of T_1 as:

$$T_2 \approx \frac{(p-d)T_1(1-\frac{1}{2}\theta T_1)}{d} \qquad (8)$$

Thus, the expected inventory level can be calculated as follows:

$$E\,(I) = \frac{(p-d)T_1^2}{2}+\frac{dT_2^2}{2} \qquad (9)$$

By replacing T_2 from Equation (8) into Equation (9), we have:

$$E\,(I) = p-d(\frac{T_1^2}{2})+d\left(\frac{(p-d)T_1(1-\frac{1}{2}\theta T_1)}{2d}\right)^2 \qquad (10)$$

Since θT_1 is very small, Equation (10) can be simplified as follows:

$$E\,(I) = \frac{p^2}{2d}(1-\frac{d}{p})T_1^2 \qquad (11)$$

Obviously, machine breakdown can affect on the expected inventory level. Since expected inventory level depends on machine breakdown period, Equation (11) is formulated as follows:

$$E\,(I) \cong \begin{cases} \frac{p^2}{2d}(1-\frac{d}{p})T_p^2 & T_p \le T_1 \\ \frac{p^2}{2d}(1-\frac{d}{p})T_1^2 & T_p > T_1 \end{cases} \qquad (12)$$

The distribution function of machine breakdown period is exponential with parameter μ. By getting the integral of the right hand side of Equation (12), the expected inventory level can be written as follows:

$$E\,(I) = \frac{p(p-d)(1-e^{-\mu T_1}-\mu T_1 e^{-\mu T_1})}{d\mu^2} \qquad (13)$$

According to Figure 1, the expected number of deteriorated items per cycle is:

$$E(R) = pT_1 - d(T_1+T_2) \qquad (14)$$

By substituting T_2 from Equation (8) into relation (14), the expected number of deteriorated items per cycle is:

$$E(R) = pT_1 - d\left(T_1+\frac{(p-d)T_1(1-\frac{1}{2}\theta T_1)}{d}\right) \qquad (15)$$

After simplifying Equation (15) and considering machine breakdown, the expected number of deteriorated items per cycle can be written as follows:

$$E\,(R) \cong \begin{cases} \frac{p}{2}(1-\frac{d}{p})\theta T_p^2 & T_p \le T_1 \\ \frac{p}{2}(1-\frac{d}{p})\theta T_1^2 & T_p > T_1 \end{cases} \qquad (16)$$

As T_p follows from exponential distribution, the expected number of deteriorated items per cycle can be obtained by getting the integral from the right hand side of Equation (16) with the use of derivative function as follows:

$$E\,(R) = \frac{(p-d)\theta(1-e^{-\mu T_1}-\mu T_1 e^{-\mu T_1})}{\mu^2} \qquad (17)$$

In the next sub-sections, two cases of exponentially and uniformly distributed repair times are considered.

2. 1. Exponential Repair Time Let the repair time follow from an exponential distribution function with parameter of λ. The expected shortage time can be written as follows:

$$E\,(T_3) = \int_{T_p=0}^{T_1}\int_{t=T_2}^{\infty}(t-T_2)\lambda e^{-\lambda t}\mu e^{-\mu T_p}\,dt\,dT_p \qquad (18)$$

After computing the previous integral, expected shortage time is formulated as follows:

$$E(T_3)=\frac{e^{T_1\left(\frac{\lambda(p-d)}{2d}\left(-2+\theta T_1\right)+\frac{\lambda p}{d}+\mu\right)}-e^{\lambda T_1\left(\frac{T_1 p\theta}{2d}+1-\frac{\theta T_1}{2}\right)}}{e^{T_1\left(\frac{\lambda p}{d}+\mu\right)}} \quad (19)$$

Since a working cycle is the sum of production, non-production and shortage periods, then the expected time of a working cycle is:

$$E(T)=E(T_1+T_2)+E(T_3) \quad (20)$$

$$E(T)=\frac{p\left(1-e^{-\mu T_1}\right)}{d\mu}+\frac{e^{T_1\left(\frac{\lambda(p-d)}{2d}\left(-2\theta T_1\right)+\frac{\lambda p}{d}+\mu\right)}-e^{\lambda T_1\left(\frac{T_1 p\theta}{2d}+1-\frac{\theta T_1}{2}\right)}}{e^{T_1\left(\frac{\lambda p}{d}+\mu\right)}} \quad (21)$$

Also, the probability of machine breakdown during production period is:

$$P(M_c)=(1-e^{-\mu T_1}) \quad (22)$$

So, it is clear that the expected repair cost can be formulated as follows:

$$E(M_c)=M(1-e^{-\mu T_1}) \quad (23)$$

Unsatisfied demand is divided into the backorder and lost sales. The probability of backlogging is a decreasing function of time *t*, where *t* is the waiting time up to the next replenishment. Conversely, the probability of lost sales is an increasing function of time *t*. The expected volume of backlogs and lost sales can be formulated as follows, respectively:

$$E(S_1)=d\int_{T_p=0}^{T_1}\int_{t=T_p}^{\infty}(t-T_2)\,f(t)e^{-\sigma(t-T_2)}\mu e^{-\mu T_p}dtdT_p \quad (24)$$

$$E(S_2)=d\int_{T_p=0}^{T_1}\int_{t=T_2}^{\infty}(t-T_2)\,f(t)(1-e^{-\sigma(t-T_2)})\mu e^{-\mu T_p}dtdT_p \quad (25)$$

Thus, the total expected cyclic costs due to lost sales, backorders, setups, repair, inventory holding, and inventory deterioration can be written as follows:

$$TC(T_1,T_2)=E\left[K+M(1-e^{-\mu T_1})+h\times E(I)+C\times E(R)+\pi E(S_1)+\hat{\pi}E(S_2)\right] \quad (26)$$

$$TC(T_1,T_2)=E\left[K+M(1-e^{-\mu T_1})+h\times\frac{p(p-d)(1-e^{-\mu T_1}-\mu T_1e^{-\mu T_1})}{d\mu^2}+C\times\frac{(p-d)\theta(1-e^{-\mu T_1}-\mu T_1e^{-\mu T_1})}{\mu^2}\right.$$
$$\left.+\pi d\int_{T_p=0}^{T_1}\int_{t=T_2}^{\infty}(t-T_2)f(t)(1-e^{-\sigma(t-T_2)})\mu e^{-\mu T_p}dtdT_p+\hat{\pi}d\int_{T_p=0}^{T_1}\int_{t=T_2}^{\infty}(t-T_2)f(t)e^{-\sigma(t-T_2)}\mu e^{-\mu T_p}dtdT_p)\right] \quad (27)$$

Consequently, the expected total cost per unit time can be written as:

$$TCT(T_1,T_2)=\frac{k+\mu(1-e^{-\mu T_1})+(h\frac{p}{d}+C\theta)(\frac{(p-d)(1-e^{-\mu T_1}-\mu T_1e^{-\mu T_1})}{\mu^2})}{\frac{p(1-e^{-\mu T_1})}{d\mu}+\int_{T_p=0}^{T_1}\int_{t=T_2}^{\infty}(t-T_2)f(t)\mu e^{-\mu T_p}dtdT_p}$$
$$+\frac{\pi d\int_{T_p=0}^{T}\int_{t=T_2}^{\infty}(t-T_2)f(t)(1-e^{-\sigma(t-T_2)})\mu e^{-\mu T_p}dtdT_p+\hat{\pi}d\int_{T_p=0}^{T_1}\int_{t=T_2}^{\infty}(t-T_2)f(t)e^{-\sigma(t-T_2)}\mu e^{-\mu T_p}dtdT_p}{\frac{p(1-e^{-\mu T_1})}{d\mu}+\int_{T_p=0}^{T_1}\int_{t=T_2}^{\infty}(t-T_2)f(t)\mu e^{-\mu T_p}dtdT_p} \quad (28)$$

Further, TCT is a convex function of T_1 under the following condition:

$$M<\frac{\left(\frac{hp}{d}+C\theta\right)(p-d)-\left(\frac{\pi d\left(\sigma^2+2\sigma\lambda\right)}{(\sigma+\lambda)^2}+\frac{\hat{\pi}d\lambda^2}{(\sigma+\lambda)^2}\right)\left(2\left(\frac{\lambda\mu(p-d)}{d}-\mu^2\right)\right.}{\mu^2}$$

A detailed proof is available upon request from authors. Then, the optimal value of T_1 can be found by getting the derivative of Equation (28) with respect to T_1 and equaling the result to zero:

$$\frac{dTCT}{dT_1}=\frac{M\mu e^{-\mu T_1}+\left(\frac{hp}{d}+C\theta\right)\left(h(p-d)T_1e^{-\mu T_1}\right)\left(e^{T_1\left(\frac{\lambda p}{d}+\mu\right)}\right)}{\left(\frac{p\left(1-e^{-\mu T_1}\right)}{d\mu}\right)\left(e^{T_1\left(\frac{\lambda p}{d}+\mu\right)}\right)}-A_e+B_e$$
$$-\frac{\frac{\pi\left(\sigma^2+2\sigma\lambda\right)+\hat{\pi}\lambda^2}{(\sigma+\lambda)^2}d\left(\left(\lambda\left(\frac{T_1p\theta}{d}\right)+1-\theta T_1+\frac{p}{d}+\frac{\mu^{T_1}}{\lambda}\right)+\left(\frac{\lambda(d-p)}{d}+\frac{(p-d)\lambda\theta T_1}{d}\right)B_e\right)}{\left(p\frac{\left(1-e^{-\mu T_1}\right)}{d\mu}\right)\left(e^{T_1\left(\frac{\lambda p}{d}+\mu\right)}\right)}-A_e+B_e \quad (29)$$

$$\frac{-C_e\left(\left(\frac{hp}{d}+C\theta\right)\left(\frac{(p-d)\left(1-e^{-\mu T_1}-\mu T_1 e^{-\mu T_1}\right)}{\mu^2}\right)\left(e^{T_1\left(\frac{\lambda p}{d}+\mu\right)}\right)\right)}{\left(\frac{p(1-e^{-\mu T_1})}{d\mu}e^{T_1\left(\frac{\lambda p}{d}+\mu\right)}-A_e+B_e\right)}$$

$$\frac{-C_e\left(k+M\left(1-e^{-\mu T_1}\right)-\left(\left(\frac{\pi d\left(\sigma^2+2\sigma\lambda\right)}{(\sigma+\lambda)^2}+\frac{\hat{\pi}d\lambda^2}{(\sigma+\lambda)^2}\right)\times\frac{e^{\frac{-\lambda(p-d)T_1}{d}}}{\lambda}\right)\right)}{\left(\frac{p(1-e^{-\mu T_1})}{d\mu}e^{T_1\left(\frac{\lambda p}{d}+\mu\right)}-A_e+B_e\right)}$$

where, A_e, B_e and C_e are:

$$A_e=e^{\lambda T_1\left(\frac{T_1\theta p}{d}+1-0/5\theta T_1\right)} \quad (30)$$

$$B_e=e^{T_1\left(\frac{\lambda(p-d)}{d}+\frac{\lambda(p-d)\theta T_1}{2d}+\frac{\lambda p}{d}+\mu\right)} \quad (31)$$

$$C_e=\frac{pe^{-\mu T_1}}{d}-\frac{\lambda\left(\frac{T_1 p\theta}{2d}+1-0/5\theta T_1-\frac{p}{d}-\frac{\mu}{\lambda}\right)e^{A_e}+\left(\frac{\lambda(p-d)}{d}+\frac{(p-d)\lambda\theta T_1}{d}\right)e^{B_e}}{\left(e^{\lambda_1\left(\frac{\lambda p}{d}+\mu\right)}\right)} \quad (32)$$

Unfortunately, it is not easy to obtain a closed-form solution by finding the parametric roots of Equation (29) with respect to T_1. Hence, an efficient method such as Newton-Raphson or bi-section method should be hired to find the solution numerically.

2. 2. Uniform Repair Time In this section, uniform distribution function with 0 and b parameter is supposed for repair time. Expected repair time can be calculated as follows:

$$E(T_3)=\frac{\left((b\mu d)^2-2b(p-d)d\mu+2(p-d)^2\right)\left(1-e^{-\mu T_1}\right)-e^{-\mu T_1}\mu T_1(p-d)\left((p-d)(2\mu T_1)-2b\mu d\right)}{2b\mu^2 d^2} \quad (33)$$

Combine Equations (20) and (33), expected time of planning period is as follows:

$$E(T)=\frac{p(1-e^{-\mu T_1})}{d\mu}+\frac{\left((b\mu d)^2-2b(p-d)d\mu+2(p-d)^2\right)\left(1-e^{-\mu T_1}\right)-e^{-\mu T_1}\mu T_1(p-d)\left((p-d)(2\mu T_1)-2b\mu d\right)}{2b\mu^2 d^2} \quad (34)$$

The probability of backlogging is β and the probability of lost sales is (1-β). The expected value of backlogging and lost sales can be formulated as follows:

$$E(S_1)=d\int_{T_p=0}^{T_1}\int_{t=T_p}^{\infty}(t-T_2)\,f(t)\beta\mu e^{-\mu T_p}\,dt\,dT_p \quad (35)$$

$$E(S_2)=d\int_{T_p=0}^{T_1}\int_{t=T_2}^{\infty}(t-T_2)\,f(t)(1-\beta)\mu e^{-\mu T_p}\,dt\,dT_p \quad (36)$$

The total cost function of t can be derived as follows:

$$TCT(T_1)=\frac{k+M\left(1-e^{-\mu T_1}\right)+\frac{hp(p-d)\left(1-e^{-\mu T_1}-\mu T_1 e^{-\mu T_1}\right)}{\mu^2 d}+C\theta(p-d)\theta\left(1-e^{-\mu T_1}-\mu T_1 e^{-\mu T_1}\right)}{\frac{p\left(1-e^{-\mu T_1}\right)}{d\mu}+\frac{\left((b\mu d)^2-2b(p-d)\mu d+(p-d)^2\right)\left(1-e^{-\mu T_1}\right)-e^{-\mu T_1}\mu T_1(p-d)\left((p-d)(2+\mu T_1)-2b\mu d\right)}{2b\mu^2 d^2}}$$
$$+\frac{\hat{\pi}\beta d\frac{\left((b\mu d)^2-2b(p-d)\mu d+(p-d)^2\right)\left(1-e^{-\mu T_1}\right)-e^{-\mu T_1}\mu T_1(p-d)\left((p-d)(2+\mu T_1)-2b\mu d\right)}{2b\mu^2 d^2}}{\frac{p\left(1-e^{-\mu T_1}\right)}{d\mu}+\frac{\left((b\mu d)^2-2b(p-d)\mu d+(p-d)^2\right)\left(1-e^{-\mu T_1}\right)-e^{-\mu T_1}\mu T_1(p-d)\left((p-d)(2+\mu T_1)-2b\mu d\right)}{2b\mu^2 d^2}}$$
$$+\frac{\pi(1-\beta)d\frac{\left((b\mu d)^2-2b(p-d)\mu d+(p-d)^2\right)\left(1-e^{-\mu T_1}\right)-e^{-\mu T_1}\mu T_1(p-d)\left((p-d)(2+\mu T_1)-2b\mu d\right)}{2b\mu^2 d^2}}{\frac{p\left(1-e^{-\mu T_1}\right)}{d\mu}+\frac{\left((b\mu d)^2-2b(p-d)\mu d+(p-d)^2\right)\left(1-e^{-\mu T_1}\right)-e^{-\mu T_1}\mu T_1(p-d)\left((p-d)(2+\mu T_1)-2b\mu d\right)}{2b\mu^2 d^2}} \quad (37)$$

Derivation of Equation (37) from T_1 is as follows:

$$\frac{dTCT(T_1)}{dT_1}=\frac{M\mu e^{-\mu T_1}+(h\frac{p}{d}+c\theta)\left((p-d)T_1e^{-\mu t_1}\right)-\left(\hat{\pi}\beta+\pi(1-\beta)\right)\left(\frac{\mu^3e^{-\mu T_1}\left(bd\left(-bd+2(p-d)T_1\right)-T_1(p-d)^2\right)}{2db\mu^2}\right)}{\frac{p\left(1-e^{-\mu T_1}\right)}{d\mu}+\frac{\left(\left((b\mu d)^2-2b(p-d)\mu d+(p-d)^2\right)\left(1-e^{-\mu T_1}\right)-e^{-\mu T_1}\mu T_1(p-d)((p-d)(2+\mu T_1)-2b\mu d)\right)}{2b\mu^2d^2}}$$
$$-\frac{A\left(K+M\left(1-e^{-\mu t_1}\right)-\frac{(h\frac{p}{d}+c\theta)\left((p-d)\left(\mu t_1e^{-\mu t_1}+e^{-\mu t_1}-1\right)\right)}{\mu^2}\right)}{\left(\frac{p\left(1-e^{-\mu T_1}\right)}{d\mu}+\frac{\left(\left((b\mu d)^2-2b(p-d)\mu d+(p-d)^2\right)\left(1-e^{-\mu T_1}\right)-e^{-\mu T_1}\mu T_1(p-d)((p-d)(2+\mu T_1)-2b\mu d)\right)}{2b\mu^2d^2}\right)^2}$$
$$-\frac{A\left((\hat{\pi}\beta+\pi(1-\beta))d\left(\frac{\left(\left((b\mu d)^2-2b(p-d)\mu d+(p-d)^2\right)\left(1-e^{-\mu T_1}\right)-e^{-\mu T_1}\mu T_1(p-d)((p-d)(2+\mu T_1)-2b\mu d)\right)}{2b\mu^2d^2}\right)\right)}{\left(\frac{p\left(1-e^{-\mu T_1}\right)}{d\mu}+\frac{\left(\left((b\mu d)^2-2b(p-d)\mu d+(p-d)^2\right)\left(1-e^{-\mu T_1}\right)-e^{-\mu T_1}\mu T_1(p-d)((p-d)(2+\mu T_1)-2b\mu d)\right)}{2b\mu^2d^2}\right)^2} \quad (38)$$

where A is as follows:

$$A=\frac{\left(\mu^3e^{-\mu T_1}\left(bd\left(-bd+T_1(p-d)\left(2-(p-d)\right)\right)\right)\right)}{2b\mu^2d^2} \quad (39)$$

The optimal value of T_1 value can be found by using Maple software with regards to Equation (38) to zero. Like Poisson repair time model, total cost function should be convex to deriving T_1 value if parameters are under this condition:

$$M<\frac{\left(\frac{hp}{d}+C\theta\right)(p-d)-\left(\frac{\pi d\left(\sigma^2+2\sigma\lambda\right)}{(\sigma+\lambda)^2}+\frac{\hat{\pi}d\lambda^2}{(\sigma+\lambda)^2}\right)\left(2\left(\frac{\lambda\mu(p-d)}{d}-\mu^2\right)\right)}{\mu^2} \quad (40)$$

The proof of total cost convexity is shown in appendixes.

3. NUMERICAL EXAMPLE

Here, we will do some sensitivities numerically on the proposed model. In this regard, a numerical example with the following input parameters will be solved in this section:

d=7500	*h=1*	$\lambda=2$
P=10000	$\hat{\pi}=2$	*M=200*
Θ=0.2	$\pi=3$	*C=5*
K=50	*b=0.1*	$\mu=0.2$
S=5		

Moreover, the Matlab software is used to solve the Equation (29) resulting in T_1=0.1443. The optimum total cost per unit time can be calculated by substituting T_1 in Equation (28) resulting in TCT= \$692.0716. These are the result when repair time following Uniform distribution and for Exponential distribution according to Equation (38) T_1=0.2017 and by substituting Equation (37) resulting in TCT=\$590.9. If the values do not apply to the unequal convexity condition of the numerical method, Newton -Raphson is used to solve Equations (29) and (38), respectively.

Figure 2 shows the comparison between partial backordering and lost sales during different repair time. It is illustrated that partial backordering case has less total cost, the difference between them are greater by increasing the value of production up time. It is concluded that partial backordering is more economical and pursuant to real world conditions.

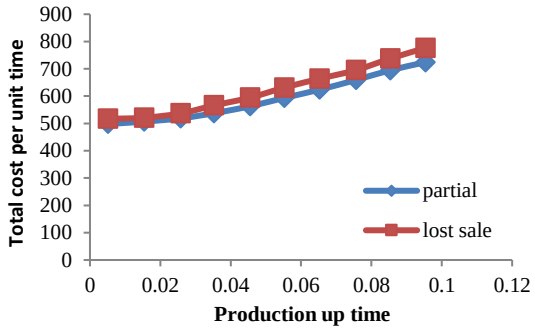

Figure 2. Total cost comparison for different production up time

4. CONCLUSION AND FUTURE RESEARCH

This paper studied an EPQ problem while considering new flavors from real world, including: (a) shortages in the form of partial backordering, (b) stochastic inventory deterioration, (c) stochastic machine breakdown, and (d) two types of stochastic repair time (i.e. uniform and exponential distributions). The two cases are formulated and necessary convexity conditions are discussed. Then, the corresponding optimality conditions are written that led to finding the roots of two equations. As it was hard to obtain a closed-form solution, the solution is obtained numerically by means of Newton-Raphson method. This research can be extended in various directions such as:

- other types of distributions (e.g. Normal) can be considered for repair times,
- the machine could experience different types of modes such as working normally, working abnormally by producing a number of defective items (i.e. a partial failure), and being unable to continue working (i.e. a complete failure) [40], the system can hire inspection procedures for forecasting future machine failures that can result in less number of emergency repairs/ maintenances [41]. Other types of inventory deterioration can be considered (e.g. fixed life time products) [42], multiple items can be produced on the machine, due to the complexity of the proposed model, various heuristics and meta-heuristics [43-45] and generally approximation methods [46-47] can be considered to address it optimality demand can be changed dynamically and/or stochastically [48-49].

5. REFERENCES

1. Safaeian, M., Fathollahi-Fard, A. M., Tian, G., Li, Z., and Ke, H., "A multi-objective supplier selection and order allocation through incremental discount in a fuzzy environment." ***Journal of Intelligent & Fuzzy Systems***, Vol. 37, No. 1, (2019), 1435-1455. https://doi.org/10.3233/JIFS-182843.
2. Misra, R.B., "Optimum production lot-size model for a system with deteriorating inventory." ***International Journal of Production Research***, Vol. 13, No. 5, (1975), 495–505. https://doi.org/10.1080/00207547508943019
3. Kim, C.H., and Hong, Y., "An optimal production length in deteriorating production processes." ***International Journal of Production Economics***, Vol. 58, (1999), 183-189. https://doi.org/10.1016/S0925-5273(98)00119-4
4. Samanta, G.P. & Roy, A., "A production inventory model with deteriorating items and shortages." ***Yugoslav Journal of Operations Research***, Vol. 14, No. 2, (2004), 219-230. https://doi.org/10.2004/00207547508943019
5. Baten, M.A. and Kamil, A.A., "Optimal control of a production inventory system with generalized Pareto distributed deterioration items." ***Journal of Applied Science***, Vol. 10, (2010), 116-123.
6. Yang, H.L., Teng, J.T. and Chern, M.S., "An inventory model under inflation for deteriorating items with stock-dependent consumption rate and partial backlogging shortages." ***International Journal of Production Economics***, Vol. 123, (2010), 8-19. https://doi.org/10.1016/j.ijpe.2009.06.041
7. Mak, K.L., "Determining optimal production-inventory control policies for an inventory system with partial backlogging." ***Computers & Operations Research***, Vol. 14, No. 4, (1987), 299-304. https://doi.org/10.1016/0305-0548(87)90067-0
8. Balkhi, Z.T., "The effects of learning on the optimal production lot size for deteriorating and partially backordered items with time varying demand and deterioration rates." ***Applied Mathematical Modelling***, Vol. 27, (2002), 763-779. https://doi.org/10.1016/S0307-904X(03)00081-7
9. Lo, S.T., Wee, H.M., and Huang, W.C., "An integrated production-inventory model with imperfect production processes and Weibull distribution deterioration under inflation." ***International Journal of Production Economics***, Vol. 106, (2007), 248-260. https://doi.org/10.1016/j.ijpe.2006.06.009
10. Cheung, L.L. and Hausman, W.H., "Joint determination of preventive maintenance and safety stocks in unreliable production environment," ***Naval Research Logistics,*** Vol. 44, (1997), 257-272. https://doi.org/10.1002/(SICI)1520-6750(199704)44:3<257::AID-NAV2>3.0.CO;2-7
11. Abboud, N.E., "A simple approximation of the EMQ model with Poisson machine failures." ***Production Planning & Control***, Vol. 8, No. 4, (1997), 385-397. https://doi.org/10.1080/095372897235190
12. Arreola-Risa, A. and DeCroix, G.A., "Inventory management under random supply disruptions and partial backorders." ***Naval Research Logistics***, Vol. 45, (1998), 687-703. https://doi.org/10.1002/(SICI)1520-6750(199810)45:7<687::AID-NAV3>3.0.CO;2-7
13. Giri, B.C., Yun, W.Y., and Dohi, T., "Optimal design of unreliable production–inventory systems with variable production rate." ***European Journal of Operational Research***, Vol. 162, (2005), 372-386. https://doi.org/10.1016/j.ejor.2003.10.015
14. Chakraborty, T., Giri, B.C., and Chaudhuri, K.S. "Production lot sizing with process deterioration and machine breakdown." ***European Journal of Operational Research***, Vol. 185, (2008), 606-618.
15. Chakraborty, T., Giri, B.C., and Chaudhuri, K.S., "Production lot sizing with process deterioration and machine breakdown under inspection schedule." ***Omega***, Vol. 37, No. 2, (2009), 257-271. https://doi.org/10.1016/j.ejor.2007.01.011
16. Widyadana, G.A., and Wee, H.M., "Production inventory models for deteriorating items with stochastic machine unavailability time, lost sales and price-dependent demand." ***Journal Teknik Industrial***, Vol. 12, No. 2, (2010), 61-68.
17. Widyadana, G.A. and Wee, H.M. "optimal deteriorating items production inventory models with random machine breakdown and stochastic repair time." ***Applied Mathematical Modelling***, Vol. 35, (2011), 3495-3508 https://doi.org/10.1016/j.apm.2011.01.006
18. Chung, C.J., Widyadana, G.A. and Wee, H.M. "Economic production quantity model for deteriorating inventory with random machine unavailability and shortage." ***International Journal of Production Research***, Vol. 49, No. 3, (2011), 883-902. https://doi.org/10.1080/00207540903460232
19. Chiu, Y.S.P. Chen, K.K. and Ting, C.K. "Replenishment run time problem with machine breakdown and failure in rework." ***Expert Systems with Applications***, Vol. 39, (2012), 1291-1297. https://doi.org/10.1016/j.eswa.2011.08.005
20. Taleizadeh, A.A., Akhavan Niaki, S.T., and Najafi, A.A. "Multiproduct single-machine production system with stochastic scrapped production rate, partial backordering and service level constraint." ***Journal of Computational and Applied Mathematics***, Vol. 233, (2010), 1834-1849. https://doi.org/10.1016/j.cam.2009.09.021
21. Sarkar, B. "A production-inventory model with probabilistic deterioration in two-echelon supply chain management." ***Applied Mathematical Modelling***, Vol. 37, (2013), 3138–3151. https://doi.org/10.1016/j.apm.2012.07.026
22. Chang H.C. "An analysis of production-inventory models with deteriorating items in a two-echelon supply chain." ***Applied Mathematical Modelling***, Vol. 36, (2013), 174-183. https://doi.org/10.1016/j.apm.2013.07.031
23. Sarkar M., and B. Sarkar, "An economic manufacturing quantity model with probabilistic deterioration in a production system." ***Economic Modelling,*** Vol. 31, (2013), 245-252. https://doi.org/10.1016/j.econmod.2012.11.019
24. Sarkar, B., and S. Sarkar, "An improved inventory model with partial backlogging, time varying deterioration and stock-

dependent demand." ***Economic Modelling***, Vol. 30, (2013), 924-932. https://doi.org/10.1016/j.econmod.2012.09.049

25. Taleizadeh, A. A., "An EOQ model with partial backordering and advance payments for an evaporating item." ***International Journal of Production Economics***, Vol. *155*, (2014), 185-193. https://doi.org/10.1016/j.ijpe.2014.01.023
26. De, S. K., Goswami, A., and Sana, S. S., "An interpolating by pass to Pareto optimality in intuitionistic fuzzy technique for an EOQ model with time sensitive backlogging." ***Applied Mathematics and Computation***, Vol. *230*, (2014), 664-674. https://doi.org/10.1016/j.amc.2013.12.137
27. Khan, M., Jaber, M. Y., and Ahmad, A. R., An integrated supply chain model with errors in quality inspection and learning in production. ***Omega***, Vol. 42, No. 1, (2014), 16-24. https://doi.org/10.1016/j.omega.2013.02.002
28. De, S. K., and Sana, S. S., "Backlogging EOQ model for promotional effort and selling price sensitive demand-an intuitionistic fuzzy approach." ***Annals of Operations Research***, Vol. *233*, No. 1, (2015), 57-76. https://doi.org/10.1007/s10479-013-1476-3.
29. Palanivel, M., and Uthayakumar, R., "Finite horizon EOQ model for non-instantaneous deteriorating items with price and advertisement dependent demand and partial backlogging under inflation." ***International Journal of Systems Science***, Vol. *46*, No. 10, (2015), 1762-1773. https://doi.org/10.1080/00207721.2013.835001
30. Pal, S., Mahapatra, G. S., and Samanta, G. P., "A three-layer supply chain EPQ model for price-and stock-dependent stochastic demand with imperfect item under rework." ***Journal of Uncertainty Analysis and Applications***, Vol. *4*, No. 1, (2016), 10-17. https://doi.org/10.1186/s40467-016-0050-3.
31. Mohanty, D. J., Kumar, R. S., and Goswami, A., "A two-warehouse inventory model for non-instantaneous deteriorating items over stochastic planning horizon." ***Journal of Industrial and Production Engineering***, Vol. *33*, No. 8, (2016), 516-532. https://doi.org/10.1007/s10479-017-2492-5.
32. Chanda, U., and Kumar, A., "Optimisation of fuzzy EOQ model for advertising and price sensitive demand model under dynamic ceiling on potential adoption." ***International Journal of Systems Science: Operations & Logistics***, Vol. *4*, No. 2, (2017), 145-165. https://doi.org/10.1080/23302674.2016.1151961
33. Manna, A. K., Das, B., Dey, J. K., and Mondal, S. K., "Multi-item EPQ model with learning effect on imperfect production over fuzzy-random planning horizon." ***Journal of Management Analytics***, Vol. 4, No. 1, (2017), 80-110. https://doi.org/10.1080/23270012.2016.1217755
34. Qiu, Y., Ni, M., Wang, L., Li, Q., Fang, X., and Pardalos, P. M., "Production routing problems with reverse logistics and remanufacturing." ***Transportation Research Part E: Logistics and Transportation Review*,** Vol. 111, (2018), 87-100. https://doi.org/10.1016/j.tre.2018.01.009
35. Marchi, B., Zanoni, S., Zavanella, L. E., and Jaber, M. Y. "Supply chain models with greenhouse gases emissions, energy usage, imperfect process under different coordination decisions." ***International Journal of Production Economics***, Vol. 211, (2019), 145-153. https://doi.org/10.1016/j.ijpe.2019.01.017
36. Marchi, B., Zanoni, S., and Jaber, M. Y., "Economic production quantity model with learning in production, quality, reliability and energy efficiency." ***Computers & Industrial Engineering***, Vol. 129, (2019), 502-511. https://doi.org/10.1016/j.cie.2019.02.009
37. Walid W. Nasr, and Jaber, M. Y., "Supplier development in a two-level lot sizing problem with non-conforming items and learning", ***International Journal of Production Economics***, Vol. 216, (2019), 349-363. https://doi.org/10.1016/j.ijpe.2019.06.022
38. Chen, B., Chao, X., and Ahn, H. S., "Coordinating pricing and inventory replenishment with nonparametric demand learning." ***Operations Research***, Vol. 67, No. 4, (2019), 1035-1052. https://doi.org/10.1287/opre.2018.1808
39. Yang, P.C. and Wee, H.M., "A collaborative inventory system with permissible delay in payment for deteriorating items," ***Mathematical Computer Modeling***, Vol. 43, (2006), 209-221. https://doi.org/10.1016/j.mcm.2005.09.029
40. Sana, S., S.K. Goyal, and K.S. Chaudhuri, "A production-inventory model for a deteriorating item with trended demand and shortages." ***European Journal of Operational Research***, Vol. 157, (2004), 357-371. https://doi.org/10.1016/S0377-2217(03)00222-4
41. Saha, S., and Sen, N., "A study on inventory model with negative exponential demand and probabilistic deterioration under backlogging." ***Uncertain Supply Chain Management***, Vol. *5*, No. 2, (2017), 77-88. https://doi.org/10.5267/j.uscm.2016.10.006.
42. Pakhira, N., Maiti, M. K., and Maiti, M., "Two-level supply chain of a seasonal deteriorating item with time, price, and promotional cost dependent demand under finite time horizon." ***American Journal of Mathematical and Management Sciences***, Vol. *36*, No. 4, (2017), 292-315. https://doi.org/10.1080/01966324.2017.1334605
43. Fathollahi-Fard, A. M., Govindan, K., Hajiaghaei-Keshteli, M., and Ahmadi, A., "A green home health care supply chain: New modified simulated annealing algorithms." ***Journal of Cleaner Production***, Vol. 214, (2019), 118200. https://doi.org/10.1016/j.jclepro.2019.118200
44. Fathollahi-Fard, A. M., Ranjbar-Bourani, M., Cheikhrouhou, N., and Hajiaghaei-Keshteli, M., "Novel modifications of social engineering optimizer to solve a truck scheduling problem in a cross-docking system." ***Computers & Industrial Engineering***, Vol. 137, (2019), 106103. https://doi.org/10.1016/j.cie.2019.106103
45. Fathollahi-Fard, A. M., Hajiaghaei-Keshteli, M. and Tavakkoli-Moghaddam, R., "Red deer algorithm (RDA): a new nature-inspired meta-heuristic," ***Soft Computing***, (2020), https://doi.org/10.1007/s00500-020-04812-z.
46. Fathollahi-Fard, A. M., Hajiaghaei-Keshteli, M., Tian, G., and Li, Z. "An adaptive Lagrangian relaxation-based algorithm for a coordinated water supply and wastewater collection network design problem." ***Information Sciences***, Vol. 512, (2020), 1335-1359. https://doi.org/10.1016/j.ins.2019.10.062
47. Fathollahi-Fard, A. M., Ahmadi, A., Goodarzian, F., and Cheikhrouhou, N., "A bi-objective home healthcare routing and scheduling problem considering patients' satisfaction in a fuzzy environment." ***Applied Soft Computing***, Vol. 93, (2020), 106385. https://doi.org/10.1016/j.asoc.2020.106385
48. Hajiaghaei-Keshteli, M., and Sajadifar, S. M., "Deriving the cost function for a class of three-echelon inventory system with N-retailers and one-for-one ordering policy." ***The International Journal of Advanced Manufacturing Technology***, Vol. 50, No. 1-4, (2010), 343-351. https://doi.org/10.1007/s00170-009-2486-9
49. Hajiaghaei-Keshteli, M., Sajadifar, S. M., and Haji, R., "Determination of the economic policy of a three-echelon inventory system with (R, Q) ordering policy and information sharing. ***The International Journal of Advanced Manufacturing Technology***, Vol. *55*, No. 5-8, (2011), 831-841. https://doi.org/10.1007/s00170-010-3112-6.

6. APPENDIXES

6. 1. Appendix A In order to prove that the $TCT(t_1)$ is differentiable and also has a single root, firstly the following mathematical theory should be regarded:

Property: If the $f(x)=\frac{g(x)}{h(x)}$ and the domain and range values for both the functions are the same, the $f(x)$ is a convex function under the following conditions:

1. $g(x)$ is convex on the domain interval and $g(x)\geq 0$ for all x in this interval.
2. $h(x)$ is concave on the domain interval and $h(x)\geq 0$ for all x in this interval.
3. Both $g(x)$ and $h(x)$ functions are differentiable.

Here $f(x)$ is the total cost per unit time, $g(x)$ is the total cost and $h(x)$ is the total replenishment period. Basically if $g(x)$ convex and $h(x)$ is concave then the $f(x)$ will be convex. In the following the convexity in presence of the small values for λ,μ is investigated:

The expected replenishment time can be drived as follows:

$$E(T_E)=\frac{p\left(1-e^{-\mu T_1}\right)}{d\mu}+\left(\frac{-e^{+\lambda T_1\left(0/5\theta T_1\frac{(p-d)}{d}+1\right)}+e^{\lambda T_1\left(0/5\theta T_1\frac{(p-d)}{d}+\frac{\mu}{\lambda}+1\right)}}{e^{\lambda_1\left(\frac{\lambda p}{d}+\mu\right)}}\right)$$

Moreover, the second derivative of the expected replenishment time is:

$$\frac{dT_E^2}{d^2T_1}=\left(-\lambda\left(\frac{\theta(p-d)}{d}\right)e^{T_1\left(0/5\theta T_1\lambda\frac{(p-d)}{d}+\lambda\right)}-\left(\theta T_1\lambda\frac{(p-d)}{d}+\lambda\right)^2e^{T_1\left(0/5\theta T_1\frac{\lambda(p-d)}{d}+\lambda\right)}+\frac{(p-d)}{d}\lambda\theta e^{T_1(0/5\theta T_1\lambda)\times\frac{(p-d)}{d}+\lambda+\mu}\right.$$

$$\left.+\left(\theta T_1\lambda\frac{(p-d)}{d}+\lambda+\mu\right)^2e^{T_1\left(0/5\theta T_1\lambda\frac{(p-d)}{d}+\lambda+\mu\right)}\right)e^{\frac{1}{T_1\left(\frac{hp}{d}+\mu\right)}}$$

$$-2\left(-\left(\theta T_1\lambda\left(\frac{p-d}{d}\right)+\lambda\right)e^{T_1(0/5\theta T_1\lambda)\left(\frac{p-d}{d}\right)+\lambda}\right.$$

$$\left.+\left(\theta T_1\lambda\left(\frac{p-d}{d}\right)+\lambda+\mu\right)e^{T_1\left(0/5\theta T_1\lambda\left(\frac{p-d}{d}\right)+\lambda+\mu\right)}\frac{\left(\lambda\frac{p}{d}+\mu\right)}{e^{T_1\left(\frac{\lambda p}{d}+\mu\right)}}\right)$$

$$+\left(-e^{T_1\left(0/5\theta T_1\lambda\left(\frac{p-d}{d}\right)+\lambda\right)}+e^{T_1\left(0/5\theta T_1\lambda\left(\frac{p-d}{d}\right)+\lambda+\mu\right)}\right)\frac{\left(\lambda\frac{p}{d}+\mu\right)^2}{e^{T_1\left(\frac{\lambda p}{d}+\mu\right)}}<0$$

This term can be simplified as:

$$\frac{dT_E^2}{dT_1^2}=\frac{-p\mu e^{-\mu T_1}}{d}+\left(-\lambda\left(\frac{\theta(p-d)}{d}\right)A-(\theta T_1\lambda)\frac{(p-d)}{d}+\lambda\right)^2A+\frac{(p-d)}{d}\lambda\theta Ae^{\mu T_1}$$

$$+\left(\theta T_1\lambda\left(\frac{p-d}{d}\right)+\lambda+\mu\right)^2Ae^{\mu T_1}\frac{1}{e^{T_1\left(\frac{\lambda p}{d}+\mu\right)}}-2\left(-\left(\theta T_1\lambda\frac{(p-d)}{d}+\lambda\right)A+\left(\theta T_1\lambda\frac{(p-d)}{d}+\lambda+\mu\right)Ae^{\mu T_1}\right)\times\frac{\left(\frac{\lambda p}{d}+\mu\right)}{e^{T_1\left(\frac{\lambda p}{d}+\mu\right)}}$$

$$+\left(-A+Ae^{\mu T_1}\right)\frac{\left(\frac{\lambda p}{d}+\mu\right)^2}{e^{T_1\left(\frac{\lambda p}{d}+\mu\right)}}<0 \qquad A=e^{T_1\left(0/5\theta T_1\frac{\lambda(p-d)}{d}+\lambda\right)}$$

So it can be rewritten as following equation:

$$\frac{d^2T_E}{d^2T_1}=dT_{E_1}+dT_{E_2}$$

$$dT_{E_1}=-\frac{p\mu e^{-\mu T_1}}{d}$$

$$dT_{E_2}=\left(\lambda\left(\frac{\theta(p-d)}{d}\right)\left(-1+e^{\mu T_1}\right)-\left(\theta T_1\lambda\left(\frac{(p-d)}{d}\right)+\lambda\right)^2A+\left(\theta T_1\lambda\left(\frac{(p-d)}{d}\right)+\lambda+\mu\right)^2Ae^{\mu T_1}\right.$$

$$\left.+2\left(\left(\theta T_1\lambda\frac{(p-d)}{d}+\lambda\right)A-\left(\theta T_1\lambda\frac{(p-d)}{d}+\lambda+\mu\right)Ae^{\mu T_1}\right)\left(\frac{\lambda p}{d}+\mu\right)\right.$$

$$\left.+\left(-A+Ae^{\mu T_1}\right)\left(\frac{\lambda p}{d}+\mu\right)^2\right)$$

The second term in the mentioned formula can be simplified to the following equation:

$$dT_{E_2}=\left(\frac{\lambda(\theta)(p-d)}{d}\right)\left(-1+e^{\mu T_1}\right)-(A_a-C)^2A+(A_b-C)^2Ae^{\mu T_1}$$

$$A_a=\theta T_1\lambda\frac{(p-d)}{d}+\lambda \qquad C=\left(\frac{\lambda p}{d}+\mu\right)$$

$$A_b=\theta T_1\lambda\frac{(p-d)}{d}+\lambda+\mu$$

In this term if $A_b>A_a$ then $dT_{E_2}>0$. Accordingly the expected replenishment time is convex if :

$$\frac{p\mu e^{-\mu T_1}}{d}>\lambda\left(\frac{\theta(p-d)}{d}\right)\left(-1+e^{\mu T_1}\right)-(A_a-C)^2A+(A_b-C)^2Ae^{\mu T_1}$$

If θ and T_1 take small values the above condition can be rewritten as follows:

$$\frac{p\mu e^{-\mu T_1}}{d}>\lambda\left(\frac{\theta(p-d)}{d}\right)\left(-1+e^{\mu T_1}\right)-(\lambda-C)^2e^{\lambda T_1}+(\lambda+\mu-C)^2e^{(\lambda+\mu)T_1}$$

And in presence of small values for the μ,λ and θT_1 the condition can be simplified as:

$$2\left(\frac{p(\lambda-0/5)-\lambda d}{d}\right)-\mu<0$$

Here if $\lambda<0/5$ or $\lambda<\frac{d\mu+p}{2(p-d)}$ the expected replenishment time will be convex.

In the second part the concavity of the total cost function is investigated; its function is as follows:

$$TC_E = k+\mu\left(1-e^{-\mu T_1}\right)+\frac{h(p)(p-d)\left(1-e^{-\mu T_1}-\mu T_1 e^{-\mu T_1}\right)}{\mu^2 d}+\frac{C\theta(p-d)(\theta)\left(1-e^{-\mu T_1}-\mu T_1 e^{-\mu T_1}\right)}{\mu^2}$$

$$+\left(\frac{\pi d\left(\sigma^2+2\sigma\lambda\right)}{(\sigma+\lambda)^2}+\frac{\hat{\pi}d\lambda^2}{(\sigma+\lambda)^2}\right)\left(\frac{e^{-\lambda T_1\left(0/5\theta T_1\frac{(p-d)}{d}+1\right)}+e^{\lambda T_1\left(0/5\theta T_1\frac{(p-d)}{d}+1+\frac{\mu}{\lambda}\right)}}{e^{T_1\left(\frac{\lambda p}{d}+\mu\right)}}\right)$$

Its second derivative is:

$$\frac{dTC_E^2}{dT_1^2}=-M\mu^2e^{-\mu T_1}+\left(\frac{hp}{d}+C\theta\right)(p-d)\left(e^{-\mu T_1}\right)(1-\mu T_1)$$

$$+\left(\frac{\pi d\left(\sigma^2+2\sigma\lambda\right)}{(\sigma+\lambda)^2}+\frac{\hat{\pi}d\lambda^2}{(\sigma+\lambda)^2}\right)\frac{1}{e^{T_1\left(\frac{\lambda p}{d}+\mu\right)}}\left(-\lambda\left(\theta\frac{(p-d)}{d}e^{T_1\left(0/5\theta T_1\lambda\frac{(p-d)}{d}+\lambda\right)}-\left(\theta T_1\frac{\lambda(p-d)}{d}+\lambda+\mu\right)^2\times e^{T_1\left(0/5\theta T_1\lambda\frac{(p-d)}{d}+\lambda\right)}\right.\right.$$

$$\left.\left.+\frac{(p-d)}{d}\lambda\theta e^{T_1\left(0/5\theta T_1\lambda\left(\frac{p-d}{d}\right)+\lambda+\mu\right)}+\left(\theta T_1\lambda\frac{(p-d)}{d}+\lambda+\mu\right)^2e^{T_1\left(0/5\theta T_1\lambda\frac{(p-d)}{d}+\lambda+\mu\right)}\right)\right.$$

$$\left.-2\left(-\left(\theta T_1\lambda\frac{(p-d)}{d}\right)+\lambda\right)e^{T_1\left(0/5\theta T_1\left(\frac{p-d}{d}\right)+\lambda\right)}+\left(\theta T_1\lambda\frac{(p-d)}{d}+\lambda+\mu\right)e^{T_1\left(0/5\theta T_1\left(\frac{p-d}{d}\right)+\lambda+\mu\right)}\right)\frac{\left(\frac{\lambda p}{d}+\mu\right)}{e^{T_1\left(\frac{\lambda p-d}{d}\right)+\mu}}$$

$$+\left(\left(-e^{T_1\left(0/5\theta T_1\lambda\frac{(p-d)}{d}+\lambda\right)}+-e^{T_1\left(0/5\theta T_1\lambda\frac{(p-d)}{d}+\lambda+\mu\right)}\right)\frac{\left(\frac{\lambda p}{d}+\mu\right)^2}{e^{T_1\left(\frac{\lambda p}{d}+\mu\right)}}\right)$$

If μ , λ , T_1 are small we will have:

$$\frac{d^2TC_E}{d^2T_1}=-M\mu^2+\left(\frac{hp}{d}+C\theta\right)(p-d)-\left(\frac{\pi d\left(\sigma^2+2\lambda\sigma\right)}{(\sigma+\lambda)^2}+\frac{\hat{\pi}d\lambda^2}{(\sigma+\lambda)^2}\right)\left(\left(\lambda-\left(\frac{\lambda p}{d}+\mu\right)^2+\left(\lambda+\mu-\left(\frac{\lambda p}{d}+\mu\right)^2\right)\right)\right)$$

So the total cost functions is convex if:

$$M<\frac{\left(\frac{hp}{d}+C\theta\right)(p-d)-\left(\frac{\pi d\left(\sigma^2+2\sigma\lambda\right)}{(\sigma+\lambda)^2}+\frac{\hat{\pi}d\lambda^2}{(\sigma+\lambda)^2}\right)\left(2\left(\frac{\lambda\mu(p-d)}{d}-\mu^2\right)\right)}{\mu^2}$$

So based on the mentioned property, if this condition is verified by the problem parameters, the function is convex.

6. 2. Appendix B

For the total cost function we have:

$$TC_u=K+M\left(1-e^{-\mu t_1}\right)-\frac{(h\frac{p}{d}+c\theta)\left((p-d)\left(\mu t_1e^{-\mu t_1}+e^{-\mu t_1}-1\right)\right)}{\mu^2}$$

$$+(\hat{\pi}\beta+\pi(1-\beta))d(\frac{\left(\left((b\mu d)^2-2b(p-d)\mu d+(p-d)^2\right)\left(1-e^{-\mu T_1}\right)-e^{-\mu T_1}\mu T_1(p-d)((p-d)(2+\mu T_1)-2b\mu d)\right)}{2b\mu^2d^2})$$

The second derivative of the total cost function is as follows:

$$\frac{dTC_U^2}{d^2T_1}=-M\mu^2e^{-\mu T_1}+\left(\frac{hp}{d}+c\theta\right)\left((p-d)(1-b\mu)e^{-\mu T_1}\right)$$

$$-(\hat{\pi}\beta+\pi(1-\beta))\left(\frac{\left(e^{-\mu T_1}\right)\mu^4\left(bd\left(bd+2T_1(p-d)+T_1^2(p-d)^2\right)+2e^{-\mu T_1}\right)\mu^3\left(bd\left(bd(p-d)-2T_1\left((p-d)^2\right)\right)\right)}{2db\mu^2}\right)$$

If $T_1=0$:

$$\frac{dTC_U^2}{d^2T_1}=-M\mu^2+\left(\frac{hp}{d}+c\theta\right)(p-d)-\left(\hat{\pi}\beta+\pi(1-\beta)\right)\left(\frac{\mu bd\left(\mu bd+2(p-d)\right)}{2}\right)$$

If the following condition will be satisfied this equation is convex:

$$M\prec\frac{\left(\frac{hp}{d}+c\theta\right)(p-d)-\left(\hat{\pi}\beta+\pi(1-\beta)\right)\left(\frac{\mu bd\left(\mu bd+2(p-d)\right)}{2}\right)}{\mu^2}\text{ In}$$

presence of the $T_1=\frac{db\left(1-\frac{\theta b}{2}\right)}{(p-d)}$:

$$\frac{dTC_U^2}{d^2T_1}=\frac{1}{d}\left(h\left(8p(p-d)-4pb\mu d(2+b\theta)\right)-\left(\hat{\pi}\beta+\pi(1-\beta)\right)\left(4\mu bd\theta(p-d)+b(\mu bd\theta)^2\right)+c\left(40d\left(2p-2d-2pdb\mu-\mu^2d\theta\right)\right)-M\mu^2d\right)$$

$$\times e^{\left(-\frac{\mu db(2+\theta b)}{2(p-d)}\right)}$$

This equation is convex if:

$$M<\frac{(hp+cd\theta)\left(8(p-d)-4b\mu d(2+b\theta)\right)-\left(\hat{\pi}\beta+\pi(1-\beta)\right)\left(\mu bd\theta\left(4(p-d)+\mu b^2d\theta\right)\right)}{\mu^2d}$$

So based on the stated property, in presence of this condition the function is convex.

Persian Abstract

چکیده

پیشرفت های اخیر در سیستم های تولید، مطالعات متعددی را برای تمرکز بر مساله تولید اقتصادی (EPQ) ایجاد می کند. اگرچه چندین بخش EPQ وجود دارد، این مقاله با در نظر گرفتن برخی از پارامترهای دنیای واقعی مانند: (الف) کمبود به شکل بازسفارش جزئی، ب) موجودی که می تواند به صورت تصادفی رو به وخامت بگذارد، (ج) دستگاه می تواند به طور تصادفی شکسته شود، و (د) زمان تعمیر دستگاه ممکن است بر اساس وضعیت خرابی دستگاه تغییر کند. تا آنجا که می دانیم، هیچ مطالعه ای در مورد همه این فرضیات در چارچوب EPQ وجود ندارد. علاوه بر این توسعه، دو شکل از زمان تعمیر یکنواخت و نمایی توزیع شده تدوین شده و شرایط همرفت ضروری مورد بحث قرار گرفته است. سپس، شرایط بهینه مربوطه نوشته می شود که منجر به یافتن ریشه های دو معادله می شود. به دلیل دشواری در دستیابی به راه حل با فرم بسته، محلول با استفاده از روش نیوتن–رافسون به صورت عددی بدست می آید. سرانجام، برخی از تجزیه و تحلیل های حساسیت برای توضیح قابلیت کاربرد مدل ارائه شده است. عملی و کارایی روش پیشنهادی در این زمینه باعث می شود وزن EPQ پیشنهادی با عناصر پیچیده تر و کاربرد آن بطور گسترده تری ایجاد شود.

International Journal of Engineering

Journal Homepage: www.ije.ir

Temperature Effect on Creep and Fracture Behaviors of Nano-SiO_2-composite and AlSi12Cu3Ni2MgFe Aluminum Alloy

M. Azadi*, H. Aroo

Faculty of Mechanical Engineering, Semnan University, Semnan, Iran

PAPER INFO

Paper history:
Received 21 February 2020
Received in revised form 26 March 2020
Accepted 07 June 2020

Keywords:
Creep Property
Piston Aluminum Alloy
Aluminum Alloy Matrix Nano-composite
Temperature Effect
Fracture Behavior

ABSTRACT

In the presented article, the temperature effect was studied on creep properties and fracture behaviors of AlSi12Cu3Ni2MgFe aluminum-silicon alloys, unreinforced and reinforced with SiO_2 nano-particles. For such objective, standard specimens were fabricated by gravity casting and stir-casting methods, for aluminum alloys and nano-composites, respectively. Then, force-controlled creep testing was performed on standard specimens at 250, 275 and 300°C, under 100 MPa. Then, to find failure mechanisms, the fracture surface of test samples was also analyzed by the field emission scanning electron microscopy. Experimental results depicted the temperature changed creep behaviors of both materials, effectively. Moreover, a significant improvement in creep properties was observed by reinforcing the aluminum matrix with nano-particles, besides a heat treatment process. Such an increase in the creep lifetime was higher at 300°C. In addition, the fracture surface investigation of both materials implied the same brittle behavior, with quasi-cleavage marks. The failure location changed from inside the intermetallic phase into boundaries of the intermetallic phase in the nano-composite.

doi: *10.5829/ije.2020.33.08b.16*

1. INTRODUCTION

Nowadays, aluminum alloys have been vastly utilized in engine and automotive industries, due to advantages such as good casting behavior, low density, proper wear resistance and moderate thermal behavior [1-3]. In order to improve these characteristics, especially at higher temperatures for engine piston applications, the addition of the nickel element to the alloy and the heat treatment process could be used. As an innovative approach, ceramic-reinforced aluminum matrix composites have been developed by adding nano-particles.

According to the operation condition of engine pistons, high-temperature behaviors of the material should be investigated, such as the creep lifetime and the stress relaxation. In this field of study, different articles were presented for aluminum-silicon alloys. Although investigations about creep properties of metal matrix composites are still rare. In following paragraphs, a literature review could be seen for aluminum alloys, not in details. Since the main topic is to highlight the nano-composite.

Ishikawa et al. [4] studied creep behaviors of highly pure aluminum at lower temperatures. They showed that the creep rate depended upon the applied stress and the cyclic stress had an effect on the creep lifetime. Jenabali Jahromi [5] presented creep behaviors of the spray-cast heat-treatable AlZnMgCuZr aluminum alloy. Their creep rate results at 120°C indicated a much lower rate of the alloy, compared to the ingot-cast 7075 aluminum alloy. Ishikawa and Kobayashi [6] found that the minimum strain rate was seen instead of the steady state condition in creep and rupture behaviors of the A5083 aluminum-magnesium alloy. Dobes and Milicka [7] studied creep behaviors of Al-5.5wt.%Mg and Al-13.7wt.%Zn aluminum solid solutions, at 300 to 500°C. Srivastava et al. [8] investigated the low-stress creep behavior of the 7075 high strength aluminum alloy, at 350-410°C to find the stress exponent. Lin et al. [9] demonstrated that the stress had a significant effect on the whole creep

*Corresponding Author Institutional Email: *m_azadi@semnan.ac.ir* (M. Azadi)

Please cite this article as: M. Azadi, H. Aroo, Temperature Effect on Creep and Fracture Behaviors of Nano-SiO_2-composite and AlSi12Cu3Ni2MgFe Aluminum Alloy, International Journal of Engineering (IJE), IJE TRANSACTIONS B: Applications Vol. 33, No. 8, (August 2020) 1579-1589

deformation process at 250°C for the pure copper and at 150°C for the aluminum alloy.

Requena and Degischer [10] presented creep behaviors of unreinforced and short fiber reinforced AlSi12Cu3Ni2MgFe aluminum alloys at 300°C. They found that 15 vol.% of the reinforcement was the highest creep resistant, while 20 vol.% had lower creep resistant than 10 and 15 vol.%, due to its higher defect density and larger interface area. Couteau and Dunand [11] studied the creep behavior of aluminum syntactic foams at 500°C and showed that the minimum strain rate varied with the stress, by changing the stress exponent. Kandare et al. [12] modeled creep-based lifetime prediction of aluminum in fire. The model was validated by fire structural tests, performed on a non-age-hardening 5083 H116 aluminum alloy. Li et al. [13] presented modeling of high-temperature creep behaviors of 7075 and 2124 aluminum alloys by continuum damage mechanics, with a good agreement. Maximov et al. [14] modeled strain hardening and creep behaviors of the 2024-T3 aluminum alloy at different temperatures. The constitutive model authenticity was proved experimentally, besides finite element simulations.

Zhan et al. [15] studied effects of process parameters on mechanical properties and the microstructure of creep-aged 2124 aluminum alloys. Their results implied that the creep strain and the creep rate increased by increasing the ageing time, the temperature and the stress. Fernandez-Gutierrez and Requena [16] investigated the effect of the spheroidization heat treatment on the creep resistance of a cast AlSi12CuMgNi aluminum alloy. They indicated that the highest creep resistance gradually decreased by increasing the solution treatment time, due to the loss of the load bearing capability of rigid phases. Zhang et al. [17] evaluated asymmetric tensile and compressive creep behaviors in the ZL109 aluminum alloy. They found that at high temperatures or high stress levels, the ratio between tensile and compressive creep rates was as large as 10. Spence and Makhlouf [18] indicated that residual compressive stresses on the machined surface caused the material to creep and the creep rate increased by increasing the temperature in 4032-O and 6061-T6 aluminum alloys. Yang et al. [19] simulated the AA2524 aluminum alloy in creep age forming at temperatures of 180-200°C.

Lie et al. [20] showed that due to fine transgranular precipitates, the creep-aged 7050 aluminum alloy with initial tempers of the solution and the re-solution exhibited higher mechanical properties than that of the retrogression with coarse transgranular precipitates. Erdeniz et al. [21] studied the effect of vanadium micro-alloying on microstructural and creep behaviors of Al-Er-Sc-Zr-Si aluminum alloys, with and without $L1_2$-ordered coherent Al_3(Er,Sc,Zr) nano-scale precipitates. Xu et al. [22] found that the creep strain magnitude of the 2524 aluminum alloy greatly increased with increasing the pre-strain due to the precipitation process, reducing the average size of Al_2CuMg phases. Li et al. [23] developed a unified constitutive model for creep-ageing of the AA2050-T34 Al-Cu-Li alloy. Yang et al. [24] investigated the effect of the pre-deformation on creep age forming of the 2219 aluminum alloy. Their results indicated that the pre-deformation could prolong the duration of the primary creep stage and considerably facilitated the creep strain.

Spigarelli and Sandstrom [25] presented basic creep modelling of the pure aluminum, which was compared to experimental data. Lei et al. [26] investigated thermal-mechanical loading sequences related creep ageing behaviors of the 7050 aluminum alloy. They showed that the alternative of the ageing furnace or the autoclave could cause inverse thermal-mechanical loading sequences, including loading prior to heating in the ageing furnace or heating prior to loading in the autoclave. El Amri et al. [27] performed thermal and also thermo-mechanical simulations in the 6061 aluminum alloy. They applied a numerical procedure to assess the thermo-mechanical damage at high temperatures, using the ABAQUS software. They depicted that the performance of the proposed model was good. Belodedenko et al. [28] studied fatigue resistance models of structures for the risk-based inspection. They proposed two basic models, including the lifetime general equation and the lifetime dispersion equation.

Consequently, in the mentioned literature review, all articles were about creep behaviors of aluminum alloys. However, in the following, more details of another literature review could be seen for aluminum matrix composites whose articles are rare in comparison to those of aluminum alloys.

Cadek et al. [29] studied the threshold creep behavior of discontinuous aluminum and aluminum alloy matrix composites. They showed that the creep-strengthening effect of silicon carbide particulates, silicon carbide whiskers and alumina short fibers was high, although particulates, whiskers and short fibers did not represent effective obstacles to dislocation motions. Ji et al. [30] investigated the creep behavior of TiC_P/2618 aluminum matrix composite at 250, 300 and 350°C. Their results indicated that both the stress exponent and the apparent activation energy of the composite were higher than those of the 2618 aluminum alloy. They depicted that the existence of TiC particles significantly improved the high-temperature creep property of the 2618 aluminum alloy. On this research, Gonzalez-Doncel and Fernandez [31] presented some comments. They improved the creep response of 2618Al with 15 and 20 vol.% of TiC_P, assuming a mechanism of the load transfer from the aluminum alloy matrix to TiC_P. Fernandez and Gonzalez-Doncel [32] checked the creep fracture behavior of aluminum alloys and aluminum alloy metal matrix composites. They found a good correlation between

experimental data and results of the phenomenological Monkman-Grant model.

Choi and Bae [33] investigated creep properties (at 250°C) of aluminum-based composites, containing 4.5 vol.% of multi-walled carbon nanotubes (CNT). They depicted that the composite had higher creep resistance at the applied stress, higher than 200 MPa. Below 110 MPa, the composite showed a negligible dependency of the strain rate on the stress, due to the diffusional flow of the matrix, which was significantly restricted by nanotubes. Sudharshan Phani and Oliver [34] performed a comparison of high-temperature nano-indentation creep and uniaxial creep measurements 27-550°C for the commercial purity aluminum. Uniaxial power-law creep parameters (the stress exponent and the pre-exponential term) were calculated from indentation data, for the comparison of results to uniaxial data. Their results demonstrated a good agreement with literature values. Saberi Kakhki et al. [35] studied impression relaxation behaviors of Al/4%-SiC nano-composites. They showed a constant relation between the stress relaxation and the compression creep rate. SiC nano-particles acted as work-hardening areas, the porosity and the non-symmetrical distribution of SiC caused variations of the steady state relaxation rate or creep rate. Zhao et al. [36] improved elevated-temperature mechanical properties of Al-Mn-Mg, containing TiC nano-particles. They indicated that TiC nano-particles significantly increased the strength at the ambient temperature and at 200°C. At higher temperatures, such strengthening effect diminished, due to the activated dislocation climb.

As a conclusion on the second part of the literature review, it could be concluded that several articles were published on creep properties of aluminum alloys. Moreover, creep properties of the nano-composite were rarely published. Different nano-particles were introduced such as CNT [33], SiC [35], TiC [37], Al_2O_3 and CuO [38], with the weight percentage of 1-4% [35,38]. In addition, creep behaviors of piston aluminum-silicon alloys, with and without SiO_2 nano-particles, as a special case study, were experimentally studied in this research. This could be the novelty, since no report could be found on such a material. Besides, this article has been presented to complete previous researches [1-3]. It should be noted that in the literature [38], 2% SiO_2 nano-particles were added to the aluminum alloy, which led to lower creep properties. In this report, the weight percentage of nano-particles reduced to 1% and creep experiments were done under different temperatures. For this objective, standard test samples were casted, machined and tested under creep loading under a constants load. Then, obtained results are presented in figures and tables. Therefore, the structure of this article includes the introduction, experimental works, results, the discussion and conclusions.

2. EXPERIMENTAL WORKS

In this article, the studied material was a piston aluminum alloy. The chemical composition of this material was 12.5 wt.% Si, 0.4 wt.% Fe, 2.4 wt.% Cu, 0.7 wt.% Mg and 2.2 wt.% Ni, besides the aluminum matrix. The flowchart for the whole stages of experimnetal works in this research is shown in Figure 1.

To reinforce the material, SiO_2 nano-particles were used to add into the aluminum matrix. Azadi and Aroo [38] reported that 2% SiO_2 nano-particles reduced the creep lifetime of the material. Therefore, in this research, the weight percentage was considered as 1%. For this objective, nano-particles were firstly coated by aluminum micro-powders in a planetary ball mill device. More details of such works were presented in the literature [1-3]. As an important note and based on previous reports [1-3], the X-ray diffraction (XRD) analysis and images of the transmission electron microscopy (TEM) showed a proper process for coating.

The fabrication technique for the piston aluminum-silicon alloy was the gravity casting approach. The production method for the aluminum matrix nano-composite was the stir-casting process. Cylindrical specimens were initially casted in a cast-iron permanent mold for aluminum-silicon alloys, unreinforced and reinforced by nano-particles. After casting, nano-composite specimens were also heat treated at 500°C for 5 h, quenched in water and aged at 180°C for 9 h [39]. More details for fabricating samples could be seen in the literature [38].

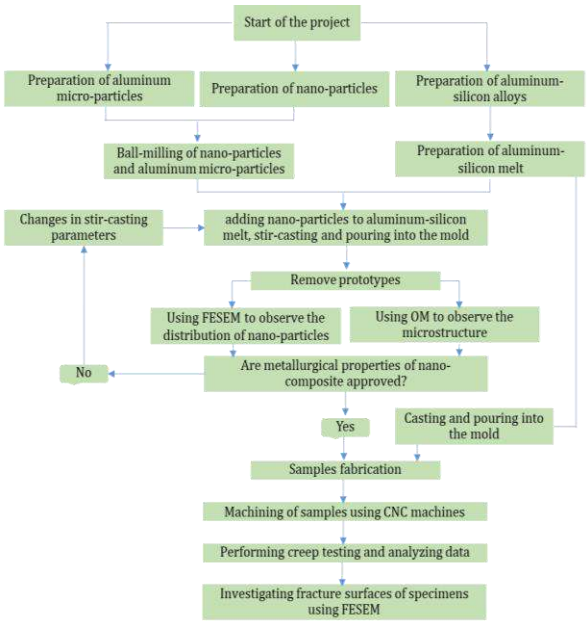

Figure 1. The flowchart of experimnetal works in this research.

For the experimental investigation, creep tests were carried out on the studied material, based on the ASTM-E139-11 standard [40]. The applied stress was 100 MPa in all creep tests on both materials. This loading case was considered due to working conditions of engine pistons [38]. However, the temperature was considered as 250, 275 and 300°C. Since the maximum temperature of pistons in internal combustion engines has been around 300°C [10, 16]. The creep specimen geometry is depicted in Figure 2. Dimensions are in millimeter in Figure 2. Standard specimens were machined from casted cylinders, made from the aluminum-silicon alloy and the aluminum alloy nano-composite. Creep tests were performed by the SCT-300 creep testing machine (SANTAM Company). More descriptions of tests could be observed in the literature [41].

To study the fracture surface, the field-emission scanning electron microscopy (FE-SEM) was used based on the MIRA TESCAN model, in the secondary mode. In addition, the energy dispersive X-ray spectroscopy (EDS) map was utilized to indicate the chemical composition of materials, in the back-scattered mode of FE-SEM images. In addition, the other objective of the back-scattered FE-SEM image was to check the distribution of nano-particles in the matrix. Then also, to find the effect of the heat treatment and nano-particles, before testing, microstructures were examined by the optical microscopy (OM), using the Olympus model. For such objective, a polishing process was firstly performed on specimens and then, a Keller etchant was used [1,3].

3. RESULTS and DISCUSSION

As a first result, the microstructure of aluminum-silicon alloys, unreinforced and reinforced with nano-particles, before creep testing, can be seen in Figure 3, including OM images. It should be noted that the nano-composite was also heat treated, as mentioned. According to Figure 3, both materials had almost the same microstructure, based on observed phases. However, the size of different phases was not the same in the aluminum-silicon alloy, with and without nano-particles.

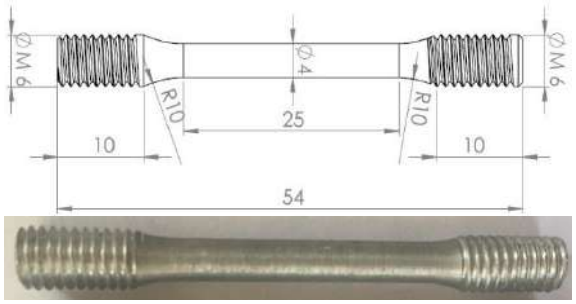

Figure 2. The specimen geometry in millimeter of creep testing, based on the ASTM-E139-11 standard

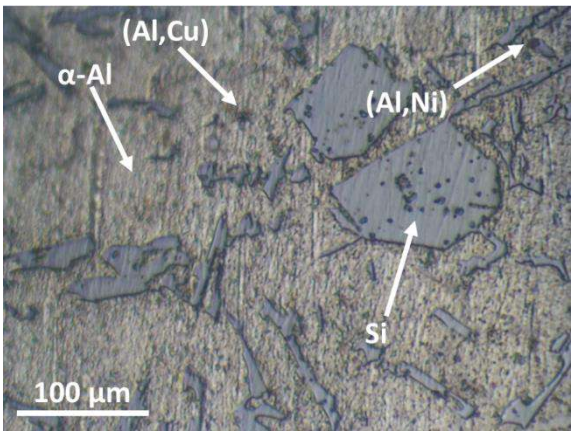

(a)

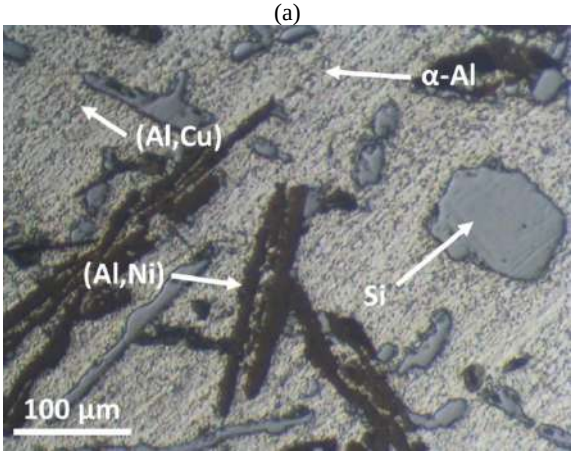

(b)

Figure 3. Microstructures of aluminum alloys, (a) unreinforced and (b) reinforced with nano-particles, before creep testing.

The investigated material had different phases [1,3]. The first phase was the matrix (α-Al) whose color was light gray. The second phase was Si, which was homogeneously distributed in the matrix in a blocky form, including polyhedral crystals with a flaky morphology. Zainon et al. [42] reported that there were two types of Si phase, including the flake-like form and the coarse primary Si particle. The intermetallic phase was (Al,Ni), which could be seen in a black-colored regime. Another intermetallic phase was (Al,Cu) with a brown color. Such obtained results are consistent with those reported in the literature [43-45].

The heat treatment increased the amount of the (Al,Ni) intermetallic phase in the aluminum matrix. Such phenomenon could enhance and improve the strength of the material. In addition, the shape of the Si phase, after the heat treatment, became the flake-like morphology. Then also, adding SiO_2 nano-particles to the aluminum matrix caused to change the morphology of the (Al,Ni) intermetallic phase, into the flaky shape. Besides, nano-particles were joined to the Si phase and therefore, higher amount of Si could be seen in the microstructure of the

nano-composite. However, the size of the Si phase decreased by nano-particles. As a result, the ratio of the diameter to the length for intermetallic phases and the Si phase decreased. Such presented results were reported in the literature [45-46]. In addition, Issa et al. [47] found a decrease in the grain size, when ceramic nano-particles reinforced the matrix.

Besides OM images, in order to illustrate the distribution of nano-particles in the aluminum matrix, the back-scattered FE-SEM image was also checked. More details about this investigation could be found in the literature [1,3]. As a result, based on the reported results in previous works [48-49], the maximum size of nano-particles in the matrix was less than 100 nm, which showed no agglomeration. Besides, the distribution of nano-particles in the aluminum matrix was also proper.

Obtained results from creep testing, including curves of the strain versus the time and the strain rate versus the time can be seen in Figures 4 and 5. It should be noted that a logarithmic scale was used for the time and the strain rate, to show all data in a wide range. As another note, one creep test was stopped for the nano-composite at 250°C, due to limitation of facilities. This long creep time was more than 46.8 h, which is equal to about 2 days of testing. As another note, for data at 300°C, curves of the strain and also the strain rate were logically differentiated from curves for two other temperatures. The reason for such a behavior was the creep lifetime at 300°C, which was too short (1.6 min and 33.4 min for specimens, without and with nano-particles), comparing to other creep lifetimes at two other temperatures.

Besides creep curves, Table 1 shows creep results, including the minimum strain rate, the rupture strain and the rupture time. Based on these results, as expected, by increasing the temperature, the creep lifetime of materials decreased. This creep lifetime of the nano-composite improved 1135 (at least), 46 and 1988%, when compared to the creep lifetime of the aluminum-silicon alloy, at 250, 275 and 300°C, respectively. The second value (46%) for such improvement at 275°C of the material by

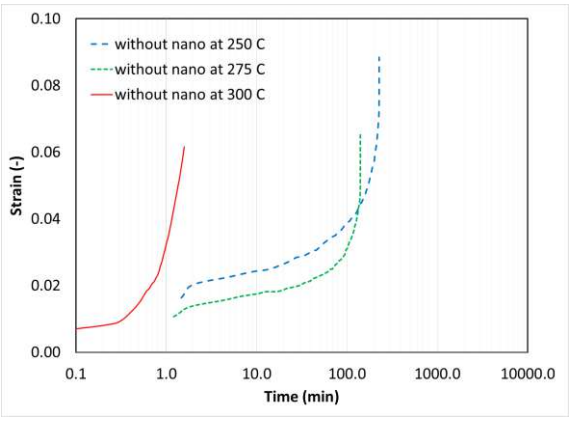

(a)

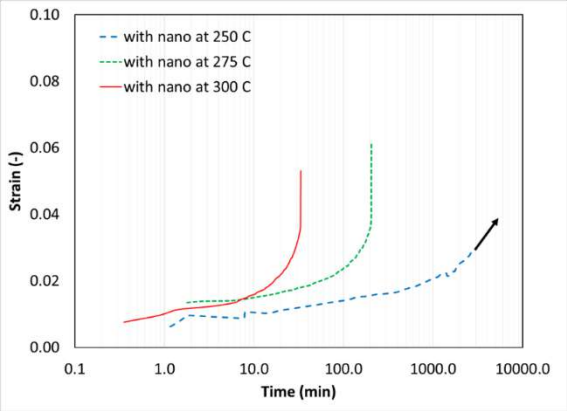

(b)

Figure 4. The strain versus the time for aluminum alloys, (a) unreinforced and (b) reinforced with nano-particles

(a)

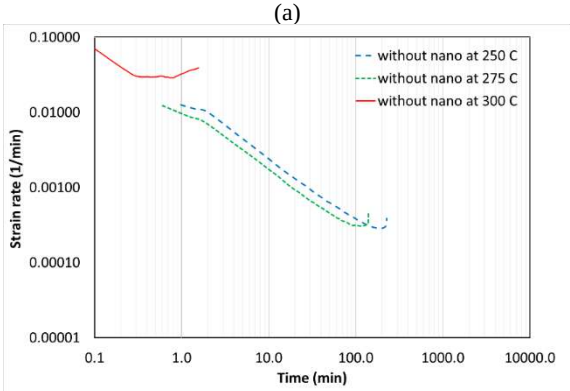

(b)

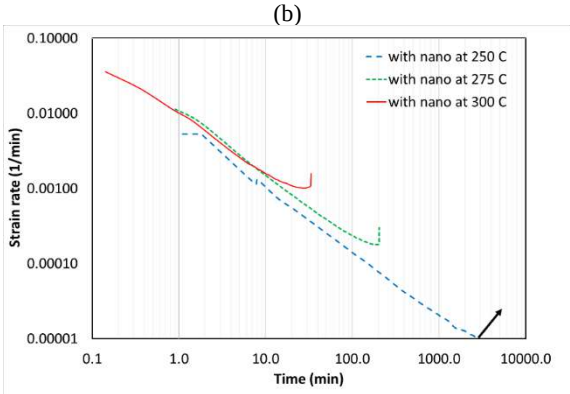

Figure 5. The strain rate versus time for aluminum alloys, (a) unreinforced and (b) reinforced with nano-particles

adding SiO_2 nano-particles was not in the order of other enhancement values. It means that the sample could have higher creep lifetime. The reason was to have a big microstructural defect due to the casting process. However, the creep lifetime of the nano-composite was still higher than that of the aluminum alloy, without nano-particles. This claim could be proved by FE-SEM images of the fracture surface as follows.

TABLE 1. Results of creep testing on aluminum alloys, unreinforced and reinforced with nano-particles

Temperature (°C)	Minimum strain rate (1/min)	Rupture strain (-)	Rupture time (min)
	Without nano-particles		
250	0.000286	0.0885	227.3
275	0.000306	0.0658	140.1
300	0.028907	0.0616	1.6
	With nano-particles		
250	Not finished	Not finished	>2807.1 Not finished
275	0.000179 Diff.: 42%	0.0618 Diff.: 6%	205.1 Diff.: 46%
300	0.001014 Diff.: 96%	0.0531 Diff.: 14%	33.4 Diff.: 1988%

*Diff.: Percentage difference comparing to data without nano-particles.

The rupture strain decreased, when the temperature enhanced, for both aluminum-silicon alloys, unreinforced and reinforced one with nano-particles. The rupture strain for the nano-composite was lower than the rupture strain of the aluminum-silicon alloy, at all temperatures. Besides, by increasing the temperature, the minimum strain rate increased. This minimum strain rate decreased when nano-particles were added to the aluminum alloy, without nano-particles. Such results were also represented in the literature [6,12], for aluminum alloys. Ishikawa and Kobayashi [6] indicated that the minimum strain rate had the dependence to the applied stress and the temperature. Besides, increasing the temperature caused to the enhancement of the minimum strain rate. Such same results were observed in the research. Kandarea et al. [12] showed that by increasing the temperature, the creep lifetime decreased, which showed a good agreement with the obtained results of this article.

To find the activation energy (Q) for the creep behavior in aluminum-silicon alloys, unreinforced and reinforced with nano-particles, the following equation could be used [50]:

$$\dot{\varepsilon}_{min} = Aexp\left(\frac{-Q}{RT}\right) \quad (1)$$

in which, $\dot{\varepsilon}_{min}$ is the minimum strain rate, A is a material constant, R is the gas global constant, which is 8.314 J/mol.K and T is the temperature in Kelvin. By using a logarithmic scale for such equation and curve fitting, one obtains:

$$ln(\dot{\varepsilon}_{min}) = ln(A) - \left(\frac{Q}{R}\right)\frac{1}{T} \quad (2)$$

And comparing to a linear equation, such as $Y = \bar{Y} - \bar{X}X$, where:

$$Y = ln(\dot{\varepsilon}_{min}), \bar{Y} = ln(A), \bar{X} = \frac{Q}{R}, X = \frac{1}{T} \quad (3)$$

the material constant and the activation energy could be found. Obtained results for such investigation is shown in Figure 6.

The coefficient of determination for the aluminum-silicon alloy, without nano-particles, was about 74%, according to the mentioned problem for the sample at 300°C (having a sudden failure and very low creep lifetime and high minimum strain rate). For the nano-composite, there were only two data, since the creep test at 250°C was not finished. However, it was over-predicted in Figure 6. Therefore, no proper conclusion could be generally obtained from these results, since there was a non-proper variation in experimental data. In further investigations, the repeatability of testing would be performed for a proper conclusion. However, the number of experimental data was enough for comparing results of aluminum alloys, with and without nano-particles. Thus, is could be claimed that reported experimental data was reliable.

However, based on obtained results in Figure 6, the activation energy was calculated as 181.2 and 226.6 kJ/mol, for aluminum-silicon alloys, unreinforced and reinforced with nano-particles, respectively. Consequently, the addition of nano-particles into the matrix reduced the activation energy of the material. However, this statement could not be correct due to the non-proper variation in testing. In other words, this range of activation energy (181.2-226.6 kJ/mol) was due to the low repeatability of testing and it seems that nano-particles have no significant effect on the activation energy. The only claim for such values is that the range of the obtained activation energy for aluminum alloys was in agreement with presented values (in the range of 142-249 kJ/mol) in the literature [6-8, 27-30, 34]. Ji et al. [30] represented the activation energy for aluminum matrix composites in the range of 226-272 kJ/mol.

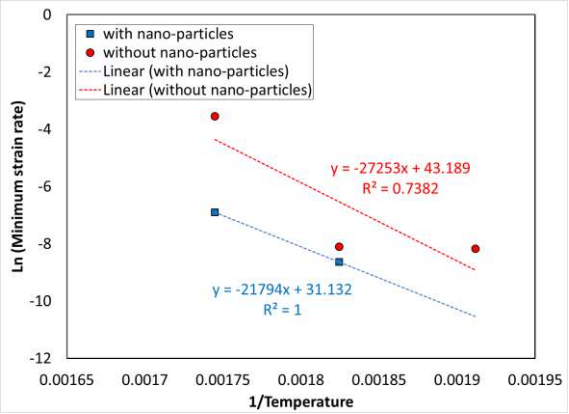

Figure 6. The curve for $ln(\dot{\varepsilon}_{min})$ versus $\frac{1}{T}$ for aluminum alloys, unreinforced and reinforced with nano-particles

Besides the activation energy, the material constant, A, for the nano-composite had lower value (3.3×10^{13}), comparing to that of the aluminum-silicon alloy (5.7×10^{18}). Therefore, the nano-composite had lower minimum strain rate and higher creep lifetime.

FE-SEM images in different magnifications for aluminum-silicon alloys, unreinforced and reinforced with nano-particle, after creep tests is depicted in Figure 7, to check failure mechanisms based on fracture surfaces. Based on this figure, both materials had a brittle fracture behavior, according to the observed quasi-cleavage marks on all fracture surfaces. In addition, micro-cracks could be seen on quasi-cleavage planes. Such marks were reported by Wang et al. [46,51] for the piston aluminum alloy, under cyclic loadings at 120-425°C. They indicated that at 280°C, brittle quasi-cleavage fractures of the aluminum matrix, with broken silicon platelets and other intermetallic particles, were observed at fracture surfaces. At 350°C, the fracture surface morphology was same as that of 280°C, with some dimples, as a ductile fracture mark. However, at 425°C, the fractography of aluminum alloys changed to a typical ductile fracture with micro-dimples and broken silicon platelets [46]. In other words, increasing the temperature caused to change in fracture characteristics, from brittle to ductile fractures. Such behavior showed that the temperature had a significant effect on mechanical properties and fracture behaviors of aluminum-silicon alloys. It should be noted that fracture surfaces of the aluminum-silicon sample at 300°C had a sudden rupture, since the creep lifetime was 1.6 (min). Therefore, there was no clear cleavage planes and no plastic deformation induced. As another result, the cleavages plane seemed to be bigger for the nano-composite. Bigger cleavage areas and less tear ridges showed the poor ductility [49]. In the literature [46], such results, including lower elongations for the nano-composite, were obtained.

Two important notes for Figure 7(b) are about the sample with nano-particles and low improvement of the creep lifetime at 275°C. For the first note, the standard sample at 250°C was not broken, since the creep test was stopped after about two days. As the second note, it should be mentioned that at 250°C, since there was no fracture, the crept surface of the cylindrical specimen could be compared to the initial sample surface, before testing. After creep testing, the roughness of the specimen surface increased, according to the plastic deformation. For the third note, lower improvement of the creep lifetime at 275°C was due to a big microstructural defect (on the left-hand side of the fracture surface), as mentioned before. Although the sample could experience higher creep lifetime than 205.1 min.

Figure 8 shows back-scattered FE-SEM images with EDX maps for aluminum-silicon alloys, unreinforced and reinforced with nano-particles, after creep testing at 275°C under 100 MPa. As can be seen in Figure 8, the gray-colored regime included Al and Si elements and the white-colored regime included the Ni element, which showed the (Al,Ni) intermetallic phase. As a note, the distribution of other elements had no meaning, in both materials. Based on the EDX map, micro-cracks were observed more inside the intermetallic phase, in the aluminum alloy, without nano-particles. However, in the nano-composite, such micro-cracks were observed at boundaries of the intermetallic phase.

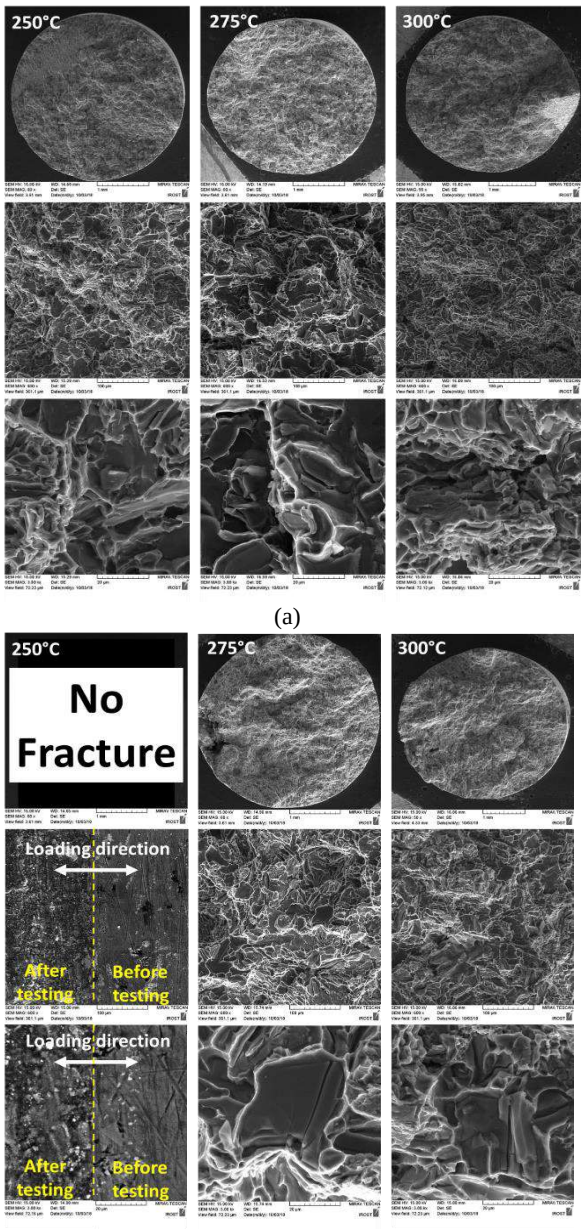

Figure 7. The FE-SEM images of fracture surfaces for aluminum alloys, (a) unreinforced and (b) reinforced with nano-particles

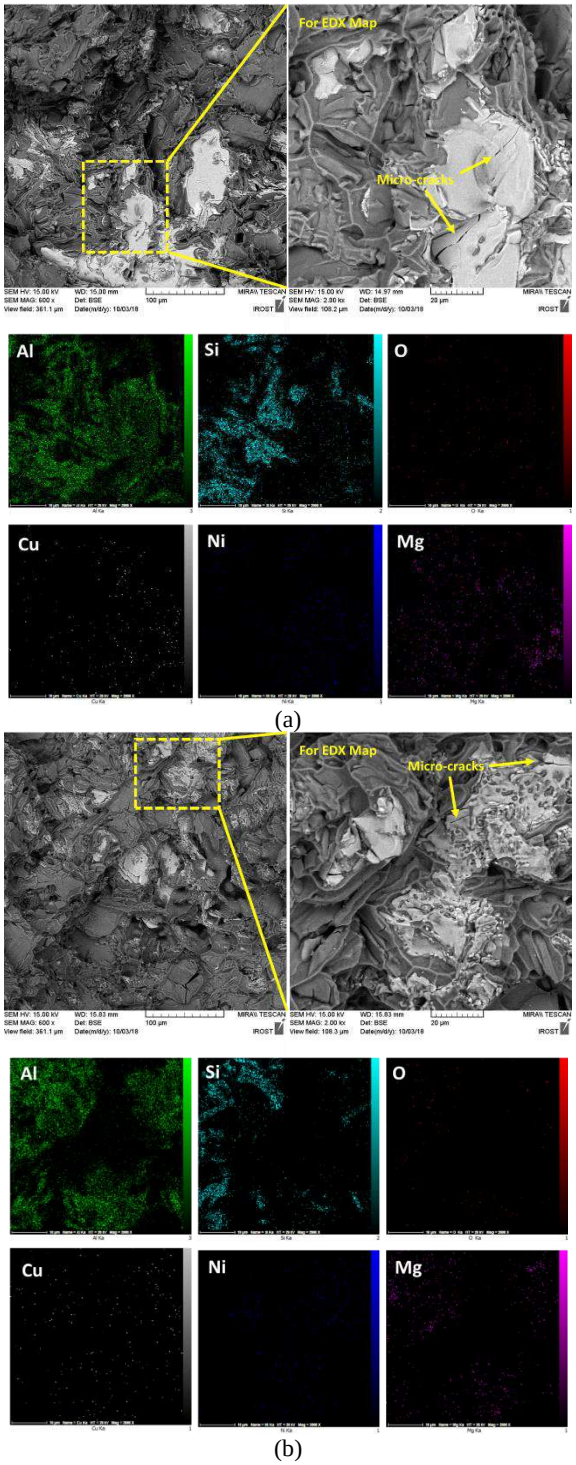

Figure 8. The back-scattered FE-SEM image with the EDX map for aluminum alloys, (a) unreinforced and (b) reinforced with nano-particles, after creep tests at 275°C under 100 MPa.

It seems that the failure mechanism improved, when nano-particles were added to the aluminum matrix. The crack path changed from inside the intermetallic phase into boundaries between (Al,Ni) intermetallic and Si phases. Therefore, the creep lifetime increased for the nano-composite. The crack length in the nano-composite was less than the crack length in the aluminum-silicon alloy, without nano-particles.

Zolfaghari et al. [49] reported that in aluminum-silicon alloys, the failure could be initiated by cleavage marks from intermetallic or Si phases. They added nano-particles in the aluminum matrix to decrease the size of Si phases in the matrix and therefore, increased the fatigue lifetime of the nano-composite. At this condition, Al/Si interface debonding occurred as the failure mechanism, due to the weak interfacial strength. Then, adding nano-particles would increase the strength of the Al/Si interface in the nanocomposite [49].

As another failure mechanism, they also implied that intermetallic phases had significant influences on brittle fractures of aluminum-silicon alloys [49,52]. Rezanezhad et al. [52] presented that the dispersed distribution of tiny intermetallic phases would increase mechanical properties of aluminum-silicon alloys. After Si particles, the second phase, which had higher phase percentage in the microstruture, was related to the (Al,Ni) intermetallic phase [52]. The third phase in the matrix was the (Al,Cu) intermetallic phase [52]. They claimed that lower content of the (Al,Ni) intermetallic phase could enhance the fatigue lifetime. In this case, the crack nucleated usually from large intermetallic phases. Then, these cracks encountered intermetallic phases and they might progress along intermetallic phases [52]. Therefore, lower amount of the (Al,Ni) intermetallic phase caused higher lifetime.

4. CONCLUSIONS

In the present article, the temperature influence on creep and fracture behaviors of the aluminum matrix nano-composite was investigated and then, compared to those of the AlSi12Cu3Ni2MgFe aluminum-silicon alloy. Experimental data can be described as follows,

- The effect of the temperature on the creep lifetime of materials was significant. There was a decreasing trend for the creep lifetime by increasing the temperature. Besides, by increasing the temperature, the minimum strain rate increased.
- The improvement of the creep lifetime by the addition of SiO_2 nano-particles to the matrix was severely significant. Besides, the minimum strain rate for the nano-composite was lower than the minimum strain rate of the aluminum alloy.
- FE-SEM images of the fracture surface indicated a brittle fracture behavior, based on quasi-cleavage marks, for aluminum alloys, unreinforced and reinforced with nano-particles. However, the cleavages plane was bigger for the nano-composite.

- Back-scattered FE-SEM images with EDX maps showed more micro-cracks inside the intermetallic phase, in the aluminum alloy. However, in the nano-composite, the failure location changed to boundaries of the intermetallic phase.

5. ACKNOWLEDGEMENT

Authors thank Motorsazi Pooya Neyestanak (MPN) Company, located in Isfahan, Iran for their financial supports.

6. REFERENCES

1. Azadi, M., Safarloo, S., Loghman, F., Rasouli, R., "Microstructural and thermal properties of piston aluminum alloy reinforced by nano-particles", ***AIP Conference Proceedings***, Vol. 1920, (2018), 020027. DOI: https://doi.org/10.1063/1.5018959
2. Azadi, M., Zolfaghari, M., Rezanezhad, S., Azadi, M., "Preparation of various aluminum matrix composites reinforcing by nanoparticles with different dispersion methods", Proceedings of Iran International Aluminum Conference, Iran, (2018).
3. Azadi, M., Zolfaghari, M., Rezanezhad, S., Azadi, M., "Effects of SiO_2 nano-particles on tribological and mechanical properties of aluminum matrix composites by different dispersion methods", ***Applied Physics A***, Vol. 124, No. 5, (2018), 377. DOI: https://doi.org/10.1007/s00339-018-1797-9
4. Ishikawa, K., Okuda, H., Kobayashi, Y., "Creep behaviors of highly pure aluminum at lower temperatures", ***Materials Science and Engineering A***, Vol. 234-236, (1997), 154-156. DOI: https://doi.org/10.1016/S0921-5093(97)00204-9
5. Jenabali Jahromi, S.A., "Creep behavior of spray-cast 7XXX aluminum alloy", ***Materials and Design***, Vol. 23, (2002), 169-172. DOI: https://doi.org/10.1016/S0261-3069(01)00065-6
6. Ishikawa, K., Kobayashi, Y., "Creep and rupture behavior of a commercial aluminum-magnesium alloy A5083 at constant applied stress", ***Materials Science and Engineering A***, Vol. 387-389, (2004), 613-617. DOI: https://doi.org/10.1016/j.msea.2004.01.099
7. Dobes, F., Milicka, K., "Comparison of thermally activated overcoming of barriers in creep of aluminum and its solid solutions", ***Materials Science and Engineering A***, Vol. 387-389, (2004), 595-598. DOI: https://doi.org/10.1016/j.msea.2004.02.095
8. Srivastava, V., Williams, J.P., McNee, K.R., Greenwood, G.W., Jones, H., "Low stress creep behavior of 7075 high strength aluminum alloy", ***Materials Science and Engineering A***, Vol. 382, (2004), 50-56. DOI: https://doi.org/10.1016/j.msea.2004.04.047
9. Lina, J., Kowalewskib, Z.L., Caoa, J., "Creep rupture of copper and aluminum alloy under combined loadings - Experiments and their various descriptions", ***International Journal of Mechanical Sciences***, Vol. 47, (2005), 1038-1058. DOI: https://doi.org/10.1016/j.ijmecsci.2005.02.010
10. Requena, G., Degischer, H.P., "Creep behavior of unreinforced and short fiber reinforced AlSi12CuMgNi piston alloy", ***Materials Science and Engineering A***, Vol. 420, (2006), 265-275. DOI: https://doi.org/10.1016/j.msea.2006.01.024
11. Couteau, O., Dunand, D.C., "Creep of aluminum syntactic foams", ***Materials Science and Engineering A***, Vol. 488, (2008), 573-579. DOI: https://doi.org/10.1016/j.msea.2008.01.022
12. Kandare, E., Feih, S., Kootsookos, A., Mathys, Z., Lattimer, B.Y., Mouritz, A.P., "Creep-based life prediction modelling of aluminum in fire", ***Materials Science and Engineering A***, Vol. 527, (2010), 1185-1193. DOI: https://doi.org/10.1016/j.msea.2009.10.010
13. Li, L.T., Lin, Y.C., Zhou, H.M., Jiang, Y.Q., "Modeling the high-temperature creep behaviors of 7075 and 2124 aluminum alloys by continuum damage mechanics model", ***Computational Materials Science***, Vol. 73, (2013), 72-78. DOI: https://doi.org/10.1016/j.commatsci.2013.02.022
14. Maximov, J.T., Duncheva, G.V., Anchev, A.P., Ichkova, M.D., "Modeling of strain hardening and creep behavior of 2024T3 aluminum alloy at room and high temperatures", ***Computational Materials Science***, Vol. 83, (2014), 381-393. DOI: http://dx.doi.org/10.1016/j.commatsci.2013.11.057
15. Zhan, L.H., Li, Y.G., Huang, M.H., "Effects of process parameters on mechanical properties and microstructures of creep aged 2124 aluminum alloy", ***Transactions of Nonferrous Metals Society of China***, Vol. 24, (2014), 2232-2238. DOI: https://doi.org/10.1016/S1003-6326(14)63338-0
16. Fernandez-Gutierrez, R., Requena, G.C., "The effect of spheroidisation heat treatment on the creep resistance of a cast AlSi12CuMgNi piston alloy", ***Materials Science and Engineering A***, Vol. 598, (2014), 147-153. DOI: http://dx.doi.org/10.1016/j.msea.2013.12.093
17. Zhang, Q., Zhang, W., Liu, Y., "Evaluation and mathematical modeling of asymmetric tensile and compressive creep in aluminum alloy ZL109", ***Materials Science and Engineering A***, Vol. 628, (2015), 340-349. DOI: http://dx.doi.org/10.1016/j.msea.2015.01.032
18. Spence, T.W., Makhlouf, M.M., "The effect of machining-induced residual stresses on the creep characteristics of aluminum alloys", ***Materials Science and Engineering A***, Vol. 630, (2015), 125-130. DOI: http://dx.doi.org/10.1016/j.msea.2015.02.020
19. Yang, Y.L., Zhan, L.H., Li, J., "Constitutive modeling and spring-back simulation for 2524 aluminum alloy in creep age forming", ***Transactions of Nonferrous Metals Society of China***, Vol. 25, (2015), 3048-3055. DOI: https://doi.org/10.1016/S1003-6326(15)63932-2
20. Lei, C., Yang, H., Li, H., Shi, N., Zhan, L.H., "Dependences of microstructures and properties on initial tempers of creep aged 7050 aluminum alloy", ***Journal of Materials Processing Technology***, Vol. 239, (2016), 125-132. DOI: https://doi.org/10.1016/j.jmatprotec.2016.07.004
21. Erdeniz, D., Nasim, W., Malik, J., Yost, A.R., Park, S., Luca, A.D., Vo, N.Q., Karaman, I., Mansoor, B., Seidman, D.N., Dunand, D.C., "Effect of vanadium micro-alloying on the microstructural evolution and creep behavior of Al-Er-Sc-Zr-Si alloys", ***Acta Materialia***, Vol. 124, (2017), 501-512. DOI: http://dx.doi.org/10.1016/j.actamat.2016.11.033
22. Xu, Y., Zhan, L., Li, W., "Effect of pre-strain on creep aging behavior of 2524 aluminum alloy", ***Journal of Alloys and Compounds***, Vol. 691, (2017), 564-571. DOI: http://dx.doi.org/10.1016/j.jallcom.2016.08.291
23. Li, Y., Shi, Z., Lin, J., Yang, Y.L., Rong, Q., "Extended application of a unified creep-ageing constitutive model to multistep heat treatment of aluminum alloys", ***Materials and Design***, Vol. 122, (2017), 422-432. DOI: http://dx.doi.org/10.1016/j.matdes.2017.03.023
24. Yang, Y., Zhan, L., Shen, R., Yin, X., Li, X., Li, W., Huang, M., He, D., "Effect of pre-deformation on creep age forming of 2219 aluminum alloy: Experimental and constitutive modelling",

Materials Science and Engineering A, Vol. 683, (2017), 227-235. DOI: http://dx.doi.org/10.1016/j.msea.2016.12.024

25. Spigarelli, S., Sandstrom, R., "Basic creep modelling of aluminum", ***Materials Science and Engineering A***, Vol. 711, (2018), 343-349. DOI: https://doi.org/10.1016/j.msea.2017.11.053
26. Lei, C., Li, H., Zheng, G.W., Fu, J., "Thermal-mechanical loading sequences related creep aging behaviors of 7050 aluminum alloy", ***Journal of Alloys and Compounds***, Vol. 731, (2018), 90-99. DOI: https://doi.org/10.1016/j.jallcom.2017.10.035
27. Cadek, J., Oikawa, H., Gustek, V., "Threshold creep behavior of discontinuous aluminum and aluminum alloy matrix composites: An overview", ***Materials Science and Engineering A***, Vol. 190, (1995), 9-23. DOI: https://doi.org/10.1016/0921-5093(94)09605-V
28. El Amri, A., El Haddou, M., Khamlichi, A., "Thermal-mechanical coupled manufacturing simulation in heterogeneous materials", ***Civil Engineering Journal***, Vol. 2, No. 11, (2016), 600-606. DOI: 10.28991/cej-2016-00000062
29. Belodedenko, S., Hanush, V., Baglay, A., Hrechanyi, O., "Fatigue resistance models of structural for risk based inspection", ***Civil Engineering Journal***, Vol. 6, No. 2, (2020), 375-383. DOI: 10.28991/cej-2020-03091477
30. Ji, F., Ma, M.Z., Song, A.J., Zhang, W.G., Zong, H.T., Liang, S.X., Osamu, Y., Liu, R.P., "Creep behavior of in situ TiC_P/2618 aluminum matrix composite", ***Materials Science and Engineering A***, Vol. 506, (2009), 58-62. DOI: https://doi.org/10.1016/j.msea.2008.11.010
31. Gonzalez-Doncel, G., Fernandez, R., "Comments on "Creep behavior of in situ TiC_P/2618 aluminum matrix composite"", ***Materials Science and Engineering A***, Vol. 527, (2010), 3288-3292. DOI: https://doi.org/10.1016/j.msea.2008.11.010
32. Fernandez, R., Gonzalez-Doncel, G., "Understanding the creep fracture behavior of aluminum alloys and aluminum alloy metal matrix composites", ***Materials Science and Engineering A***, Vol. 528, (2011), 8218-8225. DOI: https://doi.org/10.1016/j.msea.2011.07.027
33. Choi, H.J., Bae, D.H., "Creep properties of aluminum-based composite containing multi-walled carbon nanotubes", ***Scripta Materialia***, Vol. 65, (2011), 194-197. DOI: https://doi.org/10.1016/j.scriptamat.2011.03.038
34. Sudharshan Phani, P., Oliver, W.C., "A direct comparison of high temperature nano-indentation creep and uniaxial creep measurements for commercial purity aluminum", ***Acta Materialia***, Vol. 111, (2016), 31-38. DOI: http://dx.doi.org/10.1016/j.actamat.2016.03.032
35. Saberi Kakhki, Y., Nategh, S., Mirdamadi, T.S., "Impression relaxation and creep behavior of Al/SiC nano-composite", ***Materials and Technology***, Vol. 50, No. 4, (2016), 611-615. DOI: 10.17222/mit.2015.113
36. Zhao, Q., Zhang, H., Zhang, X., Qiu, F., Jiang, Q., "Enhanced elevated-temperature mechanical properties of Al-Mn-Mg containing TiC nano-particles by pre-strain and concurrent precipitation", ***Materials Science and Engineering A***, Vol. 718, (2018), 305-310. DOI: https://doi.org/10.1016/j.msea.2018.01.123
37. Barzegar, M.H., Fallahiyekta, M., "Increasing the thermal efficiency of double tube heat exchangers by using nano hybrid", ***Emerging Science Journal***, Vol. 2, No. 1, (2018), 11-19. DOI: http://dx.doi.org/10.28991/esj-2018-01122
38. Azadi, M., Aroo, H., "Creep properties and failure mechanisms of aluminum alloy and aluminum matrix silicon oxide nano-composite under working conditions in engine pistons", ***Materials Research Express***, Vol. 6, No. 11, (2019), 115020. DOI: https://doi.org/10.1088/2053-1591/ab455f
39. Zeren, M., "The effect of heat-treatment on aluminum-based piston alloys", ***Materials and Design***, Vol. 28, (2007), 2511-2517. DOI: https://doi.org/10.1016/j.matdes.2006.09.010
40. Standard test methods for conducting creep, creep-rupture and stress-rupture tests of metallic materials, ASTM-E13911, ASTM International, (2012).
41. Azadi, M., Azadi, M., "Evaluation of high-temperature creep behavior in Inconel-713C nickel-based superalloy considering effects of stress levels", ***Materials Science and Engineering A***, Vol. 689, (2017), 298-305. DOI: https://doi.org/10.1016/j.msea.2017.02.066
42. Zainon, F., Rafezi Ahmad, K., Daud, R., "Effect of heat treatment on microstructure, hardness and wear of aluminum alloy 332", ***Applied Mechanics and Materials***, Vol. 786, (2015), 18-22. DOI: https://doi.org/10.4028/www.scientific.net/AMM.786.18
43. Han, L., Sui, Y., Wang, Q., Wang, K., Jiang, Y., "Effects of Nd on microstructure and mechanical properties of cast Al-Si-Cu-Ni-Mg piston alloys", ***Journal of Alloys and Compounds***, Vol. 695, (2017), 1566-1572. DOI: https://doi.org/10.1016/j.jallcom.2016.10.300
44. Humbertjean, A., Beck, T., "Effect of the casting process on microstructure and lifetime of the Al-piston-alloy AlSi12Cu4Ni3 under thermo-mechanical fatigue with superimposed high-cycle fatigue loading", ***International Journal of Fatigue***, Vol. 53, (2013), 67-74. DOI: https://doi.org/10.1016/j.ijfatigue.2011.09.017
45. Mollaei, M., Azadi, M., Tavakoli, H., "A parametric study on mechanical properties of aluminum-silicon/SiO_2 nano-composites by a solid-liquid phase processing", ***Applied Physics A***, Vol. 124, (2018), 504. DOI: https://doi.org/10.1007/s00339-018-1929-2
46. Wang, M., Pang, J.C., Li, S.X., Zhang, Z.F., "Low-cycle fatigue properties and life prediction of Al-Si piston alloy at elevated temperature", ***Materials Science and Engineering A***, Vol. 704, (2017), 480-492. DOI: https://doi.org/10.1016/j.msea.2017.08.014
47. Issa, H.K., Taherizadeh, A., Maleki, A., Ghaei, A., "Development of an aluminum/amorphous nano-SiO_2 composite using powder metallurgy and hot extrusion processes", ***Ceramics International***, Vol. 43, (2017), 14582-14592. DOI: https://doi.org/10.1016/j.ceramint.2017.06.057
48. Rezanezhad, S., "Investigation of heat treatment effect on bending high-cycle fatigue properties in aluminum-silicon alloy, with and without nano-particles", MSc Thesis, Semnan University, Iran, (2018).
49. Zolfaghari, M., Azadi, M., Azadi, M., "Characterization of high-cycle bending fatigue behaviors for piston aluminum matrix SiO_2 nano-composites in comparison with aluminum-silicon alloys", ***International Journal of Metalcasting***, (2020), DOI: https://doi.org/10.1007/s40962-020-00437-y
50. Bahmanabadi, H., Rezanezhad, S., Azadi, M., Azadi, M., "Characterization of creep damage and lifetime in Inconel-713C nickel-based superalloy by stress-based, strain/strain rate-based and continuum damage mechanics models", ***Materials Research Express***, Vol. 5, No. 2, (2018), 026509. DOI: https://doi.org/10.1088/2053-1591/aaab04
51. Wang, M., Pang, J.C., Zhang, M.X., Liu, H.Q., Li, S.X., Zhang, Z.F., "Thermo-mechanical fatigue behavior and life prediction of the Al-Si piston alloy", ***Materials Science and Engineering A***, Vol. 715, (2018), 62-72. DOI: https://doi.org/10.1016/j.msea.2017.12.099
52. Rezanezhad, S., Azadi, M., Azadi, M., "Influence of heat treatment on high-cycle fatigue and fracture behaviors of piston aluminum alloy under fully-reversed cyclic bending", ***Metals and Materials International***, (2019), DOI: https://doi.org/10.1007/s12540-019-00498-7

Persian Abstract

چکیده

در این مقاله، تاثیر دما بر خواص خزشی و رفتار شکست آلیاژ AlSi12Cu3Ni2MgFe آلومینیوم- سیلیسیوم، تقویت نشده و تقویت شده با ذرات نانو، مورد بررسی قرار گرفت. برای این منظور، نمونه‌های استاندارد به روش ریخته‌گری ثقلی و ریخته‌گری گردابی، به ترتیب برای آلیاژ آلومینیوم و نانوکامپوزیت، ساخته شدند. آزمون خزش نیرو- کنترل، بر روی نمونه‌های استاندارد در سطوح دمایی ۲۵۰، ۲۷۵ و ۳۰۰ درجه سانتیگراد و سطح تنش ۱۰۰ مگاپاسکال انجام شد. سپس، برای شناسایی مکانیزم‌های خرابی، سطح شکست نمونه‌های آزمون با میکروسکوپ الکترون روبشی نشر میدانی، مورد مطالعه قرار گرفت. نتایج تجربی نشان داد که دما، بصورت موثری، رفتار خزش هر دو ماده را تغییر می‌دهد. بعلاوه، با افزودن ذرات نانو و عملیات حرارتی به ماتریس آلومینیوم، بهبود قابل توجهی در خواص خزشی مشاهده شد. چنین افزایشی در عمر خزشی، در دمای ۳۰۰ درجه سانتیگراد بیشتر بود. همچنین، بررسی سطح شکست هر دو ماده نشان داد که رفتار شکست بصورت ترد با آثار شبه‌کلویج بود. در نمونه‌های نانوکامپوزیتی، موقعیت شکست از داخل فازهای بین‌فلزی به مرزهای فازهای بین‌فلزی تغییر کرد.

International Journal of Engineering

Journal Homepage: www.ije.ir

The Effect of Linear Change of Tube Diameter on Subcooled Flow Boiling and Critical Heat Flux

K. DolatiAsl, Y. Bakhshan, E. Abedini*, S. Niazi

Department of Mechanical Engineering, University of Hormozgan, BandarAbbas, Iran

P A P E R I N F O

Paper history:
Received 03 February 2020
Received in revised form 03 April 2020
Accepted 11 June 2020

Keywords:
Fluid Flow Boiling
Critical Heat Flux
Euler-Euler Model
Changing Diameter

A B S T R A C T

One of the major industry problems is the flow boiling, where reaching to the critical heat flux (CHF) condition can lead to a temperature jump and damage of the systems. In the present study, the effects of a uniform change in tube diameter on subcooled flow boiling and CHF was numerically investigated. The Euler-Euler model was used to investigate the relationship between the two liquid and vapor phases. The ANSYS Fluent code was used for simulation. According to the results, a linear increase in the tube diameter leads to increase of vapor volume fraction adjacent to the tube wall, as compared to a regular tube with a fixed-diameter, which leads to increase of the tube wall temperature due to the low value of the heat transfer coefficient. At CHF conditions, where the tube wall temperature is much higher than that in subcooled flow boiling, an increase in tube diameter may lead to higher tube wall temperature before the temperature jump, as compared to the post-jump temperature of a tube with a constant diameter. The best approach for decreasing the tube wall temperature was found to be a linear decrease in tube diameter. For the tube diameter change angles of $\theta < -0.0383°$, tube wall temperature exhibited a decreasing trend from the inlet of the tube to its end.

***doi**: 10.5829/ije.2020.33.08b.17*

1. INTRODUCTION

In many industrial applications, the fluid flow is used for heat transfer, such as heating spaces, electricity production, etc [1, 2]. Also, fluid flow boiling is used for heat transfer because during the fluid phase change, the amount of heat transfer is much higher than the convection heat transfer [3, 4]. By increasing the vapor volume fraction adjacent to the heated wall, which causes decreasing the heat transfer coefficient, the tube wall temperature increases, which can eventually lead to thawing and degradation of the wall. The heat flux at which temperature jump occurs is called the critical heat flux (CHF) [5, 6]. Therefore, CHF should be prevented. Also, in order to have higher heat transfer, the CHF should be increased. A useful way to increase the heat transfer coefficient and CHF value is using nanofluids [7, 8]. Also, the convectional heat transfer and the amount of CHF depends on various factors such as geometry, fluid and nanofluid properties, surface roughness, and working conditions [7-10].

Many studies on enhancement of the CHF by adding nanoparticles to base fluid, have shown that when nanofluid is used instead of pure fluid, the CHF increases significantly (up to 100% has been reported) [10, 11].

The nucleation site density (NSD) on the heated wall where the vapor bubbles are formed is generally estimated using the Lemmert-Chawla model [12], which is a very simple relation and depends only on the fluid saturation temperature and the heated wall temperature. This relationship has been widely used to simulate the subcooled flow boiling that has good accuracy [5, 13]. Also, some researchers have used this relationship to simulate the pure fluid flow boiling at CHF conditions that have achieved acceptable results [14].

Also, working conditions such as pressure and the fluid inlet temperature, affect the fluid flow boiling and the CHF value. By increasing the working pressure of the fluid flow, the saturation temperature will also increase,

*Corresponding Author Email: *abedini@hormozgan.ac.ir* (E. Abedini)

Please cite this article as: K. DolatiAsl, Y. Bakhshan, E. Abedini, S. Niazi, The Effect of Linear Change of Tube Diameter on Subcooled Flow Boiling and Critical Heat Flux, International Journal of Engineering (IJE), IJE TRANSACTIONS B: Applications Vol. 33, No. 8, (August 2020) 1590-1597

which will increase the amount of heat received by the liquid to occur evaporation, thereby increasing the CHF [15]. Increasing the fluid inlet temperature also causes the liquid to evaporate at lower heat flux, then reduces the amount of CHF [16].

Netz et al. [17] experimented vertical channel with a wavy wall with 0.25, 0.5, and 0.75 mm amplitude. They observed that at 0.25 and 0.75 mm amplitude wavy wall, the mean wall temperature decreases and increases respectively at constant heat flux in comparison to the straight channel. They concluded that more experimental analysis is needed to find the best wavy amplitude for reducing the wall temperature.

In a study carried out by Patil et al. [18], the experimental and simulation data showed that by using the bump in the divergent channel, the heat transfer coefficient increases 25 to 35% as compared to the plain divergent channel. Also, they observed that pressure drop is reduced by using the divergent channel with internal bump instead of the cylindrical tube. They observed that using the water-ethylene glycol mixture will increase the Nusselt number in comparison with pure water.

After the experimental study on sinusoidal wavy minichannel by Khoshvaght-Aliabadi et al. [19], they proposed two correlations for Nusselt number and friction factor for convective fluid flow inside sinusoidal wavy minichannel. Their correlations were based on Re, Pr, wavy amplitude, hydraulic diameter, and tube length. Al-Asadi et al. [20] simulated laminar fluid flow convection in the microchannel, which used a cylindrical vortex generator. They observed that using the quarter-circle vortex generator was not effective on increasing the heat transfer coefficient, but half-circle spanned the whole width of the microchannel and increased the heat transfer coefficient.

Akbarzadeh et al. [21] examined the flow of fluid through channels with different walls and found that the channel with the sinusoidal wall had the highest heat transfer rate. Vo et al. [22] investigated the nanofluid flow inside the sinusoidal channel. The used nanoparticles with different shapes, which eventually showed that the platelet shape and brick shape nanoparticles had the highest and lowest heat transfer coefficients, respectively. The results showed that the Nusselt number had a sudden change in the location of bumps and indents of the channel wall. Also, the fluid temperature in those locations was higher than elsewhere.

In this study, the effect of the linear changing tube diameter on subcooled flow boiling and CHF value of water flow is investigated. For validating the simulation results, the results of subcooled flow boiling in regular tubes with a uniform diameter are used. The results reported by Krepper et al. [13] are used for the simulation of subcooled flow boiling and the results presented by Kim et al. [23] are used for validating the simulation at the CHF condition. The main purpose of the present study is to reduce the temperature of the tube wall and to increase the amount of CHF. After verification of the numerical results with the experimental data, tubes with different changing diameters are modeled, and the subcooled flow boiling at constant heat flux is simulated. To estimate the CHF value, in each tube, the flow boiling is simulated at the desired heat flux; if temperature jumping didn't occur on the tube wall, the simulation would be repeated by an increased heat flux; and this procedure is continued until temperature jump occurs, which indicates the CHF.

2. MATHEMATICAL MODELLING

In the simulation carried out in this study, subcooled flow boiling has been used. During boiling, two phases of liquid water and vapor have been used. The Euler-Euler model has been used to investigate the relationship between the two liquid and vapor phases.

Euler-Euler conservation equations include mass, momentum, and energy conservation equations for each of the phases. The governing equations have been described in our previous research [5].

To simulate the turbulent fluid flow, including boiling in the CHF state, the turbulent k-ε model, and the near-wall conditions have been used.

3. GEOMETRY AND BOUNDARY CONDITIONS

In this study, for simulation of subcooled flow boiling (case 1), the data of Krepper et al. [13] is used and to investigate the simulation results of subcooled flow boiling at the CHF condition (case 2), the data of Kim et al. [23] is used. Table 1 presents the geometry and operating conditions of each case.

In order to investigate the effect of tube diameter change on flow boiling, in each of the studied cases, it is assumed that the tube diameter change is uniform with angle θ relative to the inlet tube diameter (Figure 1 (a)). If θ is equal to zero, the tube diameter is constant and represents the original state (according to Table 1). If the value of θ is greater than zero, the tube diameter is

TABLE 1. Geometry specifications and working conditions of the samples

Conditions	Case 1 [13]	Case 2 [23]
Tube length (m)	2	0.1
Tube diameter (mm)	15.4	5.53
Pressure (kPa)	4500	101
Mass flux (kg/m^2·s)	900	2000-2500
Heat flux (kW/m^2)	570	4500-6000

incremental, and if the value of θ is negative, the tube diameter is considered as decreasing relative to the base tube diameter (as shown in Table 1). Also, a sample grid is shown in Figure 1 (b). The used grids for the tube domain are structured, and all cells are rectangular.

4. RESULTS

The results of the simulations in this section are divided into two parts: simulation of subcooled flow boiling and subcooled flow boiling at CHF condition.

4. 1. Subcooled Flow Boiling Simulation

Krepper et al. [13] used 20 cells in the radial direction and 150 cells in the longitudinal direction of the tube for simulating the flow boiling according to case 1. In this paper, a domain with different grids was used to investigate the independence of the results from the grid (based on Figure 1(b)). Figures 2 and 3 show the simulation results for different grids. Based on the results and to facilitate the simulations, a grid with 32 cells in the radial direction and 500 cells in the longitudinal direction of the tube was used, while Krepper et al. [13] used 20 cells in the radial direction and 150 cells in the longitudinal direction of the tube.

In Figures 4 and 5, the results obtained in this study are compared with the experimental results, which have very similarities and can be used for other simulations.

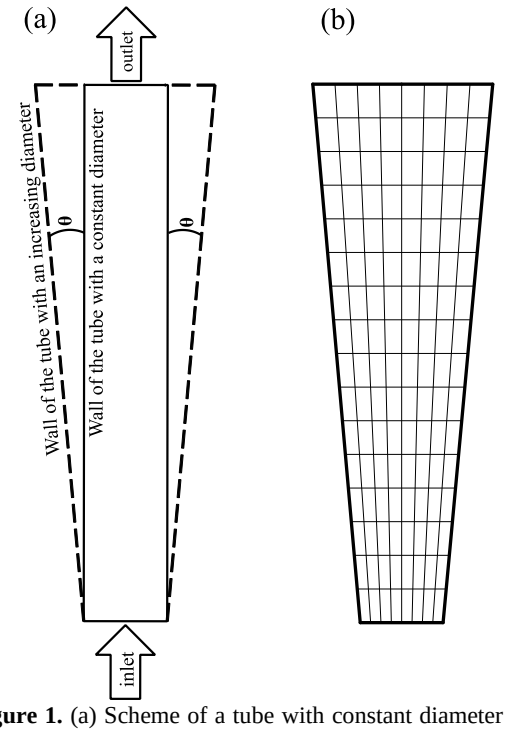

Figure 1. (a) Scheme of a tube with constant diameter and linear variable diameter with positive θ [deg] and (b) a sample of structured grid

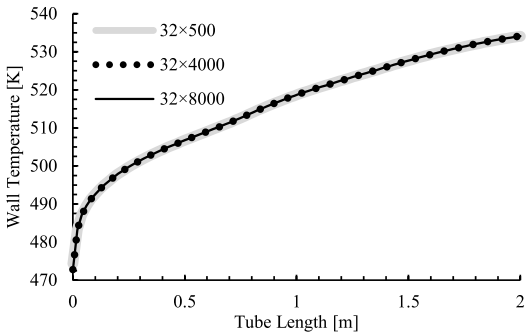

Figure 2. Influence of grid size on tube wall temperature

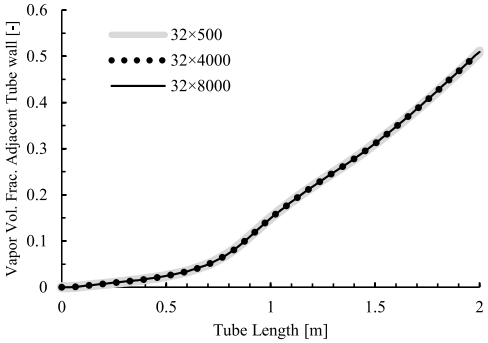

Figure 3. Influence of grid size on vapor volume fraction adjacent to the tube wall

Figure 6 shows the velocity profiles for each of the tubes with constant, decreasing, and increasing diameters at 1m distance from the tube inlet. It should be noted that the diameter of the tube is proportional to the θ [deg], which is why the maximum vertical axis value for the tubes are different. At constant mass flux, as the tube diameter increases linearly, the axial velocity decreases, and as the tube diameter decreases, the axial velocity increases. Increasing the velocity adjacent to the tube wall causes the vapor bubbles to be separated more rapidly from the surface of the tube wall.

Figure 7 shows the vapor volume fraction on the tube wall. Due to apply of constant heat flux to the tube wall, the vapor volume fraction increases consistently. It can be seen in Figure 7 that vapor volume fraction in tubes with an increasing diameter ($\theta = 0.0192°$ & $0.0383°$) is higher than the constant diameter tube. On the other hand, decreasing the tube diameter leads to a decrease in vapor volume fraction. As mentioned earlier in Figure 6, the main reason for the variation of vapor volume fraction adjacent to the wall is due to changes in velocity profile, which as the fluid flow velocity in the decreasing diameter tube increases, the vapor volume fraction adjacent the tube wall decreases.

Figure 8 shows the tube wall temperature. It is observed that if the diameter decreases linearly, the tube wall temperature decreases in comparison with the tube with a constant diameter, and as the diameter

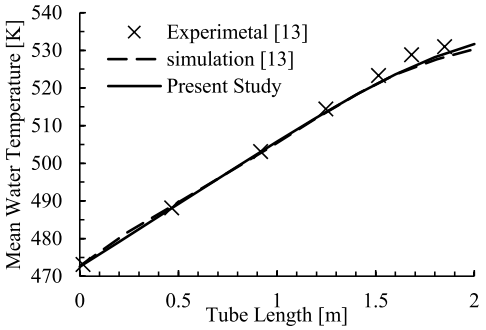

Figure 4. Comparison of experimental [13] and simulated results of mean fluid flow temperature (case 1)

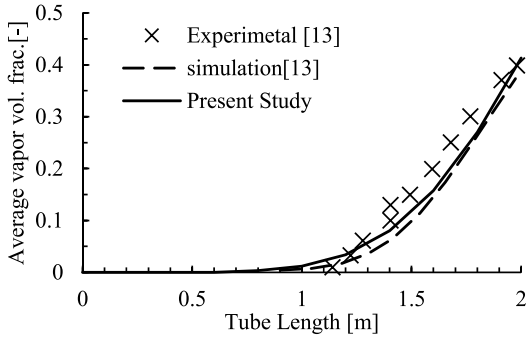

Figure 5. Comparison of experimental [13] and simulated results of mean vapor volume fraction (case 1)

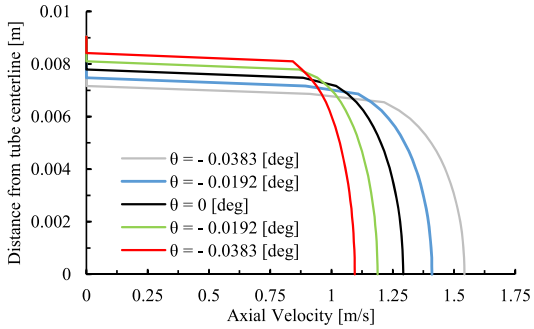

Figure 6. The axial velocity profile in the radial direction in the middle of the tube (based on case 1)

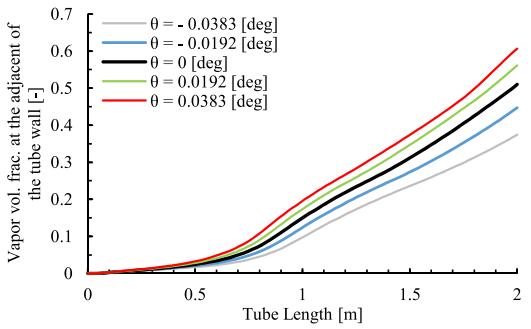

Figure 7. Vapor volume fraction adjacent the tube wall (based on case 1)

increases, the tube wall temperature increases in comparison with the tube with a constant diameter.

According to Figures 7 and 8, when the vapor volume fraction adjacent the tube on the tube wall increases, it means that the heat transfer coefficient from the tube wall to the fluid flow decreases, thereby increasing the tube wall temperature. For this reason, by increasing the vapor volume fraction on the tube wall in tubes with increasing diameter, the tube wall temperature is also higher.

Figures 9 and 10 show the mean fluid temperature and mean volume fraction in the tube, respectively. It is observed that by increasing the diameter of the tube compared to the tube with a constant diameter, the mean fluid temperature increases in different sections.

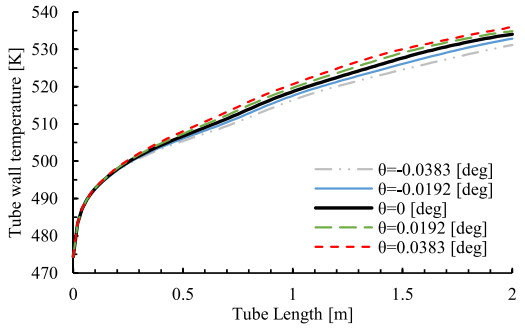

Figure 8. Tube wall temperature (based on case 1)

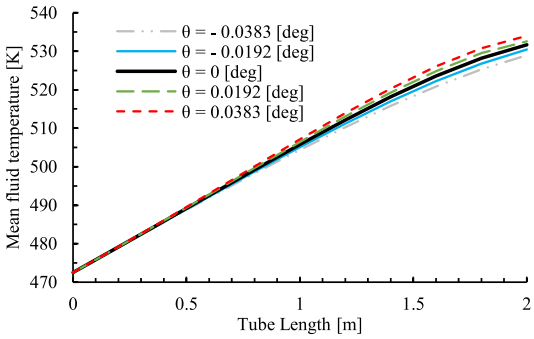

Figure 9. Mean fluid temperature (based on case 1)

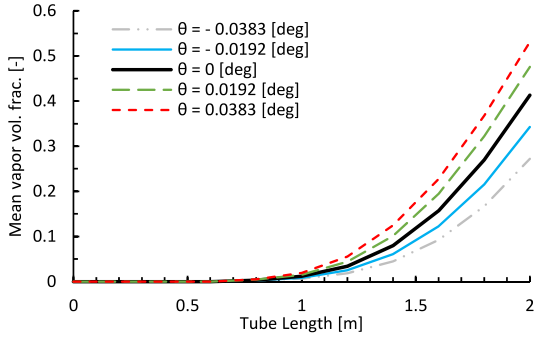

Figure 10. Mean vapor volume fraction (based on case 1)

In this study, the amount of heat flux applied to the tube wall is constant, which is defined as W/m^2. As the tube diameter varies, the total heat applied to the tube also changes, which means that as the tube diameter increases, the total heat flux applied to the tube increases, and vice versa, which naturally will be effective on the amount of produced vapor on the tube wall. Figure 11 shows the total heat applied to tubes with varying diameters. As the tube diameter and surface area increase, the amount of heat applied to the tube and fluid flow increases, which itself increases the vapor production.

Then, assuming that for all tubes with varying diameters, the total value of applied heat is equal to the amount of heat applied to the tube with a constant diameter, the vapor volume fraction and tube wall temperature are investigated (Figures 12 and 13). Assuming a heat flux value of q=570 kW/m^2 and a constant diameter of 0.0154 m, the total heat absorbed by the tube with a constant diameter will be Q=55.14 kW. By using this value, the value of heat flux is estimated for different types of tubes.

According to Figure 12, the vapor volume fraction on the tube wall decreases with decreasing tube diameter, which mentioned in describing Figure 7. It should be noted, however, that in tubes with increased diameter, the amount of vapor fraction is somewhat equal to the amount of vapor fraction in the tube with a constant diameter. The tube wall temperature is equal for different tubes (Figure 13); the main reason is that the amount of heat absorbed by the tube is constant, while the vapor on the tube wall is also somewhat equal for the tubes, and causing the heat transfer coefficient from the tube wall to the fluid flow be close together for different tubes.

Figure 14 shows the vapor volume fraction at the outlet of different tubes. If the amount of applied heat flux to the tube wall is constant, due to the change in diameter and surface area of the tube, the total amount of heat received by the fluid flows will be changed, which results in a decrease or increase in the vapor volume fraction at the tube outlet. However, when the total amount of heat received by fluid flow is constant to the total heat applied to the tube with a constant diameter (q=570 kW/m^2), the vapor volume fraction at the tube outlet is approximately constant for different tubes.

4. 2. Subcooled Flow Boiling Simulation at Chf Condition For simulating fluid flow boiling based on case 2, a grid with 15 cells in radial and 500 cells in the axis direction of the tube was used. Figure 15 shows the simulated tube wall temperature. At the heat flux of 5400 kW/m^2, the tube wall temperature increases with a uniform slope, but when the heat flux is increased to 5500 kW/m^2 (less than 2%), the wall temperature at the end of the tube rises sharply. The corresponding heat

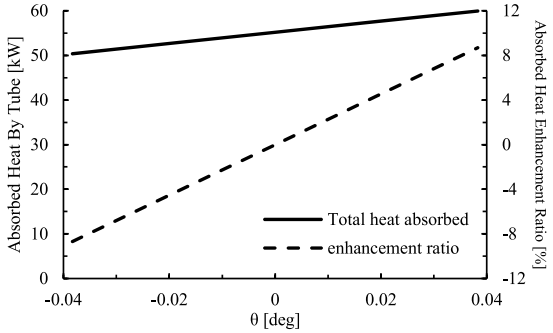

Figure 11. Effect of changing tube diameter (by θ) on the amount of heat applied to the tube

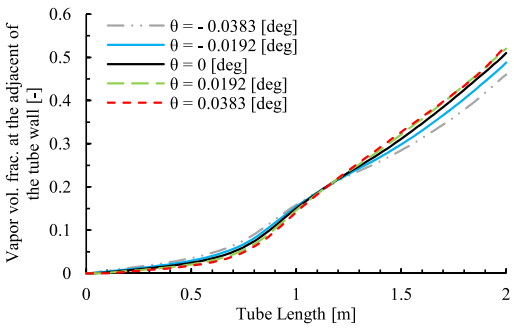

Figure 12. Vapor volume fraction adjacent the tube wall (based on case 1 & Q=55.14 kW)

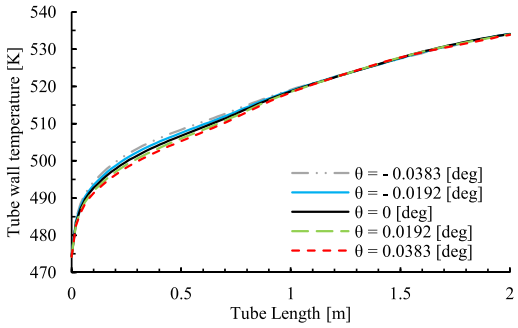

Figure 13. Tube wall temperature (based on case 1 & Q=55.14 kW)

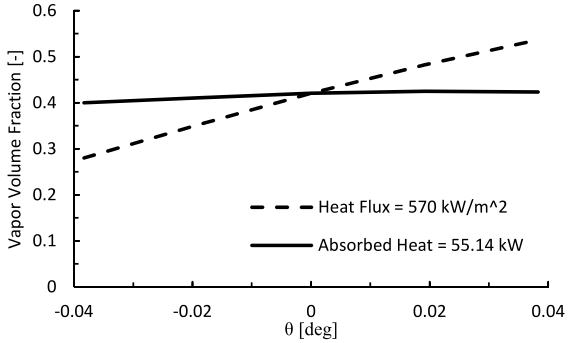

Figure 14. Outlet vapor volume fraction for constant heat flux and constant total heat (based on case 1)

flux is referred to as CHF. As shown in Figure 15, the CHF value is determined when the tube wall temperature has a sudden jump. Preventing the sudden rise in temperature that occurs at CHF is essential to prevent tube damage.

In Figure 16, the CHF values estimated in the present study are compared with the experimental data [23], which indicates the reliability of the simulation results.

Figure 17 shows the temperature for different tubes, based on case 2. The amount of heat flux applied in each state of Figure 17 is assumed to be just before the sudden jump of temperature. It is observed that when the angle of change of tube diameter is greater than $\theta > -0.0383°$, the temperature of the tube wall gradually increases from the inlet to the end of the tube, but when the angle of change of tube diameter is less than $\theta < -0.0383°$, the tube wall temperature gradually decreases from the inlet to the end of tube.

It is noticeable in Figure 17, in the tube with increasing diameter, the wall temperature (before the temperature jumps) increases to near the jumped temperature in the tube with a constant diameter. Accordingly, the use of CHF and temperature jump to determine the critical working condition of fluid flow boiling in the tube cannot be defended in this case. The main purpose of the CHF determination is to prevent the drastic rise in tube temperature and tube degradation, but it is observed that the tube wall temperature before the jump may increase sharply which in turn can lead to tube damage.

Because different tubes are of different materials and the critical temperatures are different and cannot be accurately accessed, Figure 18 shows the CHF which causes the sudden temperature jump occurring at the end of the tube. Based on the previous results, the tube wall temperature was studied in different states, and it is observed that the amount of heat flux, causing the temperature to jump in different tubes has no systematic changes. According to Figure 18, in tubes with diameter change in the range of $-0.0477° < \theta < 0.0477°$ the amount of heat flux associated with the temperature jump at $\theta = 0.0962°$ & $\theta = 0°$ has the highest values. Based on Figure 17, the tube with an angle of change of $\theta = -0.00962°$ is the best choice for increasing the CHF, because it increase the CHF significantly by slightly increasing the tube wall temperature compared to the tube with a constant diameter.

Figure 19 shows the total amount of heat applied to the tube by considering the area of the tube and the amount of heat flux, according to Figure 18. It is observed that the effect of the tube surface area changes on the total amount of heat is much less than the effect of

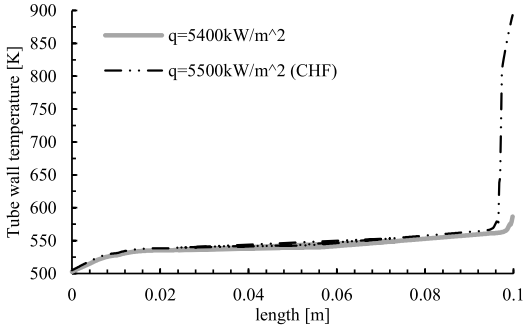

Figure 15. Tube wall temperature at q=5400 & 5500 kW/m^2 (based on case 2)

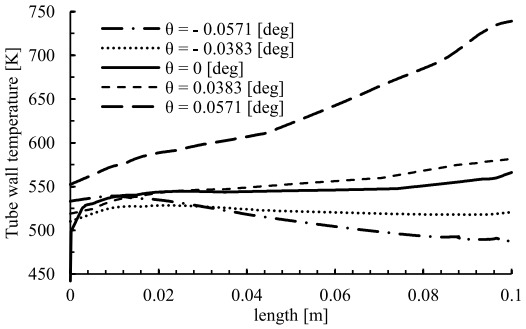

Figure 17. CHF and tube wall temperature before sudden temperature jump (based on case 2 & G= 2500 kg/m^2·s)

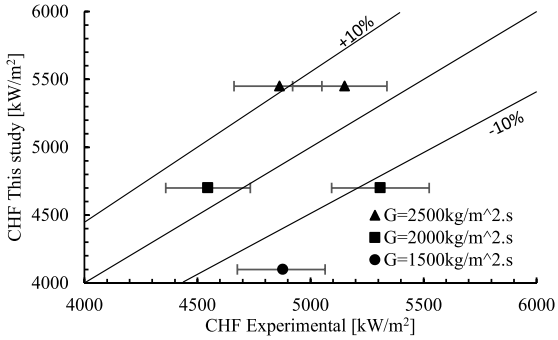

Figure 16. Comparison of simulated result and experimental data [23] of CHF (based on case 2)

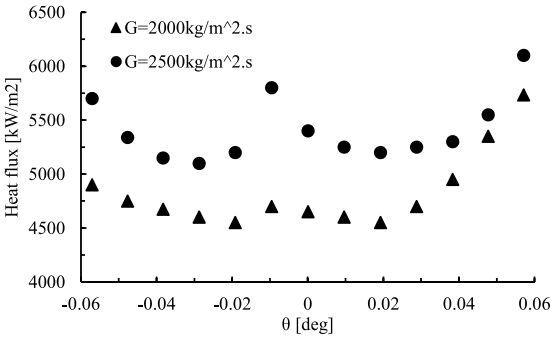

Figure 18. Heat flux at a sudden jump in temperature at the end of the tube (based on case 2)

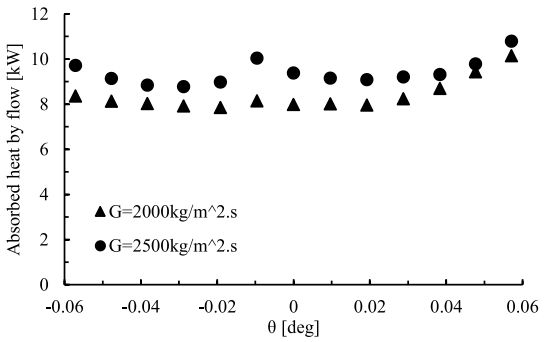

Figure 19. The total amount of heat applied to the tube, based on the heat flux in Figure 18 (based on case 2)

the heat flux changes on the tube, so that even with increasing diameter and area of the tube, the total heat content decreased which is due to the reduced heat flux applied to the tube.

5. CONCLUSION

The main purpose of this study was to investigate the effect of linearly decreasing or increasing tube diameter on subcooled flow boiling and CHF values. Based on the theory of the fluid momentum, the results show that in increasing diamter, the vapor phase attracted to the tube wall decreases and in the linearly decreasing diameter, the vapor volume fraction on the tube wall deascreses. Increasing or decreasing tube diameter, increases or decreases the fluid heat transfer coefficient, respectively. Due to the low heat transfer of the wall by the vapor phase compared to the liquid phase, the tube wall temperature increases as the tube diameter increases. The best way to reduce the wall temperature is using the tube with a decreasing diameter. In the tube with increasing diameter, the temperature of the tube wall at the end of the tube before the sudden jump is almost equal to the temperature after the sudden jump in the tube with a constant diameter, indicating that the use of the definition of the sudden jump of the wall temperature is not the correct way to determine the CHF because the purpose of CHF determination is to prevent the sudden rise in tube wall temperature and to prevent tube degradation. For the mass fluxes of 2000 and 2500 kg/m^2·s, when using a tube with a changing diameter of $\theta = -0.00962°$ compared to the tube with a constant diameter, the CHF values increased about 2.5% and 8%, respectively, and the total amount of heat transfer also increased by about 2% and 7%, respectively. If the total heat applied to the tube considered constant in the subcooled flow boiling, increasing or decreasing the tube diameter does not affect the tube wall temperature.

6. REFERENCES

1. Sarafraz, M.M., Hormozi, F., Peyghambarzadeh, S.M. and Vaeli, N., "Upward Flow Boiling to DI-Water and Cuo Nanofluids Inside the Concentric Annuli", ***Journal of Applied Fluid Mechanics,*** Vol. 8, No. 4, (2015), 651-659. doi:10.18869/acadpub.jafm.67.223.19404.
2. Sengupta, A.R., Gupta, R. and Biswas, A., "Computational Fluid Dynamics Analysis of Stove Systems for Cooking and Drying of Muga Silk", ***Emerging Science Journal***, Vol. 3, No. 5, (2019), 285-292. doi:10.28991/esj-2019-01191.
3. DolatiAsl, K., Bakhshan, Y., Abedini, E. and Niazi, S., "Correlations for estimating critical heat flux (CHF) of nanofluid flow boiling", ***International Journal of Heat and Mass Transfer***, Vol. 139, No. 2019, (2019), 69-76. doi:10.1016/j.ijheatmasstransfer.2019.04.146.
4. Sikarwar, B.S., Shukla, R.K. and Sharma, S.K., "Experimental Study for Investigating the Mechanism of Heat Transfer Near the Critical Heat Flux in Nucleate Pool Boiling", ***International Journal of Engineering, Transactions B: Applications***, Vol. 28, No. 8, (2015), 1241-1250. doi:10.5829/idosi.ije.2015.28.08b.18.
5. DolatiAsl, K., Bakhshan, Y., Abedini, E. and Niazi, S., "Numerical Investigation of Critical Heat Flux in Subcooled Flow Boiling of Nanofluids", ***Journal of Thermal Analysis and Calorimetry***, Vol. 139, No. 3, (2020), 2295-2308. doi:10.1007/s10973-019-08616-8.
6. Barzegar, M.H. and Fallahiyekta, M., "Increasing the Thermal Efficiency of Double Tube Heat Exchangers by Using Nano Hybrid", ***Emerging Science Journal***, Vol. 2, No. 1, (2018), 11-19. doi:10.28991/esj-2018-01122.
7. Adibi, T., Razavi, S.E. and Adibi, Q., "A Characteristic-based Numerical Simulation of Water-titanium Dioxide Nano-fluid in Closed Domains", ***International Journal of Engineering, Transactions A: Basics***, Vol. 22, No. 1, (2020), 158-163. doi:10.5829/ije.2020.33.01a.18.
8. Shahriari, A., Jahantigh, N. and Rakani, F., "Assessment of Particle-size and Temperature Effect of Nanofluid on Heat Transfer Adopting Lattice Boltzmann Model", ***International Journal of Engineering, Transactions A: Basics***, Vol. 31, No. 10, (2018), 1749-1759. doi:10.5829/ije.2018.31.10a.18.
9. Zeinali Heris, S., Nassan, T.H., Noie, S.H., Sardarabadi, H. and Sardarabadi, M., "Laminar convective heat transfer of Al2O3/water nanofluid through square cross-sectional duct", International Journal of Heat and Fluid Flow, Vol. 44, (2013), 375-382. doi:10.1016/j.ijheatfluidflow.2013.07.006.
10. Kim, T., Chang, W.J. and Chang, S.H., Flow boiling CHF enhancement using Al_2O_3 nanofluid and an Al2O3 nanoparticle deposited tube, ***International Journal of Heat and Mass Transfer***, Vol. 54, No. 9–10, (2011), 2021-2025. doi:10.1016/j.ijheatmasstransfer.2010.12.029.
11. Song, S.L., Lee, J.H. and Chang, S.H., CHF enhancement of SiC nanofluid in pool boiling experiment, ***Experimental Thermal and Fluid Science***, Vol. 52, (2014), 12-18, doi: 10.1016/j.expthermflusci.2013.08.008.
12. Lemmert, M. and Chawla, J.M., "Influence of flow velocity on surface boiling heat transfer coefficient", ***Heat Transfer in Boiling,*** (1977), 237-274.
13. Krepper, E., Koncar, B., and Egorov, Y., "CFD modelling of subcooled boiling-Concept, validation and application to fuel assembly design", ***Nuclear Engineering and Design***, Vol. 237, No. 7, (2007), 716-731. doi:10.1016/j.nucengdes.2006.10.023.
14. DolatiAsl, K., Abedini, E., Bakhshan, Y., "Heat transfer analysis and estimation of CHF in vertical channel", ***Journal of Applied Dynamic Systems and Control***, Vol. 2, No. 1, (2019), 18-23.

15. Wang, Y., Deng, K., Wu, J., Su, G. and Qiu, S., "The Characteristics and Correlation of Nanofluid Flow Boiling Critical Heat Flux", ***International Journal of Heat and Mass Transfer***, Vol. 122, (2018), 212-221. doi:10.1016/j.ijheatmasstransfer.2018.01.118.

16. Vafaei, S. and Wen, D., "Critical Heat Flux of Nanofluids inside a Single Microchannel: Experiments and Correlations", ***Chemical Engineering Research and Design***, Vol. 92, No. 11, (2014), 2339-2351. doi:10.1016/j.cherd.2014.02.014.

17. Netz, T., Shalem, R., Aharon, J., Ziskind, G. and Letan, R., "Incipient Flow Boiling in a Vertical Channel With a Wavy Wall", in Proceedings of the 14th International Heat Transfer Conference, Washington, DC, USA, (2010). doi:10.1115/IHTC14-22809.

18. Patil, A.S., Kulkarni, A.V. and Pansare, V.B., "Experimental analysis of convective heat transfer in divergent channel", ***International Journal of Engineering Research and General Science***, Vol. 3, No. 6, (2015), 691-698.

19. Khoshvaght-Aliabadi, M., Sahamiyan, M., Hesampour, M. and Sartipzadeh, O., "Experimental study on cooling performance of sinusoidal–wavy minichannel heat sink", ***Applied Thermal Engineering***, Vol. 92, (2016), 50-61. doi:10.1016/j.applthermaleng.2015.09.015.

20. Al-Asadi, M.T., Alkasmoul, F.S. and Wilson, M.C.T., "Heat transfer enhancement in a micro-channel cooling system using cylindrical vortex generators", ***International Communications in Heat and Mass Transfer***, Vol. 74, (2016), 40-47. doi:10.1016/j.icheatmasstransfer.2016.03.002.

21. Akbarzadeh, M., Rashidi, S. and Esfahani, J.A., "Influences of corrugation profiles on entropy generation, heat transfer, pressure drop, and performance in a wavy channel", ***Applied Thermal Engineering***, Vol. 116, (2017), 278-291. doi:10.1016/j.applthermaleng.2017.01.076.

22. Vo, D.D., Alsarraf, J., Moradikazerouni, A., Afrand, M., Salehipour H. and Qi C., "Numerical investigation of γ-AlOOH nano-fluid convection performance in a wavy channel considering various shapes of nanoadditives", ***Powder Technology***, Vol. 345, (2019), 649-657. doi:10.1016/j.powtec.2019.01.057.

23. Kim, S.J., McKrell, T., Buongiorno, J. and Hu, L.W., "Experimental Study of Flow Critical Heat Flux in Alumina-Water, Zinc-Oxide-Water, and Diamond-Water Nanofluids", ***Heat Transfer***, Vol. 131, (2009), 043204-1-7. doi:10.1115/1.3072924.

Persian Abstract

چکیده

یکی از مسائل مهم در صنایع، جوشش جریان سیال است که رسیدن به شرایط شار حرارتی بحرانی، منجر به وقوع پرش دمایی و ایجاد خسارت به سیستم‌ها می‌شود. در مطالعه حاضر به بررسی عددی تاثیر تغییر یکنواخت قطر لوله بر جوشش جریان سیال مادون سرد و در شرایط شار حرارتی بحرانی پرداخته شده است. مدل اویلر–اویلر برای تحلیل ارتباط بین دو فاز مایع و بخار مورد استفاده قرار گرفته است. برای انجام شبیه‌سازی‌ها نیز از نرم‌افزار انسیس فلوئنت استفاده شده است. با توجه به نتایج بدست آمده، در مقایسه با لوله معمولی دارای قطر ثابت، افزایش قطر لوله سبب افزایش کسر حجمی بخار در کنار دیواره لوله می‌شود که با کاهش مقدار ضریب انتقال حرارت از دیواره لوله به جریان سیال، سبب افزایش مقدار دمای لوله می‌شود. در محدوده شار حرارتی بحرانی که مقدار دمای دیواره لوله نسبت به شرایط جوشش مادون سرد بیشتر است، افزایش مقدار قطر لوله نسبت به شرایط لوله با قطر ثابت، افزایش دمای لوله قبل از پرش ناگهانی دما را در پی دارد. بهترین روش برای کاهش دمای دیواره لوله، کاهش قطر لوله است. در شرایط تغییرات قطر لوله با زاویه $\theta < -۰/۰۳۸۳^{o}$، دمای دیواره لوله از ابتدا تا انتهای لوله نسبت به لوله با قطر ثابت، دارای کاهش است.

International Journal of Engineering

Journal Homepage: www.ije.ir

Taguchi Approach and Response Surface Analysis for Design of a High-performance Single-walled Carbon Nanotube Bundle Interconnects in a Full Adder

S. Ghorbani[a], S. Ghorbani[b], K. Reza Kashyzadeh*[b]

[a] *Department of Electrical Engineering, Islamshahr Branch, Islamic Azad University, Islamshahr, Iran*
[b] *Department of Mechanical and Instrumental Engineering, Academy of Engineering, Peoples' Friendship University of Russia (RUDN University), 6 Miklukho-Maklaya Street, Moscow, 117198, Russian Federation*

PAPER INFO

Paper history:
Received 07 February 2020
Received in revised form 16 April 2020
Accepted 11 June 2020

Keywords:
Carbon Nanotube Bundle Interconnects
Full Adder
Power Dissipation
Propagation Delay
Response Surface Method
Taguchi Approach

ABSTRACT

In this study, it was attempted to design a high-performance single-walled carbon nanotube (SWCNT) bundle interconnects in a full adder. For this purpose, the circuit performance was investigated using simulation in HSPICE software and considering the technology of 32-nm. Next, the effects of geometric parameters including the diameter of a nanotube, distance between nanotubes in a bundle, and width and length of the bundle were analyzed on the performance of SWCNT bundle interconnects in a full adder using Taguchi approach (TA). The results of Taguchi sensitivity analysis (TSA) showed that the bundle length is the most effective parameter on the circuit performance (about 51% on the power dissipation and 47% on the propagation delay). Moreover, the distance between nanotubes greatly affects the response compared to other parameters. Also, response surface method (RSM) indicated that an increase in the length of interconnects (L) improves the output of power dissipation. As the width of interconnects (W) and diameter of CNTs (D) increase the power dissipation also increases. Decrease in the distance between CNTs in a bundle (d) leads to an increase in power dissipation. The highest value of power dissipation is achieved if the maximum values for the parameters of length and width of interconnects (L, W), and diameter of CNTs (D) and the minimum value of the distance between CNTs in a bundle (d) are considered. It is also revealed that an increase in the length of interconnects (L) increases the propagation delay. Eventually, the optimum parameters are reported and the performance of the optimized system is compared using different methods (TA and RSM). Results indicate that the difference between the performance of optimal design of SWCNT bundle interconnects in a full adder predicted by different methods is less than 6% which is acceptable according to engineering standards.

***doi**: 10.5829/ije.2020.33.08b.18*

1. INTRODUCTION

As the design and fabrication of highly compact integrated circuits are developing, efforts to shrink the on-chip feature sizes down to 30 nm and below continue. However, for interconnect materials based on copper (Cu), such reduction in fabrication sizes adversely affects the performance (increase in propagation delay through interconnect) and reliability because of an increased resistance and current density [1]. Application of the traditional interconnects based on Cu in the nanometer region is limited due to the low thermal and electrical conductivity [2], short mean free path [3], high resistivity [4], and electro-migration [5]. Therefore, innovative technological solutions and alternative material combinations are required for the interconnect applications, which exceed the performance of Cu and are superior to Cu in reliability. So far, various technologies presented by researchers are based on Carbon Nanotube Field Effect Transistor (CNTFET), Single Electron Transistors (SET), Quantum-Dot Cellular Automata (QCA), and Multi Gate Field Effect Transistor (MUGFET) [6–9].

CNT bundles are specific scientific interest and are an appropriate choice for replacing copper interconnects because of their intrinsic characteristics such as high

*Corresponding Author's Email: *reza-kashi-zade-ka@rudn.ru* (K. Reza Kashyzadeh)

Please cite this article as: S. Ghorbani, S. Ghorbani, K. Reza Kashyzadeh, Taguchi Approach and Response Surface Analysis for Design of a High-performance Single-walled Carbon Nanotube Bundle Interconnects in a Full Adder, International Journal of Engineering (IJE), IJE TRANSACTIONS B: Applications Vol. 33, No. 8, (August 2020) 1598-1607

resistance, electrical, thermal, magnetic, and mechanical properties. The van der Waals forces form stabilized bundles of CNTs [10]. Current density of CNT is 1011 A/cm^2 or more, which is higher than that of Cu (depending on the fabrication process and used capping layer is in the range of 106-107 A/cm^2) [11]. Therefore, due to the high carrying current densities of CNT, damage could be prevented where the highest current densities are expected, even at high temperatures [12]. Additionally, Srivastava and Banerjee [13] have reported that the minimum value of interconnect propagation delay occurs at the optimum density. This optimal density is always less than the maximum packing density of CNT bundles. Also, it has been stated in previous research that the thermal conductivity and tensile strength of CNTs are respectively three and two times larger than those of Cu wires [14]. Moreover, due to the weak influence of the CNT's length of resistance, the distance between the interconnect levels can be increased [11].

A CNT bundle interconnect can consist of single-walled carbon nanotubes (SWCNT) or multi-walled carbon nanotubes (MWCNT). In MWCNTs, achieving ballistic transport over long lengths is problematic, however the MWCNTs are metallic [13]. A SWCNT uses a single graphene sheet rolled up into a cylindrical tube with a variable diameter (0.4 to 4 nm). Depending on the chirality vector, the SWCNT could be either metallic or semi-conducting [15]. In general, semi-conductive nanotubes are applied for the channel of carbon nanotube field-effect transistors (CNFETs) [5]. It is noteworthy that the average electron free paths of SWCNT are about one micron [16]. According to the result obtained by Rai and Sarkar [12], the power dissipation increases as CNT's diameter increases and capacitance in SWCNT interconnect decreases. Thus, in the manufacturing process of SWCNT samples, technologists cope with the challenges in controlling the SWCNT's length, diameter, width, and the preparation due to control of equivalent circuit impedance parameters [17].

Resistances and capacitances are the main effective factors on the stability and the time domain responses of an inductance interconnect [18]. Some research efforts have addressed the different stability prospects of CNTs. In this regard, Xu et al. [19] have reported the mechanical and thermal stability of CNTs. They claimed that a zigzag CNT has a better stability than that of an armchair CNT with the same diameter. Chiodarelli et al. [11] focused on the optical stability of CNTs. Fathi and Forouzandeh [3] presented the Nyquist stability diagrams of CNTs interconnects. The authors offered a new concept for CNT interconnects named as "relative stability". They stated that the relative stability of the CNT bundle increases as the diameter and the length of the CNT bundle increase. Moreover, Zhao et al. [10] demonstrated that the technology advancement may lead to increased damping property and suppress the fluctuation in the time domain step response. Shin et al. [20] have discussed about the chemical stability of CNTs. They suggested general guidelines for ensuring the stability of CNTs against acid treatments.

CNFET transistors are used to design the full adder cell as one of the essential blocks of the arithmetic circuits because of its high performance and low power consumption properties [21]. It is well known that the full adder plays an important role in ALUs, CPUs, address generation and memory access units since its functionality has a great impact on the whole system's functionality [22]. Several groups have proposed the enhanced performance of full adder circuits in terms of functionality. For instance, Nejadzadeh and Reshadinezhad [22] have improved the performance of CNFET-based full adder regarding time delay and PDP by reducing the transistors count and critical paths and increasing the reliability of the circuit. Zhao et al. [10] have proposed a full adder based on hybrid-CMOS that was implemented by 24 transistors. Also, the new full adder based on CNFETs circuit improved the PDP, power consumption, and performance of the full adder cell [23]. Ghanaghestani et al. [24] have suggested a full adder cell based on a parallel design using CNFETs. The suggested model affects the power consumption and speed, which results in reducing the critical path delay. A CNFET full adder circuit design demonstrated by Ghorbani et al. [25] significantly improved both delay and power outputs, which is able to work in a wide range of temperatures, load capacitors, and frequencies. Sharifi et al. [26], in their approaches, significantly reduced the complexity and energy consumption of the full adder's design by using novel quaternary-to-binary and binary-to-quaternary converters. The validation process of the performance of the proposed model has been done using HSPICE simulator. Torkzadeh Mahani and Keshavarzian [27] have proposed new full adder circuits based on CNTFET and GDI structure, which result in better drive capacity and output swing, less energy consumption, power consumption, delay, EDP, and better parameters in higher frequencies.

Despite all past researches, the simultaneous effects of the geometric parameters of SWCNT bundle interconnects on the power dissipation and propagation delay in a full adder have not been investigated. Therefore, for the first time this was accomplished by applying Design of Experiment (DOE) techniques including Taguchi approach and response surface method. Finally, the geometrical parameters (diameter of a nanotube, distance between nanotubes in a bundle, and width and length of the bundle) were optimized to achieve the best system performance. The obtained results were verified by comparison with the HSPICE simulator.

2. DETAILED DISCUSSIONS REGARDING THE THEORIES OF CURRENT MODELS BY SWCNT BUNDLE IN A FULL ADDER

An equivalent circuit model of an isolated SWCNT interconnect, including various electrical components (e. g., resistance, capacitors, and inductance) is shown in Figure 1, in which, parameters R, L, and C are the resistance, inductance and capacitor, respectively. Also, the indices C, Q, S, M, K, and E represent connection, quantum, diffraction, magnetic, kinetic, and electrostatic, respectively. The single-walled carbon nanotube structure on a ground plane is illustrated in Figure 2, in which, Y is distance between the SWCNT center and the ground plane. The diameter of outermost shell of SWCNT is referred to D. SWCNTs are composed of one shell of carbon atoms. SWCNTs adhere strongly to each other forming ropes or bundles of nanotubes. The diameter of the most SWCNTs is about one nanometer, and the tube length can be several thousands times longer. The structure of a SWCNT can be achieved by folding an atomic thick layer of graphene into a tubular structure. SWCNT is characterized by its chirality, which determines its properties and diameter. The chirality is represented with a pair of indices (n, m), which is called the chiral vector. The chiral vector traces the CNT around its circumference from one carbon atom back to itself. CNTs are classified into three groups: armchair nanotubes for n = m, zigzag nanotubes for m = 0 or n = 0, and chiral nanotubes for any other combination [28]. The conductive properties of CNTs are determined by its helicity, diameter, and chirality.

Next, a brief description of the theories related to each of the electrical components used in the proposed model (Figure 1) is discussed.

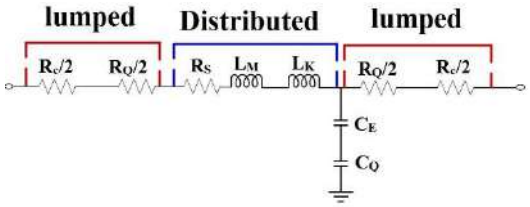

Figure 1. Details of the circuit model of an isolated SWCNT interconnect

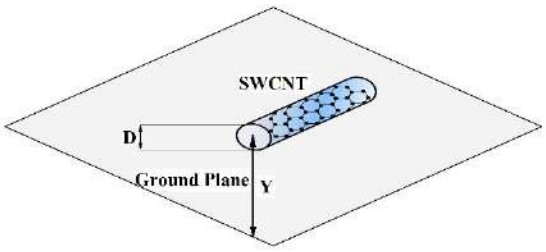

Figure 2. SWCNT structure on a ground plane

2. 1. Resistance of SWCNT The total resistance of a SWCNT (R_{CNT}) is calculated by applying Equation (1). The value of R_C is in the range of 10 Ω to 100 kΩ [29]. Also, the values of quantum resistance (R_Q) and diffraction resistance (R_S) may be obtained as follows:

$$R_{CNT} = \sum R_i = R_C + R_Q + R_S \quad (1)$$

$$R_Q = \frac{h}{4e^2} \quad (2)$$

$$R_S = \begin{cases} R_Q \times \frac{L}{\lambda_{mfp}} & if\ L > \lambda_{mfp} \\ 0 & if\ L < \lambda_{mfp} \end{cases} \quad (3)$$

where *e* is the electron charge, *h* is the Planck constant, *L* is the length of a carbon nanotube, and λ_{mfp} is the mean free distance ($\lambda_{mfp} = 2 \times 10^3 \times r_{CNT}$, and r_{CNT} is the radius of a carbon nanotube) [30].

2. 2. Capacitor of SWCNT The electrostatic capacitor (C_E) and quantum capacitor (C_Q) are defined as:

$$C_E = \frac{2\pi\varepsilon_r\varepsilon_0}{Ln\frac{Y}{D}} \quad (4)$$

$$C_Q = \frac{4e^2}{hV_f} \quad (5)$$

As previously expressed in Figure 2, Y and D are the distance of carbon nanotube's center from ground and diameter of carbon nanotube, respectively. Also, the relative and vacuum dielectric coefficients are called ε_r and ε_0, respectively. Moreover, V_F is Fermi velocity equal to $8 \times 10^5\ m/s$ for graphene and carbon nanotube [31].

2. 3. Inductance of SWCNT The kinetic and magnetic inductances are also calculated by employing Equations (6) and (7). Since the value of L_M is less than that of L_K, it must be ignored [32].

$$L_K = \frac{h}{4e^2V_f} \quad (6)$$

$$L_M = \frac{\mu_0}{2\pi} \times \ln\left(\frac{Y}{D}\right) \quad (7)$$

where μ_0 is the carrier mobility. Figure 3 shows the cross-section of the SWCNT bundle. Also, the total number of nanotubes (N_{CNT}) may be obtained as following:

$$N_{CNT} = \begin{cases} N_X N_Z - \frac{N_Z}{2} & if\ N_Z = even \\ N_X N_Z - \frac{N_Z - 1}{2} & if\ N_Z = odd \end{cases} \quad (8)$$

where N_X and N_Z are the number of nanotubes in directions X and Z, respectively.

$$N_X = \frac{W-D}{X} \quad (9)$$

$$N_Z = \frac{2(t-D)}{\sqrt{3}\,X} + 1 \quad (10)$$

In these equations, W and t are the width and thickness of bundle, D is the diameter of nanotubes, and X is the distance between centers of two adjacent carbon nanotubes. Also, the specifications of interconnects in different lengths and also their drivers in 32-nm technology based on ITRS 2013 are presented in Table 1. Next, values of resistance, capacitor, and inductance of carbon nanotube bundles are calculated based on Equations (11)-(13) [13].

$$R \rightarrow R_{Bundle} = \frac{R_C + R_Q + R_S}{N_{CNT}} \quad (11)$$

$$C \rightarrow \begin{cases} C_Q^{Bundle} = C_Q \times N_{CNT} n \\ C_E^{Bundle} = 2C_{En} + \frac{N_X - 2}{2} \times C_{Ef} + \frac{3(N_Z - 2)}{5} \times C_{En} \\ C_{En} = \frac{2\pi\varepsilon_r\varepsilon_0}{ln\left(\frac{S}{D}\right)} \quad and \quad C_{Ef} = \frac{2\pi\varepsilon_r\varepsilon_0}{ln\left(\frac{S+W}{D}\right)} \\ C_{Bundle} = L \times \frac{C_Q^{Bundle} \times C_E^{Bundle}}{C_Q^{Bundle} + C_E^{Bundle}} \end{cases} \quad (12)$$

$$I \rightarrow \begin{cases} L_m^{Bundle} = L_m \\ L_k^{Bundle} = \frac{L_k}{N_{CNT}} \\ L_{Bundle} = \frac{L \times L_k^{Bundle}}{N_{CNT}} \end{cases} \quad (13)$$

Eventually, the full adder's block diagram used in the present research is depicted in Figure 4. It was simulated in 32-nm technology using HSPICE software. In simulations, the carbon nanotube-based field effect transistors were used. In this scheme, interconnects are shown by red color and short circuit is the ideal state. But these lines can be made up of cooper in new technologies and carbon nanotube bundles in nanoscale.

3. TAGUCHI APPROACH

In this method, according to certain rules, a set of tables is prepared as an orthogonal array. These arrays make it possible to examine the main and interaction effects of different parameters by performing the least number of experiments. In fact, it is the biggest advantage of the Taguchi method over other DOE techniques. Taguchi proposes two models for analyzing results (standard and signal to noise ratio). The standard model works based on the calculating the effect of factors and performing analysis of variance. The second method examines the scattering near a certain amount. As the value of this ratio (signal to noise) increases, the amount of scattering decreases, and in this case the effect of that parameter will be more important.

In the present research, four geometric parameters with three different levels as reported in Table 2, were used to perform Taguchi analysis. To this end, a used general algorithm including the input variables and responses is depicted in Figure 5.

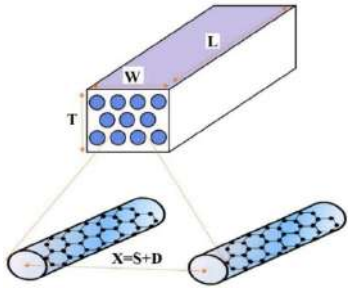

Figure 3. Cross section of a carbon nanotube bundle

TABLE 1. Specifications of interconnects in 32-nm technology

Parameter	Unit	Value	
		Global	Local & intermediate
V_{DD}	V	0.9	0.9
Width (W)	nm	40	32
Thickness (T)	nm	120	64
Aspect ratio (A/R)	-----	3	2
Oxide thickness (t_{OX})	nm	93.6	54.4
Dielectric constant	-----	2.77	2.25
Separation between adjacent bundles	nm	40	32
Center to center SWCNT in bundle (d)	nm	0.34	0.34
Diameter of SWCNT (D)	nm	1	1
ρ_0 for cu	uΩ cm	3.66	4.81
R_t	kΩ	13.85	13.85
C_{out}	fF	0.07	0.07
C_{in}	fF	0.25	0.25

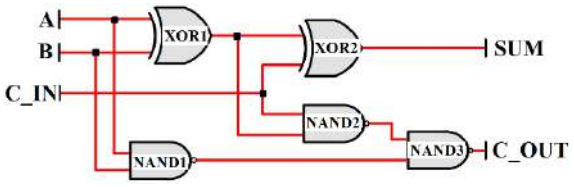

Figure 4. The full adder's block diagram used in this study

TABLE 2. Variables and their levels used as input data in the Taguchi-based DOE

Parameters	Symbol	Levels		
		L1	L2	L3
Length of interconnects	L	10 um	50 um	100um
Width of interconnects	W	30 nm	40 nm	50 nm
Diameter of CNTs	D	1 nm	2 nm	4 nm
Distance between CNTs in a bundle	d	0 nm	0.34 nm	1 nm

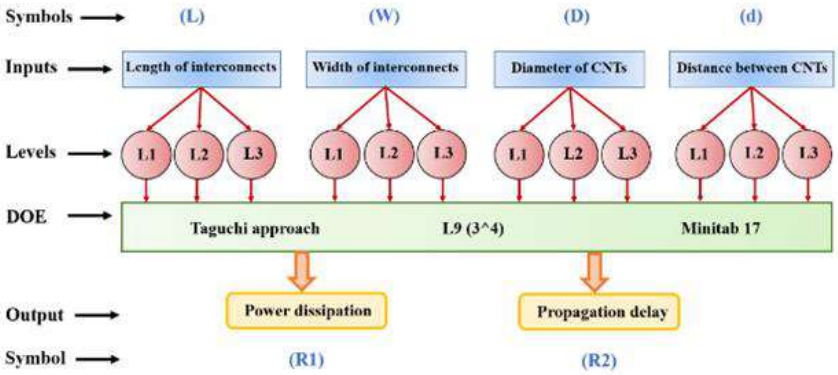

Figure 5. The scheme of Taguchi-based design of experiments used in this study

4. RESPONSE SURFACE ANALYSIS

RSM is a set of measurable systems and applied science to develop test models. The point of such plan is to optimize the output which is influenced by a few factors. Thusly, variations of the factors are made to detect the reasons for changes in the response [33, 34]. To decrease the computational costs (e. g., simulation and solving time), the prediction algorithm of Taguchi was utilized to estimate the desired cases [33].

5. RESULTS AND DISCUSSION

The circuit performance of CNT bundle interconnects in a full adder for the various cases (suggested by DOE) was analyzed using simulation in HSPICE software and considering the technology of 32-nm. The obtained results of simulation are presented in Table 3. In the current research, two outputs including power dissipation and propagation delay were investigated as representing the performance of the system. In general, research seeks to reduce propagation delay or reduce power dissipation in the system, both of which mean an increase in system performance. Therefore, the viewpoint of smaller is better was considered for both responses as follows [35]:

$$S/N = -10Log\left[\frac{1}{n}(y_1^2 + y_2^2 + \cdots + y_n^2)\right] \quad (14)$$

where y_1, y_2 , and y_n are the measured bent angles in the bending process, and each bending condition is repeated n times.

Afterward, the influences of S/N and mean ratios at every level were analyzed and the results are demonstrated in Figures 6 and 7 for power dissipation and propagation delay, respectively. It is clearly obvious from Figures 6 and 7, the number of experiments with 4 factors in three levels is enough to conduct TA. Because, the trend of S/N ratios diagram is completely reverse

TABLE 3. HSPICE simulation results extracted for TA

Experiment No.		Power dissipation (uw)	Propagation delay (ns)
1	L=10 um W=30 nm D=1 nm d=0 nm	1.3285	1.7334
2	L=10 um W=40 nm D=2 nm d=0.34 nm	1.3274	1.7478
3	L=10 um W=50 nm D=4 nm d=1 nm	1.320	1.7310
4	L=50 um W=30 nm D=2 nm d=1 nm	1.4551	1.7436
5	L=50 um W=40 nm D=4 nm d=0 nm	1.7609	1.7535
6	L=50 um W=50 nm D=1 nm d=0.34 nm	1.5224	1.7531
7	L=100 um W=30 nm D=4 nm d=0.34 nm	1.9607	1.7794
8	L=100 um W=40 nm D=1 nm d=1 nm	1.6009	1.7764
9	L=100 um W=50 nm D=2 nm d=0 nm	2.0892	1.7504

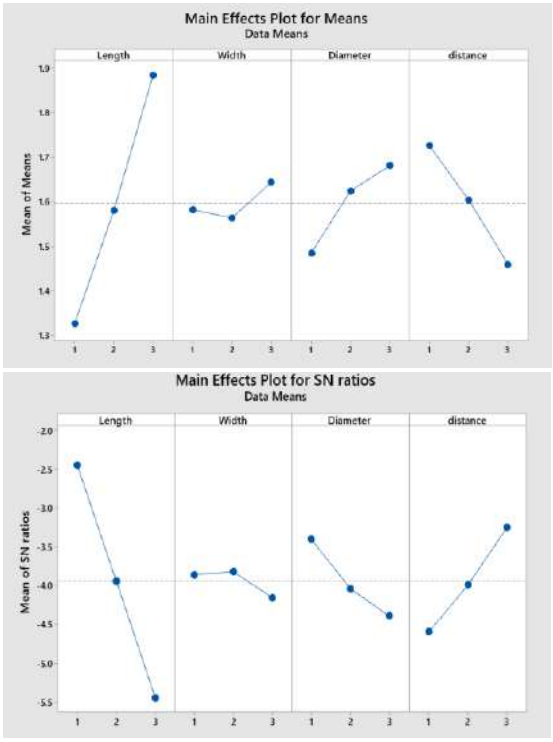

Figure 6. Influences of S/N and mean ratios of all parameters related to power dissipation

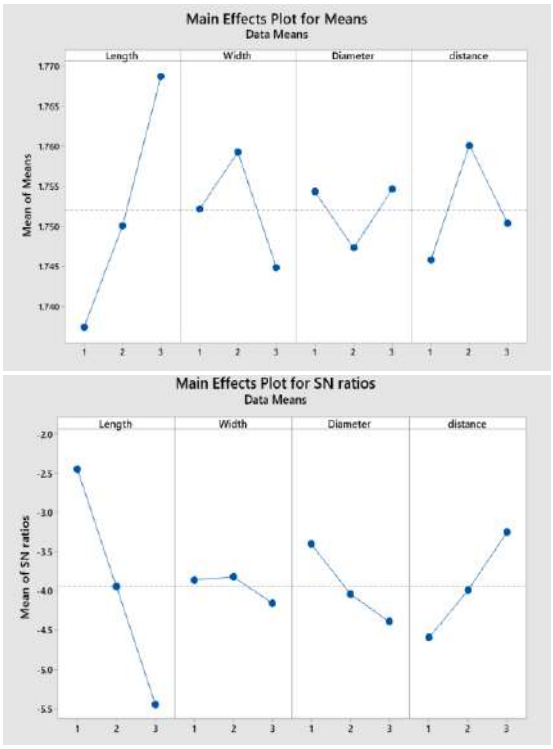

Figure 7. Influences of S/N and mean ratios of all parameters related to propagation delay

compared with trend of mean ratios diagram. As shown in Figure 7, the trend of power dissipation changes in terms of all parameters (L, D, and d) is linear except for the width of the bundle (W). This behavior is also seen at the output of the propagation time. Therefore, the value of this parameter (W) can affect the behavior of the response to other parameters. As a result, it is strongly necessary to examine the behavior of the system in a multi-dimensional way (the interaction effects of parameters).

Also, Figure 8 demonstrates the influence ranking of the geometric parameters of CNT bundle interconnects on both outputs including power dissipation and propagation delay. The Taguchi results reveal that the length of interconnects has the greatest effect on the performance of SWCNT bundle interconnects (its efficiency is 51% and 47% on the power dissipation and propagation delay, respectively). However, the least effective geometric parameter differs in power dissipation and propagation delay. According to Figure 8 (A), width of interconnects has low impact on the power dissipation (about 7%). And so on, based on Figure 8 (B), diameter of CNTs is the most ineffective parameter (about 11%) on the propagation delay. In summary, the distance between CNTs is in the second rank of importance from performance viewpoint. Next, the Taguchi prediction algorithm was utilized to estimate the performance of desired cases (Table 4). These data were used to perform response surface analysis.

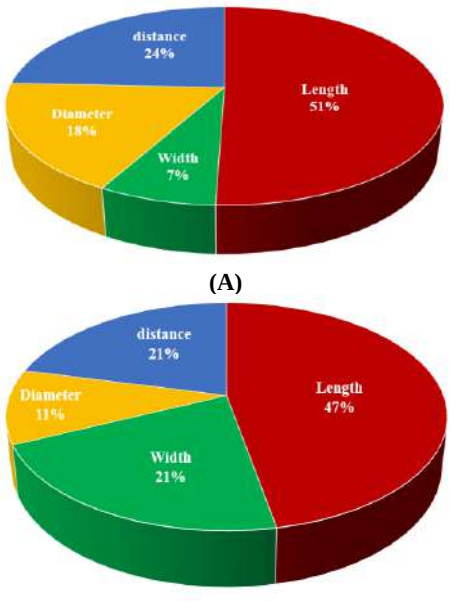

Figure 8. The quantitative effects of geometric parameters of CNT bundle interconnects on the circuit performance including (A) power dissipation and (B) propagation delay

TABLE 4. The estimated circuit performance for different settings of geometric parameters using Taguchi prediction algorithm

Case No.	Length of interconnects, um	Width of interconnects, nm	Diameter of CNTs, nm	Distance between CNTs, nm	Power dissipation, uw	Propagation delay, Ns
1	100	40	2	0.34	1.885	1.779
2	100	50	4	1	1.878	1.762
3	100	30	1	1	1.619	1.769
4	100	30	4	0	2.083	1.765
5	100	50	1	0	1.949	1.757
6	100	50	1	1	1.681	1.762
7	100	50	4	0	2.145	1.757
8	100	30	1	0	1.886	1.764
9	100	30	4	1	1.815	1.769
10	50	50	2	0.34	1.662	1.746
11	50	40	2	0	1.704	1.746
12	50	30	2	0.34	1.599	1.753
13	50	40	4	0.34	1.638	1.767
14	50	40	1	0.34	1.441	1.767
15	50	40	2	0.34	1.581	1.760
16	50	40	2	1	1.436	1.750
17	10	50	1	1	1.123	1.730
18	10	50	4	0	1.587	1.726
19	10	30	1	0	1.328	1.733
20	10	30	4	1	1.257	1.738
21	10	30	4	0	1.525	1.733
22	10	50	4	1	1.320	1.731
23	10	50	1	0	1.390	1.726
24	10	30	1	1	1.060	1.737
25	10	40	2	0.34	1.327	1.747

The results of RSM analysis for power dissipation and propagation delay are displayed in Figures 9 and 10, respectively. It should be noted that in these analyses, the constant parameter was assumed to be the average level value (L2). Eventually, the most significant findings from the RSM contours are:

1. The output of power dissipation also enhances by increasing length of interconnects (L).
2. By increasing both width of interconnects (W) and diameter of CNTs (D), the power dissipation increases. But this development is limited to power dissipation < 1.4.
3. As the distance between CNTs in a bundle (d) decreases, the power dissipation increases.
4.To achieve the highest value of power dissipation, the maximum values for the parameters of length and width of interconnects (L, W), and diameter of CNTs (D) must be considered. Moreover, the distance between CNTs in a bundle (d) should be set to minimum value.
5. It is clear that increasing the length of interconnects (L) will increase the propagation delay.
6. The variations of CNTs' diameter (D) do not have a significant effect on propagation delay. In other words, this parameter is ineffective.
7. There is a specific middle area for both the width of interconnects (W) and the distance between CNTs in a bundle (d) which is relevant to the maximum value of propagation delay. And the propagation delay is reduced by moving away from that area. In other words, the farthest from that area results in the least amount of propagation delay. Moreover, the form of the function is circular between two independent parameters W and d.
8. The lowest propagation delay in the system is achieved when we have the shortest L, d, and maximum W.

Next, the optimization was performed to design a high-performance CNT bundle interconnects in a full adder. This process was performed using a multi-objective function. The optimal values for minimizing power dissipation and propagation delay were obtained simultaneously. Afterwards, the optimal system efficiency was compared using various techniques in Table 5.

Results show that the difference between performance of optimal design of SWCNT bundle interconnects in a full adder predicted by different techniques is less than 6% which is acceptable according to engineering standards.

TABLE 5. Comparison of the optimal system efficiency using various techniques

Parameter	Optimal value	Power delay product (PDP=power dissipation × propagation delay)	
		Taguchi approach	Response surface analysis
L	10 um	Power dissipation = 1.1234	Power dissipation = 1.06097
W	50 nm		
D	1 nm	Propagation delay = 1.73067	Propagation delay = 1.72610
d	1 nm		
Final result		PDP = 1.944	PDP = 1.831

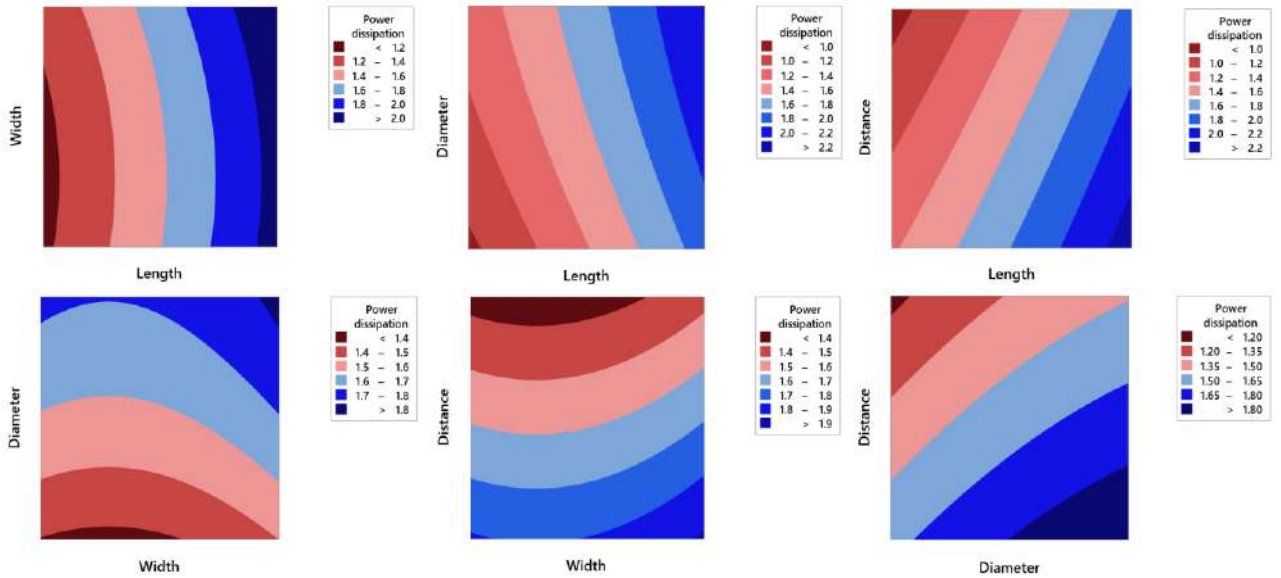

Figure 9. RSM results for power dissipation of the SWCNT bundle interconnects in a full adder

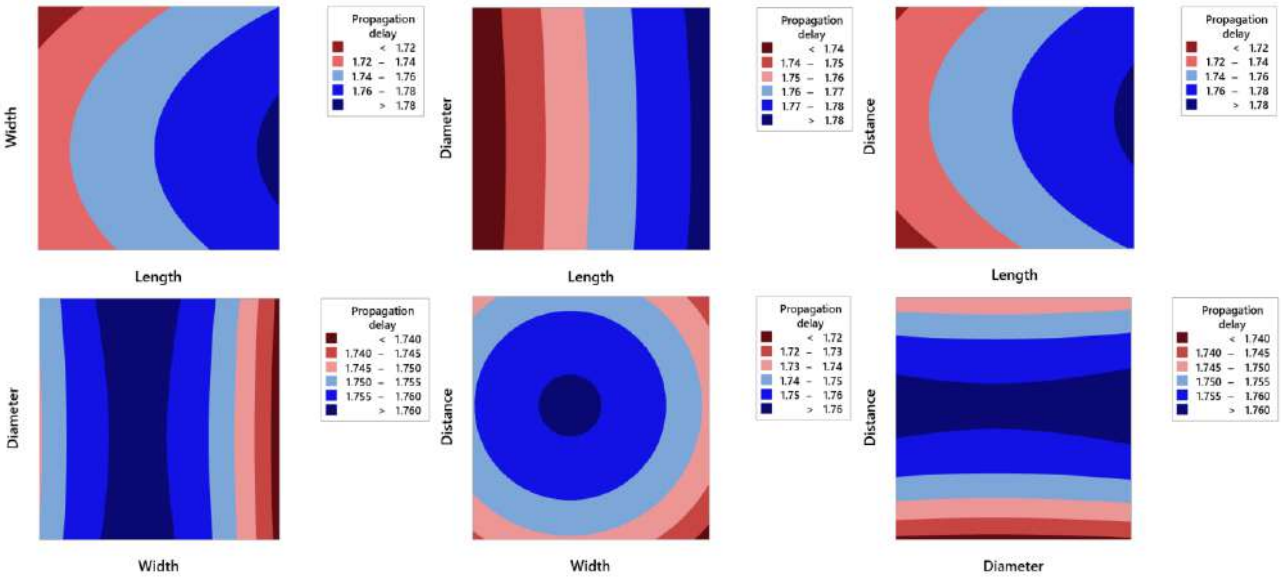

Figure 10. RSM results for propagation delay of the SWCNT bundle interconnects in a full adder

6. CONCLUSION

The current study has attempted to investigate the effects of different geometric parameters of SWCNT bundle interconnects in a full adder on the power dissipation and propagation delay. To achieve this purpose, HSPICE simulation, TA, and RSM were used. Based on the obtained results from all techniques, the parameters of length of interconnects (L), width of interconnects (W), diameter of CNTs (D), and distance between CNTs in bundle (d) were considered as input variables. Also, the power dissipation and propagation delay were considered as performance of the system. Taguchi results indicated that the length of interconnects had the most impact on power delay product (PDP). Next, RSM was used to investigate the interaction impacts of different factors on the circuit performance of carbon nanotube bundle interconnectors in a full adder. In addition, it stated that in order to have the lowest propagation delay in the system, the parameters L and d must be set to the minimum levels and inverse for the parameter W (maximum level of W). Also, the changes in D are ineffective on propagation delay. Eventually, a new design was presented to improve the circuit performance of SWCNT bundle interconnects in a full adder using different data mining techniques such as Taguchi approach and response surface analysis.

7. ACKNOWLEDGMENTS

The study was conducted with the support of the "RUDN University Program 5-100".

8. REFERENCES

1. Steinhögl, W., Schindler, G., Steinlesberger, G., Traving, M. and Engelhardt, M., "Comprehensive study of the resistivity of copper wires with lateral dimensions of 100 nm and smaller", ***Journal of Applied Physics***, Vol. 97, No. 2, (2005), 023706. https://doi.org/10.1063/1.1834982
2. Lu, Q., Zhu, Z., Yang, Y. and Ding, R., "Analysis of propagation delay and repeater insertion in single-walled carbon nanotube bundle interconnects", ***Microelectronics Journal***, Vol. 54, (2016), 85–92. https://doi.org/10.1016/j.mejo.2016.05.012
3. Fathi, D. and Forouzandeh, B., "A novel approach for stability analysis in carbon nanotube interconnects", ***IEEE Electron Device Letters***, Vol. 30, No. 5, (2009), 475–477. https://doi.org/10.1109/LED.2009.2017388
4. Zhang, K., Tian, B., Zhu, X., Wang, F. and Wei, J., "Crosstalk analysis of carbon nanotube bundle interconnects", ***Nanoscale Research Letters***, Vol. 7, No. 1, (2012), 1–5. https://doi.org/10.1186/1556-276X-7-138
5. Shabalin, M. and Fuks, D., "Density functional theory study of the influence of segregation of S or Fe impurities on electromigration in nano-grained copper interconnects", ***Journal of Applied Physics***, Vol. 117, No. 19, (2015), 195303. https://doi.org/10.1063/1.4919922
6. Deng, J., Patil, N., Ryu, K., Badmaev, A., Zhou, C., Mitra, S. and Wong, H. P., "Carbon nanotube transistor circuits: Circuit-level performance benchmarking and design options for living with imperfections", In Digest of Technical Papers - IEEE International Solid-State Circuits Conference, USA, (2007). https://doi.org/10.1109/ISSCC.2007.373592
7. Put, S., Simoen, E., Collaert, N., Claeys, C., Van Uffelen, M. and Leroux P., "Geometry and strain dependence of the proton radiation behavior of MuGFET devices", ***IEEE Transactions on Nuclear Science***, Vol. 54, No. 6, (2007), 2227–2232. https://doi.org/10.1109/TNS.2007.911420
8. Porod, W., Lent, C., Bernstein, G. H., Orlov, A. O., Hamlani, I., Snider, G. L. and Merz, J. L., "Quantum-dot cellular automata: Computing with coupled quantum dots", ***International Journal of Electronics***, Vol. 86, No. 5, (1999), 549–590. https://doi.org/10.1080/002072199133265
9. Deng, G. and Chen, C., "Hybrid CMOS-SET arithmetic circuit design using coulomb blockade oscillation characteristic", ***Journal of Computational and Theoretical Nanoscience***, Vol. 8, No. 8, (2011), 1520–1526. https://doi.org/10.1166/jctn.2011.1845
10. Zhao, W. S., Wang, G., Hu, J., Sun, L. and Hong, H., "Performance and stability analysis of monolayer single-walled carbon nanotube interconnects", ***International Journal of Numerical Modelling: Electronic Networks, Devices and Fields***, Vol. 28, No. 4, (2015), 456–464. https://doi.org/10.1002/jnm.2027
11. Chiodarelli, N., Kellens, K., Cott, D. J., Peys, N., Arstila, K., Heyns, M., De Gendt, S., Groeseneken, G. and Vereecken, P. M., "Integration of Vertical Carbon Nanotube Bundles for Interconnects", ***Journal of The Electrochemical Society***, Vol. 157, No. 10, (2010), 211-217. https://doi.org/10.1149/1.3473810
12. Rai, M. K. and Sarkar, S., "Influence of tube diameter on carbon nanotube interconnect delay and power output", ***Physica Status Solidi (A)***, Vol. 208, No. 3, (2011), 735–739. https://doi.org/10.1002/pssa.201026314
13. Srivastava, N. and Banerjee, K., "Performance analysis of carbon nanotube interconnects for VLSI applications", In IEEE/ACM International Conference on Computer-Aided Design, Digest of Technical Papers, ICCAD, USA, Vol. 2005, (2005), 383-390. https://doi.org/10.1109/ICCAD.2005.1560098
14. Wei, C., Cho, K. and Srivastava, D., "Tensile strength of carbon nanotubes under realistic temperature and strain rate", ***Physical Review B - Condensed Matter and Materials Physics***, Vol. 67, No. 11, (2003), 115407. https://doi.org/10.1103/PhysRevB.67.115407
15. Vanpaemel, J., Sugiura, M., Barbarin, Y., De Gendt, S., Tökei, Z., Vereecken, P. M. and van der Veen, M. H., "Growth and integration challenges for carbon nanotube interconnects", ***Microelectronic Engineering***, Vol. 120, (2014), 188–193. https://doi.org/10.1016/j.mee.2013.09.015
16. McEuen, P. L., Fuhrer, M. S., and Park, H., "Single-walled carbon nanotube electronics", ***IEEE Transactions on Nanotechnology***, Vol. 1, No. 1, (2002), 78–84. https://doi.org/10.1109/TNANO.2002.1005429
17. Massoud, Y. and Nieuwoudt, A., "Modeling and design challenges and solutions for carbon nanotube-based interconnect in future high performance integrated circuits", ***ACM Journal on Emerging Technologies in Computing Systems***, Vol. 2, No. 3, (2006), 155–196. https://doi.org/10.1145/1167943.1167944
18. Bagheri, A., Ranjbar, M., Haji-Nasiri, S. and Mirzakuchaki, S., "Modelling and analysis of crosstalk induced noise effects in bundle SWCNT interconnects and its impact on signal stability", ***Journal of Computational Electronics***, Vol. 16, No. 3, (2017), 845–855. https://doi.org/10.1007/s10825-017-1028-1

19. Xu, Z., Zhang, W., Zhu, Z., Ren, C., Li, Y. and Huai, P., "Effects of tube diameter and chirality on the stability of single-walled carbon nanotubes under ion irradiation", ***Journal of Applied Physics***, Vol. 106, No. 4, (2009), 043501. https://doi.org/10.1063/1.3194784
20. Shin, Y. R., Jeon, I. Y., and Baek, J. B., "Stability of multi-walled carbon nanotubes in commonly used acidic media", ***Carbon***, Vol. 50, No. 4, (2012), 1465–1476. https://doi.org/10.1016/j.carbon.2011.11.017
21. Moaiyeri, M. H., Mirzaee, R. F., Navi, K. and Momeni, A., "Design and analysis of a high-performance CNFET-based Full Adder", ***International Journal of Electronics***, Vol. 99, No. 1, (2012), 113–130. https://doi.org/10.1080/00207217.2011.623269
22. Nejadzadeh, P. and Reshadinezhad, M. R., "Modern Education and Computer Science", ***Modern Education and Computer Science***, Vol. 4, No. 4, (2018), 43–50. https://doi.org/10.5815/ijmecs.2018.04.06
23. Ghadiry, M.H., Abd Manaf, A., Ahmadi, M.T., Sadeghi, H. and Senejani, M.N., "Design and Analysis of a New Carbon Nanotube Full Adder Cell", ***Journal of Nanomaterials***, Vol. 2011, (2011), 1-6. https://doi.org/10.1155/2011/906237
24. Ghanatghestani, M. M., Ghavami, B., and Salehpour, H., "A CNFET full adder cell design for high-speed arithmetic units", ***Turkish Journal of Electrical Engineering & Computer Sciences***, Vol. 25, No. 3, (2017), 2399–2409. https://doi.org/10.3906/elk-1512-8
25. Ghorbani, A., Sarkhosh, M., Fayyazi, E., Mahmoudi, N. and Keshavarzian, P., "A Novel full adder cell based on carbon nanotube field effect transistors", ***International Journal of VLSI design & Communication Systems***, Vol. 3, No. 3, (2012), 33-42. https://doi.org/10.5121/vlsic.2012.3304
26. Sharifi, F., Moaiyeri, M. H., Navi, K. and Bagherzadeh, N., "Quaternary full adder cells based on carbon nanotube FETs", ***Journal of Computational Electronics***, Vol. 14, No. 3, (2015), 762–772. https://doi.org/10.1007/s10825-015-0714-0
27. Torkzadeh Mahani, A. and Keshavarzian, P., "A novel energy-efficient and high speed full adder using CNTFET", ***Microelectronics Journal***, Vol. 61, (2017), 79–88. https://doi.org/10.1016/j.mejo.2017.01.009
28. Dolati, S., Fereidoon, A. and Reza Kashyzadeh, K., "A comparison study between Boron nitride nanotubes and carbon nanotubes", ***International Journal of Emerging Technology and Advanced Engineering***, Vol. 2, Issue. 10, (2012), 470-474. http://citeseerx.ist.psu.edu/viewdoc/download?doi=10.1.1.441.2623&rep=rep1&type=pdf
29. Srivastava, N., Li, H., Kreupl, F. and Banerjee, K., "On the applicability of single-walled carbon nanotubes as VLSI interconnects", ***IEEE Transactions on Nanotechnology***, Vol. 8, No. 4, (2009), 542–559. https://doi.org/10.1109/TNANO.2009.2013945
30. Lamberti, P. and Tucci, V., "Impact of the variability of the process parameters on CNT-based nanointerconnects performances: A comparison between SWCNTs bundles and MWCNT", ***IEEE Transactions on Nanotechnology***, Vol. 11, No. 5, (2012), 924–933. https://doi.org/10.1109/TNANO.2012.2207124
31. Das, P. K., Majumder, M. K., Kaushik, B. K. and Dasgupta, S., "Analysis of propagation delay in mixed carbon nanotube bundle as global VLSI interconnects", ***Asia Pacific Conference on Postgraduate Research in Microelectronics and Electronics***, (2012), 118–121. https://doi.org/10.1109/PrimeAsia.2012.6458638
32. Subash, S. and Chowdhury, M. H., "Mixed carbon nanotube bundles for interconnect applications", ***International Journal of Electronics***, Vol. 96, No. 6, (2009), 657–671. https://doi.org/10.1080/00207210902791702
33. Farrahi, G. H., Reza Kashyzadeh, K., Minaei, M., Sharifpour, A. and Riazi, S., "Analysis of resistance spot welding process parameters effect on the weld quality of three-steel sheets used in automotive industry: Experimental and finite element simulation", ***International Journal of Engineering, Transactions A: Basics***, Vol. 33, No. 1, (2020), 148–157. https://doi.org/10.5829/ije.2020.33.01a.17
34. Maleki, E., Unal, O., and Reza Kashyzadeh, K., "Efficiency Analysis of Shot Peening Parameters on Variations of Hardness, Grain Size and Residual Stress via Taguchi Approach", ***Metals and Materials International***, Vol. 25, No. 6, (2019), 1436–1447. https://doi.org/10.1007/s12540-019-00290-7
35. Li, K., Yan, S., Zhong, Y., Pan, W. and Zhao, G., "Multi-objective optimization of the fiber-reinforced composite injection molding process using Taguchi method, RSM, and NSGA-II", ***Simulation Modelling Practice and Theory***, Vol. 91, (2019), 69–82. https://doi.org/10.1016/j.simpat.2018.09.003

Persian Abstract

چکیده

در پژوهش حاضر، نویسندگان سعی کردند تا به طراحی یک اتصال نانو لوله کربنی تک جداره با کارآیی بالا در یک مدار تمام جمع‌کننده بپردازند. برای دستیابی به این هدف، عملکرد مدار با استفاده از شبیه‌سازی در نرم‌افزار اچ اسپایس و با در نظر گرفتن تکنولوژی ۳۲ نانومتری مورد بررسی قرار گرفت. سپس، اثر پارامترهای هندسی مانند قطر نانو لوله، فاصله بین نانو لوله‌ها در یک باندل، طول و عرض باندل بر توان مصرفی و زمان تاخیر انتشار با استفاده از روش طراحی آزمایش تاگوچی مورد بررسی قرار گرفت. نتایج تحلیل حساسیت تاگوچی نشان داد که طول باندل موثرترین پارامتر در عملکرد مدار است (حدود ۵۱٪ اثرگذاری بر توان مصرفی و ٤٧٪ اثرگذاری بر زمان تاخیر انتشار). پس از آن، فاصله بین نانو لوله‌ها در مقایسه با سایر پارامترها تاثیر بیشتری بر روی پاسخ دارد. همچنین روش پاسخ سطح نشان داد که افزایش طول باندل منجر به افزایش اتلاف انرژی می‌شود. همچنین با افزایش عرض باندل و قطر نانو لوله کربنی، اتلاف انرژی افزایش می‌یابد. کاهش فاصله بین نانو لوله‌های کربنی در یک باندل منجر به افزایش اتلاف انرژی می‌گردد. بدین ترتیب، بیشترین مقدار اتلاف انرژی در صورتی حاصل می‌شود که مقادیر پارامترهای طول و عرض اتصال و قطر نانو لوله کربنی بیشینه و فاصله بین دو نانو لوله حداقل باشد. همچنین نشان داده شد که افزایش طول اتصال منجر به افزایش تاخیر در انتشار می‌شود. در نهایت، پارامترهای بهینه گزارش شد و عملکرد مدار بهینه پیشنهادی با استفاده از روش‌های مختلف (تاگوچی و پاسخ سطح) مقایسه شد. نتایج نشان داد که میزان عملکرد طراحی بهینه اتصال نانو لوله کربنی تک جداره در یک مدار تمام جمع کننده توسط دو روش کمتر از ٦ درصد اختلاف پیش‌بینی شده که مطابق با استانداردهای مهندسی قابل قبول است.

IJE TRANSACTIONS B: Applications Vol. 33, No. 8, (August 2020) 1608-1619

International Journal of Engineering

Journal Homepage: www.ije.ir

Emission Reduction Strategies for Small Single Cylinder Diesel Engine Using Valve Timing and Swirl Ratio

A. Jain*[a], E. Porpatham[b], S. S. Thipse[a]

[a] *The Automotive Research Association of India, Pune, India*
[b] *Vellore Institute of Technology University, Vellore, India*

PAPER INFO

Paper history:
Received 25 February 2020
Received in revised form 08 June 2020
Accepted 12 June 2020

Keywords:
Diesel Engine Emission
Intake Valve Opening
Small Diesel Engine
Start of Injection
Swirl Ratio
Valve Timing

ABSTRACT

Small diesel engines are widely used for commercial vehicle and passenger car applications due to their higher torque requirements, fuel economy, and better thermal efficiency. These engines are exposed to different operating and environmental conditions and hence emissions from these engines are erratic. Strategies are required to enhance performance and reduce engine-out emissions considering environmental pollution and regulations. The main objective of this experimental study is to develop strategies for performance improvement and emission reduction for naturally aspirated engines, which can further be used for emission reduction of the multicylinder engine. Experimental work has been carried out on a single-cylinder naturally aspirated diesel engine to study the impact of engine operating parameters like valve timing, swirl ratio, and injection pressure on engine performance and emissions. Parameters considered for the study are: three intake valve opening timings, two fuel injection pump pressures, two-cylinder head swirls, and three start of injection timings. Results showed improvement in performance, lower exhaust gas temperature, and reduction of engine-out emission. Exhaust gas temperature was reduced by 5-18% with advanced valve opening and lower cylinder head swirl option. NO_x emission was reduced by 5-50% at advanced intake valve opening (IVO) options with retarded start of injection (SOI) and lower swirl cylinder head. This has a penalty on CO and HC emissions since the availability of fresh air is less due to higher internal exhaust gas recirculation (EGR). Higher pressure fuel injection pump helps in improving engine torque with an adverse effect on engine-out NO_x emission. As these engines are of low power capacity segment and are used in few countries, research on these engines is limited. All research work has been carried out in the field of intake valve closing timings, swirl ratio and injection timings; however, very limited research is available for the effect of intake valve opening timings due to practical limitations of the lower valve to piston clearance in diesel engines.

***doi**: 10.5829/ije.2020.33.08b.19*

NOMENCLATURE

CO	Carbon Monoxide	IVO	Intake Valve Opening
HC	Hydrocarbon	IVC	Intake Valve Closing
NO_x	Oxides of Nitrogen	LIVC	Late Intake Valve Closing
DI	Direct Injection	EVO	Exhaust Valve Opening
Abbreviations		EIVC	Early Intake Valve Closing
CRDI	Common Rail Diesel Injection	VVT	Variable Valve Timing
EGR	Exhaust Gas Recirculation	BSFC	Brake Specific Fuel Consumption
VVA	Variable Valve Actuation	CA	Crank Angle
TDC	Top Dead Center	SOI	Start of Injection

1. INTRODUCTION

Small diesel engines are widely used for commercial vehicle and passengers car applications in Asia. Its fuel economy along with minimum operational and maintenance cost make it more popular for urban and

*Corresponding Author Email: *ashish.edl@araiindia.com* (A. Jain)

Please cite this article as: A. Jain, E. Porpatham, S. S. Thipse, Emission Reduction Strategies for Small Single Cylinder Diesel Engine Using Valve Timing and Swirl Ratio, International Journal of Engineering (IJE), IJE TRANSACTIONS B: Applications Vol. 33, No. 8, (August 2020) 1608-1619

rural markets. These small engines are used in 3 wheelers, 4 wheelers and modified/make to order vehicles for different applications. Vehicles fitted with these engines are used in rough and narrow roads and extreme physical and environmental conditions. Being unmonitored, these vehicles emit higher emission than expected under various driving conditions. These emissions include CO, HC, and NO_x emissions which are among the major sources of environmental pollution. Stringent emission norms are brought by the government to curb these pollutions and make the environment cleaner and greener. All vehicle and engine manufacturers are working to meet these norms by upgrading engine and combustion using the latest technologies available in the market. This includes after-treatment devices, variable valve timing, twin-turbocharging, supercharging, low-temperature combustion, higher and cooler EGR, modern fuel injection pump, and nozzles. Research is also ongoing all around the world with these technologies individually or in combination for emission reduction. The present work is to study the effect of intake valve opening timing, injection pressure, start of injection (SOI), and swirl ratio on performance and emission reduction for small single cylinder naturally aspirated diesel engine.

Diesel engine development is mainly driven by stringent emission standards imposed by the government [1]. Emission legislation and control, new fuels, improved combustion and advanced concepts for energy saving are the major areas of combustion development [2, 3]. Oil-based fuel availability is also a problem due to limited reserves and political influences, which leads to significantly increased fuel costs [4]. Future diesel engine development is of importance to cope with increasing demands concerning emissions, energy consumption and due to the forecasted increase in road transport within India. The NO_x formation in diesel engines is mainly attributed to engine thermal management which increase exponentially with the temperature [5, 6]. The transport sector is one of the major contributors to global warming and environmental pollution [7].

Variable valve timing and variable injection timings with in-cylinder combustion are possible ways to meet upcoming restrictive emissions' requirements like NO_x and soot for DI diesel engines [8]. Zhang et al. [9] have studied the effect of late intake valve closing and rebreathing strategies on diesel engine performance and emission at low load, high-pressure CRDI system with Ex-EGR, and electro-hydraulic VVA system. Increasing valve lift and valve duration in 2IVO strategy were used to minimize CO and HC emissions. Fuel injection timings were kept closed to TDC with external EGR to control NO_x emissions with 3 IVC strategy. They concluded that a low level of NO_x was emitted with heavy EGR however, LIVC strategy was beneficial for smoke reduction. 2EVO strategy resulted in the lowest CO and HC emission with a penalty in smoke emission, while 2IVO maintained all emission at a low level with a slight penalty in fuel economy.

Zammit et al. [10] experimentally investigated the effect of EIVC and cylinder deactivation on 4 cylinder, turbocharged CRDI diesel engine on fuel economy and emission. At 2 bar BMEP and fixed NO_x level, soot emissions reduced with an increase in CO and HC emission. However, as the load increased the benefit of soot emission diminishes and the fuel economy penalty was negligible. They also observed that the compression ratio decreased from 15.2:1 to 13.7:1 during the earliest timing and VVA. EIVC increased ignition delay and 30% soot reduction was achieved while the increased level of CO and HC was lowered by lean mixture through injection pressure reduction. Experimental investigation of diesel engine for reducing NO_x emission by comparing standard dual cycle and Miller cycle was carried out by Wang et al. [11]. The Miller cycle was used to reduce the in-cylinder temperature at the end of compression and to achieve lower temperatures at the end of combustion which resulted in the reduction of NO_x emission. Results showed that NO_x emission was reduced by 4.4% to 17.5% for varying load when three versions of the Miller cycle were applied to a diesel engine in which Miller cycle 1 gave the best reduction by 11.0% to 17.5%.

Tomoda et al. [12] studied the effect of VVT and variable valve lift to improve the thermal efficiency of the diesel engine and maintain low emission level. The benefits of the valve overlap approach were reduced pumping losses, enhancement of volumetric efficiency, and control of residual EGR fraction. To vary swirl ratio continuously, IVC timing of VVT system was changed continuously. At high loads, the used VVT system could flexibly change the engine parameter, which resulted in 40% reduction in NO_x emission and 4% improvement in fuel economy. Low-end torque increased by 40% by matching EVO and overlap of IVO and EVO around TDC which resulted in the utilization of exhaust pressure pulsation. Experimental investigation on modification of in-cylinder gas thermodynamic condition by advancing the IVC angle in a HD diesel engine was studied by Benjas et al. [13]. They observed, advancing IVC reduced the total mass flow rate and decreased the effective compression ratio. Both pressure and density were reduced by 21.5% whereas temperature was decreased by only 2.3% at TDC as compared with the nominal IVC profile. Advancing IVC resulted in an increase of soot and CO emission, extremely low HC emission with the reduction in thermal and engine efficiency. To obtain low NO_x level, intake oxygen mass concentration was maintained at 17.4%.

Deng and Stobart [14] carried out BSFC investigation using VVT on a HD diesel engine and observed that engine performance and fuel efficiency were significantly influenced by IVC due to its huge effect on

volumetric efficiency. About 2.3% BSFC benefit was produced in either EIVC or LIVC as it has reduced pumping losses at part load and 1600 rpm; however, at 2200 rpm and full load condition 6% BSFC benefit was achieved by LIVC. Retarded exhaust valve phasing produced 1% BSFC benefit however, BSFC increased with delayed EVO. Therefore, as a result of investigation maximum 6% BSFC benefit could be achieved in different VVT strategies. Ghajar et al. [15] proposed a semi-empirical model, with engine speed, load, and valve timing for the prediction of volumetric efficiency. The developed model, its accuracy, and generalizability correlated with experimental data over an extensive working range of three distinct engines. Normalized test errors achieved were 0.0316, 0.0152, and 0.24 for three engines, respectively.

VVA is a standard technology to maximize volumetric efficiency over a wide range of engine speeds and loads [16]. Kim et al. [17] examined the effect of LIVC strategies in a single-cylinder compression ignition engine. IVC timings of 28˚CA, 44˚CA, 68˚CA, and 88˚CA with multiple injection strategies were studied for NO_x emission reduction. They observed that the volumetric efficiency decreased owing to the backflow of the cylinder charge into the manifold which implied that intake boosting was necessary. It was observed that the decrease in effective compression ratio from 16:1 to 13.7:1 at IVC timing 88˚CA resulted in 24.1% reduction of NO_x concentration, whereas reduction in O_2 concentration from 21% to 15% resulted in 78% reduction of NO_x concentration. Prolonged ignition delay, which provided a longer time for mixture formation, resulted in a reduction in the smoke emission.

Previous studies showed the effect of IVC, EVO, and EVC valve strategy on performance and emissions reduction. The majority of the works involved CRDI system or Ex-EGR or EIVC or LIVC strategy or a combination of these at varying load conditions for NO_x, CO, and HC emission reduction. IVO timing remained unchanged in most of the studies due to the practical limitation of the valve-piston clearance at TDC for diesel engines. Therefore, it is necessary to develop effective strategies to achieve low NO_x, CO, and HC emissions while maintaining performance. The main objective of this experimental work is to study the effect of valve timing, injection pressure, SOI, and swirl on small diesel engines for performance improvement and emission reduction. This study also explores intake valve timing strategies for internal EGR to reduce engine-out NO_x emission for naturally aspirated diesel engines.

2. EXPERIMENTAL TEST SETUP

Experimental work has been carried out on air-cooled four-stroke single-cylinder direct injection diesel engine with a displacement volume of 0.43 liter and compression ratio of 19:1. The power output produced by the engine was 5.5 kW at 3600 rpm. Detailed specifications of the engine are given in Table 1. The test setup is shown in Figure 1a and b, wherein in-cylinder pressure is measured by a piezoelectric pressure transducer (Kistler make). The pressure transducer is flush-mounted in cylinder head bottom surface for accurate measurement and to avoid hindrance due to fuel spray. Fuel is supplied from an overhead tank to the fuel conditioning unit and from there it is supplied at the pressurized condition with the return line carrying the bypass. The turbine flow meter is used for the measurement of the intake air flow rate. AVL make encoder (consisting of an optical disc) is mounted on the engine dynamometer side for engine rpm measurement. The engine is instrumented to measure the inlet and exhaust gas temperature and Chromel-alumel (K-type) thermocouple is mounted at a distance of 50-100 mm for accurate measurement. Cylinder pressure, top dead center (TDC), crank position, and all other signals are acquired by a high speed digital multifunctional I/O module, A-D converters, signal conditioner for data acquisition and control (AVL Puma Graz, Austria). AVL AMA emission analyzer is used for the emission measurement, where it takes a certain amount of sample from the exhaust emission at temperatures higher than 200˚C. Separate lines are used for the measurement of NO_x, and HC emission. Flame ionization detector (FID) is utilized for determining the unburned hydrocarbon emission level from the combustion chamber. Nitric oxide emission in the exhaust is measured with a chemiluminescence analyzer. Various sensors and uncertainty are shown in Table 2.

TABLE 1. Brief engine specifications

Type	**Four strokes, air-cooled, single-cylinder, CI engine**
Fuel	Diesel
Number of cylinders	One
Bore/Stroke	1.146
Compression ratio	19±0.5
Rated power	5.5 kW @ 3600 rpm
Rated torque	18 Nm @ 2000-2400
Valve timing	Inlet valve opening (IVO) : 7° before TDC
	Inlet valve closing (IVC) : 45° after BDC
	Exhaust valve opening (EVO):35° before BDC
	Exhaust valve closing (EVC) :28° after TDC
	Valve last 0.6-0.7 mm
	Max lift for intake and exhaust: 7.6 mm

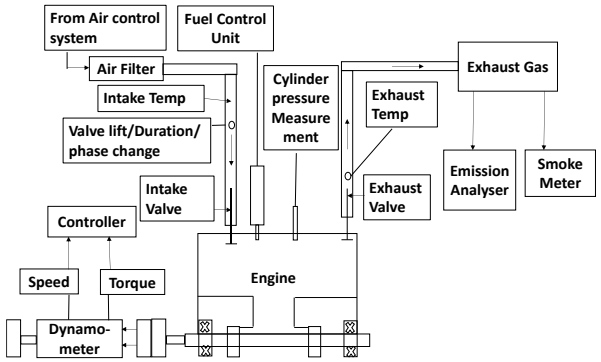

(a)

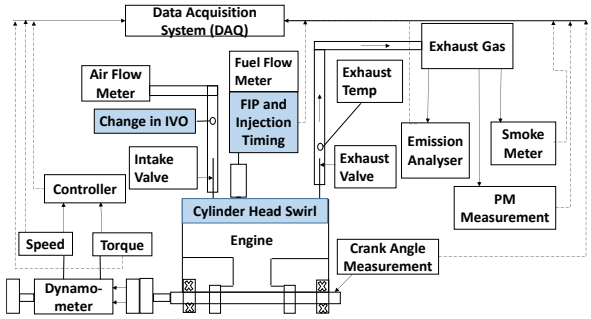

(b)

Figure 1. (a) Schematic view of the experimental set up; (b) Engine mounting view on test bed

3. TEST MATRIX

Initially, baseline engine performance and emission are measured, and thereafter effect of FIP in terms of injection pressure, valve timing, swirl ratio, and SOI are analyzed. The effect of each parameter is analyzed individually and in combination and few cases of performance and emission improvement are discussed. Three IVO timing, two swirl ratios, two FIP injection pressure, and three SOI are analyzed; the test cluster and test matrix are mentioned in Table 3. All engine specifications and other parameters remain the same for all the cases except the parameters mentioned in Table 3. Total 12 cases will be discussed, wherein the effect of individual parameters and combination is analyzed and discussed for different IVO, FIP SOI, and swirl ratios.

4. RESULT AND DISCUSSIONS

Initially, baseline engine testing is carried out and results are analyzed. Baseline engine performance and emission results are shown in Figure 2a and b. Peak engine torque measured was 19.5 Nm@2000 rpm with engine out exhaust gas temperature of 672˚C. NO_x and CO emission curves are shown in Figure 2.

The effect of various engine operating parameters is discussed in further sections.

4. 1. Effect of Fuel Injection Pump (FIP) An increase in fuel injection pump pressure increases the injector end pressure. The injector injects fuel at a higher pressure into the combustion chamber. This higher pressure gives better atomization and hence helps in better fuel-air mixing. This increases the quality of combustion and affects performance and emissions. Increased injection pressure fuel pump on baseline engine configuration increases NO_x emission by 15% for max torque speed, however, rated speed NO_x remains unchanged as shown in Figure 3a. Exhaust temperature (Figure 3b) also follows the same trends with lower values at rated speed with akin values at other engine

TABLE 2. Various measuring instruments and its uncertainty

Sr.No.	Measuring instruments	Make	Accuracy	Uncertainty (%)
1	Airflow meter	ABB SENSYFLOW-SFI-05	± 0.5% full scale reading	± 0.9
2	Fuel flow meter	Emerson, India-FI-05	± 0.5% of full-scale reading	± 0.9
3	Pressure pick up Piezo-electric	KISTLER, Switzerland-HSDA-01	± 0.4% full-scale reading	±0.85
4	Pressure pick up Piezo-resistive	KISTLER, Switzerland-HSDA-02	± 0.4% full-scale reading	±1.05
5	Emission analyzer	AVL Emission Test Systems, Germany-AVL AMA i60-03	CO: ± 0.07% of full-scale reading CO_2: ± 0.53% of full-scale reading NO_x : 0.53% of the full-scale reading THC : 0.53% of full-scale reading	± 3.92
6	Torque speed	Benz Systems, India	± 0.25% of full-scale reading ± 0.54% of full-scale reading	± 2 ± 0.5
7	PM measurement	AVL Emission Test Systems, Germany-AVL 472-04(A)	±0.53% of full-scale reading	± 3.9
8	Smoke	AVL Opcimeter439-05	± 0.25% of full-scale reading	± 0.9
9	Charge amplifier	KISTLER, Switzerland	± 1% full-scale reading	
10	Crank angle encoder	AVL, Austria	0.1 °CA	
11	Digital data acquisition system	AVL Puma Graz, Austria	± 2 bit	
12	Thermocouple (K-type)	HI-TECH Transducers & Devices, India	± 0.75% of full-scale reading	± 2

TABLE 3. Test cluster and matric

Parameters	Considered values
IVO timing	a) 15° bTDC b) 30° bTDC c) 45° bTDC
FIP pressure (bar)	a) Baseline FIP-1: 327 and b) FIP-2 - 364 bar
Swirl ratio	a) Head-1 swirl 2.5 and b)Head -2 swirl 2.0
SOI	11°, 9°and 7° bTDC
Case No	**Parameters description**
Case-1	Baseline engine configuration
Case-2	FIP-1, IVO-15˚, Head-1, SOI-11˚ bTDC
Case-3	FIP-2, IVO-30˚, Head-1, SOI-11˚ bTDC
Case-4	FIP-2, IVO-45˚, Head-1, SOI-9˚ bTDC
Case-5	FIP-1, IVO-45˚, Head-2, SOI-11˚ bTDC
Case-6	FIP-2, IVO-30˚, Head-2, SOI-9˚ bTDC
Case-7	FIP-2, IVO-45˚, Head-1, SOI-7˚ bTDC
Case-8	FIP-1, IVO-45˚, Head-1, SOI-9˚ bTDC
Case-9	FIP-1, IVO-45˚, Head-2, SOI-9˚ bTDC
Case-10	FIP-1, IVO-45˚, Head-2, SOI-7˚ bTDC
Case-11	FIP-2, IVO-45˚, Head-1, SOI-9˚ bTDC
Case-12	FIP-2, IVO-45˚, Head-2, SOI-7˚ bTDC

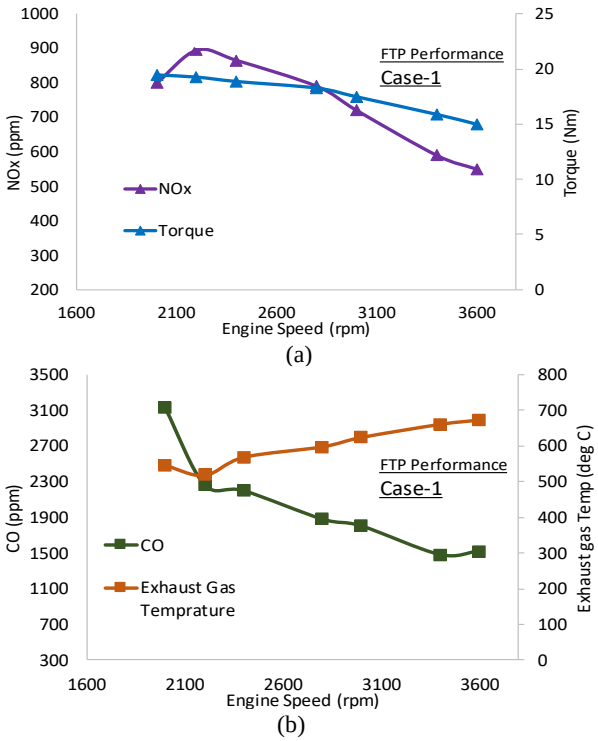

Figure 2. (a) NO_x emission and engine torque vs engine speed for baseline engine configuration; (b) CO emission and exhaust gas temperature vs engine speed for baseline engine configuration

speeds. As shown in Figure 3a, engine maximum torque is increased by 5% with a reduction in CO emission. It is due to higher in-cylinder pressure and consequently, the temperature which is a favorable condition for NO_x formation and this is the main reason for higher NO_x emission. As other engine parameters are the same, HC emission increases with reduction in CO emission. These results are in line with the results of Zammit et al. [10] and Kim et al. [17].

The effect of higher injection pressure with advanced IVO and retarded SOI is discussed in further sections.

4. 2. Effect of Early Intake Valve Opening

Advance IVO timing opens the intake valve earlier than TDC and provides higher valve overlap between intake and exhaust valve. This higher valve overlap allows us to send back a portion of high-temperature exhaust gases into the intake manifold. During suction, these high-temperature exhaust gases come back into the combustion chamber with fresh air. This mixing of exhaust gases with fresh air dilutes the intake air and increases incoming air temperature. Higher injection pressure also contributes to increased combustion chamber pressure and temperature. This initial higher temperature incoming air along with higher combustion temperature are favorable conditions for the formation of NO_x emission, however, diluted air reduces the oxygen

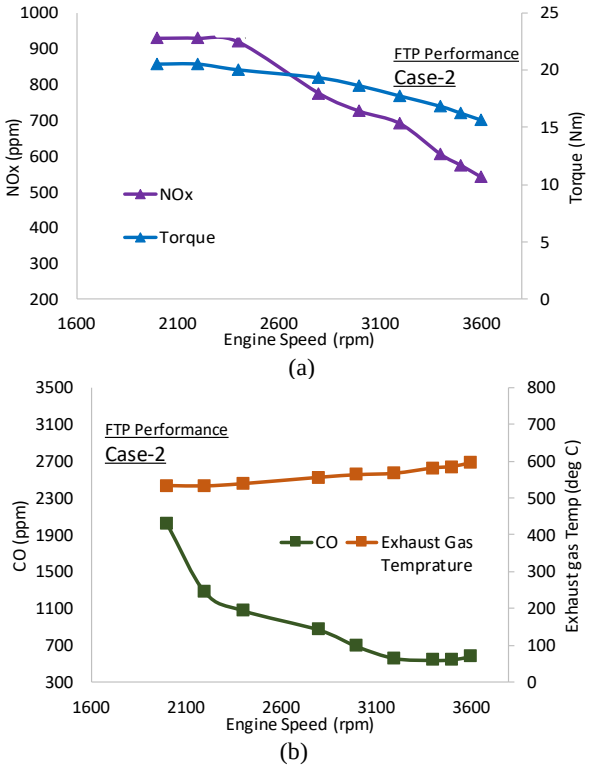

Figure 3. (a) NO_x emission and engine torque vs engine speed for FIP-2; (b) CO emission and exhaust gas temperature vs engine speed for FIP 2

availability and hence reduces NO_x emission [11]. The practical issue of adapting advanced IVO is intake valve to piston clearance which reduces as we advance IVO. Valve pocket needs to be provided on the piston to avoid this problem which increases the piston bowl volume and decreases the compression ratio. Baseline engine didn't have a pocket, however, the pocket of 1.6 and 2.5 mm depth is provided to maintain minimum valve to piston clearance of 1% of bore size for intake valve.

Advancing the IVO timing to 30˚bTDC leads to NO_x emission reduction by 10% for rated engine speed as shown in Figure 4a. This effect is uniform except at maximum torque speed where it is slightly higher than the baseline engine. Higher valve overlap duration minimizes the fresh air availability due to dilution with exhaust gases. This helps in the reduction of NO_x emission as limited oxygen is available for NO_x formation. Exhaust gas temperature trends also justify this, as it is decreased by 50°C (9%) for rated engine speed while was approximately the same for engine torque-speed. As shown in Figure 4b, CO emission also reduced in the range of 17-56% at various engine speeds compared to the baseline engine. HC emission from the engine also increased. It shows incomplete combustion due to lower oxygen availability. As combustion and exhaust gas temperatures are lower, they help in the reduction of CO formation. Higher engine speed favors higher valve overlap as it helps in feeding more air into the combustion chamber in shorter time, however, at low engine speeds, this higher valve overlap leads to higher backflow of air and thus reduces volumetric efficiency.

Advancing IVO to 45˚bTDC with retarded SOI, further reduces the NO_x emission for all engine speeds. In this case engine torque is increased by 2.5-5% at various engine speed ranges compared to the baseline engine, however, slightly lower than 30˚bTDC case. Exhaust gas temperature is also reduced by 3.6 to 11% at various engine speeds with minimum reduction at max torque speed. Advanced IVO increases valve overlap duration, which further minimizes the fresh air availability. This deteriorates the combustion quality, thus exhaust gas temperature is also reduced. CO emission is reduced due to lower peak combustion pressure and temperature, this increases HC emission due to incomplete combustion [13]. The effect of 45˚bTDC IVO on performance and emission is shown in Figure 5a and 5b.

Incomplete combustion and rich/lean fuel-air mixture are the reason for CO emission wherein, maximum combustion temperature is ≤1250˚C. Higher injection pressure with advanced injection timing also leads to higher penetration of fuel droplets and these fuel droplets

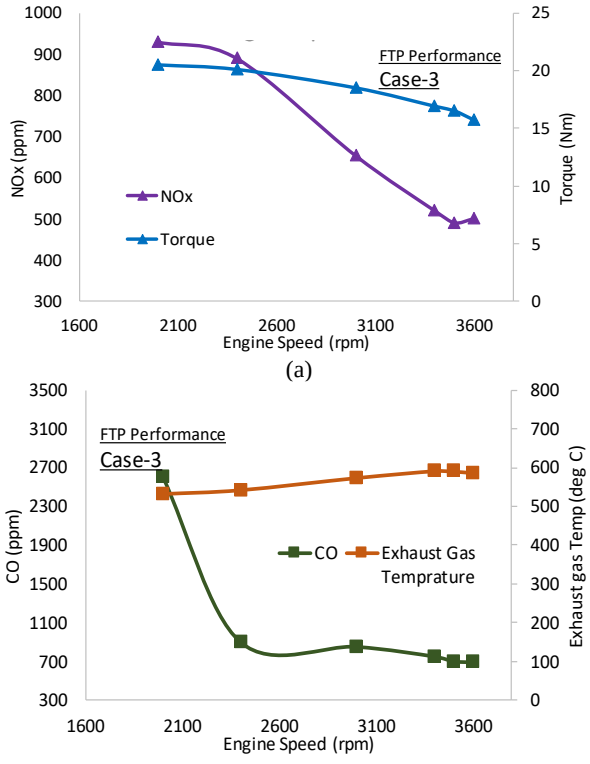

Figure 4. (a) NO_x emission and engine torque vs engine speed for 30˚bTDC IVO; (b) CO emission and exhaust gas temperature vs engine speed for 30˚bTDC IVO

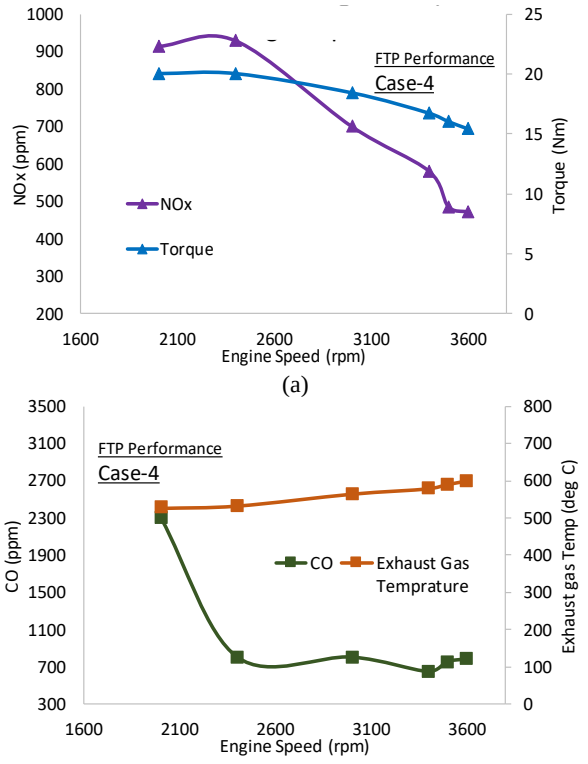

Figure 5. (a) NO_x emission and engine torque vs engine speed for 45˚bTDC IVO; (b) CO emission and exhaust gas temperature vs engine speed for 45˚bTDC IVO

lead to partial and incomplete combustion and contribute to higher CO and HC emission. As the reverse flow phenomenon is higher for lower engine speeds, it contributes more to max torque speed and consequently, the emission is higher at this speed.

4. 3. Effect of Swirl Ratio Cylinder head swirl helps in mixing of air with injected fuel. This swirling motion of air helps in breaking fuel droplets and automization. The flow coefficient of the intake port shows the resistance of the port. It should allow maximum air with minimum resistance along with the desired swirl for better mixing. Swirl is the rotational momentum of air about the arbitrary axis parallel to the cylinder axis. Higher swirl helps in better mixing of fuel with air, however higher swirl leads to higher NO_x emission.

Cylinder head mounted on the baseline engine is tested for the swirl ratio and flow coefficient on the steady-state swirl test rig. It is found that the baseline cylinder head swirl is 2.59 with flow coefficient of 0.279. The flow coefficient of the baseline cylinder head is on the lower side and needs to be modified to reduce the port restrictions and to increase the flow coefficient. Cylinder head swirl is modified on steady-state swirl rig and this increases the flow coefficient on 2nd cylinder head. The baseline performance of 2nd cylinder was similar to the baseline cylinder head. The modified swirl ratio and flow coefficient for 2nd cylinder head are 1.91 and 0.310. These values are 26% lower for the swirl ratio and 11% higher for the flow coefficient compared to the baseline cylinder head. Performance comparison of the swirl ratio and flow coefficient is shown in Figure 6. The 2nd cylinder head is used on the engine with various IVO timings, SOI timing, and FIP pump to analyze the effect of the swirl ratio.

Lower swirl (Swirl -2) cylinder head with advanced IVO of 45˚ bTDC and baseline FIP configuration shows reduction of NO_x emission by 27%. CO emission in this case also reduces by 21.5% compared to the baseline engine. HC emission increases in this case. Peak engine torque is increased by 3% with 12.5% reduction in exhaust gas temperature. Figure 7 shows the effects of performance and emission for this case. Lower swirl increases mixture formation time and this delay in fuel-air mixing leads to incomplete combustion of fuel. This affects CO and HC emission. In-cylinder airflow pattern and squish inside the bowl are the other reasons for this higher HC emission.

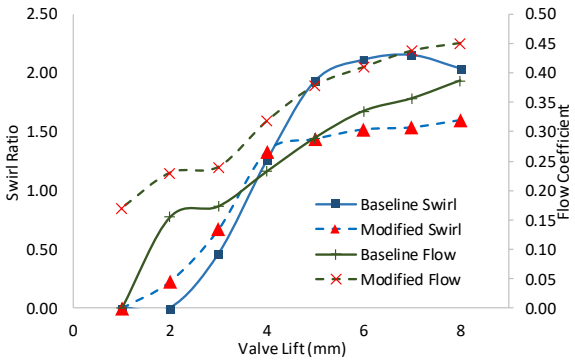

Figure 6. Swirl ratio and flow coefficient for baseline and modified cylinder head

4. 4. Effect of Start of Injection Timing Injection timing influences fuel atomization, ignition delay, premixed combustion, and main combustion. Hence combustion rate is directly governed by SOI timing. Advancing and retarding SOI controls the combustion and hence performance and emission. SOI timing is modified by changing the shim thickness as the injection system is a unit injector pump with fuel cam.

Retarded SOI of 9˚ with 30° bTDC IVO shows peak torque improvement of 7.2% (Figure 8a). This increases in HC emission by 200% with reduction of CO emission by 49% (Figure 8b). Retarded SOI and swirl-2 head increase fuel-air mixing time however, higher injection pressure and in-cylinder pressure affect combustion. Exhaust gas temperature is reduced by 6%. It is due to lower swirl and advanced IVO, which reduces oxygen

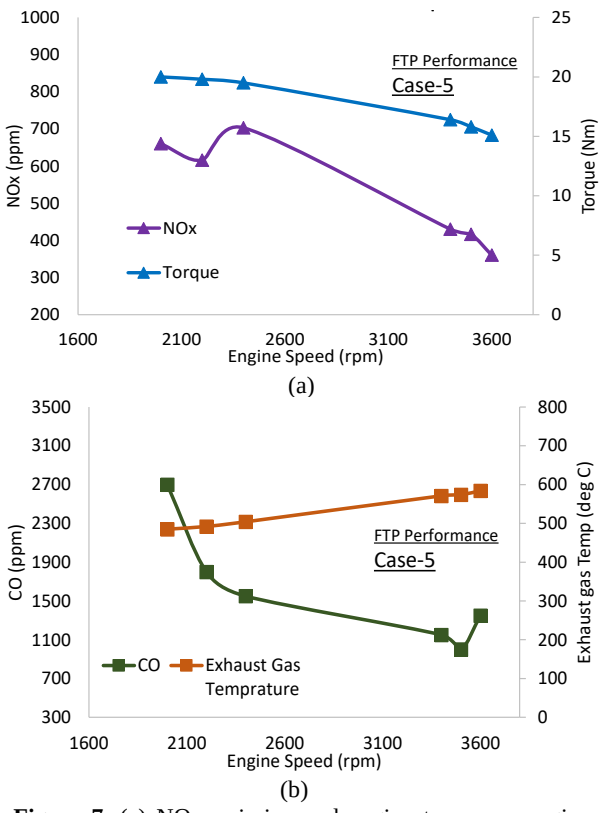

Figure 7. (a) NO_x emission and engine torque vs engine speed for swirl-2 cylinder head & 45˚bTDC IVO; (b) CO emission and exhaust gas temperature vs engine speed for swirl-2 cylinder head & 45˚bTDC IVO

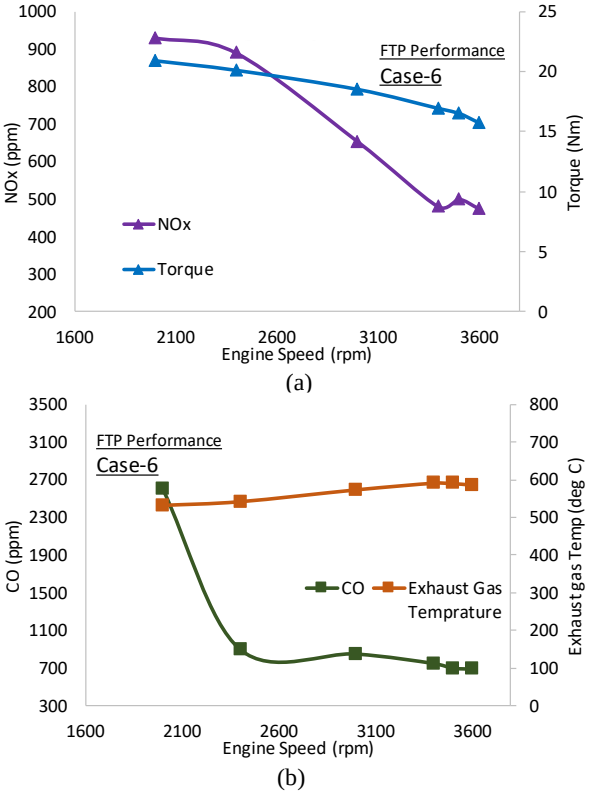

Figure 8. (a) NO_x emission and engine torque vs engine speed for 9˚ SOI; (b) CO emission and exhaust gas temperature vs engine speed for 9˚ SOI

availability and momentum of air inside the combustion chamber. NO_x emission in reduced by 11% compared to the baseline engine.

Retarded SOI of 7˚, with advanced IVO of 45° bTDC leads to reduction in NO_x emission by 15% with rated speed NO_x reduction by 22.9%, however, this effect is minimum at max torque engine speeds where this improvement is limited to only 2% as shown in Figure 9a. CO emission (Figure 9b) is increased by 100%, while HC emission is increased by 8%. Advanced intake valve opening leads to higher exhaust backflow and higher internal EGR, which increases the incoming air temperature. Retarded SOI delays injection and consequently fuel-air mixing, however higher in-cylinder pressure and temperature helps in rapid combustion. This increases the combustion rate with abruptly high pressure and temperature. Due to lower compression ratio, mixing quality, atomization, and oxygen availability favor for NO_x emission reduction [10, 16] as shown in Figure 9a. Due to abrupt combustion, exhaust gas temperature is higher (Figure 9b) and the same as per the baseline engine.

4. 5. Effect of Variation of SOI, FIP, IVO and Swirl

Injection timing influences the combustion rate, peak pressure, temperature, and emissions. FIP helps in better atomization of fuel and helps in the mixing of fuel with air. IVO helps in diluting the air and consequently the combustion and emission. Swirl ratio also plays a role in reduction of NO_x emission. The effect of variation in these parameters on performance and emission is discussed in this section.

SOI of 9˚ with advanced IVO of 45° bTDC, baseline FIP, and cylinder head reduces NO_x emission by 6%. Rated speed NO_x is reduced by 32%, however, max torque-speed NO_x is slightly higher. CO emission, in this case, is less than the baseline engine and lowest among all the cases discussed with a slight penalty in HC emission. It is due to better fuel-air mixing due to higher swirl and retarded SOI. Advanced IVO timing also maintains oxygen availability required for combustion, which restricts NO_x and CO formation. Exhaust gas temperature is reduced in the range of 8-15% at wide engine speeds. The effect of retarded SOI of 9˚ with advanced IVO of 45° bTDC is shown in Figure 10. This strategy is good for CO emission reduction.

Retarded SOI of 9˚, IVO of 45˚bTDC, baseline FIP, and swirl-2 cylinder head strategy show the reduction in NO_x emission by 29% and reduction in exhaust temperature by 10% as shown in Figure 11a and b. CO emission increased in this case compared to the baseline engine. This points out to the availability of oxygen in a

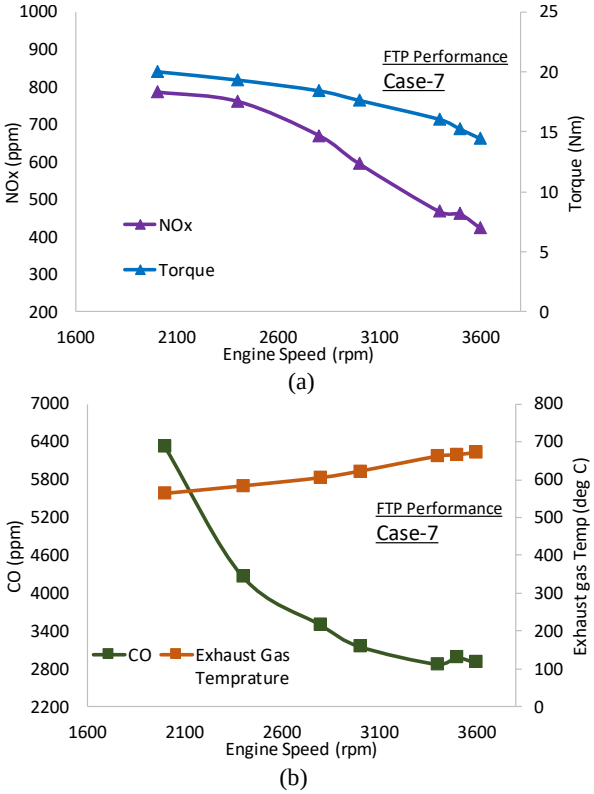

Figure 9. (a) NO_x emission and engine torque vs engine speed for 7˚ SOI; (b) CO emission and exhaust gas temperature vs engine speed for 7˚ SOI

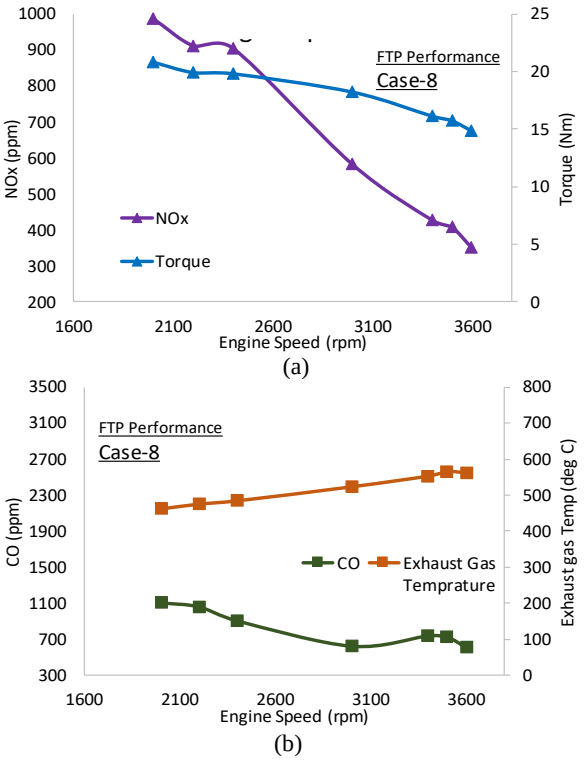

Figure 10. (a) NO_x emission and engine torque vs engine speed for 9˚ SOI and 45° IVO; (b) CO emission and exhaust gas temperature vs engine speed for 9˚ SOI and 45° IVO

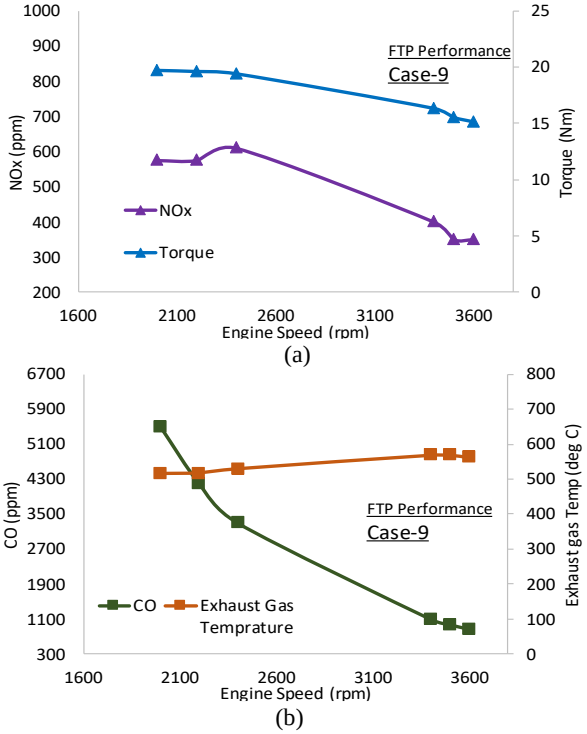

Figure 11. (a) NO_x emission and engine torque vs engine speed for 9˚ SOI, 45˚ IVO and swirl-2 cylinder head; (b) CO emission and exhaust gas temperature vs engine speed for 9˚ SOI, 45˚ IVO and swirl-2 cylinder head

small naturally aspirated engine with very advanced IVO timing. The compression ratio and volumetric efficiency of the engine decrease with advanced IVO, higher valve overlap, and internal EGR effect [10]. The engine torque for this combination strategy remains the same as the baseline engine. Rated speed CO emission is reduced by 42%, however max torque CO emission is increased by 75%. Retarded SOI, lower injection pressure FIP, and swirl resulted in uneven air-fuel mixing and lower oxygen availability due to advanced IVO which are the reasons for uneven CO emission as shown in Figure 11b.

Swirl-2 cylinder head, SOI of 7˚, IVO of 45˚bTDC and FIP-2, reduce the NO_x emission by 44%. This emission is reduced by 50% for rated engine speed while 30% for max torque-speed [12]. CO emission is reduced by 54% with an increase in HC emission. Lower swirl delays the mixture formation and leads to diverse mixing of the fuel-air mixture. The combustion rate is increased by delayed SOI and advanced IVO dilutes the air availability. Engine torque is reduced by 16-20% at various engine speeds with peak torque value of 16.3 Nm. This incomplete combustion also lowers the exhaust temperature by 30% compared to the baseline engine. This strategy has a penalty on the BSFC of the engine [14]. The effect of lower swirl with retarded SOI and advanced IVO on engine performance and emission is shown in Figure 12a and b.

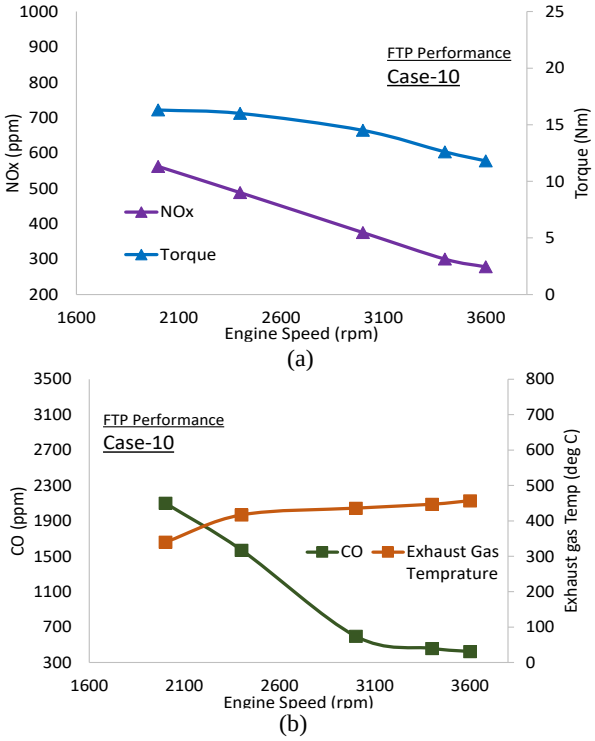

Figure 12. (a) NO_x emission and engine torque vs engine speed for 7˚ SOI, 45˚ IVO and swirl-2 cylinder head, (b) CO emission and exhaust gas temperature vs engine speed for 7˚ SOI, 45˚ IVO and swirl-2 cylinder head

SOI of 9˚, IVO of 45˚bTDC, baseline cylinder head, and FIP-2 combination strategy increases the engine's peak torque by 9% with reduction in CO emissions by 8.5% as shown in Figure 13 and Figure 14. Rated speed CO emission is reduced by 61% while max torque-speed CO emission is increased by 86%. Engine out NO_x emission also decreased marginally by 4% compared to the baseline engine. HC emission increased slightly compared to the baseline engine. Higher incoming air temperature due to internal EGR, higher swirl, and higher FIP injection pressure increase the combustion temperature. Oxygen availability due to advanced IVO is the reason for uneven CO emission and higher HC emission.

SOI of 7˚, IVO of 45˚bTDC, swirl-2 cylinder head, and higher injection pressure FIP-2 strategy reduce NO_x emission by 42%. HC emission, in this case, is also increased compared to the baseline engine. CO emission, in this case, increases by 78% with marginal increases in peak torque. Exhaust gas temperature is close to baseline engine configuration. It is due to delayed SOI and rapid combustion, which increases the exhaust gas temperature. Over lean fuel-air mixture leads to an increase in HC emission. The effect is shown in Figure 15.

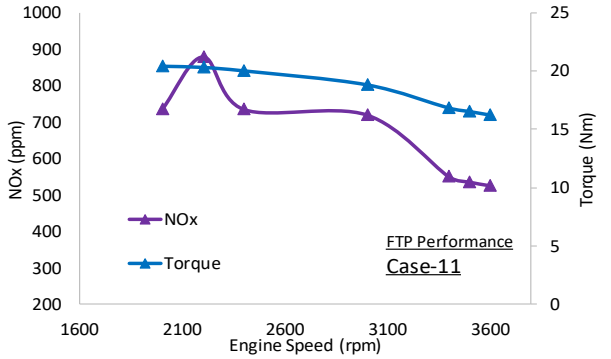

Figure 13. NOx emission and engine torque vs engine speed for 9˚ SOI, 45˚ IVO and FIP-2

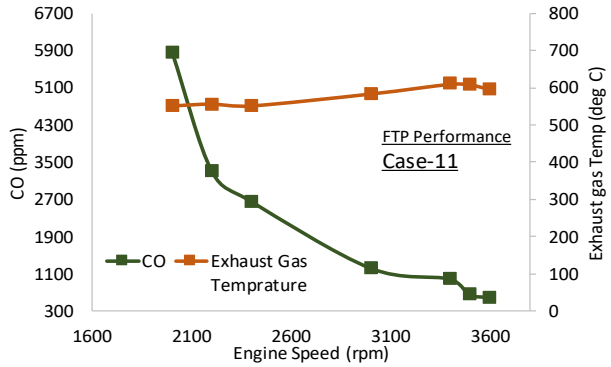

Figure 14. CO emission and exhaust gas temperature vs engine speed for 9˚ SOI, 45˚ IVO and FIP-2

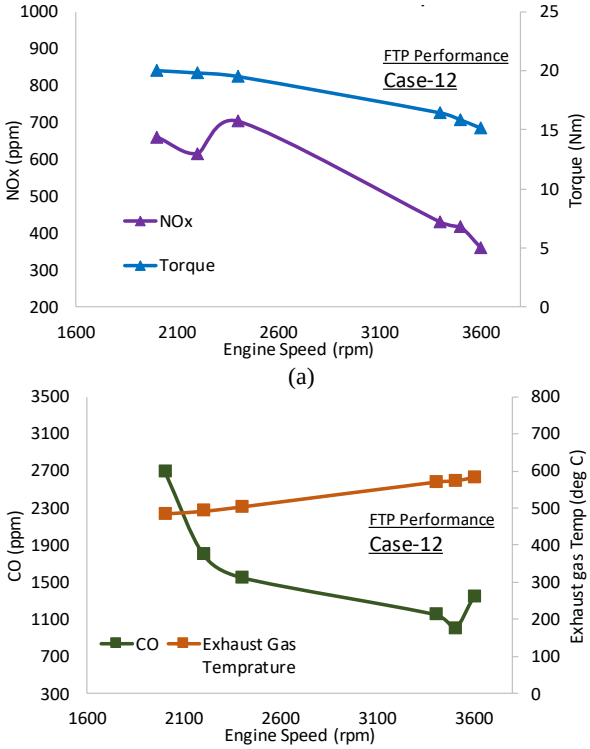

Figure 15. (a) NO_x emission and engine torque vs engine speed for 7˚ SOI, 45˚IVO, swirl-2 cylinder head, and FIP-2; (b) CO emission and exhaust gas temperature vs engine speed for 7˚ SOI, 45˚IVO, swirl-2 cylinder head, and FIP-2

Various strategies produced different results for engine performance and emission under full throttle performance. Each strategy has specific advantages and disadvantages compared to the baseline engine. These strategies show the maximum possible improvement for performance and reduction in various emission parameters under operating conditions. To further reduce emissions, we need to optimize combustion chamber geometry, external EGR, nozzles and intake ports for feeding more air.

5. CONCLUSIONS

Experimental tests were conducted on a single-cylinder naturally aspirated diesel engine to study the effect of valve timings, SOI and swirl ratio on its performance and emission characteristics. Previous studies focused on IVC timing and EGR for the reduction of NO_x emission, however, the present study is focused on the effect of IVO timing without EGR. The conclusions from the study are given below:

1. Advanced intake valve opening timing leads to higher valve overlap period and thus allows the backflow of exhaust gases into intake port and manifold which comes

back into the combustion chamber with fresh air and thus dilutes the oxygen availability in the fresh air.
2. This diluted air also helps in reducing NO_x emission as oxygen available for NO_x formation reduces and thus engine-out NO_x emission becomes lower. In the present study, engine-out emission reduced by 5-50% at different engine configurations at full throttle operating speed. Advanced IVO timing also helps in reducing in-cylinder and exhaust gas temperature.
3. The start of injection timing is an important factor affecting performance and emission as retarded SOI affects combustion rate, in-cylinder pressure, and temperature which directly affect CO, HC, and NO_x formation. In the present study, engine-out CO emission reduced by up to 50% for retarded SOI.
4. Cylinder head swirl and fuel injection pressure play a major role in in-cylinder fuel-air mixing and its uniform distribution. It also affects combustion characteristics due to pressure and temperature distribution inside the combustion chamber. Engine out NO_x emission is directly affected by swirl and injection pressure. Lower swirl strategy leads to NO_x reduction by 27%.
5. Retarded SOI, advanced IVO, and lower swirl strategy help in achieving lower NO_x and CO emission with torque improvement. This also helps in reducing exhaust gas temperature.
6. The developed strategies of SOI and advanced IVO with lower swirl can be utilized for the development of a multi-cylinder naturally aspirated engine for emission reduction. Previous studies have considered IVO with heavy exhaust EGR for reducing emission, however, a concrete solution is missing for naturally aspirated engines. Thus, this study would lead to a platform for the development of naturally aspirated engines with lower initial product cost and development time.

6. ACKNOWLEDGMENT

The authors would like to thank HoD and department staff of the Powertrain Engineering Department (PTE) of Automotive Research Association of India (ARAI), Pune, India for the support to carry out this research work.

7. REFERENCES

1. Knecht, W. "Diesel engine development in view of reduced emission standards." ***Energy***, Vol. 33, No. 2, (2008), 264–271. https://doi.org/10.1016/j.energy.2007.10.003
2. Taylor, A. M. K. P. "Science review of internal combustion engines." ***Energy Policy***, Vol. 36, No. 12, (2008), 4657–4667. https://doi.org/10.1016/j.enpol.2008.09.001
3. Agrawal, A. K., Singh, S. K., Sinha, S., and Shukla, M. K. "Effect of EGR on the exhaust gas temperature and exhaust opacity in compression ignition engines." ***Sadhana - Academy Proceedings in Engineering Sciences***, Vol. 29, No. 3, (2004), 275–284. https://doi.org/10.1007/BF02703777
4. Squaiella, L. L. F., Martins, C. A., and Lacava, P. T. "Strategies for emission control in diesel engine to meet Euro VI." ***Fuel***, Vol. 104, (2013), 183–193. https://doi.org/10.1016/j.fuel.2012.07.027
5. Jafari, B., Khatamnejad, H., Shahavi, M. H., and Ganji, D. D. "Simulation of Dual Fuel Combustion of Direct Injection Engine with Variable Natural Gas Premixed Ratio." ***International Journal of Engineering, Transactions C: Aspects***, Vol. 32, No. 9, (2019), 1327–1336. https://doi.org/10.5829/ije.2019.32.09c.14
6. Patnaik, P. P., and Acharya, S. K. "Effect of Compression Ratio on Emission of CI Engine using Neat Karanja Oil and Karanja Oil Methyl ester Blends." ***International Journal of Engineering, Transactions C: Aspects***, Vol. 27, No. 3, (2014), 403–410. https://doi.org/10.5829/idosi.ije.2014.27.03c.07
7. Boussouara, K., Merabet, A., and Kadja, M. "Modeling of Combustion and Carbon Oxides Formation in Direct Injection Diesel Engine." ***International Journal of Engineering, Transactions A: Basics***, Vol. 25, No. 3, (2012), 211–219. https://doi.org/10.5829/idosi.ije.2012.25.03a.03
8. Khatamnezhad, H., Khalilarya, S., Jafarmadar, S., Oryani, H., and Pourfallah, M. "Numerical Investigation on the Effect of Injection Timing on Combustion and Emissions in a DI Diesel Engine at Low Temperature Combustion Condition." ***International Journal of Engineering, Transactions B: Applications***, Vol. 24, No. 2, (2011), 165–179. Retrieved from http://www.ije.ir/article_71906.html
9. Zhang, X., Wang, H., Zheng, Z., Reitz, R. D., and Yao, M. "Effects of late intake valve closing (LIVC) and rebreathing valve strategies on diesel engine performance and emissions at low loads." ***Applied Thermal Engineering***, Vol. 98, (2016), 310–319. https://doi.org/10.1016/j.applthermaleng.2015.12.045
10. Zammit, J. P., McGhee, M. J., Shayler, P. J., Law, T., and Pegg, I. "The effects of early inlet valve closing and cylinder disablement onfuel economy and emissions of a direct injection diesel engine." ***Energy***, Vol. 79, No. C, (2015), 100–110. https://doi.org/10.1016/j.energy.2014.10.065
11. Wang, Y., Zeng, S., Huang, J., He, Y., Huang, X., Lin, L., and Li, S. "Experimental investigation of applying miller cycle to reduce NO_x emission from diesel engine." ***Proceedings of the Institution of Mechanical Engineers, Part A: Journal of Power and Energy***, Vol. 219, No. 8, (2005), 631–638. https://doi.org/10.1243/095765005X31289
12. Tomoda, T., Ogawa, T., Ohki, H., Kogo, T., Nakatani, K., and Hashimoto, E. "Improvement of Diesel Engine Performance by Variable Valve Train System." ***International Journal of Engine Research***, Vol. 11, No. 5, (2010), 331–344. https://doi.org/10.1243/14680874JER586
13. Benajes, J., Molina, S., Martín, J., and Novella, R. "Effect of advancing the closing angle of the intake valves on diffusion-controlled combustion in a HD diesel engine." ***Applied Thermal Engineering***, Vol. 29, No. 10, (2009), 1947–1954. https://doi.org/10.1016/j.applthermaleng.2008.09.014
14. Deng, J., and Stobart, R. "BSFC investigation using variable valve timing in a heavy duty diesel engine." In SAE Technical Papers. SAE International. https://doi.org/10.4271/2009-01-1525
15. Ghajar, M., Kakaee, A. H., and Mashadi, B. "Semi-empirical modeling of volumetric efficiency in engines equipped with variable valve timing system." ***Journal of Central South University***, Vol. 23, No. 12, (2016), 3132–3142. https://doi.org/10.1007/s11771-016-3379-3
16. Sürmen, A., Arslan, R., Kopmaz, O., Avci, A., Karagöz, I., and Karamangil, M. I. "Development of a variable-profile cam to enhance the volumetric efficiency of IC engines." ***International Journal of Vehicle Design***, Vol. 73, No. 1, (2017), 63–75. https://doi.org/10.1504/IJVD.2017.082581

17. Kim, J., Park, S. S., and Bae, C. "The effects of late intake valve closing and different cam profiles on the in-cylinder flow field and the combustion characteristics of a compression ignition engine." ***Proceedings of the Institution of Mechanical Engineers, Part D: Journal of Automobile Engineering***, Vol. 232, No. 7, (2018), 853–865. https://doi.org/10.1177/0954407017711357

Persian Abstract

چکیده

موتورهای دیزلی کوچک به دلیل نیازهای گشتاور بالاتر، صرفه‌جویی در مصرف سوخت و راندمان حرارتی بهتر، برای کاربردهای تجاری و وسایل نقلیه مسافربری بسیار مورد استفاده قرار می‌گیرند. این موتورها در معرض شرایط مختلف عملیاتی و محیطی قرار دارند و از این رو انتشار این موتورها نامناسب است. استراتژی‌های لازم برای افزایش کارایی و کاهش انتشار موتور با توجه به آلودگی محیط زیست و مقررات لازم است. هدف اصلی از این مطالعه تجربی، تدوین استراتژی‌هایی برای بهبود عملکرد و کاهش انتشار موتور برای موتورهای دارای فشار طبیعی است که می‌توان از آنها برای کاهش انتشار موتور چندسیلندر استفاده کرد. کار تجربی بر روی یک موتور دیزلی تک سیلندر انجام شده است تا تاثیر پارامترهای عملیاتی موتور مانند زمان سوپاپ، نسبت چرخش و فشار تزریق بر عملکرد موتور و تولید گازهای گلخانه ای بررسی شود. پارامترهای در نظر گرفته شده برای مطالعه عبارتند از: سه زمان باز کردن شیر ورودی، دو فشار پمپ تزریق سوخت، چرخش سر دو سیلندر و سه شروع زمان تزریق. نتایج نشان‌دهنده بهبود عملکرد، کاهش دمای گاز اگزوز و کاهش انتشار موتوراست. دمای گازی اگزوز ۵–۱۸٪ با باز شدن دریچه پیشرفته و چرخش سر سیلندر کمتر، کاهش می‌یابد. میزان انتشار NOx در حالت IVO (میزان باز شدن شیر مکش) پیشرفته با SOI (شروع تزریق) کم شده و چرخش کمتر سرسیلندر، ۵–۵۰٪ کاهش می‌یابد. این موجب کاهش انتشار گازهای CO و HC می‌شود چرا که دسترسی به هوای تازه به دلیل EGR (چرخش گاز اگزوز) داخلی بالاتر، کمتر است. پمپ تزریق سوخت با فشار بالاتر با تأثیر منفی بر انتشار NOx موتور، در بهبود گشتاور موتور کمک می‌کند. از آنجا که این موتورها از قطعات ظرفیت پایین برخوردار هستند و در معدود کشورها مورد استفاده قرار می‌گیرند، تحقیقات در مورد این موتورها محدود است. کلیه کارهای تحقیقاتی در زمینه زمانبندی بستن دریچه ورودی، زمان نسبت چرخش و زمانبندی تزریق انجام شده است. با این وجود تحقیقات بسیار محدودی در مورد اثر زمانبندی باز کردن دریچه ورودی موجود است که این مساله به محدودیت فاصله شیر پایین و پیستون در موتورهای دیزلی مربوط می‌شود.

International Journal of Engineering

Journal Homepage: www.ije.ir

Augmented Reality System and Maintenance of Oil Pumps

N. Koteleva*[a], G. Buslaev[b], V. Valnev[a], A. Kunshin[b]

[a] *Department of Automation of Technological Processes and Production, Saint-Petersburg Mining University, Saint-Petersburg, Russian Federation*
[b] *Department of Wells Drilling, Saint-Petersburg Mining University, Saint-Petersburg, Russian Federation*

PAPER INFO

Paper history:
Received 06 March 2020
Received in revised form 22 March 2020
Accepted 12 June 2020

Keywords:
Augmented Reality
Oil Pump
Maintenance
Digitalisation

ABSTRACT

Qualification of employees who operate technological processes directly influences the safety of production. However, the employees'' qualification cannot completely exclude human factor. Today, there are many technologies that can minimize or eliminate human factor impact on production safety ensuring. The augmented reality technology is an example of this technology. Nowadays, the augmented reality technologies and industrial technologies integration process moves to a new level of development. These technologies have huge experience, which has been accumulated in a long period of time. -This new level turns available by this experience combination and integration; it brings additional profit to the enterprise and can be a basis for completely new technologies. This paper shows an example of combination of augmented reality technology and oil pumps maintenance. For researching of efficiency of augmented reality system for oil pump maintenance, the laboratory unit with Grundfos vertical electric centrifugal pump (CR15-4 A-FGJ-AE-HQQE) was used. The laboratory unit is a physical model of one of the continuous oil processes. The oil pump of this laboratory unit is object of this research. The algorithm of servicing of oil pump was developed. The test of system and algorithms were carried out with four groups of people: the first one had only instructions to use on hand, the second one only used the internal recommendations of the system, the third one used only the help of an expert, and the fourth used internal recommendations and, if necessary, contacted the expert. The results show the efficiency and actuality of augmented reality technology for maintenance of industrial equipment, especially for the equipment operated in remote Arctic conditions.

***doi**: 10.5829/ije.2020.33.08b.20*

1. INTRODUCTION

Oil and gas industry is a large, dynamic and complex sector that offers great employment opportunities for a large number of people all over the world. The oil and gas industry's prosperous development or retention will depend on the latest technological achievements implementation. Therefore, recently, it has been proposed to implement the augmented reality technologies in oil industry [1].

Analysts believe that production upgrading in the oil and gas industry is possible by the introduction of augmented reality technologies into production process. The Extension of capabilities of the oil industry will make it possible to find new solutions to the actual topical issues such as exploration and production of hard-to-recover oil, the sea shelf fields construction, and transportation of oil from the Far North (in Russia) [2].

The use of augmented reality technology opens up medium-term prospects for employee's safety and efficiency improvement, and further with the digital double technology development, it would be possible to predict technical systems' failures, giving time for response or take measures for repair.

Any technical system, even the most reliable, requires qualified service and repair in case of failure. At the same time, due to the complexity and variety of equipment used in oil and gas industry, presence of a wide range of specialists is necessary. Otherwise, even one element failure will cause downtime enhance, which increases

*Corresponding Author Institutional Email: *Koteleva_NI@pers.spmi.ru* (N. Koteleva)

Please cite this article as: N. Kotelev, G. Buslae, V. Valnev, A. Kunshin, Augmented Reality System and Maintenance of Oil Pumps, International Journal of Engineering (IJE), IJE TRANSACTIONS B: Applications Vol. 33, No. 8, (August 2020) 1620-1628

proportionally with the facility remoteness and logistics complexity.

Elimination of non-production time (equipment downtime required for repair and maintenance) is an urgent area to reduce costs in oil and gas sector. This is especially pronounced in terms of modern realities, when the general amount of hydrocarbon reserves includes more and more hard-to-recover reserves, and its extraction requires significantly more financial, material and labor resources [3].

According to expert estimates, the Russian oil enterprises suffer over 4.5 thousand downtime cases every year due to equipment failure. At the same time, the equipment repair costs are more than 2.5 billion Rubles. In this regard, the company loses the raw materials amounting up to 500,000 tons of oil [4]. In addition, the lost marginal income is about 3.8 billion Rubles. The described problem is gaining weight for the Russian oil and gas industry, as exploration and production moves to more and more remote and northern regions, including Arctic territories, where with the technology development, the "maximum automation and minimum people" paradigm becomes relevant [5].

-Operation in the remote Arctic territories is associated with a number of factors those determine the necessity of careful design and maintenance and repair measures planning:

- Short navigation period for marine transport. During the summer navigation period, a significant part of cargo can be delivered via the Northern Sea Route and river transport to such ports as Varandey, Dikson, Dudinka, Pevek, Tiksi, etc. Nevertheless, most of the year (up to 10 months of the year) the Arctic Ocean from Murmansk until Sakhalin is covered with ice. It is possible to deliver goods and food to the Arctic ports only during two months a year. Therefore, careful planning is necessary, as well as accounting for the supply of equipment and spare parts for remote oil and gas projects; poor development of ground communications and infrastructure. Despite the availability of waterways, most of cargo is delivered to the Yamal Peninsula by vehicle and winter roads, which are prepared, rolled snow and ice, artificially formed in some areas [6].

- Bad weather conditions. It is advisable to transport personnel to and from the work place by air or helicopter. For the significant distances, it is advisable to organize special advanced bases with residential premises, fuel and food supplies, because in the Arctic region due to storms and severe climatic conditions, non-flying weather conditions can last up to several weeks.

In connection with the above, the most popular solution in the field of augmented reality in the near future is to provide maintenance personnel with technological systems' operating data, equipment design and the procedure for its maintenance in case of malfunction. If there is not any described solution, then the specialists' remote connection could be applied . He will be able to quickly study the collected data, visualy inspect the equipment by means of camera in the headset and give detailed recommendations for troubleshooting. Previously, the situations like this required phone connection with specialist, instructions and regulatory documents study, as well as long correspondence with technical specialists and designers in case of unusual situation.

The oil pump maintenance is one of the important measures that can decrease oil pump failures. There are three methods of maintenance: by schedule, by operating time and by actual state [7]. The maintenance by schedule shows which type of equipment and when needs to be maintained. In this case the list of equipment specifying maintenance periods is issued. So, the positions and time periods are previously known. Moreover, the time intervals between repairs are strictly defined and do not depend on the current state of the equipment. During maintenance, according to the actual state, some parameters are monitored, and on this basis, it is determined whether equipment repair is necessary or not. This method of maintenance is the most preferred because repairs are carried out only when necessary [8].

However, this method of maintenance has a range of disadvantages. It is possible that the monitored parameters show an incomplete picture, wrong status of the pump. In this case, even after maintenance, the pump failure is possible and consequently, production process stops.

According to the statistics of one of the top-ranked oil producing companies, electrical centrifugal pumps account for 40% of all types of pumps [9]. Figure 1 shows the dependence of running hours on the number of pump repairs. As we can see this dependence is linear. Regardless of the type and brand of pump manufacturers, the number of repairs is directly proportional to the running time. This means that repair of pump equipment is carried out according to the operating time for failure and only in rare cases according to their actual condition, Figure 1.

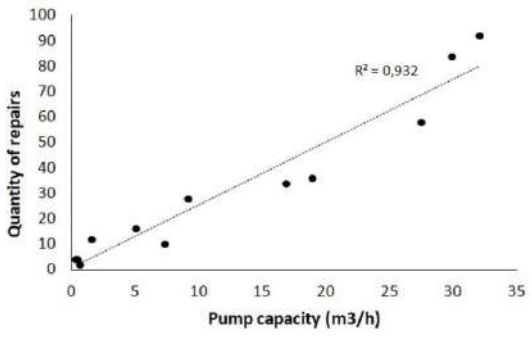

Figure 1. Dependence of the number of repairs on the pump capacity (for 6 months operation)

Furthermore, according Figure 2, the pump capacity is practically independent of average time spent on one repair.

Indirectly, we can conclude that the same type of repair operations are not affected at types and capacity, and therefore size of pumps. All in all, operator support system while repairing pump using template repairing function could show operator's efficiency, Figure 2.

Most customers are interested in less expensive pumps and lower maintenance costs during the pump lifetime. They are not interested in expensive pumps. Therefore, there is tendency to get more efficient repair.

The goal of this research is to determine the efficiency of implementing augmented reality system into the oil pump maintenance process.

2. LITERATURE REVIEW

In [10], the authors consider a photovoltaic pump station management platform using an augmented reality system with processing unit image processing (ARIMA) in an operator service application. This technological solution helps the operator in the station diagnostics and control. This support includes application of the augmented reality system covering all technological units as well as servicing algorithms specification using various modes and scenarios. Operational management and the station control is achieved by technological units' status monitoring in real time to make the workflow safe, uninterrupted and comfortable. The disadvantages of the authors' solution include the lack of adaptability of the user interface for the considered tasks and bulkiness of the control and monitoring devices.

In [11], the authors pay attention to the development and integration of virtual and augmented reality in hazardous industries, the education quality upgrade in educational institutions and training centers. The value of the study resides in the approach, which includes

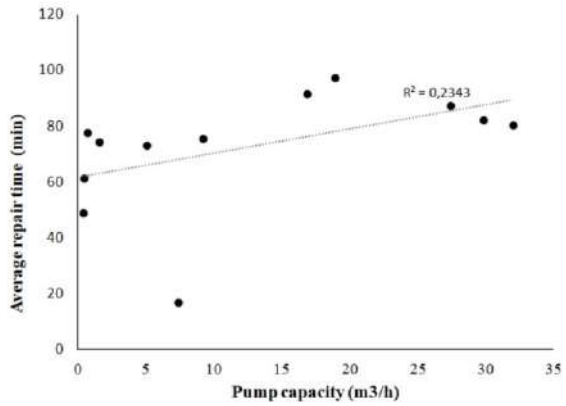

Figure 2. Dependence of the average repair time on the pump capacity

different points of view of the VR / AR systems development dynamics: technical and technological features; dangerous situations monitoring; improving production processes safety approaches. These approaches differ from the traditional ones; they are changing and improving with the VR / AR systems implementation and development of by sensors and diagnostic systems application for operating environment where technological operations are strictly carried out by personnel in accordance with certain scenarios and algorithms [12]. If the scenario was not executed according to the given algorithms, the specialists evaluated critical deviations from the rated values and applied more ergonomic and safe options of the equipment monitoring and control and control decreasing the influence of human factor. The authors note that the study is not a comprehensive one and its application is limited only to the construction area and further research should be focused on the safe and competent management of complex technological facilities in other sectors. Also, the study does not cover the laboratory studies of applications at the experimental, technical and operational levels, as well as the methods of influencing and assessment of VR / AR systems application in various projects and work scenarios.

In [13] the authors consider the VR / AR systems application in digital twins to improve the connection and interaction of physical and virtual realities. Moreover, their approach allows to increase the effectiveness of the digital twin system based on many sides comparison of the AR / VR systems' differences and similarities in the design, production, technological facilities maintenance. Based on the created VR and AR solutions in digital twins, a structure is proposed for integrating these systems into a five-dimensional digital twin, to increase the operator's ability to manage large amounts of interactive data and production scenarios. The program structure is built based on the operator's requirements. The concept of constructing AR / VR structures in digital twins proposed by the authors is presented as a literature review. Just like previous authors, the study lacks its own laboratory and experimental studies; therefore, this material should be regarded as reference information for their own test benches and applications development and can be used for solutions search in a particular production area.

In [14-15], the authors consider training VR simulator application for operation modeling, diagnostics and technological equipment repair. The simulator is purposed for oil and gas production sector specialists' training aimed to improve the safety and faultless production, capital and operating training costs reduction by saving on purchase of equipment physical samples for staff training. The following disadvantages of the equipment's physical version are noted: high risks; equipment failures due to specialist errors during

preparation; the impossibility of the equipment upgrading and the compelled purchase of newer models, etc. The authors argue that the training VR simulators will allow the specialists to have relevant equipment samples; perform manipulations without any risk for health; reduce training time by means of automation the operation process involving tools; application of various scenarios for the learner's skills development and his thinking strategies in non-standard situations. The study does not provide any statistical data on the studied object, the global experience of similar systems application and the experimental results are poorly described; that makes it difficult to reproduce the experiment and apply its results in order to improve the presented techniques.

3. METHOD

Augmented Reality (AR) overlays virtual 3-Dimensional (3D) objects on the real-world and gets inside training and education [16-17] area.

AR is a set of innovative techniques (e.g., real- time data acquisition, human computer interaction, scene capture, real- time tracking and registration, etc.), and can augment the view of physical world by embedding computer-generated elements or objects [18-19]. The goal of this technology is to put the virtual world on the screen and interact with it in real world [20].

With the advent of augmented reality (AR), the tendency to capitalize on immersive AR applications to create enabling environments for visualizing complex situations in the workplace, building knowledge on risk prevention and training has become apparent. AR technology can meet the goal of improving human perception of virtual prototyping with real objects. This gives the virtual world an improved connection with the real world, while maintaining the flexibility of the virtual world [21]. Via AR, the real environment can be augmented with text, labels, models, and videos, which will conduce to fewer mistakes, faster speed, and higher quality of the service process.

Instead of simply interacting with 3D content in a purely computer environment, users are now able to realize an extremely exciting, holistic and realistic experience based on synthesized digital and physical information about the world presented using more sophisticated software and hardware [22-23].

The use of augmented reality technologies in oil facilities is not so widespread, and is just about to be implemented. This is due to uncertainty in the technical aspects associated with the use and maintenance of systems based on augmented reality technology. In connection with the above, in the near future the most popular solution in the field of augmented reality will be to provide maintenance personnel with information on the operation of the technological system, equipment design, and the way to maintain it in case of malfunction. If the current situation has not the described solution, then there is a possibility to connect specialist to the process remotely, who is able to examine the collected data quickly, provide the equipment visual inspection by means of camera in the headset and give detailed recommendations for troubleshooting. The specialist can give his recommendations on the screen and a person at site will see on the display equipped with AR [24].

Previously, such a situation required to call a specialist, studying instructions and regulatory documents, as well as lengthy correspondence with technical specialists and designers in case of an unusual situation.

The study examines the augmented reality technology effectiveness for oil pumps servicing. According to the method used in the study, the effectiveness analysis is carried out as follows:

1. Determination of the object to study. The research object should have several properties: it is a part of the technological process, service operations with the object are complex, i.e. its servicing implies a complex algorithm; moreover, the object should be of wide application at oil and gas industry facilities.
2. The object servicing algorithm development. When developing this servicing algorithm, the following manipulations with the object are mandatory: assembly/disassembly from any existing technological installation, the equipment parts replacement, the equipment actual status assessment according to the process parameters in real time mode.
3. Testing system components. At this stage, it checks the health of the system as a whole, the health of data transmission channels, as well as the health of individual system modules and the health of the modules in conjunction with each other.
4. Determination of the system efficiency. At this stage, the test was carried out with four groups of people: the first (No. 1) had only instructions to use on hand, the second (No. 2) used only the internal recommendations of the system, the third (No. 3) used only the help of an expert, and the fourth (No. 4) used internal recommendations and, if necessary, contacted the expert. During the experiment, some of the most important functions and actions for each group recorded the execution time of each operation. Function 1 - dismantling the pump, function 2 - removing the coupling guard, function 3 - removing two halves of the clutch, function 4 - removing the pin, function 5 - dismantling the engine section.

Thus, we expect to get a numerical expression of effectiveness for every of these four ways of the augmented reality application, by fixing the execution time of each function for each group of experimenters. Herewith, the method No1 that allows using only manuals for servicing and Internet does not use the

augmented reality system functionality; therefore, it is given as a standard for service comparison before the system is implemented and after its implementation. Method No 4, where for pump servicing they use just the expert assistance is also an extreme option. This is because in this method the augmented reality system provides the possibility of "single window" and a "single point of view" between the service engineer and the expert and then the expert, totally involved in the service process, obviously is not able to increase the system efficiency.

4. IMPLEMENTATION

The research team of Saint-Petersburg Mining University had carried out work on creating an AR application for servicing the Grundfos vertical electric centrifugal pump (CR15-4 A-FGJ-AE-HQQE) of the oil transfer demonstration unit (Figure 3). The laboratory unit consists of two tanks and pumps those transfer liquid from one tank to another, a heat exchanger, valves, sensors and actuators.

The system consists of four modules (Figure 4). The first one is the laboratory unit module. It consists of control elements and equipment which help collecting the technological processes data, acquire and transmit it to a higher level. For the purpose of implementation, the basic unified protocols should be used for low level equipment [25]. The OPC-protocols are used for integration in the system. The second module is data acquisition and storage. It is an important module and it combines different modules together. For example, the module of augment reality cannot be connected with controller and SCADA-system without this module element. The third module is the additional software. It can be used for linking AR-software and different analytical modules. For example, the analytical module can analyze the quality, and predict the quantity of maintenance, it can evaluate the service engineer's actions and advise them, etc. All the analytical functions are based on the high level calculations capacity.

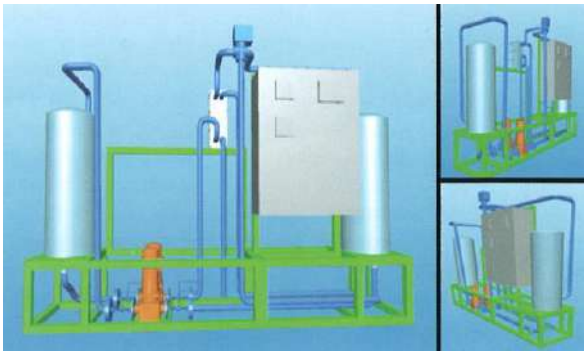

Figure 3. Laboratory unit

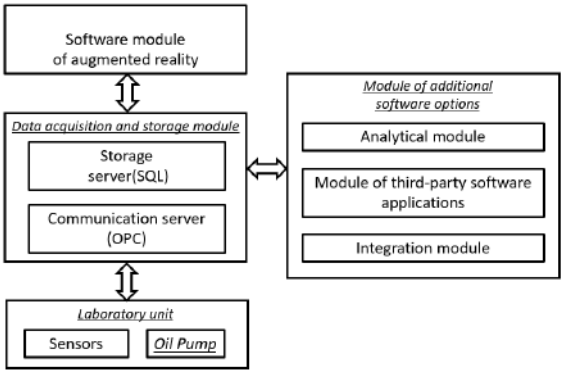

Figure 4. The system structure

Therefore, the divided architecture is more flexible and capable to adapt compared to a single one. The AR-system uses not just the technological system data, it can use the ERP-system data and other one. The other example of the analytical module is the maintenance steps templating inside the system. Many typical functions are realized in each maintenance project. Similar actions can be templated. Prior to the new project implementation, the system at the first step searches for the actions template. If the template is absent, you add this action as a new action, or change the template. The third module helps to link AR-module with other modules and systems. The fourth module is the AR-system software. It can be implemented on the different software platforms. In this project, The Unity with Vufiria is used.

The pump was dismantled by a technical specialist, each step was marked and recorded for further algorithm development. Then, the pump was assembled back recording the actions sequence. The assembly / disassembly algorithm was used to write a pump maintenance procedure for various technological operations on replacing consumables or cleaning deposits.

Figures 5 shows the system operation. Using the developed application, it is possible to carry out the unit/ disassembly of the pump, assembly/ disassembly, monitor installation parameters, study the documentation and fill out a report (Figure 5).

Figure 5. The start window of the system

If it is necessary to repair the pump or carry out maintenance, and if the site service is impossible, the system will tell you what needs to be done to disconnect the pump from the production line (Figure 6).

To control the process parameters, the head of the workshop (unit) or someone else has no need to get up or call the operator room. All parameters of the sensors can be seen in the field, even if they are not indicated in field (Figure 7).

During the equipment repair (maintenance), there is no need to use paper instructions. All the necessary documentation and instructions are digitized and appear step-by-step, prompting not only the actions necessary to perform, but also the necessary tool for this (Figure 8).

Then remove the coupling guard which is shown on Figure 9.

At the next step remove the coupling assembly, unscrew 2 screws on each side of the coupling. Remove two halves of the clutch, which is already in a collapsible condition, Figure 10.

Figure 6. Removing pump from laboratory unit

Figure 7. Processes parameters

Figure 8. Unscrew two screws of coupling guard

Figure 9. Removing the coupling guard

Now, open the way to the pin which connects the central and motor parts of the pump. Pull out the pin (Figure 11).

At this stage, the motor section (shown in Figure 12) is not connected to other parts of the pump, therefore, we take it out. At this step, the first stages of the analysis has been completed, and further actions will be finalized in the next version of the program. The pump is assemble by the reverse order (Figure 12).

Figure 10. Removing two halves of the clutch

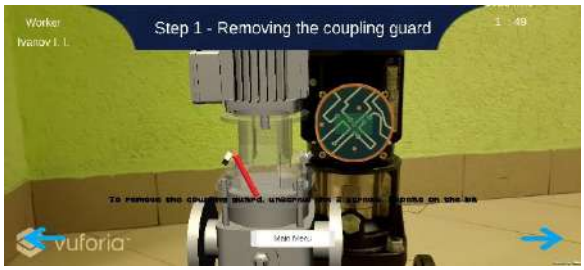

Figure 11. Removing the pin

Figure 12. Dismantling the engine section

The system developed several functions, the main ones of which are:
1. Visualization of user actions (tested in three forms - in the form of a video file, on a 3D team model displayed on top of a service part, in the form of highlighting (highlighting with light and color on a real object) of parts that require attention of service personnel (for example, highlight bolts, which you need to unscrew and the desired type of tool)
2. Display of process parameters - process parameters in real time and their values in history (in the form of trends or tables)
3. Displaying expert advice or creeping line tips
4. The possibility of video communication with the expert directly (organization of a single viewing window for the expert and service engineer)
5. The possibility of audio communication with an expert.
6. Information output of third-party applications and software modules (analytics, documentation of service information, etc.)

5. RESULTS

1. The object to study was to determine pump efficiency. It was a Grundfos vertical electric centrifugal pump (CR15-4 A-FGJ-AE-HQQE). Electrical centrifugal pumps are very popular and widely-spread in oil industry. Therefore, the testing of popular species of pumps is very important for this study.
2.The object servicing algorithm was developed.
3. The augmented reality system was developed and realized.
4. The system components were tested
5.The system efficiency was determined.

The test was carried out with four groups of people: the first (No. 1) had on hand only instructions to use, the second (No. 2) used only the internal recommendations of the system, the third (No. 3) used only the help of an expert, and the fourth (No. 4) used internal recommendations and, if necessary, contacted the expert. During the experiment, some of the most important functions and actions for each group recorded the execution time of each operation. Function 1- dismantling the pump, function 2- removing the coupling guard, function 3- removing two halves of the clutch, function 4- removing the pin, function 5- dismantling the engine section. The results of the system test are presented in Table 1.

TABLE 1. Results of experiments

Function Number \ Group Number	No 1, time, sec	No 2, time, sec	No 3, time, sec	No 4, time, sec
Experiment 1				
1	178	140	194	131
2	96	37	120	40
3	180	124	170	154
4	94	35	110	25
5	80	80	70	75
Total time	628	416	664	425
Experiment 2				
1	194	154	120	147
2	120	40	35	45
3	210	132	142	164
4	90	45	20	30
5	75	74	42	80
Total tme	689	445	359	466
Experiment 3				
1	210	135	190	175
2	95	55	110	40
3	196	120	170	165
4	87	40	80	35
5	98	62	65	73
Total time	686	412	615	488
Experiment 4				
1	180	152	110	156
2	92	45	30	37
3	214	137	145	152
4	84	38	27	40
5	115	53	45	71
Total time	685	425	357	456

6. DISCUSSION

The main hypothesis of the work is HM: The augmented reality system reduces the time for maintenance of oil pumps. To prove this hypothesis, we put forward a number of auxiliary hypotheses. Hypothesis 1: the maximum time for system maintenance will be spent by group No. 1 (the group that serviced the pump only in accordance with the paper instructions). Hypothesis 1 was not confirmed in the first experiment. It turned out that group No. 1, which serviced the pump only in accordance with paper instructions, served the pump faster than the group that used only the help of an expert (No. 3). They wasted 628 and 664 seconds, respectively. Analyzing the results, it was found that this was caused by the fact that at first the subjects tried to figure it out

themselves and only in case of failure they used the help of an expert. Therefore, as a result, they spent more time than everyone else did. Hypothesis 1 has been adjusted and hypothesis 2 has been put forward: the maximum time for system maintenance will be spent by group No. 1 if group No. 3 (which used only expert help) will be given instructions to use expert help immediately. Hypothesis 2 was confirmed. In the second and fourth experiment, group 3 completed the task faster than everyone else did. However, at the same time, an expert was constantly involved; that is actually not the best solution. The fact that the group that used the internal instructions of the system and the expert' s help at the same time involved the expert in all experiments only once could be considered as a proof. At the same time, the time to complete the task is not significantly longer than that in the group using only the experts help. Another hypothesis was hypothesis 3: a group that used internal recommendations and, if necessary, contacted the expert (No. 4) would complete the task faster than a group that used only system recommendations (No. 2). This hypothesis has been disproved. In all experiments, the group that used only the internal recommendations of the system (No. 2) completed the task faster than group No. 4. a number of reasons could be the cause of this: first, people in the fourth group reacted more slowly to the prompts of the system as a whole, and the second factor, the ability to contact an expert relaxed the participants and they turned to him even when it was not necessary and spent more time on the assignment. Group No. 1 presents an imitation of the work of service engineers without using an augmented reality system. In all four experiments, she showed the worst results compared to the averaged results for other groups. This fact is a proof of the main hypothesis - the Augmented Reality system reduces the time for maintenance of oil pumps.

7. CONCLUSIONS

In the era of information technologies development, more and more digital solutions find their application in industry, in particular oil and gas industry. One of the solutions is AR Augmented Reality Technology. The results show the effectiveness of using augmented reality technology for servicing oil pumps. Provided that there is a complete description of all the actions that must be performed during maintenance, visualization gives a significant reduction in the time spent on servicing one unit of pumping equipment. Connecting to an expert help system gives conflicting results, if there is a complete instruction, expert help increases the time it takes to carry out actions, but in situations of emergency and beyond the scope of the instructions, expert help will significantly increase the overall performance of the system.

In further studies, according to the authors, it is necessary to further develop mechanisms involving an expert in the pump maintenance system. The correct distribution of the expert's time, the development of manipulators that can remotely carry out certain actions by the hands of a service engineer and the organization of a single view of the object are relevant issues for further research. In addition, there are others actual terms for future research, including the integration with other systems, positioning, markers, date storage and analysis etc.

8. REFERENCES

1. Litvinenko, V.S., "Digital economy as a factor in the technological development of the mineral sector", ***Natural Resources Research***, Vol. 29, No. 3, (2020), 1521-1541. DOI: 10.1007/s11053-019-09568-4
2. Cherepovitsyn A.E., Lipina S.A., Evseeva O.O. "Innovative Approach to the Develop-ment of Mineral Raw Materials of the Arctic Zone of the Russian Federation", ***Journal of Mining Institute***, Vol. 232, (2018), 438-444. DOI:10.31897/PMI.2018.4.438
3. Hongfang Lu, Lijun Guo, Mohammadamin Azimi, Kun Huang, «Oil and Gas 4.0 era: A systematic review and outlook», ***Computers in Industry,*** Vol. 111, (2019), 68–90. DOI: doi.org/10.1016/J.COMPIND.2019.06.00
4. Necci, A., Tarantola, S., Vamanu, B., Krausmann, E. and Ponte, L., "Lessons learned from offshore oil and gas incidents in the arctic and other ice-prone seas", ***Ocean Engineering***, Vol. 185, (2019), 12-26. DOI: 10.1016/j.oceaneng.2019.05.021
5. NedosekinA.O., Rejshahrit E.I., KozlovskijA.N., "Strategic Approach to Assessing Economic Sustainability Objects of Mineral Resources Sector of Russia", ***Journal of Mining Institute***, Vol. 237, (2019), 354-360. DOI: 10.31897/PMI.2019.3.354
6. Rob Montenegro, Nils Hökby, «Optimizing operational efficiency in submersible pumps», ***World Pumps,*** (2004). DOI: 10.1016/s0262-1762(04)00174-9
7. Zhukovskiy, Y. and Koteleva, N., "Development of augmented reality system for servicing electromechanical equipment", ***Journal of Physics: Conference Series***, Vol. 1015, (2018), 042068. DOI: 10.1088/1742-6596/1015/4/042068
8. Dvoynikov, M.V., Nutskova, M.V. and Blinov, P.A., "Developments made in the field of drilling fluids by saint petersburg mining university", ***International Journal of Engineering***, Vol. 33, No. 4, (2020), 702-711. DOI: 10.5829/IJE.2020.33.04A.22
9. M. E. Haque, M. R. Islam, M. S. Islam, H. Haniu, M. S. Akhter, «Life cycle cost and energy consumption behavior of submersible pumps using in the Barind area of Bangladesh», ***Energy Procedia,*** Vol. 110, (2017) 479-485. DOI: 10.1016/j.egypro.2017.03.172
10. Benbelkacem, S., Belhocine, M., Bellarbi, A., Zenati-Henda, N. and Tadjine, M., "Augmented reality for photovoltaic pumping systems maintenance tasks", ***Renewable Energy***, Vol. 55, (2013), 428-437. DOI: 10.1016/j.renene.2012.12.043
11. Xiao Li, Wen Yi, Hung-Lin Chi, Xiangyu Wang, Albert P.C. «A critical review of virtual and augmented reality (VR/AR) applications in construction safety», ***Automation in Construction,*** Vol. 86, (2018), 150-162. DOI:

https://doi.org/10.1016/j.autcon.2017.11.003

12. Herbert, B., Ens, B., Weerasinghe, A., Billinghurst, M. and Wigley, G., "Design considerations for combining augmented reality with intelligent tutors", ***Computers & Graphics***, Vol. 77, (2018), 166-182. DOI: 10.1016/j.cag.2018.09.017
13. Index, in Digital twin driven smart manufacturing, F. Tao, M. Zhang, and A.Y.C. Nee, Editors. 2019, Academic Press.257-269 DOI: 10.1016/b978-0-12-817630-6.00026-6
14. Garcia, C.A., Naranjo, J.E., Ortiz, A. and Garcia, M.V., "An approach of virtual reality environment for technicians training in upstream sector", ***IFAC-PapersOnLine***, Vol. 52, No. 9, (2019), 285-291. DOI:10.1016/j.ifacol.2019.08.222
15. Necci, A., Tarantola, S., Vamanu, B., Krausmann, E. and Ponte, L., "Lessons learned from offshore oil and gas incidents in the arctic and other ice-prone seas", ***Ocean Engineering***, Vol. 185, (2019), 12-26. DOI: 10.1016/j.oceaneng.2019.05.021
16. Radu I. Augmented reality in education: a meta-review and cross-media analysis. Pers Ubiquitous Comput, Vol. 18, No.6, (2014), 1533-1543. DOI:10.1007/ s00779-013-0747-y.
17. Azuma, R., Baillot, Y., Behringer, R., Feiner, S., Julier, S. and MacIntyre, B., "Recent advances in augmented reality", ***IEEE Computer Graphics and Applications***, Vol. 21, No. 6, (2001), 34-47. DOI: 10.1109/38.963459
18. MarininM.A.,Khokhlov S.V., Isheyskiy V.A., "Modeling of the Welding Process of Flat Sheet Parts by an Explosion", ***Journal of Mining Institute***, Vol.237, (2019), 275-280. DOI: 10.31897/PMI.2019.3.20.
19. Jacobs, T., "Ar headsets give oil and gas sector the quicker fix", ***Journal of Petroleum Technology***, Vol. 70, No. 7, (2018), 32-34. DOI: 10.2118/0718-0032-JPT
20. X. Wang, S.K. Ong, A.Y.C. Nee, A comprehensive survey of augmented reality assembly research, ***Advanced Manufacturing,*** Vol. 4, No. 1, (2016), 122. DOI: 10.1007/s40436-015-0131-4
21. Amelessodji Kokougan Etonam, Giulio Di Gravio, Patrick W. Kuloba, Jackson G. Njiri, «Augmented Reality (AR) Application in Manufacturing Encompassing Quality Control and Maintenance», ***International Journal of Engineering and Advanced Technology***, Vol. 9, No. 1, (2019), 197-204. DOI: 10.35940/ijeat.A1120.109119
22. Tanita Fossli Brustad "Preliminary Studies on Transition Curve Geometry: Reality and Virtual Reality", ***Emerging Science Journal,*** Vol. 4, No. 1, (2020). DOI: https://doi.org/10.28991/esj-2020-01204
23. Mehmet Özüağ, İsmail Cantürk, Lale Özyilmaz, «A New Perspective to Electrical Circuit Simulation with Augmented Reality», ***International Journal of Electrical and Electronic Engineering & Telecommunications*** Vol. 8, No. 1, (2019), 9-13. DOI: 10.18178/ijeetc.8.1.9-13
24. Wei Zhang, Xianzhao Yang, Tao Wang, Xueyuan Peng, Xiaolin Wang, "Experimental Study of a Gas Engine-driven Heat Pump System for Space Heating and Cooling", ***Civil Engineering Journal*** , Vol. 5, No. 10, (2019), 2282-2295. DOI: 10.28991/cej-2019-03091411
25. Sunitha, R. and Chandrikab, J., "Evolutionary computing assisted wireless sensor network mining for qos-centric and energy-efficient routing protocol", ***International Journal of Engineering***, ***Transactions B: Applications,*** Vol. 33, No. 5, (2020), 791-797. DOI: 10.5829/IJE.2020.33.05B.10

Persian Abstract

چکیده

صلاحیت کارکنانی که فرایندهای تکنولوژیکی را انجام می‌دهند به طور مستقیم بر ایمنی تولید تأثیر می‌گذارد. لیکن، صلاحیت کارکنان نمی‌تواند عامل انسانی را کاملاً مستثنی کند. امروزه فناوری‌های زیادی وجود دارد که می‌توانند تأثیر عامل انسانی بر ایمنی تولید را به حداقل رسانده یا از بین ببرند. فناوری واقعیت افزوده نمونه‌ای از این فناوری است. امروزه، ادغام فناوری‌های واقعیت افزوده و فناوری‌های صنعتی به سطح جدیدی از توسعه رسیده است. این فناوری‌ها تجربه‌ی شگرفی دارند که در مدت زمان طولانی انباشته شده است. این سطح جدید توسط ترکیب و یک‌پارچه‌سازی تجربه در دسترس قرار می‌گیرد، سود اضافی را برای شرکت به ارمغان می‌آورد و می‌تواند مبنایی برای فناوری‌های کاملاً جدید باشد. این مقاله نمونه‌ای از ترکیب فناوری واقعیت افزوده و نگهداری پمپ های نفتی را نشان می‌دهد. به‌منظور تحقیق در مورد کارایی سیستم واقعیت افزوده برای نگهداری پمپ روغن از واحد آزمایشگاهی با پمپ گریز از مرکز عمودی برقی Grundfos (CR15-4 A-FGJ-AE-HQQE) استفاده شد. واحد آزمایشگاهی یک مدل فیزیکی یکی از فرایندهای پیوسته‌ی روغن است. پمپ روغن این واحد آزمایشگاهی هدف این تحقیق است .الگوریتم سرویس پمپ روغن ایجاد شد. آزمایش سیستم و الگوریتم‌ها با چهار گروه از افراد انجام شده است: دسته‌ی اول فقط از دستورالعمل‌های در دست، گروه دوم فقط از توصیه‌های داخلی سیستم، دسته‌ی سوم فقط به کمک یک متخصص و گروه چهارم توصیه‌های داخلی و در صورت لزوم تماس با کارشناس را به کار می‌گرفتند. نتایج بهره‌وری و دقت فناوری واقعیت افزوده برای نگهداری تجهیزات صنعتی، به‌ویژه برای تجهیزات کار شده در شرایط دورافتاده قطب شمال را نشان می‌دهد.

International Journal of Engineering

Journal Homepage: www.ije.ir

Control of Electric Wheelchair Suspension System based on Biodynamic Response of Seated Human Body

A. Saghafi*, M. Bagheri Hosseinabadi, N. Khomarian

Department of Mechanical Engineering, Birjand University of technology, Birjand, Iran

PAPER INFO

Paper history:
Received 10 April 2020
Received in revised form 28 May 2020
Accepted 12 June 2020

Keywords:
Wheelchair
Human Biodynamic Model
Body Vibration
Active Control
Suspension

ABSTRACT

Electric wheelchair is one of the equipment to be used by the incapacitated and disable people. Constant exposure to vibration affects human comfort and health. Reducing the vibrations transmitted to the human body is important in the electric wheelchair design and becomes a healthcare industry demand. This paper deals with the study on vibration control of the electric wheelchair suspension system. A generalized model of the electric wheelchair suspension, including the biodynamic model of seated human body is presented. In order to achieve optimal suspension performance, an active control for wheelchair suspension is designed based on H-infinity control criterion. Numerical simulations are carried out to demonstrate the effectiveness of the proposed wheelchair suspension system. The simulation results show that the proposed control system can effectively attenuate the vibration amplitude and improve the wheelchair suspension performance. This control system could be used for electric wheelchair design and assist with improving human comfort.

doi: *10.5829/ije.2020.33.08b.21*

1. INTRODUCTION

Numerous research studies have focused on the ride comfort of vehicles which has effects on driver fatigue and health. Suspension systems are designed to reduce the transmission of vibration from road surface disturbances. Semi active and active suspension systems have been more attractive for researchers during the last several decades [1-10].

To minimize vertical vibration transmitted to a driver, an active seat suspension system is developed by Alfadhli et al. [7]. Performance of the active suspension is evaluated using experimental and simulation. Moghadam-Fard et al. [8] presented an active control of quarter car suspension system based on adaptive neuro fuzzy (ANFIS). Moaaz et al. [9] used fuzzy and PID control approach to investigate the performance of automotive active suspension system. It was found that controlled suspension can provide much better performance in the ride comfort compared with uncontrolled system. In the study by Nouby et al. [10] a quarter vehicle active suspension control model is developed. Suspension model controlled using H-infinity control approach.

Study performed in these literature [11-14] showed that human body is considered mainly as a rigid mass mounted on the suspension system. Human body exposed to vibrations is a complex dynamic system. An investigation of the dynamic response of human body helps to a better understanding of the effects of vibration on human comfort, and is important for the analysis and improvement of suspension system performance.

Modeling and analysis of the dynamic response of human body are interesting topics for research. To study the dynamic response of human body, many biodynamic models have been developed. These models could be mainly classified as lumped parameter, multi-body, and finite element models [15, 16]. For example, using beam, spring and mass elements, a 2-DOF model for human body is presented by Griffin [17]. Wei et al. [18] used two models of human body, 1-DOF and 2-DOF, to investigate the vibration transmissibility. It was observed that 2-DOF model provided better prediction. Tewari et al. [19] developed and investigated a 3-DOF model of tractor seat

*Corresponding Author Email: *a.saghafi@birjandut.ac.ir* (A. Saghafi)

Please cite this article as: A. Saghafi, M. Bagheri Hosseinabadi, N. Khomarian, Control of Electric Wheelchair Suspension System based on Biodynamic Response of Seated Human Body, International Journal of Engineering (IJE), IJE TRANSACTIONS B: Applications Vol. 33, No. 8, (August 2020 2020) 1629-1636

suspension. A dynamic model for a seated human body in a sitting posture is presented by Abbas et al. [20]. The vibration transmissibility and dynamic responses are evaluated. In the study conducted by Aisyah et al. [21], the suspensions seat transmissibility and seat effective amplitude transmissibility values for a seated human body exposed to vibration in tractor are investigated. Optimization based on genetic algorithms is used by Baumal et al. [22] to design and control an active suspension system. In the study by Desai et al. [23] a 2-dimensional, 20 DOF sitting posture multi-body model for seated human is developed, and model parameters are optimized by using genetic algorithm. Dong et al. [24] developed a 3-dimensional finite element model of the body-seat system to study the effect of sitting posture and seat on the dynamic response of human body.

Electric wheelchair is one of the equipment to be used by the incapacitated and disable people. The effects of vibration exposure and also longed wheelchair riding on user discomfort have been approved. Minimizing the vibrations transmitted to the wheelchair user is important in the electric wheelchair design and becomes a healthcare industry demand. It can be addressed through the suspension system design [25-27]. For example, Garcia-Mendez et al. [26], evaluated vibration exposure to wheelchair user for different types of wheelchair frames. They determined the effect of wheelchair suspension in reducing vibration transmitted to the body. In a study by Cooper et al. [27], vibrations in manual wheelchairs with and without suspension are investigated.

A thorough survey of literature indicates that although the wheelchair suspension performance is investigated, active control of wheelchair suspension and also the biodynamic response of wheelchair user are not considered. The purpose of this study is to apply suspension system in the design of wheelchair. In order to control and improve the wheelchair performance, active control of wheelchair suspension model by considering the biodynamic model of seated human body is proposed. Then, H-infinity static output feedback controller is designed to control and improve the wheelchair performance .

This paper is organized as follows. The model of a wheelchair suspension, including the seated human model, is described in section 2. Based on H-infinity control technique, active controller design is formulated. Section 3 presents the simulation results and controller performance evaluations. Finally, conclusions are given in section 4.

2. MODEL DESCRIPTION AND CONTROLLER DESIGN

2. 1. Biodynamic Model of Human Body human body can be modeled as several rigid mass connected by sets of spring and damper. In this study, a 1-DOF model of human body is employed, proposed by Wei and Griffin in 1998 [18]. Analytical studies and experimental validations have shown that this model is suitable for studying the dynamic response of human body. In this model, the seated person is composed of a support structure "m_b" and a sprung mass "m_h", connected by spring, "k_h", and damper, "c_h". Schematic of this model is depicted in Figure 1.

2. 2. Wheelchair and Suspension model A 2-DOF active suspension model is employed to investigate the dynamic response and control of electric wheelchair. This suspension system schema is shown in Figure 2. Sprung mass, m_s, is the mass of wheelchair chassis and seat. Unsprung mass, m_w, represents the wheel assembly mass. Tire is simulated by a spring with stiffness, k_t, and it is assumed that it always contacts with the road surface.

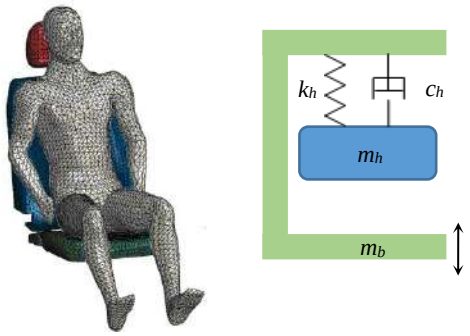

Figure 1. The biodynamic model of human body proposed by Wei et al. [13]

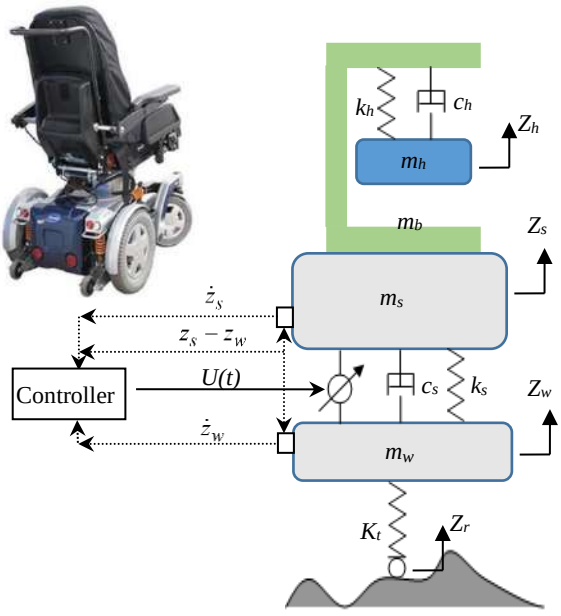

Figure 2. Wheelchair suspension model

k_s and c_s are stiffness and damping of the passive suspension component. The controller output *U(t)*, represents the input control force can be generated by the actuator.

The dynamic equation for the wheelchair suspension and human body can be derived as:

$$m_h \frac{d^2 z_h}{dt^2} = -k_h(z_h - z_s) - c_h(\frac{dz_h}{dt} - \frac{dz_s}{dt}) \quad (1\text{-a})$$

$$(m_b + m_s)\frac{d^2 z_s}{dt^2} = k_h(z_h - z_s) + c_h(\frac{dz_h}{dt} - \frac{dz_s}{dt})... - k_s(z_s - z_t) - c_s(\frac{dz_s}{dt} - \frac{dz_w}{dt}) + U \quad (1\text{-b})$$

$$m_w \frac{d^2 z_w}{dt^2} = k_s(z_s - z_w) + c_s(\frac{dz_s}{dt} - \frac{dz_w}{dt})... - k_t(z_w - z_r) - U \quad (1\text{-c})$$

The state variables can be defined as: $x_1(t) = (z_h - z_s)$, $x_2(t) = dz_h / dt$, $x_3(t) = (z_s - z_w)$, $x_4(t) = dz_s / dt$, $x_5(t) = z_w$, $x_6(t) = dz_w / dt$. $w(t) = z_r$ represents road surface disturbance. The state space model for this suspension system can be written as:

$$\dot{x} = Ax + B_1 w + B_2 u \quad (2)$$

where:

$$A = \begin{pmatrix} 0 & 1 & 0 & -1 & 0 & 0 \\ -\frac{k_h}{m_h} & -\frac{c_h}{m_h} & 0 & \frac{c_h}{m_h} & 0 & 0 \\ 0 & 0 & 0 & 1 & 0 & -1 \\ \frac{k_h}{m_b + m_s} & \frac{c_h}{m_b + m_s} & \frac{-k_s}{m_b + m_s} & \frac{-c_h - c_s}{m_b + m_s} & 0 & \frac{c_s}{m_b + m_s} \\ 0 & 0 & 0 & 0 & 0 & 1 \\ 0 & 0 & \frac{k_s}{m_w} & \frac{c_s}{m_w} & -\frac{k_t}{m_w} & -\frac{c_s}{m_w} \end{pmatrix}$$

$$B_1 = \begin{bmatrix} 0 & 0 & 0 & 0 & 0 & \frac{k_t}{m_w} \end{bmatrix}^T, B_2 = \begin{bmatrix} 0 & 0 & 0 & \frac{1}{m_b + m_s} & 0 & -\frac{1}{m_w} \end{bmatrix}^T$$

2. 3. Controller Design To improve the suspension performance, this section is devoted to the controller design for the wheelchair suspension system. A static output feedback controller is considered as: *U=Ky*, where, y is the input of the controller. *K* and *U* are the controller gain matrix and the output of the controller, respectively. Measured signals feedback to the controller. The controller sends a signal to the actuator to generate a compensation force to eliminate vibration (Figure 2). Schematic of this control system is shown in Figure 3 [28]. The suspension deflection and also the seat and upper body velocity are measured variables which are selected as input variable to the controller. So, the control law can be expressed as:

$$U(t) = ky = \begin{bmatrix} k_1 & k_2 & k_3 \end{bmatrix} \begin{bmatrix} z_s - z_w \\ \dot{z}_s \\ \dot{z}_h \end{bmatrix} \quad (3)$$

For this suspension controller design, ride comfort and road holding are the main desired objective [6]. For this purpose, the control objectives are defined as: $\ddot{z}_h$, $\ddot{z}_s$ and, $z_w - z_r$, which are the controlled output, Z. Now, by considering the dynamic Equation (1), the control model for the wheelchair suspension can be described as:

$$\begin{pmatrix} \dot{x} \\ z \\ y \end{pmatrix} = \left(\begin{array}{c|cc} A & B_1 & B_2 \\ \hline C_1 & D_{11} & D_{12} \\ C_2 & D_{21} & D_{22} \end{array}\right) \begin{pmatrix} x \\ w \\ u \end{pmatrix} \quad (4)$$

where:

$$C_1 = \begin{pmatrix} -\frac{\alpha_1 k_h}{m_h} & -\frac{\alpha_1 c_h}{m_h} & 0 & \frac{\alpha_1 c_h}{m_h} & 0 & 0 \\ \frac{\alpha_2 k_h}{m_b + m_s} & \frac{\alpha_2 c_h}{m_b + m_s} & \frac{-\alpha_2 k_s}{m_b + m_s} & \frac{-\alpha_2 (c_h + c_s)}{m_b + m_s} & 0 & \frac{\alpha_2 c_s}{m_b + m_s} \\ 0 & 0 & 0 & 0 & \alpha_3 & 0 \end{pmatrix}$$

$$D_{11} = \begin{pmatrix} 0 \\ 0 \\ -\alpha_3 \end{pmatrix}, D_{12} = \begin{pmatrix} 0 \\ \frac{\alpha_2}{m_b + m_s} \\ 0 \end{pmatrix}, C_2 = \begin{pmatrix} 0 & 0 & 1 & 0 & 0 & 0 \\ 0 & 0 & 0 & 1 & 0 & 0 \\ 0 & 1 & 0 & 0 & 0 & 0 \end{pmatrix},$$

$$D_{21} = \begin{pmatrix} 0 \\ 0 \\ 0 \end{pmatrix}, D_{22} = \begin{pmatrix} 0 \\ 0 \\ 0 \end{pmatrix}$$

α_1, α_2, and α_3 are the weighting coefficients which represent the trade-off between the control objectives. Transfer function for the state space model of Equation (4) is obtained as:

$$P(s) = \begin{bmatrix} C_1 \\ C_2 \end{bmatrix} (sI - A)^{-1} \begin{bmatrix} B_1 & B_2 \end{bmatrix} + \begin{bmatrix} D_{11} & D_{12} \\ D_{21} & D_{22} \end{bmatrix} = \left[\begin{array}{c|c} P_{11} & P_{12} \\ \hline P_{21} & P_{22} \end{array}\right] \quad (5)$$

For this static output feedback controller, the closed loop transfer function from the disturbance input *w(t)* to the controlled output Z, can be obtained as:

$$T_{zw}(s) = P_{11} + P_{12} K (I - P_{22} K)^{-1} P_{21} \quad (6)$$

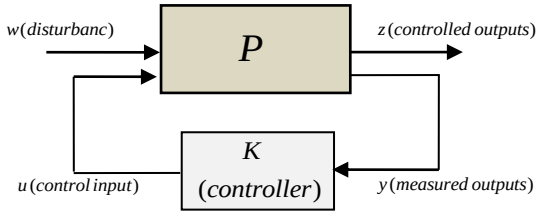

Figure 3. Schematic of the control system [28]

The active suspension controller is implemented by H-infinity control technique. The control objective is to determine a controller gain matrix $K=[k_1\ k_2\ k_3]$, in a way the system would be stable and the H-infinity norm of the closed loop transfer function $\|T_{zw}(j\omega)\|_\infty$, could be minimized. In practice, the actuator force is limited by its physical capability and should be considered in controller design. This limitation can be expressed as: $\|K\|_\infty \le K_{\max}$. Therefore, the H-infinity controller design problem for suspension can be expressed as the following constrained optimization problem [28, 29]:

$$\min(\|T_{zw}(j\omega)|k=\begin{bmatrix}k_1 & k_2 & k_3\end{bmatrix}\|_\infty) \quad s.t.: T_{zw}(s)\ is\ stable\ \&\ \|k\|_\infty \le k_{\max} \tag{7}$$

This multi-objective minimization problem is formulated in MATLAB and solved by using particle swarm optimization (PSO) algorithm [30, 31].

3. SIMULATION RESULTS

In this section, in order to demonstrate the proposed controller performance, numerical simulations are conducted. The simulation parameters of the wheelchair suspension and human are listed in Table 1. In this simulation, the weighting coefficients and controller gain limitation for the actuator are considered as: $\alpha_1=\alpha_2=2$, $\alpha_3=1$, $\|K\|_\infty \le 200$ and $\|K\|_\infty \le 3000$, respectively. Optimization is performed using the PSO algorithm. H-infinity norms of transfer function are obtained as: $\|T_{zw}(j\omega)\|_\infty = 10376$ and $\|T_{zw}(j\omega)\|_\infty = 5467.7$. Also, the optimal controller gains are obtained as:

$$K_{opt,1}=\begin{bmatrix}-200 & -200 & 200\end{bmatrix}\ \ st.\|K\|_\infty \le 200$$
$$K_{opt,2}=\begin{bmatrix}142.48 & -3000 & 3000\end{bmatrix}\ \ st.\|K\|_\infty \le 3000 \tag{8}$$

The frequency responses of closed loop system (active suspension with optimal control gains $K_{opt,1}$ and $K_{opt,2}$) for upper body acceleration, lower body acceleration and tire deflection are compared with those of open loop system (passive suspension system without controller), and are depicted in Figures 4-6, respectively. Figures 4 and 5 present the frequency responses of the upper and lower body acceleration, respectively. As it can be seen, the proposed control system reduces body acceleration more effectively compared to the uncontrolled system especially in the resonance regions (Around 2.63, and 10.5 *Hz*).

In the resonance region (Around 10.5 *Hz*), the controller attenuates the upper body acceleration around 15% for controlled system with control gain $K_{opt,1}$, and also 52% for system with higher control gain $K_{opt,2}$. Also, about 16 and 56% amplitude reduction for the lower body acceleration is observed, compared with the closed loop system. As it can be seen, the best control performance has been achieved by using the optimal control gain $K_{opt,2}$. As expected, the control performance can be improved by using the higher control gain.

Figure 6 presents frequency responses of tire deflection. At resonance frequencies, around 2.63, and

TABLE 1. Parameters of the wheelchair and human body

Parameter	Unit	Value
m_h	kg	43.4
m_b	kg	8.8
m_s	kg	20
m_w	kg	30
c_h	N.s/m	1485
c_s	N.s/m	150
k_h	N/m	44130
k_s	N/m	31000
k_t	N/m	100000

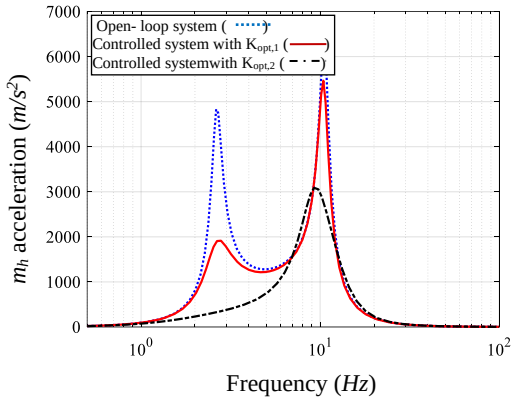

Figure 4. Frequency response of upper body acceleration

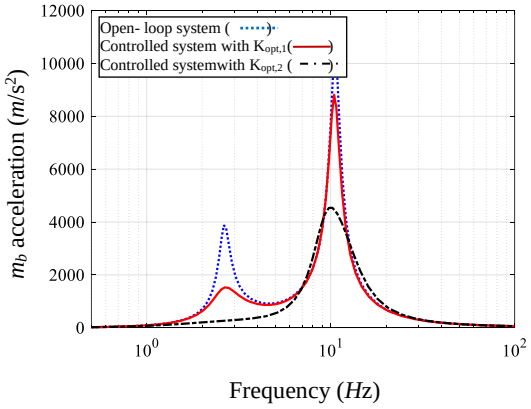

Figure 5. Frequency response of lower body acceleration

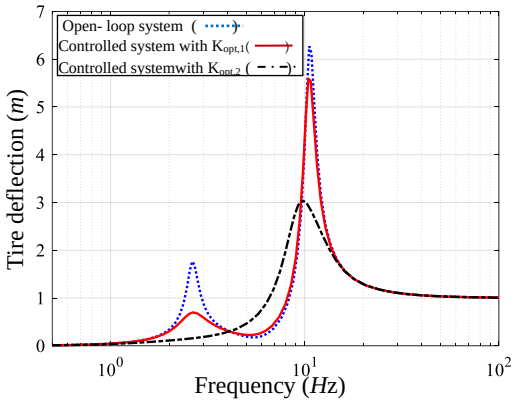

Figure 6. Frequency response of tire deflection

10.5 *Hz*, the active controller provides a significant vibration reduction. Comparing the controlled and uncontrolled system shows that the maximum amplitudes are attenuated 11 and 52% around the resonance (10.5 *Hz*). The maximum values of frequency responses for open loop and closed loop system are also listed in Table 2. The simulation results presented in Figures 4-6 and also Table 2 indicate that active suspension performance can be substantially improved by employing the proposed control strategy.

Furthermore, the optimal control gains are obtained for five values of the controller gain limitation. For obtained optimal control gains, the frequency responses of the upper body acceleration and also tire deflection are shown in Figures 7(a) and 7(b). As expected, the control performance can be improved by using the higher control gain. It is clear that the actuator force is limited by its physical capability and also increasing the controller gain more than a limit does not produce significant difference in optimal solution (see controlled system with $\|K\|_\infty \leq$ *5000* and $\|K\|_\infty \leq$ *10000*). As a result, increasing the controller gain limitation, only to a given limit, is reasonable and of engineering justification.

Also, the simulations for controlled system with control gain $K_{opt,2}$ are performed in the time domain under random road excitation displacement. The road excitation displacement is shown in Figure 8. The simulation results for upper body acceleration, lower body acceleration and tire deflection are illustrated in Figures 9-11, respectively. It is seen from these figures that the proposed control system significantly reduces the vibration amplitude compared with the uncontrolled suspension system. The Root Mean Square (RMS) values of the time domain responses under the random road disturbance are also listed in Table 3. The decrease in the RMS values of the responses for active suspension is observed. Obviously, the proposed control system is effective and can provide much better performance compared to uncontrolled system.

TABLE 2. The maximum values of the frequency responses for controlled and uncontrolled system

	Uncontrolled system	Controlled system with $K_{opt,1}$	Improvement %	Controlled system with $K_{opt,1}$	Improvement %
Upper body acceleration (m/s^2)	6.38e3	5.44e3	15	3.07e3	52
Lower body acceleration (m/s^2)	1.04e4	8.7e3	16	4.53e3	56
Tire deflection (m)	6.26	5.57	11	3.01	52

.

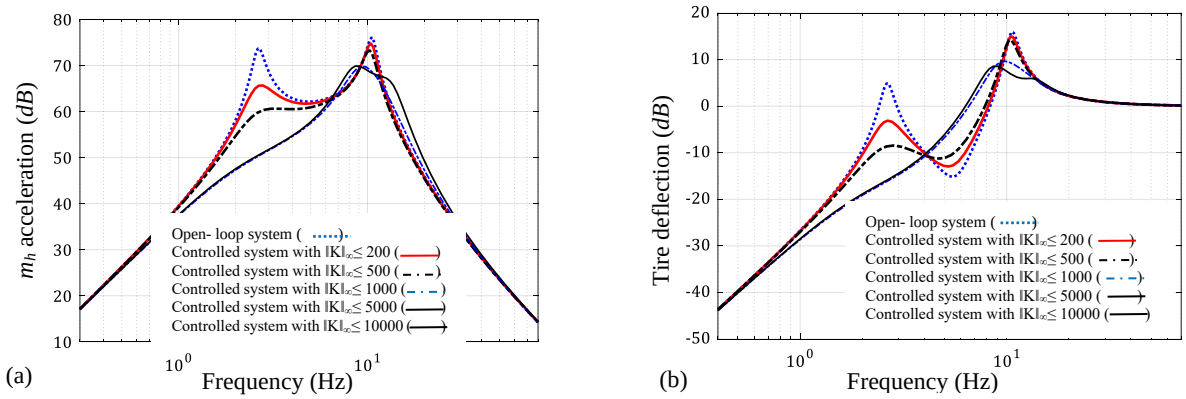

Figure 7. Frequency responses for different controller gain limitations. (a): upper body acceleration, and (b): tire deflection

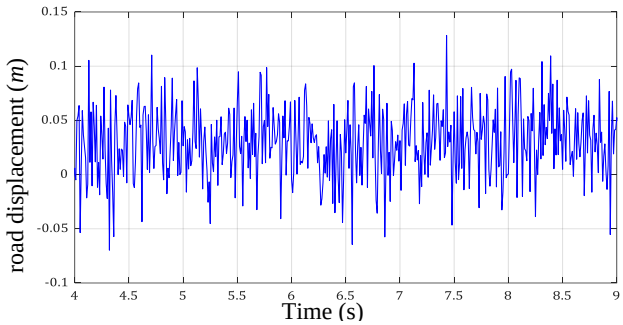

Figure 8. Road excitation displacement

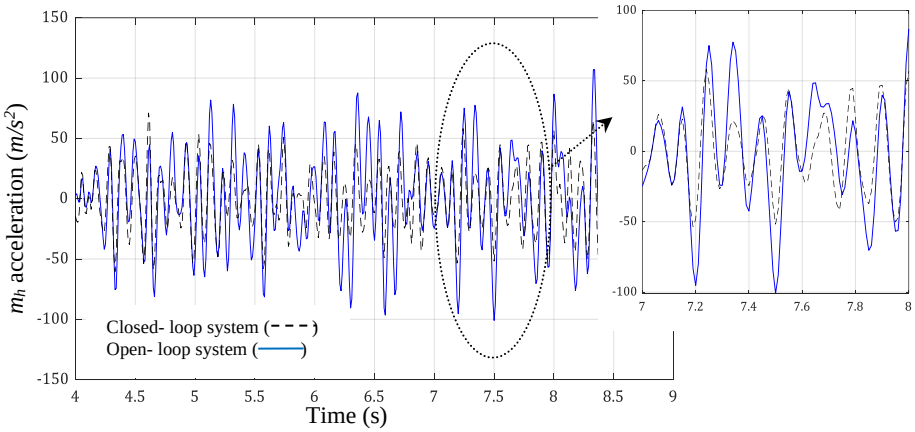

Figure 9. Time response of upper body acceleration under road excitation displacement

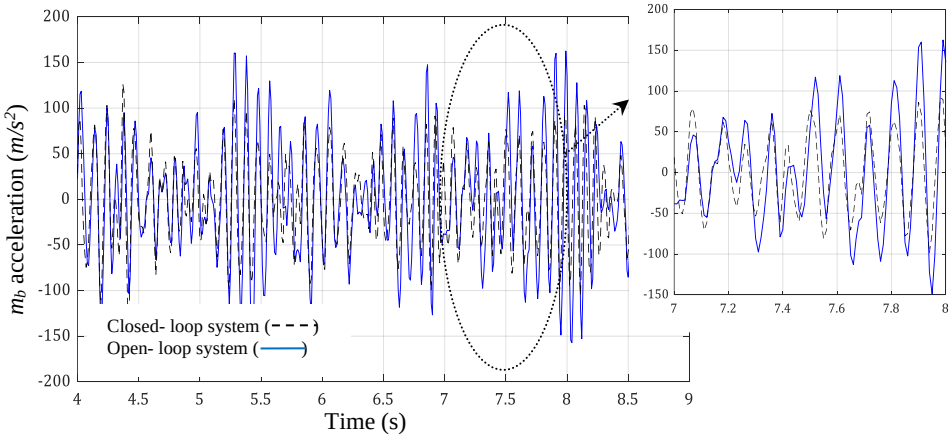

Figure 10. Time response of lower body acceleration under road excitation displacement

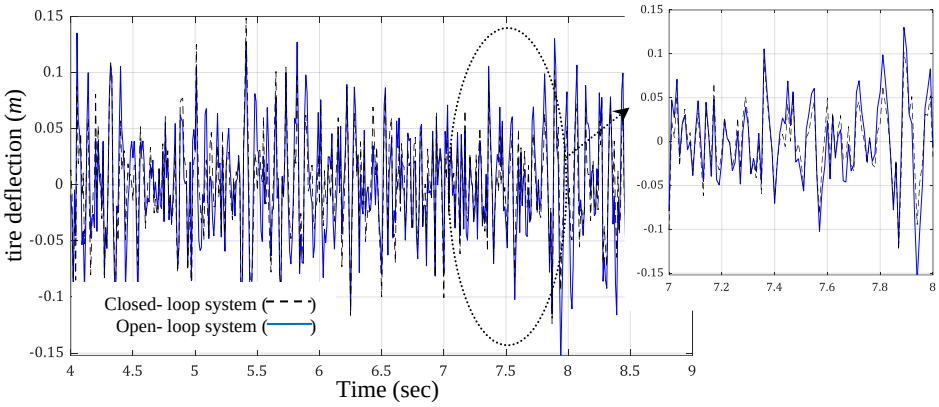

Figure 11. Time response of tire deflection under road excitation displacement

TABLE 3. RMS values of the wheelchair suspension response under road excitation displacement

	Uncontrolled System	Controlled System	Improvement %
Upper Body Acceleration	39.41	26.58	32
Lower Body Acceleration	57.22	41.86	27
Tire Deflection	0.047	0.042	11

4. CONCLUSION

In this paper, vibration control of an electric wheelchair suspension system has been evaluated. A 1-DOF model of human body has been employed in the design of active wheelchair suspension. A model of the wheelchair suspension, including the biodynamic model of seated human body presented. The static output feedback controller based on H-infinity control criterion was designed to control and improve the wheelchair performance. It has been demonstrated that the control system proposed in this study has significantly suppressed the vibration amplitude and improved the suspension performances. Results of this study could potentially help in the electric wheelchairs design and assist with improving ride quality and wheelchairs user health.

5. REFERENCES

1. Toloei, A., Zarchi, M., Attaran, B., "Numerical Survey of Vibrational Model for Third Aircraft based on HR Suspension System Actuator Using Two Bee Algorithm Objective Functions", ***International Journal of Engineering, Transactions C: Aspects***, Vol. 30, No. 6, (2017), 887-894. doi: 10.5829/ije.2017.30.06c.09
2. Rajamani, R., Larparisudthi, S., "On invariant points and their influence on active vibration isolation", ***Mechatronics***, Vol. 14, (2004), 175-198. doi: 10.1016/S0957-4158(03)00029-1.
3. Miaomiao, D., Dingxuan, Z., Yang, B., Lili, W., "Terminal sliding mode control for full vehicle active suspension systems", ***Journal of Mechanical Science and Technology,*** Vol. 32, No. 6, (2018), 2851-2866. doi: 10.1007/s12206-018-0541-x.
4. Gohrle, C., Schindler, A., Wagner, A., Sawodny, O., "Design and vehicle implementation of preview active suspension controllers", **IEEE *Transactions on Control Systems Technology***, Vol. 22, No. 3, (2014), 1135-1142. doi: 10.1109/TCST.2013.2272342
5. Pang, H., Chen, Y., Chen, J., Liu, X., "Design of LQG controller for active suspension without considering road input signals", ***Shock and Vibration***, Vol. 2017, (2017), doi: 10.1155/2017/6573567
6. Du, H., Lam, J., Sze, K.Y., "Non-fragile output feedback H∞ vehicle suspension control using genetic algorithm", ***Engineering Applications of Artificial Intelligence***, Vol. 16, (2003), 667–680. doi: 10.1016/j.engappai.2003.09.008
7. Alfadhli, A., Darling, J., Hillis, A.J., "The control of an active seat with vehicle suspension preview information", ***Journal of Vibration and Control***, Vol. 24, No. 8, (2017), 1412-1426. doi: 10.1177/1077546317698285
8. Moghadam-Fard, H., Samadi, F., "Active Suspension System Control Using Adaptive Neuro Fuzzy (ANFIS), Controller", ***International Journal of Engineering, Transactions C: Aspects***, Vol. 28, No. 3, (2015), 396-401 doi: 10.5829/idosi.ije.2015.28.03c.08
9. Moaaz, Ahmad O., Ghazaly, Nouby M., "Fuzzy and PID Controlled Active Suspension System and Passive Suspension System Comparison", ***International Journal of Advanced Science and Technology***, Vol. 28, No. 16, (2019), 1721-1729.
10. Ghazaly, N., Sharkawy, A. Ali, A. & Abdel-Jaber, G., "H∞ Control of Active Suspension System for a Quarter Car Model", ***International Journal of Vehicle Structures and Systems***, Vol. 8. (2016), 35-40. doi: 10.4273/ijvss.8.1.07
11. Bovenzi, M., Hulshof, C.T., "An updated review of epidemiologic studies on the relationship between exposure to whole-body vibration and low back pain (1986-1997)**",** ***International Archives of Occupational and Environmental Health***, Vol. 72, No. 6, (1999), 351-365. https://doi.org/10.1007/s004200050387
12. Tiemessen, I.J., Hulshof, C.T.J., Frings-Dresen, M.H.W., "An overview of strategies to reduce whole-body vibration exposure on drivers: a systematic review", ***International Journal of***

Industrial Ergonomics, Vol. 37, No. 3, (2007), 245-256. https://doi.org/10.1016/j.ergon.2006.10.021

13. Hill, T.E., Desmoulin, G.T., Hunter, C.J., "Is vibration truly an injurious stimulus in the human spine?" ***Journal of Biomechanics***., Vol.42, No. 16 (2009), 2631-2635. https://doi.org/10.1016/j.jbiomech.2009.10.001
14. Salvendy, G., "Handbook of Human Factors and Ergonomics", 2nd Edition, John Wiley & Sons, Inc., New York, (2005).
15. Zhou, Z., Griffin, M.J., "Response of the seated human body to whole-body vertical vibration: biodynamic responses to mechanical shocks", ***Ergonomics***, Vol. 60, No. 3, (2017), 333-346. doi: 10.1080/00140139.2016.1179793
16. Toward, M.G.R., Griffin, M.J., "The transmission of vertical vibration through seats: Influence of the characteristics of the human body", ***Journal of Sound and Vibration***, Vol. 330, No. 26, (2011), 6526–6543. doi: 10.1016/j.jsv.2011.07.033
17. Kitazaki, S., Griffin, M.J., "A modal analysis of whole-body vertical vibration, using a finite element model of the human body", ***Journal of Sound and Vibration***, Vol. 200, No. 1, (1997), 83-103. doi: 10.1006/jsvi.1996.0674
18. Wei, L., Griffin, M.J., "The Prediction of seat transmissibility from measures of seat impedance", ***Journal of Sound and Vibration***, Vol. 214, No.1, (1998), 121-137. doi: 10.1006/jsvi.1998.1540
19. Tewari, V. K., Prasad, N., "Three-DOF Modelling of Tractor Seat-Operator System", ***Journal of Terramechanics***, Vol. 36, No. 4, (1999), 207-219. doi: 10.1016/S0022-4898(99)00008-7
20. Abbas, W., Abouelatta, O.B., El-Azab, M., Elsaidy, M., Megahed, A.A., "Optimization of Biodynamic Seated Human Models Using Genetic Algorithms", ***Engineering***, Vol. 2, (2010), 710-719. doi: 10.4236/eng.2010.29092
21. Adam, S. A. Abdul Jalil, N.A., "Vertical Suspension Seat Transmissibility and SEAT Values for Seated Person Exposed to Whole-body Vibration in Agricultural Tractor Preliminary Study", ***Procedia Engineering***, Vol. 170, (2017), 435- 442. doi: 10.1016/j.proeng.2017.03.070
22. Baumal, A. E., McPhee, J. J., Calamai, P. H., "Application of Genetic Algorithms to the Design Optimization of an Active Vehicle Suspension System", ***Computer Methods in Applied Mechanics and Engineering***, Vol. 163, No. 1, (1998), 87-94. doi: 10.1016/S0045-7825(98)00004-8
23. Desai, R., Guha, A., Seshu, P., "Multibody Biomechanical Modelling of Human Body Response to Direct and Cross Axis Vibration", ***Procedia Computer Science***, Vol. 133, (2018), 494–501. doi: 10.1016/j.procs.2018.07.062
24. Dong, R., He, L., Du, W., Cao, Z., Huang, Z., "Effect of sitting posture and seat on biodynamic responses of internal human body simulated by finite element modeling of body-seat system", ***Journal of Sound and Vibration***, Vol. 438, (2019), 543-554. doi: 10.1016/j.jsv.2018.09.012
25. Ding, D., Cooper, R. A., "Electric powered wheelchairs", ***IEEE Control Systems Magazine***, Vol. 25, No. 2, (April 2005), 22-34. doi: 10.1109/MCS.2005.1411382
26. Garcia-Mendez Y., Pearlman L. J., Boninger L.M., Cooper A.R., "Health risks of vibration exposure to wheelchair users in the community", ***The Journal of Spinal Cord Medicine***, Vol. 36, No.4 (2013), 365-375. doi: 10.1179/2045772313Y.0000000124
27. Cooper R. A., , Wolf E., Fitzgerald Sh.G., , Boninger M. L., Ulerich R., Ammer W.A., "Seat and Footrest Shocks and Vibrations in Manual Wheelchairs With and Without Suspension", Arch Phys Med Rehabil, Vol. 84, (2003), 96-102. doi: 10.1053/apmr.2003.50069
28. Farshidianfar, A., Saghafi, A., Kalami, S.M., Saghafi, I., "Active vibration isolation of machinery and sensitive equipment using H∞ control criterion and particle swarm optimization method", ***Meccanica***, Vol. 47, (2012), 437-453. doi: 10.1007/s11012-011-9451-z
29. Skogestad, S., Postlethwaite, I., "Multivariable feedback control: analysis and design", 2nd ed., Wiley Interscience, New York, (2005).
30. Schutte, J.F., Groenwold, A.A., "A study of global optimization using particle swarms", ***Journal of Global Optimization***, Vol. 31, (2005), 93–108. doi: 10.1007/s10898-003-6454-x
31. Zhan, Z., Zhang, J., Li, Y., Chung, H. S., "Adaptive Particle Swarm Optimization", ***IEEE Transactions on Systems, Man, and Cybernetics, Part B (Cybernetics)***, Vol. 39, No. 6, (2009), 1362-1381. doi: 10.1109/TSMCB.2009.2015956

Persian Abstract

چکیده

ویلچر برقی از جمله تجهیزات پرکاربردی است که توسط معلولین و افراد ناتوان مورد استفاده قرار می گیرد. قرار گرفتن مداوم بدن انسان در معرض لرزش همواره به عنوان یک عامل آزار دهنده مطرح می شود که تاثیراتی منفی بر راحتی و سلامت انسان دارد. کاهش ارتعاش منتقل شده به بدن انسان نقشی تعیین کننده و مهم در طراحی ویلچر داشته و به یک تقاضای مهم در حوزه مراقبت های بهداشتی تبدیل شده است. در این پژوهش، به منظور بهبود عملکرد ویلچرهای برقی، کنترل ارتعاش در سیستم تعلیق ویلچر و با درنظر گرفتن مدل بیودینامیکی بدن انسان ارائه شده است. برای دستیابی به عملکرد بهینه در سیستم تعلیق ویلچر، کنترل فعالی بر اساس معیار کنترل H∞ طراحی و مورد ارزیابی قرارگرفته‌است. نتایج شبیه سازی نشان می دهد که سیستم کنترلی پیشنهادی به طور موثر سبب کاهش پاسخ ارتعاشی بدن و درنتیجه بهبود عملکرد سیستم تعلیق می شود. بکارگیری این سیستم کنترلی در طراحی سیستم تعلیق ویلچرهای برقی به منظور بهبود راحتی سواری پیشهاد می شود.

IJE TRANSACTIONS B: Applications Vol. 33, No. 8, (August 2020) 1637-1642

International Journal of Engineering

Journal Homepage: www.ije.ir

Effect of Wire Pitch on Capacity of Single Staggered Wire and Tube Heat Exchanger Using Computational Fluid Dynamic Simulation

F. R. Akbar, I. M. Arsana*

Department of Mechanical Engineering, Universitas Negeri Surabaya, East Java, Indonesia

P A P E R I N F O

Paper history:
Received 12 January 2020
Received in revised form 25 March 2020
Accepted 11 June 2020

Keywords:
Single Staggered Wire and Tube Heat Exchanger
Heat Transfer
Natural Convection
Computational Fluid Dynamic

A B S T R A C T

Single staggered is a design development of normal wire and tube heat exchanger that wires are welded with staggered configuration on two sides. Capacity of wire and tube heat exchanger is the ability of the heat exchanger to release heat. The objective of this study is to analyse the effect of wire pitch (p_w) on capacity of single staggered wire and tube heat exchanger. The research method uses Computational Fluid Dynamic (CFD) simulation by ANSYS Fluent to analyse heat transfer of wire and tube; also to analyse airflow at surface the wire and tube. The simulation is experimentally validated by measuring temperatures at some points of wire and tube. Based on results, temperature contours increasing capacity of heat exchanger depend on smaller wire pitch that the highest value is 72.02 W at p_w 7 mm. The reason is smaller wire pitch increases area of convection heat transfer surface. Whereas, airflow patterns show air move slowly at the wire and tube surface and flow with free convection. This study contributes new design of wire and tube heat exchanger with CFD and it can be applied to improve the performance of this heat exchanger in refrigeration system and other applications.

doi: *10.5829/ije.2020.33.08b.22*

NOMENCLATURE

cp	Specific heat (J/kgK)	T_s	Surface temperature (K)
d_t	Tube diameter (m)	T_∞	Ambient air temperature (K)
d_w	Wire diameter (m)	**Greek Symbols**	
g	Gravity (m/s^2)	β	Expansion coefficient of air (1/K)
H	Wire and tube height (m)	ε	Thermal emissivity
h_c	Coefficient convection (W/m^{2}K)	μ	Dynamic viscosity (Ns/m^2)
h_o	Coefficient overall (W/m^{2}K)	ρ	Density (kg/m^3)
h_r	Coefficient radiation (W/m^{2}K)	Φ	Wire and tube specific ratio
k	Thermal conductivity of air (W/mK)	σ	Stefan-boltzmann constant 5.67 x 10-8 W/m^{2}K^4
$\dot{m}$	Massflow rate (kg/s)	**Subscripts**	
Nu	Nusselt number	c	Convection
p_t	Tube pitch (m)	in	Inlet tube
p_w	Wire pitch (mm)	o	Overall
q	Heat rate (W)	out	Outlet tube
Ra	Rayleigh number	r	Radiation
S_t	Tube specific ratio	s	Surface of wire and tube
S_w	Wire specific ratio	t	Tube
T_{in}	Inlet temperature (K)	w	Wire
T_{out}	Outlet temperature (K)	∞	Ambient air

*Corresponding Author Institutional Email: *madearsana@unesa.ac.id* (I. M. Arsana)

Please cite this article as: F. R. Akbar, I. M. Arsana, Effect of Wire Pitch on Capacity of Single Staggered Wire and Tube Heat Exchanger Using Computational Fluid Dynamic Simulation, International Journal of Engineering (IJE), IJE TRANSACTIONS B: Applications Vol. 33, No. 8, (August 2020) 1637-1642

1. INTRODUCTION

Wire and tube heat exchanger is commonly used as component of refrigeration system in industry or life. Wire and tube consists of a concentric tube with wires welded on two sides of the tube. Wires as a fin in this wire and tube were welded in the inline arrangement and facing each others. Wires are used to increase total area of convention heat transfer. The more area contact in a heat exchanger will increase value of heat transfer [1]. This is applied by Topcuoglu [2] that used coiled tube for increasing heat transfer. Zhang et al. [3] studied condenser in gas engine-driven heat pump for heating and cooling application.

Many development designs are investigated to improve performance wire and tube heat exchanger with inline arrangement wire. For examples, reasearch was to develop wire and tube model with mathematical approach using finite element methods [4-6].

Research by Arsana et al. [7] showed a new design of wire and tube with single staggered arrangement of wires has better heat transfer rate. This research used three variations of wire pitch (7 mm, 14 mm, and 21 mm) and developed numerical modelling to optimize design. It still needs further investigation, especially to concern effect of small wire pitch on heat transfer. At the small wire pitch, the capacity will be optimal but it is still more investigation to find out optimal design precisely.

Nowadays, researches often use CFD simulation to investigate in heat transfer. Such as Arsana et al. [8] investigated natural convection heat transfer from single staggered wire and tube comparing with normal direction. Gonul et al. [9] investigated air side force convection on several variation of wire and tube. Sengupta et al. [10] investigated combustion gases of stove system for cooking. Teja et al. [11] analysed surface temperature on water harvesting.

Based on thoughts above, single staggered arrangement of wires still needs further investigation about the effect of wire pitch on heat transfer of this heat exchanger in free convection conditions. So, present study investigates effect of wire pitch with three variations (7 mm, 9 mm, and 11 mm) on capacity of single staggered design.

2. MATERIALS AND METHODS

2. 1. Materials Steel is used as material of wire and tube and oil thermo-32 is used as hot working fluid which flows inside tube. This study used three inlet variations to figure out the effect of wire pitch at low to high temperature [8]. Beside this, detailed objects as shown in Table 1.

TABLE 1. Detailed specification of some single staggered wire and tubes

Property	Value or Information
Wire and tube material	Steel
Heat exchanger height	0.445 m
Heat exchanger width	0.431 m
Tube out diameter	0.0048 m
Tube in diameter	0.0032 m
Property	**Value or Information**
Wire diameter	0.0012 m
Wire pitch	7, 9, 11 mm
Total concentric tube	12
Number of wires in p_w 7 mm	62
Number of wires in p_w 9 mm	48
Number of wires in p_w 11 mm	40
Tube pitch	0.4 m
Fluid	Thermo oil-32
Mass flow rate	0.0012 kg/s
Inlet temperature	313 K, 333 K, and 353 K
Specific heat (Cp)	2000 J/kg K
Density (ρ)	856 kg/m^3

2. 2. Simulation Setup This research was conducted by developing models using CFD simulations by ANSYS Fluent with experimental validation. first step, a simulation model at p_w 7 mm was validated by using experiment. Then, the data is used as a reference for other simulations.

There were three steps to simulate model was pre-processing, processing, and post-processing [12]. In the initial stage of conducting CFD simulation was created 3D geometry model. There were two types of geometry models. Wire and tube geometry models were used for flow simulation inside tubes and air geometry models were used for airflow simulation at wire and tube surface. The mesh method chosen for the wire and tube models were unstructured mesh with hexahedral mesh [13]. While the mesh method chosen for the wire and tube air models were unstructured mesh with tetrahedral mesh [13].

After meshing, next step determines physical-mathematical modeling, material, operating conditions, boundary conditions, and completion techniques. First, determining general conditions, where conditions generally used pressure-based by including the influence of gravity in solving and steady-state conditions [11]. Second, choosing the physical equations used for this simulation were the energy equation, and the viscous model k-epsilon for wire and

tube geometry models [14] and k-omega STT for air at surface wire and tube geometry models [15].

2. 3. Experimental and Validation Method Simulations were validated by the experiment. Data validation used only at wire and tube p_w 7 mm and inlet temperature at 313 K. Validation was conducted by measuring inlet, outlet and nine temperatures of the wire and tube [7-8]. The data of p_w 7 mm was compared to simulations result with maximum error limit of ± 5% [7-8]. Furthermore, when the data had been valid, the data applied as reference to simulated at pw 9 mm and pw 11 mm; installation experiment are shown in Figure 1

2. 4. Data Analysis Capacity of a heat exchanger [5] can be related as follows:

$$q = \dot{m}\, c_p\, (T_{in} - T_{out}) \quad (1)$$

Wire and tube heat exchanger naturally releases heat to ambient air. According to Bansal and Chin [5] free convection is overall convection coefficient consisting radiation and convection coefficients. The equations are shown below:

$$h_o = h_c + h_r \quad (2)$$

$$h_r = \varepsilon.\sigma.(T_s^4 - T_\infty^4)/(T_s - T_\infty) \quad (3)$$

$$Nusselt\ Number\ (Nu) = \frac{h_c \cdot H}{k} \quad (4)$$

Empirical equation for Nusselt Number [5] is shown below:

$$Nu = 0.66\,(\frac{Ra \cdot H}{dt})^{0.25}\,\{1 - [1 - 0.45\,(\frac{Ra \cdot H}{H})^{0.25}]\,Exp(-\frac{Sw}{\varphi}) \quad (5)$$

$$R_a = (\frac{\beta \rho^2 cp}{\mu k}).\ g\,(T_s - T_\infty).H^3 \quad (6)$$

$$\phi = (\frac{2s_t 2}{H})^{0.4} . S_w^{0.9} . S_t^{-1} + (\frac{2s_t 2}{H})^{0.8} .[\frac{264}{Ts - T\infty}]^{0.5}.S_w^{-1.5}. S_t^{-0.5} \quad (7)$$

$$S_w = (p_w - d_w)/d_w,\ dan\ S_t = (p_t - d_t)/d_t \quad (8)$$

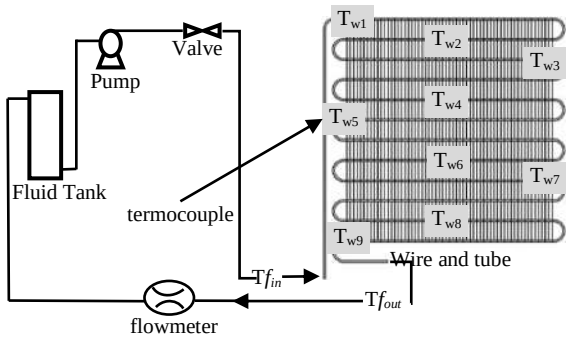

Figure 1. Experiment set up for validation

Basedon above equations, capacity of wire and tube can be found by determining heat transfer inside wire and tube (1) and overall convection coefficient in outside wire and tube heat exchanger (2).

3. RESULT AND DISCUSSION

3. 1. Grid Independence In simulation process, grid independence used for simulation models is the smallest error [5]. There are three meshes to figure it out at pw 7 mm. The results are shown in Figures 2 and 3.

Based on Figures 2 and 3, the chosen wire and tube mesh is mesh 3 because the mesh 3 produces an average error of 1.32% which is smaller than the others. Meanwhile, the smallest average error of air model at wire and tube is mesh 1 with 3.97%.

3. 2. Simulation Result Figure 4(a) (b) and (c) show almost the same outlet temperature around 305 K which means three wire and tubes have almost the same heat transfer. However, p_w 7 has better heat transfer because it reaches 305 K faster than the others. It is indicated by reaching 305 K at third row than p_w 9 and p_w 11 reached at fourth and fifth rows. Wire and tube at 313 K inlet just obtains little heat transfer because of small temperature difference between inlet and ambient air [8].

Figure 4(d) (e) and (f) show wire and tubes at 333 K inlet work more optimal than inlet at 313 K. That can be

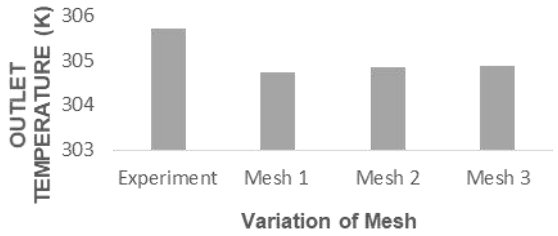

Figure 2. Grid independence of wire and tube heat exchanger models.

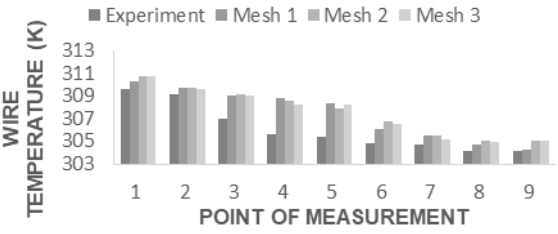

Figure 3. Grid independence of air models at surface wire and tube heat exchanger.

seen from the change in inlet to outlet. P_w 7 mm has the highest heat transfer with temperature difference from 333 K to 307 K. Whereas, p_w 9 mm reaches temperature difference from 333 K to 309 K and p_w 11 mm reaches from 333 K to 311 K.

Figure 4(g) (h) and (i) have highest capacity of heat transfer because they produce significant temperature difference from inlet to outlet is from 353 K to 323 K. These data show the higher inlet temperature will increase heat transfer of wire and tube. The highest temperature difference in order is p_w 7 with 353 K to 323 K, p_w 9 mm with 353 K to 326 K and p_w 11 mm with 353 K to 328 K. These results indicate the smaller wire pitch will increase heat transfer because it has more contact area of heat transfer [5]. These results are supported by Arsana's research [7-8] showed temperature of wire and tube at p_w 7 with 333 K has difference temperature around 26 K from inlet to outlet. However, this simulation is more complete than reported data.

Figure 5 shows the air velocity distribution viewed from the side of wire and tube is very small. That is because the heat transfer of wire and tube occurs from the surface object to ambient air without any external force. The airflow of wire and tube moves due to the temperature difference in each tube row from top part to the bottom part. That causes the air is spread.

The highest velocity occurs at p_w 11 mm as the largest wire pitch has small resistance [8]. Besides, highest velocity occurs at middle tube because there was smallest resistance to flow freely. According to previous research [6] [7] and [10] this is because of the air move following the change in heat of each row on the wire and tube. Air is exposed to heat and expands then from that expansion the air became lighter and raised to the top.

Figure 6 shows correlation between each wire and tube and heat transfer rate. The largest heat transfer is 72.07 W at pw 7 mm with 353 K inlet, and the smallest heat transfer rate is 16.06 W at pw 11 mm with 313 K inlet. It shows smaller wire pitch increasing heat transfer due to more heat transfer area. Figure 6 also shows at the 313 K inlet, heat transfer at the three wire and tubes are not much different. That concludes

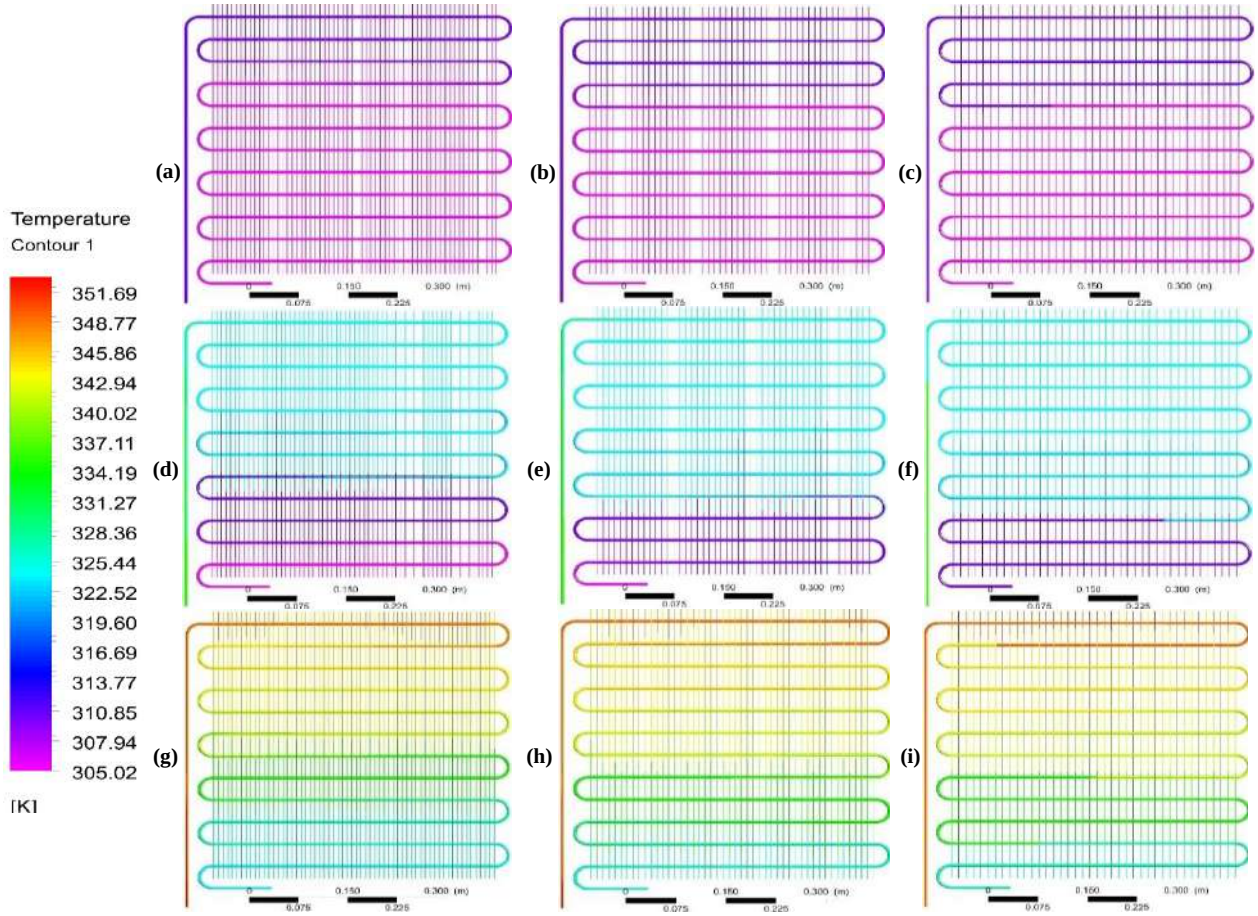

Figure 4. Temperature contours of: **(a)** p_w 7 mm at 313 K inlet. **(b)** p_w 9 mm at 313 K inlet. **(c)** p_w 11 mm at 313 K inlet. **(d)** p_w 7 mm at 333 K inlet. **(e)** p_w 9 mm at 333 K inlet. **(f)** p_w 11 mm at 333 K inlet. **(g)** p_w 7 mm at 353 K inlet. **(h)** p_w 9 mm at 353 K inlet. **(i)** p_w 11 mm at 353 K inlet

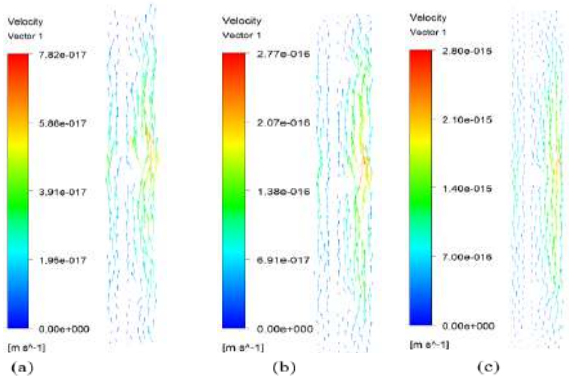

Figure 5. Air current speed vector at wire and tube heat exchangers of inlet 313 K. **(a)** p_w 7 mm. **(b)** p_w 9 mm. **(c)** p_w 11 mm

the low inlet temperature does not require a lot of wires.

This is in line with Arsana's research [7] stated that increasing the number of wires would increase the rate of heat transfer by using inline wire and tube at p_w 7, 14, and 21 mm with 333 K inlet which results in the best rate at p_w 7 mm.

Figure 7 shows the largest coefficient at p_w 7 mm with 353 K inlet is 13.27 W/m^{2}K. While the smallest value at p_w 11 mm with 313 K inlet is 8.68 W/m^{2}K. Figure 9 shows convection coefficient increasing because of smaller wire pitch and the larger inlet temperature. Meanwhile, the radiation coefficient will produce almost the same value because the average temperature of all wire and tubes is not too large so that it emits little radiation. These results are supported by previous studies such as Bansal and Chin [5], Arsana et al. [7] which obtained the best capacity value was proportional to the area of heat transfer.

Correlation between heat transfer and overall convection coefficient is interconnected with each other. Heat transfer rate is proportional with overall heat transfer coefficient because high heat transfer rate increases air thermal conductivity. This is in line with

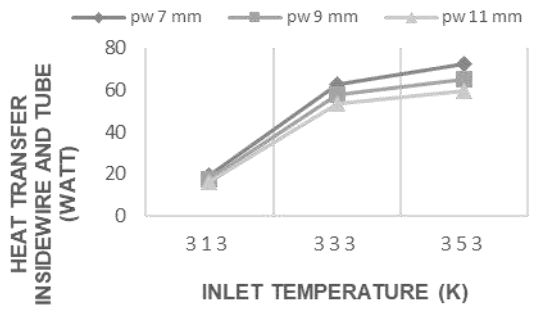

Figure 6. Heat transfer at each inlet temperature and each wire pitch

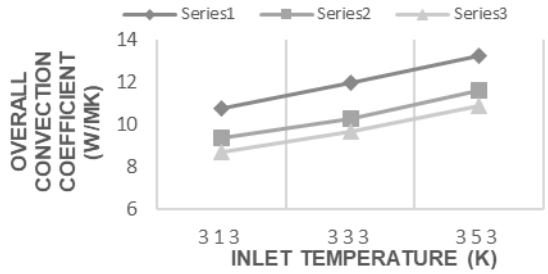

Figure 7. Air convection coefficient at each wire and tube.

previous study by Barzegar and Fallahiyekta [16] stated that increasing heat transfer depends on increasing fluid thermal conductivity and decreases boundary layer thickness.

4. CONCLUSION

Based on the research that the smaller wire pitch makes greater heat exchanger capacity at each inlet temperature. But, Wire and tube with small wire pitch does not work optimally at low temperature because the small wire pitch causes the heat transfer working only on top part instead bottom part of wire and tube heat exchanger.

Air simulation shows current convection flowing from the bottom to the top at wire and tube surface it is because the air became lighter when it is exposed by heat from inside tube. The simulation result can help understand heat transfer phenomenon to occur outside surface of single staggered wire and tube heat exchanger. These results can be used as a reference for using optimal wire and tube heat exchanger. If it is used at low temperature, it is recommenced to use wire and tube with large wire pitch

5. REFERENCES

1. Omer, A., "Heat Exchanger Technology and Applications in Heat Exchanger Engineering", ***Advances in Nanoscience and Nanotechnology,*** Vol. 3. (2019), 1-3. Doi: 10.33140/ann.03.01.01
2. Topcuoglu, K., "Trombe Wall Application with Heat Storage Tank", ***Civil Engineering Journal,*** Vol. 5, No. 7, (2019), 1477-1489. Doi: 10.28991/cej-2019-03091346
3. Zhang, W., Yang, X., Wang, T., Peng, X., Wang, X., "Experimental Study of a Gas Engine-diven Heat Pump System for Space Heating and Cooling", ***Civil Engineering Journal,*** Vol. 5, No. 10, (2019), 2282-2295. Doi: 10.28991/cej-2019-03091411
4. Kumra, A., Rawal, N., Samui, P., "Prediction of Heat Transfer Rate of a Wire-on-Tube Type Heat Exchanger: An Artificial Intelligence Approach", ***Procedia Engineering,*** No. 64, (2013), 74-83. Doi: 10.1016/j.proeng.2013.09.078

5. Bansal, P.K., and Chin, T.C., "Modelling and Optimisation of Wire and Tube Condenser", ***International Journal of Refrigeration,*** No. 26, (2003), 601-603. Doi: 10.1016/s0140-7007(02)00044-0
6. Ahmed A. M. Saleh, "Correlation of Overall Heat Transfer Coefficient in Three Zones of Wire and Tube Condenser", ***Journal of Mechanical Engineering Research and Deveopment (JMERD),*** Vol. 42 No. 1, (2019), 96-103. Doi: 10.26480/jmerd.01.2019.96.103
7. Arsana, I. M., Budhikardjono, K., Susianto., Altway, A., "Optimization of The Single Staggered Wire and Tube Heat Exchanger", ***MATEC Web of Conference,*** No. 58, (2016). Doi: 10.1051/matecconf/20165801017
8. Arsana, I Made., Budhikardjono, Kusno., Susianto., and Altway, Ali., "Modelling of The Single Staggered Wire and Tube Heat Exchanger", ***International Journal of Applied Engineering Research***, Vol. 11, No. 8, (2016), 5591-5599.
9. Gonul, A., Agra, O., Atayilmaz, O., Demir, H., Sevendir, Kemal, M., Teke, "Experimental and Numerical Investigation of Air Side Forced Convection on Wire-on-Tube Condensers", ***International Journal of Thermal Science,*** Vol. 151, (2020), 106241. Doi: 10.1016/j.ijthermalsci.2019.106241
10. Sengupta, A. R., Gupta, R., Biswas, A., "Computational Fluid Dynamic Analysis of Stove Systems for Cooking and Drying of Muga Silk", ***Emerging Science Journal,*** Vol. 3, No. 5 (2019), 285-292. Doi: 10.28991/esj-2019-01191
11. Teja, S.T.G. Krishna., Karthikeyan, C. P., and Kumar, M. B. Shyam., "Investigation of Radiative Cooling Using a Photonic Composite Material for Water Harvesting", ***International Journal of Engineering, Transaction A: Basic,*** Vol. 30, No. 10, (2017), 1573-1582. Doi: 10.5829/ije.2017.30.10a.19
12. Davarnejad, R., Barati, S., Zakeri, M., "Simulation of Comvective Heat Transfer of a Nanofluid in a Circular Cross-section", ***International Journal of Engineering, Transaction C: Aspects***, Vol. 26, No. 6, (2013), 571-576. Doi: 10.5829/idosi.ije.2013.26.06c.02
13. Djodikusumo, I., Diasta, I.N., Awaluddin, I.S., "Geometric Modelling of a Propeller Turbine Runner Using ANSYS BladeGen Meshing Using ANSYS TurboGrid and Fluid Dynamic Simulation Using ANSYS Fluent", ***Trans Tech Publications, Ltd.,*** Vol. 842, (2016), 164-177. Doi: 0.4028/www.scientific.net/amm.842.164
14. Patel, S.D., Parmar, R.R., Prajapati, V.M., "CFD Analysis of Shell and Tube Heat Exchanger", ***International Research Journal of Engineering and Technology (IRJET),*** Vol. 2, (2015), 2231-2235. Doi: 10.23883/ijrter.2017.3386.jcalx
15. Vazifeshenas, Y., Delavar, M.A., "Investigation of Thermo-hydraulic Performance of Circular Tube Fitted with Center-cleared Twisted Tape Using CFD Modeling", ***International Journal of Engineering, Transaction C: Aspects,*** Vol. 28, No. 3, (2015), 476-482. Doi: 10.5829/idosi.ije.2015.28.03c.19
16. Barzegar, M.H., Fallahiyekta, M., "Increasing Thermal Efficiency of Double Tube Heat Exchangers by Using Nano Hybrid", ***Emerging Journal Science,*** Vol. 2, No. 1, (2018), 11-19. Doi: 10.28991/esj-2018-01122

Persian Abstract

چکیده

توسعه طراحی مبدل حرارتی تیغه دار معمولی و لوله ای است که انحناع از دو طرف با پیکربندی مبهم جوش داده می شوند. ظرفیت مبدل حرارتی تیغه دار و لوله ، توانایی مبدل حرارتی در انتشار گرما را دارند. هدف از این مطالعه ، بررسی تأثیر ضخامت موانع تیغه دار بر ظرفیت حرارتی یک مبدل حرارتی لوله منفرد است. روش تحقیق از شبیه سازی دینامیکی سیالات محاسباتی (CFD)بکمک نرم افزار ANSYS Fluent برای تجزیه و تحلیل انتقال حرارت مبدل تیغه دار و لوله استفاده می کند. همچنین برای تحلیل جریان هوا در سطح تیغه و لوله. این شبیه سازی به صورت آزمایشی با اندازه گیری دما در برخی از نقاط تیغه و لوله تأیید می شود. بر اساس نتایج ، کانتورهای دما که ظرفیت مبدل حرارتی را افزایش می دهد ، به تیغه کوچکتر بستگی دارد که بیشترین مقدار آن ۷۲.۰۲ W در 7 pw میلی متر است. دلیل این است که خمش تیغه کوچکتر باعث افزایش سطح انتقال حرارت همسو می گردد. در حالی که ، الگوهای جریان هوا نشان می دهد هوا به آرامی در سطح تیغه و لوله حرکت می کند و با انتقال حرارت بطور آزاد جریان می یابد. این مطالعه به طراحی جدید مبدل حرارتی تیغه و لوله با استفاده از CFD کمک می کند و می تواند برای بهبود عملکرد این نوع مبدل حرارتی در سیستم تبرید و سایر کاربردها کاربرد داشته باشد.

International Journal of Engineering

Journal Homepage: www.ije.ir

A Semi-empirical Model to Predict the Attached Axisymmetric Shock Shape

A. R. Davari*

Aerospace Division, Department of Engineering, Science and Research Branch, Islamic Azad University, Tehran, Iran

P A P E R I N F O

Paper history:
Received 21 April 2020
Received in revised form 22 May 2020
Accepted 12 June 2020

Keywords:
Semi Vertex
Mach Wave
Shock Shape
Conical Flow

A B S T R A C T

In this work, a simple semi-empirical model is proposed, based on Response Surface Model, RSM, to determine the shape of an attached oblique shock wave emanating from a pointed axisymmetric nose at zero angle of attack. Extensive supersonic visualization images have been compiled from various nose shapes at different Mach numbers, along with some others performed by the author for the present paper. The method is based on the relationship between the body shape and the shock shape. The body shape and the free stream Mach number determine the shape of the oblique shock standing ahead. From the statistical data bank containing the visualization tests and employing the RSM, an analytic relationship has been established between the body and the shock shape. From this relationship, knowing the body shape and the Mach number, one can simply determine the shock shape. The visualization tests performed by the author for some other cases have approved the accuracy of the proposed relationship. However, the approach is restricted to attached shocks emanating from sharp noses at zero angle of attack. Despite the limitations, this relationship can effectively be used in model scale determination for wind tunnel tests to prevent shock reflection from the walls that could lead to erroneous results.

***doi**: 10.5829/ije.2020.33.08b.23*

NOMENCLATURE

M	Free stream Mach number	**Greek Symbols**	
x	Longitudinal distance along the axis of symmetry from the apex	δ	The nose semi vertex angle
y_b	The local ordinates of the nose contour	μ	Mach wave angle
y_s	The local ordinates of the shock	**Subscripts**	
l	The nose length	s	Shock
d	The nose diameter at the base	b	Body/Nose

1. INTRODUCTION

In a supersonic flight, the shock wave emanating from the nose or other components of the aircraft, may impinge somewhere on another solid surface or intersect other waves. Such intersections and interactions are important in the practical design and analysis of the vehicle. This is also the case when a model is to be placed in the wind tunnel test section to avoid any shock intersection with the wall and reflection from it [1-3].

The shape of the attached shock has long been recognized as a subject of remarkable importance, particularly in the solution of interference problems. One of the primary assumptions to estimate the shock shape of an arbitrary nose shape was to consider it as a straight cone of the same vertex angle as the nose, which is greatly restricted in application. An accurate evaluation of interference requires a careful representation of the curved shock [4].

Some methods have already been proposed to predict the attached shock shape. Among them, the approach based on linear theory, introduced by Whitham [5] has perhaps met with as much success and received as much attention as any others. However, the range of applicability of this method is severely restricted. This method does not give accurate quantitative results when

*Corresponding Author Institutional Email: *ardavari@srbiau.ac.ir*
(A. R. Davari)

Please cite this article as: A. R. Davari , A Semi-empirical Model to Predict the Attached Axisymmetric Shock Shape, International Journal of Engineering (IJE), IJE TRANSACTIONS B: Applications Vol. 33, No. 8, (August 2020) 1643-1651

the semi-nose angle is larger than 20° and beyond the Mach number of about 3.0.

Love et al [6] proposed a different approach to obtain the axisymmetric shock shape emanating from a pointed nose. Based on the known shock slope at the apex and that at the end of the nose where the body slope vanishes, he considered an equation for a so-called unspecified shock shape. He suggested that this unspecified shock shape belongs to a circular arc in general. If this arc is put on the given nose contour and adjusted to cover the nose, the unspecified shock and the one correspond to the given nose will be coalesced on each other. This method, despite claims to give good results, is not easy to follow and requires many manual adjustments, which does not grab the interests nowadays.

For calculating shock shape over wide ranges of Mach number and nose shape, the method of characteristics, though being laborious, is still a popular tool. However, in recent years, with the advent of modern processors, the computational methods as well as the experimental surveys are widely used to determine the shock shape and its stand-off distance for the bow and detached shocks [7-10].

Up to now, extensive surveys, mostly numerical, have been performed to study the shock shape, either attached oblique shock or detached one in the form of a bow shock and valuable information have been obtained so far to discover the impact of free stream condition and the body mold line on the shape of the shock wave. However, no attempt has so far been reported in the literature to obtain a neat and easy-to-use analytic relationship between the shock and the body shapes.

The shape of an oblique shock is a key feature to design and determine the scale of the model for supersonic wind tunnel tests. The shock waves emanating from various parts of the model, with an improper scale, could impinge the walls and reflect over the model [11, 12]. This remarkably decreases the accuracy of measurement and the data fidelity. The shock shape is also a major contributor in aerodynamic interference between the components of a supersonic vehicle. The shock-shock, shock-body interactions add lot of complexities to design and analysis of supersonic vehicles [13, 14].

Such applications necessitate accurate shock shape prediction in a minimum time. The numerical calculations to get the shape of the shock for a given flow condition and body shape, is a time-consuming task. Since various conditions have to be examined to get the best results, this would be an iterative process and the numerical calculations cannot be helpful. A rapid engineering, analytic or empirical/semi-empirical relation can be a convenient surrogate tool to determine whether or not, the shock wave impinges to the wind tunnel wall or to another part of the aircraft or to the shock wave emanating from other parts of the vehicle.

Several attempts have already been made to develop an analytical or relationship. The most successful one was proposed by Love [6]. However, he did not offer a ready-to-use and specific relation for any nose shape. He instead, proposed a graphical algorithm in which the user should swing a circular arc along the line normal to the slope of the nose under consideration. This circular arc should be fitted on the front portion of the nose and in this way, a proper scale factor is determined to relate the general shock shape to the specific nose under consideration (Figure 1). The method is cumbersome and hard to use. As stated earlier, it requires many manual adjustments and change of the constants during the process. It soon became obsolete and the researchers kept seeking for proper surrogates.

On the other hand, in recent years the statistical methods using response surface methodology, RSM, has become a popular tool to construct mathematical models based on experimental observations [15-17]. The RSM has provided a promising road for various aerospace applications including the aerodynamic problems. In this methodology, the dependent variable is expressed in the form of a polynomial, in terms of the independent variables engaged in the problem [18]. This process is based on ample experimental observations.

In this paper, a simple semi-empirical model has been proposed, based on RSM methodology, to predict the shock shape on a pointed axisymmetric nose at zero incidence. Several images from various shock visualization methods have been examined and the shock shape for different bodies and different Mach numbers were extracted. With these data, a response surface model was constructed to establish a relationship between the shock shape, as the dependent variable, and the nose geometric parameters and the free stream Mach number as the independent variables.

The proposed regression model was then compared with the data that have not already been used in the regression process. These data were extracted from the Schlieren tests performed by the author and were used to check the model accuracy and validity. The comparisons show a remarkable agreement between the experimental findings, both the data found in the literature and the exclusive ones performed in this paper, and those predicted by the proposed model. The model works for

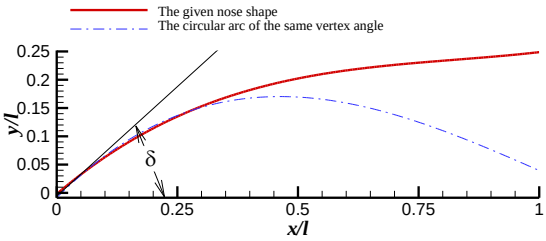

Figure 1. The circular arc fit on the given nose shape

any attached shock ahead of arbitrary axisymmetric pointed bodies of revolution at zero angle of attack. For the case of two-dimensional shock from a wedge, the same approach with a simpler model can be obtained, as well.

2. IDENTIFICATION OF A RESPONSE SURFACE MODEL

The Response Surface Methodology, RSM, encompasses a set of mathematical and statistical methods to model the problems in which a dependent variable is expressed as a function of some independent factors [19].

For m independent variables, x_1, x_2, …, x_m, the dependent or response variable, y, can be considered to be an unknown function of the independent variables, i.e. $y= f(x_1, x_2, \ldots, x_m)$. For each of N experimental runs carrying out on m design variables and for a single response y, a general form of the regression equation can be considered in the form of Equation (1):

$$y = B_o + \sum_{i=1}^{m} B_i x_i + \sum_{i=1}^{m} B_{ii} x_i^2 + \sum_{i=1}^{m} B_{iii} x_i^3 + \sum_{i=1}^{m} \sum_{j\neq i} B_{ij} x_i x_j + \cdots + \varepsilon \quad (1)$$

where ε is the regression error term and the B_{ij}'s are the regression coefficients and are determined by the Least Square method based on several observations of the dependent variable for a given set of the independent parameters [20].

Note that all of the terms in Eq. (1) do not necessarily appear in every problem and some of them according to their functionality and the physical nature of the problem under consideration may be disregarded.

In this paper, the response variables are the terms in the proposed equation for the shock shape and the independent variables are the terms describing the equation of the nose contour as well as the free stream Mach number.

3. THE EXPERIMENTAL DATA COMPENDIUM

Extensive visualization tests have already been performed on various body shapes in supersonic flow to reveal the shock and expansion waves and study their behavior. Some of the clearest ones have been selected from the literature, mostly from Van Dyke's collection [17]. Figure 2 shows these pictures that include different pointed noses at an extensive range of Mach numbers and at zero angle of attack.

In addition to the data bank, shown in Figure 2, which were used to construct a regression model for the shock shape, further Schlieren visualization tests have been performed by the author to check the accuracy of the proposed model. These tests were carried out for various nose shapes at different Mach numbers.

The experiments have been conducted in two supersonic wind tunnels, one having a 60 cm×60 cm test section and the other, which was a small educational tunnel, has a rectangular test section of 2.5 cm×2.8 cm. Figure 3 shows the Schlieren arrangement including the light source, the mirrors, the knife edges and the digital camera recorder for the second tunnel. Shown in Figure 4 are some of the test results.

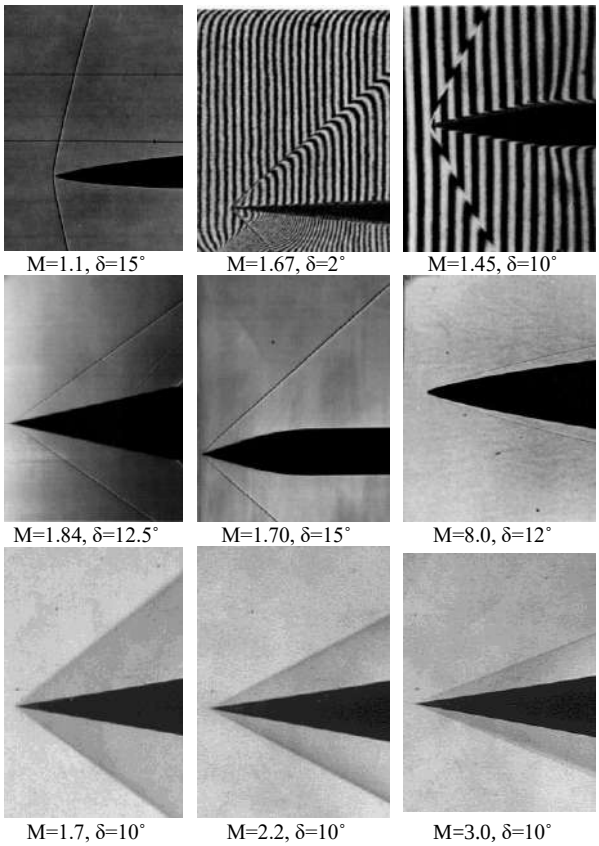

Figure 2. Various attached shocks compiled from the literature [17-19]

Figure 3. The Schlieren arrangement for the small test section wind tunnel

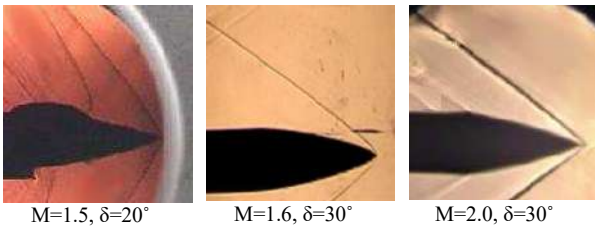

M=1.5, δ=20˚ M=1.6, δ=30˚ M=2.0, δ=30˚

Figure 4. The Schlieren tests performed in the present experiments

The first model is the well-known Standard Dynamics Model, SDM, which is a generic airplane model extensively used to study the dynamic stability behavior and to check the validity of the dynamic test rigs all over the world. The two others are the ogive-cylinder combinations with different nose shapes. The middle nose is a tangent ogive, while the two others are secant.

3. THE SCHILIEREN IMAGE PROCESSING

Picking up the exact points on the shock from the Schlieren images is actually an erroneous task and care must be taken in measuring the shock points. When the image is zoomed-in to pick up the points on the shock, the dark pixels on the shock form discrete saw-tooth cells and cannot be easily distinguished from the background pixels.

To enhance the accuracy of the measurements, an image processing routine was developed using MATLAB®. In the first step, and to simplify the process, the original RGB image, Figure 5(a), was changed to gray scale, Figure 5(b). A histogram plot of the color spectrum from absolute black to absolute white for the image of Figure 5(b) is shown in Figure 5(c). As observed, the intensity peaks are mainly concentrated at two specific regions while the rest of the spectra are nearly empty.

By stretching the color map, the intensity values in grayscale image, Figure 5(b), have covered the entire spectra and were re-scaled in Figure 5(d), such that 1% of data is saturated at low and high intensity regions in Figure 5(b). This increases the contrast of the output image, Figure 5(d). Note that the pixels in the original image have not been displaced by this process, and the shock shape is thus preserved. The improved histogram of the intensities in the spectrum after stretching is shown in Figure 5(e), which approves that the intensities over the gray scale spectra has been stretched and provided a more uniform contrast between the shock and the background pixels. The background color was also removed to get a more distinguished boundary between the shock and the surrounding, Figure 5(f). Finally, using Otsu's method [24], a global threshold was computed that could be used to convert the intensity image to a binary one in which the variance of the black and white pixels is minimized. This can reduce the saw-tooth edges between the pixels and makes them nearly smooth.

The final results would be a clearer boundary between the shock and the environment and is shown in Figure 5(g). The boundary between the dark and the bright zones is actually the outer edge of the shock wave and the points on it were detected and measured with more accuracy. By this method, the shock shape and position have not been changed or displaced, so the shock points recognition have been much easier and more accurate than any classical and conventional methods. The measured quantities from the images were the longitudinal and lateral positions of the points on the nose as well as the ones on the shock all the way from apex to the end of the nose section, along with the nose semi vertex angle, δ. Figure 6 schematically shows the measured parameters.

4. THE REGRESSION MODEL

The shape of a vast range of tangent ogive pointed noses can be expressed in the form of a 4th order polynomial, i.e.

$$y_b=a_1x+a_2x^2+a_3x^3+a_4x^4 \quad (2.a)$$

where both x and y_b are normalized by l, and therefore x is between 0 and 1. For non-tangent noses, including the secant types, this approximation still works. Figure 7 shows several tangent, power-law and secant type noses

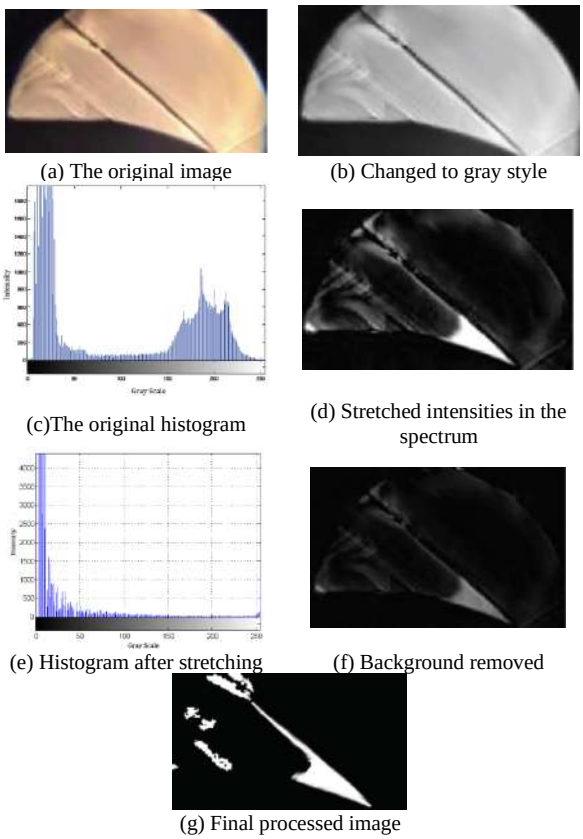

(a) The original image (b) Changed to gray style

(c)The original histogram (d) Stretched intensities in the spectrum

(e) Histogram after stretching (f) Background removed

(g) Final processed image

Figure 5. The image processing steps to obtain clear images with a smooth shock boundary

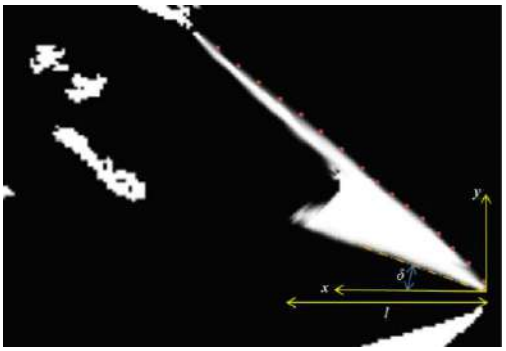

Figure 6. The parameters measured from the processed images

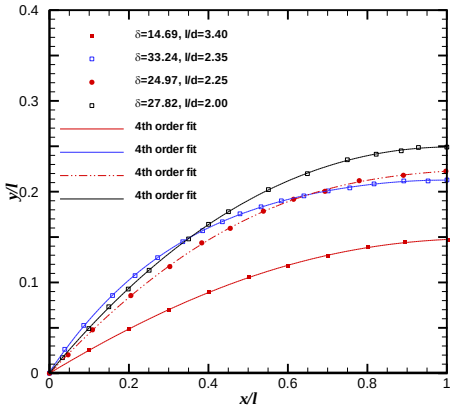

(a) Tangent and power-law type

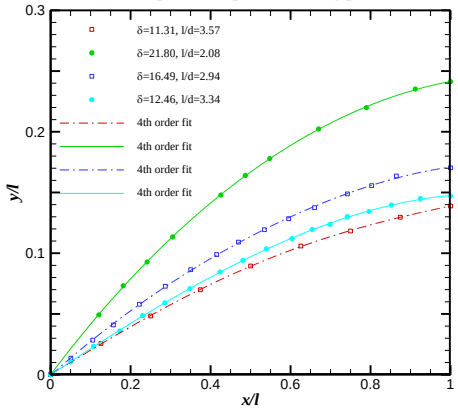

(b) Secant type

Figure 7. The 4th order polynomial fit on several pointed noses

fitted by a 4th order polynomial, where the markers are the actual points on each nose and the lines of the same color, show the polynomial fit for that nose.

Note that the expansion waves emanating from the front half of the nose usually impinge the nose shock and affect its slope and curvature. After a certain distance from the nose apex, the expansion waves no longer intersect the shock. These stations that are at the rear most of the nose can be deemed to have no effect on shock shape. This has been previously shown by exploiting method of characteristics on both two-dimensional and axisymmetric pointed bodies [6].

The 4th order polynomial is thus a good approximation for any pointed nose, having a smooth contour, to determine the corresponding shock shape. The shape of the oblique shock emanating from the nose apex would be of the same family of polynomials indicated by Equation (2.a). Evidently, certain relationships must exist between the corresponding coefficients of the two polynomials.

$$y_s=b_1x+b_2x^2+b_3x^3+b_4x^4 \quad (2.b)$$

Again, both x and y_s are normalized by l. First, note that the shock slope at x=0 can be considered to be the same as that for an equivalent conical shock angle emanating from a cone of the same semi vertex angle as the body under consideration. At large values of x, i.e. the rear most of the nose, the shock slope reduces to that of the corresponding Mach wave, that is arcsin (1/M). Therefore:

At x/l=0: dy/dx=tan β

At $x/l\rightarrow$1: dy/dx=tan μ

where β is the shock angle at the apex and μ the Mach wave angle. Thus, the coefficient b1 in the shock shape equation must be a function of the body slope, as well as the free stream Mach number. Since the shock slope everywhere decreases with Mach number and increases with the body semi vertex angle, δ, the ratio M/δ plays a decisive role in the shape of the shock.

Note that δ/M is the dominant factor near x=1. Since the curvature in the shock shape near x= 0 is higher than the other longitudinal positions, a third power of a1 is included to the regression equation for b1 as well as an interaction term a_1a_2 to match the behaviors at the two limits x/l=0 and x/l=1.0 and represent a continuous curve. The following functional form can thus be proposed for the constant b_1 in shock equation:

$$b_1 = B_{01}+B_{11}a_1M/\delta +B_{21}a_1\delta/M +B_{31}a_1a_2 +B_{41}a_1^3 \quad (3)$$

The coefficient of the second order term of the shock equation, b_2, determines the second derivative of the shock equation at the apex. It also depends on M/δ at the front and δ/M at the rear halves of the nose.

This coefficient, b_2, must also be in accordance with the corresponding value a_2 in the body equation. From the shock shape, it is required for the second derivative in Equation (2) to be always negative. The interaction terms a_1a_2 and a_3a_2 are included to take the dependencies in a_1 and a_3 into account. These terms are necessary to model the impingement of the expansion waves from the nose and the oblique shock originating at the apex. As a consequence, of this impingement, the oblique shock curvature evidently changes. Thus, the regression equation for b_2 may be suggested as:

$$b_2 = B_{02}+B_{12}a_2^2 + B_{22}a_2\, M/\delta + B_{32}a_2\delta/M +B_{42}a_1a_2 +B_{52}a_3a_2 \quad (4)$$

Similar regression models have been considered for b_3 and b_4, knowing the constants a_1 through a_4 from the given nose shape. The third order coefficient for the shock, b_3, can be modeled to be functions of the products a_3M/δ for the front part and a_3δ/M for the rear part of the body, along with the interaction terms a_1a_3 and a_1a_2 to adjust the changes in shock slope as the nose local slope changes.

The same arguments work for b_4 which includes the M/δ and M/δ ratios for both near x=0 and near x=1 respectively, and the interaction terms to express the shock shape as the body slope changes.

$$b_3 = B_{03} + B_{13}a_3\,M/\delta + B_{23}a_3\delta/M + B_{33}a_1a_3 + B_{43}a_1a_2 \quad (5)$$

$$b_4 = B_{04} + B_{14}a_1\,M/\delta + B_{24}a_1a_4 + B_{34}a_1a_2 + B_{44}a_4\delta/M \quad (6)$$

To make sure that all of the terms added to the response surface model for each coefficient in Equation (3) to (6), were the major contributors to the response variable, the statistical hypothesis test in RSM is performed to determine the p-value [15]. For each term in the regression, the null hypothesis implies that the term under consideration does not have any significant effect on the response variable.

From the Anderson–Darling test [25], if the p-value for that term is greater than a certain pre-defined value, known as the significance level and is usually set to 0.05, the null hypothesis is accepted. This means that the term under consideration does not have any remarkable effect on the coefficients b_1, b_2, b_3 or b_4.

On the other hand, if the p-value is less than the significance level, there would be enough evidence to reject the null hypothesis. The p-values for all of the coefficients were measured to be nearly zero. On this basis, within 95% confidence level, all of the terms used in the regression equation for each coefficient can be considered to have strong impact on the response variables, i.e. b_1 through b_4.

Each regression equation for b_1, b_2, b_3 and b_4 was solved individually using the least square method based on the shock shape measurements already performed for various bodies and the unknown regression constants B_{ij} have been determined.

The regression coefficient, R^2, in RSM is a measure of the model performance in fitting the data. Theoretically, the closer be R^2 to the unity, the better would be the estimation of regression [25]. The regression coefficient, R^2, and the adjusted regression coefficient, R_{adj}^2 [25], for each coefficient in Equation (2) have been calculated and shown in Table 1.

Finally, the regression coefficients for Equation (2.b) have been evaluated and are presented in Tables 2-5.

Once the constants b_1 through b_4 are evaluated using the associated regression models, the shock shape is determined from Equation (2.b). This equation holds for any axisymmetric shock on a pointed nose at zero angle of attack.

TABLE 1. The coefficients of regression for each coefficient in the shock shape equation

Coefficient	R^2 (%)	R_{adj}^2 (%)
b_1	99.99	99.97
b_2	99.75	98.50
b_3	98.99	96.96
b_4	99.74	99.21

TABLE 2. The regression constants for b_1

B01	B11	B21	B31	B41
0.748396	-4.50195	0.101269	0.295592	0.933427

TABLE 3. The regression constants for b_2

B02	B12	B22	B32	B42	B52
-0.10824	-19.2161	1.22114	0.21092	-15.2768	-15.2215

TABLE 4. The regression constants for b_3

B03	B13	B23	B33	B43
0.002284	-4.08483	- 0.173138	5.44873	-1.47554

TABLE 5. The regression constants for b_4

B04	B14	B24	B34	B44
0.0698898	-2.73123	8.64948	0.346297	-0.280287

To sum up, the procedure followed in this paper to determine the shock shape is elucidated. The problem starts with a given nose at a given Mach number at zero angle of attack. From the geometry of the nose, a 4th order polynomial is fitted on the nose and the coefficients a_1 through a_4 in Equation (2.a) are determined. With these data, the Mach wave angle, μ, and the nose semi vertex angle, δ, can be calculated. Now the shock equation can be determined from Equation (2.b) where the constants b_1 through b_4 are in Equations (4) through (6). The constants in these equations are presented in Tables (2) to (6). The numerical constants have been evaluated from the RSM model, Equation (1), and using several shock shapes obtained from visualization tests.

5. RESULTS AND DISCUSSIONS

Having determined the regression coefficients for the shock shape, Equation (2.b), given a nose shape, the equation of the attached shock can be determined. Various noses at different Mach numbers which have not been used in the regressions to determine B_{ij}, as well as

those exclusively tested in the wind tunnel for the present experiments will be considered in this section to evaluate the performance of the model in Equation (2.b).

The shock shapes ahead of two different noses at a Mach number of M=1.62 have been predicted by Equation (2) and compared with the experiment [6]. The prediction accuracy for the nose with δ=19.8˚ in Figure 8 is much higher than the other nose shown in Figure 9. This shows that the present approach works better for small nose angles. The agreement between the predicted and measured sock shapes that both the equivalent cone concept at the shock origin and the limit of the shock slope at the end of the nose that have been implemented in Equation (2) worked satisfactorily.

However for δ=27.83˚, some small discrepancies are observed between the predicted shock shape and that measured in the experiment. These discrepancies are in the rear half of the nose near the base. From axisymmetric flow theories in supersonic regime, the maximum vertex angle for which, an attached shock is possible at M=1.62 is about 30 degrees [26], beyond which the shock will detach the nose and the prediction accuracy decreases.

Similar behavior for another nose with δ=30˚ at M=1.6 can be observed in Figure 10. The visualization tests for this nose was performed by the author for the present paper, and shows subtle errors in the shock shape predicted by Equation (2) comparing to that measured from the Schlieren tests. For a high supersonic speed of M=5.05, Figure 11 shows a good performance for Equation (2) in predicting the shock shape comparing to the experimental data of reference 6. Note that the shock lies closer to the body as the free stream Mach number increases. This makes the shock shape more complicated than the one at smaller Mach numbers and the local slope of the shock would be more sensitive to the nose shape.

Another cases whose Schlieren tests were performed by the author, are shown in Figure 12 for M=1.5, δ=20˚ and Figure 13 for M=1.5, δ=20˚. Both noses were secant ogives and one can still observe a remarkable accuracy in shock shape prediction. For the nose in Figure 12, even though the vertex angle is not too large, the nose local slopes are fairly high which adds a lot of complexities to the shock shape. For this reason, some small differences can be seen near the nose base between the predicted and the measured values.

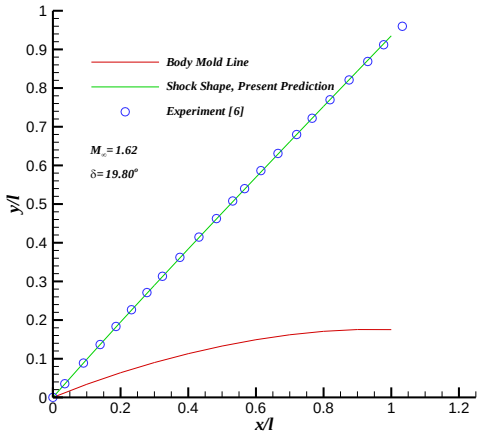

Figure 8. The predicted shock shape for M=1.62, δ=19.8˚ compared to data of Ref. 6

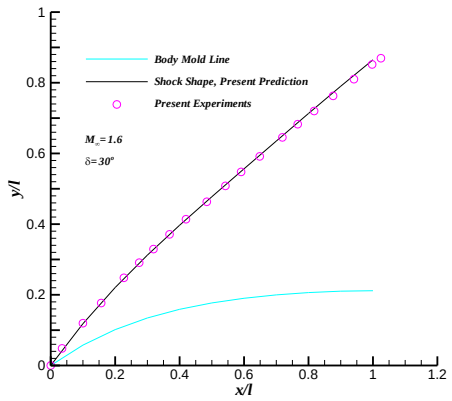

Figure 10. The predicted shock shape for M=1.6, δ=30˚ compared to the present experiments

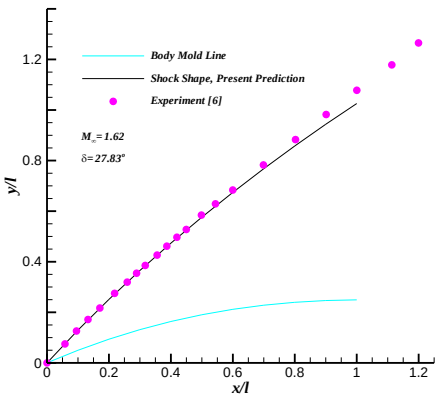

Figure 9. The predicted shock shape for M=1.62, δ=27.83˚ compared to data of Ref. 6

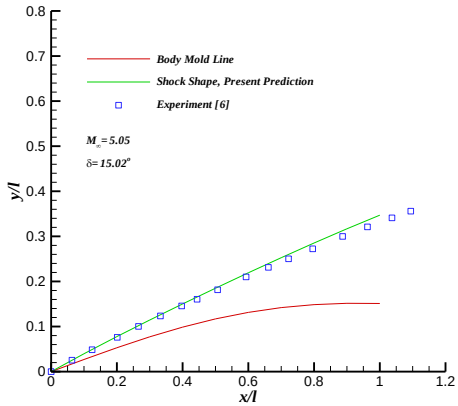

Figure 11. The predicted shock shape for M=5.05, δ=15.02˚ compared to data of ref. 6

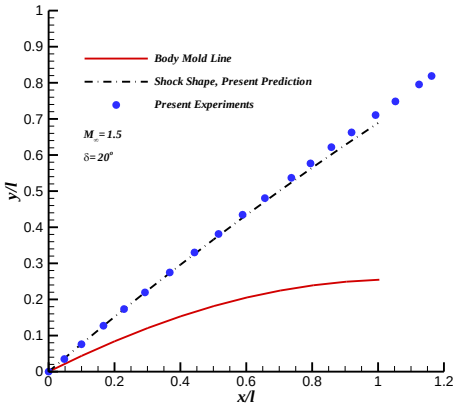

Figure 12. The predicted shock shape for M=1.5, δ=20˚ compared to the present experiments.

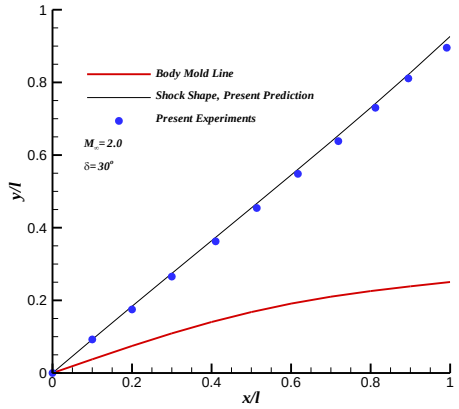

Figure 13. The predicted shock shape for M=2, δ=30˚ compared to the present experiments

6. CONCLUSION

A semi-empirical model has been proposed to determine the shape of the shock wave emanating from a pointed nose, knowing the nose geometric parameters and the free stream Mach number. The method is based on a relationship between the shock shape and the body shape. A series of supersonic flow visualization tests have been compiled and the shock shapes have been correlated to their associated nose shapes. A response surface methodology has been exploited to describe the mathematical model for this relationship. Once the regression coefficients for the model have been determined, it can be used to calculate the shape of the shock, knowing the geometric parameters of the nose. Several Schlieren tests have been performed in this paper to check the validity of the model. The results show a good agreement between the shock shape predicted by this regression model and the ones measured directly from the visualization images for a vast range of nose geometric parameters and free stream Mach numbers. Based on the nature of this model and the supersonic flow properties, the prediction accuracy is likely to slightly decrease for high Mach numbers where the shock lays closer to the nose surface and at high nose vertex angle where the shock curvature increases and stays away from the nose. The shape of the shock is of great importance when a model of a supersonic vehicle is to be tested in wind tunnel, to avoid shock reflections from the walls.

6. REFERENCES

1. Martínez-Ruiz, D., Huete, C., Sánchez, A.L., and Williams, F.A., "Interaction of Oblique Shocks and Laminar Shear Layers", ***AIAA Journal***, Vol. 56, (2018), pp. 1023-1030. DOI: 10.2514/1.J056302.
2. Mason, F. and Kumar, R., "Study of Shock Wave Boundary Layer Interactions on an Axisymmetric Body", AIAA 2019-0342, AIAA Scitech Forum, Shock Boundary Layer Interaction Session, (2019), CA, USA
3. Farahani, M. and Jaberi, A., "Experimental Investigation of Shock Waves Formation and Development Process in Transonic Flow", ***Scientia Iranica, Transaction B***, Vol. 24, No. 5 (2017), 2457-2465. DOI: 10.24200/sci.2017.4309.
4. Kulkarni, M.D., "Shape Sensitivity for High-speed Flows with Shocks", AIAA 2020-0888, AIAA Scitech Forum, Aerodynamic Shape Optimization Session, (2020), FL, USA
5. Whitham, G.B., "The Flow Pattern of a Supersonic Projectile", ***Communications on Pure and Applied Mathematics***, Vol. 5, No. 3, (1920), 301-348. DOI: 10.1002/cpa.3160050305.
6. Love, E.S. and Long, R.H., "A Rapid Method for predicting Attached-Shock Shape", NACA TN-4167, 1957.
7. Martel, J.D., and Jolly, B., "Analytical Shock Standoff and Shape Prediction with Validation for Blunt Face Cylinder", AIAA 2015-0523, AIAA Atmospheric Flight Mechanics Conference, (2015).
8. Sinclair, J. and Cui, X., "A theoretical approximation of the shock standoff distance for supersonic flows around a circular cylinder", ***Physics of Fluids,*** Vol. 29, (2017), 026102. DOI: 10.1063/1.4975983
9. Hunt, R.L., and Gamba, M., "Shock Train Unsteadiness Characteristics, Oblique-to-Normal Transition, and Three-Dimensional Leading Shock Structure", ***AIAA Journal***, Vol. 56, (2018), 1569-1587. DOI: 10.2514/1.J056344
10. Davari, Ali, R., and Soltani, M.R., "On the Relationship between Unsteady Forces and Shock Angles on a Pitching Airplane Model", ***Scientia Iranica, Transaction B***, Vol. 17, No. 2, (2010) 102-107. DOI: 10.1063/1.4821520
11. Jin J., Li G., Wei Z., Dong J., Zhang J. "Calibration of the Versatile Platform and the Supersonic Integrated Section" in CAAA. The Proceedings of the 2018 Asia-Pacific International Symposium on Aerospace Technology (2019), Springer, Singapore, Vol. 459. 915-929, DOI: 10.1007/978-981-13-3305-7_72
12. Chernyshev, S.L., Ivanov, A.I., Streltsov, E.V., And Volkova, A.O., "Numerical and Experimental Research of New Methods For Wall Interference Reduction In Wind Tunnels of Transonic and Low Supersonic Velocities", Proceeding of the 7th European Conference on Computational Fluid Dynamics, ECFD 7, (2018), Glasgow, UK
13. Martínez-Ruiz, D., Huete, C., Sánchez, A.L., and Williams, F.A., "Interaction of Oblique Shocks and Laminar Shear Layers," ***AIAA Journal***, Vol. 56, (2018), 1023-1030. DOI: 10.2514/1.J056302
14. Mason, F. and Kumar, R., "Study of Shock Wave Boundary Layer Interactions on an Axisymmetric Body," AIAA 2019-0342, AIAA Scitech 2019 Forum, Shock Boundary Layer Interaction Session, (2019), CA, USA, DOI: 10.2514/6.2019-0342

15. Fenrich, R.W., and Alonso, J., "A Comparison of Response Surface Methods for Reliability Analysis using Directional Simulation", AIAA 2018-0437, AIAA Non-Deterministic Approaches Conference, (2018). DOI: 10.1016/S0167-4730(03)00022-5
16. Vasu, A., and Grandhi, R.V., "A Response Surface Model Using the Sorted k-fold Approach", AIAA 2014-1485, 10th AIAA Multidisciplinary Design Optimization Conference, (2014). DOI: 10.2514/1.J052913
17. Kucuk, U.C., "Application of Response Surface Methodology to Optimize Aerodynamic Performance of NACA Inlet," AIAA 2017-4991, 53rd AIAA/SAE/ASEE Joint Propulsion Conference, (2017).
18. Lawson, J., Design and Analysis of Experiments with R, First Edition, CRC Press, (2015).
19. Myers, R.H., and Montgomery, D.C., Response Surface Methodology: Process and Product Optimization Using Designed Experiments, Fourth edition, John Wiley & Sons Inc., (2016). DOI: 10.1080/00224065.2017.11917988
20. Fenrich, R.W., and Alonso, J.J., "A Comparison of Response Surface Methods for Reliability Analysis using Directional Simulation", AIAA 2018-0437, 5th AIAA Non-Deterministic Approaches Conference, (2018), FL, USA. DOI: 10.2514/6.2018-0437
21. Van Dyke, M., An Album of Fluid Motion, The Parabolic Press., (1982). DOI: 10.1002/aic.690280628
22. D. K. Weimer, C. H. Fletcher, and W. Bleakney, "Transonic Flow in a Shock Tube", ***Journal of Applied Physics***, Vol. 20, No. 4, (1949), 418-421. DOI: 10.1063/1.1698393
23. Freeman, N.C., Cash, R.F. and Bedder, D., "An experimental investigation of asymptotic hypersonic flows", ***Journal of Fluid Mechanics***, Vol. 18, (1964), 379-384. DOI: 10.1017/S0022112064000271
24. Otsu, N., "A Threshold Selection Method from Gray-Level Histograms," *IEEE Transactions on Systems, Man, and Cybernetics*, Vol. 9, No. 1, (1979), 62-66. DOI: 10.1109/TSMC.1979.4310076
25. Kenett, R.S., Zacks, S., and Amberti, D., Modern Industrial Statistics, Second Edition, John Wiley & Sons Ltd, (2014). DOI: 10.1002/9781118763667
26. Ferreyra, R.T., "Supersonic Cones at Zero Incidence," AIAA 2016-4275, 46th AIAA Fluid Dynamics Conference, (2016). DOI: 10.2514/6.2016-4275

Persian Abstract

چکیده

در این مقاله یک روش نیمه‌تجربی برمبنای سطح پاسخ پیشنهاد داده شده است که به کمک آن می‌توان شکل موج ضربه‌ای مایل که از یک دماغه‌ی با تقارن محوری در زاویه‌ی حمله‌ی صفر درجه ایجاد می‌شود را تخمین زد. به این منظور، یک بانک اطلاعاتی گشترده از تصاویر آشکارسازی جریان فراصوتی حول دماغه‌های مختلف در اعداد ماخ متفاوت جمع‌آوری شده و شکل موج ضربه‌ای برای همه‌ی آنها استخراج گردید. همچنین، چندین آزمایش آشکارسازی دیگر با استفاده از امکانات داخلی و در دو تونل باد فعال موجود در کشور توسط نویسنده انجام گرفته و از نتایج آنها برای بررسی دقت تخمین روش مذکور استفاده شده است. در این روش، ثابت شد که انواع مختلف دماغه‌های با تقارن محوری را می‌توان با یک منحنی درجه‌ی چهار توصیف نمود. بر این اساس، معادله‌ی شکل موج ضربه‌ای نیز یک منحنی درجه‌ی چهار درنظر گرفته شد است که هر یک از ضرایب آن خود تابعی از عدد ماخ جریان و پارامترهای هندسی دماغه می‌باشند. این ضرایب ثابت با استفاده از بانک اطلاعاتی تدوین شده و به کمک روش سطح پاسخ تعیین شده و برای استفاده از روش مذکور، کافیست عدد ماخ جریان و ضرایب معادله‌ی درجه چهار از شکل دماغه مشخص باشند. به کمک اطلاعات مذکور و رابطه‌ی به دست آمده در این مقاله، می‌توان معادله‌ی درجه‌ی چهار از شکل موج ضربه‌ای ایجاد شده را به‌راحتی تخمین زد. چنین محاسباتی برای به دست آوردن مقیاس مدل مورد آزمایش در تونل باد و به منظور اجتناب از انعکاس شوک از دیواره‌های تونل باد، یک ابزار مهم و کاربردی بوده و نقش مهمی در کاهش خطاهای ناشی از تداخل شوک و دیواره خواهدداشت.

International Journal of Engineering

Journal Homepage: www.ije.ir

Design and Experimental Study of a Combined Pneumatic Plot Seed-metering Device for Cotton

L. Yudao*[a], S. Xuezhen[b]

[a] College of Mechanical and Electronic Engineering, Shandong Agricultural University, Tai'an, China
[b] College of Agricultural, Shandong Agricultural University, Tai'an, China

PAPER INFO

Paper history:
Received 10 May 2020
Received in revised form 2 June 2020
Accepted 12 June 2020

Keywords:
Combined Pneumatic
Seed-metering Device
Orthogonal Test
Uniformity Coefficient
Seeding Rate

ABSTRACT

This study presents a combined pneumatic seed-metering device (SMD) that could not only fill, carry, and meter seeds, but also switch quickly between seed-metering and seed-cleaning modes, and clean seeds thoroughly and rapidly. The seed-filling, seed-carrying, and seed-metering modes of the SMD were analyzed based on a theoretical kinematic model. Furthermore, a three-factor, three-level orthogonal test was conducted by using a performance test bench arranged for the SMD as well as Design-Expert software. The combination of parameters that led to the lowest mis-seeding rate (0.59%) was as follows: an air pressure of 2.67 kPa, a slot width of 2.83 mm, and a seed-metering speed of 20 r/min. The optimized scheme that resulted in a relatively low multiple-seeding rate (4.3%) and met other requirements at the same time was as follows: an air pressure of 2.35 kPa, a slot width of 2.78 mm, and a seed-metering speed of 20 r/min. A field test was subsequently performed by using a combined pneumatic plot cotton planter prototype. While the mis-seeding and re-seeding rates obtained from the field test were both somewhat higher than those obtained from the laboratory bench test, they still met precision planting requirements. The field test validated the accuracy of the theoretical analysis and bench test and served as a foundation for future prototype production and popularization.

***doi**: 10.5829/ije.2020.33.08b.24*

NOMENCLATURE

d	Width of the guide slot on the guide slotted disk (m)	G	Force of gravity exerted on each cotton seed (N)
l	Distance between the center of gravity of the seed and the guide slotted disk (m)	g	Gravitational acceleration (m/s^2)
Q	Resultant force of G, F, and J (N)	v	Distance between the cotton seed and the center (m)
P	Suction force generated by the seed-suction hole on the seed (N)	λ	Comprehensive seed friction coefficient
F	Sliding friction force between the seed and the guide slot (N)	K_1	Seed suction reliability coefficient (K_1=1.8–2.0)
N	Force (i.e., the sum of N1 and N2) exerted by the air-suction hole on the seed (N)	K_2	External conditions influence coefficient (K_2=1.6–2.0)
S	Area of the air-suction hole (m^2)	K_3	Seed moisture content influence coefficient (K_3=1.1–1.2)
H	Critical degree of vacuum in the SMD air-suction hole (Pa)	μ	Dynamic friction coefficient
		m	Seed group weight (kg)

1. INTRODUCTION

The cotton industry plays an important role in agricultural production system of China. Cotton is closely linked to daily life. In 2019, the total cotton planting area in China was 3,339,200 ha, which was 15,200 ha smaller than in 2018. This represents a 0.5% decrease. In 2019, China's total cotton production reached 5,889,000 tons, which is 213,000 tons or 3.5% less than in 2018. (data from the National Bureau of Statistics of China). Cotton breeding substantially affects the cotton planting area and the production quality. Plot breeding is an important step in the selection and breeding of new cotton cultivars. Due to the large number of cotton cultivars and seeds available for selection, cotton is planted across many plots during cotton selection and breeding. Strict requirements are applied to cotton selection [1].

*Corresponding Author Institutional Email: *liyudao@sdau.edu.cn* (L. Yudao)

Please cite this article as: L. Yudao, S. Xuezhen, Design and Experimental Study of a Combined Pneumatic Plot Seed-metering Device for Cotton, International Journal of Engineering (IJE), IJE TRANSACTIONS B: Applications Vol. 33, No. 8, (August 2020) 1652-1661

Cotton planting in plots differs from that in fields. When cotton is planted in a plot, there are strict position requirements for the start and end of planting. In addition, precise row and plant spacings and planting depths are required. Moreover, rapid, thorough seed cleaning is required after cotton planting is completed and seeds are rapidly discharged in the subsequent plot.

Currently, plot planters are used in China primarily for crops such as wheat, maize, and soybeans. The 2BJ-2 planter developed by Hebei Suning Agricultural Machinery Research Institute is used primarily to plant wheat in plots [2]. Li et al. [3] designed an automatic control system based on a conical compartment tray-type seed-metering device (SMD). Xu et al. [4] designed a conical canvas belt-type plot planter for wheat. Shang's team studied plot planting of wheat extensively during the project termed "Development and Demonstration of Precision Planting and Harvesting Equipment for Plots of Crop Varieties—an Industrial Science and Technology Project of China". Li et al. designed a precision plot planter for maize [5]. Huang et al. designed a precision plot planter for soybeans [6]. Cotton seeds differ from wheat, maize, and soybean seeds. Therefore, it is necessary to further explore and design machinery for breeding and planting cotton in plots using planters similar to those currently used in China.

Internationally, enterprises that have been somewhat successful in crop breeding machinery development, including Wintersteiger in Austria, Haldrup in Germany, Almaco in the United States, and Baural in France, have all manufactured various plot planter models for various crops [7-10]. The agricultural parameters (e.g., plant and row spacings and planting depths) used with cotton differ from those for wheat, maize, and soybeans. Therefore, it is necessary to design precision plot planters for cotton that can accurately meter and rapidly and thoroughly clean seeds. These plot planters must be relatively easy to operate within the agricultural requirements of cotton [11-13].

According to the needs of cotton planting, we have designed a combined air suction cotton planter (Figure 1). This machine is mainly composed of seed metering device, opener, vacuum fan, air pump, waste seed recovery room, etc. The seed meter is the most critical component. Therefore, this paper combines the agricultural material characteristics of cotton seeds to design the structure of the combined air-suction seed meter and study the optimal working parameters.

2. STRUCTURE AND OPERATING PRINCIPLE OF THE COMBINED PNEUMATIC SMD FOR COTTON PLOT PLANTERS

The components of the SMD included a seed-metering shell, a drive disk, a guide slotted disk, a suction disk, a forced seed-metering disk, and a seed-storage shell. The seed-metering shell could be fixed onto a furrow opener using bolts. The drive disk could rotate via a bearing when driven by the drive sprocket. The guide slotted disk was fixed onto the guide slotted disk via a positioning slot. The air-suction disk and the forced seed-metering disk rotated together with the drive disk across three slots that were evenly distributed on the drive disk. As demonstrated in Figure 2(b), seeds that are intended for planting are discharged through the seed-discharge opening during seed metering. Guided by the seed-guide tube, the seeds fall into the seed-storage shell. The vacuum fan provides vacuum, which is transferred to the air-suction disk via the guide slotted disk.

Figure 3(a) shows a schematic of the approximately rectangular air-suction holes formed by the combination of the guide slotted disk and the air-suction disk.

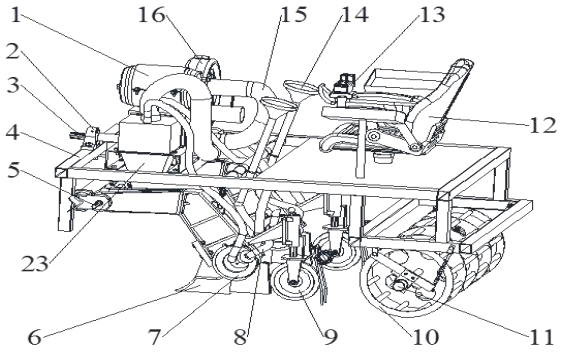

Figure 1. 3D drawing of seeder
1. Air pump 2. Bearing 3. Power input shaft 4. frame 5. Spline shaft 6. Opener 7. Seed metering device 8.Guided seed tube 9. Press wheel 10. Land wheel 11. Encoder 12. Work platform 13. Electromagnetic valve 14. Aid seed funnel 15. Vacuum tube 16. Vacuum fan 23. Wasteseed seed recovery room

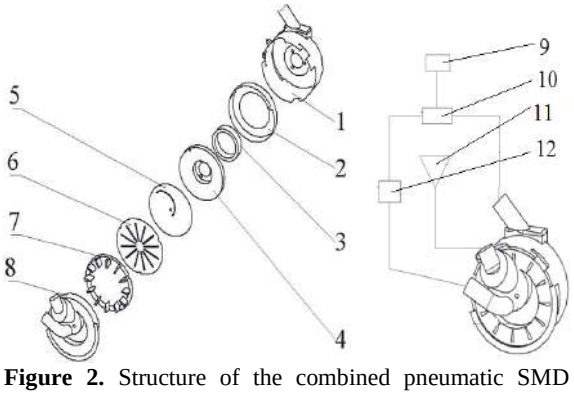

Figure 2. Structure of the combined pneumatic SMD (a) Exploded-view drawing (b) Assembly drawing
1. Seed-metering shell 2. Drive disk 3. Rolling bearing 4.Guide slotted disk-fixing device 5. Guide slotted disk 6.Air-suction disk 7. Forced seed-metering disk 8. Seed-storage shell 9. Vacuum fan 10. Three-way switch valve 11. Seeding funnel 12. Waste seed-recycling chamber

The figure also shows cotton seeds. Cotton seeds move towards the circumference of the air-suction disk as it rotates. The air-suction disk is in the front in the photograph in Figure 3(b).

Upon reaching the circumference of the air-suction disk, a seed enters the closed space formed by the three surfaces of the seed-storage shell, the two sides of the forced seed-metering disk, and the bottom surface of the air-suction disk, as shown in Figure 4. The seed rotates in the closed space with the forced seed-metering disk. Upon moving to the bottom, gravity causes the seed to fall through the opening at the bottom of the seed-metering shell to the furrow opened by the furrow opener. Thus, seed metering is completed.

After the planting in one cotton plot was completed, a three-way switch valve was controlled via an air system to direct vacuum to the waste-seed recycling chamber and transfer vacuum to the seed-suction opening. As a result, the seeds were sucked back to the waste seed-recycling chamber. This ensured that no seeds intended for the previous plot were stored in the SMD. When planting the subsequent plot, seeds were again discharged via the seed-discharge opening.

3. THEORETICAL FORCE ANALYSIS OF THE SEED-FILLING STAGE OF THE SMD

3. 1. Description of the Seed-filling, Seed-Carrying, and Seed-metering Stages of the SMD

The combined pneumatic SMD relies primarily on the negative pressure provided by vacuum to individuate single cotton seeds from a cotton seed group and arrange them into a uniform, orderly seed flow that rotates with the air-suction disk. The SMD carries and meters seeds via this mechanism. During this operation, the SMD is affected by factors such as disturbances from the seed group, negative pressure, the centrifugal force, and gravity. Here, a cotton seed force model is preliminarily established for each stage to facilitate force analysis. Based on the motion of and forces on a

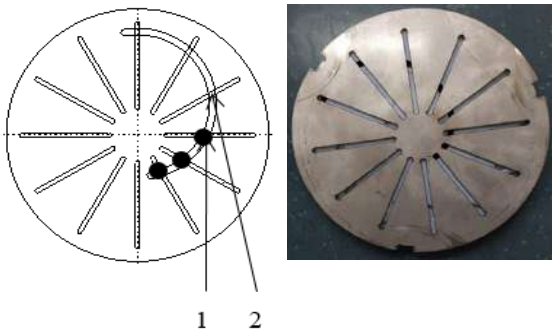

Figure 3. Air-suction holes formed by the combination of the guide slotted disk and the air-suction disk; (a) Two dimensional graph (b) Prototype; 1. cotton seed 2. air-suction holes

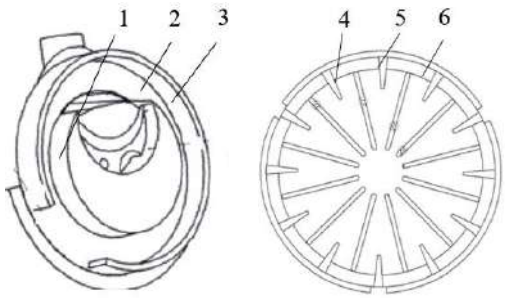

Figure 4. The closed space (a) Seed-storage shell (b) Air-suction disk and forced seed-metering disk

cotton seed, the seed-metering operation of the SMD is divided into three stages, as shown in Figure 5.

As the air-suction disk starts to rotate counterclockwise, the suction holes between approximately 0° and 60° on the seed-metering disk are under negative pressure. Under the negative pressure provided by the fan, the cotton seeds inside the seed storage chamber are sucked onto the suction holes and rotate with them as a seed group. This is the seed-filling stage. Between approximately 60° and 180° on the seed-metering disk, the air-suction holes are under vacuum. Under the negative pressure provided by the fan, the cotton seeds are sucked onto the suction holes, where they rotate synchronously with the seed-metering disk.

This is the seed-carrying stage. Between approximately 180° and 270° on the seed-metering disk, the suction holes are no longer under vacuum, the negative pressure provided by the fan disappears, and gravity causes the cotton seeds to fall into the closed space formed by the forced seed-metering disk and the seed-storage shell. The seeds rotate synchronously with the forced seed-metering and air-suction disks. The seed-metering operation is complete when the seeds eventually rotate to the opening at the bottom of the seed-storage shell. This is the seed-metering stage.

The following assumptions are made to facilitate analysis of the three stages of seed-metering operation:
(1) Cotton seeds are ideal, rigid ellipsoidal bodies with a uniform and consistent shape and size and do not

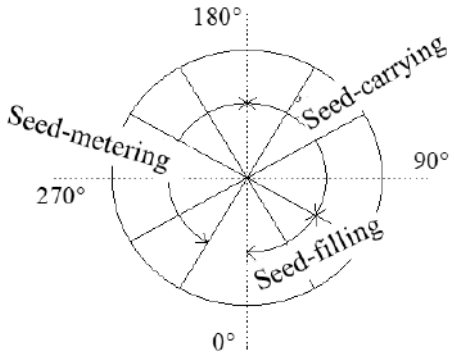

Figure 5. Three stages of the SMD

undergo elastic deformation. In addition, all external forces to which each cotton seed is subject act on its centroid.
(2) The seed-metering disk rotates at a uniform, constant speed.
(3) During seed-metering, the negative pressure difference provided by the fan is uniform and stable.

3. 2. Force Analysis of the Seed-filling Stage of the SMD Seed-filling performance is a key factor in seed-metering that directly affects the seed-metering quality index [14-16]. Figure 6 shows a force diagram of a single cotton seed during the seed-filing stage. The diagram was produced based on the suction position of the cotton seed and a theoretical analysis of the vertical-disk air suction-type SMD. The air-suction hole is formed by the combination of the guide slot and a straight air-suction slot. As this combined air-suction hole moves continuously, the magnitudes and angles of the forces from centrifugal inertia and sliding friction on the seed that is sucked onto the air-suction hole also change continuously. The forces on the seed are complex and varied.

Therefore, it is necessary to make several assumptions to facilitate the subsequent force analysis [17-19]:
(1) The distance between seed-suction holes is greater than their length and width. In addition, the dimensions of each seed-suction hole are smaller than the projected seed dimensions in all directions. This ensures that each seed-suction hole can suck and hold exactly one seed. The forces on a cotton seed at a seed-suction hole were investigated.
(2) During operation, the air-flow field in the closed vacuum chamber inside the SMD is uniform, and its parameters are set to steady-state values.

Figures 6(a) and 6(b) analyze the forces on a seed sucked onto the guide slot within the horizontal and vertical planes, respectively, during seed-metering. In Figure 6, G is the gravitational force on the seed sucked onto the guide slot, J is the centrifugal inertial force generated by of rotation of the seed (which is held onto the guide-slotted disk by suction) with the air-suction disk. The direction of J changes with the angle of rotation α. F is the sliding friction force generated by movement of the cotton seed on the guide slot during rotation of the air-suction disk and R is the resultant force from gravity and the centrifugal inertial force. In the force analysis shown in Figure 6, P is the suction force generated by the air chamber inside the SMD, while N_1 and N_2 are the reaction forces generated by the suction force on the guide slot. The suction force is itself generated by the SMD air chamber.

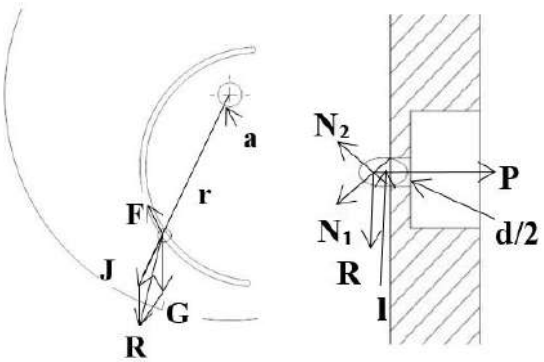

Figure 6. Force analysis of a cotton seed (a) The horizontal direction (b) The vertical direction

For a cotton seed to be sucked onto an air-suction hole, stably rotate with the air-suction disk, and undergo no sliding movement [20,21], the following force balance conditions should be satisfied at any location on the guide slot [22, 23]:

$$P\frac{d}{2} \geq Ql \tag{1}$$

The minimum pressure can be determined from the relationship between P and the degree of vacuum:

$$H = \frac{P}{S} \tag{2}$$

To suck and hold one cotton seed, an air-suction hole must at least meet the following condition:

$$P = \frac{2lQ}{d} \tag{3}$$

The critical degree of vacuum in an air-suction hole can be determined based on Equations (2) and (3):

$$H = \frac{2lQ}{Sd} \tag{4}$$

Q can be determined using the parallelogram rule of forces. First, one uses the parallelogram rule of forces to determine R, which is the resultant force of G and J:

$$R = \sqrt{G^2 + J^2 + 2GJ\cos\alpha} \tag{5}$$

Then, Q, which is the resultant force of R and F, is determined:

$$Q = \sqrt{R^2 + F^2 + 2RF\cos\beta} \tag{6}$$

Substituting Equations (5) and (6) into Equation (4) produces:

$$H = \frac{2lQ}{Sd}\sqrt{\begin{matrix}G^2 + J^2 + 2GJ\cos\alpha + F^2 + \\ 2\sqrt{G^2 + J^2 + 2GJ\cos\alpha}F\cos\beta\end{matrix}} \tag{7}$$

In ideal conditions, when cos α = 1 and cos β = 1, Equations (2)-(7) produces:

$$H = \frac{2K_1K_2K_3lG}{Sd}(1 + \frac{1}{g}\frac{v^2}{r} + \lambda) \tag{8}$$

The cotton seed dynamic friction coefficient was measured experimentally. The combined mass of the tested seed group and the shell was 435.38 g. The mass of the shell was 51 g. The mass of the weights used to pull the shell such that it moved horizontally was 275 g. F could be determined using the following equation:

$$F = mg\mu \tag{9}$$

Thus, μ could be determined using the following equation:

$$\mu = \frac{F}{mg} \tag{10}$$

Equation (10) was used to determine that μ was 0.72. The Shandong Cotton-37 cotton cultivar was used in the test. The cotton seed weight was set to 95.35 g/1000 seeds. The seed diameter was set to 5.3 mm and the area of each air-suction hole was set to 12 mm^2 (i.e., the width of the guide slot and the width of the air-suction straight slots were set to 4 mm and 3 mm, respectively). θ was set to 36.1°. K_1, K_2, and K_3 were set to 2.0, 1.8, and 1.1, respectively. The comprehensive coefficient was set to 7.2. The rotational speed of the air-suction disk was 15 r/min. Thus, the critical degree of vacuum was calculated to be 2180.89 Pa. When the air-suction disk rotated at a speed of 25 r/min, the critical air pressure was 2157.3 Pa. The calculation results of these theoretical values can provide numerical reference for subsequent experimental design.

4. SMD PERFORMANCE TEST

4. 1. Test Material and Methods Based on the operating principle of the combined pneumatic SMD, the degree of vacuum (i.e., air pressure) in each combined hole, the air-suction disk slot width, and seed-metering rotational speed of the air-suction disk are the primary parameters that affect seed-metering quality[24]. Seed-metering quality includes multiple-seeding and mis-seeding rates. Test data were obtained using a JPS-12 test bench and subsequently analyzed using Design-Expert software. The effects of each parameter on seed-metering performance were analyzed. Thus, a partially optimized combination of seed-metering parameters was selected to further improve planting precision in cotton plots.

During the test, the vacuum required for the SMD was provided by a vacuum tube on the test bench. The degree of vacuum was altered by controlling the rotational speed of the vacuum fan via the test bench control system [25]. The SMD air-suction disk slot width was varied by using previously designed air-suction disks with various slot widths. SMD rotation was powered by a drive motor. The rotational speed was controlled by a pulse signal from the control system. The control system was designed primarily to allow the SMD to be installed on real-world cotton plot planters. When used on the test bench, the seed-bed belt speed was set to mimic the advancing speed of a planter operating in a field [26]. Thus, all of the dependent variables (i.e., the degree of vacuum, slot width, and seed-metering speed) associated with the SMD during operation could be controlled. Figure 7 shows the test bench configuration and seed-metering results.

Tests were performed at the Seed-metering Performance Laboratory at the College of Mechanical and Electronic Engineering, Shandong Agricultural University. A Shannongmian-37 cotton cultivar was used. The following cotton seed parameters were measured: weight of 1000 seeds—96.7 g; density—0.886 g/cm3; angle of repose—19°; angle of sliding friction—25.3°; average length—9.66 mm; average thickness—5.22 mm.

During the tests, analytical and statistical models were established using Design-Expert software to investigate the effects of the air pressure, slot width, and rotational speed on multiple-seeding and mis-seeding rates. Air pressure, slot width, and rotational speed test values were determined based on previous kinematic analyses and the pre-testing. In addition, a three-factor, three-level central composite design (CCD) was developed, as shown in Table 1. In Table 1, X_1, X_2, and X_3 represent the air pressure, slot width, and rotational speed, respectively. In the data analysis, Y_1 and Y_2 represent the multiple-seeding and the mis-seeding rates, respectively.

The CCD parameters in Table 1 were imported into Design-Expert [27-29]. Based on the response-surface test design scheme, the software automatically generated 20 CCD schemes. Tests were performed

(a) SMD on JPS-12

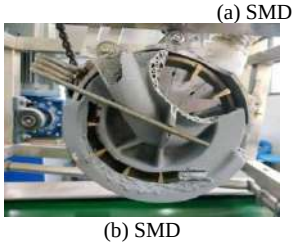

(b) SMD

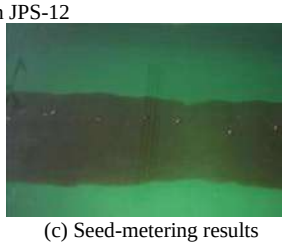

(c) Seed-metering results

Figure 7. SMD performance test, 1. Drive motor 2. SMD 3. Control system 4.Vacuum tube

based on these CCD schemes. The results were subsequently imported into the Design-Expert software and the effects of each factor on the multiple-seeding and mis-seeding rates were analyzed. A suitable combination of parameters was determined by comprehensively considering multiple-seeding and mis-seeding rates. During the test, the SMD rotated approximately 12 times and theoretically metered approximately 240 seeds under the parameters corresponding to each number. The numbers of seeds corresponding to multiple seeding and missed seeding, respectively, were recorded when approximately 240 seeds were metered. Table 2 summarizes the CCD schemes and results.

TABLE 1. Test factor code

Code	Factors		
	X_1/kPa	X_2/mm	X_3/(r/min)
-1.414	3.7	3.24	46.82
-1	3.2	3.1	40
0	2.6	2.9	30
1	2.0	2.7	20
1.414	1.5	2.56	13.18

TABLE 2 Response-surface test schemes and results

Testing No.	Factor			Result	
	X_1/kPa	X_2/mm	X_3/(r/min)	Y_1/%	Y_2/%
1	2.6	2.9	30	3.71	1.299
2	1.5	2.9	30	3.64	1.54
3	2.0	3.1	20	4.1	4.25
4	2.6	2.9	30	3.24	4.58
5	2.6	2.56	30	3.65	2.52
6	3.2	3.1	40	2.3	4.08
7	2.6	2.9	30	3.34	1.64
8	2.6	2.9	30	2.41	3.54
9	2.6	3.24	30	4.53	2.13
10	3.2	3.1	20	2.3	3.25
11	2.6	2.9	30	2.1	2.54
12	2.6	2.9	13.18	1.62	4.21
13	2.0	2.7	20	1.3	1.54
14	2.0	2.7	40	3.62	1.2
15	3.2	2.7	20	1.36	1.47
16	3.2	2.7	40	1.4	1.87
17	2.6	2.9	46.82	1.45	2.03
18	2.6	2.9	30	1.63	1.89
19	2.0	3.1	40	1.42	1.96
20	3.7	2.9	30	1.36	1.54

4. 2. Test Results and Analysis

4. 2. 1. Mis-seeding Rate Data and Analysis

The test data were subject to analysis of variance using Design-Expert. Table 3 summarizes the regression equation significance test results. The mis-seeding rate (Y_1) goodness-of-fit is significant (P<0.01), whereas the lack-of-fit is insignificant (P=0.1006). This suggests that there are no other principal influencing factors. Air pressure exerts the most significant impact on the quality index, followed by rotational speed and slot width. The following multivariate quadratic response surface regression model was obtained via a quadratic response-surface regression analysis performed using Design–Expert (Version 8.0.6):

$$Y1(\%)=78.93728-10.97592X_1-40.64099X_2-0.18529X_3-0.38541X_1X_2-0.02812X_1X_3-0.011875X_2X_3-2.324X_1^2+7.17705X_2^2+0.004X_3^2 \quad (11)$$

TABLE 3. Mis-seeding rate processing results

Source	Sum of square	df	Mean square	F	P
Model	16.95	9	1.88	3.36	0.0363**
X_1	3.55	1	3.55	6.33	0.0306**
X_2	0.0758	1	0.0758	0.1351	0.7208
X_3	0.0609	1	0.0609	0.1085	0.7486
X_1X_2	0.0171	1	0.0171	0.0305	0.8648
X_1X_3	0.2278	1	0.2278	0.4062	0.5382
X_2X_3	0.0045	1	0.0045	0.0080	0.9303
X_1^2	10.09	1	10.09	18.00	0.0017
X_2^2	1.19	1	1.19	2.12	0.1762
X_3^2	3.59	1	3.59	6.40	0.0298
Residual	5.61	10	0.5608		
Lack of Fit	5.56	5	1.11	109.10	0.053
Pure Error	0.0509	5	0.0102		
Cor total	22.56	19			

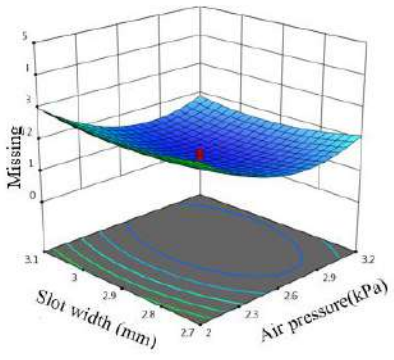

Figure 8. The slot width and air pressure impacts on the mis-seeding rate

The P-value of the model is 0.0363, which suggests that the model is significant. The X_1, X_2, X_3, X_1^2, and X_3^2 in the model are all significant terms. The lack-of-fit in this test is insignificant (P=0.053) and can be used to analyze data.

As demonstrated in Table 3, the slot width and air pressure each exert significant impacts on the mis-seeding rate. Thus, the effects of interactions between the slot width and air pressure on the mis-seeding rate were analyzed. To a certain extent, an increase in the slot width results in a lower mis-seeding rate (Figure 8). An increase in the air pressure also decreases the mis-seeding rate. However, the effects on the multiple-seeding rate should also be considered. Thus, the first scheme provided by the software is optimized and meets requirements. The optimized parameters that produce the lowest mis-seeding rate (0.59%) are as follows: an air pressure of 2.67 kPa, a slot width of 2.83 mm, and a seed-metering speed of 20 r/min.

4. 2. 2. Multiple-seeding Rate Data and Analysis

The test data was subjected to analysis of variance using Design-Expert [30-32]. Table 4 summarizes the significance test results for the regression equation. The goodness-of-fit of the mis-seeding rate (Y_2) is significant (P<0.0001) and the lack-of-fit (0.1551) is insignificant. This suggests that there are no other principal influencing factors. The slot width exerts the most significant impact on the quality index, followed by air pressure and rotational speed. A quadratic response-surface regression equation for the multiple-seeding rate was obtained via a response-surface analysis of the multiple-seeding rate using Design-Expert (Version 8.0.6):

$$Y2(\%)=102.77096-8.21243X_1-78.23229X_2+1.22112X_3+0.446875X_1X_2+0.060188X_1X_3-0.463187X_2X_3+1.1267X_1^2+16.14963X_2^2-0.000669X_3^2 \quad (12)$$

The P-value of the model is less than 0.0001 suggests that the model is significant. In this model, X_1, X_2, X_1X_3, X_1^2, and X_2^2 are all significant terms. The F-value of the lack-of-fit is 0.1551. This suggests that the lack-of-fit is insignificant, the goodness-of-fit is high, and the original data are reasonably accurate. The coefficient of adjusted determination is 0.9586. This suggests that 95.86% of the multiple-seeding rate is related to the three test factors, that the goodness-of-fit is high, and that the equation is satisfactorily simulated. However, 4.14% of the total multiple-seeding rate cannot be explained using the established surface model.

As demonstrated in Table 4, the slot width and air pressure each exert significant impacts on the multiple-seeding rate. Thus, the effects of the interaction between the slot width and air pressure on the multiple-seeding rate were analyzed. As demonstrated in Figure 9, increasing the slot width results in an increase in multiple-seeding rate to a certain extent. Increasing the air pressure also increases the multiple-seeding rate. Thus, the multiple- seeding rate data produces the following scheme optimized to produce the lowest multiple-seeding rate of 4.3%: an air pressure of 2.35 kPa, a slot width of 2.78 mm, and a seed-metering speed of 20 r/min.

TABLE 4. Multiple seeding data processing results

Source	Sum of square	df	Mean square	F	P
Model	16.95	9	1.88	3.36	0.0363**
X_1	2.56	1	2.56	26.28	0.0004
X_2	3.99	1	3.99	40.90	< 0.0001
X_3	0.0155	1	0.0155	0.1595	0.6980
X_1X_2	0.0230	1	0.0230	0.2360	0.6376
X_1X_3	1.04	1	1.04	10.70	0.0084
X_2X_3	6.87	1	6.87	70.42	< 0.0001
X_1^2	2.35	1	2.35	24.10	0.0006
X_2^2	6.01	1	6.01	61.69	< 0.0001
X_3^2	0.0570	1	0.0570	0.5847	0.4622
Residual	0.9749	10	0.0975		
Lack of Fit	0.7071	5	0.1414	2.64	0.1551
Pure Error	0.2677	5	0.0535		
Cor total	23.53	19			

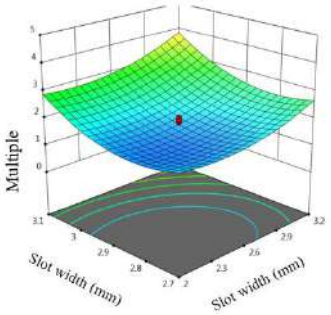

Figure 9. The slot width and air pressure impacts on the multiple-seeding rates

5. FIELD TEST

In June of 2019, a field test was performed using a prototype machine at the Agricultural Test Station on the south campus of Shandong Agricultural University (shown in Figure 10). During the test, the planter was driven by a Lovol 350 tractor (power: 26 kW). The field soil consisted of loam and had a moisture content of 23.2%. The primary equipment used in this test included

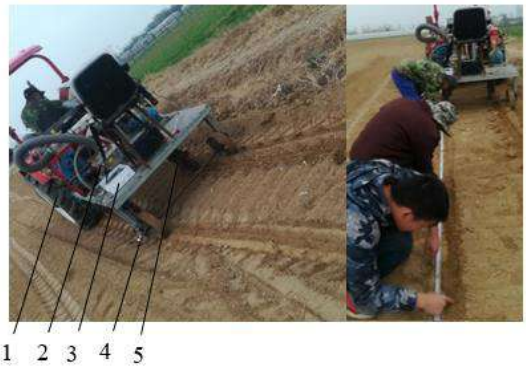

Figure 10. Field test 1. Tractor 2.Waste seed-recycling chamber 3. Control system 4.Encoder 5.SMD

TABLE 5. Field test results

	First group	Second group
Mis-seeding rate (%)	1.53	4.96
Multiple-seeding rate (%)	1.69	5.34

a cotton planter, straight rulers, a stopwatch, and a moisture meter. The test results show that the planter is able to complete the relevant processes, exhibits good seed-planting performance, and can plant single seeds precisely. In addition, the distances between the seeds planted by this planter are reasonably consistent.

The parametric settings for the first test group are as follows: a vacuum of 2.67 kPa, a slot width of 2.83 mm, and a seed-metering speed of 20 r/min. The mis-seeding and multiple-seeding rates for the first test group are 1.53 and 4.96%, respectively. The parametric settings for the second test group are as follows: a vacuum of 2.35 kPa, a slot width of 2.78 mm, and a seed-metering speed of 20 r/min.

6. CONCLUSION

This study presented a combined pneumatic SMD design. This SMD could fill, carry, and meter seeds and could switch rapidly between seed-metering and seed-cleaning modes. In addition, this SMD could meter seeds precisely and thoroughly and rapidly clean seeds. Thus, this SMD could improve the accuracy and speed of cotton planting in plots.

The seed-filling, seed-carrying, and seed-metering modes of the SMD were analyzed theoretically based on a theoretical kinematic model. The results provided a basis for identifying SMD structural and motion parameters. The critical air pressure for stable seed suction was calculated to be 2,161.6 Pa. This data provided support for subsequent bench and field tests.

A three-factor, three-level orthogonal test was performed using a performance test bench arranged for the SMD and Design-Expert software. SMD parameters that produced relatively good performance were determined during the test and used as a source of parameters for the field planting test. The combination of parameters that led to the lowest mis-seeding rate (0.59%) was as follows: an air pressure of 2.67 kPa, a slot width of 2.83 mm, and a seed-metering speed of 20 r/min. The optimized scheme that led to a relatively low multiple-seeding rate of 4.3% and otherwise met requirements was as follows: an air pressure of 2.35 kPa, a slot width of 2.78 mm, and a seed-metering speed of 20 r/min.

A field test was performed using a combined pneumatic cotton plot planter prototype. While the mis-seeding and multiple-seeding rates obtained from the field test were both somewhat higher than those obtained from the laboratory bench test, they still met precision planting requirements. The results of bench test and field test verify the accuracy of theoretical analysis. This validated provided a foundation for subsequent prototype production and popularization. The combined pneumatic cotton plot planter designed in this study could precisely meter and rapidly and thoroughly clean seeds. This design could meet cotton plot planting requirements.

7. REFERENCES

1. Karayela, D., Wiesehoffb, M., Özmerzia, A., Muller, J.. "Laboratory measurement of seed drill seed spacing and velocity of fall of seeds using high-speed camera system". ***Computers and Electronics in Agriculture***, Vol. 5, No. 2, (2006), 89-96. DOI: 10.1016/j.compag.2005.05.005
2. Vianna, L. R., Reis, A. V., Machado, A. L. T. "Development of a horizontal plate meter with double seed outlets". ***Revista Brasileira De Engenharia Agricola EAmbiental,*** Vol. 18, No. 10, (2014), 1086-1091. DOI: 10.1590/1807-1929/agriambi.v18n10p1086-1091
3. Correia, T. P., De Sousa, S. F., Silva, P. R., Dias, P. P., Gomes, A. R.. "Sowing performance by a metering mechanism of continuous flow in different slope conditions", ***Engenharia Agrícola***, Vol. 36, No. 5, (2016), 839-845. DOI: 10.1590/1809-4430-Eng.Agric.v36n5p839-845/2016
4. Ghosal, M. K., Din, M. "Design and development of cup in cup feed metering seed drill for seed pattern characteristics study of paddy seeds". ***Ama-Agricultural Mechanization in Asia Africa and Latin America***, Vol. 47, No. 3, (2016), 54-59. DOI: 10.5829/IJE.2019.32.12C.13
5. Li, Y., He, X. T., Cui, T., Zhang, D. X.., Shi, S., Zhang, R., Wang, M. T.. "Development of mechatronic driving system for seed meters equipped on conventional precision corn planter". ***International Journal of Agriculture and Biological Engineering***, Vol. 8, No. 4, (2015), 1-9. DOI: 10.3965/j.ijabe.20150804.1717
6. Wang, J, W., Han, T., Wang, J. F., Li, X., Hang, H. N. "Optimization design and experiment on ripple surface type pickup finger of precision maize seed metering device". ***International Journal of Agriculture and Biological Engineering***, Vol. 10, No. 1, (2017), 61-71. DOI: 10.3965/j.ijabe.20171001.2050

7. Horabik, J., Molenda, M., Parafiniuk, P. "Discharge of rapeseeds from a model silo: Physical testing and discrete element method simulations", ***Computers and Electronics in Agriculture***, Vol. 97, (2013), 40-46. DOI: 10.1016/j.compag.2013.06.008
8. Luo, X. W., Ou, Z., Jiang, E.C., Li, Z.W., Huang S. X.. "Experimental research on precision rice direct-seeder with hill sowing". ***Transactions of the Chinese Society for Agricultural Machinery***, Vol. 36, No. 9, (2005), 37-40. DOI: 10.3969/j.issn.1000-1298.2005.09.010
9. Yu, J. J., Ding, Y. C., Liao, Y. T., Cong, J. L., Liao, Q. X.. "High-speed photography analysis of dropping trajectory on pneumatic metering device for rapeseed". ***Journal of Huazhong Agricultural University***, Vol. 33, No. 3, (2014), 103-108. DOI: 10.13300/j.cnki.hnlkxb.2014.03.018
10. Searle, C. L., Kocher, M. F., Smith, J. A., & Blankenship, E. E.. "Field slope effects on uniformity of corn seed spacing for three precision planter metering systems". ***Applied Engineering in Agriculture***, Vol. 24, No. 5, (2008), 581-586. DOI: 10.13031/2013.25270
11. Barr, J. B., Desbiolles, J. M. A., "Fielke John M. Minimising soil disturbance and reaction forces for high speed sowing using bentleg furrow openers". ***Biosystems Engineering***, Vol. 151, (2016), 53-64. DOI: 10.1016/j.biosystemseng.2016.08.025
12. Kocher, M. F., Coleman, J. M., Smith, J. A., & Kachman, S. D. "Corn seed spacing uniformity as affected by seed tube condition". ***Applied Engineering in Agriculture,*** Vol. 27, No. 2, (2011), 177-183. DOI: 10.13031/2013.36484
13. Brosh, T., Kalman, H., Levy, A., Peyron, I., Ricard, F.. "DEM-CFD simulation of particle comminution in jet-mill". ***Powder Technol***, Vol. 257, (2014), 104-112. DOI: 10.1016/j.powtec.2014.02.043
14. Yuan, G. Z., Zhang, T., Liu, Y. Q., . "Design of a Spoon Wheel Type Seed Metering Device and Simulation of Soybean Seeds By Discrete Elemen". ***Journal of Agricultural Mechanization Research***, Vol. 11, (2017), 25-29. DOI: 10.13427/j.cnki.njyi.2017.11.004
15. Liu, T., He, R. Y., Lu, J.,.Zou, Y., Zhao, M. M.. "Simulation and verification on seeding performance of nest hole wheel seed-metering device based on EDEM". ***Journal of South China Agricultural University***, Vol. 37, (2016), 126-132. DOI: 10.7671/j.issn.1001-411X.2016.03.020
16. Shi, S., Zhang, D. X., Yang, L., Cui, T., Li, K. H., Yin, X. W.. "Simulation and verification of seed-filling performance of pneumatic-combined holes maize precision". ***Transactions of the Chinese Society of Agricultural Engineering,*** Vol. 31, No. 3, (2015), 62-69. DOI: 10.3969/j.issn.1002-6819.2015.03.009
17. Safari, M., Joudaki, J., Ghadiri, Y.. "A Comprehensive Study of the Hydroforming Process of Metallic Bellows: Investigation and Multi-objective Optimization of the Process Parameters", ***International Journal of Engineering, Transactions B: Applications***, Vol. 32, No. 11, (2019) 1681-1688. DOI: 10.5829/IJE.2019.32.11B.19
18. Kazemian, M. E., Gandjalikhan, Nassab, S. A., "Thermodynamic Analysis and Statistical Investigation of Effective Parameters for Gas Turbine Cycle using the Response Surface Methodology", ***International Journal of Engineering, Transactions B: Applications***, Vol. 33, No. 5, (2020), 894-905. DOI: 10.5829/IJE.2020.33.05B.22
19. Patel, S. S., Prajapati, J. M., "Experimental Investigation of Surface Roughness and Kerf Width During Machining of Blanking Die Material on Wire Electric Discharge Machine", ***International Journal of Engineering, Transactions A: Basics*** Vol. 31, No. 10, (2018), 1760-1766. DOI: 10.5829/ije.2018.31.10a.19
20. Wang, J. W., Tang, H., Wang, Q., Zhou W. Q., Yang, W. P., Shen, H. G.. "Numerical simulation and experiment on seeding performance of pickup finger precision seed-metering device based on EDEM". ***Transactions of the Chinese Society of Agricultural Engineering***, Vol. 31, No. 21, (2015), 43-50. DOI: 10.11975/j.issn.1002-6819.2015.21.006
21. Cao, X. Y., Liao, Y. T., Cong, J. L.. "Design and Experiment on Metering Hole Structure of Centrifugal Precision Metering Device for rapeseed". ***Transactions of the Chinese Society for Agricultural Machinery***, Vol. 45, (2014), 40-46. DOI: 10.6041/j.issn.1000-1298.2014.S0.007
22. Ding L., Yang L., Zhang D.X., Cui T. G., Xiao J., "Design and experiment of seed plate of corn air suction seed metering device based on DEM-CFD". ***Transactions of the Chinese Society for Agricultural Machinery***, Vol. 50, No. 5, (2019), 50-60. doi: 10.6041/j.issn.1000-1298.2019.05.006
23. Shi S., Zhou J.L., Liu H., Fang H.M., Jian S.Ch., Zhang R.F., "Design and experiment of pneumatic precision seed-metering device with guided assistant seed-filling". ***Transactions of the Chinese Society for Agricultural Machinery***, Vol. 50, No. 5, (2019), 61-70. doi:10.6041/j.issn.1000-1298.2019.05.007
24. Kamgar, S., Eslami, M. J., Maharlouie, M. M.. "Design, development and evaluation of a mechatronic transmission system to improve the performance of a conventional row crop planter". ***International Journal of Agronomy and Plant Production***, Vol. 4, No. 3, (2012), 480-487. DOI: 10.13031/2013.41987
25. Yang, L., Yan, B. X., Cui, T., Yu, Y. M., He, X. T., Liu, Q. W., Liang, Z. J., Yin, X. W., Zhang, D. X.. "Global overview of research progress and development of precision maize planters". ***International Journal of Agricultural and Biological Engineering***, Vol. 9, No. 1, (2016), 9-26. DOI: 10.3965/j.ijabe.20160901.2285
26. Wang, X. Y.. "Improve design and experiment on spoon of spoon precision seed metering device". ***Journal of Northeast Agricultural University***, Vol. 46, No. 12, (2015), 79-85. DOI: 10.19720/j.cnki.issn.1005-9369.2015.12.012
27. JB/T10293-2001 "Single grain (precision) planter technical conditions". ***People's Republic of China machinery industry standard***, (2001). DOI: 10.3969/j.issn.1002-6819.2014.08.005
28. Shi, L. R., Wu, J. M., Sun, W., Zhang, F. W., Sun, B. G., Liu, Q. W., Zhao, W.Y.. "Simulation test for metering process of horizontal disc precision metering device based on discrete element method". ***Transactions of the Chinese Society of Agricultural Engineering***, Vol. 30, No. 8, (2014), 40-48. DOI: 10.3969/j.issn.1002-6819.2014.08.005
29. Singh, R.C., Singh, G., Saraswat, D.C.. "Optimisation of design and operational parameters of a pneumatic seed metering device for planting cottonseeds". ***Biosystems Engineering***, Vol. 92, No. 4, (2005), 429-438. DOI: 10.1016/j.biosystemseng.2005.07.002
30. Xu, D. "Research and Application of Wheat Precision Seeding Machinery". ***Agricultural Science & Technology and Equipment***, Vol. 6, (2015), 79-80. DOI: 10.16313/j.cnki.nykjyzb.2015.06.030
31. Wang, J. W., Tang, H., Wang, J. F.. "Analysis and Experiment of Guiding and Dropping Migratory Mechanism on Pickup Finger Precision Seed Metering Device for Corn". ***Transactions of the Chinese Society for Agricultural Machinery,*** Vol. 8, No. 1, (2017), 29-37. DOI: 10.6041/j.issn.1000-1298.2017.01.005
32. Lei, X. L., Liao, Y. T., Liao, Q. X. "Simulation of Seed Motion in Seed Feeding Device with DEM-CFD Coupling Approach for Rapeseed and Wheat". ***Computers and Electronics in Agriculture,*** Vol. 131, (2016), 29-39. DOI: 10.1016/j.compag.2016.11.006

Persian Abstract

چکیده

این مطالعه یک دستگاه اندازه‌گیری پنوماتیکی ترکیبی (SMD) دانه (بذر)را ارائه می‌دهد که نه تنها می‌تواند ظرف بذرها را پر، حمل و اندازه‌گیری کند، بلکه می‌تواند سریعاً بین حالت‌های اندازه گیری و تمیز کردن بذر تغییر عملکرد دهد و دانه‌ها را به‌طور کامل و سریع تمیز کند. حالت‌های تمیزکردن، انتقال و روش‌های اندازه گیری بذر در SMD بر اساس یک مدل سینماتیکی نظری انجام شد. علاوه بر این ، یک آزمون سه عاملی و سه سطحی متعامد با استفاده از یک میز آزمون عملکرد تنظیم‌شده برای SMD و نرم افزار Design-Expert انجام شد. ترکیبی از پارامترهایی که منجر به کمترین میزان بذرپاشی نادرست (۰.۵۹٪) شد، فشار هوای ۲.٦۷ کیلو پاسکال و عرض شکاف ۲.۸۳ میلی متر بود. طرح بهینه‌شده که منجر به سرعت کاشت بذر چندگانه‌ی نسبتاً پایین (٤.۳٪) و در عین حال برآورده کردن سایر نیازها شد به شرح زیر است: فشار هوای ۲.۳۵ کیلو پاسکال، عرض شکاف ۲.۷۸ میلی متر و سرعت اندازه گیری بذر از ۲۰ r/min. سپس، یک آزمایش میدانی با استفاده از یک نمونه آزمایشی بذرپاش پنبه ترکیبی پنوماتیکی انجام شد. با این که میزان کاشت بذر نادرست و جوانه‌زنی مجدد در آزمایش میدانی هر دو تا حدودی بالاتر از مقادیری بود که از آزمایش میز آزمایشگاهی به دست می‌آمد، اما هنوز هم نیازهای کاشت دقیق را برآورده می‌کردند. آزمون میدانی صحت تحلیل نظری و آزمون میز آزمایشگاهی را تأیید کرده و به عنوان پایه‌ای برای تولید نمونه اولیه و مقبولیت آن عمل می‌کند.

International Journal of Engineering

Journal Homepage: www.ije.ir

Mechanical Properties Analysis of Bilayer Euler-Bernoulli Beams Based on Elasticity Theory

Z. Zhang*[a], C. Zhang[b]

[a] *Zhejiang Sci-Tech University, Hangzhou, Zhejiang Province – 928, No.2 Avenue, Xiasha, China*
[b] *Minmetals Yingkou Medium Plate CO., LTD, Yingkou, Liaoning Province, China*

PAPER INFO

Paper history:
Received 11 March 2020
Received in revised form 04 April 2020
Accepted 12 June 2020

Keywords:
Bilayer Beam
Euler-Bernoulli Hypothesis Model
Natural Frequency
Static Deflection

ABSTRACT

This paper analyzes the effects of structures and loads on the static bending and free vibration problems of bilayer beams. Based on static mechanical equilibrium and energy equilibrium, the static and dynamic governing equations of bilayer beam are established. It is found that the value of the thickness ratio has a significant effect on the static and dynamic responses of the beam, and the structure factors have their own critical value. When the value of the relative thickness is lower than its critical value or the length thickness ratio is greater than its critical value, the static and dynamic responses of the beam increase obviously. The results reveal that a critical value exists in bilayer beam, the value has noticeable influence on the mechanical properties of bilayer beams. Therefore, investigators should predict the critical structures accurately, when they design the bilayer beam.

***doi**: 10.5829/ije.2020.33.08b.25*

NOMENCLATURE

M	Bending moment (N·mm)	$w(x,t)$	Amplitude (mm)
F_s	Shear force (N)	La	Lagrange's function
q	Uniformly distributed load (N/mm)	k	The stiffness of an elastic foundation
L	Beam length (mm)	u_i	Displacement vector
h	Thickness (mm)	$m=E_1/E_2$	Ratio of elasticity modulus
b	Width (mm)	**Greek Symbols**	
w	Deflection (mm)	$\boldsymbol{\sigma}$	Stress tensor
E	Material elastic modulus (GPa)	ε	Strain tensor
I	Second moment of cross-sectional area (mm^4)	ω	Natural frequency (Hz)
d	Distance from the neutral layer to the bottom layer	ξ	Relative thickness
A	Cross-sectional area of the beam (mm^2)	υ	Poisson's ratio
$\boldsymbol{U}$	Strain energy (J)	ρ	Density (kg/m^3)
$\boldsymbol{V}$	Work done by the external forces (J)	**Subscripts**	
$\boldsymbol{T}$	Kinetic energy(J)	e	Bilayer beam

1. INTRODUCTION

Beams are one of the major structures used widely in mechanical systems, such as energy harvesters [1], sensors [2] and the construction industry [3]. Haghpanah [4] and Laminou [5] found that the structure size and load would have a significant impact on the mechanical properties of the mechanical systems. Hence, a lot of work has been undertaken to explore the mechanical properties of beams.

*Corresponding Author Institutional Email: *zzj512682701@126.com* (Z. Zhang)

Please cite this article as: Z. Zhang, C. Zhang, Mechanical Properties Analysis of Bilayer Euler-Bernoulli Beams Based on Elasticity Theory, International Journal of Engineering (IJE), IJE TRANSACTIONS B: Applications Vol. 33, No. 8, (August 2020) 1662-1667

Scarpa [6] and Damanpack [7] analyzed the elastic mechanical properties of a single layer beam model. However, with the research continuing in-depth, many researchers have found that the power output of mechanical systems applied to composite beam structures are higher than that on monolayer beam structures. Kok et al. [8] found that the multilayer piezoelectric cantilever beam has a higher power output efficiency than monolayer. Chun et al. [9] observed that increasing the number of actuator piezoelectric layer can improve the actuator power output effectively.

To predicate the beams mechanical properties accurately, some researchers use the business software [10-11]. For example, Al-Qasem et al. [12] calculated the shear stress in a cantilever beam by ANSYS software. However, theoretical basis is lacked in this approach. Therefore, many researchers used a mathematical calculation which are based on mechanical theory to study the mechanical properties of beams. For example, Lotfavar [13] and Alashti [14] applied Hamilton's variational principle to establish the governing equations of monolayer beams. Torabi et al. [15] investigated free vibration of a beam in variational iteration method which is based on mechanical theory. JafarSadeghi-Pournaki [16] analyed static deflection problem of beams by Galerkin.

Physical properties of the materials in each layer in the multilayer beam vary. Therefore, to calculate the location of neutral axis of the multilayer beam, an alternative two-variable method has been used to solve the bending problem of bilayer beam subjected to external moments and internal stresses by Zhang et al. [17]. Rastegarian and Sharifi [18] studied inter-story drifts in conventional RC multilayer moment frames. Based on the elastic equivalent relationship, T-J. Subsequently, Zhang et al. [19] analyzed the elastic bending deformation of bilayer beams by alternative two variable methods. Hsueh et al. [20] presented a new analytical model to obtain the mechanical properties of the multilayer beams. They also studied the multilayer problems of stress distribution [21] and elastic thermal stresses in two dissimilar materials [22]. Although, they have taken a lot of work on the mechanical properties of the multilayer beams, but most cases they neglected the effect of the structures on the mechanical properties of the multilayer beams.

In summary, based on the classical elastic theory, the object of this research is to find out the effects of structures and loads on the static bending and free vibration problems of bilayer beams.

The structure of the article is arranged as following; Based on the bilayer Euler-Bernoulli beams elasticity mechanical theory model including static governing equations and dynamic governing equations are established in section 2. In Section 3, the effect of loads and structures on the static and dynamic response of the beam are assessed. Finally, conclusion of this paper appears in Section 4.

2. GOVERNING EQUATION

The two-dimensional schematic diagram of a Euler-Bernoulli beam is shown in Figure 1. The hypothesis of Euler–Bernoulli beam ignores the effect of the centroidal axis rotation angle of the beam. The displacement field is written as:

$$u_x = z\frac{dw(x)}{dx}, u_y = 0, u_z = w(x) \tag{1}$$

where u_x, u_y, u_z are the displacement vector, and $w(x)$ the deflection of the beam.

The beam strain Equation (2) and stress Equation (3).

$$\varepsilon_{xx} = \frac{du_x}{dx} = z\frac{d^2w(x)}{dx^2} \tag{2}$$

$$\sigma_{xx} = Ez\frac{d^2w(x)}{dx^2} \tag{3}$$

The relation between bending moment, shear force and displacement is shown as Equation (4).

$$\begin{cases} M = -EI\dfrac{d^2w}{dx^2} \\ F_s = -\dfrac{d}{dx}\left(EI\dfrac{d^2w}{dx^2}\right) \end{cases} \tag{4}$$

2. 1. Static Theoretical Model The location of the neutral axis can be calculated by Equation (5) [23], d represents the distance from the neutral layer to the bottom layer.

$$d = \left[1 + \frac{me(1+e)}{1+me}\right]\frac{h_2}{2} \tag{5}$$

where $m=E_1/E_2$, $e=h_1/h_2$, E_1 and E_2 represent the material elastic moduli of layers no.1 and 2, h_1 and h_2 represent the thickness of layers no. 1 and 2. Equation (6) is the equivalent unit length mass equation of the

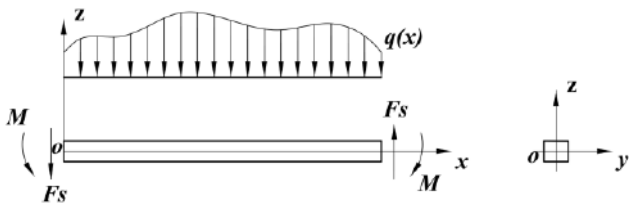

Figure 1. Schematic diagram of Euler-Bernoulli beam

bilayer beam. Equation (7) is the equivalent bending stiffness equation of the bilayer beam.

$$(\rho A)_e = \rho_1 A_1 + \rho_2 A_2 \tag{6}$$

$$(EI)_e = E_1 I_1 + E_2 I_2 + E_1 A_1 \left(h_2 + \frac{h_1}{2} - d \right)^2 + E_2 A_2 \left(d - \frac{h_2}{2} \right)^2 \tag{7}$$

where A is the cross-sectional area of the beam and I is the second moment of cross-sectional area.

Inserting Equations (6) and (7) into Equation (4), yields the bilayer beam static governing equation.

$$(EI)_e \frac{d^4 w(x)}{dx^4} = -q(x) - kw(x) \tag{8}$$

Solving Equation (8) then gives:

$$w(x) = C_1 \cos(\beta x)\cosh(\beta x) + C_2 \sin(\beta x)\sinh(\beta x) + C_3 \cos(\beta x)\sinh(\beta x) + C_4 \sin(\beta x)\cosh(\beta x) - \frac{q}{k} \tag{9}$$

where

$$\beta = \left(\frac{k}{4(EI)_e} \right)^{1/4} \tag{10}$$

As shown in Figure 2, the characterized of a cantilever beam is that one end is clamped, the other end is free. The boundary conditions are shown in Equation (11).

$$w(0) = 0, \frac{dw(0)}{dx} = 0, \frac{d^2 w(L)}{dx^2} = 0, \frac{d^3 w(L)}{dx^3} = 0 \tag{11}$$

Substituting Equation (9) into Equation (11), then the value of C_1, C_2, C_3, and C_4 can be obtained.

2. 2. Dynamic Theoretical Model Energy equilibrium is applied to solve the dynamic problem in this paper. The strain energy $\boldsymbol{U}$ is given by:

$$\mathrm{U} = \frac{1}{2} \int_{\mathrm{V}} \sigma_{ij} \varepsilon_{ij} dV \qquad (i, j = x, y, z) \tag{12}$$

Inserting Equations (2) and (3) into Equation (12), yields the bilayer beam strain energy $\boldsymbol{U}$:

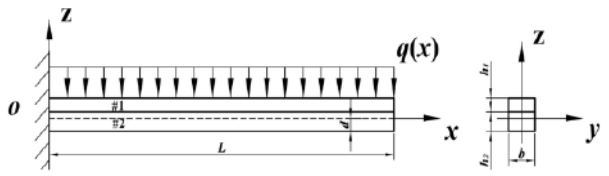

Figure 2. Cantilever beam in static distributed load

$$\boldsymbol{U} = \frac{1}{2} \int_0^L (EI)_e \left(\frac{\partial^2 w(x,t)}{\partial x^2} \right)^2 dx \tag{13}$$

The work done by the external forces $\boldsymbol{V}$ as shown in Figure 1, reads:

$$\boldsymbol{V} = -\int_0^L q(x,t) w(x,t) dx \tag{14}$$

And the kinetic energy $\boldsymbol{T}$ can be written as:

$$\boldsymbol{T} = \frac{1}{2} \int_0^L \rho(x) A(x) \left(\frac{\partial w(x,t)}{\partial t} \right)^2 dx \tag{15}$$

By means of Hamiltonian principle, the dynamic governing equation can be determined.

$$\delta \left\{ \int_{t_1}^{t_2} (\boldsymbol{T} - \boldsymbol{V} - \boldsymbol{U}) dt \right\} = 0 \tag{16}$$

Substituting Equations (13), (14) and (15) into Equation (16), then leads to:

$$\delta \int_{t_1}^{t_2} \int_0^L \left[\frac{1}{2} (\rho A)_e \left(\frac{\partial^2 w(x,t)}{\partial t^2} \right)^2 - \frac{1}{2} (EI)_e \left(\frac{\partial^2 w(x,t)}{\partial x^2} \right)^2 + q(x,t) w(x,t) \right] dx dt = 0 \tag{17}$$

Lagrange's function:

$$La = \frac{1}{2} \rho A \left(\frac{\partial^2 w(x,t)}{\partial t^2} \right)^2 - \frac{1}{2} (EI) \left(\frac{\partial^2 w(x,t)}{\partial x^2} \right)^2 + qw \tag{18}$$

Through the calculation, Equation (17) can be written as:

$$\int_{t_1}^{t_2} \int_0^L \left[-(EI)_e w^{(4)} - \rho A \ddot{w} + q \right] \delta w dx dt - \int_{t_1}^{t_2} \left[(EI)_e w^{(4)} \delta w \right]_0^L dt - \int_{t_1}^{t_2} \left[(EI)_e w' \delta w' \right]_0^L dt + \int_0^L \left(\dot{w} \delta w \right)_{t_1}^{t_2} dx = 0 \tag{19}$$

where

$$w' = \frac{\partial w}{\partial x}, w^{(3)} = \frac{\partial^3 w}{\partial x^3}, w^{(4)} = \frac{\partial^4 w}{\partial x^4}, \ddot{w} = \frac{\partial^2 w}{\partial t^2} \tag{20}$$

According to Equation (19), without any external force, $q(x,t)$=0, the dynamic governing equation of the bilayer beam will transform as the free vibration Equation (32):

$$(\rho A)_e \frac{\partial^2 w(x,t)}{\partial t^2} + (EI)_e \frac{\partial^4 w(x,t)}{\partial x^4} = 0 \tag{21}$$

where $w(x,t)$ is a function of the coordinate x and time t, and the variable separation approach can be added to solve Equation (21).

$$w(x,t) = W(x) \bullet H(t) \tag{22}$$

Inserting Equation (22) into Equation (21), yields:

$$-\frac{(EI)_e}{(\rho A)_e} \bullet \frac{\frac{d^4W(x)}{dx^4}}{W(x)} = \frac{\frac{d^2H(t)}{dt^2}}{H(t)} \tag{23}$$

where the function variables on both sides of the equal sign is different. Equation (23) can be set up only when both equations are equal to a constant. Suppose the constant equals to $-\omega^2$, the ordinary differential equation of $W(x)$ can be given as:

$$(EI)_e \frac{d^4W(x)}{dx^4} - \omega^2 (\rho A)_e W(x) = 0 \tag{24}$$

Solving Equation (24) then gives amplitude equation:

$$W(x) = C_5 \sin(\gamma x) + C_6 \cos(\gamma x) + C_7 \sinh(\gamma x) + C_8 \cosh(\gamma x) \tag{25}$$

where

$$\gamma = \left(\frac{(\rho A)_e \omega^2}{(EI)_e} \right)^{1/4} \tag{26}$$

Then yields the natural frequency ω:

$$\omega = (\gamma L)^2 \sqrt{\frac{(EI)_e}{(\rho A)_e L^4}} \tag{27}$$

The schematic diagram of the cantilever beam in free vibration is shown as Figure 3. Substituting amplitude Equation (25) into the boundary condition of cantilever beam Equation (11), then leads to:

$$\cos(\gamma_i L)\cosh(\gamma_i L) = -1 \tag{28}$$

2. 3. Analytical Flowchart Calculation program for static and dynamic responses is accomplished using MATLAB. The analytical flowchart is shown in Figure. 4.

3. RESULTS AND DISCUSSIONS

To illustrate the static and dynamic responses of bilayer beam, the PZT film / Si substrate bilayer system is considered as an example. In this case, the material constants are: elastic modulus of layer no. 1, E_1=101GPa, elastic modulus of layer no. 2, E_2=168.9GPa, $\rho_1=7.5\times10^3$kg/m^3, $\rho_2=2.331\times10^3$kg/m^3 [24]. The width is set as $b=4h$ and the length is set as $L=200h$. h represents total thickness of the beam $h=h_1+h_2=0.5\times10^{-3}$m. The ratio of the thicknesses h_1/h_2 is set to 1/9.

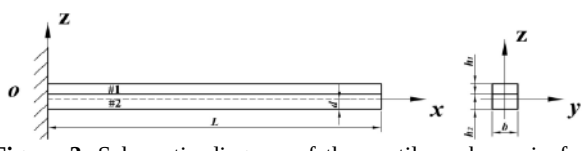

Figure 3. Schematic diagram of the cantilever beam in free vibration

3. 1. Static Responses of Bilayer Beams

Effect on the deflection with respect to different loads for a cantilever beam is shown as Figure 5. Under the material and structure dimension remain constant, the static deflection of the cantilever beam increases as the static distributed load increase. The maximum deflection of the cantilever beam is appeared at the free end of the beam (at $x=L$). In the process of the distributed load increases from 10N/m to 50N/m, the

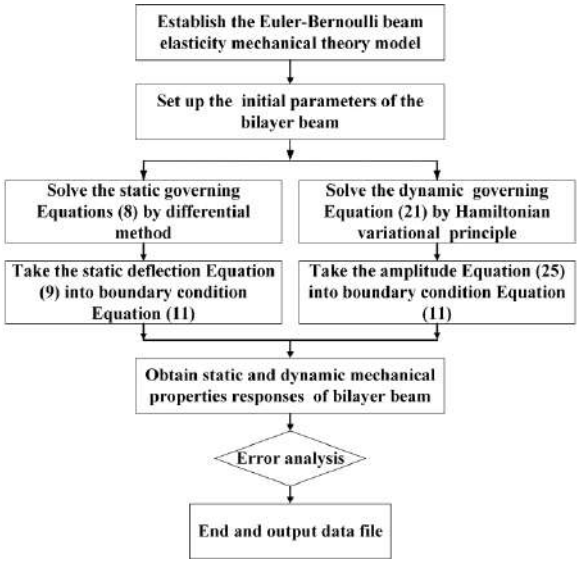

Figure 4. Analytical flowchart of the bilayer beam

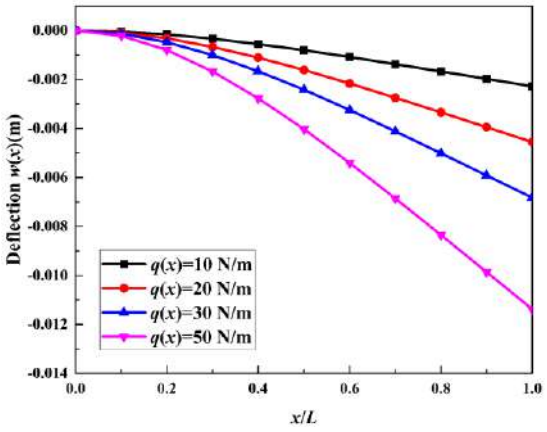

Figure 5. Deflection of the cantilever bilayer beam based on four different distributed load

beam maximum deflection increases from 0.01mm to 0.09mm.

The thickness ratio is an important factor. With the distributed load $q(x)$=20N/m, the effect of the thickness ratio on cantilever beam deflection at $x=L$ is analyzed. From Figure 6, it is found that the cantilever deflection decreases as the increases of the upper layer h_1 thickness proportion with the total thickness remain constant. When the ratio of h_1/h_2 increases from 1 to 8, absolute value of deflection of the cantilever rapidly decreases from 0.053mm to 0.046mm. However, when the thickness ratio increases from 8 to 30, the absolute value of deflection increases only 0.002mm. It is observed that when the thickness ratio of the bilayer cantilever beam exceeds 8, the effect of the thickness ratio on beam deflection can be ignored.

3. 2. Dynamic Responses of Bilayer Beams

The influence of the relative thickness on natural frequency of the cantilever beam, ω, in free vibration is shown in Figure 7. The dimensionless relative thickness

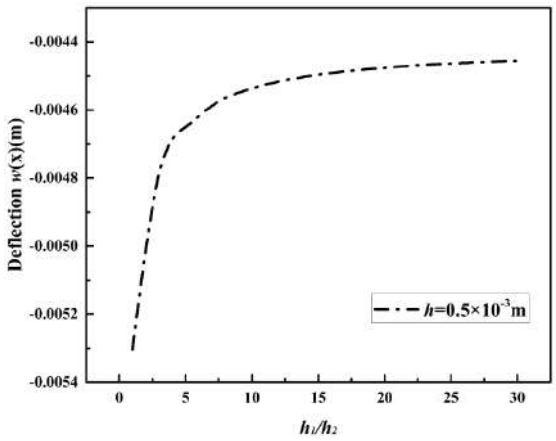

Figure 6. Effect of thickness ratio on cantilever bilayer beam deflection

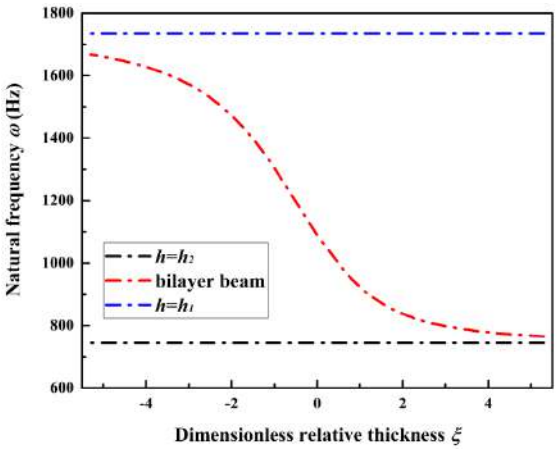

Figure 7. Effect of relative thickness on natural frequency of the cantilever bilayer beam

equation is shown as Equation (43). With the total thickness remains constant, when the value of the relative thickness is larger than 4 (the value of the thickness of layer no. 1 is 17 times greater than the value of layer no. 1), the natural frequency of the bilayer beam is approximately equal to that of the single layer no. 2 beam 744.86 Hz. When the value of the relative thickness is less than -4 (the value of the thickness of layer no. 2 beam is 1/17 times less than the value of layer no. 1), the natural frequency of the bilayer beam is approximately equal to that of the single layer no. 1 beam 1734.4Hz.

$$\xi = \frac{\left(h_1 - h_2\right)}{\sqrt{h_1 h_2}} \tag{43}$$

4. CONCLUSIONS

This paper analyzes the static and dynamic problems of the Euler-Bernoulli bilayer beams on the basis of elasticity theory. The static and dynamic governing equations of bilayer beam are established by static mechanical equilibrium and energy equilibrium. It is found that the loads and beam structure have a significant effect on the static and dynamic responses of the bilayer beam. Under the static loads, the deflection increases with the increase of the static load. The thickness ratio and the length thickness ratio of the bilayer beam have their own critical values. When the thickness ratio is less than its critical value or value of the length thickness ratio is higher than its critical value, the static deflection of bilayer beam will change significantly. Under the free vibration, with the increase of the relative thickness, the natural frequency of bilayer beam is gradually transferred from the single layer beam of one material to the single layer beam of another material. When the relative thickness exceeds its critical value, the natural frequency of the bilayer beam is approximately equal to that of the single beam.

5. REFERENCES

1. Wang, L., Ding, J. J., Jiang, Z. D., Jiang, Z. D., Luo, G. X. Zhao, L., Lu, D. J., Yang, X. and Maeda, R., "A packaged piezoelectric vibration energy harvester with high power and broadband characteristics", ***Sensors and Actuators A: Physical***, Vol. 295, (2019), 629-636. DOI: 10.1016/j.sna.2019.06.034
2. Ferraria,M., Alghisi, D., Baù, M. and Ferrari,V., "Nonlinear Multi-Frequency Converter Array for Vibration Energy Harvesting in Autonomous Sensors", in 26th European Conference on Solid-State Transducers (Eurosensors) in Wroclaw Univ Technol, Fac Microsystem Elect & Photon, Krakow, POLAND 2012, Procedia Engineering, Vol. 47, (2012). DOI: 10.1016/j.proeng.2012.09.171
3. Khorramshahi, M. R. and Mokhtari, A., "Automatic

Construction by Contour Crafting Technology", ***Emerging Science Journal***, Vol. 1, No. 4, (2017), 1-28. DOI: 10.28991/esj-2017-01113

4. Haghpanah, F. and Foroughi H., "Size and Shape Optimization of Space Trusses Considering Geometrical Imperfection-Sensitivity in Buckling Constraints", ***Civil Engineering Journal***, Vol. 3, No. 12, (2018), 1314-1326. DOI: 10.28991/cej-030960
5. Laminou, L. M., Liu, Z. J., and Chen, X. H., "Extreme Events design and Mitigation Methods: A Review", ***Civil Engineering Journal***, Vol. 5, No. 6, (2019), 1424-1439. DOI: 10.28991/cej-2019-03091342
6. Scarpa, F., Adhikari, S. and Phani, A. S., "Effective elastic mechanical properties of single layer graphene sheets", ***Nanotechnology***, Vol. 20, No. 6, (2009), 1-11. DOI: 10.1088/0957-4484/20/6/065709
7. Damanpack, A. R., Bodaghi, M., Aghdam, M. M. and Shakeni, M., "On the vibration control capability of shape memory alloy composite beams", ***Composite Structures***, Vol. 110, (2014), 325-334. DOI: 10.1016/j.compstruct.2013.12.002
8. Kok, S. L., White, N. M. and Harris, N. R., "Fabrication and characterization of free-standing thick-film piezoelectric cantilevers for energy harvesting", ***Measurement Science and Technology***, Vol. 20, No. 12, (2009), 1-13. DOI: 10.1088/0957-0233/20/12/124010
9. Chun, D. M., Sato, M. and Kanno, I., "Precise measurement of the transverse piezoelectric coefficient for thin films on anisotropic substrate", ***Journal of Applied Physics***, Vol. 113, No. 4, (2013), 044111.1-044111.19. DOI: 10.1063/1.4789347
10. Alameh, A. H., Gratuze, M. and Nabki, F., "Impact of Geometry on the Performance of Cantilever-Based Piezoelectric Vibration Energy Harvesters", ***IEEE Sensors Journal***, Vol. 22, No. 15, (2019), 10316-10326. DOI: 10.1109/JSEN.2019.2932341
11. Wang, L., Zhao, L. B., Jiang, Z. D., Luo, G. X., Yang, P., Han, X. G., Li, X. and Maeda, R., "High accuracy Comsol simulation method of bimorph cantilever for piezoelectric vibration energy harvesting", ***AIP Advances***, Vol. 9, No. 9, (2019), 095067.1-095067.7. DOI: 10.1063/1.5119328
12. Al-Qasem, I., Hasan, A. R., Abdulwahid, M. Y. and Galobardes, I., "Comparison between Analytical Equation and Numerical Methods for Determining Shear Stress in a Cantilever Beam", ***Civil Engineering Journal***, Vol. 4, No. 2, (2018), 258-265. DOI: 10.28991/cej-030989
13. Lotfavar, A. and Mosalaeifard, A. H., "Three-dimensional Vibration Suppression of an Euler-Bernoulli Beam via Boundary Control Method", ***International Journal of Engineering-Transactions B: Applications***, Vol. 28, No. 5, (2015), 755-763. DOI: 10.5829/idosi.ije.2015.28.05b.14
14. Alashti, R. A, and Abolghasemi, A. H., "A Size-dependent Bernoulli-Euler Beam Formulation based on a New Model of Couple Stress Theory", ***International Journal of Engineering-Transactions C: Aspects,*** Vol. 27, No. 6, (2014), 951-960. DOI: 10.5829/idosi.ije.2014.27.06c.14
15. Torabi, K., Ghassabib, M., Heidari-Rarania, M., and Sharific, D., "Variational Iteration Method for Free Vibration Analysis of a Timoshenko Beam under Various Boundary Conditions" , ***International Journal of Engineering- Transactions A: Basics***, Vol. 30, No. 10, (2017), 1565-1572. DOI: 10.5829/ije.2017.30.10a.18
16. JafarSadeghi-Pournaki, I., Zamanzadeh, M. R., Madinei, H. and Rezazadeh, G., "Static Pull-in Analysis of Capacitive FGM Nanocantilevers Subjected to Thermal Moment using Eringen's Nonlocal Elasticity", ***International Journal of Engineering-Transactions A: Basics***, Vol. 27, No. 4, (2014), 633-642. DOI: 10.5829/idosi.ije.2014.27.04a.15
17. Zhang, N. H. and Chen, J. Z., "Elastic bending analysis of bilayered beams by an alternative two-variable method", ***European Journal of Mechanics, A/Solids***, Vol. 28, No. 2, (2009), 284-288. DOI: 10.1016/j.euromechsol.2008.07.004
18. Rastegarian, S. and Sharifi, A., "An Investigation on the Correlation of Inter-Story Drift and Performance Objectives in Conventional RC Frames", ***Emerging Science Journal***, Vol. 2, No. 3, (2018), 140-147. DOI: 10.28991/esj-2018-01137
19. Zhang, N. H. and Xing, J. J., "An alternative model for elastic bending deformation of multilayered beams", ***Journal of Applied Physics***, Vol. 100, No. 10, (2006), 103519.1-103519.5. DOI: 10.1063/1.2372578
20. Hsueh, C. H., "Thermal stresses in elastic multilayer systems", ***Thin Solid Films***, Vol. 418, No. 2, (2002), 182-188. DOI: 10.1016/S0040-6090(02)00699-5
21. Hsueh, C. H., "Stress distribution and curvature in graded semiconductor layers", ***Journal of Crystal Growth***, Vol. 258, No. 3-4, (2003), 302-309. DOI: 10.1016/S0022-0248(03)01563-X
22. Hsueh, C. H., and Lee, S., "Modeling of elastic thermal stresses in two materials joined by a graded layer", ***Composites Part B-Engineering***, Vol. 34, No. 8, (2003), 747-752. DOI: 10.1016/S1359-8368(03)00088-X
23. Chuang, T. J. and Lee, S., "Elastic flexure of bilayered beams subject to strain differentials", ***Journal of Materials Research***, Vol. 15, No. 12, (2000), 2780-2788. DOI: 10.1557/JMR.2000.0397
24. Deshpande, M. and Saggere, L., "PZT thin films for low voltage actuation: Fabrication and characterization of the transverse piezoelectric coefficient", ***Sensors & Actuators A***, Vol. 135, No. 2, (2007), 690-699. DOI: 10.1016/j.sna.2006.07.022

Persian Abstract

چکیده

در این مقاله اثر ساختارها و بارها بر روی خیز استاتیکی و مشکلات لرزش آزاد تیرهای دولایه بررسی شده است. براساس تعادل مکانیکی (استاتیکی) و تعادل انرژی، معادلات حاکم استاتیکی و دینامیکی تیر دولایه برقرار می‌شوند. مشخص شده است که مقدار نسبت ضخامت تأثیر معنی‌داری در واکنش استاتیکی و دینامیکی تیر دارد و عوامل سازه دارای اهمیت بحرانی خود هستند. هنگامی که مقدار ضخامت نسبی پایین‌تر از مقدار بحرانی آن است، یا نسبت ضخامت به طول از مقدار بحرانی آن بیشتر است، پاسخ های استاتیکی و دینامیکی تیر به وضوح افزایش می‌یابد. نتایج نشان می‌دهد که این مقدارهای بحرانی تأثیر چشم‌گیری بر خصوصیات مکانیکی تیرهای دولایه دارد. بنابراین، پژوهش‌گران در هنگام طراحی تیر دولایه باید ساختارهای بحرانی را به دقت پیش‌بینی کنند.

International Journal of Engineering

Journal Homepage: www.ije.ir

Vibration and Noise Reduction Optimization Design of Mine Chute with Foam Aluminum Laminated Structure

K. Yang*[a], J. Zou[a], J. Shen[b]

[a] College of Mechanical Engineer and Automation, Liaoning University of Technology, Jinzhou, China
[b] College of Mechanical Engineering, Liaoning Technical University, Fuxin, China

PAPER INFO

Paper history:
Received 06 February 2020
Received in revised form 25 March 2020
Accepted 11 June 2020

Keywords:
Chute
Foam Aluminum
Vibration Reduction
Noise Reduction
Experimental Research

ABSTRACT

The mining chute is an important equipment in the process of coal transportation and coal screening preparation. During the working process, the mining chute generates a lot of vibration and noise because of constant friction and impact of gangue and coal blocks. In order to reduce the vibration and noise during the operation of the chute, a new type of foam aluminum laminated structure is used to manufacture the mining chute. According to the characteristic of chute, the laminated structure is optimized by taking the vibration amplitude as the objective function and the thickness of the steel plate and the foam aluminum core plate as the design variables. Then, the vibration and noise reduction performance of two types of chute are evaluated through experiments and finite element simulation method. Results show that use of foam aluminum laminate structure to manufacture the chute can obviously increase the damping ratio of the system, which can effectively reduce the vibration amplitude of the chute. The average sound insulation performance of foam aluminum laminated chute is better than prototype chute, especially in the middle and high frequency section, which can be reduced by about 7.1 dB on average in comparison with prototype chute. So, the foam aluminum laminated structure chute has a more significant sound insulation and vibration reduction effects than the prototype chute.

***doi**: 10.5829/ije.2020.33.08b.26*

NOMENCLATURE

A	Steady-state amplitude of vibration (m)	V_0	Chute volume (m^3)
A_0	Equivalent static displacement (m)	V_1	Volume in the height direction of the chute (m^3)
F	Amplitude of exciting force (N)	M	Bending moment of chute panel
k	System equivalent stiffness	t_0	Thickness of the prototype chute plate (m)
w_c	Deflection of simply supported beam	g	Gravity (m/s^2)
$z(x)$	Cross section width	**Greek Symbols**	
x	Height in x-axis direction	β	Vibration amplification factor
y	Width in y-axis direction	λ	Frequency ratio
I_{xf}	Inertia moment of steel plate	ξ	Damping ratio
I_{xp}	Inertia moment of foam aluminum plate	ϕ	Inclination angle of the chute panel
s	Thickness of foam aluminum plate (m)	ρ_m	Density of coal
t	Thickness of steel plate (m)	ρ_f	Density of the Q235 steel
$(EI)_{eq}$	Equivalent bending stiffness	ρ_p	Density of the foam aluminum
E_f	Elastic module of Q235 (MPa)	σ_f	Maximum stress of the prototype chute
E_p	Elastic module of foam aluminum (MPa)	σ_{ps}	Yield stress of foam aluminum
m	Quality of foam aluminum chute panel (kg)	σ_{eq}	Maximum stress of the foam aluminum chute
V_f	Volume of the Q235 steel plate (m^3)	σ_p	Maximum stress of the foam aluminum plate

*Corresponding Author Institutional Email: *yangkunwh@163.com* (K. Yang)

Please cite this article as: K. Yang, J. Zou, J. Shen, Vibration and Noise Reduction Optimization Design of Mine Chute with Foam Aluminum Laminated Structure, International Journal of Engineering (IJE), IJE TRANSACTIONS B: Applications Vol. 33, No. 8, (August 2020) 1668-1676

V_p	Volume of the foam aluminum plate (m^3)	**Subscripts**	
Q	Gravity of coal	*f,p*	Inner and outer plate "*f*", foam aluminum plate"*p*"
F_t	Total pressure received by each chute panel		

1. INTRODUCTION

The mining chute is an important equipment in the process of coal transportation and coal preparation plant screening and grading. It plays the role of reloading, distributing, concentrating, aliquoting and adjusting the process flow, so that the materials conveyed continuously run along the line specified in the process flow to achieve the purpose of continuous production [1-3]. The mining chute is constantly subjected to the friction and impact of vermiculite and lump coal in the work process, which will generate a lot of vibration and noise. The noise level can reach more than 100 dB, and the highest can reach 115 dB or more, which seriously endangers the health of workers. It also causes noise pollution to the surrounding environment [4].

The vibration and noise reduction of mine chutes has always been a problem in China. The structure of the traditional chute is generally manufactured by the method of welding the inner liner of the steel plate, and the inner lining plate is mainly made of cast iron, carbon steel and polymer materials. For ordinary cast iron liner, its wear resistance is poor and impact toughness is low; cast stone and polymer liner have good wear resistance but low toughness; carbon steel and stainless steel liner have high toughness but low wear resistance; rubber liner have good toughness and strong shock absorption performance, but easy to fall off and block, and the service life is low [5]. Therefore, there is an urgent need for a new material preparation chute to achieve the purpose of vibration and noise reduction, thereby improving the service life of the chute and reducing the noise during operation.

Foam aluminum is a new type of structural and functional porous material that has developed rapidly in recent years. It has light weight, high specific stiffness and high specific strength, high damping and sound absorption, sound insulation, heat insulation, flame retardant, vibration damping, absorbing impact energy, electromagnetic shielding and other physical properties [6-8]. The laminated board with foam aluminum as the core can not only have many excellent properties of the foamed aluminum material, but also can solve the disadvantage of low strength of the single foam aluminum plate. At present, foam aluminum laminate materials have been applied in many fields of automobile manufacturing, mechanical engineering, civil engineering, aviation and aerospace engineering [9-10]. In this study, a new type of mining chute with foam aluminum laminated structure is established. As we know, the main part of chute operation noise is the impact noise caused by the collision of the coal block and the metal plate in the chute. Reducing the vibration of structure is an effective way to reduce the noise. So, the laminated structure is designed by taking vibration amplitude as optimization objective, and the thickness of steel plate and foam aluminum core plate as design variables. And then, the vibration and noise insulation performance of two types of chute are studied by the method of experiment and finite element simulation. The research flowchart is shown in Figure 1.

2. FREE VIBRATION PRINCIPLE AND OPTIMIZATI ON DESIGN OF FOAM ALUMINUM CHUTE

2. 1. Prototype and Foam Aluminum Laminated Chute In this study, a certain type of chute commonly used in coal mine was taken as an example; the shape and size are shown in Figure 2(a). This prototype chute is mainly used at the bottom of the vibration screen, and it is an additional transfer device for the purpose of centralizing the screened coal blocks. The size of the inlet and outlet parts depends on the requirements of the connected equipment. The width of the screen mesh is 600×600 mm, the drop from the bottom of the screen to the conveyor is 618 mm, and the conveyor width is 460 mm. Therefore, the cross section shape of the chute is square, the longitudinal section is a pyramid structure with the start side length of 600 mm, the end side length of 420 mm and the height of 468 mm. The thickness of steel plate on each side is 10 mm. The material of the prototype chute is Q235 steel plate, and its performance parameters are shown in Table 1.

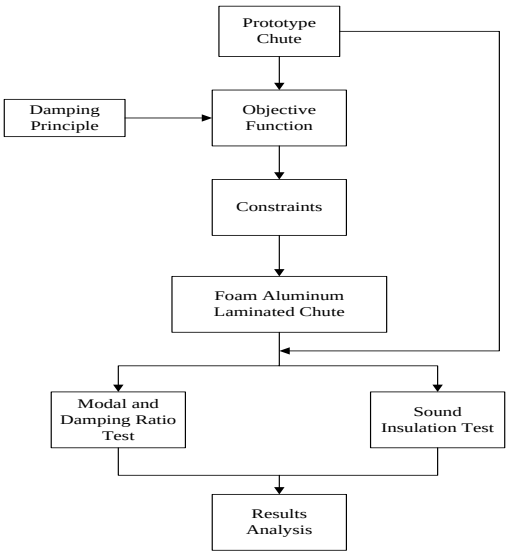

Figure 1. General framework of the study

TABLE 1. Material parameters

Material	Density/ (kg/m^3)	Elastic modulus/ GPa	Poisson's ratio	Yield strength/ MPa
Q235	7860	200	0.288	235
Foam aluminum	500	12	0.34	8.1

According to the prototype chute structure, the overall dimensions of the foam aluminum laminated chute are kept unchanged, but the original 10 mm thick steel plate is replaced by the thickness of the inner and outer steel plates *t* and the thickness of foam aluminum lamination plate *s*. The structural board is shown in Figure 2(b).

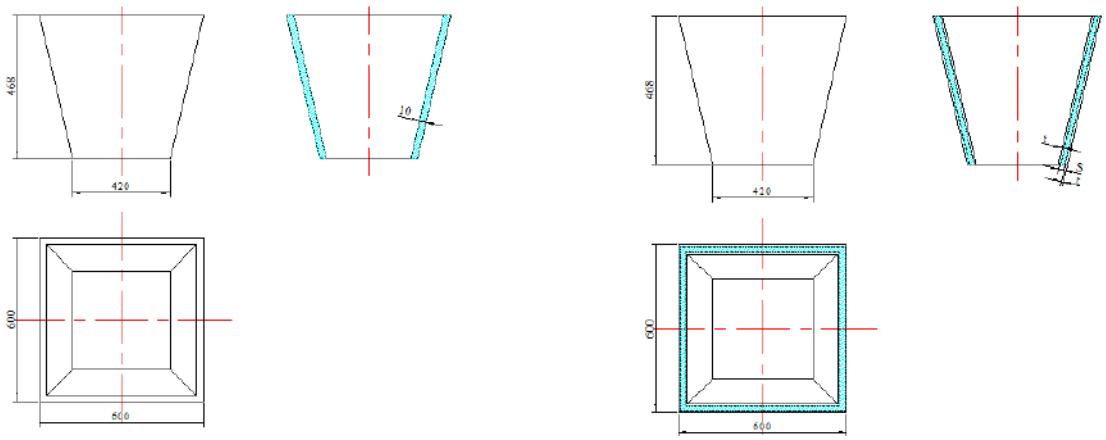

(a) Prototype chute (b) Foam aluminum chute

Figure 2. Chute structure size

2. 2. Principle of Free Vibration During the operation of foam aluminum chute, the chute panel is forced to vibrate by the continuous impact of materials. The steady-state amplitude of forced vibration which is the product of equivalent static displacement A_0 and the vibration amplification factor β [11-13], can be expressed as follows:

$$A=A_0 * \beta = \frac{F}{k\sqrt{(1-\lambda^2)^2+(2\xi\lambda)^2}} \quad (1)$$

where $A_0 = F / k$ is the equivalent static displacement, F is the amplitude of the exciting force, 387 N, k is the system equivalent stiffness, $\lambda = \omega / \omega_n$ is the frequency ratio, ω is the minimum excitation frequency, 500 Hz, $\omega_n = \sqrt{k / m}$ is the natural frequency of the system, m is the system quality, $\xi = c / c_0$ is the damping ratio and $c_0 = 2\sqrt{km}$ is the critical damping. The relationship of the amplification factor β, the frequency ratio λ and the damping ratio ξ are shown in Figure 3.

According to Equation (1), if the exciting force F is fixed, the amplitude of the system is affected by the spring coefficient k, the frequency ratio λ, and the damping ratio ξ. According to Figure 2, in order to reduce the amplitude of the system, the natural frequency of the system should be much smaller than the excitation frequency or increase the damping ratio ξ of the system.

According to the literature [14], the damping ratio of the open-cell foam aluminum laminate structure is 0.03 to 0.06. So, the damping ratio of laminated plate can be set as 0.04 initially.

The way to reduce the natural frequency of the system is to increase the mass of the system m or reduce the system equivalent stiffness k. But reducing the stiffness of the system also increases the equivalent static displacement of the system, which may cause the amplitude of the system to increase, so the design parameters require system considerations.

2. 3. Optimization Design of Foam Aluminum Chute The optimization purpose is to minimize the vibration amplitude of the foam aluminum chute, through

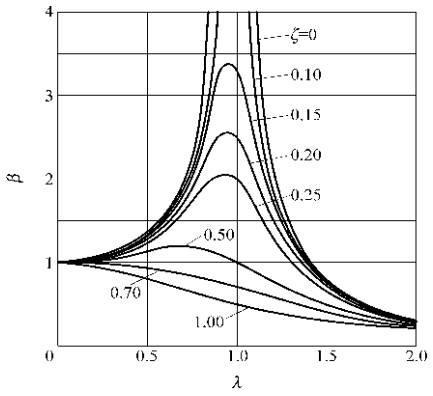

Figure 3. Magnification factor curve

determining the thickness of foam aluminum plate *s* and the thickness of steel plate *t*. So, the objective function is min *A(s, t)*.

In order to calculate the inertia moment of the chute panel, the coordinate system as shown in Figure 4 is established.

According to Figure 4, the cross-section width $z(x)$ of the panel is linearly changed along the height in x-axis direction, and it is satisfied as:

$$z(x) = 5x/13 + 0.42 \tag{2}$$

The inertia moment of a section of any foamed aluminum laminated structural panel can be divided into three parts, the inertia moment of the inner and outer steel plates I_{zf} , and the inertia moment of the aluminum foam plate I_{zp} . And the inner and outer steel plates have the same moment of inertia. Because of continuous variation of the foam aluminum layer and the cross-section of the panel, the total moment of inertia on the x-axis can be expressed as follows:

$$I_{zf} = \int_{-t/2}^{t/2} (y + \frac{t}{2} + \frac{s}{2})^2 (\frac{5}{13}x + 0.42)dy \tag{3}$$

$$I_{zp} = \int_{-s/2}^{s/2} y^2 (\frac{5}{13}x + 0.42)dy \tag{4}$$

Equations (3) and (4) are the total moments of inertia on the x-axis. The average moment of inertia is also divided by the height of the panel in the x-axis direction. Therefore, the equivalent bending stiffness of the foam aluminum chute panel can be determined:

$$\begin{aligned}(EI)_{eq} &= [2E_f I_{zf} \int_0^{0.168} dx + E_p I_{zp} / \int_0^{0.468} dx] = \\ &[2E_f \int_0^{0.168} \int_{-t/2}^{t/2} (y + \frac{t}{2} + \frac{s}{2})^2 (\frac{5}{13}x + 0.42)dydx + \\ &E_p \int_0^{0.468} \int_{-s/2}^{s/2} y^2 (\frac{5}{13}x + 0.42)\, dydx] / \int_0^{0.468} dx\end{aligned} \tag{5}$$

where E_f and E_p are the elastic module of Q235 and foam aluminum, respectively.

The quality of the foam aluminum chute panel is:

$$m = [2V_f \rho_f + V_p \rho_p] = 0.468 \times [(0.6 + 0.42)t\rho_f + \frac{(0.6 + 0.42)}{2} s\rho_p] \tag{6}$$

where V_f and V_p are the volume of the Q235 steel plate and the foam aluminum plate, respectively and ρ_f and ρ_p are the density of Q235 steel and the foam aluminum, respectively.

$$\begin{aligned}k = \frac{F}{w_c} = \frac{48(E\bar{I})_{eq}}{l^3} = 48[2E_f \int_0^{0.468} \int_{-t/2}^{t/2} (y + \frac{t+s}{2})^2 (\frac{5}{13}x + 0.42)dydx + \\ E_p \int_0^{0.468} \int_{-s/2}^{s/2} y^2 (\frac{5}{13}x + 0.42)dydx] / [(\int_0^{0.468} dx)^4]\end{aligned} \tag{7}$$

Using Equations (1), (6) and (7), the optimization objective function can be expressed as follow:

$$\begin{aligned}\min A(s,t) = 387 / \{&[2.4 \cdot 10^{11} s^3 + 8 \cdot 10^{12} t(3s^2 + \\ &6st + 4t^2) - 3140^2 (3750t + 119.3s)]^2 + \\ &251^2 [2.4 \cdot 10^{11} s^3 + 8 \cdot 10^{12} t(3s^2 + 6st + 4t^2)](3750t + 119.3s)\}^{0.5}\end{aligned} \tag{8}$$

In order to improve the static performance of foam aluminum chute, the maximum static stress of the foam aluminum chute should be smaller than the maximum stress of the prototype chute. So, this relationship can be expressed as follow:

$$\begin{aligned}\sigma_{eq} = \frac{M(s+2t)}{2(2I_{zf} + I_{zp})} < \sigma_f = \frac{Mt_0}{2I_z} \Rightarrow \\ (s/2 + t) - [2s^3 + (3s^2 + 6st + 4t^2)t] \times 10^4 < 0\end{aligned} \tag{9}$$

where σ_{eq} , σ_f are the maximum stress of the foam aluminum chute and the prototype chute, respectively, *M* is the bending moment received from the chute panel and t_0 is the thickness of the prototype chute steel plate.

In order to prevent the pores of the foam aluminum from being crushed and to reduce the damping, the maximum stress of the foam aluminum plate should be less than its yield stress.

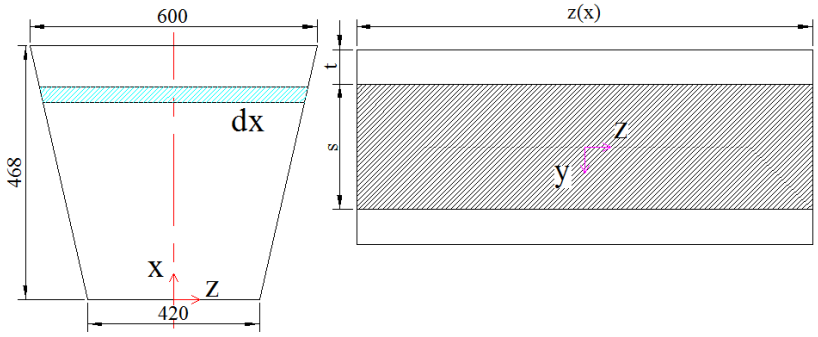

Figure 4. Panel height and width

According to the analysis, the force model of the chute panel can be considered as the force model of the simply supported beam with variable cross section, and its system equivalent stiffness *k* satisfies the equation as follow:

$$\sigma_p = \frac{Ms}{2(2I_{zf} + I_{zp})} < \sigma_{ps} = 8.1\times10^6 \text{ Pa} \Rightarrow \\ \frac{49.8s}{17s^3 + 34t(3s^3 + 6st + 4t^2)} - 8.1\times10^6 < 0 \quad (10)$$

where σ_{ps} is the yield stress of foam aluminum.

In order to prevent the material transportation from being affected, the thickness of the foam aluminum panel can not be increased too much and the thickness of inner and outer panel cannot exceed 5 mm. So, the thickness of the two types panel should satisfy the following conditions:

$$\left.\begin{matrix} 0 \le t \le 0.005 \\ 0 \le s \le 0.02 \end{matrix}\right\} \quad (11)$$

According to the established optimization objective function (Equation (8)) and Constraints (9), (10) and (11), the optimized thickness of the steel plate and foam aluminum is obtained 4.912 mm and 2.6341 mm by using the fmincon function in MATLAB [15,16]. Taking into account the thickness specification of the steel plate, the thickness of the steel plate is set as 5 mm. The thickness of foam aluminum plate is set as 2.6 mm, because of the difficulty in processing the foam aluminum material and that the thickness has a large influence on the natural frequency of the system.

3. STATIC SIMULATION ANALYSIS OF CHUTE

3. 1. Finite Element Model Based on the size of prototype and optimization results, the three-dimensional models of the two types of chutes are created using Pro/E software. The relevant material performance parameters are given in Table 1. Every panel of the chute is mainly subjected to the pressure of the coal block under the condition of full loading, and its force analysis is shown in Figure 5. According to the actual situation at full load, the total pressure received by each chute panel can be calculated by Equation (12).

$$F_t = Q\cos\phi = \rho_m \cdot (V_0 - V_1) \cdot g \cdot \cos\phi \quad (12)$$

where V_0 is the chute volume, V_1 is the volume in the height direction of the chute discharge port, g is the acceleration of gravity, ρ_m is the density of coal and ϕ is the inclination angle of the chute panel.

Bringing the relevant data into Equation (12), the calculated pressure on the chute panel is 155.352 N. According to the working condition of the chute, the fixed constraints are added to the four entrance vertices of the chute, and the y-axis and z-axis direction constraints are also added to the four exit vertices of the chute.

3. 2. Result Analysis The equivalent stress and strain analysis results of the two types of structural chutes obtained by ANSYS software are shown in Figures 6 and 7.

The main data of simulation results are listed in Table 2 for the convenience of comparison.

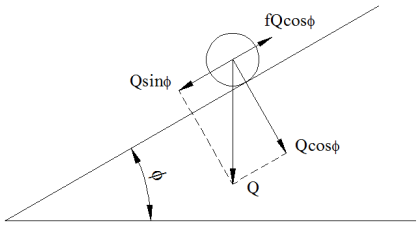

Figure 5. Chute stress analysis

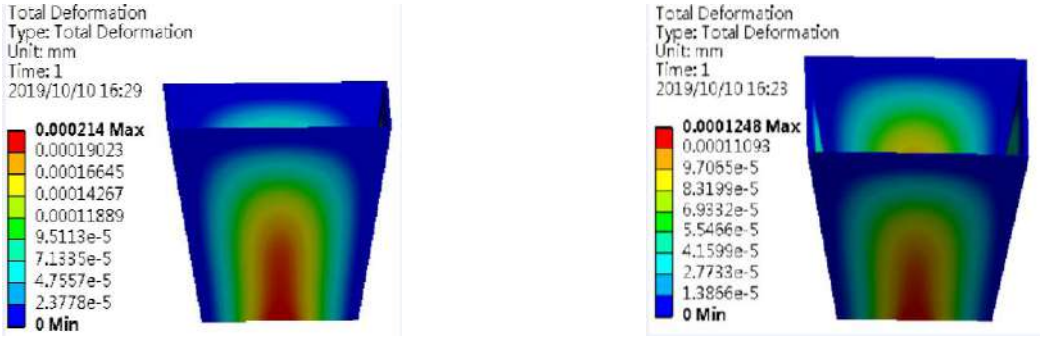

(a) Prototype chute (b) Foam aluminum chute

Figure 6. Equivalent strain of the two types of chute

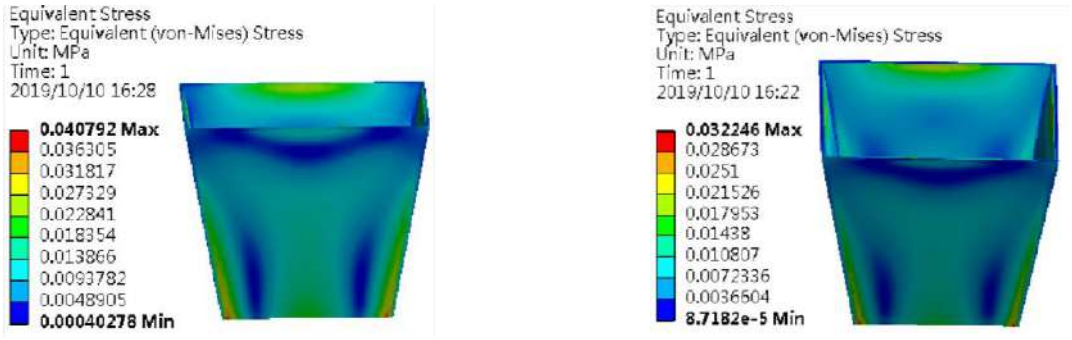

(a) Prototype chute (b) Foam aluminum chute

Figure 7. Equivalent stress of the two types of chute

TABLE 2. Simulation results of the chute

Category	Prototype	Foam aluminum
Maximum deformation/m	21.4×10^{-5}	12.48×10^{-5}
Maximum stress/MPa	0.0407	0.0322

According to Table 2, the maximum strain of the foam aluminum chute is reduced by 41.68% compared with the prototype chute, and the maximum stress is also reduced by 20.88%, which proves that the designed foam aluminum chute has better static characteristics than the prototype chute.

4. MODAL EXPERIMENT

The impact noise caused by the impact of the coal block and the metal plate in the chute is the main part of the chute noise. That is the sound energy radiated by the free vibration which gradually attenuates after the structure impacted by the impact force. So, it is necessary to study the vibration characteristics of the chute structure. According to the shape and size of the two types of chutes, the test specimen is prepared according to the ratio of 1:1. The foam aluminum layer of laminated structure chute specimen is bonded with epoxy resin adhesive between other panels. The prepared test specimens of the foam aluminum chute and the prototype chute are shown in Figure 8.

The test system is mainly composed of excitation system, acceleration sensor, measurement and analysis system, as shown in Figure 9. The measurement and analysis system use the DH5922N dynamic signal test produced by Jiangsu Donghua Testing Technology Co., Ltd. During the test, the test piece is suspended with soft rope to achieve the approximation of free condition. In order to minimize the influence of suspension, the connection point of the suspended test piece shall be selected at or close to the node with as many modes as possible. So, the middle points of the 4 sides at the inlet are selected as the suspension point.

During the experiment, the hammer stroke is used as the excitation signal, and the single-point excitation method is used while hammer striking. The acceleration sensor is used to detect the response signal by multi-point picking, which is to measure the response signals of all nodes on each panel at one time. The measured excitation signal and response signal are amplified by the amplifier, then are inputted into the analysis system for analysis to obtain the response function of each response point.

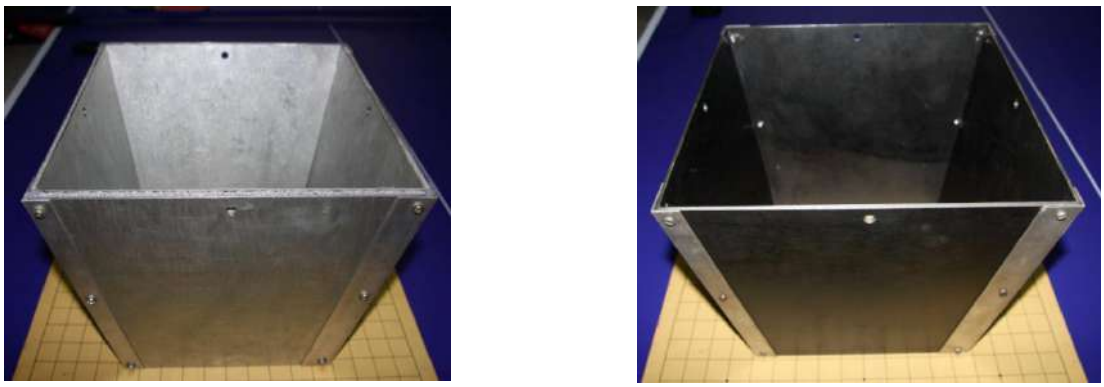

(a) Foam aluminum chute (b) Prototype chute

Figure 8. Test specimens of the two types of chute

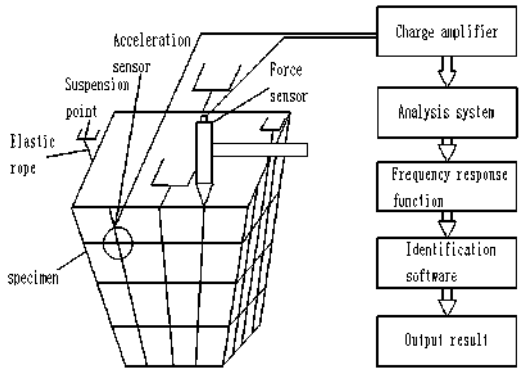

Figure 9. Schematic representation of modal analysis system

And then the response function is subjected to modal recognition processing by special recognition software. The final output is the experimental modal results of the chute. The experimental environment is shown in Figure 10.

The first 5 natural frequencies measured in the experiment and finite element simulation results of the two structural chutes are shown in Table 3. The first 5 natural frequencies of the foam aluminum laminated chute are higher than original chute. The maximum relative error of the natural frequencies obtained by the two methods is less than 3.85%, and the minimum increase of damping ratio of foam aluminum chute is 6.54 % (first order) and the maximum increase is 89.55% (third order). It is proved that the foam aluminum chute can increase the damping ratio of the system and play a role of vibration reduction, as well as reducing the impact noise of the chute.

5. SOUND INSULATION EXPERIMENT

The foam aluminum laminated structure has also a good noise reduction performance. It is necessary to compare the sound insulation performance of the two structural chutes by experiment.

5. 1. Experimental Equipment and Composition

The purpose of this test is to measure the sound insulation of two different structure chutes. The amount of sound insulation can be expressed by three methods, including the sound pressure level, sound intensity level and sound power level. In this test, the method of measuring the sound pressure level is used. The experimental system mainly consists of AWA5680 multi-function sound level meter and analog sound source.

A special sound spectrum generating software is used to simulate the noise source by computer and sound reinforcement equipment. The noise generated by the analog sound source can directly read the sound pressure value on the instrument. During the experiment, there are three conditions to measure the sound pressure value of the noise source, such as without a chute, a prototype chute, and a foam aluminum laminated structure chute. And then, the measurement results can be compared and analyzed. The test system is shown in Figure 11.

5. 2. Experiment Method In this study, the sound insulation performance is represented by the average sound insulation of six octaves with center frequencies of125, 250, 500, 1000, 2000, and 4000 Hz commonly used in engineering. In order to reduce the influence of

Figure 10. Experimental site

TABLE 3. First 5 natural frequencies and damping ratios

Order	Prototype			Aluminum foam		
	Experimental frequency/Hz	Simulation frequency/Hz	Damping ratio/%	Experimental frequency/Hz	Simulation frequency/Hz	Damping ratio/%
1	295.257	301.59	5.351	196.615	200.45	5.701
2	401.886	411.41	3.247	277.538	282.91	4.823
3	397.262	413.07	0.134	278.895	285.30	0.254
4	590.681	310.46	3.083	403.976	413.94	5.140
5	638.933	657.00	3.565	412.668	421.00	5.685

Figure 11. Sound test system

the sound diffraction during the experiment, a foam plate with thickness of 10 mm is added to the upper opening part of the chute specimen.

The noise measurement test is carried out when the laboratory is relatively quiet, and both the room wall and the ground are noise reflection surfaces. According to the size of the chute specimen, the noise source is placed in the middle position of the chute and 0.3 m from the ground. And the sound level meter is placed 1 m outside the chute specimen at a height of 0.3 m from the ground.

5. 3. Experiment Results Analysis The test results are shown in Figure 12. The three curves in the figure are the equal curve of bare test, prototype structure and foam aluminum laminated structure.

It can be seen from Figure 11 that the sound pressure level fluctuates greatly with the change of the frequency under the pure tone of the same loudness level, and the equal sound curve is divided into two parts. The first part is the frequency range of 125~1000 Hz. In this frequency range, the measured sound pressure level of the two structure chutes increases with the increasing of the frequency, and tends to stabilize after reaching a certain degree. The second part is the frequency range of 1000~4000 Hz. In this range, the sound pressure level of two kinds of structure chutes decreases with the increasing of frequency, which indicates that the two structural chutes have better sound insulation effect on higher frequency noise. However, due to the small space

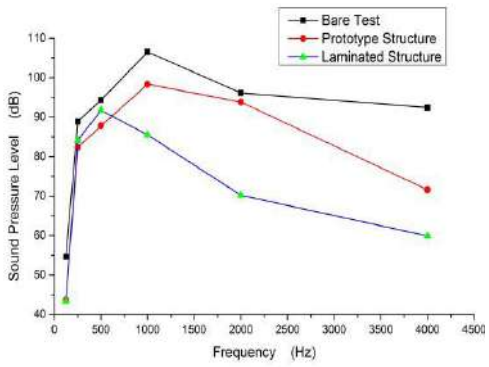

Figure 12. Relationship between frequency and noise

in the test room, the echo of the room, the resonance of the desktop and the interference of the external environment during the test can have a certain impact on the experimental results.

By comparing the results of the three sets of tests, it can be found that both of the foam aluminum laminated structure chute and the prototype structure chute have different degrees of sound insulation effect. In the frequency range of 125-500 Hz, the average sound insulation of the prototype chute is 6.6 dB, and the average sound insulation of the laminated structure chute is 3.7 dB. The foam aluminum laminated structure is 2.9 dB smaller than the prototype. In the frequency range of 1000~4000Hz, the average sound insulation of the foam aluminum laminated structure chute is 26.5dB, and the average sound insulation of the prototype chute is 10.4 dB. The sound insulation of the foam aluminum laminated structure chute is 16.1 dB larger than the sound insulation of the prototype chute. However, from the average sound insulation of six octaves, the sound insulation effect of the foam aluminum laminated structure chute is better than that of the prototype chute, and the average sound insulation is increased by about 7.1 dB. It can be seen that the foam aluminum laminated structure chute has a more significant function of noise reduction effect than the prototype chute.

6. CONCLUSIONS

In this paper, a new type of foam aluminum laminate materials is used to design the mining chute, which has been commonly applied in many fields. And in order to reduce the vibration as more as possible and not to affect the working efficiency of the chute, the structure parameters of the chute are optimized. According to the established optimization objective function and constraints, the optimized thickness of the steel plate and foam aluminum plate is 4.912 mm and 2.6341 mm by using the fmincon function in MATLAB. Taking the difficulty of processing, the foam aluminum material and the thickness which has a large influence on the natural frequency of system into account, the thickness of the steel plate and the foam aluminum plate is set as 5 mm and 2.6 mm, respectively.

In order to verify if the stiffness and strength of the foam aluminum laminated structure chute can meet the working requirements, the static properties of the two types of structure chute are numerically calculated. According to the stress distribution and deformation of the two structural chutes under external load, the equivalent stress and strain is reduced by 41.68% and 20.88% compared with the prototype chute, respectively. This shows that the foam aluminum laminated structure chute has better static mechanical properties.

Through experiments, it can be found that the foam

aluminum chute can increase the damping ratio of the system. The minimum increase of damping ratio of foam aluminum chute is 6.54% (first order) and the maximum increase is 89.55% (third order) compared with prototype chute. Both of the foam aluminum laminated chute and the prototype chute have different degrees of sound insulation. However, the average sound insulation performance of foam aluminum laminated chute is better than the prototype chute, especially in the middle and high frequency section. The average sound pressure level can be reduced by about 7.1 dB. It can be seen that the foam aluminum laminated structure chute has a more significant sound insulation and vibration reduction effect than the prototype chute. The superiority of the foam aluminum laminated structure provides a new way to improve the vibration and noise reduction performance of the mining chute. But we only take the vibration amplitude as the objective function, without considering the purchase and processing cost of materials. Thus, it is necessary to carry out a multi-objective optimization design in the future.

7. REFERENCES

1. Khoshnood, A.M., Khaksari, H., Roshanian, J. and Hasani, S.M., "Active noise cancellation using online wavelet based control system: numerical and experimental study", ***International Journal of Engineering-Transactions A: Basics,*** Vol. 30, No. 1, (2017), 120-126. DOI:10.5829/idosi.ije.2017.30.01a.15
2. Kamesh, D., Pandiyan, R. and Ghosal, A., "Passive vibration isolation of reaction wheel disturbances using a low frequency flexible space platformv", ***Journal of Sound and Vibration***, Vol. 331, No. 6, (2012), 1310-1330. DOI:10.1016/j.jsv.2011.10.033
3. Masterson, R.A., Miller, D.W. and Grogan, R.L., "Development and validation of reaction wheel disturbance models: Empirical model", ***Journal of Sound and Vibration***, Vol. 249, No. 3, (2002), 575-598. DOI:10.1006/jsvi.2001.3868
4. Mellinger, P., Döhler, M. and Mevel, L., "Variance estimation of modal parameters from output-only and input/output subspace-based system identification", ***Journal of Sound and Vibration***, Vol. 379, (2016), 1–27. DOI:10.1016/j.jsv.2016.05.037
5. Masterson, R.A., Miller, D.W. and Grogan, R.L., "Development and validation of reaction wheel disturbance models: empirical model", ***Journal of Sound and Vibration***, Vol. 249, No. 3, (2002), 575-598. DOI:10.1006/jsvi.2001.3868
6. CHO, H. and CHO, J., "Damage and penetration behavior of aluminum foam at various impacts", ***Journal of Central South University***, Vol. 9, (2014), 3442-3448. DOI:10.1007/s11771-014-2320-x
7. Raja, R.E. and Daniel,B.S.S, "Structural and compressive property correlation of closed-cell aluminum foam", ***Journal of Alloys and Compounds***, Vol. 467, No. 1, (2009), 550-556. DOI:10.1016/j.jallcom.2007.12.040
8. Shafiq, B. and Quispitupa, A., "Fatigue characteristics of foam core laminated composites", ***International Journal of Fatigue***, Vol. 28, No. 2, (2006), 96-102. DOI:10.1016/j.ijfatigue.2005.05.002
9. Yu, Y.H. and Yu G.J., "Study on reduction noise properties offo amed aluminum laminated structure acoustical enclosure for ball mill", ***Journal of China Coal Society***, Vol. 37, No. 1, (2012), 158-161. DOI:10.1007/s11783-011-0280-z
10. Xu, P., Yang, K. and Yu Y.H., "Simulation research on machine worktable filled with foam aluminum/epoxy resin", ***Ordnance Material Science and Engineering***, Vol. 36, No. 1, (2013), 94-96. DOI:10.3969/j.issn.1004-244X.2013.01.021
11. Qin, H.X. and Yang, D.Q., "Vibration reduction design method of metamaterials with negative poisson's ratio", ***Journal of Materials Science***, Vol. 54, No. 22, (2019), 14038-14054. DOI:10.1007/s10853-019-03903-z
12. Simon, S.K., Chakyar, S.P., Sebastian, A., Jose, J., Andrews, A. and Joseph, V.P., "Broadside coupled split ring resonator as a sensitive tunable sensor for efficient detection of mechanical vibrations", ***Sensing and Imaging***, Vol. 20, No. 1, (2019), 1-11. DOI:10.1007/s11220-019-0240-4
13. Kudzaev, A.B., Korobeinik, I.A., Tsgoev, A.E., Tsgoev, D.V., Kalagova, R.V., Urtaev, T.A., "Development of closed-circuit elastic mounting for working bodies in the interrow cultivator", ***Civil Engineering Journal***, Vol. 4, No. 12, (2018), 3027-3037. DOI:10.28991/cej-03091218
14. Shotorbani, A.R. and Saghai, H.R., "Modeling and implementing nonlinear equations in solid-state lasers for studying their performance", ***Emerging Science Journal***, Vol. 2, No. 2, (2018), 78-84. DOI:10.28991/esj-2018-01130
15. Centeno-González, F.O., "Programming the inverse thermal balance for a bagasse-fired boiler, including the application of a optimization method in MATLAB", ***Sugar Tech***, Vol. 20, No. 5, (2018), 585-590. DOI:10.1007/s12355-017-0573-z
16. Matalkah，F., Bharadwaj, H., Balachandra, A. and Soroushian, P., "Aerated concrete produced using locally available raw materials", ***Civil Engineering Journal***, Vol. 3, No. 4, (2017), 214-220. DOI:10.28991/cej-2017-00000087

Persian Abstract

مجرای سرریز (ناودان) معدن یکی از تجهیزات مهم در فرآیند حمل و نقل ذغال سنگ و غربالگری آن است. در طی فرایند کار، ناودان معدن به دلیل اصطکاک مداوم و اثر کلوخه و بلوک‌های ذغال سنگ، لرزش و سر و صدای زیادی ایجاد می کند. به منظور کاهش لرزش و سر و صدا از ناودان در حین کار، از نوع جدیدی از سازه روکش شده آلومینیومی فوم برای ساخت ناودان معدن استفاده می‌شود. با توجه به ویژگی‌های ناودان، ساختار چند لایه با بهره‌گیری از دامنه ارتعاش به عنوان تابع هدف و ضخامت صفحه فولادی و صفحه اصلی آلومینیوم فوم به عنوان متغیرهای طراحی، طراحی شده است. سپس عملکرد لرزش و کاهش سر و صدا در دو نوع ناودان از طریق آزمایشات و روش شبیه سازی عنصر محدود ارزیابی می‌شود. نتایج نشان می‌دهد که استفاده از سازه ورقه ورقه آلومینیومی فوم برای تولید ناودان می‌تواند موجب افزایش نسبت کاهش میرایی سیستم شود، که در نتیجه می‌تواند به طور موثری دامنه ارتعاش ناودان را کاهش دهد. متوسط عملکرد عایق صوتی فوم آلومینیومی نسبت به نمونه اولیه بهتر است، خصوصاً در بخش فرکانس میانی و بالا، که می‌تواند به طور متوسط در حدود ۷.۱ دسی‌بل در مقایسه با نمونه اولیه کاهش یابد. بنابراین، ناودان سازه‌ای با روکش آلومینیوم فوم دارای خاصیت عایق صوتی قابل توجهی نسبت به نمونه اولیه است و موجب کاهش لرزش می‌شود.

International Journal of Engineering

Journal Homepage: www.ije.ir

Characteristics of Shale Gas Reservoir in Jiyang Depression and its Significance in Drilling and Exploitation

X. Liu[a,b], R. Jiang*[a], J. Li[c], W. Huang[a]

[a] *School of Petroleum Engineering, China University of Petroleum, Qingdao, Shandong, China*
[b] *Dongsheng Jinggong Petroleum Development Group Co., Ltd., Shengli Oilfield Company, SINOPEC, Dongying, Shandong, China*
[c] *Exploration and Development Research Institute, Sinopec Shengli Oilfield Company, Dongying, Shandong, China*

P A P E R I N F O

Paper history:
Received 12 February 2020
Received in revised form 04 April 2020
Accepted 11 June 2020

Keywords:
Shale Gas Reservoir
Physical and Chemical Characteristics
Adsorption Isothermal
High Pressure Mercury Intrusion
Shale Stability Index

A B S T R A C T

Physical and geochemical characteristics of shale play conclusive role in confirming operation measures during drilling and stimulation. The properties of shale samples from Jiyang depression were investigated through X-ray diffraction, scanning electron microscope, adsorption isothermal, high pressure mercury intrusion, methylene blue trihydrate, pressure pulse decay, tests of specific water wettability and shale stability index. Correlations, geological and engineering significances of them were discussed. Results show that shale reservoir in Jiyang depression has exploitation value corroborated by good characteristic parameters: 2.86% TOC, 69.9% brittle mineral, 26.14% clay mineral, high permeability of 0.011×10^{-3}μm^2, large Langmuir volume (5.82 cm^3/g) and Langmuir specific area (0.91 m^2/g), effective porosity (3.77%) and thickness (130.66m). Langmuir specific area is the key control on methane adsorption and storage verified by its moderate positive relativity with Langmuir volumes rather than TOC. High illite content (69.29%) may lead to instability of borehole and velocity sensitivity damage. Microfractures provide channels for filtration, invasion and loss of drilling fluid. Large specific water wettability (4.36×10^{-7}g/m^2) and smaller shale stability index (19.99 mm) dispalyed that shale formation were unstable once contacting with fresh water. Countermeasures must be adopted during drilling and fracturing to reduce reservoir damage and complex downhole conditions.

***doi**: 10.5829/ije.2020.33.08b.27*

NOMENCLATURE

API	American Petroleum Institute	H_i	Needle penetration of shale before water sucking (mm)
CEC	Cation exchange capacities	ΔH	Swelling capacity of shale (mm)
HPMI	High pressure mercury intrusion	S_w	Specific water wettability of shale (10^{-7}g/m^2)
I/S	Mixed-layer of illite and smectite	w_2	Weight of shale power after water sucking (g)
MBT	Methylene blue trihydrate	w_1	Weight of shale power oven dried 5 hours under 105℃ before water sucking (g)
NA	Nitrogen adsorption	w_0	Weight of container (g)
P_L	Langmuir pressure	S_s	Specific surface area of shale powder (m^2/g)
SEM	Scanning electron microscope	x_i, y_i	i=1,2,3,…n
SSI	Shale stability indexes	$\bar{x}$,$\bar{y}$	Averages of being analysed variables
TOC	Total organic carbon	r	Pearson product-moment correlation coefficient
V_L	Langmuir volume	**Subscripts**	
XRD	X-ray diffraction analysis	*w*	Water
T	Temperature	*s*	Shale powder
H_f	Needle penetration of shale after water sucking (mm)		

1. INTRODUCTION

With the development of horizontal drilling technology, segregated fracturing technology and the increase of global energy demand, more and more attentions were paid on shale gas exploration and exploitation. Results of geological prospect show that shale gas reservoir may mainly distribute in Sichuan, Ordos, Bohai Gulf,

*Corresponding Author Email: *jrzhong@126.com* (R. Jiang)

Please cite this article as: X. Liu, R. Jiang, J. Li, W. Huang, Characteristics of Shale Gas Reservoir in Jiyang Depression and its Significance in Drilling and Exploitation, International Journal of Engineering (IJE), IJE TRANSACTIONS B: Applications Vol. 33, No. 8, (August 2020) 1677-1686

Songliao, Jianghan, Tuha, Tarim and Junggar basin in China [1]. Nevertheless, mineral composition, organic content, microstructure of rock, reservoir thickness and burial depth of shale formation in these basins are different from which in North America. Especially, deeper burial depth of shale gas reservoirs in China make operations such as drilling, completion, fracturing very difficult, leading that many key technology problems should be solved before shale gas could be produced commercially in large scale [2]. Shale gas reservoirs explored and had been put into commercial exploitation were only found in South China especially in Sichuan basin up to now. Logging data analysis indicated that there were three sets of grey brown oil shale formation (thickness is 92m, 233m, 37m separately, $\Sigma(C_1\text{-}C_4)$ from tank top gas logging analysis results of many cuttings was up to 25587.277 μL/L) developed in Shahejie Group of Paleogene System in Jiyang depression of Bohai Gulf [3]. Because of the characteristics of low porosity and low permeability of shale, it is difficult to detect shale physical properties and influencing factors, which restricts the development of shale property evaluation [4]. Logging and laboratory experiments were the main methods to analyze the physical properties of shale gas reservoirs. Physical property evaluation of shale gas reservoir mainly includes porosity, permeability and saturation of reservoir [5]. Therefore, the purpose of this paper is to investigate the physical and chemical properties of shale from Shahejie group of Jiyang depression for making sure that whether this shale gas reservoir is suitable for producing commercially and give the guides for drilling and exploitation.

2. EXPERIMENTAL

2. 1. Materials Shale cores and fragments were collected from Shahejie group of Jiyang depression located in Bohai Gulf. There were several sets of gas source rocks including Stone carbon-dyas paralic hydrocarbon source rocks, Mesozoic erathem limnetic facies source rocks and Paleogene System lacustrine facies bearing rocks. Other additives and chemicals were all analytical grade and purchased from Sinopharm Chemical Reagent Co., Ltd (SCRC), Peking, China.

2. 2. Analysis of Compositions and Microstructure Some of shale fragments were first ground into powder: a part of them less than 150 μm; others no bigger than 58μm. About 30 grams shale powder smaller than 58μm were used in mineral composition analysis through X-ray diffraction (XRD) using Rigaku D/max-IIIA to test whole rock mineral and relative contents of clay minerals. About two grams of shale powder smaller than 150μm were used in total organic carbon (TOC) analyzing by CS230 carbon-sulfur analyzer purchased from LECO Company of United States [6]. Several shivers of shale rock were shattered with fresh section for observing microstructure through S-4800 scanning electron microscope (SEM).

2. 3. Measurements of Porosity, Pore Diameter, Specific Area and Permeability True density, porosity, pore diameter and Langmuir specific area were all measured through nitrogen adsorption (NA) in low temperature using shale cores [7]. True density and porosity were tested by 3H-2000TD2 full automatic true density and porosity measuring instrument, pore diameter and Langmuir specific area were determined by 3H-2000PS1 full nitrogen adsorption surface area and pore size analyzer after shale cores dried and outgassed at 423 K for 5 hours, ensuring the removal of bound water adsorbed in the clays. For comparison, pore diameters were also tested by high pressure mercury intrusion (HPMI) through AutoPore 9505 equipment (SY/T 5346-2005) using core samples [8], specific area was measured by methylene blue trihydrate method (MBT) using shale powder less than 150 μm. The permeability of shale cores was tested by the pressure pulse decay method on TEMCO PDP-200 with high purity methane as medium according to American Petroleum Institute Standard (API RP-40).

2. 4. Tests of Adsorption Isotherm Adsorption of methane on shale surface adhere to Langmuir adsorption isotherm relationship, volume of methane in free state can be figured out by gas equation of real state after adsorption equilibrium achieved. The analytical results include Langmuir volume and Langmuir pressure. Shale powder samples whose diameter between 178 μm and 250 μm were sieved and dried for 24 hours at 105℃ before the methane adsorption experiments. All methane adsorption was measured at temperatures of 25℃, 50℃, 75℃ and under pressures up to a consistent pressure of 6 MPa.

2. 5. Analysis of other Physicochemical Properties The cation exchange capacities (CEC) of shale from Shahejie group of Jiyang depression were determined by methylene blue trihydrate method after ground less than 150 μm [9]. The hydration properties were tested through shale dispersion experiment for dispersion properties using fragment with size between 2mm and 5mm, shale expansion experiment for swelling properties using shale powder smaller than 150 μm according to API standard. The shale stability indexes (SSI) were measured by needle penetration method using small shale particles between 250 μm and 180 μm. The SSI can be calculated through the following Equation (1).

$$SSI=102-2(H_f-H_i)-4\Delta H \quad (1)$$

where, H_f is the needle penetration of shale after water sucking, mm; H_i is the needle penetration of shale before

water sucking, mm; ΔH is swelling capacity of shale, mm.

Moreover, the specific water wettability (SWW) defined as water absorbing capacity on unit area of shale was figured out using total suction divided by specific surface area:

$$S_w = \frac{w_2 - w_1}{10000 * S_s (w_1 - w_0)} \quad (2)$$

where S_w is the specific water wettability of shale, 10^{-7} g/m^2; W_2 is the weight of shale power after water sucking, g; W_1 is the weight of shale power oven dried 5 hours under 105℃ before water sucking, g; W_0 is the weight of container, g; S_s is the specific surface area of shale powder, m^2/g. The total water suction was determined by water vapour adsorption, the specific surface area through methylene blue trihydrate method [10].

3. RESULTS AND DISCUSSION

3. 1. Inorganic Mineral and TOC It can be seen from XRD analysis results listed in Table 1 that main inorganic mineral compositions of shale from Shahejie group of Jiyang depression are quartz, calcite and clay. The specific content of them is shown in Table 1. The brittleness indexes, which means the percentage of brittle mineral (quart, calcite, feldspar, dolomite) in total inorganic mineral (quart, calcite, feldspar, dolomite, clay and so on), ranged from 62 to 79% and averaged 69.9%. High brittleness index leads to the formation of fractures, which are the main seepage channels of shale gas. So shale in Jiyang depression is excellent fracturing formation. The clay mineral and their relative amount are presented in Table 2. Main components of clay mineral in shale are illite, mixed-layer of illite and smectite (I/S), whose average relative content are 69.29 and 27.38%, respectively. Illite has the characteristics of weak expansion and breakable, and high content of illite is favorable for fracturing. In shale samples, the TOC content is 2.86% on average, and ranges from 1.84% to 4.92%, with small diversity and wirkungsgehalt forming shale gas reservoirs (Table 1).The sulphur content ranges from 2.45 to 7.93%, with an average of 4.90% (Table 1), which may have a high concentration of sulphur-bearing shale gas.

TABLE 1. Results of mineral composition analysis by X-ray diffraction

Sample	Quartz (%)	Potash Feldspar (%)	Anorthose (%)	Calcite (%)	Ankerite (%)	Siderite (%)	Iron pyrite (%)	Clay (%)	TOC (%)	Sulfur content (%)	Brittleness Index (%)
D1	25	6	15	22	3	1	4	24	2.61	7.21	71
D2	28	7	15	11	3	1	4	31	4.92	6.50	64
D3	29	0	7	32	0	4	3	25	2.63	4.87	68
D4	31	5	3	26	3	0	0	32	2.82	6.29	68
D5	26	8	12	33	0	2	1	18	2.96	7.93	79
D6	29	7	14	28	1	1	3	17	2.34	4.67	79
D7	34	4	8	19	3	1	5	26	1.96	3.82	68
D8	32	0	11	26	2	1	4	24	3.27	4.95	71
D9	23	1	12	30	1	0	2	31	2.98	2.88	67
D10	28	3	13	27	3	2	1	23	3.18	6.78	74
D11	31	3	15	24	0	2	4	21	3.06	5.04	73
D12	27	7	6	31	1	3	3	22	2.88	6.31	72
D13	31	5	5	22	4	2	2	29	2.47	4.84	67
D14	30	8	8	27	5	1	0	21	2.52	5.45	78
D15	27	6	3	30	0	4	0	30	1.84	3.77	66
D16	29	5	0	28	1	3	2	32	2.28	4.19	63
D17	35	0	4	27	0	1	0	33	2.66	3.36	66
D18	29	6	7	31	2	1	3	21	3.69	2.82	75
D19	28	4	6	32	1	0	4	25	2.84	5.93	71
D20	25	3	9	25	0	2	3	33	2.72	2.45	62
D21	27	6	11	21	1	1	2	31	3.41	4.50	66

TABLE 2. Results of the relative content analysis of clay minerals

Sample	Kaolinite (%)	Chlorite (%)	Illite (%)	I/S (%)	Interlaying Ratio of I/S (%)
D1	2	2	67	29	20
D2	2	2	69	27	20
D3	2	1	69	28	20
D4	2	2	67	29	20
D5	2	2	69	27	20
D6	2	1	69	28	20
D7	1	1	71	27	20
D8	2	1	74	23	20
D9	1	1	74	24	20
D10	1	1	72	26	20
D11	3	1	68	28	20
D12	1	2	64	33	20
D13	1	1	67	31	20
D14	2	2	65	31	20
D15	2	2	72	24	20
D16	1	3	70	26	20
D17	1	2	68	29	20
D18	3	1	69	27	20
D19	2	1	65	32	20
D20	3	1	73	23	20
D21	2	2	71	25	20

3. 2. Microstructure SEM images of shale sample D1 and D21 are shown in Figures 1 and 2, respectively. The microfracture and micropore were developed. The parallel lamellation were found in the images. The microfracture is important drainage channel for shale gas. But filtration and slurry of drilling fluid can invade into formation through these channels. So these microfractures must be plugged during drilling. The lamellation is helpful to form horizontal fracture during fracturing stimulation. The microstructure characteristics of shale from Shahejie group of Jiyang depression indicate that the objective formation possess a certain permeability for shale gas, but also maybe lead loss of drilling fluid, instability of well bore, velocity sensitivity damage.

3. 3. Porosity, Pore Diameter, Specific Area and Permeability The average porosity of shale samples is 3.77%, and the average methane permeability is 0.011×10-3 cm^2, which is larger than the permeability of shale in Sichuan Basin [10]. The average true density

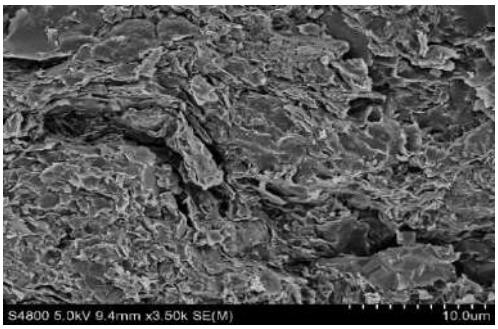

(a) Clay mineral filling in pore (6000 times)

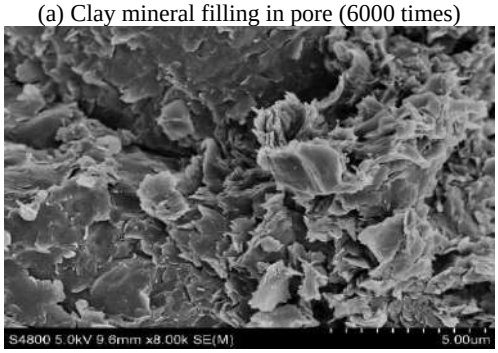

(b) Clay mineral (8000times)

Figure 1. SEM images of shale sample D1

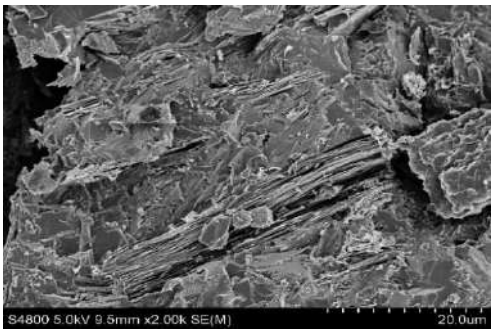

(a) Parallel lamellation development (2000 times)

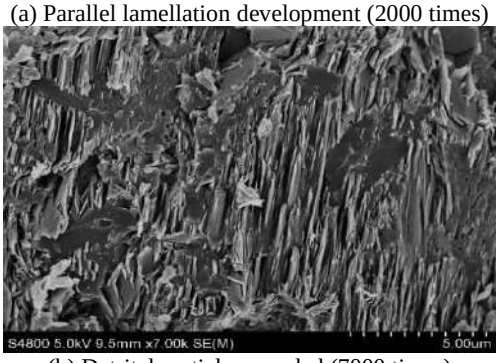

(b) Detrital particle corroded (7000 times)

Figure 2. SEM images of shale sample D21

is 2.69 g/cm^3, which is basically consistent with the average true density of natural shale. Pore diameters tested by nitrogen adsorption (test curve of sample D21 shown in Figure 3) ranged from 3.92 to 11.24 nm, with

an average of 7.64 nm. While pore diameters measured by high pressure mercury intrusion ranged from 4.38 to 14.78 nm, with an average of 10.46 nm (test curve of sample D21 shown in Figure 4), which is larger than NA ones. The reason is that the high capillary force must be overcome to drive mercury enter pindling pore. Even the test pressure in experiment was up to 227.545 MPa. There are still many pores that have not been filled with mercury. (Figures 4 and 5). Test results of NA pore diameter could be affected by adsorption state of nitrogen on internal wall of shale pores, for example whether this adsorption follows Langmuir rules or not. There was a well positive correlation between results measured by two different methods (r=0.79, Figure 6). The nitrogen adsorption method was better for characterizing shale samples with smaller pores. Internal surface area of shale cores measured by nitrogen adsorption (Langmuir surface area) averaged 0.91 m^2/g and ranged from 0.4 to 1.34 m^2/g, while surface area of shale powder tested through methylene blue trihydrate (MBT) method ranged from 45 to 68.6 m^2/g with a larger average of 57.56 m^2/g, which has positive correlation with Langmuir surface area (Figure 7). Langmuir surface area could reflect shale's adsorption features, and MBT surface area has better guidance for hydration characteristic of shale, which were used in calculating specific water wettability.

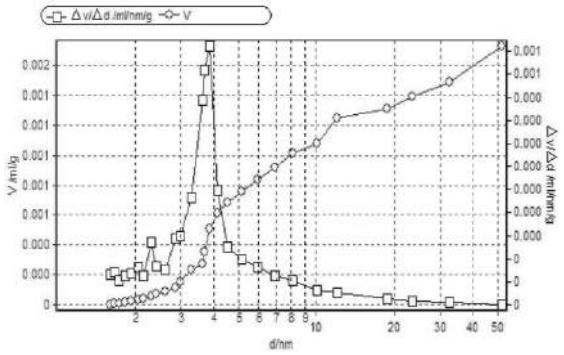

Figure 3. BJH differential, integration hole volume and pore diameter curve of sample D21

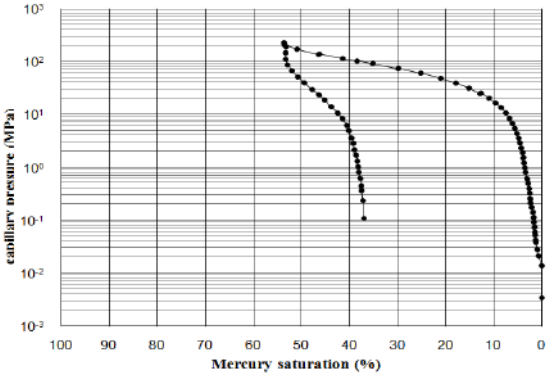

Figure 4. Capillary pressure curve of sample D21

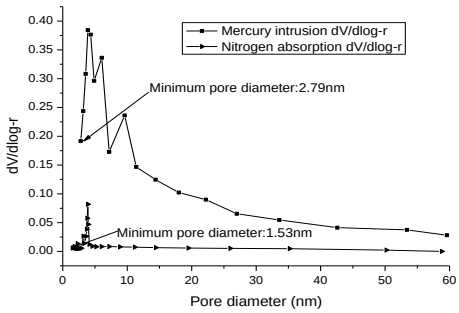

Figure 5. Differential volume and pore diameter curve of sample D21 by N_2 adsorption and mercury intrusion

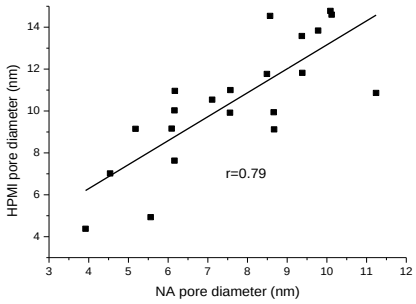

Figure 6. Relation between NA pore diameters and HPMI pore diameters

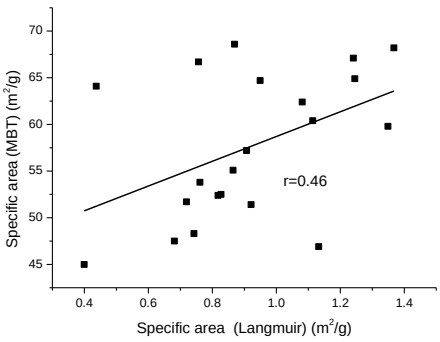

Figure 7. Relation between NA specific areas and MBT specific areas

3. 4. Adsorption Characteristic for Methane and its Relativity with other Parameters

3. 4. 1. Effect of Temperature and Pressure Langmuir volumes of methane adsorbed on shale samples averaged 5.82 cm^3/g (between 3.48 cm^3/g and 7.69 cm^3/g) at 25 ℃, 4.83 cm^3/g (from 2.94 cm^3/g to 6.38 cm^3/g) at 50 ℃ and 4.01 cm^3/g (between 2.62 cm^3/g and 5.38 cm^3/g) at 75℃. As temperature increased, the Langmuir volume droped, while the Langmuir pressure

enlarged. Adsorptive capacity of methane adsorbed on shale samples grew with pressure increasing and reduced at elevated temperature (Figure 8). The reason is that molecular kinetic of methane gas intensify with temperature rising, and the differential pressure of methane in adsorption tank enlarges with pressure increasing. This phenomenon indicates that shale gas is easier to desorb from internal surface of shale pores by lower pressure and keep the formation temperature.

3. 4. 2. Relation between Langmuir Volumes and other Parameters In statistics, Karl Pearson correlation theory is the most simple, intuitionistic and conventional method used in investigating the correlation between two variables. The Pearson product-moment correlation coefficient (r) reflects the degree of linear relationship between two variables. It can be computed through Equation (3) [11]:

$$r = \frac{\sum_{i=1}^{n}(x_i - \bar{x})(y_i - \bar{y})}{\sqrt{\sum_{i=1}^{n}(x_i - \bar{x})^2 \sum_{i=1}^{n}(y_i - \bar{y})^2}} \quad (3)$$

where, x and y are two variables; (x_i, y_i) (i=1,2,3,…n) are n pairs of variables; $\bar{x}$ and $\bar{y}$ are averages of variables. The "r" ranges from +1 to -1. A correlation of +1 means that there is a perfect positive linear relationship between variables. -1 means that there is a perfect negative linear relationship between variables. 0 means there is no linear relationship between the two variables. The linear relationship between variables can be classified into four grades according to the value of $|r|$: weak correlation ($|r|$ =0~0.3), low correlation ($|r|$ =0.3~0.5), moderate correlation ($|r|$ =0.5~0.8), high correlation ($|r|$ =0.8~1). The relationship between Langmuir volumes and other parameters was studied in detail by Karl Pearson correlation theory. Pearson product-moment correlation coefficient and linear fitting between Langmuir volumes and other parameters were listed in Table 3. It can be seen from Table 3 that Langmuir volumes of shale samples were positively correlated with TOC, content of clay mineral, Langmuir specific area and pore diameter under 25 ℃, 50 ℃ and 75 ℃. As literature had shown that methane adsorption capacity of shales is dependent on geological control factors including TOC content, kerogen types, mineralogy, pore structure. TOC was thought as a critical control on methane adsorption and storage for shale because CH_4 bituminite. There was a low positive relationship between TOC and Langmuir volume of shale in Jiyang depression evidenced by smaller Pearson coefficient (Figure 9) attributed to it lower content and the effect of clay mineral (Figure 10). Clay minerals can adsorb methane and the adsorption capacity depends on the development of nano-scale micropore and the specific surface area size specific area [12]. Role of clay mineral in methane adsorption and storage would be enhanced when the content of organic matter in shale was lower. There is a moderate positive relationship between Langmuir volume and Langmuir specific area of shale in Jiyang depression with big Pearson coefficient (Figure 11). This indicates that Langmuir specific area is a key of methane adsorption and storage of shale from Shahejie group in Jiyang depression. The relation line does not go through the origin of the Langmuir specific area - Langmuir volume plot, which may be related to dissolution of methane gas in matrix bituminite. Micropore and microfracture mainly serve as shale gas transport channel,s so pore diameter size have a weak positive correlation with Langmuir volumes of shale samples with smallest r shown in Figure 12. Pore structure affects the permeability, porosity and internal surface area of shale and plays an important role in the storage and exploitation.

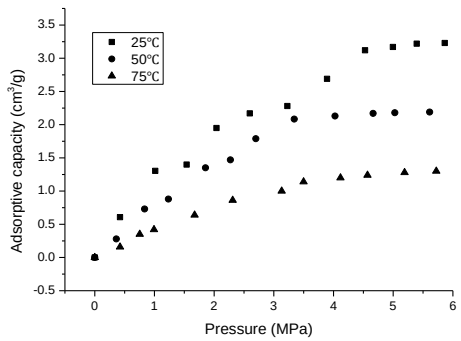

Figure 8. Adsorptive capacity of methane adsorbed on shale sample D1 under different temperature

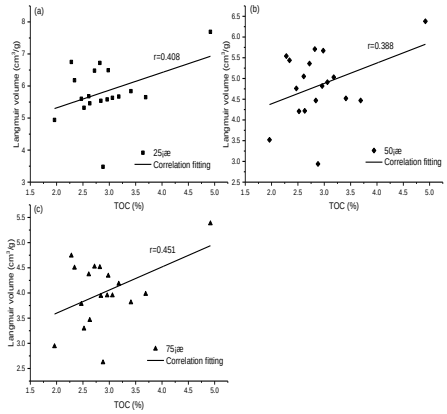

Figure 9. Relation between Langmuir volumes and TOC under different temperature

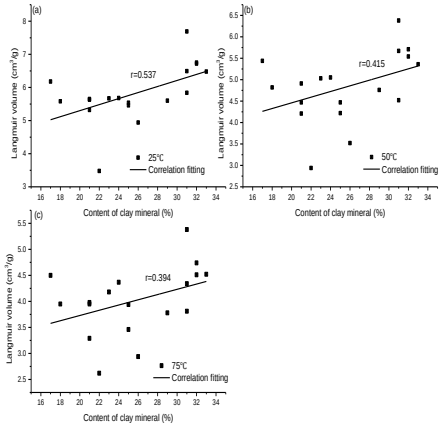

Figure 10. Relation between Langmuir volumes and content of clay mineral under different temperature

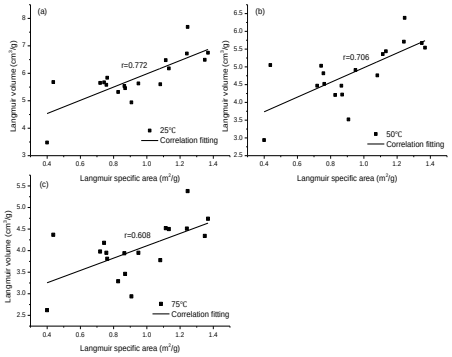

Figure 11. Relation between Langmuir volumes and Langmuir specific area under different temperature

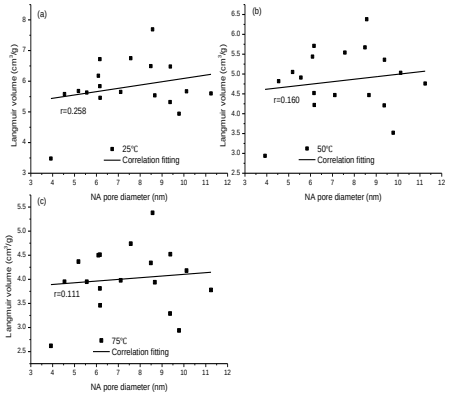

Figure 12. Relation between Langmuir volumes and NA pore diameter under different temperature

3. 5. CEC, Hydration Capacity, Specific Water Wettability and SSI Other physicochemical properties of shale samples from Shahejie group in Jiyang depression were tested. CEC of samples ranged from 21.84 mmol/kg to 30.82 mmol/kg with a smaller an average of 92.57%, showing that the analysed shale has weak hydration dispersing capacity. Linear swelling rates were between 6.04 and 9.49% with an average of 7.43%, indicating that the shale samples has lower hydrating and swelling performance. But swelling rates were very high at the initial stage, and it increased slowly after half an hour and run up to maximum within 8 hours (Figure 13). Specific water wettability was considered to be a more effective index in reflection of hydration repulsion of mud rock and shale because its physical significance is the thickness of hydration shell. The bigger SWW is, the higher hydration swelling pressure will be and the easier well bore collapse. The average of SWW is 4.36×10^{-7} g/m^2, illustrating that hydration repulsion of shale samples were huge and would cause the borehole collapse. The shale stability index is a comprehensive indicator used to denote the stability of mud rock and shale formation, which can reflect the hydration dispersion, swelling and strength after sample contact with tested fluid (water or drilling fluid) synthetically. The stability of formation can be divided into four ranks according to the value of SSI: high stability (SSI>90 mm), moderate stability (SSI=60~90 mm), low stability (SSI=30~60 mm), weak stability (SSI <30 mm). SSI of shale samples, with an average of 19.99 mm (<30mm), showed shale formation of Shahejie group in Jiyang depression has poor stability [13].

3. 6. Geological and Engineering Significance Statistical test results of shale samples listed in Table 4 indicated that shale reservoir in Jiyang depression has fairly good physical and chemical characteristics: suitable TOC (2.86%) for hydrocarbon generation; enough brittle mineral (69.9%), less clay mineral

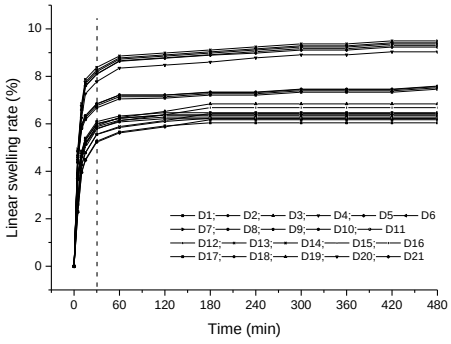

Figure 13. Linear swelling rate changes of shales from Shahejie group in Jiyang depression with time

TABLE 3. Linear fitting between Langmuir volumes and other parameters

Variable 1(X)	Variable 2(Y)		Fitting equation	Pearson coefficient	Relationship
TOC	Langmuir volume	25 ℃	Y=4.216+0.551X	0.408	Low
		50 ℃	Y=3.407+0.492X	0.388	Low
		75 ℃	Y=2.682+0.459X	0.451	Low
Content of clay mineral	Langmuir volume	25 ℃	Y=3.473+0.091X	0.537	Moderate
		50 ℃	Y=3.136+0.067X	0.415	Low
		75 ℃	Y=2.722+0.050X	0.394	Low
Langmuir specific area	Langmuir volume	25 ℃	Y=3.569+2.412X	0.772	Moderate
		50 ℃	Y=2.907+2.689X	0.706	Moderate
		75 ℃	Y=2.683+1.429X	0.608	Moderate
Pore diameter	Langmuir volume	25 ℃	Y=5.013+0.108X	0.258	Weak
		50 ℃	Y=4.366+0.062X	0.160	Weak
		75 ℃	Y=3.753+0.034X	0.111	Weak

(26.14%) for fracturing; higher permeability (0.011V) for methane supplying better flow channel; appropriate porosity (3.77%) and Langmuir specific area (0.91 m^2/g) for storage of shale gas in free and adsorbed states; effective thickness of 130.66m for recovery.

Meanwhile, there were several problems related to reservoir damage, instability of borehole and loss circulation during drilling and exploiting determined from results of physical and chemical properties. High content of illite (69.29%) maybe lead to serious fine migration and velocity sensitivity damage. Also, nanoscale pore and microfracture (7.64 nm) caused high capillary force (up to 227.545MPa) and water lock is easy to cause permeability reduction of formation and check flow back of fracturing liquid.

Down hole problems include borehole instability caused by large SWW ($4.3610^{-7}g/m^2$) and small SSI (19.99mm) of shale formation in Shahejie group of Jiyang depression, filtration, invasion and loss of drilling fluid due to microfracture and lamellation.

So some countermeasures must be adopted during drilling and fracturing. Oil based drilling fluid; water based working fluid with micro and nano materials, asphalt, membrane-forming agent are wellbehaved working fluid, which can reduce filtration, improve salinity and enhance plugging capacity.

TABLE 4. Physical and chemical characteristics of shale samples from Jiyang depression and their significance in drilling and exploitation

Items	Parameters	Range of results	Averages	Geological significance	Engineering values	
					Drilling	Exploitation
Organic matter	TOC (%)	1.84-4.92	2.86	Meet reservoir forming condition	---	---
Inorganic mineral	Brittle mineral content (%)	62-79	69.9	Meet reservoir forming condition	Be fit for Improving speed	Be fit for fracturing
	Clay mineral Content (%)	17-33	26.14	Meet reservoir forming condition	Lead to side wall unstable	Be fit for fracturing
	Content of expansive clay minerals (%)	20	20	Meet reservoir forming condition	Lead to side wall unstable	Be fit for fracturing
Properties of reservoir	Porosity by NA (%)	0.92-8.18	3.77	Meet reservoir forming condition	---	Adaptive for recovery
	Permeability ($10^{-3}\mu m^2$)	0.0037-0.0204	0.011	Better physical properties	---	Need be fractured
	Pore diameter by NA (nm)	3.92-11.24	7.64	Better physical properties	---	Adaptive for recovery

	Pore diameter by HPMI (nm)	4.38-14.78	10.46	Better physical properties	---	Adaptive for recovery
	Specific area by NA (m^2/g)	0.4-1.37	0.91	Better physical properties	---	---
	Specific area by MBT (m^2/g)	45-68.6	57.56	---	Calculating SWW	---
Adsorption	V_L(25℃) (cm^3/g)	3.48-7.96	5.82	Better physical properties	---	Adaptive for recovery
	CEC (mmol/kg)	21.84-30.82	26.32	---	Lead to side wall unstable	---
	Swelling rate (%)	6.04-9.49	7.43	---	Lead to side wall unstable	---
Hydration properties and stability of borehole	Recovery (%)	88.74-96.97	92.57	---	Lead to side wall unstable	---
	SWW ($10^{-7}g/m^2$)	2.75-5.77	4.36	---	Lead to side wall unstable	---
	SSI (mm)	7.34-32.48	19.99	---	Lead to side wall unstable	---
Thickness of shale		67-233	130.6	Meet reservoir forming condition	Difficult to drill through	Adaptive for recovery

4. CONCLUSIONS

The following conclusions have been reached based on the measurement of physical and chemical characteristics of shale samples, the detail discussion of their correlation, the geological and engineering significances. Pore diameters of samples tested by high pressure mercury intrusion were larger than that by nitrogen adsorption. Nitrogen adsorption method is suitable for characterizing smaller pores of shale. There was a well positive correlation between results tested by two different methods. Internal surface area of shale cores measured by nitrogen adsorption (Langmuir surface area) has a positive correlation with surface area of shale powder tested through methylene blue trihydrate. Langmuir surface area could reflect shale's adsorption features very well, MBT surface area had better guidance for hydration characteristic of shale and was used in calculating specific water wettability. Langmuir volumes of shale samples were positively correlated with TOC, clay mineral content, Langmuir specific area, pore diameter under 25 ℃, 50 ℃, 75 ℃ and affected by several geological factors at the same time evidenced by the lower Pearson coefficient between Langmuir volume and each factor. There were several problems related to reservoir damage, instability of borehole and loss circulation during drilling and exploiting determined from results of physical and chemical properties.

5. ACKNOWLEDGEMENTS

This work was financially supported by the National Natural Science Foundation of China (NO. 51974351; NO. 51704322; Major Program, NO. 51991361), the National Science and Technology Major Project of China (NO. 2016ZX05040-005), and PCSIRT (IRT_14R58).

6. REFERENCES

1. Tonglou, G., "Key geological issues and main controls on accumulation and enrichment of chinese shale gas", ***Petroleum Exploration and Development***, Vol. 43, No. 3, (2016), 349-359. http://doi.org/10.1016/j.energy.2011.09.001
2. Chen, S., Zhu, Y., Wang, H., Liu, H., Wei, W. and Fang, J., "Shale gas reservoir characterisation: A typical case in the southern sichuan basin of china", ***Energy***, Vol. 36, No. 11, (2011), 6609-6616. http://doi.org/10.1016/s1876-3804(16)30042-8
3. Nie, H., Zhang, J. and Li, Y., "Accumulation conditions of the lower cambrian shale gas in the sichuan basin and its periphery", ***Acta Petrolei Sinica***, Vol. 32, No. 6, (2011), 959-967.
4. Romero-Sarmiento, M.-F., Ducros, M., Carpentier, B., Lorant, F., Cacas, M.-C., Pegaz-Fiornet, S., Wolf, S., Rohais, S. and Moretti, I., "Quantitative evaluation of toc, organic porosity and gas retention distribution in a gas shale play using petroleum system modeling: Application to the mississippian barnett shale", ***Marine and Petroleum Geology***, Vol. 45, No., (2013), 315-330. http://doi.org/10.1016/j.marpetgeo.2013.04.003
5. GUO, X., HU, D., LI, Y., LIU, R. and WANG, Q., "Geological features and reservoiring mode of shale gas reservoirs in longmaxi formation of the jiaoshiba area", ***Acta Geologica Sinica-English Edition***, Vol. 88, No. 6, (2014), 1811-1821. http://doi.org/10.1111/1755-6724.12347
6. Akhtarmanesh, S., Shahrabi, M.A. and Atashnezhad, A., "Improvement of wellbore stability in shale using nanoparticles", ***Journal of Petroleum Science and Engineering***, Vol. 112, No., (2013), 290-295. http://doi.org/10.1016/j.coal.2012.06.012
7. Klaver, J., Desbois, G., Urai, J.L. and Littke, R., "Bib-sem study of the pore space morphology in early mature posidonia shale

from the hils area, germany", ***International Journal of Coal Geology***, Vol. 103, No., (2012), 12-25. http://doi.org/10.1016/j.petrol.2013.11.022

8. Labani, M.M., Rezaee, R., Saeedi, A. and Al Hinai, A., "Evaluation of pore size spectrum of gas shale reservoirs using low pressure nitrogen adsorption, gas expansion and mercury porosimetry: A case study from the perth and canning basins, western australia", ***Journal of Petroleum Science and Engineering***, Vol. 112, No., (2013), 7-16.
9. Shaobo, T.H.Z.S.L. and ZHANG, H., "Determination of organic-rich shale pore features by mercury injection and gas adsorption methods [j]", ***Acta Petrolei Sinica***, Vol. 3, No., (2012). http://doi.org/10.1180/claymin.2009.4.421
10. Środoń, J., "Quantification of illite and smectite and their layer charges in sandstones and shales from shallow burial depth", ***Clay Minerals***, Vol. 44, No. 4, (2009), 421-434. http://doi.org/10.1016/j.petrol.2013.11.017
11. Yang, F., Ning, Z. and Liu, H., "Fractal characteristics of shales from a shale gas reservoir in the sichuan basin, china", ***Fuel***, Vol. 115, No., (2014), 378-384. http://doi.org/10.1016/j.fuel.2013.07.040
12. Ji, L., Qiu, J., Xia, Y. and Zhang, T., "Micro-pore characteristics and methane adsorption properties of common clay minerals by electron microscope scanning", ***Acta Petrolei Sinica***, Vol. 33, No. 2, (2012), 249-256.
13. Xu, Y.-M., He, D.-M., Guan, J. and Zhang, Q.-M., "Preparation of alumina from retorting residue of oil shale", ***Oil Shale***, Vol. 29, No. 1, (2012). http://doi.org/10.3176/oil.2012.1.04

Persian Abstract

چکیده

خصوصیات فیزیکی و ژئوشیمیایی شیل نقش موثری در تأیید اقدامات عملیاتی حین حفاری و تحریک دارد. خواص نمونه های شیل از پراکنش جیانگ از طریق پراش اشعه ایکس ، میکروسکوپ الکترونی روبشی ، ایزوترمال جذب ، نفوذ جیوه با فشار بالا ، تری هیدرات متیلن آبی ، پوسیدگی فشار پالس ، تست مقاومت به خاصیت خیس شدن آب و شاخص پایداری شیل بررسی گردید. همبستگی ، اهمیت زمین شناسی و مهندسی آنها مورد بحث قرار گرفت. نتایج نشان می دهد که مخزن شیل در پراکنش جیانگ دارای ارزش بهره برداری با پارامترهای مشخصه خوب تأیید شده است: ٢/٨٦٪ TOC، ٦٩.٩٪ مواد معدنی شکننده ، معدنی خاک رس ٢٦.١٤٪ ، نفوذپذیری بالا از μm^2 ×١٠$^{-٣}$ 0.011، حجم بزرگ لانگمویر (٥.٨٢ g/cm^3)و منطقه خاص لانگمویر (٠/٩١ مترمربع در گرم) ، تخلخل مؤثر (٣/٧٧٪) و ضخامت (١٣٠/٦ متر). منطقه خاص لانگمیر کنترل اصلی در جذب و ذخیره متان است که با توجه به نسبت نسبی مثبت آن با حجم لانگمویر به جای TOC تأیید شده است. محتوای بالای Illite 69.29٪ (ممکن است به بی ثباتی آسیب چاه و حساسیت به سرعت منجر شود. ریزساختارها کانالهایی را برای تصفیه ، تهاجم و از بین رفتن مایع حفاری فراهم می کنند. خاصیت خیس شدن خاص آب (١٠$^{-٧}$ ×٤/٣٦گرم بر مترمربع) و شاخص پایداری شیل کوچکتر (١٩/١٩ میلی متر) باعث شده است که تشکیل شیل یک بار در تماس با آب شیرین ناپایدار باشند. اقدامات متقابل باید در حین حفاری و شکستگی اتخاذ شود تا آسیب مخزن و شرایط پیچیده فروپاشی کاهش یابد.

International Journal of Engineering

Journal Homepage: www.ije.ir

Study on Rheological Property Control Method of "Three High" Water Based Drilling Fluid

P. Lijuan[a,c], L. Xiaoping[b], L. Wu[b], Z. Fuhao[b], W. Tongliang[b], W. Huang*[b], W. Fuwei[d]

[a] *Research Institute of Petroleum Engineering, Northwest Oil Company of SINOPEC, Urumqi, Xinjiang, China*
[b] *School of Petroleum Engineering, China University of Petroleum (East China), Qingdao, Shandong, China*
[c] *Key Laboratory of Enhancing Oil Recovery in Joint-City Reservoirs of Sinopec, Urumqi, Xinjiang, China*
[d] *Xinchun Oilfield, SINOPEC Shengli Oil Field Company, Dongying, China*

PAPER INFO

Paper history:
Received 11 April 2020
Received in revised form 01 May 2020
Accepted 12 June 2020

Keywords:
High Salinity
High Density
Water-based Drilling Fluid
Rheology
Control Method

ABSTRACT

The rheological regulation of the "three high" (high temperature, high density and high salinity) water-based drilling fluid is a worldwide problem due to the combined influence of temperature, solid content and salinity. This paper investigates the factors and regulation methods about rheological property of "three high" water based drilling fluid, and the effects of clay, salinity and weighting materials on the drilling fluid rheology. The experimental results show that base mud compound bentonite with attapulgite had good salt resistance and temperature resistance. The clay content should be kept close to 2% in high density mud (ρ=2.0g/cm^3), to control drilling fluid rheology. The sequence of rheological parameters of the "three high" water-based drilling fluid with same density was: manganese oxide> micronized barite> barite> ilmenite powder. When barite compounded with ilmenite powder or micronized barite in the ratio of 1:1 to weight drilling fluid respectively, the rheology and filtration of the "three high" water-based drilling fluid performed well. Based on the optimization of a series of mud additives including fluid loss additive, thinner, anti-collapse filtration reducing agent, lubricant with salt and calcium resistance, a formula of the "three high" water-based drilling fluid system was prepared which had excellent rheology, filtration and sedimentation stability property with the density of 2.2g/cm^3 (180℃). The expansion rate of the drilling fluid was 1.84%, shale recovery rate was 85.73%, lubrication coefficient was 0.122, and resistanced to pollution of 1% $CaCl_2$ and 10% poor clay. It also had excellent reservoir protection and plugging performance.

***doi**: 10.5829/ije.2020.33.08b.28*

1. INTRODUCTION

Salt strata, salt mud composite salt layer and high-pressure salt water layer restrictes the exploitation of oil and gas reservoir [1]. When drilling in complex salt layer, it is easy to cause downhole complex conditions such as borehole instability, lost circulation, sticking, etc. Drilling and completion fluid technology faces many challenges [2-4]. Applied "three high" water-based drilling fluid technology, to a certain extent, it solves the complex problems in the drilling process. But its rheological property control exists high temperature, high salinity, high density, and weighting difficulties, etc unresolved issues [5-10]. Boul synthesized a high-performance salt water tackifier which was based on the multi-molecular structure unit. Horton et al. [11] and Boul [12] prepared a high-density salt water system with temperature resistance of 162℃ and density of 2.3g/cm^3. Al-Ansari used potassium formate/ manganous-manganic oxide to increase the density of drilling fluid to 2.1g/cm^3, with temperature resistance of 155℃, which it was first used in Saudi Arabia [13]. Jin Chengping constructed ultra-high density (2.48g/cm^3) saturated salt water drilling fluid. This drilling fluid had excellent performance in lubricity, inhibitory, high temperature stability, and anti-pollution capacity [14]. Therefore, it has important theoretical and technical value to establish "three high" water-based drilling fluid rheological property control method and provide technical support for deep oil and gas drilling fluid under complex

*Corresponding Author Email: *masterhuang1997@163.com* (W. Huang)

Please cite this article as: P. Lijuan, L. Xiaoping, L. Wu, Z. Fuhao, W. Tongliang, W. Huang, W. Fuwei, Study on Rheological Property Control Method of "Three High" Water Based Drilling Fluid, International Journal of Engineering (IJE), IJE TRANSACTIONS B: Applications Vol. 33, No. 8, (August 2020) 1687-1695

conditions. In this paper, the effects of salinity and various factors on the rheological properties of the composite base mud are investigated by optimizing the materials to resist salt and calcium. The influence factors and mechanism of the rheological properties and stability of the "three high" water-based drilling fluid are studied. A new rheological control method of "three high" is formed to build the "three high" water-based drilling fluid system.

2. EXPERIMENTAL

2. 1. Basic Performance Test of Drilling Fluid Drilling fluid property tests were conducted according to American Petroleum Institute (API) specifications. The API filtrate volume (FL) of the mud was determined at pressure of 0.69 MPa for 30 min, using a ZNS-5A type medium-pressure filtration apparatus made by Qingdao Hai Tongda Special Instruments CO., Ltd., China. The viscosity of the mud was reflected by the rotary viscometer torque reading at a rotation speed of 600 rpm, 300 rpm, 200 rpm, 100 rpm, 6 rpm, 2 rpm through a ZNN-D6 type rotating viscometer (Qingdao Hai Tongda Special Instruments CO., Ltd., China). The high temperature and high pressure filtration under 150℃ and 3.5MPa were measured using a GGS 71 filter instrument from FANN Company, U.S.A.

2. 2. Inhibitory Test Linear swelling and hot-rolling dispersion tests were performed to evaluate the inhibition properties of drilling fluid. For the hot-rolling dispersion test, shale recovery assessments were conducted at a low temperature of 77℃ to investigate the durability of inhibition.

2. 3. Particle Size Distribution Test The particle size distribution of sample was assessed using a Bettersize2000 laser particle size tester (Dandong Bettersize Instrument Co., Ltd., China) to investigate the influence of factors on the size distribution of slurry particles.

2. 4. VSST Settlement Stability Test In this study, VVST settlement test method was used for dynamic settlement measurement. The required instruments includes: FANN35 viscometer, API drilling fluid rheometer measuring cup, heating jacket, 10mL syringe, and settlement shoes. Among them, the FANN35 viscometerprovides dynamic conditions for the measurement, the measuring cup is the drilling fluid holding container, the heating jacket is used for heating and temperature control, and the syringe is used to draw the drilling fluid sample from the bottom of the heating cup.

The specific operating procedure is: place the settling shoes in the measuring cup of the API drilling fluid rheometer, pour the drilling fluid to be measured, adjust the rotation speed of the rotary viscometer to 600 rpm, when the temperature of the drilling fluid is stable at 50 ℃, use a syringe collect the drilling fluid sample in the hole and measure its density as ρ_1. Then adjust the rotational speed of the rotary viscometer to 100 rpm, and control the temperature to 50℃. After 30 minutes, collects sample again in the collection hole and measures the density as ρ_2. Before and after calculation, measure the density difference of the drilling fluid in the collection hole. It is the dynamic density difference of drilling fluid.

2. 5. Plugging Performance Test Through the sand bed filtration test, use quartz sand with different meshes to simulate different permeability conditions of the reservoir, and evaluate the plugging performance of the experimental mud.

3. RESULTS AND DISCUSSION

3. 1. Performance Optimization of Base Mud

3. 1. 1. Optimizing Proportion of Attapulgite/Bentonite The bentonite and attapulgite were mixed into 4% base mud according to different proportion, and 5% NaCl was added, respectively. Then tested the rheological property and loss property of experimental mud before and after aging at 150℃/16h. According to Table 1, with the decrease of bentonite content, the filtration gradually increased before and after aging; poor quality of attapulgite mud cake resulted in increased filtration; The cutting force and filtration of #4 and #5 mud were larger after aging than before; # 1and #2 mud had good well building property, but low viscosity and shear force; #3 mud was selected as the base mud for the next experiment due to its moderate viscosity, shear force, and filtration.

3. 1. 2. Factors Affecting the Properties of Mixed Base Mud

3. 1. 2. 1. Particle Size of Clay Using attapulgite of different particle sizes prepared 4% base mud (bentonite: attapulgite ratio of 1:1). Then tested the rheology and fluid loss of each base mud at room temperature. According to Figure 1, bentonite played an important role in the rheology and loss property of mixed fresh water base mud, while attapulgite particle size had little effect. The fuller the attapulgite particles were ground, the lower the strength of network structure resulted in insignificant effect on the composite base mud.

TABLE 1. Effect of the different mixture ratio on rheology of base mud

The mixed proportion (bentonite: attapulgite)	condition	AV/mPa·s	PV/mPa·s	YP/Pa	Gel/Pa/Pa	FL/mL	pH
1# (3:1)	Before aging	6.25	2	4.3	2.25/2.5	94	9
	After aging	4.25	2	2.3	3.75/9	170	7
2# (2:1)	Before aging	6.25	2	4.3	2.25/2.75	106	9
	After aging	4	2.5	1.5	3.25/7.75	184	7
3# (1:1)	Before aging	6.75	1.5	5.3	2.5/3.25	122	9
	After aging	4.25	2	2.3	4.75/10	220	7
4# (1:2)	Before aging	8	1.5	6.5	3/4.25	146	9
	After aging	4.5	1	3.5	5.75/18.5	244	7
5# (1:3)	Before aging	8.75	2.5	6.3	3/4	145	9
	After aging	4.5	1	3.5	5/17	268	7

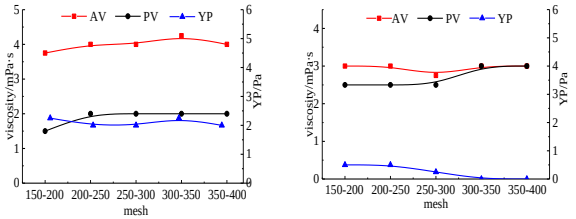

(a) Before aging (b) After aging

Figure 1. Effect of particle size of attapulgite on rheology of mixed mud

3. 1. 2. 2. Aging Temperature The base mud was aged for 16h at different temperatures, then tested their rheological property and loss property. According to Figure 2, with an increase in aging temperature, the viscosity of the mixed base mud increased, and the yield value (YP) decreased to gentle. API filtration increased linearly with aging temperature, indicating that attapulgite can improve the temperature resistance of the base mud.

3. 1. 2. 3. pH Value Regulated pH value of drilling fluid system, tested their rheological property and loss property after aging at 150℃/16h. According to Figure 3, when pH > 9 before aging or pH > 8.5 after aging, the

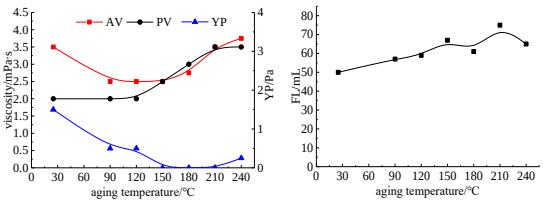

Figure 2. Effect of aging temperature on rheology of mixed mud

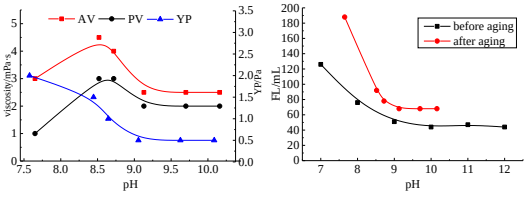

Figure 3. Effect of pH on rheology of mixed mud

surface charge number of attapulgite particles increased with an increase in pH value, and the electrostatic repulsion force was strengthened, which made the viscosity and YP of fresh water base mud to decrease. At the same time, bentonite was easy to be passivated at high temperature under strong alkali environment, which has resulted in a decrease in viscosity and YP of the mixed base mud. The API filtration was the lowest at pH=9, and then it was stable. Therefore, the drilling fluid prepared by mixed fresh water base mud the pH should be greater than 9; or higher as far as possible.

3. 1. 2. 4. Salt

(1) NaCl Rheology tests of compound base mud were carried out at room temperature under different dosage of NaCl. The experimental results are shown in Figure 4. The viscosity and YP of the base mud were ascending in first and descending at last. When attapulgite was added, the viscosity and YP of the mud did not decrease, but kept stable and slightly increased. The results showed that attapulgite can improve the salt resistance of the mud.

(2) $CaCl_2$ The rheology test of compound base mud were carried out at room temperature under different dosage of $CaCl_2$. The effect of $CaCl_2$ addition on the viscosity, filtration, and pH of the mixed base mud is shown in Figure 5. When the amount of $CaCl_2$ was less than 0.15%,

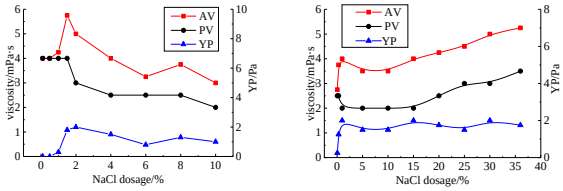

(a) Bentonite mud **(b) Mixed mud**

Figure 4. Effect of NaCl content on rheology of mixed mud

the bentonite flocculated moderately and the viscosity of the mixed mud increased. When the amount of $CaCl_2$ was more than 0.15%, the conversion degree of Na montmorillonite to Ca montmorillonite increased, and the dispersion degree of the system decreased. The viscosity and YP of the mixed mud slightly decreased, which indicated that mixed mud had certain calcium resistance performance.

3. 2. Influence of Weighting Materials on the Performance of High Salinity Drilling Fluid The physical parameters of weighting materials used in the experiment are summarized in Table 2.

3. 2. 1. Different Kinds of Weighting Agent Examined the effects of 4 weighting materials on the rheological property of drilling fluid with aging at 150℃ /16h. The formula of drilling fluid was 2% mixed mud + 1% PMHA-Ⅱ+ 3% SD-101+ 3% SPNH+ 3% ZDGF+ 3% white oil+ 0.2%Span-80+ 10% NaCl+ 1% SMT+ weighting agent (#3-1). According to Figure 6, the viscosity, YP and API filtration of the after aging mud increased as the density increases. When density increased to 1.8-1.9 g/cm^3, these properties changed greatly. At the same density, the viscosity and YP of the supermicro barite weighted mud were higher than which weighted by ilmenite powder, and this phenomenon was more significant with the increase of density. When $\rho >$ 1.9 g/cm^3, the manganese oxide weighted mud became tick and the rheological property of the mud get worse.

3. 2. 2. Mix Weighting Agents Mixed barite with ilmenite powder, and barite with supermicro barite by different mass ratio to weight high density drilling fluid #3-1, then tested their performance after aging at 150℃ /16h. According to Figure 7, when the mass ratio of barite and ilmenite powder was 1:1, the viscosity and YP of high-density brine drilling fluid were low, and the filtration was moderate. When the mass ratio of barite and supermicro barite was 1:1, the viscosity, YP and API filtration were low, and then the rheological property was optimal. The physical parameters of weighting materials used in the experiment are summarized in Table 2.

3. 2. 3. Influence of Weighting Materials on the Sedimentary Stability of Drilling Fluid Used different weighting materials to weighting drilling fluid #3-1 to different density. Tested the density difference ($\Delta\rho$) of the upper and lower layers after aging and standing 24 hours of each system. Learning from Figure 8, with an increase in weighting density, the density difference of each system decreased gradually and the sedimentary stability became better. With the same density, the sedimentary stability of supermicro barite and manganous oxide was the best, followed by barite, while ilmenite powder was the worst.

By studying the effects of mortar soil, salinity and weighted materials on the rheology and settlement stability of the "three high" water-based drilling fluid and its mechanism, it was found that the base mud performance was better after the combination of attapulgite and bentonite (1:1), and the weighting material should not be used alone, it should be mixed and weighted in a certain proportion to have a better improvement effect on the rheology of the "three high" water-based drilling fluid.

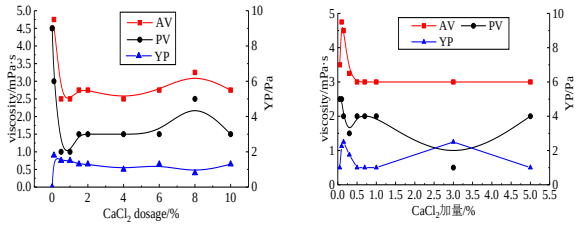

(a) bentonite mud (b) mixed mud

Figure 5. Effect of $CaCl_2$ content on rheology of mixed mud

TABLE 2. The physical parameters of weighting materials

Weighting materials	density/(g/cm$^{3)}$	Structural shape	rigidity	D_{50}/μm
Common barite	4.2	lump	3.1	18.49
Supermicro barite	4.3	sphere	3.8	2.101
Ilmenite powder	4.5	Irregular grain	6.0	23.74
manganese oxide	5.0	sphere	5.5	1.572

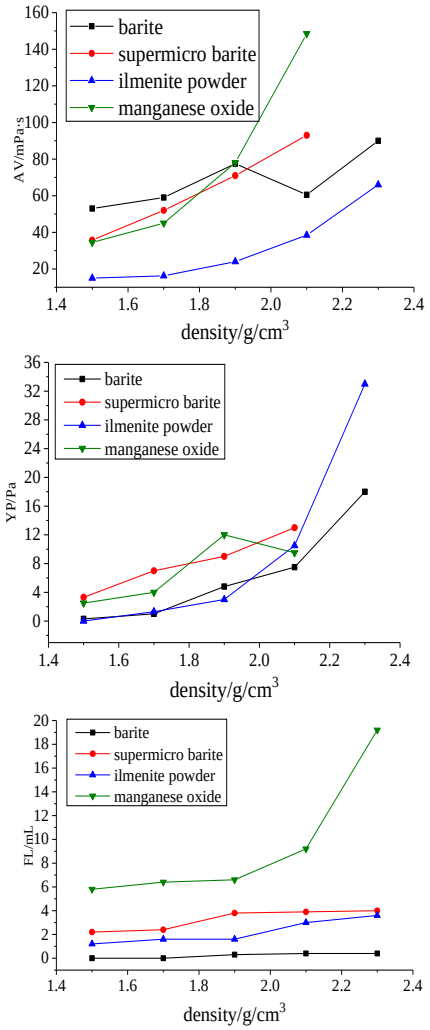

Figure 6. The effect of weighting materials on drilling fluid

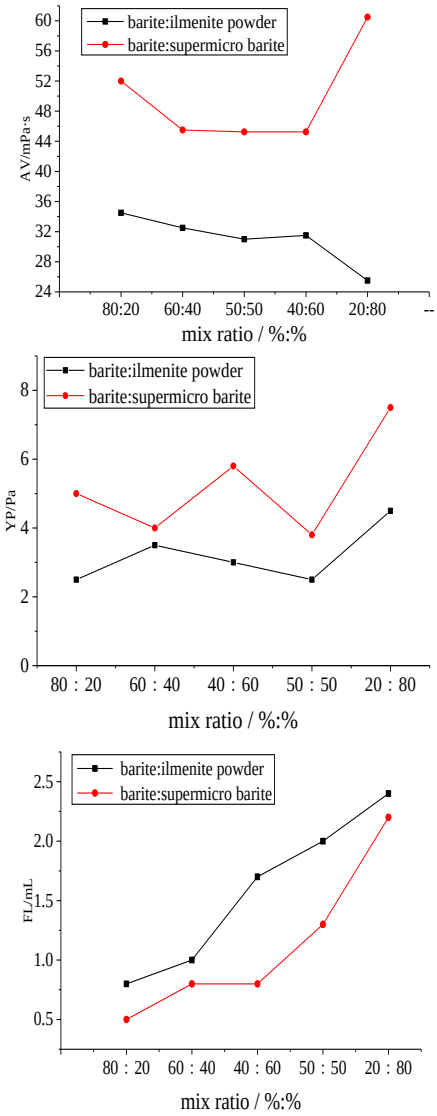

Figure 7. Effect of mixture materials on drilling fluid

3. 3. Build of the 'three high' Water-based Drilling Fluid System

3. 3. 1. Optimization of Drilling Fluid System Filter loss reducer used polymer anti-salt calcium and temperature resistance ZDP-1, resin filter loss reducer SMP-3, lignite filter loss reducer SPNH; viscosity reducer SDJN and SF-260 with good properties; ZDGF and sulfonated asphalt PLH are used as blocking. Also, anti-sagging agents; solid lubricants GRA and white oil were used as lubricants. After 28 groups of formula optimization, the best performance formula was obtained. The aging conditions were 150 °C/16h, ρ= 2.2g/cm^3, and the formula was: 2.5% base mud+ 0.4% NaOH+ 0.1% ZDP-1+ 8% SMP-3+ 2% SPNH+ 3% ZDF-1+ 2% ZDGF+ 30% NaCl+ 0.3% CaO+ 1.5% CaCO3 (2800 mesh)+ 4% white oil+ 0.4% Span-80+ barite + 1.5% SF260 (HSHD-3).

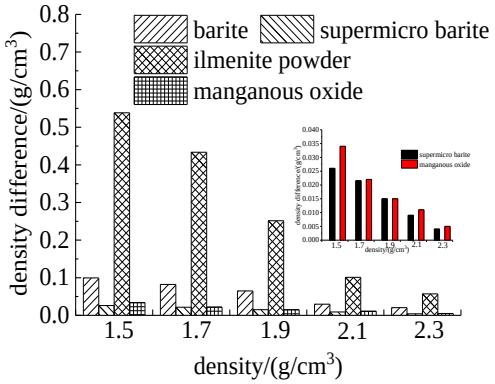

Figure 8. Effect of weighting material and density on sedimentation stability of drilling fluid

TABLE 3. Results of drilling fluid optimation experiment

Formula	Condition	AV/mPa·s	PV/mPa·s	YP/Pa	Gel/Pa/Pa	FL/mL	pH	HTHP/mL	Coefficient of lubrication
HSHD-3	Before aging	105	81	24.0	4/47.5	0	9	11	0.122
	After aging	79	64	15.0	3.75/27	0.4	9		

3. 3. 2. Evaluation of Drilling Fluid System

3. 3. 2. 1. Temperature Resistance and Temperature Stability It is known from Table 4 that the drilling fluid performance was stable after aging at 150°C/64h, which indicated that the formula had good temperature resistance and high temperature stability. After 180°C/16h aging, the filtration loss of the drilling fluid was only 1 mL, the viscosity and shear force change were relatively small, and the drilling fluid performance was stable, indicating that the formula can withstand high temperatures of 180°C.

3. 3. 2. 2. Anti-pollution Performance Prepare sieve inferior soil with 100 meshes of argillaceous siltstone from the Bashkirchik Formation. According to Table 5, after adding 1% $CaCl_2$ and 10% inferior soil, tested rheology and fluid loss at room temperature, the formula HSHD-3 had little change in viscosity, shear force and filtration loss after aging, indicating that it had better resistance to Ca^{2+} pollution and can reach inferior soil 10%.

3. 3. 2. 3. Settlement Stability The HSHD-3 formula after aging at 150℃/16h was stirred at high speed for 30min, and kept at rest for 24h. The density difference between the upper and lower sides was measured. The density difference measured by the static sedimentation method was only 0.032g/cm^3 (Table 6, Figure 9). The density difference measured by the

TABLE 4. Evaluation results on anti-temperature of drilling fluid

Experimental Conditions	Condition	AV/mPa·s	PV/mPa·s	YP/Pa	Gel/Pa/Pa	FL/mL	pH
150℃/16h	Before aging	105	81	24.0	4/47.5	0	9
	After aging	79	64	15.0	3.75/27	0.4	9
150℃/32h	Before aging	108	81	27.0	4.5/47	0	9
	After aging	81.5	67	14.5	3.25/16.5	0	9
150℃/48h	Before aging	107.5	80	27.5	5/55	0	9
	After aging	68	47	21.0	3/20.5	0.8	9
150℃/64h	Before aging	109.5	83	26.5	4.5/54	0.8	9
	After aging	61.5	53	8.5	3.5/18	0	9
160℃/16h	Before aging	111	82	29.0	6.5/6	1	9
	After aging	55	46	9.0	3.25/14.5	0.4	9
170℃/16h	Before aging	92.5	79	13.5	2.25/15	1	9
	After aging	48.5	41	7.5	3.75/20	0.6	9
180℃/16h	Before aging	101	77	24.0	6/55.5	0	9
	After aging	70.5	32	38.5	10/29	1	9

TABLE 5. Evaluation results on resisting pollution performance of drilling fluid

Experimental conditions	Condition	AV/mPa·s	PV/mPa·s	YP/Pa	Gel/Pa/Pa	FL/mL	pH
1%$CaCl_2$	Before aging	87.5	55	32.5	26.5/36.5	3	9
	After aging	61	52	9.0	1.75/9	0	9
10%Inferior soil	Before aging	140.5	101	39.5	8.5/74	0.1	9
	After aging	104	82	22.0	6/29.5	1	9

TABLE 6. Evaluation results on sedimentation stability of drilling fluid

Method	Position	Density /g/cm^3	Density difference /g/cm^3
Dynamic settlement method	upper layer	2.185	0.042
	Lower layer	2.227	
Static settlement method	upper layer	2.22	0.032
	Lower layer	2.252	

sedimentation method (VSST) was 0.042g/cm^3. Two methods showed that HSHD-3 had good sedimentation stability.

3. 3. 2.4. Inhibitory Selected mud shale of Bashkichik Formation (6-10 mesh), the shale recovery rate of the HSHD-3 formula was evaluated by rolling dispersion of mud shale, and compared with the polysulfonate drilling fluid system used in the Bashkichik formation. It can be seen from Figure 10 that the expansion rate of calcareous cores in clear water was 31.42%, the expansion rate of polysulfide drilling fluid was 15.21%, the expansion rate of HSHD-3 was only 1.84%; the recovery rate of clear water was 12.97%, and the recovery rate of polysulfonate drilling fluid used on site was 34.50%, and the recovery rate of the HSHD-3 formula was 85.73%, which indicated that the HSHD-3 formula had a strong inhibitory effect.

3. 3. 2. 5. Plugging Performance Test the "three high" water-based drilling fluid system optimized formula to penetrate the sand bed depth after aging at 150°C/16h. From Table 8, it can be seen that the sand bed penetration depth of optimized formula was very small, and the depth of 40-60 mesh medium pressure sand bed filtrate intrusion into the sand bed was 2.3 cm, indicating that the optimized formula had excellent plugging.

(a) Static settlement method (b) Dynamic settlement method

Figure 9. Measuring method of sedimentation stability

TABLE 7. Results of drilling fluid arrest to shales decentralization

Hashtag	Well section	Sample	Initial/ g	Finally/ g	Recovery rate /%
BZ-102	6728-6799m	Shimizu	30	3.89	12.97
		Polysulfide system for field use	30	10.35	34.50
		HSHD-3 Experimental pulp	30	25.75	85.83

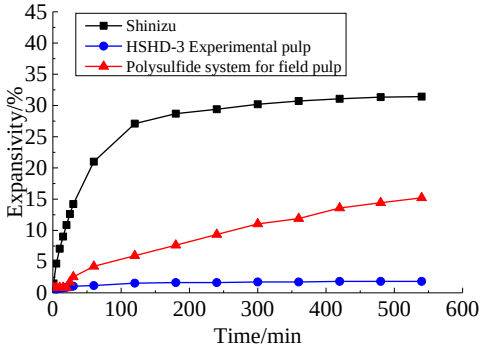

Figure 10. Results of drilling fluid arrest to shale swelling

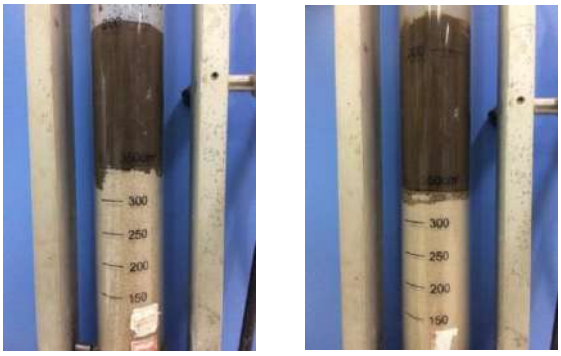

(a) 40-60 mesh (b) 80-120mesh

Figure 11. The experimental results of sand bed filtration

In the Name of God

INTERNATIONAL JOURNAL OF ENGINEERING
Transactions A: Basics

DISCLAIMER

The publication of papers in International Journal of Engineering does not imply that the editorial board, reviewers or publisher accept, approve or endorse the data and conclusions of authors.

International **J**ournal of **E**ngineering *Transactions A: Basics* (ISSN 1728-1431) (EISSN 1735-9244)
International **J**ournal of **E**ngineering *Transactions B: Applications* (ISSN 1728-144X) (EISSN 1735-9244)
International **J**ournal of **E**ngineering *Transactions C: Aspects* (ISSN 2423-7167) (EISSN 1735-9244)
Web Sites: www.ije.ir & www.ijeir.info E-mails: ije.editor8@gmail.com, Tel: (+9821) 88771578, Fax: (+9821) 88773352
Materials and Energy Research Center (MERC)

TABLE 8. The experimental results of sand bed filtration

Formula	Sand mesh	Sand particle size /mm	Intrusion sand bed depth/cm
HSHD-3	40-60	0.425-0.250	2.3
	80-120	0.180-0.125	1.2

Based on this, the "three high" water-based drilling fluid formulation, with a temperature resistance of 180°C, provides new research ideas for deep high-temperature and high-pressure oil and gas production. Combined with the increasingly stringent environmental protection requirements, the environmental protection indicators of the system should also be regarded as key research.

4. CONCLUSION

(1) The suitable ratio of attapulgite to bentonite is 1: 1. The compound base mud has good resistance to salt and calcium and temperature. The bentonite plays a major role in the rheology and filtration of the compound base mud. When the mortar content is about 2%, the "three high" drilling fluid ($\rho = 2.0 g/cm^3$) has better rheology.
(2) When we used four kinds of weighting materials alone, the viscosity, shear force, and API filtration loss of "three high" drilling fluids increased with increasing weighting density. With high-density conditions, the viscosity, shear force, and API filtration loss of ultrafine barite and trimanganese tetroxide are difficult to control; then, use of ultrafine barite and trimanganese tetroxide are not suitable for individually weighting the "three high" drilling fluids. When the barite, ilmenite powder, and ultrafine barite are respectively mixed at a ratio of 1: 1, the "three high" drilling fluid had good rheology and filtration loss; settlement stability: ultrafine barite> trimanganese tetroxide> barite> ilmenite powder. It can be seen that the use of compound weighting and optimization of the compounding ratio can well meet the rheological control requirements of the "three high" drilling fluids, which has a good guiding significance for the selection and use of drilling fluid weighting materials in the future.
(3) The "three high" water-based drilling fluid formula with a density of 2.2 g/cm^3 (180°C) has good rheology and lubricity, the expansion rate of calcareous cores is only 1.84%, resistance to pollution of 1% $CaCl_2$ and 10% poor clay, with good reservoir protection and plugging performance. It can be better applied to the drilling and production of high temperature and high pressure oil and gas reservoirs, and has a good industrial application prospect.

5. ACKNOWLEDGMENTS

This work was financially supported by the National science and technology major project (No. 2017ZX05005-005), Sinopec scientific research project (No. P18022-1) and the National Natural Science Foundation of China (No. 51974351; No. 51704322; Major Program, No. 51991361).

6. REFERENCES

1. Omojuwa, E.O., Osisanya, S.O. and Ahmed, R., "Properties of salt formations essential for modeling instabilities while drilling", in Nigeria Annual International Conference and Exhibition, Society of Petroleum Engineers. (2011), http://doi.org/10.2118/150801-ms.
2. Wu, H.M., Lou, Y.S., Li, Z.H., Zhu, L. and Huang, W.L., "Wellbore stability research to the direction well in the salt layer", in Advanced Materials Research, Trans Tech Publ. Vol. 250, (2011), 4042-4045. http://doi.org/10.4028/www.scientific.net/amr.250-253.4042
3. Holt, C.A. and Johnson, J.B., "A method for drilling moving salt formations-drilling and underreaming concurrently", ***SPE Drilling Engineering***, Vol. 1, No. 04, (1986), 315-324. http://doi.org/10.2118/13488-pa.
4. Sheffield, J., Collins, K. and Hackney, R., "Salt drilling in the rocky mountains", in IADC/SPE Drilling Conference, Society of Petroleum Engineers. (1983). http://doi.org/10.2118/11374-ms
5. Yu, Z., Wang, W., An, C., Lv, X., Zhang, Z., Ai, G. and Wang, Z., "Comprehensive & associated drilling technology for ultra-deep well jida 4", in IADC/SPE Asia Pacific Drilling Technology Conference and Exhibition, Society of Petroleum Engineers. (2012). http://doi.org/10.2118/155837-ms
6. Villada, Y., Gallardo, F., Erdmann, E., Casis, N., Olivares, L. and Estenoz, D., "Functional characterization on colloidal suspensions containing xanthan gum (XGD) and polyanionic cellulose (pac) used in drilling fluids for a shale formation", ***Applied Clay Science***, Vol. 149, (2017), 59-66. http://doi.org/10.1016/j.clay.2017.08.020
7. Amani, M. and Hassiba, K.J., "Salinity effect on the rheological properties of water based mud under high pressures and high temperatures of deep wells", in SPE Kuwait International Petroleum Conference and Exhibition, Society of Petroleum Engineers. (2012). http://doi.org/10.2118/163315-ms
8. Mao, H., Yang, Y., Zhang, H., Zheng, J. and Zhong, Y., "Conceptual design and methodology for rheological control of water-based drilling fluids in ultra-high temperature and ultra-high pressure drilling applications", ***Journal of Petroleum Science and Engineering***, Vol. 188, (2020), 106884.
9. Bland, R.G., Mullen, G.A., Gonzalez, Y.N., Harvey, F.E. and Pless, M.L., "Hpht drilling fluid challenges", in IADC/SPE Asia

Pacific drilling technology conference and exhibition, Society of Petroleum Engineers. (2006). http://doi.org/10.2118/103731-ms

10. De Stefano, G., Stamatakis, E. and Young, S., "Meeting the ultrahigh-temperature/ultrahigh-pressure fluid challenge", ***SPE Drilling & Completion***, Vol. 28, No. 01, (2013), 86-92. http://doi.org/10.2118/153709-pa
11. Horton, R.L., Dobson Jr, J.W., Tresco, K.O., Knox, D.A., Green, T.C. and Foxenberg, W.E., "A new biopolymer-free, low solids, high density reservoir drilling fluid", in SPE European Formation Damage Conference, Society of Petroleum Engineers. (2004). http://doi.org/10.2118/87664-PA
12. Boul, P.J., Abdulquddos, S. and Thaemlitz, C.J., "High performance brine viscosifiers for high temperatures", in SPE Middle East Oil & Gas Show and Conference, Society of Petroleum Engineers. (2017). http:// doi.org/10.2118/1117-0046-jpt
13. Al-Ansari, A., Abuhamed, A.M., Abahusain, A., Pino, R., Bialy, M.E. and Zoghbi, B., "Enhance drilling performance using an optimized mud fluid system through extensive laboratory testing", in SPE Kingdom of Saudi Arabia Annual Technical Symposium and Exhibition, Society of Petroleum Engineers. (2016). http://doi.org/10.2118/182741-ms
14. Cheng, H., Chao, Z., Ming, L., Anchao, W. and Fabin, X., "Research and application of micronized barite drilling fluid in hpht wells of the western south china sea", ***International Journal of Oil, Gas and Coal Engineering***, Vol. 4, No. 2, (2016), 9-15. http://doi.org/ 10.11648/j.ogce.20160402.11

Persian Abstract

چکیده

تنظیم رئولوژیکی سیال حفاری مبتنی بر آب "سه حد بالا" (درجه حرارت بالا ، چگالی بالا و شوری زیاد) یک مشکل جهانی است که به دلیل ترکیبی دما ، محتوای مواد جامد و شوری است. در این مقاله به بررسی فاکتورها و روشهای تنظیم در مورد خاصیت رئولوژیکی سیال حفاری مبتنی بر آب "سه حد بالا" و تأثیر رس ، شوری و وزن مواد در رئولوژی مایعات حفاری می پردازیم. نتایج تجربی نشان می دهد که بنتونیت ترکیب گل و لای پایه با آتوپلولیت مقاومت خوبی در برابر نمک و دما دارد. محتوای گل رس را باید نزدیک ۲٪ در گلهای با چگالی بالا ($\rho = 2.0g / cm^3$) نگه داشت تا بتوانید رئولوژی گل حفاری را کنترل کنید. توالی پارامترهای رئولوژیکی "سیال حفاری مبتنی بر آب" سه حد بالا "با چگالی یکسان بود: اکسید منگنز> باریت میکرونیزه> باریت> پودر ایلمنیت. هنگامی که باریت به ترتیب با پودر ایلمنیت یا باریت میکرونیزه در نسبت مایع حفاری وزنی ۱: ۱ به وزن ترکیب می شود ، رئولوژی و تصفیه مایعات حفاری مبتنی بر آب "سه حد بالا" به خوبی انجام می شود. بر اساس بهینه سازی یک سری مواد افزودنی گلی از جمله افزودنی برای از بین رفتن مایعات ، نازک تر و ضد ریزش تصفیه کننده ضد آب ، روان کننده با نمک و مقاوم به کلسیم ، فرمول سیستم سیال حفاری مبتنی بر آب "سه حد بالا " تهیه شده است. خصوصیات رئولوژی ، فیلتراسیون و رسوب گذاری با چگالی $2.2g / cm^3$ $(180^\circ C)$. میزان انبساط مایع حفاری ۱.۸٤٪ ، سرعت بازیابی شیل ۸۵.۷۳٪ ، ضریب روانکاری ۰/۱۲۲ و مقاومت در برابر آلودگی ۱٪ $CaCl_2$ و ۱۰٪ خاک رس ضعیف بود. همچنین از حفاظت و مخزن بسیار عالی از مخزن برخوردار بود.

AIMS AND SCOPE

The objective of the International Journal of Engineering is to provide a forum for communication of information among the world's scientific and technological community and Iranian scientists and engineers. This journal intends to be of interest and utility to researchers and practitioners in the academic, industrial and governmental sectors. All original research contributions of significant value focused on basics, applications and aspects areas of engineering discipline are welcome.

This journal is published in three quarterly transactions: Transactions A (Basics) deal with the engineering fundamentals, Transactions B (Applications) are concerned with the application of the engineering knowledge in the daily life of the human being and Transactions C (Aspects) - starting from January 2012 - emphasize on the main engineering aspects whose elaboration can yield knowledge and expertise that can equally serve all branches of engineering discipline.

This journal will publish authoritative papers on theoretical and experimental researches and advanced applications embodying the results of extensive field, plant, laboratory or theoretical investigation or new interpretations of existing problems. It may also feature - when appropriate - research notes, technical notes, state-of-the-art survey type papers, short communications, letters to the editor, meeting schedules and conference announcements. The language of publication is English. Each paper should contain an abstract both in English and in Persian. However, for the authors who are not familiar with Persian, the publisher will prepare the latter. The abstracts should not exceed 250 words.

All manuscripts will be peer-reviewed by qualified reviewers. The material should be presented clearly and concisely:

- *Full papers* must be based on completed original works of significant novelty. The papers are not strictly limited in length. However, lengthy contributions may be delayed due to limited space. It is advised to keep papers limited to 7500 words.
- *Research* notes are considered as short items that include theoretical or experimental results of immediate current interest.
- *Technical notes* are also considered as short items of enough technical acceptability with more rapid publication appeal. The length of a research or technical note is recommended not to exceed 2500 words or 4 journal pages (including figures and tables).

Review papers are only considered from highly qualified well-known authors generally assigned by the editorial board or editor in chief. Short communications and letters to the editor should contain a text of about 1000 words and whatever figures and tables that may be required to support the text. They include discussion of full papers and short items and should contribute to the original article by providing confirmation or additional interpretation. Discussion of papers will be referred to author(s) for reply and will concurrently be published with reply of author(s).

INSTRUCTIONS FOR AUTHORS

Submission of a manuscript represents that it has neither been published nor submitted for publication elsewhere and is result of research carried out by author(s). Presentation in a conference and appearance in a symposium proceeding is not considered prior publication.

Authors are required to include a list describing all the symbols and abbreviations in the paper. Use of the international system of measurement units is mandatory.

- On-line submission of manuscripts results in faster publication process and is recommended. Instructions are given in the IJE web sites: www.ije.ir-www.ijeir.info
- Hardcopy submissions must include MS Word and jpg files.
- Manuscripts should be typewritten on one side of A4 paper, double-spaced, with adequate margins.
- References should be numbered in brackets and appear in sequence through the text. List of references should be given at the end of the paper.
- Figure captions are to be indicated under the illustrations. They should sufficiently explain the figures.
- Illustrations should appear in their appropriate places in the text.
- Tables and diagrams should be submitted in a form suitable for reproduction.
- Photographs should be of high quality saved as jpg files.
- Tables, Illustrations, Figures and Diagrams will be normally printed in single column width (8cm). Exceptionally large ones may be printed across two columns (17cm).

PAGE CHARGES AND REPRINTS

The papers are strictly limited in length, maximum 6 journal pages (including figures and tables). For the additional to 6 journal pages, there will be page charges. It is advised to keep papers limited to 3500 words.

Page Charges for Papers More Than 6 Pages (Including Abstract)	
For International Author ***	**$55 / per page**
For Local Author	**100,000 Toman / per page**

AUTHOR CHECKLIST

- Author(s), bio-data including affiliation(s) and mail and e-mail addresses).
- Manuscript including abstracts, key words, illustrations, tables, figures with figure captions and list of references.
- MS Word files of the paper.

International **J**ournal of **E**ngineering, P.O. Box 13145-1659, Tehran, I.R. Iran
Materials and Energy Research Center, 5 Ahuramazda St., Alvand Ave., Argentina Sq., Tehran, Islamic Republic of Iran
www.merc.ac.ir - www.emerc.ac.ir

THOMSON REUTERS

WEB OF SCIENCE

Scopus®

CAS®
A DIVISION OF THE
AMERICAN CHEMICAL SOCIETY

Google
Scholar